NASA Technical Memorandum 85127

(NASA-TM-85127) REPORTS OF PLANETARY GEOLOGY PROGRAM, 1982 (National Aeronautics and Space Administration) 416 p
HC A18/MF A01 CSCL 03B

N83-16270

Unclas
G3/91 08103

Reports of Planetary Geology Program - 1982

DECEMBER 1982

NASA

NASA Technical Memorandum 85127

Reports of Planetary Geology Program - 1982

Compiled by
Henry E. Holt
NASA Office of Space Science and Applications
Washington, D.C.

National Aeronautics
and Space Administration

**Scientific and Technical
Information Branch**

1982

Foreword

This is a compilation of abstracts of reports from Principal Investigators of NASA's Office of Space Science, Solar System Exploration Division, Planetary Geology Program.

The purpose is to provide a document which succinctly summarizes work conducted in this program. Each report reflects significant accomplishments within the area of the author's funded grant or contract.

No attempt has been made to introduce editorial or stylistic uniformity; on the contrary, the style of each report is that of the Principal Investigator and may best portray his research. Bibliography information will be included in a separately published document.

Full reports of selected abstracts were presented to the annual meeting of Planetary Geology Principal Investigators at Jet Propulsion Laboratory, Pasadena, California, January 12-14, 1982.

Joseph M. Boyce
Discipline Scientist
Planetary Geology Program

TABLE OF CONTENTS

CHAPTER 1 - OUTER SOLAR SYSTEM SATELLITES (continued)

CHAPTER 2 - ASTEROIDS AND COMETS

CHAPTER 3 - VENUS

CHAPTER 3 - VENUS (continued)

CHAPTER 4 - CRATERING PROCESSES AND LANDFORM DEVELOPMENT

CHAPTER 4 - CRATERING PROCESSES AND LANDFORM DEVELOPMENT (continued)

CHAPTER 5 - VOLCANIC PROCESSES AND LANDFORMS

CHAPTER 6 - AEOLIAN PROCESSES AND LANDFORMS (continued)

CHAPTER 7 - FLUVIAL PROCESSES AND LANDFORM DEVELOPMENT

CHAPTER 7 - FLUVIAL PROCESSES AND LANDFORM DEVELOPMENT (continued)

CHAPTER 8 - PERIGLACIAL AND PERMAFROST PROCESSES

CHAPTER 10 - REMOTE SENSING AND REGOLITH STUDIES (continued)

CHAPTER 10 - REMOTE SENSING AND REGOLITH STUDIES (continued)

CHAPTER 11 - GEOLOGIC MAPPING, CARTOGRAPHY AND GEODESY

CHAPTER 11 - GEOLOGIC MAPPING, CARTOGRAPHY AND GEODESY (continued)

CHAPTER 12 - SPECIAL ACTIVITIES AND PROGRAMS

Chapter 1

OUTER SOLAR SYSTEM SATELLITES

IDENTIFICATION OF TWO CLASSES OF IO'S VOLCANIC PLUMES

Alfred S. McEwen and Laurence A. Soderblom, U.S. Geological Survey, Flagstaff, Arizona 86001

Comparison of images of Io's surface, acquired by the Voyager 1 and Voyager 2 spacecraft, reveal that a major volcanic eruption, previously unnoted, occurred in the south-polar region of the satellite during the time between the two encounters. The fallout pattern from this eruption, centered on Aten Patera caldera (lat 48° S., long 311° W.), is virtually identical to that from a similar eruption, centered on the caldera named "Surt" (lat 45° N., long 338° W.), that also occurred between the two encounters (Smith et al., 1979b; Strom et al., 1981). These two plume deposits and that of Pelé (the first plume discovered; Morabito et al., 1979) are similar in scale and spectral properties, and we believe that they form a class of plume eruption distinct from the smaller active plumes. The large plumes deposit red material over areas about 1,400 km in diameter and are probably shortlived, whereas the small plumes deposit bright white material over areas approximately 300 km in diameter and are very longlived. Six small plumes were observed to be continuously active during both encounters, and simple probability indicates likely minimum durations of about 3 years. Pelewas erupting during the Voyager 1 encounter but had ceased 4 months later when Voyager 2 arrived; Surt and Aten Patera were evidently inactive during both encounters.

The probable lifetime of a large plume is on the order of days, much less than the years that a small plume is likely to be active. Other differences between the two classes of plume eruptions have implications for basic geologic processes on Io. Evidence from the Voyager Imaging Experiment, the International Ultraviolet Explorer, ground-based telescopic spectra, and the Voyager Infrared Interferometric Spectrometer (IRIS) suggest that the smaller plumes have substantial amounts of associated SO_2 and eruptive temperatures of about 300 K, whereas the large plumes are depleted rich in SO_2 and erupt at near 600 K (Sinton, 1980; Pearl and Sinton, 1981).

Two general types of models have been proposed for the plume volcanism, in which either sulfur or SO_2 is the driving volatile material (Smith et al., 1979; Reynolds et al., 1980; Kieffer, 1982). From recognition of the two classes of plume eruption, we now contend that sulfur, originating from deep reservoirs, is the driving volatile material for the large plumes, whereas SO_2 in shallow reservoirs drives the small plumes. The mobility of SO_2 as a ground fluid would provide a continuous supply of volatile materials, and so the small plumes are very longlived. Sulfur, however, is very fluid over only a narrow range of temperatures and pressures, and so this volatile supply would not be replenished, and the large plumes are shortlived.

The distribution of these two plume classes suggests a global asymmetry in Io's crust. Whereas the small plumes are concentrated in an equatorial belt around the satellite, the three large plumes and surface markings that suggest previous large plume eruptions all occur in the hemisphere centered on long 300° W. Ground-based observations

since 1926 have consistently noted that the longitude zone near 300° W. is much darker and redder than the central and eastern longitudes (Morrison et al., 1979). (The fissure named "Loki" occurs where these areas overlap, and the two plumes erupting from the east and west ends of this fissure display attributes of both plume classes.) Where the large plumes dominate, darkness of the surface in ultraviolet images suggests little SO_2 frost, and the surface is covered by many huge lava flows. Elsewhere, near the Equator, where the small plumes are concentrated, brightness of the surface in ultraviolet images suggests abundant SO_2, and few lava flows are apparent. Continuous deposition of pyroclastic materials and SO_2 by the small plumes is consistent with a low-density porous crust, whereas the crust near long 300° W. may consist mostly of lava flows.

References

Kieffer, S. W., Dynamics and thermodynamics of volcanic eruptions: Inferences for the plumes on Io, in The Satellites of Jupiter, edited by D. Morrison, Univ. Arizona Press, Tucson, in press, 1982.

Morabito, L. A., S. P. Synnott, P. M. Kupferman, and S. A. Collins, Discovery of currently active extraterrestrial volcanism, Science, 204, 972, 1979.

Morrison, D., D. Pieri, J. Veverka, and T. V. Johnson, Photometric evidence on long-term stability of albedo and colour markings on Io, Nature 280, 753-755, 1979.

Pearl, J. C., and W. M. Sinton, Hot spots of Io, NASA Technical Memorandum 82154, 48 pages, 1981.

Reynolds, R. T., S. J. Peale, and P. Cassen, Io: Energy constraints and plume volcanism, Icarus, 44 234-239, 1980.

Sinton, W. M., Io: Are vapor explosions responsible for the 5 μ outbursts? Icarus, 43, 56-64, 1980.

Smith, B. A., E. M. Shoemaker, S. W. Kieffer, and A. F. Cook II, The role of SO_2 in volcanism on Io, Nature, 280, 738-743, 1979a.

Smith, B. A., L. A. Soderblom, R. Beebe, J. Boyce, G. Briggs, M. Carr, S. A. Collins, A. F. Cook II, G. E. Danielson, M. E. Davies, G. E. Hunt, A. Ingersoll, T. V. Johnson, H. Masursky, J. McCauley, D. Morrison, T. Owen, C. Sagan, E. M. Shoemaker, R. G. Strom V. E. Suomi, and J. Veverka, The Galilean satellites and Jupiter: Voyager 2 imaging science results, Science, 206, 927-950, 1979b.

Strom, R. G., N. M. Scheider, R. J. Terrile, A. F. Cook and Candice Hansen, Volcanic Eruptions on Io, J. Geophys. Res., v. 86, n. A10, 8593-8620, 1981.

REGOLITH OUTGASSING BY SULPHUR FLOWS ON IO

Baloga, S.M., Pieri, D.C., Matson, D.L., Jet Propulsion Laboratory, Pasadena, CA 91109

Bright lateral surface markings often exist in close association with volcanic features on Io. In previous studies (1,2), we proferred the term "auras" for the bright distinctive ribbon-like markings adjacent to many of the sulphur flows observed in Voyager images. These auras generally exhibit a relatively intense image near the inner boundary with the flow and a definite surface pattern correlation with flow morphology. Aural patterns gradually take on a nebulous character toward the outer boundaries and ultimately merge into the image background or the bright markings associated with other volcanic features.

We attribute the formation of auras to volatile release activated by sulphur flows. Three alternative hypotheses for the origin of the volatile species have been examined : the regolith beneath the observed aura, the flow itself, and the regolith predominantly subjacent to the activating sulphur flow. By using high resolution Voyager mission data on the volcanic complex Ra Patera, a suite of theoretical and geomorphological arguments indicates regolith outgassing from beneath the flow as the most likely hypothesis. Moreover, the fine structure of the analysis severly constrains reasonable choices for aural material candidates as highlighted below.

Aura morphogenesis by volatile release from the regolith underlying the observed auras at Ra Patera is precluded by the lateral dimensions of the auras, typically 10-20 km, and the heat transfer properties of the regolith (3). Regolith heating at such distances from the sulphur flow, followed by local volatile outgassing, requires a time scale exceeding $O(10^{15})$ seconds. Aura formation processes requiring such a time scale are grossly inconsistent with the surface renewal estimates derived from global volcanic plume and sulphur flow averages (4,5). Consequently, the activating flow itself and the regolith in its immediate vicinity are the more likely hypotheses for the origin of aural materials.

To examine the remaining two hypotheses, we evoke a stochastic-ballistic theory for the above-surface emplacement of molecular species. This theory considers volatile effusion as a stochastic process with ballistic trajectories between the origin and the point of emplacement in the aura. Using identical independent Gaussian distributions for the vertical and lateral effusion velocity components, it can be shown that the lateral emplacement probability density is given by,

$$w(x) = (\pi L)^{-1} K_0 (x/2L) , \qquad (1)$$

where K_o is the zeroth-order modified Bessel function of the second kind, $L = \sigma^2/g$ is the characteristic length, σ^2 is the Gaussian variance, g denotes gravity at the surface of Io, and x indicates the distance from the sulphur flow. Due to the finite resolution of the Voyager images (1.25 km/pixel), matching theoretical and observed aura intensity decay curves requires division of the cumulative emplacement probability implied by (1),

$$P(x) = 2\pi^{-1} \int_0^{x/2L} K_o(s)ds \ , \qquad (2)$$

into finite size intervals. With the modest assumption that the emplacement probability, the areal density of the aural deposit, and the image intensity are all proportional, this procedure allows us to compare theoretical and Voyager scan decay curves and quantitatively fix the length scale of the intensity decay in the auras at Ra Patera. The histograms shown in Figure 1 are an example of this matching process, where the dotted histogram indicates the theoretical curve for L = 9.7 km and the solid histograms represent the envelope of Voyager observations in the violet filter for one particularly well-expressed aura. Numerous fittings and analyses of observational noise lead to a best estimate of L = 12 km for this aura with L = 15 km being the most reasonable upper bound.

To relate the resulting length scale to the physical properties of the effusion source, we borrow the random velocity $\sigma = \sqrt{kT/m}$ from the kinetic theory of gases. For a given molecular species, the observed length scale of the aural decay thus fixes a characteristic effusion temperature of the source. Table 1 gives a partial listing of materials that might be found in the bright aural markings and the characteristic temperatures using our best estimate of L = 12 km.

TABLE 1

Compound	Mass (amu)	Eff. Temp.(K)
SO_2	64	166
H_2S_2	66	171
Na_2S_4	174	451
S_8	256	664

By noting that the activating sulphur flow solidifies at about 384K, these calculated effusion temperatures differentiate the source of the effusion by molecular species. Molecules with temperatures less than sulphur solidus evolve from the regolith subjacent to the flow, while those above issue from the flow itself.

FIGURE 1

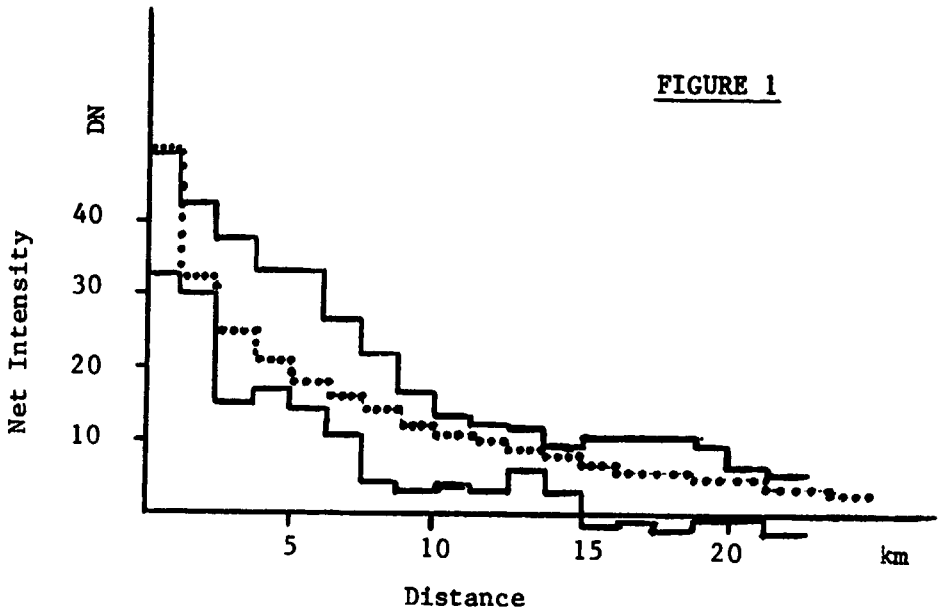

We have examined many more candidate aural materials than shown in Table 1, and, complemented by a variety of morphological arguments, precluded all species issuing directly from the flow itself. With additional considerations such as degree of volatility, spectral properties, and chemical abundance on Io, we suggest that SO_2 liberation from the regolith beneath the flow is the most likely hypothesis for explaining the existence of the auras at Ra Patera.

REFERENCES

1. Baloga, S.M., Matson, D.L., Pieri, D.C., "The Auras of Sulphur Flows on Io," Bull. AAS, 1982 (Fall DPS Meeting)

2. Baloga, S.M., Pieri, D.C., Matson, D.L., "The Auras of Sulphur Flows on Io," 1982 (in preparation for submission to JGR)

3. Matson, D.L., and Nash, D.B., "Io's Atmosphere: Pressure Control By Regolith Coldtrapping and Surface Venting," 1982 (submitted to JGR)

4. Johnson et al., "Volcanic Resurfacing Rates and Implications for Volatiles on Io," Nature, Vol. 280, pp. 746-750, 1979

5. Pieri, D.C., et al., "The Sulphur Flows of Ra Patera, Io," 1982 (in preparation for submission to Nature)

THE EJECTION OF MATERIAL FROM IO

Carl B. Pilcher, Institute for Astronomy and
Department of Physics and Astronomy,
University of Hawaii, Honolulu

We have reduced a group of ~ 50 images showing directional features in Io's sodium cloud, selected from our full data set of ~ 180 images. The images were selected on the basis of their anticipated value in providing constraints on possible models for the sodium ejection mechanism. The data reduction process encompasses the following steps. The data, including images of the scattered Jovian background radiation, are first digitized from the photographic plates. The data values are converted to intensity and the background images are then subtracted from those showing the sodium emission. A low pass filter is applied to the resulting images and these results are displayed as hard-copy contour plots. For images that are to be subjected to detailed numerical analysis, the two-dimensional instrument response function (which is non-uniform for optical reasons) is calculated. This function is then applied as a correction to the data.

Models of the process producing the directional features are being developed in collaboration with W. H. Smyth of Atmospheric and Environmental Research, Inc. (Cambridge, Massachusetts). Our hypothesis is that sodium is collisionally swept from the trailing hemisphere of Io's bound atmosphere by the nearly corotating heavy ion plasma. The swept sodium forms a hollow core which is projected onto the sky ahead of Io. In the absence of an asymmetric sodium sink, this projection would lead to the observation of a pair of directional features, oblique to and symmetric about Io's orbital plane. An asymmetric sink is provided, however, by the plasma torus, which oscillates north-south about Io's position owing to the tilt of the Jovian dipole. When the plasma is largely to one side of Io, neutral sodium in the corresponding directional feature rapidly undergoes electron impact ionization. Six-and-one-half hours later, when the plasma has reached the other extreme of its north-south oscillation, sodium in the other directional feature is similarly ionized. The apparent result is in general a single directional feature that appears to oscillate about Io's orbital plane with a period equal to Io's magnetic period. The time lag between plasma symmetry with respect to Io and feature symmetry with respect to the orbital plane is determined by the details of the ejection and ionization processes. We are using a set of observations that show the feature moving through its symmetry point to constrain the parameters in this model.

Variations in the overall intensities of the directional features can be due to variations in the sodium density in Io's bound atmosphere or to changes in the plasma density. The root of both of these effects is likely a variation in Io's volcanic activity. Dramatic evidence for such a variation is contained in images, acquired during a 4-day interval in February 1980, which show anomalously bright sodium emission surrounding Io and anomalously prominent directional features. Images of the S^+ component of the plasma torus obtained on the same nights may help us understand the origin of this unusual occurrence.

VOYAGER SURFACE AND DISK-INTEGRATED PHOTOMETRY OF IO

D. Simonelli and J. Veverka, Laboratory for Planetary Studies, Cornell University, Ithaca, N.Y.

To date most of the colors on Io have been explained in terms of various forms of elemental sulfur and sulfur compounds, including SO_2 frost. One difficulty with the universal conviction that the surface of Io is rich in elemental sulfur is that laboratory measurements show the spectral reflectance curves of sulfur allotropes to be temperature-dependent. For example, Gradie et al. (1982) find that measurable changes in reflectance and color should accompany diurnal and post-eclipse changes of surface temperature on Io, if the surface contains appreciable amounts of the brighter sulfur allotropes (especially S_8). So far no such variations have been noted either in normal Voyager coverage (Veverka et al., 1982), or in the post-eclipse sequences (Veverka et al., 1981). Before concluding that S_8 and other bright allotropes are not present in sufficient amounts to affect the satellite's spectrum, one must consider the possibility that the requisite temperature effects do occur, but that they are masked by some compensating peculiarity of Io's photometric properties. In part to resolve this question we have begun a comprehensive determination of Io's disk-integrated and disk-resolved photometric properties.

Photometry of Individual Regions: Preliminary analyses (Clancy and Danielson, 1981; McEwen and Soderblom, 1982; Veverka et al., 1982) have not produced any evidence that Io's photometric properties are in any way peculiar. At least the small phase angle Voyager data ($\alpha \leq 20°$; cf. Fig. 2) can be represented well by simple scattering functions, including Minnaert's equation (Figure 1). In our initial analysis we have chosen a three-component color classification system, labeling regions as either white, orange, or brown (where the brown material is confined largely to the polar regions). Figure 1 shows that the observations for the "orange" and "brown" regions can be described extremely well by a simple Minnaert law. The scatter in the "white" region data is larger, but a Minnaert fit is still adequate on average. The values of the limb darkening coefficients, and their dependence on the phase angle (Table 1) are reasonable. Thus, there is no indication that there is anything peculiar about the photometric properties of typical regions on Io. The relatively larger random scatter in the white region data (Fig. 1) most likely indicates that our classification in this case is too coarse. The random nature of the scatter does not support the idea that the white areas are photometrically peculiar in some systematic way.

Disk-integrated Photometry: Figure 2 shows the disk-integrated brightnesses through the Voyager orange and clear filters on a magnitude scale, graphed vs. phase angle. The low phase angle data have been rotation-corrected using the earth-based rotation curves published in Morrison and Morrison (1977). The phase coefficient for Io (appropriate to the wavelength region covered by the Voyager clear

and orange filters) derived from earth-based observations, .02 mag/deg (Morrison and Morrison, 1977), fits the low phase angle Voyager data well (Figure 2). The high phase angle data allow us for the first time to directly compute the phase integral q. We find $q = 0.75 \pm 0.2$ in both the orange and clear filters. The liberal error bars are due to the lack of coverage at phase angles between 20° and 100°. This value for q compares favorably with the earth-based determinations of q summarized in Table 12.2 of Morrison (1977); pre-Voyager estimates of q centered on either 0.6 or 0.9, although Morrison adopted a nominal value of 0.9 ± 0.2.

This research was supported in part by NASA Grant NSG 7156.

References

Clancy, R. T., and Danielson, G. E. (1981). J. Geophys. Res. 86, 8627-8634.

Gradie, J., Ostro, S., Thomas, P., and Veverka, J. (1982). Lunar Planet. Sci. 13, 275-276.

McEwen, A. S., and Soderblom, L. (1982). Personal communication.

Morrison, D. (1977). In Planetary Satellites (J. Burns, Ed.), pp. 269-301. Univ. of Arizona Press, Tucson.

Morrison, D., and Morrison, N. D. (1977). In Planetary Satellites (J. Burns, Ed.), pp. 363-378. Univ. of Arizona Press, Tucson.

Veverka, J., Gradie, J., Thomas, P., and Ostro, S. (1982). Lunar Planet Sci. 13, 823-824.

Veverka, J., Simonelli, D., Thomas, P., Morrison, D., and Johnson, T. V. (1981). Icarus 47, 60-74.

TABLE 1. Minnaert parameters (B_0 and k) for Io
Violet Filter (λ = .41 μm); Subspacecraft longitude = 20°

Image (FDS No.)	Phase Angle α (deg)		B_0	k
16345.24	4.9	White	.439 ± .009	.60 ± .02
		Orange	.285 ± .003	.70 ± .02
		Brown	.152 ± .002	.72 ± .01
20592.05	8.8	White	.39 ± .01	.55 ± .02
		Orange	.241 ± .004	.70 ± .03
		Brown	.138 ± .003	.74 ± .02
16292.33	14.5	White	.37 ± .01	.55 ± .03
		Orange	.248 ± .004	.81 ± .04
		Brown	.146 ± .004	.81 ± .03

Note: Errors are the least squares standard deviations.

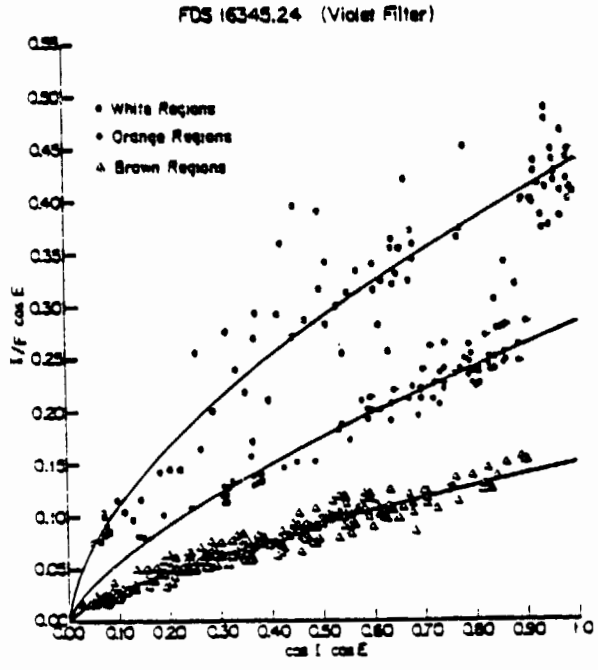

Fig. 1. Minnaert plot for the three classes of colored regions in image FDS 16345.24 (Violet Filter; $\lambda \approx 0.41$ μm). For each class, the solid line is a least-squares fit to a curve of the form $I/F \cos e = B_0(\cos i \cos e)^k$, where i is the incidence angle and e is the emission angle.

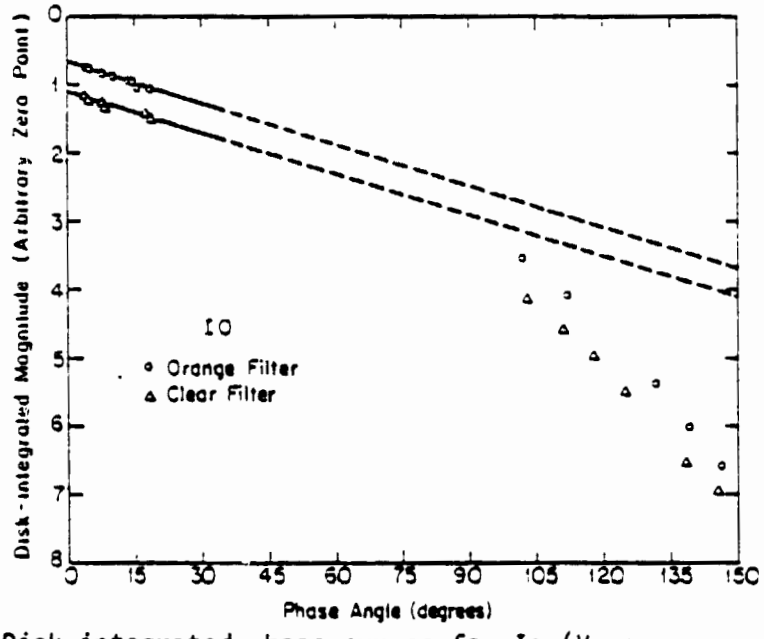

Fig. 2. Disk-integrated phase curves for Io (Voyager orange and clear filters). The disk-integrated brightness of the satellite has been computed on a magnitude scale with an arbitrary zero point. The low phase angle data have been rotation corrected using the earth-based rotation curves of Morrison and Morrison (1977). Straight lines have slopes of $\beta = .02$ mag/deg, the phase coefficient determined from telescopic observations. The approximate effective central passbands of the clear and orange filters are 0.48 and 0.59 μm respectively.

REFLECTION SPECTRUM OF LIQUID SULFUR AND ITS IMPLICATION FOR IO

R.M. Nelson, D.C. Pieri, D. Nash, and S.M. Baloga
Jet Propulsion Laboratory
Pasadena, California 91109

We have measured the spectral reflectance from 0.38 to 0.75μm of a column of liquid sulfur (figure 1) at several temperatures between the melting point (~118°C) and 173°C. Below 160°C the spectral reflectance was observed to reversibly change as a function of the temperature, without regard to the previous thermal history of the column. Once the temperature exceeded 160°C, the spectrum would not change given a subsequent decrease in temperature.

Our results show that at all temperatures at which liquid sulfur exists, its spectral reflectance ($0.35<0.75\mu m$) measured is quite low, the maximum being 19% at 118°C ($\lambda=0.75\mu m$)(figure 2). When this result is compared to the spectrophotometry of selected areas on Io reported by the Voyager Imaging Team (Soderblom et al., 1980; Clancy and Danielson, 1981) we conclude that all those Io areas are too reflective to be liquid sulfur except for the regions classified as "black caldera floor material" which have reflectivities of <25% of all Voyager camera wavelengths. Molten sulfur at any temperature would be classified as black by the Voyager imaging results.

These black areas consititute approximately 5% of Io's total surface area (Carr et al., 1978). However, groundbased thermal infrared studies put a fractional limit of $\simeq 10^{-4}$ for temperatures higher than 77°K (Morrison and Telesco, 1980). Since liquid sulfur must be hotter than 77°K, only ≈0.2% of the black spots observed on Io by Voyager could be molten sulfur. This implies that the remaining black spots are solid and subject to resurfacing from other volcanic deposits. If so, given resurfacing rates reported by Johnson et al. (1979), then the lifetime of a typical black spot (once solidified) is about 10^4 years. Using rates estimated by Pieri et al. (1982) reduces that estimate by a factor of 10. Both rates assume that 1 cm. of covering material is the minimum required to obliterate a black spot.

The finding that liquid sulfur at any temperature appears black to the Voyager cameras has several additional implications for Io volcanism. First, the uniform and low albedo of molten sulfur allows that active sulfur calderas need not have been heated to the temperature range of black sulfur, but could have any range of temperatures above 118°C. This is consistent

with the range of temperature-dependent flow morphology observed (Pieri et al., 1982). Furthermore, some isolated flows on Io appear quite dark in the Voyager imaging data. These could either be quenched black sulfur flows or active liquid flows with little or no overcrusting (Pieri et al.,1982) although thermal data (Morrison and Telesco, 1980) severely limit the area which may be liquid sulfur.

Finally, (a) if flows existed on Io during the Voyager encounters, (b) if quenching does effectively preserve the original allotropic colors (Nelson and Hapke, 1978), and (c) if the varigated and systematic color-morphology associations in flows are indeed the result of cooling of sulfur lavas (Sagan, 1979; Pieri et al., 1982; Baloga et al., 1982), then nearly all flows on Io were either inactive at the time of the Voyager encounters, or most of the active flows were roofed over by quenched sulfur crusts.

Several outstanding questions remain. It has yet ot be shown that large masses of sulfur will retain their color upon quenching. Ultrapure sulfur with respect to carbon may be required in order to preserve this effect. If so then such conditions must be consistent with the Io environment. In particular, it must be reconsidered with the presence of other surface materials, most notably the sulfides of sodium and sulfur dioxide.

This work performed under NASA contract at the Jet Propulsion Laboratory of the California Institute of Technology.

REFERENCES

Baloga, S.M., D.C. Pieri, R.M. Nelson, and C. Sagan, 1981, Volcanic Sulfur Flows on Io, E&S, 62, p.1080.

Baloga, S.M., D.C. Pieri, and D. Matson, 1982, Auras of Sulfur Flows on Io, in preparation.

Carr, M.H., H. Masursky, R.G. Strom, and R.J. Terrile, 1979, Volcanic Features on Io, Nature, 280, p.729-733.

Clancy, T. and G.E. Danielson, 1981, Journal of Geophys. Res., 86, p.8627-8634.

Fanale, F.P., T.V. Johnson, and D.L. Matson, 1974, Io: A Surface Evaporite Deposit?, Science, 186, p. 922-925

Johnson, T.V., A.F. Cook II, C. Sagan, and L.A. Soderblom, 1979, Volcanic Resurfacing Rates and Implications of Volatiles on Io, Nature, 280, p.746-750.

REFERENCES (continued)

Morrison, D. and C.M. Telesco, 1980, Io:Observational Constraints on Internal Energy and Thermophysics of the Surface, Icarus, 44, p.226-233.

Pieri, D.C., S.M. Baloga, R.M. Nelson, and C. Sagan, 1982, Sulfur Flows at Ra Patera, Io, in preparation.

Soderblom, L.A., T.V. Johnson, G.E. Danielson, B.L. Smith, J. Veverka, A. Cook II, C. Sagan, P. Kupferman, D. Pieri, J. Mosher, C. Avis, J. Gradie, and T. Clancy, 1980, Spectrophotometry of Io: Preliminary Voyager I Results, Geophysics Research Letters, 7, p. 963-966.

FIGURE CAPTIONS

Figure 1. The special glass column depicted in this figure was constructed in such a fashion that it was possible to fill the column with powdered sulfur and measure the reflection spectrum of a 3.8 cm thickness of molten sulfur through a fused silica window at one end. The column was filled under argon with USP grade sublimed sulfur manufactured by Mallincrodt Inc. It was evacuated, sealed and wrapped in heater tape over its entire length, except for the topmost portion and the window. Figure 1 shows a sketch of the glassware. The temperature was monitored by an iron-constantan thermocouple in contact with the glass on the side of the column near the window. The temperature was regulated by a temperature controller activated by a thermistor wich was also in contact with the glass near the window. The spectral reflectance of the top surface of the column of sulfur liquid was measured through the window using a Beckman DK-2 recording spectrophotometer in the spectral renge 0.375 to 0.75 microns.

Figure 2. Reflection spectra of the top of the molten liquid column at selected temperatures. Below 160°C the color changed as a function of temperature. Once the column was heated above 160°C, the color would not change if the temperature was lowered again to just above the melting point.

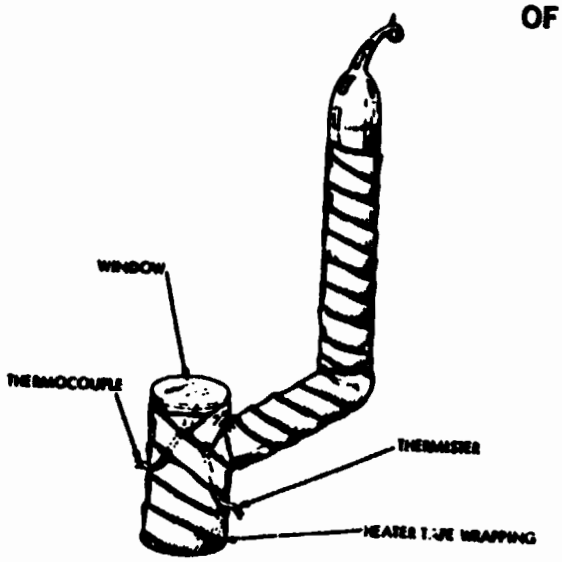

Figure 1.

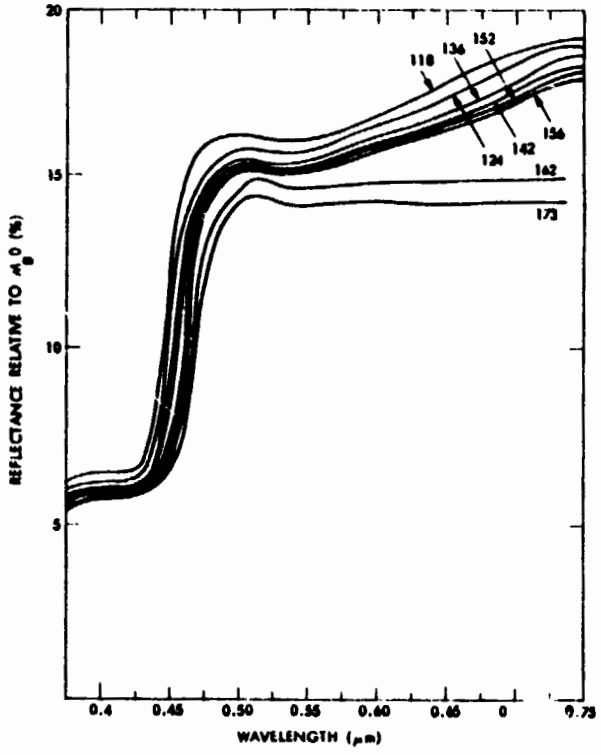

Figure 2.

COLORS OF LAVA FLOWS AT RA PATERA, IO

D.C. Pieri, S.M. Baloga, and R.M. Nelson
Jet Propulsion Laboratory
Pasadena, California 91109

Morphology and qualitative color observations have been used to argue that long (> 150 km) sinuous, radially-oriented flows at Ra Patera are the result of the eruption of molten sulfur in a temperature range of 400 to 525°K. (Pieri et al. 1981, Baloga et al., 1981). We have suggested that radiative cooling is the predominate heat-loss preocess for such volcanic features and have shown that morphology and color transitions occur at approximately the correct distances (±10%) as would be expected for molten sulfur erupting at about 500°K for the Main Flow at Ra Patera. Other flows exhibit different morphologies as well as a range of color sequences and thus a range of initial effusion temperatures is likely to be involved (Pieri et al., 1982).

We have classified flows at Ra Patera and elsewhere on Io using flow morphology and color sequence. "Complete flows" show the full sequence of color and morphology associated with sulfur lavas (Pieri et al., 1981, 1982; Baloga et al., 1981, 1982; Fink and Greeley, 1982, and Sagan, 1979). "Incomplete flows" show truncated color sequences, that is they do not exhibit the complete range of morphology and color associated with an initial eruption of the high temperature allotrope (i.e. red-black sulfur). At Ra Patera, two kinds of incomplete flows exist--those that start as dark red or black sulfur and do not show transition to the lower temperature allotrope (orange) and those that,because of color and morphology observations, appear to have originated as lower temperature and less viscous sulfur, initially.

In support of these studies we have compiled detailed photometric data on the flows at Ra Patera and at other places on Io, using high resolution decalibrated Voyager Imaging data. Some results of this effort are shown in figure 1. Here we present color data for the Upper, Middle, and Main Flows at Ra Patera which are depicted in the sketch map in figure 2. Figure 1 shows Voyager narrow angle orange to blue ratios versus downflow distance for the darkest part of the flow determined from transverse scans. Evident are clear systematic trends in the data consitent with a progressive change to higher albedo allotropes as

one moves away from the caldera. This trend appears in all three examples. On the basis of these data alone we can conclude that brightening occurs downflow consistent with allotropic transitions. Upper and Middle Flows appear to show colors consistent with primarily dark red to black sulfur near the caldera changing progressively to red sulfur downslope. The tightly sinuous morphology of these two flows is also consistent with composition mainly of dark high-viscosity (10^4cp) sulfur. These two are incomplete flows. The Main Flow at Ra Patera, however, appears to be a complete flow erupting as red-black sulfur and terminating with a distal accumulation of orange sulfur.

REFERENCES

Baloga, S.M., D.C. Pieri, R.M. Nelson, and C. Sagan, 1981, Volcanic Sulfur Flows on Io, E⊕S, 62, p.1080

Baloga, S.M. , D.C. Pieri, and D. Matson, 1982, Auras of Sulfur Flows on Io, in preparation.

Fink, J. and R. Greeley, 1982, in preparation.

Pieri, D.C., S.M. Baloga, R.M. Nelson, and C. Sagan, 1982, Sulfur Flows at Ra Patera, Io, in preparation.

FIGURE CAPTIONS

Figure 1. Blue to orange Voyager broadband filter data ratios are presented on the vertical axis versus downflow distances for the Upper, Middle, and Main Flows at Ra Patera.

Figure 2. Sketch map of Ra Patera showing the locations of the flows discussed in the text.

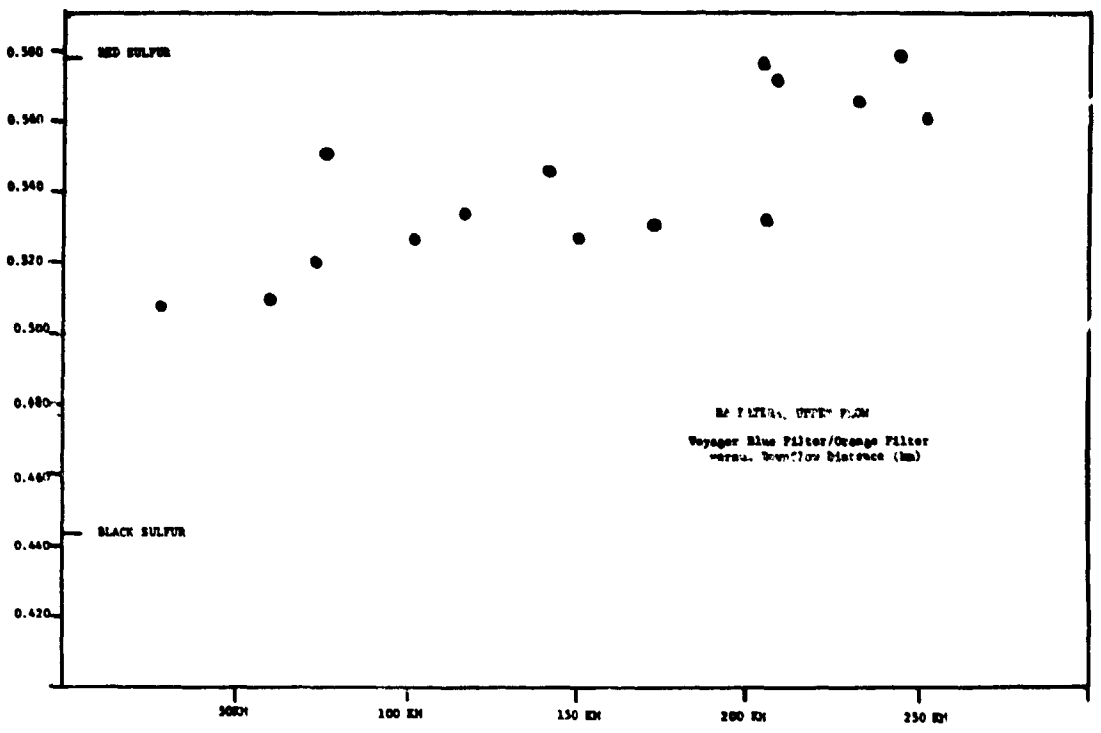

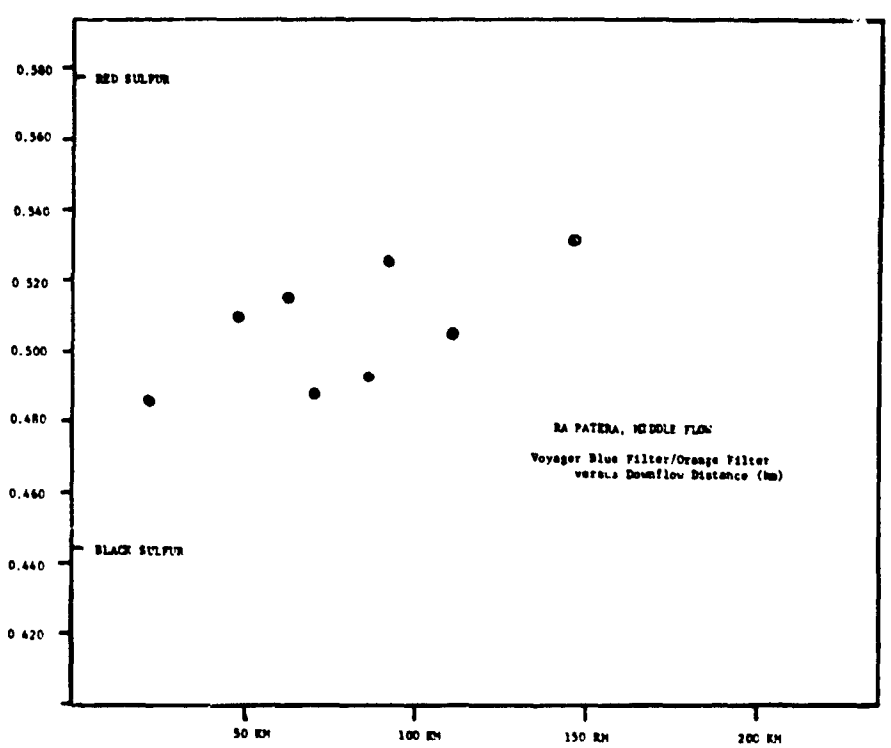

FIGURE 1

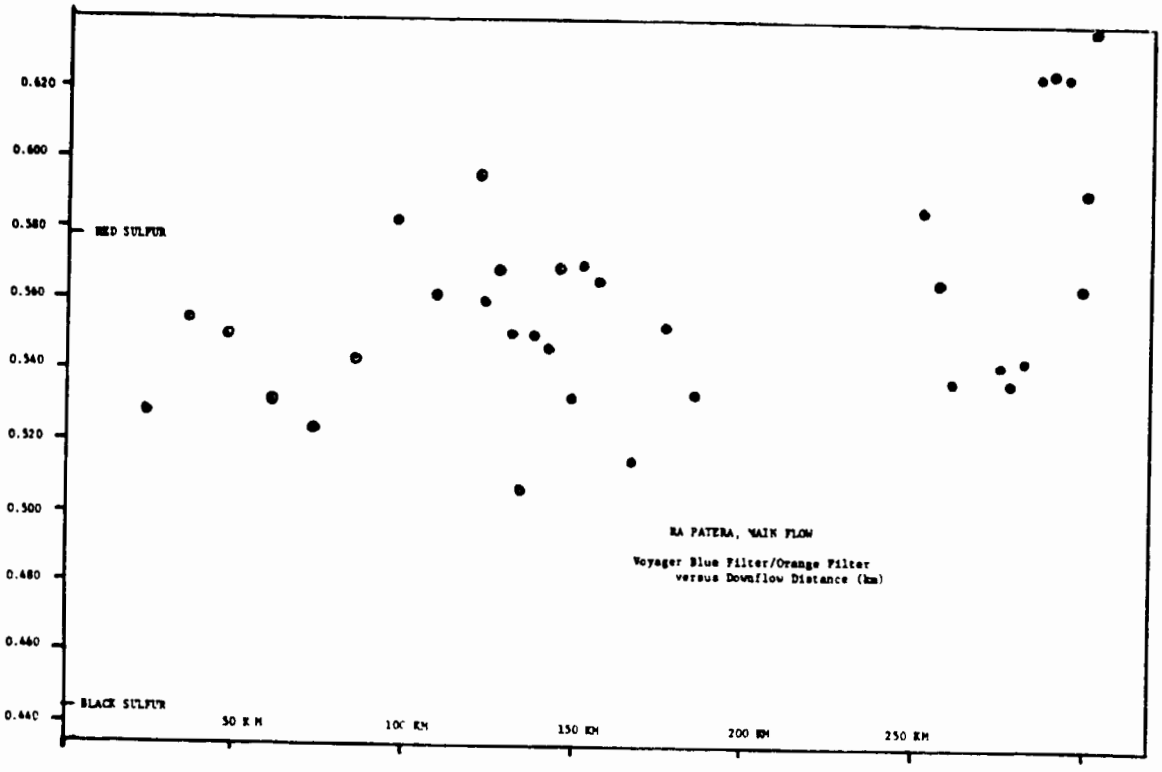

FIGURE 1 (continued)

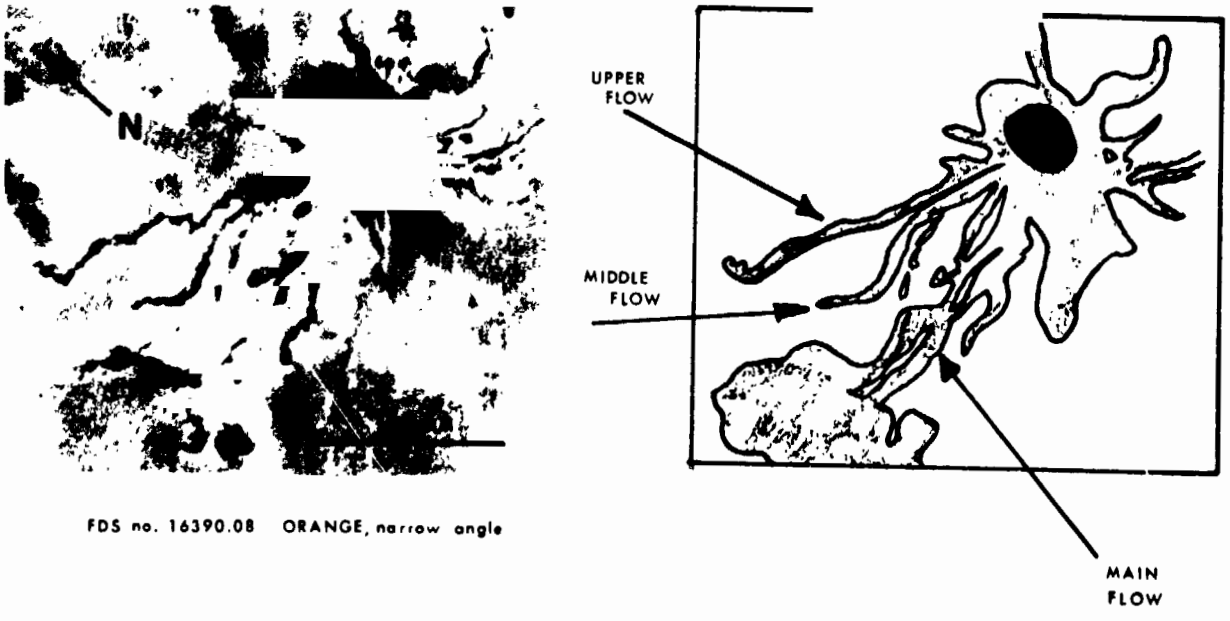

FIGURE 2

EXPERIMENTAL INSIGHTS INTO THE LACK OF IMPACT CRATERS ON EUROPA

Greeley, R., Fink, J.H., Geology Department, Arizona State University, Tempe, AZ, 85287, and Gault, D.E., Murphys Center for Planetology, Box 833, Murphys, CA 95247.

The surfaces of the icy satellites of Jupiter exhibit a wide range of impact crater densities, ranging from the intensely pitted surface of Callisto to the relatively smooth surface of Europa. These differences have generally been ascribed to variations in either crustal properties or degree of bombardment among the satellites. The lack of many visible craters on Europa has been attributed to their slow viscous relaxation in a solid ice crust having relatively high heat flow (e.g., Parmentier and Head, 1981), similar to the process of palimpsest formation proposed for Ganymede by Smith et al. (1979). Based on impact experiments, Greeley et al. (1982) and Fink et al. (1981b) proposed that palimpsest formation may involve a nearly instantaneous relaxation of craters excavated in crusts with relatively fluid rheological properties. Crustal evolution models for the Galilean satellites (e.g., Cassen et al., 1980) have generally rejected the possibilty of a liquid water mantle during all but the earliest parts of their histories. More recent calculations suggest, however, that Europa may have preserved a liquid mantle until quite recently (Squyres et al., 1983). Hence the possibility arises that the paucity of visible impact craters on Europa may be due to initial crater relaxation or resurfacing phenomena associated with impacts into a planetary surface comprised of a liquid mantle overlain by a thin brittle crust.

As part of our ongoing series of investigations at the NASA Ames Vertical Gun Range into cratering processes on icy satellites, we conducted a series of 18 experimental impacts using layered carbowax (Polyglycol 600) targets. These targets consisted of 25 cm of transparent liquid carbowax (melting point = 21°C) overlain by frozen carbowax layers ranging in thickness from 5 to 40 mm. Impacting pyrex projectiles (density = 2.3 g/cm^3) had diameters of 6 or 13 mm (1/8 or 1/4 inch), and velocities ranging from 0.91 to 2.27 km/s. Impacts took place within a vacuum chamber where the pressure was maintained between 10 and 20 mm Hg (1 mm Hg=133 Pa), and the temperature was kept between 25 and 30 °C.

Crater morphology and evolution were quite varied and depended upon crustal layer thickness, projectile diameter and velocity. For constant crustal thickness and projectile diameter, increasing projectile velocity led to a progression from (1) bowl-shaped craters entirely within the crustal layer, to (2) bowl-shaped craters that barely penetrated the liquid substrate, to (3) craters that penetrated well into the substrate, to (4) craters that totally fragmented the crustal layer. A similar progression was suggested by a series of experiments in which projectile conditions were kept nearly constant while crustal thickness was steadily decreased. However, verification of this latter trend requires further experiments.

Experiments of type (2) led to craters that had central pit-like depressions (Fink et al., 1981a), left by the draining back of small amounts of liquid substrate material. In case (3), penetration of the substrate was followed by forceful ejection of a 'plume' of liquid carbowax that filled in the crater bowl, sometimes overflowing and smoothing the initially cratered surface. For the case of total disruption (4), the fragments of crust floated

on the surface, eventually melting. In one experiment, the liquid substrate was heated to 42°C before the impact, and the crustal layer fragmented at an anomalously low projectile velocity.

Previous experimental impacts into targets with solid surfaces overlying liquid substrates (Greeley et al., 1982) demonstrated that the cratering process could vary from that characteristic of solid targets to that of liquid targets, depending upon the thickness of the crustal layer and the projectile properties. Impacts into liquids with thin or negligible surface layers produced craters that disappeared shortly after formation, leaving only a ring of bubbles or other signs of disruption. Similar results occurred for thicker crusts if the projectiles had sufficient energy.

Extending these results to the cratering record of Europa, or lack thereof, requires a series of caveats about scaling (see, for e.g., Greeley et al., 1982). Nevertheless, based on our experiments we may qualitatively suggest that the presence of a liquid mantle beneath a relatively thin ice crust on Europa could explain the paucity of visible impact craters through two mechanisms. Large impact events would essentially 'ignore' the presence of the crust and produce a transient crater that immediately relaxed hydrodynamically. The 'scar' or disrupted zone could then refreeze, leaving very little residual topography. Smaller impacts could punch through the crust, followed by the ejection of water in either a liquid or solid state which could then cover the surface of the surrounding crust. These deposits might then themselves tend o even out topography through slow viscous flow.

Additional experiments are planned to further quantify the relationships between crater morphology and crustal layer properties and thicknesses. In particular, experiments should be run at reduced temperatures to try and simulate resurfacing and re-freezing processes.

REFERENCES CITED

Cassen, P., Peale, S.J. and Reynolds, R.T. (1980) On the comparative evolution of Ganymede and Callisto. Icarus, v. 41, p. 232-239.

Fink, J.H., Greeley, R. and Gault, D.E. (1981a) Laboratory simulations of central pit craters. Amer. Astron. Soc., Div. Planetary Sciences, p. 712 [abstract].

Fink, J.H., Greeley, R. and Gault, D.E. (1981b) Impact cratering experiments in Bingham materials and the morphology of craters on Mars and Ganymede. Proc. Lunar Sci. Conference, 12th, p. 1649-1666.

Greeley, R., Fink, J.H., Gault, D.E. and Guest, J.E. (1982) Impact cratering in simulated icy satellites. In The Satellites of Jupiter (D.M. Morrison, editor) Univ. Arizona Press [in press].

Parmentier, E.M. and Head, J.W. (1981) Viscous relaxation of impact craters on icy planetary surfaces: determination of viscosity variation with depth. Icarus, v. 47, p. 100-111.

Smith, B.A. and the Voyager Imaging Team (1979) The Jovian system through the eyes of Voyager 1. Science, v. 204, 951-972.

Squyres, S.W., Reynolds, R.T., Cassen, P.M. and Peale, S.J. (1983) Liquid water and active resurfacing on Europa. Icarus [submitted].

GEOLOGICAL STUDIES OF ICY SATELLITES: EUROPA AND ENCELADUS

Steven W. Squyres, Ray T. Reynolds, Patrick M. Cassen, NASA Ames Research Center, Moffett Field, CA 94035, and Stanton J. Peale, Dept. of Physics, University of California, Santa Barbara, CA 93106.

A number of models have been suggested for the evolution and present state of Europa (1,2,3). We have recalculated its thermal state, and have obtained results consistent with a largely dehydrated silicate interior, an overlying ocean of liquid water tens of km thick, and a surface layer of ice with a mean thickness of roughly 10 km. The model incorporates radiogenic heating, and tidal heating in both the silicate core and the ice shell. The crustal thickness is found to be similar to but less than the minimum value that would permit solid state convection. If convection occurred, it would cause rapid heat loss and freezing of the ocean (4). Our results are different from those of previous models for three reasons. First, we consider tidal heating in both the shell and the interior (Cassen et al. (2,3) neglected dissipation in the interior; Ransford et al. (1) neglected tidal dissipation altogether). Second, we use a value of Q=25, appropriate for long period oscillations of the Moon (5), rather than Q=100 (2,3). Finally, we use a value of the ice activation energy constant $E/kT_{melting}$=26, which is favored by Weertman (6) and indicated by study of viscous crater relaxation (7), rather than 18 (2,3).

The theoretical calculations are consistent with a liquid ocean beneath the ice, but for confirmation we must turn to the observational evidence. The surface of Europa shows widespread evidence for fracturing of the icy crust (8). Fracturing of the crust, caused by tidal flexure or membrane stresses, would result in boiling of exposed water and deposition of the vapor as recondensed frost. Several observations provide evidence for an active frost layer. First, the paucity of impact craters indicates very rapid viscous relaxation (9) and near-surface temperatures substantially greater than the solar equilibrium temperature. A frost layer, with its very low thermal conductivity, would help to maintain high near-surface temperatures. Second, the photometric function of Europa is quite different from that of impact regolith of equal reflectance on Ganymede and Callisto (10), but consistent with a tenuous frost layer. Finally, the observation of SO_2 on Europa's trailing hemisphere (11) is explained as a result of implantation of magnetospheric sulfur ions concurrent with deposition of H_2O. From the observed SO_2 column density we calculate a minimum global mean H_2O frost deposition rate of roughly 0.1 microns per year for Europa.

Saturn's small icy moon Enceladus shows evidence for several episodes of geologic resurfacing spread over much of its history (12). Tectonic features very similar to the grooves on Ganymede are also observed, suggesting that Enceladus' crust, like Ganymede's, has undergone extension. Extension was probably caused by freezing of H_2O in the interior. Lithostatic compressive stresses are very small on Enceladus due to the low gravity, making it unlikely that the grooves there are grabens. Resurfacing took place by eruption of fresh material, perhaps

containing NH_3, to the surface. Melting in the interior may have been made more likely by the presence of NH_3, as the H_2O-NH_3 system has a eutectic point at 173°K. Tidal dissipation seems to be the only heating mechanism capable of melting Enceladus. Assuming thermal conductivity like that of pure H_2O ice, the orbital eccentricity would have to be higher by a factor of 5 to 7 than the present value of 0.0044 to maintain a molten interior. It may have to exceed the present value by as much as a factor of 20 to cause melting in an initially frozen body. Recent experimental work (13) suggests, however, that inclusion of a small amount of NH_3 could lower the conductivity as much as an order of magnitude. If this were the case, an eccentricity increase of at most a factor of 8 would suffice to initiate melting, and a molten interior could perhaps marginally be maintained by the present eccentricity.

References:

(1) Ransford, G.A., et al., Nature 289, 21 (1981).

(2) Cassen, P.M., et al., Geophys. Res. Lett. 6, 731 (1979).

(3) Cassen, P.M., et al., Geophys. Res. Lett. 7, 987 (1980).

(4) Reynolds, R.T., and Cassen, P.M., Geophys. Res. Lett. 6, 121 (1979).

(5) Cappallo, R.J., et al., J. Geophys. Res. 86, 7180 (1981).

(6) Weertman, J., In Physics and Chemistry of Ice (Roy. Soc. Can, 1973).

(7) Passey, Q.R., and Shoemaker, E.M.. Submitted to J. Geophys. Res.

(8) Smith, B.A., et al., Science 206, 927 (1979).

(9) Shoemaker, E.M., and Wolfe, R.F., In The Satellites of Jupiter (Univ. of Ariz. Press, in press).

(10) Buratti, B., and Veverka, J., Submitted to Icarus.

(11) Lane, A.L., et al., Nature 292, 38 (1982).

(12) Smith, B.A., et al., Science 215, 504 (1982).

(13) Ross, R.G., and Andersson, P., Can. Jour. Chem. 60, 881 (1982).

SPECTRAL ANALYSIS OF TOPOGRAPHY ON GANYMEDE

Robert E. Grimm, Dept. of Geological Sciences, University of Tennessee, Knoxville, TN 37996, and Steven W. Squyres, NASA Ames Research Center, Moffett Field, CA 94035.

Ganymede's bright resurfaced terrain is thought to have formed as the result of global extension (Smith et al., 1979), probably caused by internal phase changes between ice polymorphs during differentiation (Squyres, 1980). Parmentier et al., (1982) have argued that the bright bands originated as large grabens that were flooded and filled with clean ice deposits. It is not clear, however, whether the grooves that are so common in the resurfaced material represent long, very narrow grabens, extension fractures, or ductile necking features. Regular groove spacing is commonly observed and could result from extension of a brittle surface layer over a viscous layer, causing a necking instability that might result in any brittle deformation being concentrated at regular intervals (Fink and Fletcher, 1981). Squyres (1982) has pointed out that regular spacing might also result from rapid formation of a cooled, strengthened zone around an extension fracture immediately after its formation. In either case, the geothermal gradient at the time of deformation has been shown to be directly related to the spacing of grooves. Quantitative determinations of groove spacing might therefore be used to constrain this important indicator of planetary evolution.

In addition, it has been suggested that colder overall temperatures within the crust could substantially increase the stresses resulting from extensions, causing increased deep crustal normal faulting (Squyres, 1982). For this reason, one might expect topography in tectonically deformed areas to be less regular in the polar regions, where colder temperatures might result in extensive disruption of any regular groove pattern by propagation of deep normal faults to surface. If, instead, no variation of morphology with latitude exists, it may indicate the presence of a regolith with unexpectedly strong insulating properties. In order to perform a quantitative statistical analysis of groove spacing and morphology on Ganymede, we have adopted a spectral analysis technique, taking Fourier transforms of a large number of photmetric profiles across groove sets, and examining the resultant power spectra for the position and strength of peaks representing periodicities.

Approximately 160 tracks perpendicular to the trend of groove sets from 28 Voyager images were selected for study. These images provide a nearly complete sample of all the groove sets observed at moderate to high resolution by the Voyager cameras. Groove sets selected for study had to satisfy a uniqueness criterion: namely, that no grooves within a given set could be traced unbroken into adjacent sets. One representative track was chosen within each groove set. Grooves that were not nearly parallel were avoided, as were areas that were extensively cratered. In addition, features of less than a few wavelengths were not used, e.g., single grooves and groove pairs. Because of the lack of stereo coverage and the unsuitability of many images for detailed photoclinometric analysis, digital photometric intensities as recorded by the Voyager cameras through clear filters were considered to correlate with the relative amplitudes and wavelengths of surface topography.

Anomalous contrasts in reflectivity therefore had to be avoided, such as those due to bright ejecta. Similarly, those groove sets judged not to have adequate contrast to be clearly resolved from noise were not used. The latitude, longitude, and scale (in km per picture element) of each track were calculated using subspacecraft point coordinates and image frame orientation from the Voyager final SEDR document and using the photogrammetric control points of Davies and Katayama (1981).

For each desired cross-groove photometric track, a set of five adjacent parallel tracks was summed, bandpass filtered, and tapered in the spatial domain in order to reduce the effects of regional shading trends noise, aliasing, and sidelobes in the wavenumber domain. The power in a given spatial frequency is proportional to the square of the modulus of its Fourier transform:

$$\hat{A}(k) = \int_{-\infty}^{\infty} A(r) e^{i2\pi kr} dr \qquad (1)$$

$$P(k) = Re^2(\hat{A}(k)) + Im^2(\hat{A}(k)) \qquad (2)$$

At the time of this writing, we have completed track selection and data reduction, and are begining data anlaysis. A sample cross-groove track and its power spectrum are shown in Figures 1 and 2. This spectrum shows a peak at approximately 0.3 km^{-1} (about 3 km wavelength), although much of the power is dispersed at higher frequencies. Since we wish to look for variations in groove spacing and morphology with latitude, power spectra within a given latitude band will be averaged and compared with other latitutdes. The spectra will also be statistically analyzed with respect to viewing geometry parameters and spacecraft range in order to reveal any hidden systematic errors. When completed, this work will provide a global picture of the variation of groove spacing on Ganymede.

Acknowledgment: This work was supported in part by the NASA Planetary Geology Undergraduate Research Program.

References:

Davies, M.E., and Katayama, F.Y. (1981). J. Geophys. Res. 86. 8653-8677.

Fink, J.H., and Fletcher, R.C. (1981). in Reports of Planetary Geology Program, NASA T.M. 84211.

Parmentier, E.M., Squyres, S.W., Head, J.W., and Allision, M.L. (1982) Nature 295. 290-293.

Smith, B.A., and Voyager Imaging Team (1979). Science 206, 504-537.

Squyres, S.W. (1981). Geophys. Res. Lett. 7, 593-596.

Squyres, S.W. (1982) Submitted to Icarus.

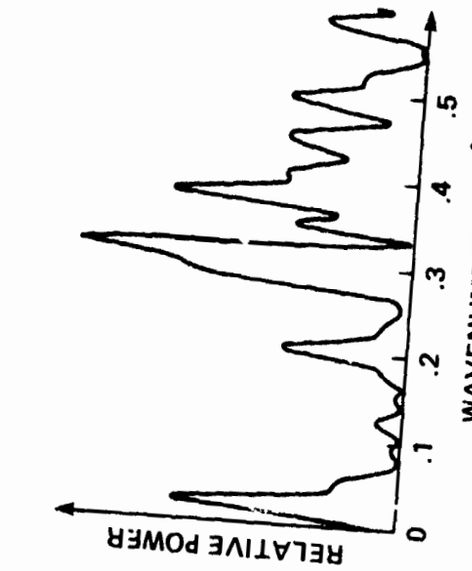

FIG. 2. Sample Ganymede Power Spectrum

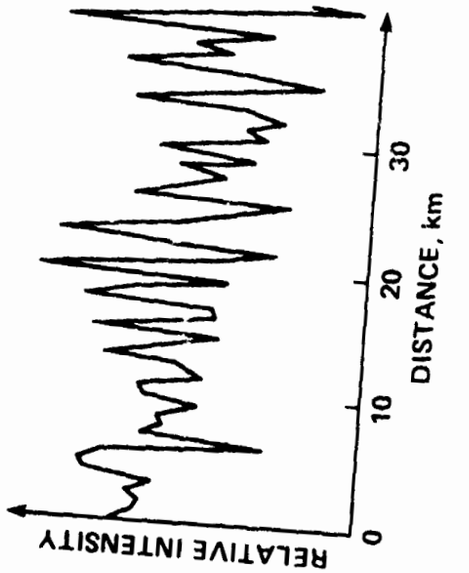

FIG. 1. Sample Ganymede Surface Scan

PEDESTAL CRATERS ON GANYMEDE: INTERIOR MORPHOLOGY

Vicki M. Horner and Ronald Greeley, Department of Geology, Arizona State University, Tempe, AZ 85287

High resolution Voyager images of Ganymede show a class of fresh craters distinguished by ejecta with a sharp terminus (1,2,3; fig. 1). Grooves are sometimes recognizable beneath the ejecta; however, crater interiors appear undisturbed by the grooves. The ejecta thus appears to have conformed to preexisting topography during emplacement. Although earlier named "rampart craters" (4), we suggest that the term "pedestal craters" better describes the appearance of this ejecta morphology.

Our data base consists of 185 craters, ranging in diameter from 6 to 89 km. They were identified from Voyager 1 and 2 images with resolutions from 0.56 to 1.49 km/pixel and solar incidence angles $>40^{o}$. There appears to be no correlation of the normalized ejecta extent (d_e/d_c; the ratio of ejecta diameter to the crater diameter) with latitude or longitude. Although it can be inferred from the data that a correlation exists between d_e/d_c and terrain types (grooved terrain and dark cratered terrain) the difference is not statistically significant (3).

The interior morphology of the craters may provide clues to the relative strength of the impact target (5,6). Figure 2 compares the distribution of central peaks and pits for pedestal craters on Ganymede with martian craters. The percent frequency curve for the distribution of central peaks for martian craters represents the fluidized ejecta craters. The curve for the distribution of central pits for martian craters is comprised of all fresh craters within a region.

Although the frequency of martian craters with central peaks increases over the diameter interval from 5 to 30 km, the frequency of central peaks in Ganymede pedestal craters decreases in this interval from a high of 91% for diameters 10 to 15 km. This can be interpreted either as an effect of differing surface gravities or the result of different target materials. Several researchers (6,7) suggest that gravity has a minimal effect on differences in crater interior features; thus, it appears that target materials of Ganymede are more conducive to the formation of central peaks than are martian target materials.

Figure 2 also shows the distribution of central pit craters on Ganymede and Mars. In general, pit crater frequency increases with diameter; however, on Mars central pits occur in smaller craters.

1. Lucchitta, B.K. (1980) Icarus 44. 481-501.
2. Strom, R.G. et al. (1981) J. Geophys. Res. 86: 8659-8674.
3. Horner, V.M. and R. Greeley (1982) Icarus 51 (in press).
4. Horner, V.M. and R. Greeley (1981) NASA TM 84211, p. 82-84 (abstr.).
5. Cintala et al. (1977) Proc. Lunar Sci. Conf. 8th, p. 3409-3425.
6. Wood, C.A. et al. (1978) Proc. Lunar Planet. Sci. Conf. 9th, p. 3691-3709.
7. Malin, M.C. and D. Dzurisin (1978) J. Geophys. Res. 83: 233-243.
8. Mouginis-Mark, P.J. (1979) J. Geophys. Res. 84: 8011-8022.

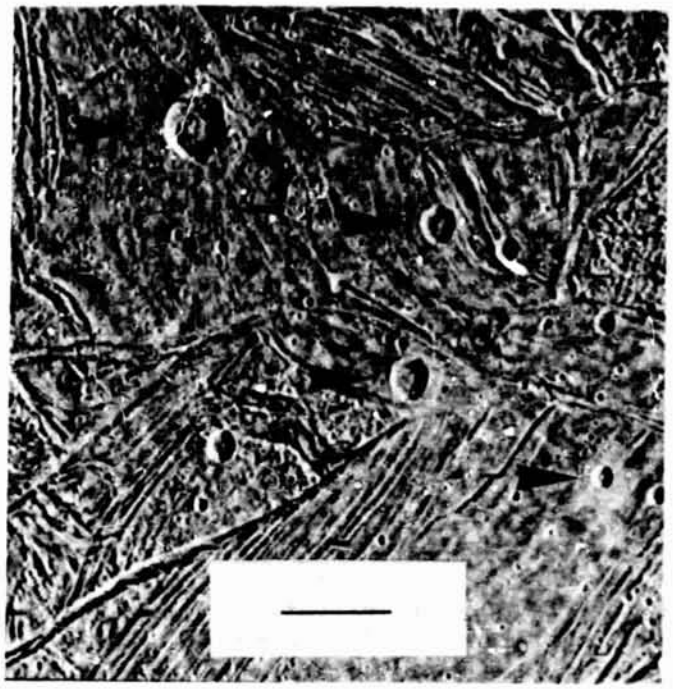

Figure 1. High resolution Voyager 2 image (FDS 20638.59) showing several pedestal craters on Ganymede (arrows). The scale bar represents 50 km.

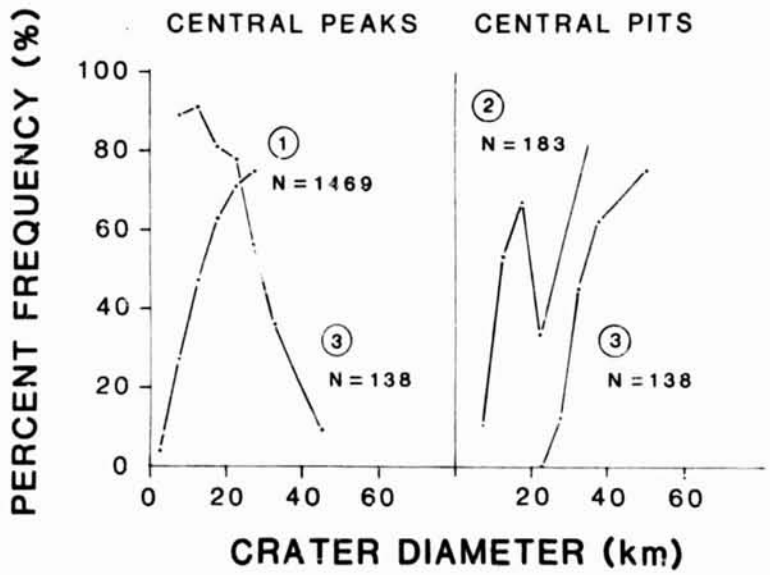

Figure 2. The percent frequency of central peaks and pits for fresh martian craters and Ganymede pedestal craters. (1) is from Mouginis-Mark, 1979, (2) is taken from Wood et al., 1978, and (3) represents the Ganymede pedestal craters. N is the total number of craters involved in each survey. For the pedestal craters, N represents the total number of craters with an unambiguous interior morphology.

EVIDENCE FOR MOBILITY OF WATER ICE ON CALLISTO

John R. Spencer, Lunar and Planetary Lab., University of Arizona
Tucson, AZ 85721

Voyager 1 images of Callisto provide good coverage of the north polar region. These images reveal that many high-latitude craters have an anomalous appearance, in that their south-facing slopes, tilted towards the sun, are darker than their north-facing slopes (figure 1). This effect is present, to a variable extent, in most regions above about 50°N, with anomalously-bright slopes facing fairly consistently northward (figure 2). Voyager 2 images of Callisto do not show high latitudes favorably and, probably for this reason, do not reveal the same phenomenon. Neither spacecraft imaged Callisto's south polar region. Bright north-facing slopes are not readily visible on Voyager Ganymede images either, but again, this may be due to unfavorable viewing geometry.

The likely explanation for this phenomenon is that north facing slopes, because of their lower mean temperatures, have accumulated deposits of a bright volatile, presumably water ice. An adaptation of modelling performed by Squyres (1980) shows that this is a reasonable mechanism. Squyres calculated one-way diurnally-averaged sublimation rates (neglecting re-impact of sublimating molecules) for ice on the Galilean satellites as a function of latitude. Assuming a typical interior crater wall slope of 15°, then for the purposes of temperature determinations, the 'effective latitude' of the north-facing interior wall of a crater at 60°N will be 75°N, and of the south-facing wall, 45°N. Applying Squyres' values for mean sublimation rates at these latitudes, it is clear that there is a large imbalance in the rates on opposite sides of the crater (figure 3). As the mean jump distance for a sublimating molecule is about 50 km (Purves and Pilcher, 1980) greater than the diameter of most Callistoan craters, frost buildup on the south interior wall is almost inevitable given a supply of surface ice and an absence of more effective redistribution processes. The presence of bright deposits on north-facing slopes is thus confirmation that ice migration on Callisto, at least on a local scale, is dominated by insolation-controlled temperature variations.

Theoretical models of ice transport on Callisto (Purves and Pilcher, 1980) predict substantial migration of ice from equatorial to temperate latitudes over the age of the solar system. Callisto's striking visual homogeneity in latitude (figure 4), is thus remarkable, especially when contrasted with Ganymede and its well-developed polar caps. Squyres (1980) attributed the lack of latitudinal brightness variations to a paucity of surface ice available for migration, but the present observations show that Callisto's bright areas, at least, are icy and that the ice is capable of local migration across the surface. In addition, earth-based reflectance spectra of Callisto have been interpreted as indicating a minimum of 30 wt.% free water ice on the surface, intimately mixed with silicates (Clark, 1980). At present, the problem of Callisto's homogeneous appearance is still unresolved - for a full discussion, see Spencer and Maloney (1983).

References

Clark (1980). Ganymede, Europa, Callisto, and Saturn's Rings: Compositional Analysis from Reflectance Spectroscopy. Icarus 44, 388-409.

Davis and Katayama (1981). Coordinates of Features on the Galilean Satellites. J. Geophys. Res. 86, 8635-8657.

Purves and Pilcher (1980). Thermal Migration of Water on the Galilean Satellites. Icarus 43, 51-55.

Spencer and Maloney (1983). Mobility of Water Ice on Callisto: Evidence and Implications. Submitted to Geophys. Res. Lett.

Squyres (1980). Surface Temperatures and Retention of H_2O Frost on Ganymede and Callisto. Icarus 44, 502-510.

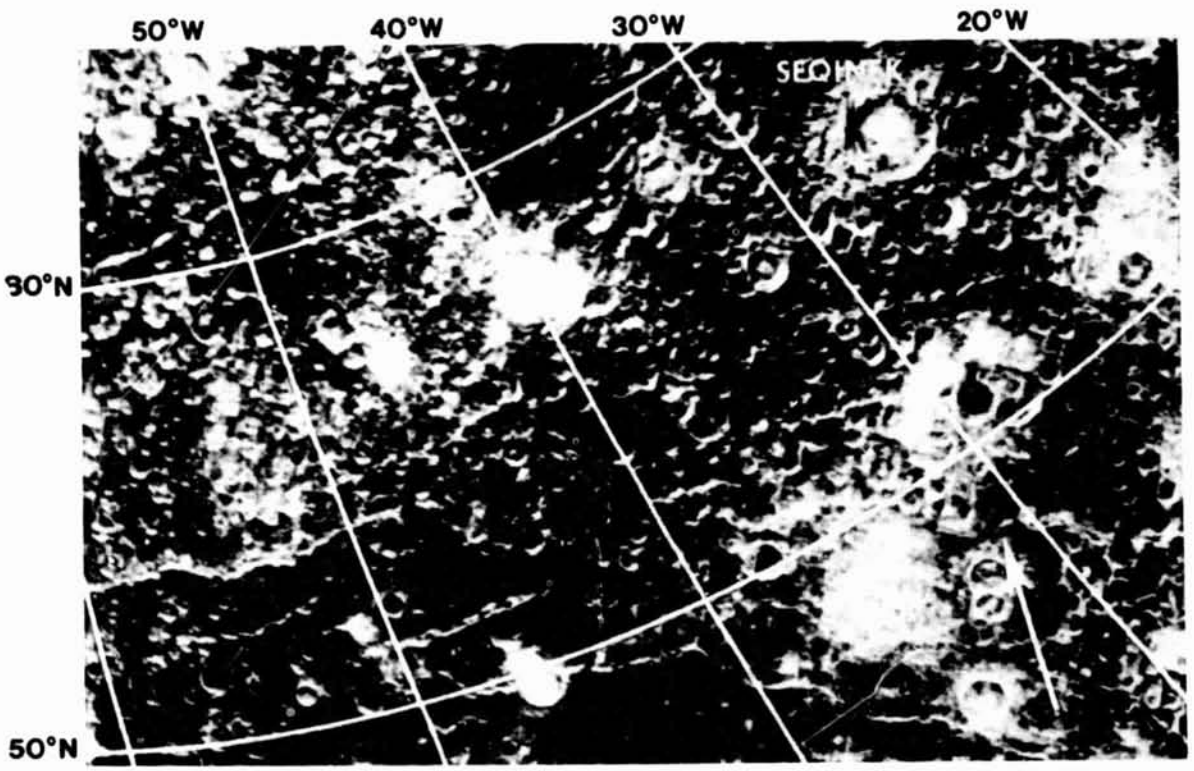

Figure 1 High latitude region of Callisto in the vicinity of the crater Seqinek, showing bright patches on north-facing crater walls, giving the effect of reversed illumination. The true illumination direction is shown by the arrow in the lower right. Distance from top to bottom of the image is about 600 km. Latitude/longitude grid on this and other figures from Davis and Katayama (1981). Portion of Voyager 1 image, FDS 16424.48.

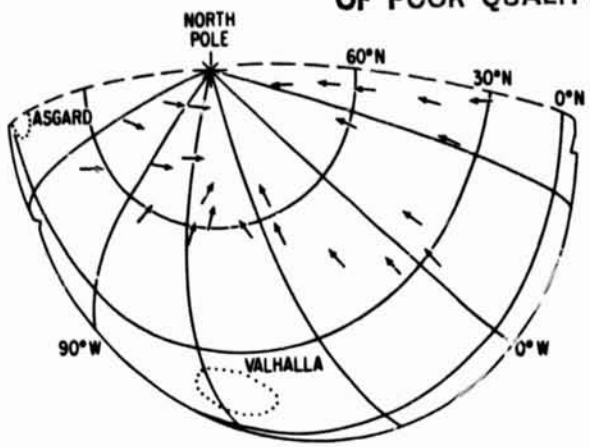

Figure 2 Map showing facing directions of anomalously-bright crater walls on Voyager 1 images of Callisto's northern hemisphere. Gaps in coverage due partly to severe image smear. Based on J.P.L. Callisto mosaic no. 4.

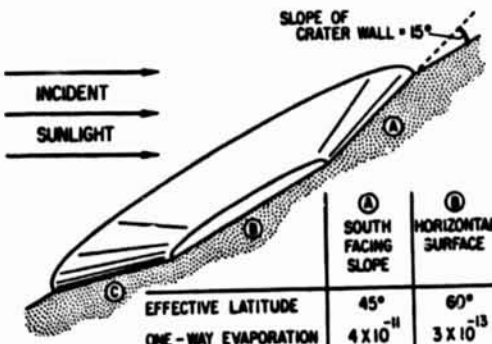

	Ⓐ SOUTH FACING SLOPE	Ⓑ HORIZONTAL SURFACE	Ⓒ NORTH FACING SLOPE
EFFECTIVE LATITUDE	45°	60°	75°
ONE-WAY EVAPORATION RATE g cm^{-2} s^{-1}	4×10^{-11}	3×10^{-13}	3×10^{-17}
TOTAL ONE-WAY EVAPORATION IN 10^9 YEARS	13 km	100 m	10 mm

Figure 3 One-way mean sublimation rates, from Squyres (1980), for various parts of a Callistoan crater at 60°N. Assumed surface ice albedo of 0.13.

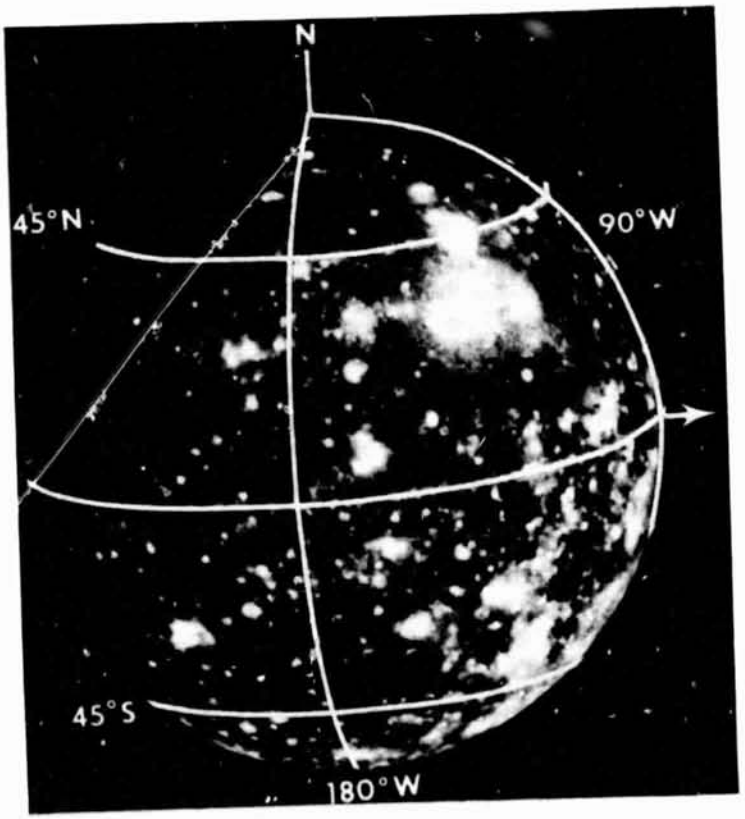

Figure 4 Global view of anti-Jupiter face of Callisto, showing the lack of correlation between surface brightness and latitude. Phase angle is 13°, accounting for the gradual darkening towards the upper left. The apex of orbital motion is indicated by an arrow. Voyager 2 image, FDS 20583.21.

VOYAGER GANYMEDE STELLAR OCCULTATION AND SURFACE ICE TEMPERATURES

John R. Spencer, Lunar and Planetary Lab., University of Arizona
Tucson, AZ 85721

Introduction In the past few years, several papers discussing ice stability and transport on the Galilean satellites have been published (e.g. Lebofsky 1975, Purves and Pilcher 1980, Squyres 1980, Spencer and Maloney, 1983). An uncertainty in these models has always been the actual surface temperature of the ice on the satellite surfaces, which is dependant on ice albedo, emissivity, and thermal properties, none of which are well known. Because of the extreme variation of ice vapor pressure and evaporation rate with temperature, these temperature uncertainties result in large variations in possible transport rates. A direct observational constraint on ice temperature can, however, be obtained by consideration of the tenuous water vapor atmospheres that these bodies must possess due to the finite vapor pressure of the exposed ice.

In the case of Ganymede, an upper limit on the surface pressure of an equilibrium water vapor atmosphere has been obtained from the Voyager 1 UVS stellar occultation. Interpretation of this upper limit, however, requires some knowledge of the behaviour of Ganymede's tenuous, vapor-pressure controlled H_2O atmosphere.

Atmosphere Behaviour A characteristic time for the adjustment of the atmospheric density to changing conditions is given by the ratio of the atmospheric column density to the surface sublimation rate. Both quantities are proportional to vapor pressure, so the adjustment time has no pressure dependance, and can be simply shown to be given by equation 1:

$$t = \frac{4H}{\bar{v}} \qquad (1)$$

Where H is the scale height and $\bar{v}$ the mean atmospheric molecular speed. For a temperature of 150°K, implying a water vapor scale height of 48km, this gives a characteristic time of about 8 minutes. Processes affecting the atmosphere with substantially longer time constants will not greatly disturb atmosphere/surface equilibrium. As Ganymede's rotation period is 7.2 days, the atmosphere can adjust effectively instantaneously to diurnal temperature variations.

Pilcher (1979) considered loss mechanisms for an H_2O atmosphere around Io. He concluded that thermal escape would be negligable, and that UV photolysis would remove molecules with a time constant of about 40 days. He also predicted loss rates due to sputtering by charged particles in Jupiter's magnetosphere that are several orders of magnitude smaller than the rates of thermal evaporation from the surface. Loss by this mechanism at Ganymede should be smaller still. Therefore, in the absence of other major loss mechanisms, Ganymede's H_2O atmosphere should be in equilibrium with the surface below it at all times.

Equilibrium entails the surface atmospheric pressure being equal to the vapor pressure of the exposed ice, and this is true whether the ice is continuous or segregated into patches surrounded by non-volatiles. The reason is that at equilibrium the downward flux of molecules impacting the surface will be the same for both the icy and non-volatile regions,

provided that the scale of segregation is smaller than the mean molecule jump distance, which is about 50 km (Purves and Pilcher, 1980). This flux will equal the upward flux from the ice patches, which is determined solely by the ice vapor pressure and thus temperature.

The surface pressure of Ganymede's H_2O atmosphere at any point on the surface can thus be used as a probe of ice temperature, without requiring assumptions about the ice's emissivity, thermal properties, detailed surface distribution, or albedo. Ice vapor pressure as a function of temperature in the temperature range of interest has been determined experimentally by Bryson et. al. (1974). Their data is shown in figure 1, together with the extrapolated curves from the International Critical Tables (1926-1933) and the CRC Handbook of Chemistry and Physics (1971) that have been used in previous studies of ice stability and mobility.

Voyager Stellar Occultation by Ganymede Occultation ingress occurred at $12.1^{o}S$, $13.5^{o}W$, at a local time of 1:30 pm (Ganymede hours) over a mixture of bright and dark terrain (figure 2). Assuming a water vapor atmosphere at $150^{o}K$, an upper limit on the surface pressure of about 3×10^{-8} mbar can be derived. (All data from B.R. Sandel, pers. comm.) This limit is only a weak function of the assumed temperature. Using the Bryson et. al. vapor pressure curve, this gives an upper limit to the surface ice temperature in this region of $146^{o}K$. Figure 3 compares this temperature upper limit to various theoretical estimates of the surface temperature at this latitude and time of day on Ganymede's surface. Equilibrium temperature is shown for two different possible emissivities, as a function of albedo, which varies with terrain type and incidence angle. The occultation occurred at a solar incidence angle of 26^{o}, at which the average albedos are about 0.26 and 0.32 for cratered and grooved terrain respectively (Squyres 1980, 1981). Temperatures for average light grooved and dark cratered terrain, derived from the thermal modelling of Squyres (1981) are also indicated.

The occultation-derived upper limit to the ice temperature is slightly below all these theoretical estimates. A likely reason for this is that the ice is somewhat segregated into bright patches so that its albedo is higher, and its temperature lower, than the 'average' surface. With the current data the degree of segregation and consequent lowering of ice temperature cannot be ascertained, but further data on the atmospheres of Ganymede and the other Galilean satellites, from Galileo for instance, could powerfully constrain ice temperatures and, consequently, models of surface ice transport.

Acknowledgement I wish to thank Dr. B.R. Sandel for generously providing and reducing unpublished Voyager UVS data necessary for this study.

References

Bryson, Cazcarra, and Levenson (1974). Sublimation Rates and Vapor Pressures of H_2O, CO_2, N_2O, and Xe. J. Chem. Eng. Data 19, 107-110

Handbook of Chemistry and Physics (1971). The Chemical Rubber Company, Cleveland, Ohio

International Critical Tables of Numerical Data, Physics, Chemistry, and Technology (1926-1933). National Research Council

Lebofsky (1975). Stability of Frosts in the Solar System. Icarus 25 205-217

Pilcher (1979). The Stability of Water on Io. Icarus 37 559-574

Purves and Pilcher (1980). Thermal Migration of Water on the Galilean Satellites. Icarus 43 51-55

Spencer and Maloney (1983). Mobility of Water Ice on Callisto: Evidence and Implications. Submitted to Geophys. Res. Lett.

Squyres (1980). Surface Temperatures and Retention of H_2O Frost on Ganymede and Callisto. Icarus 44 502-510

Squyres (1981). The Morphology and Evolution of Ganymede and Callisto. PhD. Thesis, Advances in Planetary Geology NASA TM 84412

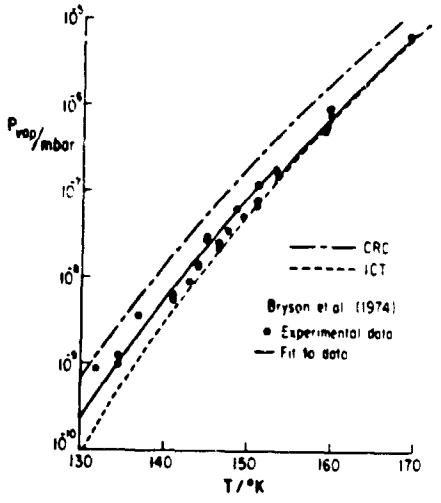

Figure 1 H_2O vapor pressure as a function of temperature. The expressions given in the 1971 CRC Handbook and the International Critical Tables, extrapolated from higher-temperature data, are compared with the experimental data of Bryson et. al. and curves fitted to this data. The break in the fitted curve corresponds to an assumed ice phase change at 153° K

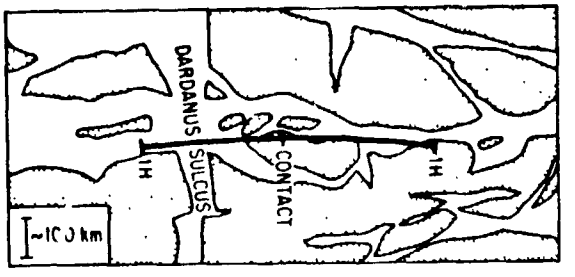

Figure 2 Map of the ingress region for the Voyager UVS stellar occultation by Ganymede. The light-path at occultation is shown up to one scale-height above the surface at either side of the contact point. Dark terrain is stippled. Mean molecular jump distance is about 50 km, so atmospheric pressure will not affect surface ice temperature variations on scales much smaller than 50 km. Taken from Voyager I image FDS 164[illegible].22

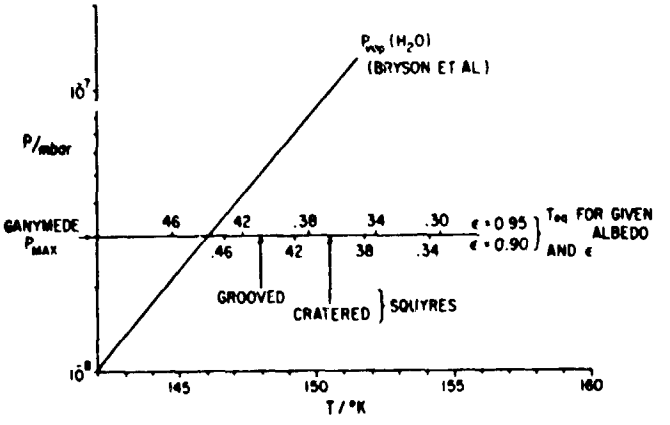

Figure 3 Comparison of the Bryson et. al. H_2O vapor pressure curve with the deduced upper limit for H_2O atmospheric pressure at the occultation point, and various theoretical surface temperatures. See text for full description.

ABSOLUTE AGES AND FLUX HISTORY FOR THE SATURNIAN SATELLITES

J.B. Plescia, Jet Propulsion Laboratory, California Institute of Technology, Pasadena, CA 91109
J. M. Boyce, NASA Headquarters, Washington, D.C. 20546

Previously we have reported the results of the crater density determinations for the various terrain types on the Saturnian satellites: Mimas, Tethys, Dione, Rhea (Plescia and Boyce 1982a) and Hyperion, Tethys, Enceladus and Iapetus (Plescia and Boyce 1982b). Thus, we have established the relative chronologies for the major events on each body. A more complete understanding of the geologic histories of the Saturnian satellites requires an estimation of the absolute flux rate of impacting bodies over time. In this way observed crater densities can be correlated with absolute time.

Several effects must be taken into account in order to compare crater densities between satellites. These include the gravitational focusing of projectiles by Saturn (Smith et al., 1982), a gradient in the cratering rate from the apex to antapex of motion on a tidally locked satellite (Shoemaker and Wolfe, 1981, Smith et al., 1981, 1982) and the viscous relaxation of large crater topography (Johnson and McGetchin, 1973). The gravitational focusing effect of Saturn produces an increase in the cratering rate with decreasing orbital radii such that the rate on Mimas in approximately 20 times that on Iapetus. Table I lists observed crater densities for various satellite surfaces, while Table II lists the same data after correction for the focusing effect nomalized to the flux at Iapetus. The gradient in cratering rate from the apex to antapex and viscous relaxation do not appear to have affected the macroscopic craters viewed on the satellites.

In developing a theoretical cumulative flux history we have made several assumptions. These include, first that the shape of the curve resembles that of the Moon (Neukum and Wise, 1976) - An initial rapid decay of the impact flux over the first few hundred million years until about 3.85 b. y. ago then a linear decrease to zero over the subsequent period. The second assumption is that Population I craters were produced during the initial rapid fall off and that Population II craters formed during the subsequent period of linear decay. The location of the bend in the curve is based upon the density at which the slopes of the observed cumulative size-frequency distributions indicate a change from Population I to II. For craters larger than 20 km diameter this is about 25 craters/10^6 km^2. These assumptions are supported by results from outer solar system orbit evolution studies (Shoemaker and Wolfe, 1981).

Using the crater densities listed in Table II and the flux history outlined above; the ages listed in Table II are indicated. These data suggest that the majority of satellites have ancient surfaces, in excess of 3.8 b. y..

Rhea, Mimas, Tethys, Hyperion, and Iapetus all have ancient surfaces. Any internal activity which occurred on those bodies transpired over a very short period of time, just a few hundred million years after formation. Enceladus has had a prolonged geologic history extending over billions of years, with the oldest regions being nearly 3.8 b. y. old and the youngest craterless areas being no more than a few hundred million years. Two intermediate age plains units on Enceladus are expected to be about 1.7 and 3.0 b. y. old. Dione has had a history that extended over a relatively shorter period of time. The youngest unit on Dione, material associated with the fractures, is estimated to be about 3.25 b. y. old. The intermediate unit is about 3.6 b. y. old and the oldest unit about 3.9 b. y. old. The relatively young age for the south pole of Mimas represents a resurfacing event which occurred about 3.7 b. y. ago. This probably represents a large impact event rather than an internally driven process. The young age for the co-orbital 1980S3 most likely records the impact event which split a larger object into the two smaller co-orbitals.

A comparison of the Lunar flux history with the Saturnian satellite impact flux history proposed here suggests that the flux of impacts was significantly lower in the Saturnian system, i.e., a factor of 2-3 lower at Mimas than on the Moon. This is consistent with orbital evolution calculations made recently by Shoemaker (oral communication) for outer solar system debris.

REFERENCES:

Johnson, T.V. and McGetchin, T.R., Icarus 18, 612-620 (1973).

Neukum, G. and Wise, D.U., Science (94, 1381-1386 (1976)

Plescia, J. B. and Boyce, J. M., Nature 295, 285-290 (1982a).

Plescia, J. B. and Boyce, J. M., submitted to Nature (1982b).

Shoemaker, E. M. and Wolfe, R., Abstr. 12th Lunar Planet. Sci. Conf. Suppl. A, 1-3 (1981).

Smith, B. A., et al., Science 212, 163-191 (1981).

Smith, B. A., et al., Science 215, 504-537 (1982).

TABLE I

DENSITIES PER 10^6 KM^2

SATELLITE		5	10	20	30	40	50	M
IAPETUS	H.C.		4500 ± 75	740 ± 30	205 ± 16	110 ± 12	68 ± 9	- 2.6
HYPERION	H.C.		940 ± 135	150 ± 58	60 ± 37	30 ± 26	18 ± 20	- 2.2
RHEA	H.C.		1400 ± 186	320 ± 89	125 ± 56	55 ± 37	32 ± 28	- 2.4
	I.C.		1200 ± 96	230 ± 42	80 ± 25	40 ± 18	25 ± 14	- 2.4
	L.C.		900 ± 119	160 ± 50	47 ± 27	25 ± 20	14 ± 15	- 2.7
	L.C.		480 ± 109	90 ± 47	35 ± 29	18 ± 21	10 ± 15	- 2.0
	BLK.		160 ± 43	15 ± 13	4 ± 7	-	-	- 3.5
DIONE	H.C.		780 ± 86	275 ± 51	100 ± 31	45 ± 21	42 ± 20	- 1.7
	I.C.		750 ± 98	45 ± 24	8 ± 10	3 ± 6	1 ± 4	- 4.1
	L.C.		260 ± 51	23 ± 15	6 ± 8	2 ± 5	1 ± 3	- 3.3
TETHYS	H.C.		2000 ± 135	500 ± 92	225 ± 62	120 ± 45	80 ± 37	- 1.9
	H.C.		690 ± 72	170 ± 36	85 ± 25	45 ± 18	28 ± 14	- 2.0
	L.C.		1000 ± 98	125 ± 34	35 ± 18	15 ± 12	3 ± 9	- 3.0
ENCELADUS	H.C.	4100 ± 455	300 ± 201	220 ± 105	100 ± 71	54 ± 52	34 ± 41	- 2.0
	I.C.	2400 ± 774	420 ± 324	85 ± 146	32 ± 89	18 ± 67	10 ± 50	- 2.4
	L.C.	1300 ± 355	175 ± 130	32 ± 56	12 ± 34	6 ± 24	3 ± 17	- 2.4

SATELLITE		5	10	20	30	40	50	M
MIMAS	R.C.		10000 ± 295	1100 ± 69	350 ± 39	105 ± 21	80 ± 19	- 3.0
	I.C.		1100 ± 178	290 ± 91	68 ± 44	45 ± 36	26 ± 27	- 2.3
	S.P.		1403 ± 174	230 ± 70	28 ± 25	22 ± 22	11 ± 15	- 2.7
CO-ORBITALS 1980S3			3000 ± 717	640 ± 331	200 ± 211	135 ± 152	80 ± 117	- 2.3
1980S1			1450 ± 603	210 ± 231	70 ± 134	35 ± 94	20 ± 72	- 2.3
			2900 ± 484	650 ± 229	270 ± 148	130 ± 103	75 ± 78	- 2.3

TABLE III

SATELLITE		DENSITIES PER 10^6 KM^2 5	10	20	30	40	50	M
IAPETUS	H.C.		4500 ± 75	740 ± 30	205 ± 16	110 ± 12	68 ± 9	- 2.6
HYPERION			336 ± 59	66 ± 25	25 ± 16	13 ± 11	8 ± 9	- 2.2
RHEA	H.C.		882 ± 117	202 ± 50	79 ± 35	35 ± 23	20 ± 18	- 2.4
	I.C.		756 ± 60	145 ± 26	50 ± 16	25 ± 11	16 ± 9	- 2.4
	L.C.		567 ± 75	101 ± 32	30 ± 17	16 ± 13	9 ± 10	- 2.7
	L.C.		302 ± 69	57 ± 30	22 ± 18	11 ± 13	6 ± 10	- 2.0
	BLK.		100 ± 27	10 ± 8	3 ± 4	-	-	- 3.3
DIONE	H.C.		226 ± 25	80 ± 15	29 ± 9	13 ± 6	12 ± 6	- 1.7
	I.C.		313 ± 28	13 ± 7	2 ± 3	1 ± 2	-	- 4.1
	L.C.		75 ± 15	7 ± 4	2 ± 2	-	-	- 3.3
TETHYS	H.C.		308 ± 34	92 ± 17	41 ± 11	22 ± 8	15 ± 7	- 3.3
	H.C.		127 ± 13	31 ± 5	16 ± 5	8 ± 3	5 ± 7	- 2.0
	L.C.		190 ± 19	24 ± 6	7 ± 3	3 ± 2	2 ± 2	- 3.0
ENCELADUS	H.C.	324 ± 36	63 ± 16	17 ± 8	8 ± 6	4 ± 4	3 ± 3	- 2.3
	I.C.	190 ± 61	33 ± 26	6 ± 12	25 ± 7	1 ± 5	0.8 ± 4	- 2.7
	L.C.	103 ± 38	14 ± 10	3 ± 4	1 ± 3	0.5 ± 2	0.2 ± 1	- 2.3

MIMAS	H.C.	494 ± 15	55 ± 4	17 ± 2	5 ± 1	4 ± 1	- 3.0
	I.C.	55 ± 9	15 ± 5	3 ± 2	2 ± 2	1 ± 1	- 2.3
	S.P.	70 ± 9	12 ± 4	1 ± 1	1 ± 1	-	- 2.7
CO-ORBITALS							
1980S3		90 ± 22	19 ± 10	6 ± 6	4 ± 5	2 ± 4	- 2.3
		43 ± 20	7 ± 8	2 ± 4	1 ± 3	0.7 ± 2	- 2.3
1980S1		87 ± 15	30 ± 7	8 ± 4	4 ± 3	2 ± 2	- 2.3

VOYAGER PHOTOMETRY OF SATURN'S SATELLITES

B. Buratti, J. Veverka, P. Thomas, Laboratory for Planetary Studies,
Cornell University, Ithaca, NY 14853

Saturn's satellites exhibit a wide range of albedos (0.05-1.0) and of surface scattering properties (Table 1). Figure 1 shows the normalized disk-integrated phase curves of Enceladus, Mimas, Tethys, Dione, and Rhea derived from Voyager imaging observations. In Figure 2 these phase curves are compared with those of Europa, Ganymede, Callisto, and the Earth's moon. There is a general tendency for darker objects (Moon, Callisto) to have steeper phase curves than brighter bodies (Enceladus, Europa).

Since the brightness of the satellites varies with orbital longitude, the data in Figure 1 have been corrected for this effect using the method of Noland et al. (1974). Rotational brightness variations derived from Voyager data for Rhea, Dione, and Tethys agree well with telescopic observations (Franz and Millis, 1975; Noland et al. (1974); those of Mimas and Enceladus, which were poorly known from Earth, are shown in Figure 3. Voyager observations indicate that the amplitudes of the rotational lightcurves of these two objects do not exceed 0.20 magnitudes (about 20%).

While the photometric properties of Phoebe, and even Dione and Rhea, can be adequately described by a lunar-like scattering law, those of Tethys, Mimas, and especially Enceladus, are more complicated and involve significant Lambert-like components. Figure 3 shows scans across the photometric equators of Rhea and Enceladus. If the data are fitted using a simplified photometric function of the form

$$I/F = Af(\alpha)\,\frac{\mu_o}{\mu + \mu_o} + (1 - A)\,\mu_o$$

TABLE 1. Disk-integrated Properties: Voyager Clear Filter ($\sim$ 0.47 μm)

	Geometric albedo, p	Phase Integral, q	pq	Phase Coefficient (mag/deg)
Mimas	0.6 ± 0.1	0.8 ± 0.1	0.5 ± 0.1	0.021 ± 0.001
Enceladus	1.0 ± 0.1	0.8 ± 0.1	0.8 ± 0.1	0.017 ± 0.002
Tethys	0.71 ± 0.07	0.9 ± 0.2	0.6 ± 0.2	0.014 ± 0.002
Dione	0.47 ± 0.08	0.5 ± 0.1	0.2 ± 0.1	0.023 ± 0.002
Rhea	0.53 ± 0.05	0.46 ± 0.06	0.2 ± 0.1	0.016 ± 0.002
Phoebe	0.060 ± 0.005* 0.046 ± 0.005	$\sim$ 0.4	$\sim$ 0.02	0.033 ± 0.001 0.036 ± 0.002

*Values correspond to the brighter and darker areas of Phoebe (Thomas et al., 1982).

where I/F is the fraction of reflected radiation, $f(\alpha)$ is the phase function, μ_0 and μ are the cosines of the incident and emission angles, and A is a parameter such that A = 1 corresponds to a lunar photometric function and A = 0 corresponds to a Lambert function, we find that for Rhea A = 1.0 is a good fit, whereas for Enceladus the best fit is 0.30.

The photometric properties of Enceladus have been studied in detail to search for photometric differences among the different geologic terrains. We find a marked uniformity of albedoes, colors, and scattering properties over Enceladus' geologically varied surface. Although some albedo variations of up to 10% occur in low-resolution Voyager 1 images, the albedoes of the four major geological units imaged in the Voyager 2 near-encounter sequence (cratered terrain, cratered plains, ridged plains and smooth plains) differ by 1-2% or less, even though the ages of these units probably differ by more than a factor of ten (4.5 to 0.1 billion years?). The lack of correlation of spectrophotometic properties with terrain type suggests that the optical characteristics of Enceladus are determined by an ubiquitous surface layer of relatively recent age. The high geometric albedo implies that the surface layer is remarkably free of opaque material and is much more backscattering than is common for natural or laboratory frost layers on Earth.

This research was supported by NASA Grant NSG 7156.

REFERENCES:

1. Buratti, B., and Veverka, J. (1982). Voyager Photometry of Europa. Submitted to Icarus.
2. Franz, O. G., and Millis, R. L. (1975). Icarus 24, 433-442.
3. Lane, A. P., and Irvine, W. (1973). Astron. J. 78, 267-277.
4. Noland, M., Veverka, J., Morrison, D., Cruikshank, D. P., Lazarewicz, A. R., Morrison, N. D., Elliot, J. L., Goguen, J., Burns, J. A. (1974). Icarus 23, 334-354.
5. Squyres, S., and Veverka, J. (1981). Icarus 46, 137-155.
6. Thomas, P., Veverka, J., Morrison, D., Davies, M., Johnson, T.v. (1982). Voyager Observations of Phoebe. Submitted to J. Geophys. Res.

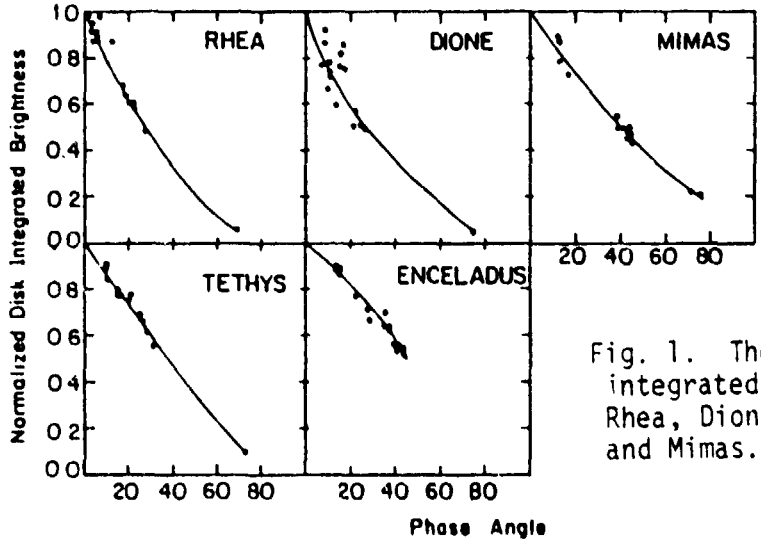

Fig. 1. The normalized disk-integrated phase curves of Rhea, Dione, Tethys, Enceladus, and Mimas.

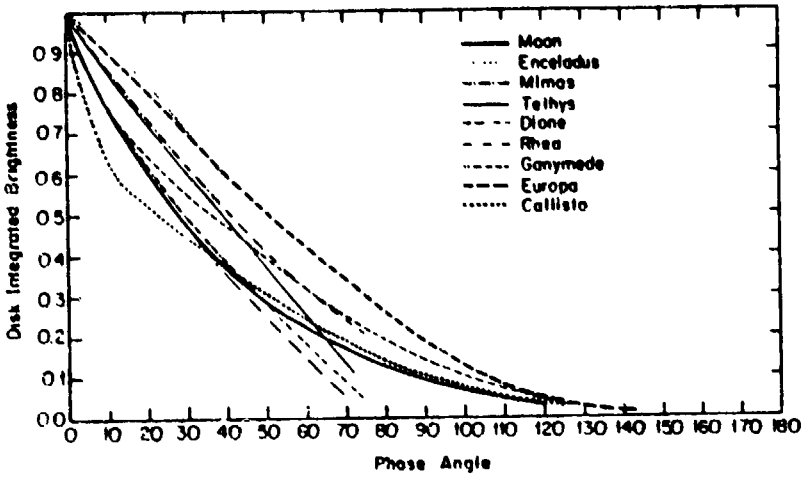

Fig. 2. Comparison of the phase curves in Fig. 1 with those of Europa, Ganymede, Callisto, and the Moon. The data for Ganymede and Callisto are from Squyres and Veverka (1981), the lunar data from Lane and Irvine (1973), and the Europa curve from Buratti and Veverka (1982).

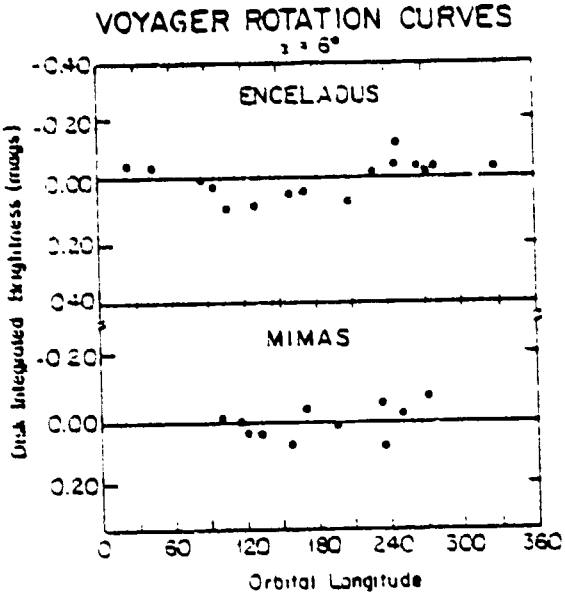

Fig. 3. Brightness variations (in magnitudes) as a function of orbital longitude for Enceladus and Mimas derived from Voyager images. All measurements have been corrected to a phase angle of 6° using the phase coefficients listed in Table 1.

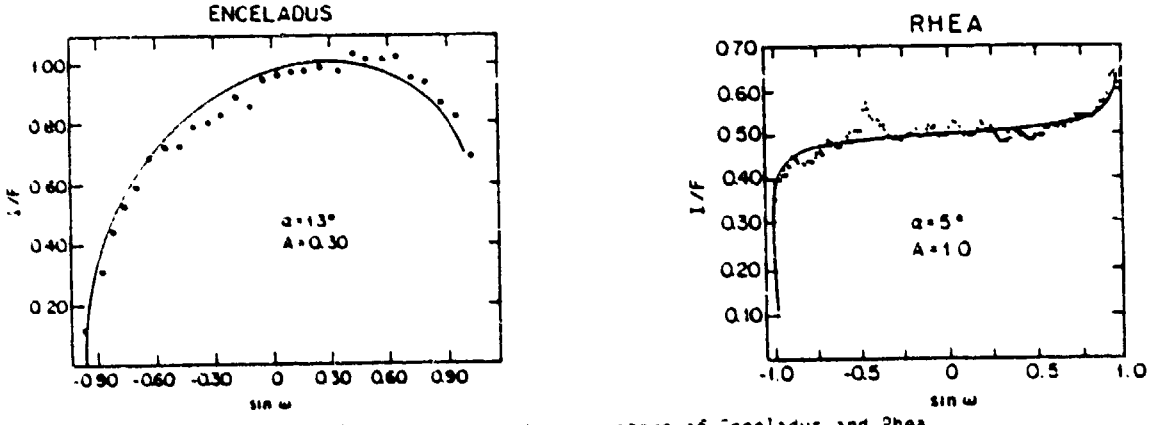

Fig. 4. Scans along the photometric equators of Enceladus and Rhea. The photometric longitude is denoted by ω. A) Enceladus: phase angle = 13° (FDS 43967.52). B) Rhea: phase angle = 5° (FDS 34925.38)

THE ALBEDO MARKINGS OF IAPETUS

Steven W. Squyres, NASA Ames Research Center, Moffett Field, CA, and Carl Sagan, Cornell University, Ithaca, NY 14853.

Voyager images of Saturn's moon Iapetus (1,2) confirm deductions made from Earth-based observations of a very dark leading hemisphere and a very bright trailing hemisphere (3,4). The darkest area lies at the apex of orbital motion, with a gradual increase in albedo toward the antapex. The trailing hemisphere is substantially (about 10 times) brighter than the apex, and the poles somewhat brighter still. The observed albedo distribution resembles the calculated areal variation of the trans-saturnian meteorite flux (5) remarkably closely. Dark areas correspond to regions with the highest calculated flux. While there is at least one dark-floored crater on the bright trailing hemisphere, no bright-floored craters are apparent anywhere on the dark leading hemisphere.

Several hypotheses have been proposed to account for the albedo asymmetry of Iapetus. Cook and Franklin (5) suggested impact erosion of a thin ice veneer from the leading hemisphere of a dark essentially silicate body. But Voyager measurements show the density of Iapetus to be 1.16 ± 0.09 g cm^{-3} (2), indicating a bulk composition of ice, not silicates. Soter (6) suggested that the leading hemisphere is coated with dark material ejected from Phoebe by impacts and dragged toward Saturn by the Poynting-Robertson effect. This hypothesis is inconsistent with both the large color differences between Iapetus and Phoebe (7) and with the observation of dark-floored craters on the trailing hemisphere. Smith *et al.* (2) have suggested that dark carbonaceous material may have been extruded to the surface preferentially on the leading hemisphere. However, for the pattern of eruptive material to so closely match that of the meteorite flux would require a coincidence of remarkable proportions. The dense N_2-CH_4 atmosphere of Titan implies that NH_3 and CH_4 were incorporated in that body when it formed. It is likely, then, that Iapetus contains significant amounts of methane and ammonia, as $CH_4 \cdot XH_2O$ and $NH_3 \cdot H_2O$. We propose that the dark material on Iapetus is composed of organic chromophores produced from CH_4-rich ice.

Surface material on Iapetus will experience ballistic diffusion from regions of high impact flux to regions of low impact flux. Depending on the amount of material coming from Phoebe, the impact mass flux may vary from leading to trailing hemisphere by as little as a factor of 2 or as much as a factor of 100. The low gravitational acceleration of Iapetus allows impact ejecta to travel large distances. Particles on the leading hemisphere will have a high probability of being ejected and landing on the trailing hemisphere, but a smaller probability of being returned by subsequent impacts to the leading hemisphere. The impact flux gradient across the body will therefore result in a net ablation of material from the leading hemisphere and a net accumulation of impact ejecta on the trailing hemisphere. Because $CH_4 \cdot XH_2O$ is much more volatile than the other ices, the net result of many impacts will be to strongly deplete any

accumulated regolith in CH_4.

Ultraviolet irradiation of water ice and simple organic ices at Iapetus ambient temperatures (about 77°K) is known to yield a variety of more complex organic products (8); despite the low temperature there is substantial free radical mobility. Visible wavelength organic chromophores that might be expected to form on prolonged UV irradiation of $CH_4/NH_3/H_2O$ ices on Iapetus include conjugated polyenes, polyaromatic hydrocarbons, and porphyrins. We calculate that very modest quantum yields are required to allow UV darkening to keep pace with ablation by impacts on the leading hemisphere.

A thin dark layer rich in organics can be maintained only on a surface that experiences no net accumulation of impact ejecta. This is because, after a sufficient number of impacts, the ejecta will have been distilled by the impact process, depleting it of CH_4 and leaving it permanently bright. Where net ablation takes place, the surface will be dark, as ice not depleted in CH_4 is continually exposed to UV irradiation by removal of overlying material. Where net deposition takes place the surface will be bright, as the accumulating material will have been depleted in CH_4. The process determining whether ablation or deposition dominates is ballistic diffusion, driven by the impact flux gradient. Because the albedo of a surface element depends on the relative rates of exposure of CH_4-rich darkenable ice and of deposition of CH_4-poor non-darkenable ice, the surface albedo contours should follow the impact flux contours, as observed. The dark-floored crater on the trailing hemisphere may be readily understood of it is a young feature: an impact has relatively recently penetrated the bright regolith, exposing CH_4-rich ice which has been UV-darkened but which has not yet had time to be buried under bright debris.

The surfaces of the uranian satellites probably also contain CH_4 and NH_3, so that the darkening process proposed here may function there as well. Because there is no known source of retrograde debris in the uranian system, these satellites should lack the strong albedo asymmetry of Iapetus. Low albedos have in fact been reported very recently for several of the uranian satellites (9). Conceivably, UV darkening is also responsible for the very low albedo of the uranian rings, as the very low gravitational acceleration of the ring particles would prevent accumulation of a CH_4-depleted regolith. There will be an opportunity to investigate these possibilities when Voyager 2 encounters Uranus in 1986.

References:

(1) Smith, B.A., et al. Science 212, 163-191 (1981).

(2) Smith, B.A., et al. Science 215, 504-537 (1982).

(3) Cassini, J.D. Phil. Trans. Roy. Soc. 8, 5178 (1671).

(4) Morrison, D. et al. Icarus 24, 157-171 (1975).

(5) Cook, A.F., & Franklin, F.A. Icarus 13, 282-291 (1970).

(6) Soter, S., paper presented at the IAU Planetary Satellite Conference, Cornell University, Ithaca, N.Y. 1974.

(7) Cruikshank, D.P., et al., paper presented at the International Colloquium on the Saturn System, Tucson, AZ, 1982.

(8) Sagan, C., & Khare, B.N. In Molecules in the Galactic Environment, M. Gordon & L. Snyder, eds. (New York: John Wiley, 1973).

(9) Brown, R.H., et al. Nature, in press.

PHOEBE: VOYAGER OBSERVATIONS

P. Thomas and J. Veverka, Laboratory for Planetary Studies, Cornell University; D. Morrison, University of Hawaii; M. Davies, Rand Corporation; T. V. Johnson, Jet Propulsion Laboratory.

Voyager 2 obtained images of Phoebe for a period of 24 hours from a range of 2 x 10^6 km. These data provide information on the size, rotation rate, surface markings, and photometric properties unavailable from earth-based observations. The average equatorial and polar diameters are 220 ± 20 km, but topography of 10-20 km probably exists. The rotation was monitored by observation of bright spots and by disk-integrated brightness variations (Fig. 1), yielding a prograde period of 9.4 ± 0.2 hours. Because of the limited resolution of the images (11 pixels across the disk) crater counts cannot be made, but a high crater density cannot be ruled out. The geometric albedo of Phoebe varies with longitude from 0.046 to 0.060 (clear filter, λ = 0.47 μm) (Table 1). The most prominent surface markings are brighter patches at high northern and southern latitudes that have reflectances as much as 50% greater than the dark, bland areas. These patches are scattered and do not appear to constitute polar caps. They may represent materials exposed by impacts. Even the brightest have reflectances of less than < 12%. The Voyager color data (Fig. 2) agree with earlier ground-based spectra and show that Phoebe has a flatter spectrum than does the dark side of Iapetus; this observation is not consistent with simple contamination of Iapetus by debris from Phoebe.

This research is supported by NASA Grant NSG 7156.

TABLE 1: Phoebe Photometric Results
(Voyager Clear Filter: 0.47 μm)

	Geometric Albedo	Phase Coefficient mag/deg	
Bright Hemisphere	0.060	0.033	disk-integrated
Dark Hemisphere	0.046	0.036	disk-integrated
Bright Equatorial	0.055	0.022	intrinsic
Dark Equatorial	0.043	0.025	intrinsic

Lightcurve Amplitude	
α = 0°	0.29 mag
α = 24°	0.36 mag

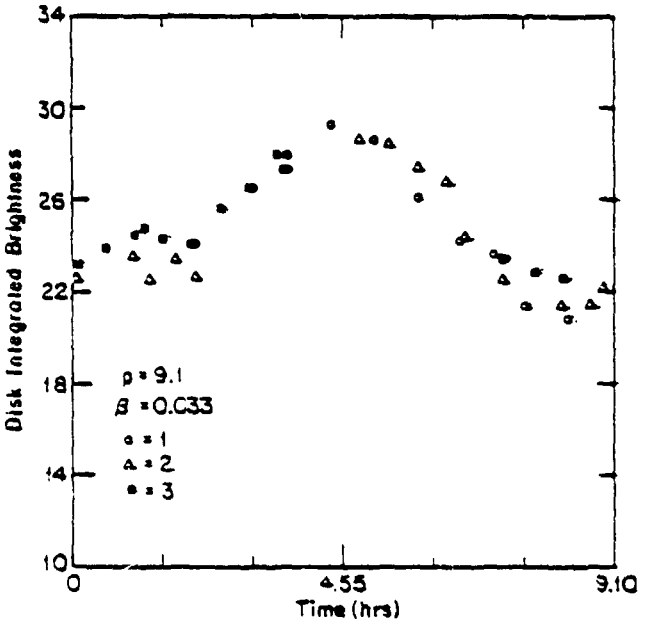

Fig. 1: Disk-integrated lightcurves of Phoebe. Numbered symbols refer to successive rotations. Period = 9.1 hours relative to spacecraft, corresponding to a sidereal period of 9.4 hours.

a) Assuming a phase coefficient of $\beta = 0.033$ mag/deg appropriate to the brighter areas on Phoebe (Table 1).

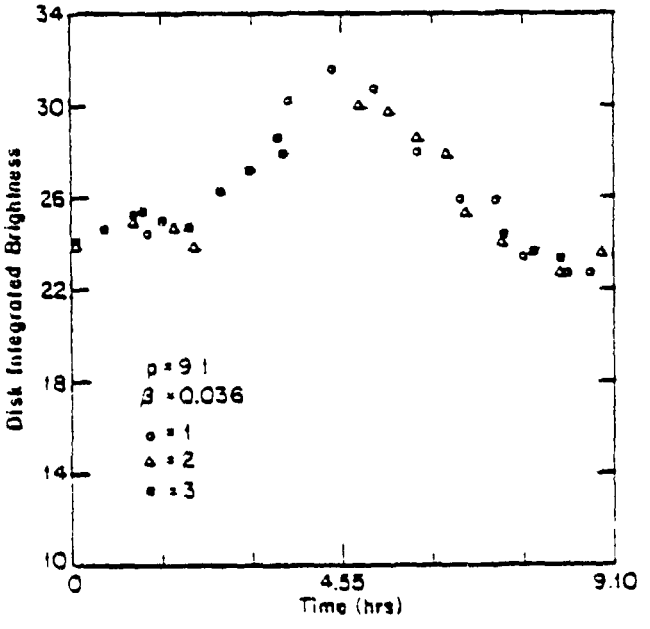

b) Assuming a phase coefficient of $\beta = 0.036$ mag/deg appropriate to the darker areas (Table 1).

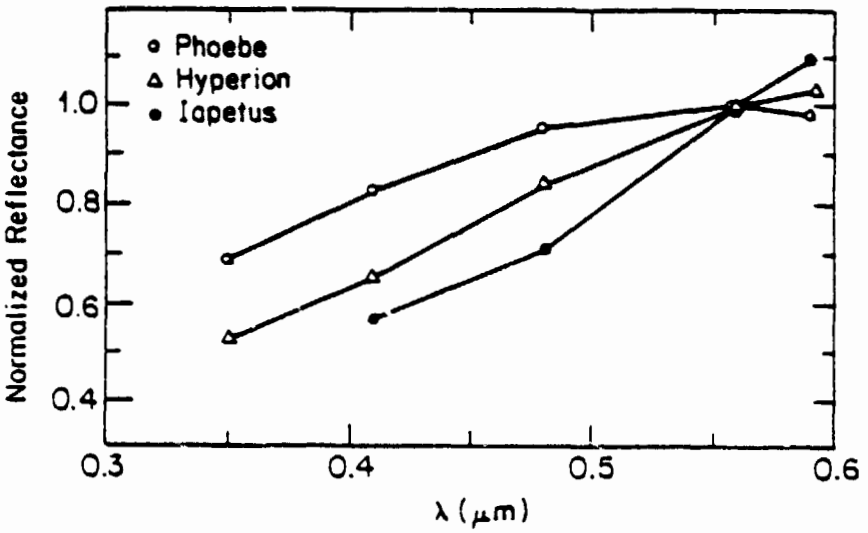

Fig. 2: Colors of Phoebe, Hyperion, and dark region of Iapetus, normalized to Voyager green filter. All Voyager 2 data.

Chapter 2

ASTEROIDS AND COMETS

The United Kingdom - Caltech Asteroid Survey

S. J. Bus, E. F. Helin, R. S. Dunbar, and E. M. Shoemaker
California Institute of Technology

J. Dawe, J. Barrow, M. Hartley, D. Morgan, K. Russell and A. Savage
Royal Observatory of Edinburgh

The U.K.-Caltech Asteroid Survey (UCAS) is a systematic survey for faint minor planets carried out with plates taken with the U.K. 48-inch Schmidt telescope at Siding Spring, Australia. The long-term goal of the survey is to establish accurate orbits for about 1,000 faint asteroids sufficient for their recovery and for physical observations at any time in the future (orbits meeting the requirements for numbering and for yearly publication of ephemerides). One immediate objective is to estimate the population of faint Mars-crossing asteroids with the precision needed to calculate collision and cratering rates on Mars, and thereby to establish the absolute chronology of the cratering and geological time scales on Mars. Longer term objectives include determination of the distribution of compositional types among small main belt asteroids, especially among the small members of the principal Hirayama families. The planned launch of the Infrared Astronomical Satellite (IRAS) was a further incentive to establish accurate orbits for faint asteroids so that the observations from IRAS could be utilized to determine albedos and sizes for an extensive sample of small asteroids.

The basic strategy of the initial UCAS survey was to photograph a 12° x 18° area of sky repeatedly for a period of 3 months. An area of sky this large was chosen in order to reduce the percentage of objects lost by motion beyond the photographed field. Six individual Schmidt fields, each 6.5° x 6.5°, are required to cover this area with some overlap along adjoining edges of the fields. This coverage is similar to that of the previous Palomar-Leiden Survey (PLS) for faint minor planets of Van Houten et al. (1970); however, in order to sample objects in high inclination orbits with less bias than the PLS, the long edge of the photographed area was oriented north-south. The area surveyed extends from ecliptic latitudes +2° to -16°. In order to follow the motions of the asteroids, the plate centers were shifted to follow the average component of motion of main belt asteroids parallel to the ecliptic plane. Weather patterns, the positions of the ecliptic and galactic planes, and the locations and phases of the moon were all factors considered in planning the timing of the photographed fields.

A total of 85 photographic plates for UCAS were obtained from February to May, 1981. Hydrogen-soaked 14 x 14 inch Kodak IIIa-J plates were exposed with a Schott glass GG-395 filter. Exposures varied in length from 45 minutes to 70 minutes to reach a preferred central sky density of 1.0 above fog. Sensitometry spots were applied to all the plates during their exposure in the telescope to aid in photographic photometry of the discovered objects. The initial observing scheme called for photographing the entire 12° x 18° area twice during each of the dark moon periods in

February and May, and at least three times during the dark periods in March and April. The center of the photographed area was selected to pass through opposition on March 20. This corresponded approximately to the equinox, and also to full moon. Thus, the surge in the brightness of objects due to the opposition effect was, to some extent, avoided. The three sets of observations in both March and April were to be spread over at least 10 days. From these observations, short arc orbits could be independently calculated for both March and April, which would simplify the process of linking observations from one dark period to the next. Weather encountered at Siding Spring during the months of the survey, however, did not allow for this strategy to be completely followed. Four observations spanning arcs of 10 to 14 days were obtained in the March dark period, but, in many cases, only one good observation in April was available. The photographs taken in February and May are adequate to determine three month arcs for most asteroids discovered, although the February and May observations were also adversely affected by the weather.

The plates were quickly inspected after processing to find any objects which needed immediate followup. Any asteroid whose motion would not be followed by the average shift of plate centers could be followed up independently. Comet 1981b was discovered by this initial scanning, but no specially fast-moving asteroids were found. Glass copies of the original plates were made at the U.K. Schmidt Telescope Unit. The originals and one set of copies were then sent to Caltech/JPL for reduction.

To date, the plates taken during March and April have been visually scanned and all measurable asteroid trails have been identified. The probability of detecting an asteroid trail by the visual methods used is about 98 percent for objects at least 0.5 magnitude above the plate limit. Owing to the exigencies of seeing conditions, the plate sensitivity varies considerably between some of the exposures, so that many faint asteroids are recorded only on the best plates.

Astrometric positions are being measured with the X-Y measuring engine of the Mt. Wilson - Las Campanas Observatories. Conversion from rectangular to celestial coordinates is made using plate constants determined from a second-order fit to approximately 50 reference stars distributed over each plate. Typical residuals from the fits made to the reference stars average 1.4 arcseconds. Owing to the small number of observations obtained during April, short arc orbits are only determined from the March observations. An ephemeris is generated from this orbit to identify the objects in April, leading to a refined orbit determined from the one month arc. The ephemeris generated from the one month arc will then be used in linking observations from February and May. These measurements, preliminary orbits, and preliminary rough estimates of the visual magnitudes are being reported to the Minor Planet Center of the Smithsonian Astrophysical Observatory for publication in the Minor Planet Circulars.

At the time of writing, plates taken in March and April of the two southern most fields had been measured and orbits for 185 asteroids had

been calculated. All but one or two of these asteroids are unnumbered. All of the objects have inclinations above 4°, owing to the ecliptic latitudes of the fields studied. Four of the new asteroids are Mars-crossers and one is an Earth-crossing Amor (Table 1). The Amor (1981 ET3) was discovered near aphelilon, at which time its apparent motion resembled that of main-belt asteroids. Several of the asteroids found have been linked to objects discovered in the Palomar-Leiden Survey.

On the basis of the asteroids detected in scanning the plates from March and April, we expect to obtain a minimum of 1,000 orbits for which the observed arc will span 2 to 3 months. Approximately 500 more objects will be reported with orbits based on relatively short arcs. In the coming years the main task of the survey will be to obtain observations at future apparitions and from plates taken in previous years, in order to establish reliable orbits for the long term. Observations for 1982 apparitions are now being taken on the Palomar 48-inch Schmidt. The Earth-crossing Amor (1981 ET3) was recovered in 1982 and its orbit is now secure. Once the astrometry and initial orbit calculations have been completed, an attempt will be made to determine accurate magnitudes for all objects from measurements by a high precision scanning densitometer. Where feasible, we will determine approximate phase coefficients for each asteroid observed.

Table 1. Planet-crossing asteroids discovered to date in the UCAS Survey

Asteroid	q(AU)	a(AU)	e	i	B(1,0)	Δ_4(AU) [1]	Δ_3(AU) [2]
1981 EF3	1.022	1.769	0.422	22°.16	~15.5	-0.685	-0.027
UCAS 3210	1.645	2.319	0.291	7°.97	~17.0	-0.078	
UCAS 3169	1.659	2.368	0.300	12°.08	~15.5	-0.037	
1981 EJ5	1.702	2.200	0.226	4°.94	~16.0	-0.056	
1981 EC3	1.783	2.357	0.244	7°.74	~17.0	-0.027	

[1] Δ_4 is the deepest overlap of the orbit of the asteroid with the orbit of Mars along the radius vector to the node as calculated by the method of Williams (1969, 1979). A negative value indicates that the radius vector to the asteroid orbit at the node is less than the radius vector to the orbit of Mars.

[2] Δ_3 is the deepest overlap of the orbit of the asteroid with the orbit of the Earth, as calculated by the method of Williams. A negative value of Δ_3 indicates that the asteroid is an Earth crosser, capable of colliding with the Earth solely as a consequence of secular perturbations of the orbits of the asteroid and the Earth.

References

Van Houten, C. J., Van Houten-Groenveld, I., Herget, P. and Gehrels, T., 1970, The Palomar-Leiden survey of faint minor planets: Astr. Astrophys. Suppl. 2, p. 339-448.

Williams, J. G., 1969, Secular perturbations in the solar system: Ph.D. dissertation, Univ. Calif. at Los Angeles.

Williams, J G., 1979, Proper elements and family memberships of the asteroids, in Gehrels (ed.) Asteroids, Univ. of Ariz. Press, p. 1040-1063.

A STOCHASTIC MODEL OF REGOLITH EVOLUTION ON SMALL BODIES

Kevin R. Housen
Shock Physics and Applied Mechanics, MS 13-20
Boeing Aerospace Company
Seattle, Washington

The geological evolution of small solar-system bodies has been dominated largely by impact cratering. A major consequence of impacts on these bodies is the formation of regoliths. Models of regolith evolution have been constructed (Housen et al., 1979; Langevin and Maurette, 1980), but have consistently approached the problem from a determinate point of view. A statistical approach, adopted here, necessarily yields a wider body of information.

Consider a fictitious population of a large number of initially indistinguishable asteroids. Each body is subjected to the same impacting-projectile population. The amount of regolith developed on any given asteroid depends primarily on three factors. (1) The number of craters as a function of size. For example, a body which has been pelted by many small impacts should develop less regolith than an asteroid with a larger proportion of big craters because large craters are the ones responsible for creating new regolith via excavations into bedrock whereas small craters merely rework existing regolith. (2) The order or occurrence of craters. The regolith should be relatively deep if the largest craters form late in the evolution. If they occur early, then much of the regolith they generate will be ejected from the asteroid by numerous small impacts. (3) The relative positions of craters. As mentioned above, new egolith is generated when craters puncture through the existing debris layer and excavate bedrock. On some bodies the larger craters will, by chance, occur in the regions where the regolith layer is very thin compared to other areas on the surface. Such bodies will develop more regolith than those asteroids on which the large craters preferentially formed in the deeper parts of the debris layer. These three quantities are all random variables, i.e., we cannot exactly predict the number of craters produced on an asteroid (even though an average crater flux might be specified exactly), their order of occurrence or their relative positions. Thus, corresponding to each body is a unique surficial distribution of regolith depths.

The distribution of regolith depth can be determined by considering the evolution at a randomly chosen point on the surface of an asteroid selected at random from the population of bodies. The depth is a random vairable for the three reasons mentioned above and because the surface point was chosen as random. The probability that the depth is less than some value, x, is denoted by P(x,t), where t denotes the evolution time. P(x,t) can be found by noting that the probability that the regolith depth is less than x at time t+dt is just the sum of two components: (1) the probability that the depth was less than x at time t and that there were no cratering events which affected the depth in the time interval dt and (2) the probability that the depth was less than some value, say x-u, at time t and that a cratering event occurred in dt which changed the depth by an amount u. That is,

$$P(x,t+dt) = P(x,t)\ (1 - \lambda\, dt) + \lambda\, dt \int_{-\infty}^{x} P(x-u,t)\, g(u)\, du \qquad (1)$$

where $\lambda\, dt$ is the probability that a cratering event affected the regolith depth at the point in the time interval dt (Poisson statistics), and g(u)du is the probability that the depth was changed by an amount u during the event. Note that λ is just the rate at which events occur. The function g is determined by crater and ejecta blanket morphology. Taking the limit as dt approaches zero one finds

$$\frac{1}{\lambda}\ \frac{\partial P(x,t)}{\partial t} = -P(x,t) + \int_{-\infty}^{x} P(x-u,t)\, g(u)du \qquad (2)$$

Housen (1981) has shown that if an asteroid does not experience a net gain of mass in an impact then P becomes independent of time, for large t. That is, the regolith settles into a state of statistical equilibrium. A characteristic time, t_e, required to reach equilibrium is given by

$$t_e = m_2/2m_1^2\lambda \qquad (3)$$

where m_1 and m_2 are the first two moments of the function g, i.e., the mean and variance of the change in regolith depth caused by a cratering event. Values of t_e and estimates of mean lifetimes against collisional fragmentation for several sizes of asteroids are listed in Table 1. For most sizes of bodies the time to reach equilibrium vastly exceeds the fragmentation lifetime and even the age of the solar system. These bodies are fragmented long before equilibrium can be attained. Hence, regolith models which assume equilibrium are questionable (e.g., Duraud et al., 1979).

The probability distribution of regolith depth at the time of a catastrophic fragmentation can be found from equation (2) by numerical methods. An example of such a numerical solution is shown in Figure 1, which applies to a 300 km diameter rocky asteroid. The mean regolith depth is found to be 3.3 km. The probability density function, i.e., the probability that the regolith depth is in some interval dx, is shown in the figure as a dashed curve (with no vertical scale). The broadness of this curve implies the regolith depth varies considerably about the mean value. In fact the standard deviation of the regolith depth is roughly equal to the mean. Thus, models of regolith evolution should address more than just average values. Note that the large standard deviation results from variations in regolith depth over the surface of any given asteroid and from variations between "otherwise similar" bodies. Housen (1981) has shown that these two components of variance are comparable in magnitude.

The mean regolith depth for three sizes of rocky asteroids and a Phobos-size body comprised of a much weaker material are listed in Table 1. The largest asteroids should develop several-kilometer thick debris layers. The depth decreases for smaller bodies because more ejecta escape and because the collisional lifetimes are shorter. Rocky asteroids smaller than a few tens of kilometers in diameter should develop very little regolith. The Phobos-size body is able to generate a substantial debris layer because ejecta velocities are rather low in the assumed weak target material. Note that Veverka and Thomas (1979) estimate the regolith depth on Phobos to be of order 100m in agreement with the estimate given in Table 1.

In all cases the standard deviation is comparable to the mean. These large stochastic variations should give rise to large differences in regolilths for asteroids of similar size. As a result, spacecraft imagery of asteroids can be expected to reveal a wide variety of surface morphologies. Indeed, the observed morphological differences between Phobos and Deimos may be largely attributable to "statistical fluctuations."

TABLE I

Asteroid	Time to reach equilibrium	Fragmentation lifetime	Mean depth at frag.
1000 km, rocky	800 b.y.	5 b.y.	7.2 km
300 km	50	2.5	3 km
100 km	1	1.5	600 m
20 km, weak	4	! m.y.	80-100 m

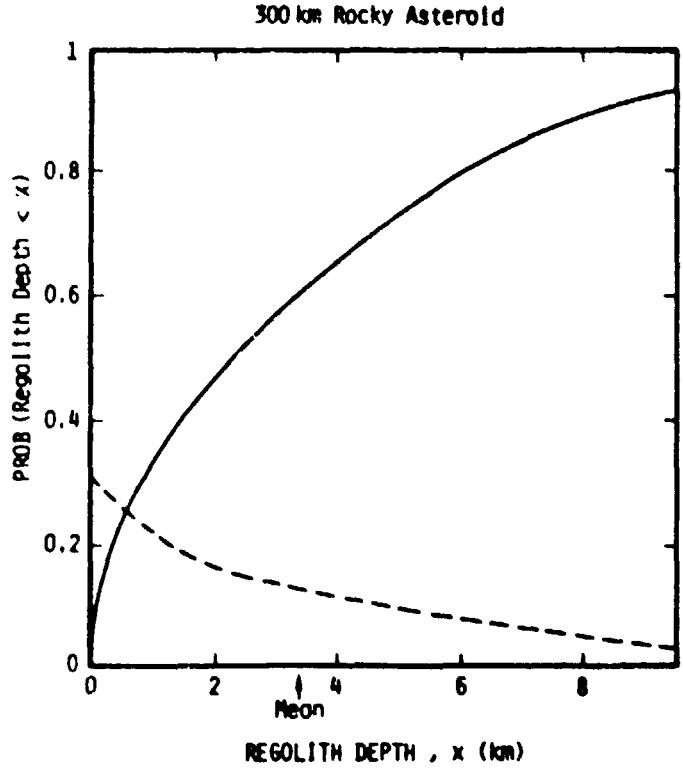

Figure 1: The probability distribution of regolith depth for a 300 km diameter rocky asteroid.

ICE-POOR REGOLITH DEVELOPMENT AND DESTRUCTION ON SMALL ICY-DUSTY OR ICY-ROCKY OBJECTS,
F.P. Fanale and J.R. Salvail, Planetary Geosciences Division, Hawaii Institute of Geophysics, University of Hawaii at Manoa, Honolulu, Hawaii 96822.

Development of ice-poor/silicate-rich "mantles" on cometary objects has been described by several investigators and has been the subject of at least one detailed quantitative model (Brin & Mendis, 1979; Brin, 1980). Ice sublimation is the creator, the "boiler"/disrupter, and the launcher of ice-poor regoliths. In our model, the major physical processes which are quantitatively described are: 1) Modification of the periodic orbital thermal "wave" that reaches buried condensed volatiles, by the finite thermal conductivity of any overlying ice-poor regolith, 2) Modification of the vapor outflux by the finite and changing vapor diffusivity of the incipient regolith, 3) The effect of volatile flux and preferential launching of smaller grains on the thickness and grain size distribution of the regolith, 4) Continuous feedback of developing regolith properties into the thermal and vapor transport described in "1." and "2." 5) The compound effects of multiple passes.

The model includes latent heat effects, H_2O and CO_2 properties, obscuration by streaming dust, and possible transitions from one dominant volatile loss mechanism to another (see below). In its preliminary form, it does not currently include scattering effects of ice halos or global effects such as systematic launching of grains from one region on a comet accompanied by their systematic accretion on another. Also, because of the complexity of the mantle development model, we have not yet coupled it with sophisticated insolation histories for comets with appropriate rotation rates, orbits and obliquities. Rather we have so far considered only two latitudes on comets with archtypical orbits and an obliquity of 90 degrees. We hope to consider more interesting and realistic orbits, obliquities and rotation rates.

Despite the preliminary stage of the investigation, our results suggest some general inferences: An object in an "archtypical" short period cometary orbit can undergo at least three distinct phases of regolith development including 1) A molecular diffusion phase, when the gas:silicate ratio of the outflux is high but the gas flux is very low. This phase is most effective ~ 3-5 AU and a comet in near circular at this heliocentric distance would probably first develop a water ice and dust regolith poor in other volatiles and then, ultimately, a permanent silicate-rich regolith. In this phase, the regolith inhibits vapor flux and thermal flux via its porosity and absorptive properties which, in turn, are determined by grain size distribution and prior history. 2) A phase (onset ~3AU) in which the thermally controlled volatile flux can in turn control the regolith geometry by regolith-disrupting processes, commencing when gas pressure exceeds lithostatic pressure. The transition from molecular diffusion through a fixed regolith matrix to volatile flux control of the matrix geometry might be analogous in some ways to the transition from still evaporative processes to boiling. During the molecular diffusion phase launching of even small grains by H_2O sublimation alone (without participation of other ices) is extremely ineffective. However, during the disruption/boiling phase, H_2O sublimation rates approach free sublimation of dusty H_2O ice, and can generally launch a substantial dust flux, albeit still strongly weighted to finer grains. 3) At small heliocentric distances (~1AU) launching of grains can become indiscriminate and at very small distances (~.3AU) even H_2O sublimation can launch large boulders. However the dependence of launch ability on heliocentric distance and ice composition is greatly moderated by latent heat effects. Table I gives a rough idea of these dependencies. However it should be borne in mind that the values in this table are for idealized thermal histories - a fixed subsolar point or a fixed 60 degrees incidence angle - and may not be generally applicable to comets. During the indiscriminate launch phase, ejectae have the same H_2O: rock flux as the comet mass, and severe erosion occurs in steady state and is not accompanied by any ice poor-regolith retention.

An ice poor regolith is "self-protecting" and mantle growth is "self-aggravating" because 1) A mantle modulates the thermal shock experienced at the buried ice interface near perihelion. Even with thermal transfer in radiative, conductive and convective modes, a static mantle of sufficient thickness and fineness can protect and enlarge itself because of its insulating properties and further suppress the volatile flux diffusing up through it for any given thermal history. Also, the thicker the existing regolith the less vulnerable it is to physical disruption by an excess of vapor pressure over its lithostatic pressure. Hence whether a particular comet undergoes the above transitions depends on whether incipient regolith growth achieved since the last perihelion is sufficient to protect the mantle against the next perihelion. If it is, then the mantle will irreversibly evolve to permanence. If not, the comet will cycle reversibly through the preceding stages until it is globally dissipated. It would appear that any virginal icy rocky object placed in an orbit with perihelion <1AU would have little chance of developing a permanent regolith (except for "global" effects mentioned above which are not considered here). Hence it would disappear after, say, hundreds of passes. On the other hand, any postulated existing initial mantle of ~4cm or more could protect itself even at a perihelion distance of ~1.7AU if only H_2O ice were present. A much greater initial thickness of ice poor mantle would be required if the comet expected to survive a typical Apollo perihelion passage at 0.7AU without beginning to cycle. If an ice-poor regolith did survive initial passage intact, it would stay in the molecular diffusion stage and would grow asymptotically with time to a thickness of perhaps several tens to hundreds of meters - depending on exact vapor diffusivity and heliocentric distances. Whether the "cometary" core of such an object would be detectable by remote sensing techniques in lieu of density measurements is a fascinating question, and the water flux itself is probably the most telling clue to such an object. The greater the sensitivity of gas flux measurements, and the greater the range of heliocentric distances at which these can be made on objects in eccentric orbits, the more chance of evaluating the actual nature of cometary regolith evolution by observing phenomena such as the sharp hypothesized transition between increasing molecular diffusion and the boiling/disruption phase or predicted strong variations in the H_2O: dust ratio.

In general, the main difference between our model results and those of others is that, where appropriate, we allow Knudsen flow (where mantle properties control the flux) and not continuum flow be the rate limiting mode of vapor transport. As a consequence, the inhibiting effect of any incipient regolith which develops toward aphelion is a very effective barrier to development of what would otherwise be a multicentimeter ice poor regolith.

Table I. Minimum* Requirements for Launching Silicates From a Comet With Albedo = 0.1, Radius = 2 km

Maximum Launchable (Radius, cm)	Required H_2O [CO_2] Flux, g/cm²sec	Required T for Flux, °K	Required Insolation erg/cm²sec	Required AU if Subsolar Point	Required AU 60° Latitude
1×10^{-4} (dust)	1.2×10^{-9} [2.3×10^{-9}]	151 [97]	2.6×10^{4} [4.5×10^{3}]	6.9 [16.8]	4.9 [11.9]
1×10^{-2} (sand)	1.1×10^{-7} [2.2×10^{-7}]	170 [113]	4.6×10^{4} [9.4×10^{3}]	5.2 [11.5]	3.7 [8.2]
1×10^{0} (pebbles)	1.1×10^{-5} [2.0×10^{-5}]	195 [135]	3.7×10^{5} [1.4×10^{5}]	1.8 [3.0]	1.3 [2.2]
1×10^{2} (boulders)	9.7×10^{-4} [1.7×10^{-3}]	229 [168]	2.8×10^{7} [1.1×10^{7}]	0.21 [0.34]	0.47 [0.76]
1×10^{3} (large boulders)	9.3×10^{-3} [1.7×10^{-2}]	250 [191]	2.6×10^{8} [1.0×10^{6}]	0.07 [0.11]	0.05 [0.08]

* assume launch accomplished with diurnal maximum flux

References: Brin, G.D. and Mendis D.A., Dust Release and Mantle Development in Comets, The Astrophysical Journal, 229, 402-408, 1979. Brin, G.D., Three Models of Dust Layers on Comet Nuclei, The Astrophysical Journal, 237, 265-279, 1980.

Albedo and morphological characteristics of asteroidal objects derived from laboratory simulations.

M.A.Barucci and M.Fulchignoni
Istituto di Astrofisica Spaziale CNR, Reparto di Planetologia, V.le dell'Università,11 00185 Roma, Italy

Asteroids are the largest population of solid bodies in the Solar System which may be the key for understanding the processess occurred during the formation of the planets from the protosolar nebula and the final phases of the planetary accretion.

Due to the lack of space missions toward the asteroids, all the available information about such an interesting set of bodies has been obtained with telescopic observations and has been collected in the TRIAD catalogue. An atlas of asteroids' photometric light curves is in preparation (Barucci et al., 1983) and it will contains all the lightcurves published in the worldwide literature.

The photometric light curve of an asteroid is affected by several parameters: 1) the shape of the object; 2) the orientation of the asteroid in space with respect to the Earth and the Sun; 3) the morphological surface characteristics; 4) the variation of the albedo properties of the surface materials. Points 3 and 4 are connected both with the chemical composition of the outer layers and with the evolutive history of each body.

The aim of our experimental research is to understand the effects of each of the above listed parameters on the light curve of an asteroidal model by means of laboratory simulations.

an attempt to reproduce esperimentally the observed asteroid light curves using 12 different rotating asteroid models (Dunlap 1971) yielded far from satisfactory results; this particular research line was therefore abandoned.

Our research program can be schematized as follows:

1. Setting up of the experimental device S.A.M. (the achronim stands for System for Asteroid Model);
2. Study of the effects of the variation of the orientation parameters on the lightcurve of regular and homogeneous bi-and triaxial ellipsoid models;
3. Study of the influence of albedo variations (black and white patches)on the amplitude and shape of the light curve.
4. Study of the influence of the surface morphological marks (craters, ridges, rilles, etc.) on the amplitude and shape of the light curve;
5. Study of the scattering properties of the models' coating materials;
6. Study of the dependence of the light curve on the chemistry of the surface materials.

The present state of the research program listed under points 1 to 6 above is as follows: work on points 1 and 2 is completed, points 3 and 4 have been looked into and some interesting results have been obtained, preliminary results are available for point 5 and more measurements are in progress while the experimental work connected with point 6 is still in a preliminary stage.

Here below we describe the states of the art and discuss the obtained results.

1. Description of the S.A.M.

The experimental device named System for Asteroid Model was built by A.Di Paoloantonio and C.Giuliani in the workshop of the Collurania Observatory (Teramo, Italy). The S.A.M. is composed by: i) a mechanical support for the asteroid models which allows the automatic variation (by means of step motors) of the model orientation parameters (i.e. aspect, obliquity and phase angles) with respect to the light source and the observer; ii) a light source which produces a parallel beam of quasi-solar light; iii) a photometer which collects the light reflected by the model; iv) an electronic interface, which drives all the mouvements of the model, i.e. rotation around the polar axis and the set-up of its orientation; v) a recording system, which gives the resulting light curves both on paper rolls and on magnetic tapes. A more detailed description of the S.A.M. can be found in Barucci et al. (1982).

2. The effects of the variation of the orientation parameters on the lightcurve of bi and triaxial ellipsoid models.

Several sets of measurements on five different bi- and triaxial ellipsoid models have been carried out, taking into account previous results both theoretical (Barucci and Fulchignoni) and numerical (Surdey and Surdey 1978). The parameters characterizing the shapes of the used models are listed in Table 1.

TABLE 1

Model N.	Shape	a	a/b	b/c	Material
1	Biaxial	10.00	1.67	1.00	wood
2	Biaxial	8.00	1.60	1.00	wood
3	Biaxial (cigar)	8.00	2.67	1.00	wood
4	Triaxial	10.00	1.43	1.17	wood
5	Triaxial(9 Metis)	8.00	1.29	1.70	Plaster of Paris

The models, all homogeneous and regularly shaped, have been sprayed with grey paint thus acquiring a uniform albedo of 0.4-0.45.

For each model we obtained 147 lightcurves, varying respectively the aspect angle from 0° to 90° (step : 15°), the obliquity angle from 0° to 20° (step : 15°) and the phase angle in the range 0° - 35° with steps of 7° (the phase angles have been selected in order to reproduce the observational conditions). The results obtained by the S.A.M. are in excellent agreement with the theoretical ones and can be summarized as follows:

- the variation of the hightcurve amplitude with the aspect is larger with increasing values of the aspect angle;
- the effect of the obliquity is negligible for small phase angles while it is predominant for phases larger than 25°-30°;
- the higher the phase angle, the larger is the maximum amplitude of the light curve;

- the amplitude of the light curve grows with the aspect angle as a function of the ratio a/b. Furthermore in the triaxial ellipsoid models as an effect of the ratio b/c, the amplitude values for intermediate aspect angles are lower than in the corresponding biaxial models.

3. Influence of albedo variations.

The data have been obtained by the S.A.M. using black (albedo 0.2) and white (albedo 0.9) circular patches on the gray models. The patches have different diameters D (2a/D ratios equal respectively to .125, .187, .250) and were located respectively i) on the pole of the model, and along the equator corresponding to ii) the minimum area side and iii) the maximum area side. The polar albedo variations do not affect the amplitude of the lightcurve, but their influence is revealed by an increase (white patches) and a decrease (black patches) in the absolute magnitude of the objects. the following significative variations in the shape of the light curves are caused by the presence of the equatorial patches: the minimum (case ii) is deeper with the black patches and more shallow with the white ones while the maximum (case iii) is higner with the white and lower with the black patches. an example of the magnitude variations and their dependence on the patches' dimensions is given in figure 1.

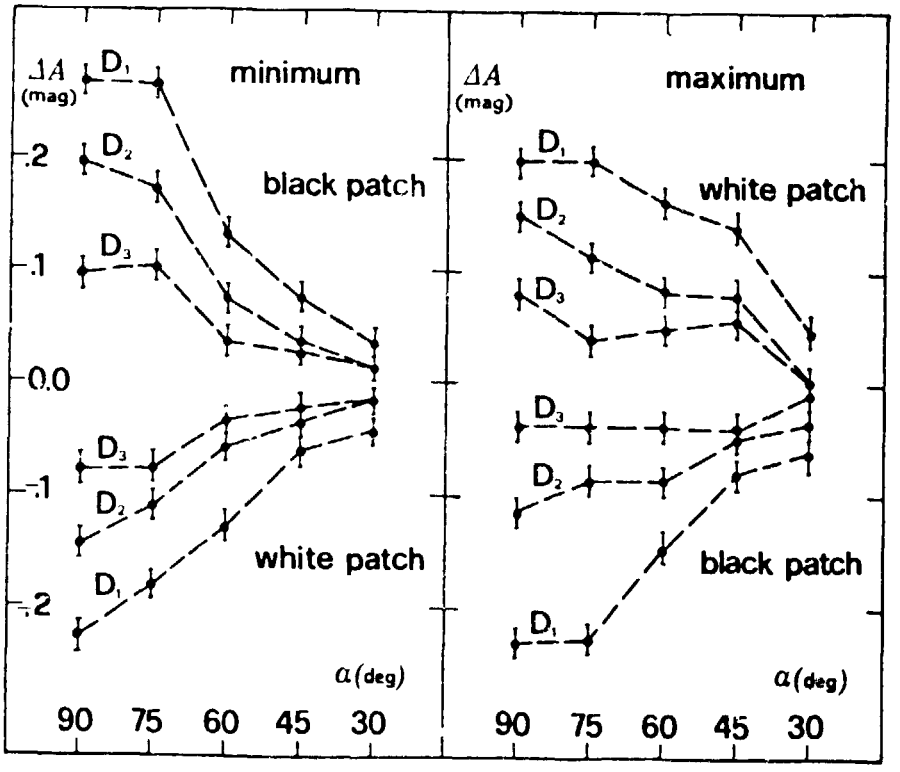

fig.1 - Variations of the lightcurve amplitude vs. aspect angle due to black and white albedo patches located respectively on the minimum area side(left)and the maximum area side(right)of an asteroidal model(a:b=1.29, b/c=1.70).The curves refer to different size ptches with diameter/a ratios $D_1 = .250$, $D_2 = .167$, $D_3 = .125$.

4. Influence of a large crater on the light curve.

The study of the influence on the light curve of the asteroid surface morphology has been recently undertaken. At the present time measurements have been carried out on models with a large crater (2a/D=.25) located in the center of both i) the minimum and ii) the maximum area side. The influence of such a crater on the light curve is negligible within the experimental errors (0.02 mag).

5.Scattering properties of the coating materials.

The scattering properties of the spray point have been investigated and some measurements are reported in fig.2.

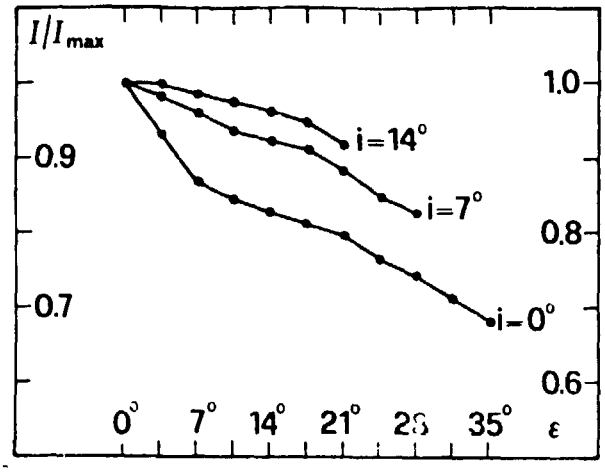

Fig.2 Ratio of the brightness (ε)/brightness (0°) of a painted plane surface vs. the angle of emergence ε per various value of the angle of incidence i.

We are studying these results in order to obtain an analytical and/or a numerical expression for the scattering, taking into account works published by Lumme and Bowell (1981), Thompson and Van Blerkom (1982) and in progress at the Cornell University (Gradie, 1982).

6.Chemistry of the surface materials.

We are working on the preparation of a coating mixture, which allows us i) to vary the chemical composition of the surface of the used models; ii) to operate easily changes in the surface morphology; iii) to ensure the control of the granulometric distribution of the adopted materials.

References.

- Barucci M.A. and Fulchignoni M (1982) "The Dependence of Asteroid Light Curves on the Orientation Parameters and the Shapes of Asteroids", The Moon and the Planets (in press).

- Barucci M.A., Casacchia R., Fulchignoni M., Burchi R., Dipaoloantonio A.,Giuliani C., Milano L., Scaltriti F., Zappalà V. (1982): "Laboratory Simultations of Photometric Asteroids' Light Curves", The Moon and the Planets (in press).
- Barucci M.A., Lagerkvist C., Zappalà V., (1983): "Atlas of photometric Asteroids' light curves (in preparation).
- Dunlap, J.L. (1971): "Laboratory Work on the Shapes of Asteroids", in T.Cherels (ed.), Physical Studies of Minor Planets, NASA SP 267.
- Gradie, J. (1982) - personal communication.
- Lumme K. and Bowell E. (1981): "Radiative Transfer in the Surfaces of Atmosphereless Bodies. I. Theory.", Astron. J.86 (11), 1694-1704.
- Surdey A. and Surdey J; (1977): "Asteroid lightcurves simulated by the rotation of a a three axis ellipsoid model",Astron., Astrophys.,66.
- Thompson W.T. and Van Blerkom D. (1982): "A Monte Carlo Approach to Scattering of Surfaces of Triaxial Ellipsoids", Icarus 49, 387-397.

L CHONDRITES: A PHOTOGEOLOGIST'S SEARCH FOR PHYSICAL PROCESSES

Charles A. Wood and Alan Silliman,* Johnson Space Center, Houston, TX 77058. *NASA Planetary Geology Intern, 1982.

Chondrites are the most common type of meteorites, comprising 51% of all known specimens, and 87% of all recovered falls (Dodd, 1981). H and L chondrites are very nearly equally represented with 589 H's and 578 L's currently known (exclusive of Antarctic finds). Despite, or perhaps because of, the large number of meteorites, meteoriticists have never compiled comprehensive catalogs of meteorites that list properties other than fall characteristics and petrologic type (e.g., Hey, 1966; Hutchison et al., 1977; and Motylewski, 1978). The large number of meteorites invites statistical investigation, and toward that end we are compiling catalogs of physical and chemical data for H and L chondrites (Wood and Lee-Berman, in prep; Wood and Silliman, in prep.). The catalogs - Houston Chondrite Register - contain the following data for each meteorite:

> name, petrologic type, fall location, fall date, fall hour, mass, Fa % in olivine, total wt. % Fe, SiO_2/MgO, shock class, metallographic shock class, ^4He abundance, U,Th-He gas retention age, K-Ar gas retention age, and exposure age.

These parameters were selected (1) to represent the basic chemical and physical characteristics of the meteorites, and (2) to ease data collection because many of them have been previously compiled in various publications. One of the major results of the cataloging effort is the realization that all of the basic data types listed above are available for only 8 meteorites (8 out of 1167!), and only mass and olivine composition are available for significantly more than 50% of the samples. A large number of analyses are still needed to provide the chemical, shock, and age data that are basic to understanding meteorites.

Partial analysis of the H chondrite data has resulted in the discovery of meteorite streams identifiable through clustering in exposure ages (Wood, 1982a, b). The L chondrites do not, apparently, travel in such well defined meteorite streams, but other interesting characteristics have been noted:

Fragmentation of L Chondrites: Few L chondrites are smaller than 2 kg, and the largest is 600 kg. Although there is considerable scatter the average mass of L chondrites decreases with increasing exposure age (Fig. 1). All L's weighing >50 kg have exposure ages <25 m.y., and no L with exposure age >25 m.y. weighs >50 kg. This relationship may be due to fragmentation both in space and in the Earth's atmosphere. A stone that was last involved in a large scale collision (which reset the exposure age) 30-50 m.y. ago may have since experienced repeated, lower energy collisions which failed to fragment it but did produce zones of weakness, resulting in significant fragmentation in the Earth's atmosphere, and thus only a small percentage of the meteorite survived. Alternative interpretations (such as higher average collisional velocities >25 m.y. ago) are possible.

Shock Histories: Strongly shocked meteorites (shock facies e and f of Dodd and Jarosewich, 1979) invariably have young gas retention ages - that is, the last big collision which reset their U,Th-He clocks occurred during the last 1.5 b.y. (Fig. 2). This confirms the original discovery, based on a smaller data set, by Heymann (1967) who interpreted the relation in terms of partial resetting of ages for meteorites that were shocked only weakly. Available Ar-Ar ages, which more accurately date the shock event, indicate that Heymann was correct, for there is no evidence for major collisions older than approximately 500 m.y. ago. This implies that L chondrites were not common as meteorites, nor presumably as crater-forming projectiles, prior to about 500 m.y. ago. The only terrestrial impact crater thought to have been formed by an L chondrite is Brent (Grieve, 1978), which is 450 m.y. old (Lozej and Beales, 1975). A second finding relates shock history to travel time to Earth: the average exposure age for L chondrites with gas retention ages >600 m.y. is 15.7 m.y. but only 7.7 m.y. for meteorites involved in the 500 m.y. shock event. Perhaps ejecta from the 500 m.y. collisional event was placed into an orbit more favorable for derivation of meteorites than material not involved in the collision. Finally, these findings suggest that exposure age is a rough guide to both shock age and intensity for L chondrites.

Enigmatic Relations: Recognizing the above exposure-shock age tendency for L chondrites we have divided the meteorites into two extreme populations. The "young" group (n = 28) consists of those stones with U,Th-He ages $\lesssim$1 g.y. and exposure ages <8 m.y; the "old" group (n = 31) has U,Th-He ages $\gtrsim$2 b.y. and exposure ages $\gtrsim$20 m.y. These two groups are remarkably different in chemistry, mass, and hour of fall, but have virtually identical distributions for month of fall and petrologic type (Table 1). Note that the difference in average % Fa (Fig. 3) is statistically significant, and that the second value for average masss discounts the single largest stone in each group. The greater mass of the young group is consistent with Figure 1, and the difference in olivine composition suggests that the two groups may represent different parent bodies. The remarkable concentration of daytime falls for the old group must reflect some unique orbital coherence or velocity structure.

References: Dodd, R. T. (1981) Meteorites, Cambridge Univ. Press. Dodd, R. T. and E. Jarosewich (1979) Earth Planet. Sci. Lett. 44, 335. Grieve, R.A.F. (1978) Proc. Lunar Planet. Sci. Conf. 9th, 2579. Hey, M. H. (1966) Catalogue of Meteorites, British Museum. Heymann, D. (1967) Icarus 6, 189. Hutchison, R., A. W. R. Bevan, and J. M. Hall (1977) Appendix to the Catalogue of Meteorites, British Museum. Lozej, G.P. and F.W. Beals (1975) Can. J. Earth Sci. 12, 606. Motylewski, K. (1978) The Revised Cambridge Chondrite Compendium, Smithsonian Astrophysical Observatory, Cambridge, Mass. Wood, C. A. (1982a) Lunar Planet. Sci. 13, 873. Wood, C. A. (1982b) 45th Ann. Met. Soc. Meeting, Abstracts, XIII-10 Lunar and Planetary Inst. Houston. Wood, C A. and R. Lee-Berman (in prep.) Houston Chondrite Register - H Chondrites. Wood, C. A. and A. Silliman (in prep.) Houston Chondrite Register - L Chondrites.

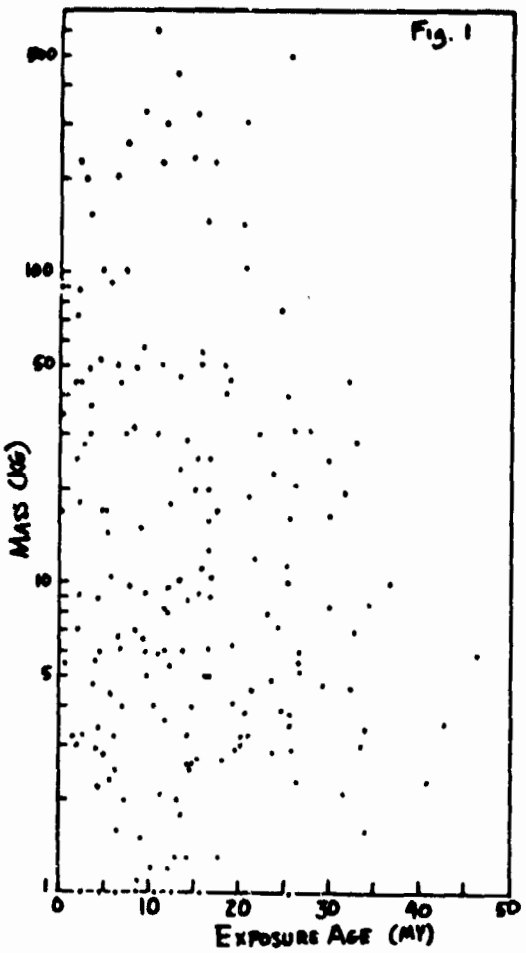

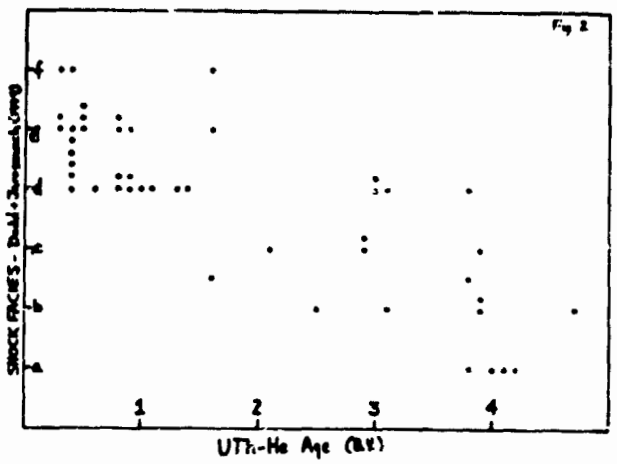

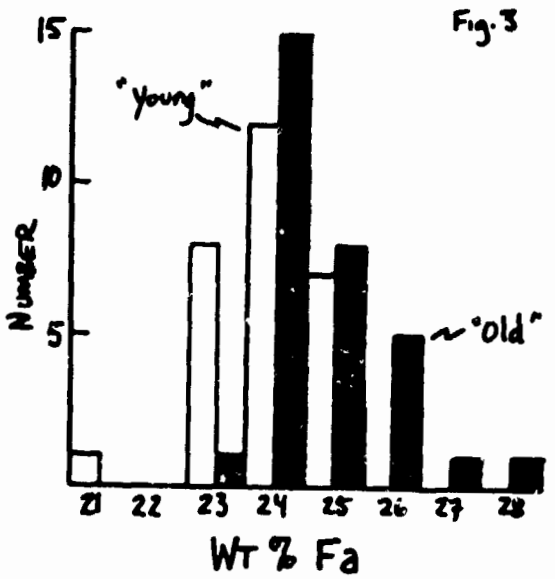

TABLE 1

	Young	Old
	U ≤ 1 BY; EA < 8 MY	U ≥ 2 BY; EA > 20 MY
Average % Fa	24.0 ± 0.8	24.8 ± 1.1
Average Mass		
Arithmetic mean	60.7 ± 77.0 kg	21.2 ± 91.3 kg
	53.6 ± 67.8	15.6 ± 28.3
Geometric mean	19.2	7.4
Hour of Fall		
1800–0600	11	1
0600–1800	9	16
Month of Fall		
April–September	14	13
October–March	6	6
Petrologic Type		
4/5/6	4/8/18	4/7/18

Double or Multiple Cometary Nuclei?

Fred L. Whipple
Smithsonian Astrophysical Observatory

The question as to whether double or multiple cometary nuclei might be responsible for comet splitting discussed by Whipple and Stefanik (1966), has been raised again by Van Flandern (1981). Because the separation of multiple cometary nuclei rendered orbitally unstable by solar gravitation would not stress the nuclei, outbursts of activity should not accompany such separations, contrary to the frequent simultaneous occurence of outbursts and splitting.

The introduction of differential nongravitational (DNG) forces into the theory drastically changes the situation. If the primary nucleus and its smaller satellites suffer DNG accelerations radial to the Sun comparable to those observed for many comets, the perturbations must exceed the direct solar differential accelerations for a fairly tightly bound system when traversing the inner solar system. The result in the coplane case (comet orbit and satellite orbit in the same plane) is simply determined and is typical of the more general case. The semimajor axis of the pair suffers no change but the orbit generally swings around so that the eccentricity of the orbit increases. Finally the satellite encounters the nucleus. This should produce a violent disruption of material even at the low velocities involved (meters/sec). Hence a violent outburst should occur, possibly two or more on successive revolutions.

It is suggested that two major outbursts of 9 magnitudes or 4000 times in brightness for two faint short-period comets, P/Tuttle-Giacobini-Kresák in 1973 and P/Holmes in 1892 may be caused by such encounters. Otherwise it is difficult to understand how such old comet nuclei, presumably the cores of much greater comets, could suddenly exhibit such violent activity.

Statistical evidence, on the other hand, suggests that comet splitting in general and most typical cometary outbursts arise from the intrinsic properties of the nucleus material. Newer comets with a greater proportion of active volatile material show a much greater chance of splitting than the remanent cores of older comets.

REFERENCES

Van Flandern, T.C. 1981, Icarus, 47, 412-430.

Whipple, F.L., and Stefanik, P., 1966, Nature et Origine des Cometes, Mem. Roy. Sci. Liège, 5th Ser. Vol. 12, 33-52.

Chapter 3

VENUS

TECTONICS AND SURFACE ROUGHNESS OF VENUS: A PROGRESS REPORT

Gerald G. Schaber, Philip Davis, Richard C. Kozak, and Eric M. Eliason - U.S. Geological Survey, Flagstaff, AZ 86001

Considerable progress was made during 1982 in the investigation of Venus' tectonics and surface-roughness variations. A formal report describing limited extension and volcanism along zones of global lithospheric weakness on Venus was published by Schaber (1982), and these data were also presented at the Planetary Rifting Conference in the Napa Valley, Calif., in December 1981.

Investigation of the distribution of surface roughness on Venus has been centered during 1982 on application of an unsupervised linear-discriminant clustering algorithm to various Pioneer-Venus (P-V) data sets. The goal was to determine regions that have the following similar properties: 100-km-scale regional slope, reflectivity, and rms slopes at 1- to 100-m scale. The three data sets used include the P-V altimetry, reflectivity (ρ factor) and the C-factor derived from the Hagfors scattering model. The side-looking-radar-image (8 X 8 imaging) P-V data set was not used as a fourth dimension in this analysis because reflectivity was already used in the preparation of the 8 X 8 data base; thus, its inclusion would give this data set double weight. The 100- to 150-km-scale slope data used in this analysis were derived from the P-V altimetry data base over regional topographic wavelengths equal to or greater than 100 km. Slope was used instead of altitude because it has greater physical significance in terms of surface characterization; the 100-km-wavelength interval represents the resolution of the altimetry data.

The advantage of the clustering algorithm over previous visual analysis (Schaber et al., 1982) is that this algorithm is totally unsupervised and depends only on the precision of the input data (Jayroe, 1976). The linear-discriminant classifier was chosen over maximum-likelihood, nearest-neighborhood, and minimum-distance algorithms because it; (1) defines cluster boundaries as hyperplanes in three-dimensional space, (2) defines hyperplane boundaries that are not restricted to the orthogonality of the three axes, (3) defines hyperplane boundaries by statistical analysis of cluster-overlap regions, and (4) defines hyperplane boundaries for each cluster whose distances from their respective cluster centroid are independent of the other hyperplane distances for that cluster. Once the hyperplane boundaries for each cluster are defined, each picture element of the input-data bases is assigned a number from 1 to n indicating the cluster to which it belongs. A map of these numbers is then constructed; this map shows the distribution of units with similar regional slope, reflectivity, and small-scale rms slopes.

Once the initial clustering of the P-V data sets is complete, the Earth-based data on Venus surface scattering from Goldstone and Arecibo will be incorporated into the investigation.

References

Jayroe, R. R., Atkinson, R., Dasarthy, B. V., Lybanon, M., and Ramapyrian, H. K., 1976, Classification software technique assessment: NASA Tech. Memo D-8240, 153 p.

Schaber, G. G., 1982, Venus: Limited extension and volcanism along zones of lithospheric weakness: Geophysical Research Letters, v. 9, no. 5, p 499-502.

Schaber, G. G., Kozak, R. C., Davis, Philip, and Eliason, Eric, 1982, Venus Pioneer: Ratios and composite maps of altimetry, rms slopes and the Fresnel reflection coefficient: Lunar and Planetary Science XIII - Pt. 2, The Lunar and Planetary Institute, Houston, TX, p. 683-684.

MORPHOLOGY AND TOPOGRAPHY OF APHRODITE TERRA, VENUS. William J. Ehmann and James W. Head, Dept. of Geol. Sci., Brown Univ., Providence, RI 02912.

Aphrodite Terra is the largest of the three major upland regions on Venus. We have defined the base of Aphrodite to be the 6051.5 km elevation level, which is the mean planetary radius (mpr) (Masursky et al., 1980). This choice delineates a continuous upland, twice the size of Africa, that covers 7.3×10^7 km^2 (16%) of the venusian surface. Aphrodite trends dominantly east-west for 22, 180 km between 45° and 255° longitude and ranges between 60° N and S latitudes (Figure 1). Within Aphrodite, a variety of geologic features exist, including broad mountains, isolated peaks, individual and aligned pits, linear and arcuate troughs, and circular structures. Using Pioneer-Venus data, we have subdivided Aphrodite Terra into six provinces on the basis of elevation, slope, and the presence or absence of specific geomorphic features, building upon earlier studies by Schaber (1981, 1982).

The Western Highlands (13.6×10^6 km^2) is the third largest province, half the size of North America, and extends 6865 km along the major east-west trend of Aphrodite. The province is dominated by Ovda Regio (6056.8 km), an elliptical and essentially continuous mountain region that is bounded by steep slopes. Hypsometric plots show that 65% of the province is above 6053 km elevation, and that the topography is nearly equally distributed among the three central 1.5 km intervals (Figure 2). The Interior Highlands (15.9×10^6 km^2) is the largest province, twice the size of Australia, and follows a NE/SW trend. A break in continuity of highland topography, broader slopes, and a zone of low reflectivity separate the province from the Western Highlands. This region contains Thetis Regio (6057.2 km), a less continuous highland than Ovda, and several scattered peaks on a broad, more gently sloping upland. Hypsometric plots reveal a shift of topography towards lower elevations, as this province contains 13% more lowlands than the Western Highlands. The Artemis Chasma province (4.4×10^6 km^2) is a generally flat, circular region 2600 km in diameter, containing two arcuate troughs. Artemis Chasma proper spans 280° of arc, averaging 200 km wide and 1 km deep for a distance of 5700 km. It is flanked on both sides by narrow, < 200 km wide ridges, although the interior wall is usually higher than the outer wall (Schaber, 1981). The smaller trough lies within the northern part of Artemis and opens east. Unlike Artemis Chasma, it is not consistently bounded by ridges, although a 200 km diameter peak lies to the south. Hypsometry shows that Artemis Chasma province has nearly twice as much area between 6051.6 and 6053 km than either the Western Highlands or the Interior Highlands. The Central Chasma region is a broad, E-W trending arch covering 11.6×10^6 km^2 of the venusian surface and cut by numerous troughs and pits. Although hypsometrically similar, the Central Chasma province differs from Artemis by the linear trends of the troughs within it. Dali Chasma runs east-west for 3600 km along the crest of the regional arch, flanked on both sides by elongate ridges which vary by as much as 2.5 km from one side of the trough to the other (Schaber, 1981). The lowland regions on either side of Dali are broadly symmetric about the trough axis. Diana Chasma trends NE/SW for 970 km along the western edge of Dali. Further to the northwest, a third trough is oriented in such a way as to suggest a continuation of Dali Chasma. The Eastern Highlands province (13.0×10^6 km^2) trends NW/SE and contains two mountain districts: four major peaks on an L-shaped upland to the north, and the pyramid-shaped Atla Regio (6057.2 km) to the south. Between them is a 600 km diameter topographic low with a peak in the center. Slopes are more gradual and uniform over all elevations than elsewhere in Aphrodite. Hypsometric data show that

ORIGINAL PAGE IS
OF POOR QUALITY

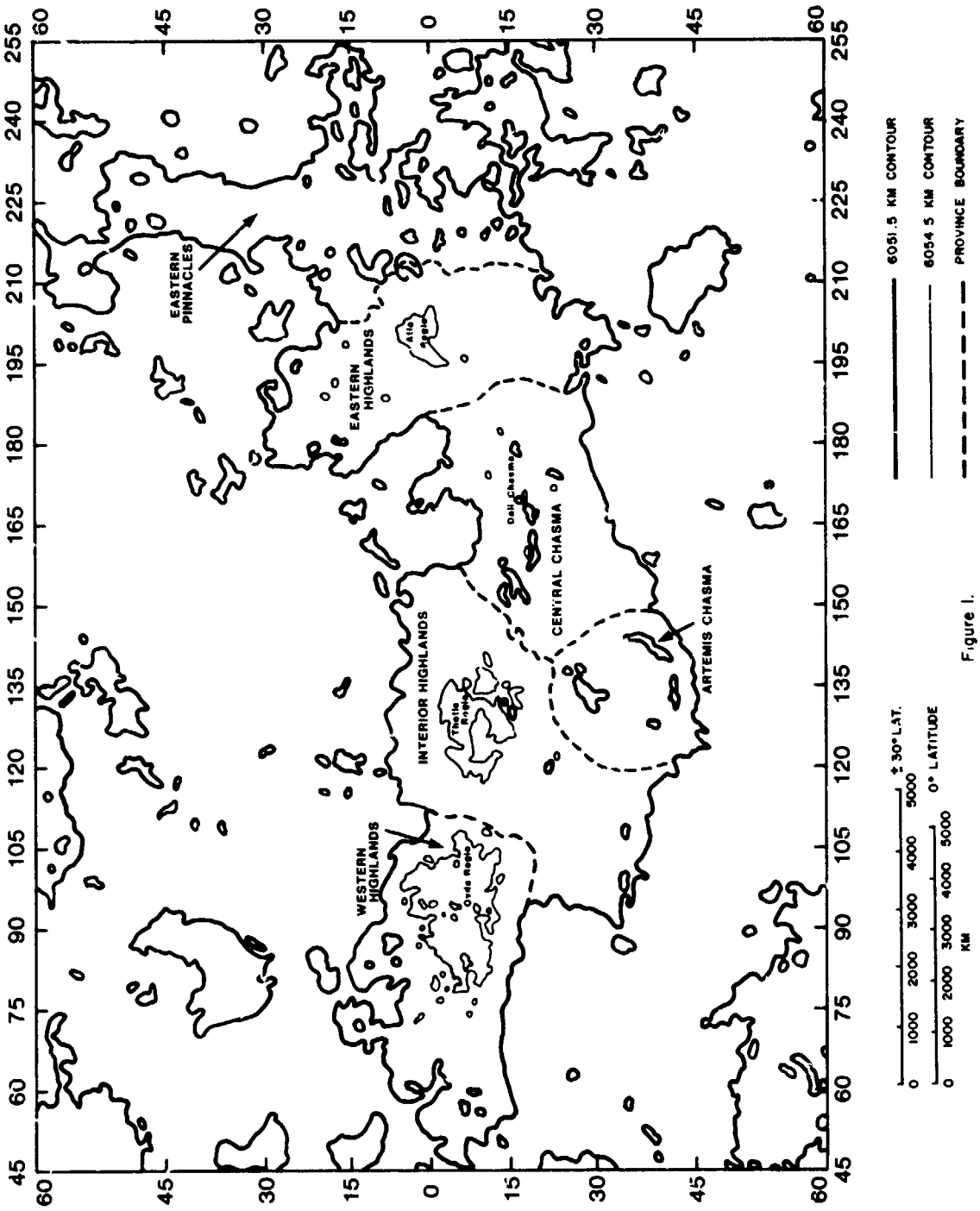

Figure 1.

the Eastern Highlands are intermediate between the chasma provinces and the Interior Highlands. The Eastern Pinnacles province covers 14.2 X 10^6 km^2 as a distinctive terrain of isolated topographic highs set on a patchwork of arcuate lows. It is separated from the Eastern Highlands by a break in topograhic continuity, roughly along the 6052 km contour line. Fourteen 300 km diameter peaks define two major, intersecting trends: a 8200 km N-S trend, and a 5400 km E-W trend which terminates near Beta Regio. Hypsometric plots suggest that the Eastern Pinnacles province is most like Artemis Chasma province, with the principle difference being the shape and orientation of peaks and lowlands.

Several Aphrodite provinces are similar in morphology and elevation to Beta Regio, but are distinct from terrain in Ishtar Terra. Each province is roughly the size of the Tharsis region on Mars. We are presently comparing the provinces and features within Aphrodite to geologic structures on the other terrestrial planets in an effort to test hypotheses for the origin and evolution of the venusian surface.

References: 1) Masursky et al. (1980) JGR 85, 8232. 2) Schaber (1981) LPI Contrib. #457, 31. 3) Schaber (1982) GRL 9, 499. 4) Schaber and Masursky (1980) NASA TM 82385, 82.

PERCENTAGE OF DATA POINTS IN AN ELEVATION RANGE FOR EACH PROVINCE IN APHRODITE

PROVINCE	ELEVATION RANGE (KM)					
	6051.6	6051.6-6053.0	6053.0-6054.4	6054.4-6056.0	6056.0	Total Range
Western Highlands	1.5	33.4	29.8	31.4	3.8	6050.8-6056.8
Interior Highlands	1.2	47.0	32.9	18.8	0.1	6049.8-6056.2
Artemis Chasma	5.3	80.8	13.4	0.5	0.0	6049.8-6055.4
Central Chasma	3.0	76.5	19.3	1.0	0.1	6049.0-6056.2
Eastern Highlands	1.2	64.2	27.8	6.8	0.0	6049.8-6057.2
Eastern Pinnacles	5.8	86.8	6.7	0.7	0.0	6049.8-6055.0

Figure 2.

IDENTIFICATION OF BANDED TERRAIN IN THE MOUNTAINS OF ISHTAR TERRA, VENUS. J. W. Head (Dept. of Geol. Sci., Brown Univ., Providence, RI 02912) and D. B. Campbell (Nat'l. Astron. and Ionosphere Ctr., Arecibo, Puerto Rico, 00612).

Critical to the understanding of the tectonic style of Venus is the origin of the major mountain ranges on Ishtar Terra (Fig. 1). These mountainous regions are unlike high topography observed on the Moon, Mars, and Mercury, which is predominantly associated with large volcanoes or the rims of large circular impact basins (1). Recently, images have been obtained of the Ishtar Terra region with the 12.6 cm wavelength radar system at the Arecibo Observatory. These images, which map the backscatter cross-section per unit area (surface reflectivity), have resolutions of 3-6 km, a significant improvement over previously published Earth-based images. Because the subearth point on Venus is restricted to ± 9° of the equator, the angle at which the surface is illuminated by the incident radar wave varies from near zero near the equator to over 65° at high latitudes. Appropriate scattering laws as a function of incidence angle, as well as methods of data acquisition and display, are discussed elsewhere (2). At the high latitudes typical of Ishtar Terra (55° to 75° N) the slope of the scattering law increases, suggesting that both small scale (wavelength-size) surface roughness, and average slope-induced changes in the scattered signal, are important. The average scattering properties of the planet have been removed (2) so that the images show the ratio of the received power to that of a homogeneous Venus surface with average scattering properties.

The new high resolution radar images show a distinctive set of high reflectivity bands extending along the strike of Akna Montes for its full extent, curving eastward at the northern end of Akna to merge into similar banded terrain in Freyja Montes. The bands begin abruptly at the southwestern edge of Ishtar where at least six parallel bands with widths of 10 to 20 km occur. These merge into two to three major bands of very high reflectivity and this major textural pattern extends the full length of the southern arcuate portion of Akna Montes. As Akna Montes turns toward the north and the terrain decreases in elevation, the bands become somewhat less distinct but can still be traced into Freyja Montes. To the east, the banded texture disappears near the base of the mountains and is not obvious in the very low reflectivity Lakshmi Planum region. To the west, bands of comparable lengths and widths but lower reflectivity, are visible to the edge of Ishtar Terra, a distance of about 400 km. The linear east-west portion of Freyja Montes is dominated by the same type of banded texture seen in Akna Montes. The banded terrain is 200-300 km wide and is composed of up to fifteen radar bright bands separated by bands of lower reflectivity. High reflectivity bands are 10-20 km in width and up to several hundred km in length. The highest reflectivity bands generally correlate with the highest topography. The 300 km wide high terrain at the eastern end of Freyja is characterized by high reflectivity but the patterns are dominated by shorter linear segments arrayed in a variety of directions. High resolution radar images of Maxwell Montes show levels of reflectivity and banded texture comparable to Akna and Freyja Montes. The distinctive banded terrain is concentrated in west-central Maxwell, in the highest region of the mountain range, and trends parallel to the long axis of the topography. On the mountain to the north and south (at lower elevations) the banded terrain merges into mottled regions of high backscatter. To the east on the lower slopes of Maxwell, the well-developed banded terrain is replaced by a circular backscatter feature over 100 km in diameter.

A number of hypotheses can be proposed to explain the nature and origin of the high reflectivity bands, including basic geological processes such as

wind activity, mass wasting, volcanism, and tectonism. Eolian processes can produce sorting of sedimentary particles into linear bands (dunes) of varying grain size, often oriented parallel to slope. However, the wide spacing of these bands coupled with the likelihood that eolian erosion on Venus is less efficient than on Earth (3), suggest that eolian activity is not the primary process responsible for the origin of the bands. Volcanic processes can produce lava flows which differ from surrounding terrain in terms of composition, surface roughness, and topography, all factors which can cause variations in radar backscatter and thus in discriminibility on radar images. In addition, 10-20 km wide lava flows of hundreds of km length are known for the Moon (4) and Mars (5), and some authors have proposed a volcanic origin for Maxwell Montes, one of the major mountain ranges where the banded terrain occurs. However, the vast majority of lava flows are oriented normal to the strike of regional slope, while the vast majority of the bands described here run parallel to the strike. Mass wasting processes are known to produce a variety of features on Earth, such as slumps and talus aprons, which produce grain size and local slope variations, and are oriented parallel to regional slopes. The distinctive topography of these mountains seem to make these features very susceptible to erosion and mass wasting processes, even though the nature of these processes is not known for Venus. However, the extremely linear and continuous nature of many of these bands over hundreds of kilometers suggests that mass wasting processes are not the primary cause of their origin, although such processes may have been significant in their enhancement. Deformational features on Earth (folds and faults) are often extremely linear and a combination of formational and degradational (erosional) processes can produce major belts of linear high topography which could be perceived as banded terrain in radar images. The Basin and Range Province of the western United States, for example, is characterized by a broad topographic high several hundred km in width, and a series of linear mountains produced by extension and block faulting, with dimensions comparable to some parts of the banded terrain. The Appalachian Mountains of the eastern United States form a broad linear topographic high approximately 1500 km in length and 100-200 km in width. The Appalachians are characterized by numerous folds and faults formed at an ancient convergent plate boundary in a compressional tectonic regime and were subsequently exposed by erosion. Fold wavelengths and fault separation distances are typically in the 5-20 km range and these features are oriented parallel to the topographic trend of the mountain range.

On the basis of the close correlation of the banded terrain occurrence and distinctive mountainous topography, the parallelism of topography and bands, and the extremely continuous nature and regular spacing of the bands, we conclude that deformational processes (folding, faulting) are a strong candidate for the origin of the banded terrain. These characteristics are more comparable to plate tectonic-related features on Earth, such as folded mountain belts, than they are to any feature known on the smaller terrestrial planets. The exact nature of potential deformational or tectonic processes remains unclear, however, both because of the lack of sufficient resolution to distinguish geological details and because of the poor understanding of potential tectonic processes on Venus (7, 8, 9). Indeed, a form of deformation associated with viscous relaxation of mountainous topography enhanced by the high temperature of Venus near-surface rocks (10) may be a factor in the formation of the banded terrain. A more quantitative assessment of the geometry and textural patterns of the banded terrain is presently underway and may provide data to further distinguish potential modes of formation of these distinctive features.

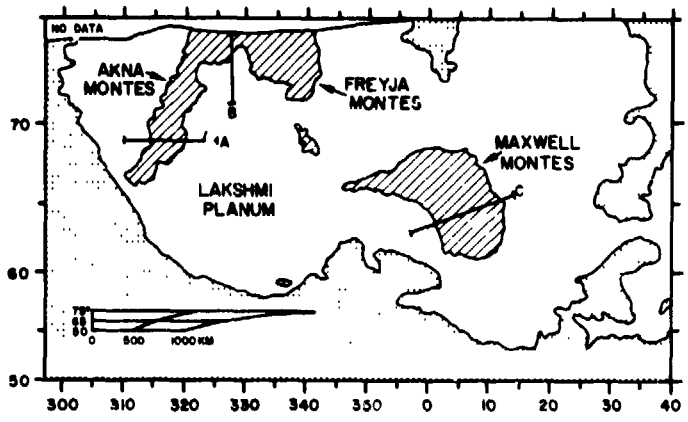

Figure 1. The mountains of western Ishtar Terra (Mercator Projection). Ishtar Terra is outlined by the 6053.0 contour which defines the base of the highlands province on Venus (6). Elevations are expressed in terms of planetary radius. Dotted regions lie below this altitude. The base of Maxwell Montes is outlined by the 6056.0 km contour. The base of all other mountains are outlined by the 6055.5 km contour. Topographic profiles of Akna, Freyja and Maxwell Montes are shown (with 50:1 vertical exaggeration) and compared to the Colorado Rocky Mountains (where elevations are in km above sea level).

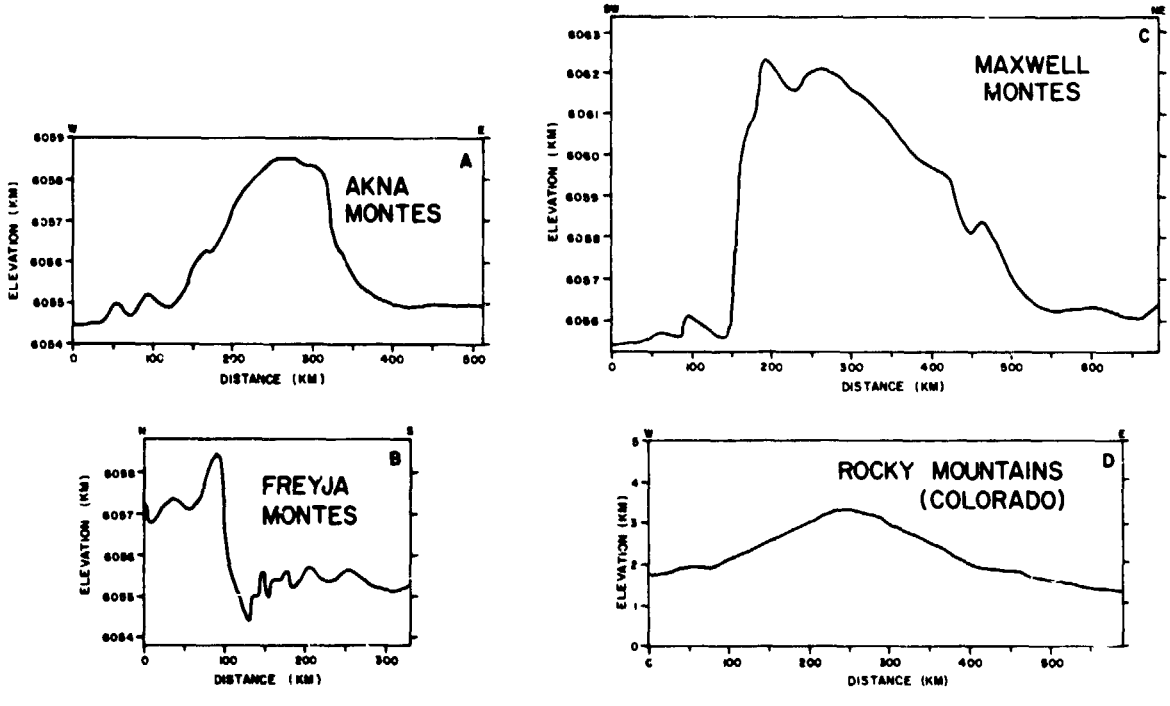

References: 1) J. W. Head and S. C. Solomon, (1981) Science, 213, 62-76. 2) D. B. Campbell and B. A. Burns (1980) J. Geophys. Res., 85, 8271. 3) B. White (1981) Icarus, 46, 226. 4) G. Schaber (1973) Geochim. Cosmochim. Acta, Supp. 4, 1. 5) G. Schaber et al. (1978) Geochim. Cosmochim. Acta, Suppl. 10, 3, 3433. 6) H. Masursky et al. (1980) J. Geophys. Res., 85, 8232. 7) S. C. Solomon and J. W. Head (1982) J. Geophys. Res., in press. 8) W. M. Kaula and R. J. Phillips (1981) Geophys. Res. Lett. 8, 1187-1190. 9) R. J. Phillips, W. M. Kaula, G. E. McGill, M. C. Malin (1981) Science, 212, 879. 10) J. Weertman (1979) Phys. Earth Planet. Inter., 19, 197-207.

UNSMOOTHED VENUS TOPOGRAPHIC DATA IN HARD COPY

George E. McGill and Susan J. Steenstrup, Department of Geology and Geography, University of Massachusetts, Amherst, MA 01003

The Pioneer Venus radar altimeter measured the radius of Venus at thousands of points between 74°N and 63°S latitudes. Computer-smoothed versions of these data have been published as small-format global topographic maps. Also, smoothed data are available on magnetic tape at NSSDC; but unsmoothed altimetry data are not now available to the profession at large. Although computer smoothing greatly enhances the appearance of global maps, and eliminates many artifacts, high-frequency real information also is lost.

A hard-copy data set is in preparation at the University of Massachusetts that shows the center of each altimeter footprint and the "elevation" corresponding to that footprint for all altimeter points except the high altitude pre-orbit-culmination points and those points deemed of doubtful validity by P. Ford of MIT. The data are printed onto 16 large sheets, 8 on Lambert polyconic projections (poleward of ±30° latitude) and 8 on Mercator projections (equatorward of ±35° latitude). The sheets are printed such that the Lambert and Mercator projections have identical scales at 30° latitude.

This data set, with accompanying explanation, will be available to planetary geologists in the near future (for information contact the first author). The sheets distributed will be ozalid copies, and each will be on the order of 1 x 1.5 meters in dimensions. It is our hope that this data set will be of particular use to those wishing unsmoothed data, to those who prefer to draw topographic maps manually, and to those without the facilities necessary to use altimetric data on magnetic tape.

RADAR-BRIGHT RINGS ON THE MOON AND VENUS, R. S. Saunders, T. W. Thompson, and A. J. Graz*, Jet Propulsion Laboratory, California Institute of Technology, Pasadena, CA 91109, *Princeton University, Princeton, NJ.

Radar images of the Moon obtained at 3.8 cm and 70 cm wavelengths may provide a basis for interpreting Venus radar images. The availability of high resolution visual images of the Moon permits a better understanding of the lunar radar images. We have examined lunar radar-bright features as possible analogs to bright-ring features on Venus. The 3.8 cm lunar images of Zisk et al. (1974) have resolutions of 1-3 km. Thompson et al. (1980) have examined the lunar radar-bright features. The suggested progression in the evolution of lunar impact craters is that they have bright floors, walls, and rims when first formed. These are the latest Copernican age craters. Many Copernican and Eratosthenian age craters appear as bright rings, with the floors having about the same reflectivity as the surrounding terrain. Most of the Imbrian and older craters have isolated bright portions but generally do not appear as bright rings, with the exception of the crater Maclear which is mapped as Imbrian. The bright ring features do not occur preferentially on either mare or terra.

We have studied the lunar bright ring features in depolarized 3.8 cm images between 0° and 60° incidence angles. Depolarized images are sensitive to surface roughness in this range of angles rather than to topography. The sample of bright rings measured included only those features with complete, circular and uniformly bright rings larger than 15 km.

The outer and inner diameters of the rings were measured and compared with the rim crest diameter of the associated crater (Figure 1).

We have concluded that the bright rings are associated with slopes both interior and exterior to the rim. The dark floors probably become smooth rather quickly by processes of mass wasting from crater walls and by meteorite comminution. Slopes have roughness elements that are continuously renewed by weathering from impact gardening and downslope movement. When slopes are reduced to those typical of Imbrian age and older craters, they no longer appear bright in the 3.8 cm images. Volcanic flooding does not appear to be a significant factor in reducing roughness since only three craters in our sample have flooded floors.

A test of the slope control hypothesis for radar-bright features is provided by Pike's (1977) relationships for the diameter of the raised crater rim versus rim crest diameter and floor diameter versus rim-crest diameter. These relationships hold for Copernican and Eratosthenian craters. The outer diameters of radar-bright rings fall close to Pike's relationship for the diameter of the raised lip versus rim crest as shown in the upper line. The inner diameters of the radar-bright rings compare closely to the floor width of Pike's relationship.

Using the same criteria for circular features in Venus images (Campbell & Burns, 1980) we have identified and plotted seven Venus bright-rings (Figure 1). The pairs of inner and outer diameters are plotted on the ordinate. The bar is of an arbitrary width placed over the Pike relationship. The pairs of bars for each feature overlap indicating at least a reasonable fit to the Pike relationship for impact craters. We suspect that slopes on Venus are much

lower than those on the Moon since the Venus images use the polarized return and see little indication of slope control. Most of the image brightness appears to be modulated by roughness variations on Venus. We postulate that these features, whether of volcanic or impact origin, are bright because of slopes and that there is a weathering process and downslope movement that is in equilibrium with the production and removal of the slopes.

If of impact origin, it appears that we may be seeing only a fraction of the craters. There is no way to estimate the rate of removal, or evolution from bright to dark, of the craters as we can on the Moon since the Venusian features may evolve very quickly or slowly. There are about a factor of ten fewer bright rings on Venus per unit area than there are on the Moon.

References:

Campbell, D. B. and Burns, B. A., 1980, Earth-based radar imagery of Venus: J. Geophys. Res., Vol. 85, p. 8271-81.

Pike, R. J., 1977, Size-dependence in the shape of fresh impact craters on the Moon: in Impact and Explosion Cratering, D. J. Roddy and R. O. Pepin, Eds., Pergamon Press, p. 489-509.

Thompson, T. W. et al., 1980, Infrared and radar signatures of lunar craters: Implications about crater evolution: in Proc. Conf. Lunar Highlands Rust, Papike, J. J. and R. B. Merrill, Eds., p. 483-499.

Zisk, S. H., Pettengill, G. H., and Catuna, G. W., 1974, High-resolution radar maps of the lunar surface at 3.8-cm wavelength: The Moon, Vol. 10, p. 17-50.

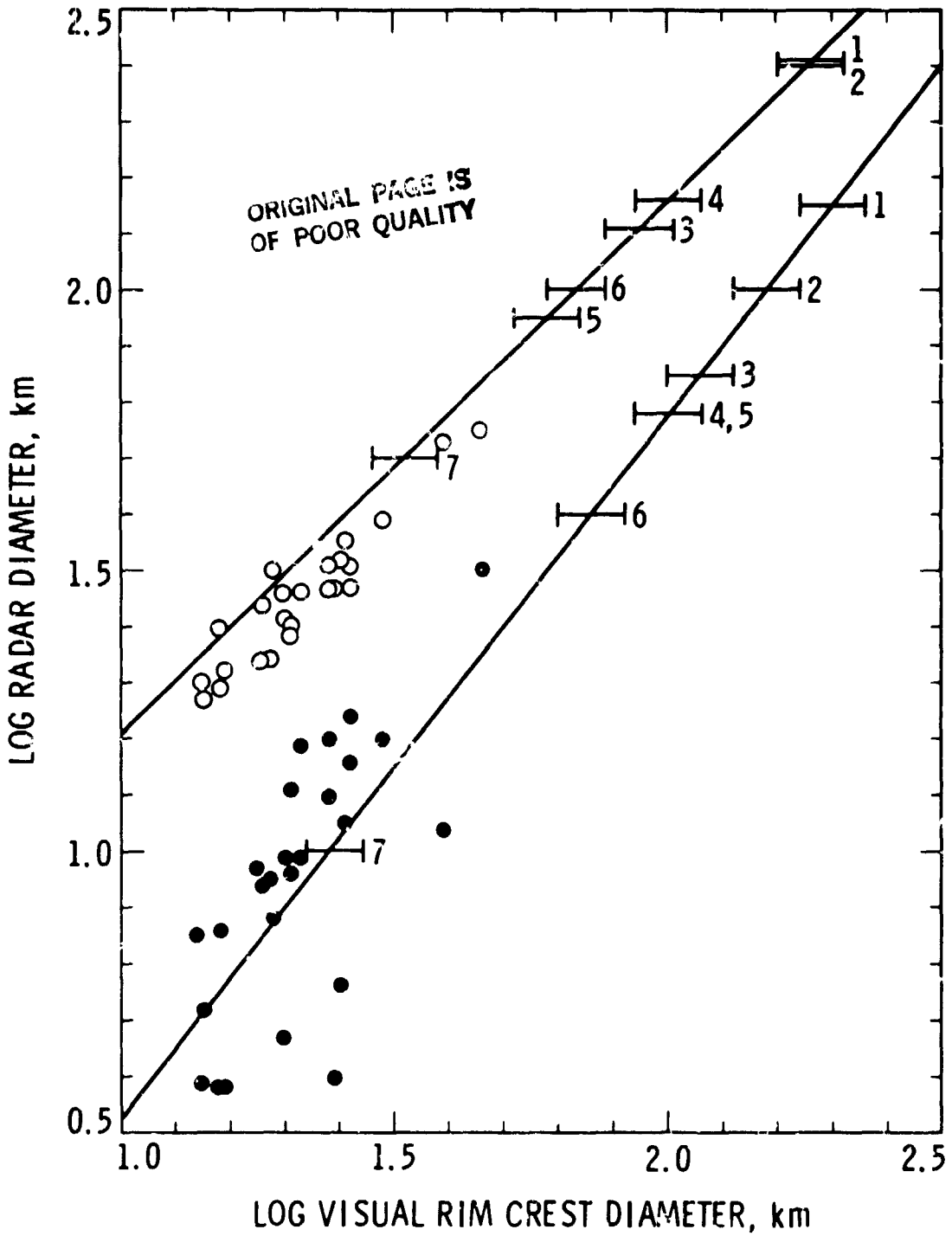

Open circles are outer diameter of lunar bright rings plotted against the rim crest diameter of the associated crater. Filled circles are corresponding inner ring diameters. Lines are from Pike (1977). Upper line is the diameter of the raised rim plotted against rim crest diameter. The lower line is the floor width versus diameter. Bars are the inner and outer rim diameters for seven Venusian bright rings placed along the Pike relationship.

RADAR ROUGHNESS AT VENUS LANDING SITES. James B. Garvin and James W. Head III, Dept. of Geol. Sci., Brown Univ., Providence, RI 02912.

Remote sensing of the surfaces of the terrestrial planets has greatly improved our understanding of the surface characteristics of these bodies at a variety of scales, ranging from millimeters to kilometers. With the advent of spacecraft capable of landing on the surfaces of the Moon, Mars, and Venus, it has been possible to observe local areas in situ with high resolution (mm to cm) cameras, and to analyze their surface properties in terms of the geologic processes that would most likely produce such landscapes. Radar observations of the Moon, Mars, and even of the Earth have recently proven to be valuable in the interpretation of planetary surface roughness at a centimeter-decameter scale over wide areas (1,2,3). The exact relationship between radar-derived measurements of surface roughness (i.e., block concentration, dune arrangement, etc.) is imperfectly known, but for the Moon and Mars, a correlation appears to exist when surface images are compared with orbital or Earth-based radar observations (1,2). Surveyor, Lunokhod, and Apollo photographs of the lunar surface show various types of terrains all of which have a characteristic local-scale roughness (i.e., fresh impact ejecta vs. mature mare regolith vs. highlands) -- this local-scale roughness correlates with orbital bistatic radar observations (1,2), and suggests that surface images can be used to calibrate our interpretation of the physical (geologic) nature of regions for which there is radar coverage. It is thus possible to extrapolate a local-scale view to an entire region using radar roughness information and surface pictures. For Mars, radar and infrared thermal inertia measurements were used to help select the Viking lander sites (4). At the Viking lander 1 site in Chryse Planitia there is good correlation between orbital and Earth-based remote sensing data and the views of the surface from the VL-1 cameras. Radar measurements give rms slope values near 5.0° which suggests a relatively rough and blocky surface (2). High resolution orbital photography (8-10 m/pixel) gives some indication that much of the region in Chryse near VL-1 is blocky and covered with meter-scale drifts or dunes. Thermal inertia data from the Viking orbiter IRTM supports the presence of blocks in the VL-1 area as well (3). On the basis of these correlations between surface roughness measured on a regional scale by radar and on a local-scale by surface cameras for the Moon and Mars, we seek to explore the nature of the venusian surface in the same manner. To accomplish this, we use the Pioneer Venus orbiter radar experiment data (roughness expressed as C-factor or rms slope in degrees) and the Venera lander panoramas (Veneras 9, 10, 13, 14) and related data. Due to the similarities between the spatial resolution and wavelength of the PV and Apollo orbital radars and the fact that the lunar radar roughness does correlate with surface photography, we are interested in comparing Venera panoramas with PV radar roughness. Is there a correlation between lander-scale roughness as seen in the Venera panoramas and the regional-scale roughness near the landing sites as measured by the PV radar instrument? Can block abundance be related to radar roughness? How do the lander site radar roughness signatures compare with the mean Venus roughness or with regional averages (i.e., for Aphrodite, Beta, Ishtar, etc.)? Here we focus on the PV radar data and the Venera lander panoramas in terms of what they can tell us of the local and regional scale geology of Venus.

Before considering the radar roughness data for the Venus landing sites (see Table I), it is appropriate to summarize the surface observations made by each spacecraft. Venera (V) 8 measured a surface albedo in excess of 0.20, suggesting bright materials; and the K, U, and Th content of surface materials using γ-ray spectrometry and found evidence for syenitic material (5,6).

V 9 and 10 produced the first photographs of the surface, measured the albedo, and used γ-ray spectrometry, discovering darker materials with K, U, Th contents similar to most basalts (5,6). The V 9 locality was littered with closely spaced fragments 5-70 cm in length and coarse fines could be observed amongst the somewhat angular blocks (7). The local terrain appeared to be sloping at a 10°-15° angle, suggesting the landing was made on a talus slope (5,7). V 10 observed plate-like outcrops amid zones of soil and small pebbles --there were few isolated blocks as at V 9. Apparently dust was more easily mobilized at V 10 than at V 9 because photometry data suggests a significant dust cloud was produced after the free-fall landing. The slope of the local terrain appears to be slight (8,9). V 11 and 12 did not obtain images, but each made photometric measurements while on the surface. The results suggest that V 11 landed on high albedo material (10). The PV Day Probe survived for over an hour on the surface--its particle detecting nephelometer recorded a post-impact disturbance that can be interpreted as a dust cloud (8,11). V 13 and 14 produced almost 360° panoramas of their local areas, as well as measuring the major element abundances in surface rocks via X-ray fluorescence (12). The V 13 locality is reminiscent of the V 10 landscape, with slabby rocks and fine materials. A landing-induced dust cloud was large enough to emplace cm-scale clods or pebbles on the lander ring. The V 14 landscape is remarkably uniform--a continuous sequence of layered rocks (at cm-scale) characterizes the local area. The site is almost devoid of fines, pebbles, or isolated fragments.

All of these observations illustrate the importance of scale in making correlations between radar and photographic observations. The radar (17 cm) is sensitive to scatterers (blocks, dunes, undulations) at 0.1 m to 10 m scales, but averaged over large areas (> 160 km^2), while the photographic observations have cm-resolution and cover an area 6 orders of magnitude smaller than the radar cell size (13). However, there is evidence from the Moon and Mars (1,3) that lander-scale areas are often representative of much larger regions.

The PV radar roughness data can be expressed in C-factor or rms slope format, and is derived from the radar altimeter measurements by means of fits to theoretical and empirical templates (13, 14). Our criteria for data selection allows only those radar data points falling within a 1° circle about the most recent lander coordinates to be considered. In addition, C-factor data with an error of over 100% are ignored. All valid data (usually ∿ 50 points) are averaged (see Table I) and compared with the global Venus averages (avg. ∿ 2.9°;17% of planet in 1.5-2.0° range). Over 60% of Venus is smoother than 3.0° rms, yet most of the lander sites are rougher than this value. Table I describes our preliminary results. Our preliminary analyses thus far permit the following general conclusions to be drawn:

1) On Venus there appears to be a positive correlation (as on the Moon) between radar roughness and roughness observed in Venera surface panoramas. The roughest (blockiest) surface images have the highest rms slopes (above 4° rms) as determined by those PV radar footprints falling within the confidence level for the Venera landing ellipses. For example, V 9 is rocky and has a high average rms slope (∿ 4°), in contrast with V 14 which is almost devoid of rocks and has a low average rms slope (∿ 2.9°). 2) Much of the surface of Venus is smoother than the terrain viewed by the Venera landers (at least in terms of 17 cm radar roughness)--only the regions around V 8 and 14 are near to the Venus mean roughness (∿ 2.9° rms). 3) The V 10 landing region has an extremely uniform radar roughness character--all of the PV radar observations within the 1° landing ellipse cluster about an rms slope of 3.5°. The standard deviation is 0.25°, versus 0.70° for the next best landing area radar

C-2

roughness. This suggests the terrain seen by the V 10 spacecraft may be regionally extensive. 4) Both the V 8 (no imaging) and V 14 landing areas display a radar roughness character (in terms of rms slope) that falls within the global Venus average range (2.5°-3.0° rms). 5) The V 9 locality, with a surface block cover of over 35% (more blocky than VL-2 on Mars), has a radar roughness that is comparable to that for the VL-1 site on Mars (at similar radar instrument wavelengths). This provides further evidence for the agreement between radar and photographic observations of surface roughness on terrestrial planets (Moon, Mars, and Venus).

References: 1) Moore, H. J. et al. (1980) Geol. Survey Prof. Paper 1046-B, Washington, D.C., 78 pp. (sec. B 34-41). 2) Pettengill, G. H. (1978) Ann. Rev. Astron. Astrophys. 16, 265. 3) Simpson, R. A. and Tyler, G. L. (1980) JGR 85, 6610. 4) Masursky, H. and Crabill, N. L. (1981) NASA SP-429, Washington, D.C., 34pp. 5) Keldysh, M. V. (1979) (ed) NASA TM-75706, Washington, D.C. 189pp. 6) Barsukov, V. L. et al. (1981) Abs. in Intl. Conf. on Venus Environment, Palo Alto, 8. 7) Florensky, C. P. et al. (1977) GSA Bull. 88, 1537. 8) Garvin, J. B. (1981) Proc. LPSC 12B, 1493. 9) Moshkin, B. E. et al. (1979) Cosmic Res. 17, 232. 10) Ekonomov, A. P. et al. (1979) Cosmic Res. 17, 590. 11) Ragent, B. and Blamont, J. (1980) JGR 85, 8089. 12) Florensky, C. P. et al. (1982) Pisma V. Astron. Zhur. 8, 429. 13) Pettengill, G. H. et al. (1980) JGR 85, 8261. 14) Pettengill, G. H. et al. (1980) IEEE Trans. Geosci. Rem. Sens. GE-18, 28.

Table I: Radar roughness of Venus landing sites as derived from Pioneer Venus orbital radar experiment data (expressed as rms slopes on a scale of 1-10 m).

Lander Site		Coordinates (lat.,lon.)	Average rms slope* (degrees)	Standard deviation rms slope (degrees)	Range of rms slopes (degrees)	Average error (%)	"Best"+ rms slope data point (degrees)
Venera 8	(1972)	-10°,335.0°	2.77	1.04	1.1-5.1	59	2.2
Venera 9@	(1975)	31.7°,290.8°	3.96	0.90	2.9-5.7	61	5.4
Venera 10@	(1975)	16.0°,291.0°	3.53	0.25	3.0-4.0	53	3.5
Venera 11	(1978)	-14.0°,299.0°	3.18	0.70	2.2-3.7	51	2.6
Venera 12	(1978)	-7.0°,294.0°	5.27	1.50	3.1-8.1	61	5.2
Venera 13@	(1982)	-7.6°,303.5°	3.57	1.20	1.9-5.7	56	3.4
Venera 14@	(1982)	-13.2°,310.1°	2.87	0.69	1.8-4.2	54	2.3
P-V Day	(1978)	-31.2°,317.0°	3.23	0.95	1.6-4.7	43	3.4
VL-1 (Mars)#@	(1976)	22.5°, 47.9°	4.7-5.0	N/A	4.0-5.7	~20	5.6

*of all P-V radar data points within ± 1° of landing site coordinates.

+the radar data point nearest the landing coordinates with the lowest error in rms slope.

#from Earth-based radar observations made at Arecibo (12.6 cm) and Viking bistatic radar data [Simpson and Tyler, 1978, 1980; Tyler et al., 1976].

@surface images exist.

MECHANISMS FOR LITHOSPHERIC HEAT TRANSFER ON VENUS: PREDICTIONS FOR SURFACE VOLCANIC AND TECTONIC FEATURES

Sean C. Solomon, Dept. of Earth and Planetary Sciences, M.I.T., Cambridge, MA 02139; and James W. Head, Dept. of Geological Sciences, Brown University, Providence, RI 02912.

Introduction. The mechanism of heat transport across the outer 100 km of a planetary interior plays a pivotal role in determining the styles and magnitudes of tectonic and volcanic activity at the planet's surface. For the Earth, heat transport is dominated by the processes of plate creation, cooling and subduction [1]. For the smaller terrestrial planets, heat transport is principally by conduction through a globally continuous lithospheric shell [2]. For Io, volcanic activity at individual eruptive centers dominates the planetary heat flux [3-4]. For the planet Venus, the evidence on the mode of lithoshperic heat transfer is equivocal [5-9]. In this paper we evaluate each of the three mechanisms observed on other solid planets and satellites (plate recycling, lithospheric conduction, and hot spot volcanism) as candidates for the dominant process of lithospheric heat transport on Venus. Further, we make specific predictions for the type and distribution of surface volcanic and tectonic features expected for each mechanism.

Plate Recycling. The creation of new lithosphere, its cooling during seafloor spreading, and its subsequent subduction account for about 65% of the current heat loss of the Earth, estimated at 4.2×10^{13} W[1]; the remainder of the heat loss is contributed by lithospheric conduction (20%) and radioactive decay in the continental crust (15%). Plate tectonics, in addition to its dominant role in heat transfer in the outer portions of the Earth, accounts for most of the characteristics of the large scale topography of this planet, including the mid-ocean ridges, the systems of trenches and island arcs, the linear mountain belts at Andean-type subduction zones or at Himalayan-type continental collisions, and ultimately the formation, growth and distribution of continents. Venus, similar in mass and radius to the Earth, is likely to have a roughly similar heat budget, an assumption consistent with the Venera measurements of surface radioactivity and the Pioneer measurements of atmospheric ^{40}Ar. Scaling by mass from the Earth gives the Venus heat loss at 3.4×10^{12} W. A reasonable hypothesis is that Venus, like the Earth, loses much of this heat by plate recycling.

This hypothesis has been challenged in the literature on the basis of several arguments: (1) that topographic features indicative of plate tectonics can't be "seen" on Venus [5,6,10]; (2) that most of the Venus surface is "ancient" on the basis of the distribution of inferred impact craters and basins[10]; (3) that because of the high surface temperature, the Venus lithosphere is less likely to subduct than oceanic lithosphere on Earth [8,11]; and (4) that because of the high surface temperature, plate recycling is a less "significant" process for removing heat than on Earth [12].

These arguments are all assumption-dependent, however, and it can be demonstrated [13,14] that none of them are sufficiently compelling to rule out plate recycling on Venus at present. In particular, the search for topographic analogs on Venus to plate tectonic features on Earth is made

difficult by the coarse horizontal resolution of Pioneer Venus altimetry and, for oceanic-type features, by the lack of an ocean and by the likely lesser temperature drop across the lithospheric thermal boundary layer on Venus [5-8]. Further, many terrestrial tectonic features may owe their principal characteristics to the abundance of surface water or to the low temperature rheology of rocks. Island arc volcanism, for instance, may require the subduction of material containing free water or hydrated minerals and the release of that water at depth to initiate melting. Notably, there are topographic features, such as linear mountain belts, continental-sized plateaus and arcuate ridges and troughs, which resemble terrestrial features of plate tectonic origin [7, 10].

The hypothesis that plate recycling dominates lithospheric heat transport on Venus leads to the prediction (Table 1) that the rolling plains and lowlands provinces [10] are analogs to terrestrial ocean basins. In order for plate recycling to remove the necessary heat, spreading centers would be characterized by rapid spreading rates and modest relief in comparison to Earth. The Venus highlands [10] would be analogs to terrestrial continents, at least in terms of greater crustal thicknesses and probably greater ages of surface units than elsewhere. Venus mountain belts would form as on Earth, by continental collision (Himalayan analog) or in the process of subduction beneath continental lithosphere (Andean analog).

Conduction. If all of the heat from Venus were transported by conduction, the lithospheric thermal gradient would be roughly twice that in terrestrial ocean basins [15], or about 24°C/km. Thus temperatures corresponding to the base of the thermal lithosphere in oceanic regions on Earth [15] would be reached at about 40 km depth. It is difficult to envision mechanisms for supporting the 13 km of relief on Venus if the thermal lithosphere is this thin. One likely implication of the hypothesis that conduction dominates heat transfer on Venus is that all surface topographic relief, at least on scales smaller than characteristic horizontal scales of mantle convection, must be geologically young.

The hypothesis that lithospheric heat flux on Venus occurs principally by conduction leads to the prediction that major topographic features are the response of a readily deformable lithosphere to shear tractions associated with mantle convection (Table 1). Modestly elevated regions in the rolling plains may be areas of recently extended and thinned crust and lithosphere, areas which will subside to lowland elevations during lithospheric cooling and thickening [16]. The more elevated highlands may be areas of thickened crust and lithosphere resulting from lithospheric compression.

Hot Spot Volcanism. If on Venus, as on Io, the dominant mechanism of lithospheric heat transfer is volcanic activity at individual vents, then there are profound implications for volcanic flux and rates of resurfacing. The most prominent hot spot on Earth, Hawaii, has an average volcanic flux for the past 42 m.y. of 2×10^{-2} km^2/yr [17]; at this rate Hawaiian volcanism contributes less than .01% of the Earth's heat loss. Whether the number of important hot spots on Earth is 20 [18] or closer to 100 [19], the total contribution of hot spot volcanism to terrestrial heat loss is minor. If all of the Venus heat were lost by hot spot volcanism, a total of 10^4 "Hawaiis" would be needed, or one "Hawaii" for each 200-km square of Venus

surface. Every 2 m.y. these hot spots would add enough volcanic material to cover the entire Venus surface to a depth of 1 km.

The hypothesis that hot-spot volcanism dominates lithospheric heat transport on Venus leads to the prediction that most topographic features are of volcanic origin (Table 1). In particular, the Venus highlands would most likely have been formed by volcanic construction. Tectonic activity in the absence of large-scale horizontal motions should be principally restricted to that associated with vertical motions of the lithosphere.

Conclusions. Without more detailed information on the Venus surface, all of the mechanisms for lithospheric heat transfer considered here should be considered as potentially important for Venus. So, too, should scenarios in which combinations of mechanisms operate [e.g., 8] or in which the dominant mechanism changes during the course of planetary history [e.g., 5]. Although the specific implications of these mechanisms for tectonic and volcanic features on the Venus surface are quite different (Table 1), each of the hypotheses that one of these mechanisms dominates leads to the prediction that many if not most of the topographic features of the Venus surface are geologically young.

Table 1. Implications of End-member Hypotheses for Lithospheric Heat Transport on Venus

Surface Characteristics	Plate Recycling	Lithospheric Conduction	Hot-Spot Volcanism
Volcanic activity	Extensive; activity dominantly at divergent boundaries	Minor	Extensive; active centers nearly cover surface
Tectonic features	Widespread; dominated by plate interactions	Possibly extensive deformation of thin lithosphere	Primarily vertical tectonics
Ages of surface units	Rolling plains and lowlands geologically young ($< 10^8$ yr)	Unconstrained; ancient impact features may be preserved	Much of surface young ($\lesssim 10^7$ yr)
Nature of mountain belts	Products of plate convergence	Anomalously thick crust and lithosphere	Volcanic constructs
Nature of highlands	Analogs to terrestrial continents	Thickened crust and lithosphere	Thickened volcanic crust
Nature of rolling plains and lowlands	Analogs to terrestrial ocean basins	Thinned crust and lithosphere	'Normal'-thickness volcanic crust

References: [1] J.G. Sclater et al., RGSP, 18, 269, 1980; [2] S.C. Solomon, GRL, 5, 461, 1978; [3] D.L. Matson et al., JGR, 86, 1664, 1981; [4] T.C. O'Reilly and G.F. Davies, GRL, 8, 313, 1981; [5] R.J. Phillips et al., Science, 212, 879, 1981; [6] R.E. Arvidson and G.F. Davies, GRL, 8, 741, 1981; [7] J.W. Head et al., Amer. Sci., 69, 614, 1981; [8] R.J. Phillips and M.C. Malin, in Venus, in press, 1982; [9] G.W. Brass and C.G.A. Harrison, Icarus, 49, 86, 1982; [10] H. Masursky et al., JGR, 85, 8232, 1980; [11] D.L. Anderson, GRL, 8, 309, 1981; [12] W.M. Kaula and R.J. Phillips, GRL, 8, 1187, 1981; [13] S.C. Solomon et al., JGR, 87, in press, 1982; [14] S.C. Solomon and J.W. Head, JGR, in press, 1982; [15] B. Parsons and J.G. Sclater, JGR, 82, 803, 1977; [16] D. McKenzie, EPSL, 40, 25, 978; [17] H.R. Shaw, BGSA, 84, 1505, 1973; [18] W.J. Morgan, Nature, 230, 42, 1971; [19] K.C. Burke and J.T. Wilson, Sci. Am., 235(2), 46, 1976.

IMPACT AND VOLCANISM REVISITED, WITH EMPHASIS ON VENUS

Wolfgang E. Elston, Department of Geology, University of New Mexico, Albuquerque, NM 87131

The great impact-versus-volcanism controversy of the 1960's seems naive in retrospect, as both processes are now well-established on the Moon and inner planets. Exploration of space coincided with the rise of terrestrial plate tectonics; both gave new perspectives to planetary evolution. We now recognize a continuum, ranging from small and relatively inert bodies like the Moon and Mercury, on which impact scars are dominant features, to larger and dynamic bodies like Earth, on which impact features are relatively obscure. However, no body of the inner solar system turned out to have been miraculously shielded from early intense accretionary bombardment, or later stages of protracted but diminished cometary and/or asteroidal bombardment. All bodies the size of the Moon or larger were shown to have complex thermal histories, sufficient for two principal stages of partial melting on the early Moon. On Earth, the internally heated lithosphere has interacted with the externally heated hydrosphere and atmosphere to create the ocean-continent dichotomy and vigorously interacting lithosphere plates. While the largest number of terrestrial volcanoes is at plate boundaries, there is a strong tendency for volcanic edifices to develop their largest sizes in plate interiors, both oceanic and continental.

Mars occupies an intermediate position between smaller and long-inert bodies like the Moon and Mercury and dynamic bodies like Earth. There is no evidence for true plate boundaries or for true continental crust. Even on topographically high regions like the Tharsis Ridge, large volcanoes take forms more characteristic of the interior of terrestrial oceanic plates (e.g., Hawaii) than of either the interior of continental plates or plate boundaries.

In the Earth-to-Moon continuum, what is the position of Venus? By analogy with Mars, there has been a tendency to interpret large constructs as volcanoes and possible crater-like features as impact sites. Actually, it is possible that large accretionary impact craters have been destroyed or obscured by processes analogous to development of thin and primitive continental crust. On Earth, formation of sial is furthered by both sedimentary and magmatic processes. Sedimentation effectively differentiates primitive basaltic crust, by removing Na to sea water and evaporites, Ca to limestone; Mg to dolomite and sea water, and Fe to specialized chemical sediments, leaving a residue enriched in Si, Al, and K (i.e., sial). Analogous processes are less efficient on Venus. Although chemical weathering may be effective, transportation and redeposition are likely to be ineffective in the absence of water. However, magmatic processes like those of the primitive Earth, leading to sialic segregations, may well have been operating on Venus, to form thin continent-like crust. It is

precisely in areas of thin or thinned contintal crust, in plate interiors, t t the largest terrestrial volcano-tectonic caldera complexes occur. In tensional tectonic regimes, crustal thinning results in rising isotherms and partial melting of sialic components. The results can be seen in large calderas and ring complexes, tens of km to > 100 km in diameter, partly buried under their own ejecta of ignimbrites and other pyroclastic materials. Poorly understood thermal events have resulted in this style of eruption over wide continental areas of Earth, sufficiently far removed from plate boundaries so that no simple connection with plate-boundary processes has been established. The Pan-African event, about 500 to 700 m.y.b.p., is a possible example; by one interpretation (Kröner, 1979) it represents a transitional stage of continental evolution, from pre-plate tectonic to plate tectonic. The truly gigantic Proterozoic ring complexes (up to 900 km diameter) postulated by Kloosterman (1966 and personal communication, 1973) in the Guiana shield of Brazil may have formed under similar circumstances. In Phanerozoic time, intraplate thermal events are more likely to have occurred in continental rifts and ensialic backarcs, where crustal thinning temporarily caused a reversion to Precambrian-like conditions. The Basin and Range province of southwestern North America is an example (Eaton, 1982). About 200 and 500 ignimbrite caldera complexes formed there between 40 and 20 m.y.b.p., over an area of 1 million km^2, during a period of massive ductile extension of the continental lithosphere.

It is proposed that terrestrial intraplate continental areas of extensional tectonic regimes and lithosphere thinning may be analogs of cratered terrains of Venus. The crater-like features on Venus would be interpreted as large calderas or volcano-tectonic depressions, formed on a thin continent-like crust in a primitive state of evolution.

REFERENCES CITED

Eaton, G.P.; 1982, The basin and Range province: Origin and tectonic significance: Ann. Rev. of Earth and Space Sciences, v. 10, p. 409-440.

Kloosterman, J.B., 1966, Granites and rhyolites of São Lourenço: A volcano-plutonic complex in southern Amazonia: Eng. Min. Met. (Brazil), v. 44, no. 262, p. 169-171.

Kröner, A., 1979, Pan African plate tectonics and its repercussions on the crust of northeast Africa: Geol. Rundschau, v. 68, p. 565-583.

VENUS, ASIAN VOLCANOTECTONICS, AND LANDSAT AND SHUTTLE IMAGERY.

J.L.Whitford-Stark, Geology Dept. Sul Ross State University, Alpine Texas 79830.

The K-U systematics of the Venusian surface materials derived by analysis of Venera 8, 9, and 10 data indicated the presence of two rock types; one with properties characteristic of tholeiitic basalts, and the other with the properties of alkali basalts and basanites(1). A similar dichotomy has been found between materials at the Venera 13 and 14 sites (2). The sites with alkali basalt characteristics(Veneras 8 and 13) are generally topographically higher than those with tholeiitic characteristics. Although alkali basalts are found on oceanic islands on Earth, the majority of alkali basalts are found in continental environments.

The author has been compiling volcanic, tectonic, and geochemical data (3,4) for mainland Asia in an attempt to relate all three, and to provide a data base for comparison with extraterrestrial bodies. The major Cenozoic volcanic areas and tectonic features of Asia are illustrated in Fig. 1. The area is one of extreme structural complexity containing areas of continent-continent collision, ocean-continent collision, back-arc basin development, rifting, transcurrent faulting, and domal uplift. Volcanism appears to be relatable to each of these environments. Fig.2 shows the compositional variation among the Asian volcanics. It is possible to distinguish three types of variation among the separate provinces. Firstly there are those provinces with little variation(B,F,H,L,M). Secondly, those with mild alkali enrichment(G), and, thirdly, those with strong alkali enrichment(A,E,J,N,P). Province J could be separated from the third group as a result of a possible "Daly" gap. In the context of a venusian comparison, two interesting areas are Provinces G(Mongolia and Mancnuria) and P (Tibet). Province G is currently located far from any plate boundary and volcanism is mostly associated with large faults. The province is dominated by alkali basalts of deep-seated origin with few silica-rich volcanics. A detailed study of the Wudalianchi area of Province G has been submitted for publication(5) and a Landsat analysis of the area is underway. The volcanics of Tibet result from the continental collision between the Indian and Eurasian plates. Although the materials are as alkaline as those of Province G, silica-rich materials abound(4). Along the Baykal rift zone (F), alkali basalts are found in quantity only at the extreme northeastern (Vitim Plateau;E) and western(Tuva;G) . Differentiated volcanics with up to 62 % SiO_2 are found on the Vitim Plateau(4). The volcanics of Province N result from the eastward subduction of the Indian Ocean and range in composition from andesitic in the west to basaltic in the east. The Tengchong district of China is thought(6) to mark the easternmost boundary of the Indian plate.Northern Tengchong, composed of olivine basalts, was imaged by the Shuttle Imaging Radar experiment(7).

On the basis of the Asian volcanic compositions, it is predicted that if plate tectonics has occured on Venus there will probably be substantial volumes of silicic volcanics. If plate tectonics has not taken place, the "continental" terrains will probably be dominated by alkali- and volatile-rich extrusives. A further feature of the continental volcanics of Asia is that they tend to form flat-lying lava fields with associated cinder cones

(4,5,7), not large central-vent volcanoes. If the topographically high features of Venus, such as Beta Regio, are of volcanic origin, an origin via a process similar to that resulting in terrestrial oceanic island formation would seem more consistent with their morphologies than a formation via plate interaction. A rift and dome analogy(8) for the Beta Regio area would not, however, be inconsistent with the Baykal data.

References: 1) Surkov,Yu.A. 1977 Proc.Lunar Planet.Sci.Conf.8th,2665-2689 2)Wilson,L. 1982 Nature 296, 607-608. 3) Whitford-Stark,J.L. 1981 Reports of Planetary Geology Program-1981. p.180-182. 4) Whitford-Stark,J.L. 1983 J.Volcanol.Geotherm.Res. in press. 5) Feng,M. and Whitford-Stark,J.L. 1983 J.Volcanol.Geotherm.Res. submitted.6Fan,P.F. 1978 Tectonophys.45, 261-267 7) Whitford-Stark,J.L. 1982. Submitted to Spaceborne Imaging Radar Symp. 8) McGill,G.E. et al 1981 Geophys.Res.Lett. 8, 737-740.

Figure Captions:

1. Volcanotectonic map of eastern Asia. Horizontal ruling represents back-arc basins; solid shading is Cenozoic volcanics - paleogeographic reconstructions for the U.S.S.R., outcrop for remaining areas; lines with solid triangles are plate boundaries; lines with hollow triangles are former plate boundaries; hachured lines are rifts; remaining lines are large faults with direction of motion indicated, where known (from 4).

2. AFM diagrams for the Asian volcanic provinces. Province A is the eastern seaboard of the U.S.S.R., B is the Aniusky Range, E is the Vitim Plateau, F is the Baykal region, G is Mongolia and parts of Manchuria and the southern U.S.S.R., H is northeast China and the eastern U.S.S.R. inland of the coastal belt, J is northern Korea, L is eastern China, M is Indochina, N is Burma, and P is Tibet.

FIG.1

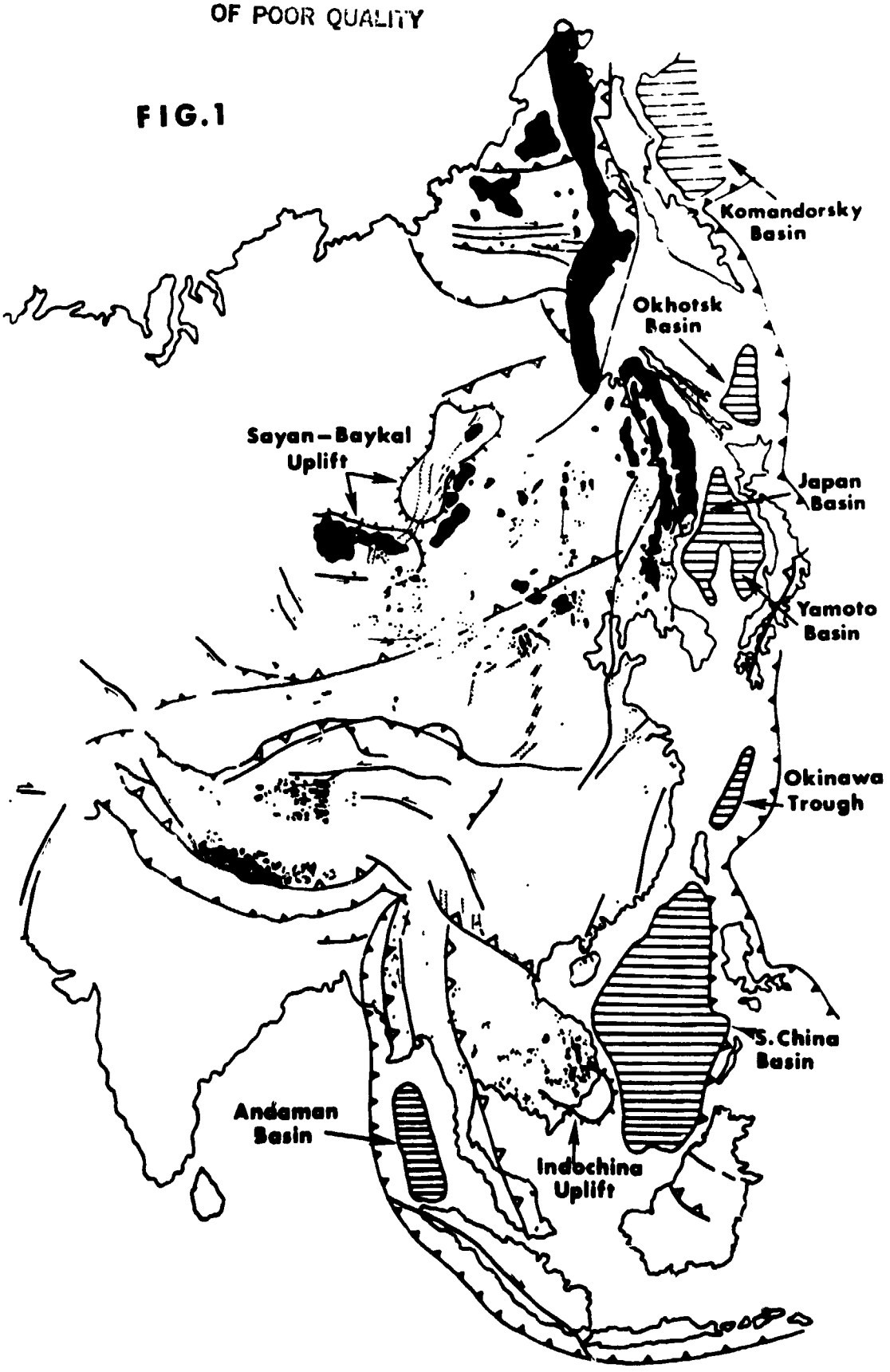

ORIGINAL PAGE IS
OF POOR QUALITY

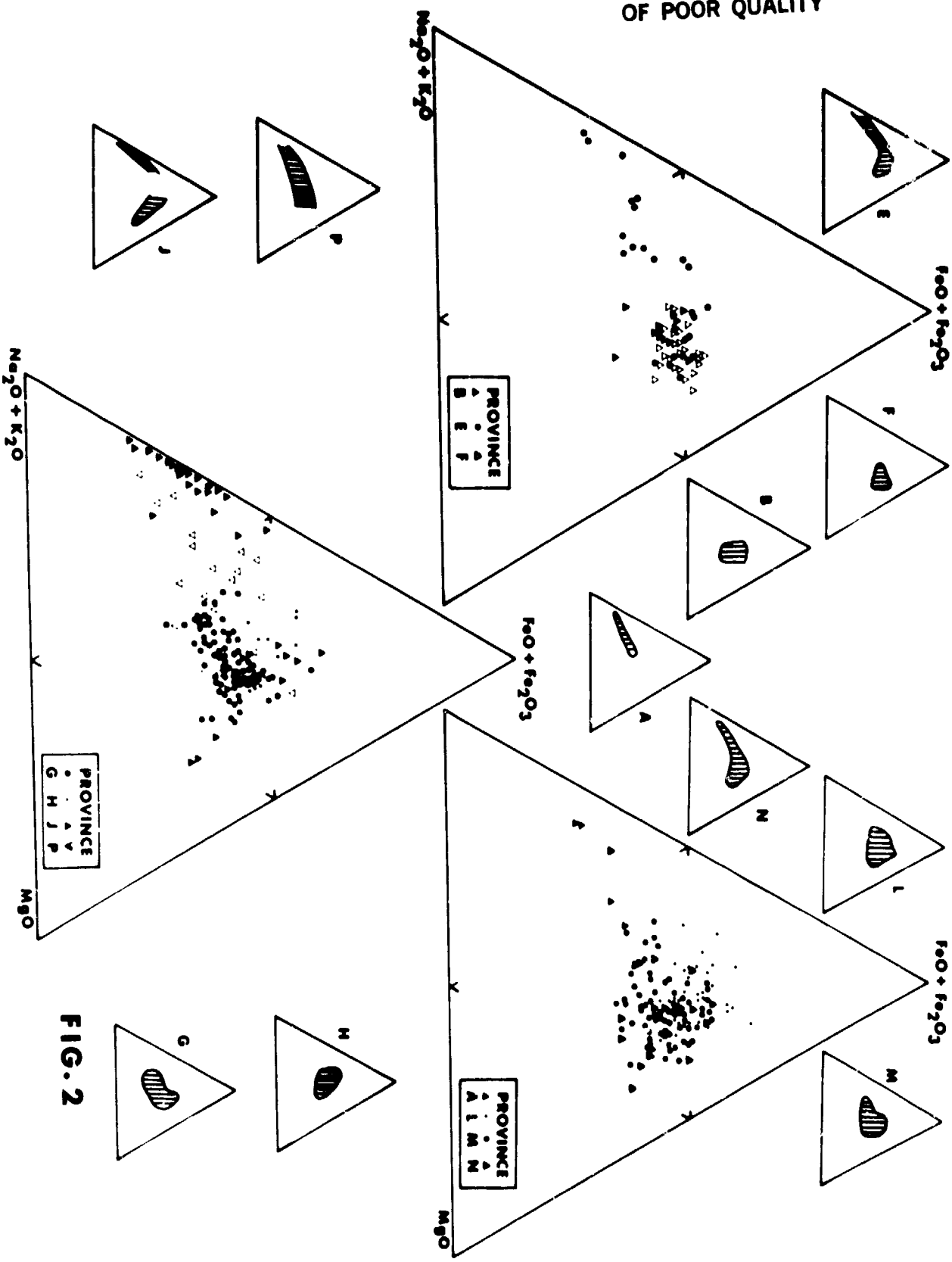

FIG. 2

Chapter 4

CRATERING PROCESSES AND LANDFORM DEVELOPMENT

THE EFFECT OF CRUSTAL VISCOSITY ON IMPACT CRATERING OF ICY SATELLITES

Fink, J.H., Greeley, R. (Geology Department, Arizona State University, Tempe, AZ 85287) and Gault, D.E. (Murphys Center for Planetology, Murphys, CA 95247)

Impact craters are the principal geologic structures available for the remote determination of planetary crustal properties. Individual craters' morphologies and the planetary statistics of crater sizes and shapes have both been used to infer the nature of regoliths, stratigraphy, and relative ages of surfaces on the Moon, Mercury and Mars. Hypervelocity impact experiments into sand and other dry targets have provided an empirical basis for scaling laws relating crater dimensions to impactor properties, gravity and the crustal strengths of these planets. The presence of near-surface volatiles on Mars has been used to explain the fluid-like ejecta morphology of some of its craters. Experiments designed to simulate such impacts require targets capable of fluid behavior, and clay slurries with Bingham type rheologies proved most successful (Gault and Greeley, 1978; Greeley et al., 1980, 1982; Fink et al., 1981).

The galilean and saturnian satellites provide new cratering conditions to evaluate which favor a different scaling relation that takes account of the viscosity of the planetary surface as well as gravity and crustal strength. In order to investigate the effects of viscosity independent of target strength, we have performed a series of 218 impact experiments at the NASA Ames Vertical Gun Facility, using homogeneous Newtonian oil targets (Fink et al., 1982). Viscosities ranged from 0.01 to 10^3 Pa-s, while surface tensions, densities and thermal properties remained nearly constant.

By measuring transient crater bowl diameters in high speed motion pictures, we were able to derive empirical relationships among crater size (V) and shape (depth-to-diameter ratio), impactor diameter (D_p), mass (m) and velocity (U), and target viscosity (η) and density (ρ). Two distinct regimes can be defined by plotting the dimensionless groups $\pi_1 = [V\rho/m][1.61gD_p/U^2]^{0.6}$ and $\pi_2 = [\eta/\rho D_p U]$. Below a value of about $\pi_2 = 0.005$, dimensionless volume (π_1) is independent of target viscosity, whereas for values of π_2 larger than about 0.1, volume decreases steadily as viscosity increases, and is independent of gravity. Crater depth-to-diameter ratios show a similar two-part dependence on viscosity. Below the transition, all craters have approximately the same shape. For larger values of π_2, craters have progressively smaller diameters for a given depth (or equivalently, craters of the same diameters are deeper).

If we assume that these criteria can be extrapolated to planetary scale craters, then viscous effects will be favored by small impacting bodies traveling at low velocities hitting planets with low values of g and high kinematic viscosities. Conditions on the icy satellites may favor this viscous regime, especially in the saturnian system where slow moving impacting bodies have been postulated and where the small satellites have low gravitational accelerations and low surface densities.

The relative ages of craters on icy satellites have been estimated from their depth-to-diameter ratios (e.g., Passey and Shoemaker, 1982). These interpretations assume that all craters form with bowl-shaped profiles and then relax by slow viscous flow over geologic time. Flatter craters are thus assigned greater ages than deeper craters. However, transient craters in viscous materials could have relatively greater depth-to-diameter ratios than

100

craters in adjacent terrains with different material properties. Thus, for example, if an icy satellite had some regions with high heat flow, these might yield more fluid slurries during impact. Rapid readjustment then could produce final craters with lower depth-to-diameter ratios than those in colder areas. Similar ambiguities could arise from impactors of different velocities or sizes hitting identical surfaces.

In summary, relative age determinations of different surfaces on the icy satellites must take into account the possibility that craters subjected to viscous scaling laws would have different shapes and volumes than those controlled solely by gravity.

REFERENCES CITED

Fink, J.H., Greeley, R. and Gault, D.E. (1982) The effect of viscosity on impact cratering of the icy saturnian satellites. Geophysical Research Letters [in press].

Fink, J.H., Greeley, R. and Gault, D.E. (1981) Impact cratering experiments in Bingham materials and the morphology of craters on Mars and Ganymede. Proc. Lunar Sci. Conference, 12th, p. 1649-1666.

Gault, D.E. and Greeley, R. (1978) Exploratory experiments of impact craters formed in viscous-liquid targets: Analogs for martian rampart craters? Icarus, v. 34, p. 486-495.

Greeley, R., Fink, J.H., Gault, D.E., Snyder, D.B., Guest, J.E. and Schultz, P.H. (1980) Impact cratering in viscous targets: Experimental results. Proc. Lunar Planet. Sci. Conf., 11th, p. 2075-2097.

Greeley, R., Fink, J.H., Gault, D.E. and Guest, J.E. (1982) Impact cratering in simulated icy satellites. In The Satellites of Jupiter (D.M. Morrison, editor) Univ. Arizona Press [in press].

Passey, Q.R. and Shoemaker, E.M. (1982) Craters and basins on Ganymede and Callisto: Morphologic indicators of crustal evolution. In The satellites of Jupiter (D.M. Morrison, ed.) Univ. Arizona Press [in press].

Mudrains on Mars -- What Causes Ejecta to Flow?

Michael C. Malin, Department of Geology, Arizona State University, Tempe, AZ 85287

Craters with multiple, lobate ejecta blankets with distal and surficial evidence of flow have been the subject of considerable and often heated debate since their identification in Viking Orbiter images. In a literature of papers and abstracts far too voluminus to cite in toto here (see e.g., 1, 2 as representative examples) numerous investigators have examined the distribution, morphology and relevant photogeological criteria, discussed possible emplacement mechanisms, and evaluated environmental or geophysical implications of these mechanisms. Laboratory experiments have sought to simulate, at least on a small scale, features of flow-ejecta craters. Theoretical models have attempted to isolate diagnostic criteria by parameterizing flow behavior. The diversity in interpretation is at least as great as the number of different names by which these craters are called.

Essentially all interpretations invoke some form of volatile-silicate rock interaction, though the details vary widely. It is probably safe to say that among the leading ideas are 1) interaction of rock ejecta with volatile atmospheric gasses (either by aerodynamic breaking (3) or by ingestion and fluidization) and 2) interaction of rock and volatile ejecta, with the ejected volatile most often discussed being liquid water. Examinations of target materials, at least in small scale laboratory impact experiments, have concentrated on relatively low viscosities ($\lesssim 10^3$ poise) and strengths.

A third idea might be to combine the ejection of volatile materials and post-ejection interaction of these materials with the ejected rock material. Such a concept would draw upon the experience of terrestrial volcanologists and sedimentologists who encounter such phenomena in the formation of accretionary lapilli and pisolites in conditions of high atmospheric water vapor and dust content (e.g., as in pyroclastic volcanic eruptions). Applying this idea to hypervelocity impact cratering might lead to the following scenerio:

1. Impact into rock and ice materials. Ice may be either interstitial or segragated. Frozen water reduces the need for special environmental, geothermal, or stratigraphic requirements.

2. Ejecta in the form of a) rock fragments, b) ice, c) steam, and d) a very small amount of water (probably negligable). It is the steam (some percent of the total available volatile) that is important.

3. As ejecta curtain expands, the steam cools and nucleates on the dust in the cloud, forming droplets. The timescale for this nucleation and droplet formation is less than the ballistic flight-time for ejecta from craters of a certain size or larger.

4. Droplets of condensed water and dust (e.g., accretionary lapilli or pisolites) cool much more slowly than steam. Timescale for freezing is greater than flight time.

5. Ejecta strikes ground as mud drops and chunks. Flowage occurs as deposit integrates, aided by liquefaction.

6. Materials ejected at differing angles and/or experiencing different heating histories during impact account for multiple deposits. "Jetted" materials have short flight-times, high, oblique velocities, and hence have little chance to allow condensation. Thus, they form distal secondary craters. Some materials fall in areas of condensation, but segragation of volatile and non-volatile phases allows concentric zones of increasing and then decreasing water content. Innermost area has materials that are again "dry" or "dryer" and give rise to thicker, more viscous flows.

7. Small craters do not have flow ejecta because travel times are less than condensation times.

References

1. Carr, M. H., et al (1977) J. Geophys. Res. 82, 4055-4065.
2. Mouginis-Mark, P. (1981) Icarus 45, 60-76.
3. Schultz, P. and Gault, D. (1979) J. Geophys. Res. 84, 7669-7687
See also numerous papers cited therein, and PGPI abstracts 1978 to present.

Spatial Distribution of Craters on the Moon and Callisto

Alex Ruzicka and Robert G. Strom, Lunar and Planetary Laboratory,
University of Arizona, Tucson, AZ 85721

The crater size/frequency distribution on Callisto (and Ganymede) has a marked deficiency of craters greater than about 30 km diameter relative to the heavily cratered regions on the terrestrial planets (Mercury, Moon and Mars). This deficiency has been attributed to either (a) an obliteration of large craters by viscous relaxation when the crust of Callisto was more thermally active (1, 2,), or (b) the impact of a population of objects which was intrinsicilly deficient in large objects (3, 4).

To distinguish between these two explanations, Woronow and Strom (4) conducted a Monte Carlo computer simulation in which a lunar highland size/frequency distribution was imprinted on a surface and craters eliminated in such a way as to produce the observed Callisto size/frequency distribution. The simulation was completely independent of any assumptions concerning the thermal history, crustal-thickness history or ice rheology of Callisto. The simulated surface (Fig. 2d) showed a crater spatial distribution markedly different from that observed on Callisto (Fig 2c). On the simulated surface, extensive uncratered areas were produced by the obliteration of large craters; a condition not observed on Callisto. Gurnis (5) carried this approach farther by using a variety of size distributions in the Monte Carlo simulation and comparing the resulting spatial distributions with that observed on Callisto by "nearest neighbor" statistical methods. This more rigorous study confirmed the previous results and set more accurate limits on the amount of large-crater obliteration on Callisto. Both studies indicate that the observed crater size/frequency distribution on Callisto is essentially a production population which differs significantly from that on the terrestial planets.

In order to further test these Monte Carlo computer results, an actual surface of the lunar farside highlands was selected to perform a somewhat similar simulation for comparison with Callisto. Although two lunar areas were initally chosen for their apparent lack of plains and secondary craters, one of these areas has a super-abundance of smaller craters relative to other regions of the lunar highlands. Until we understand the reason for this anomaly (possibly clusters of secondaries from Orientale and another nearby basin), only the more typical region will be considered in this preliminary report.

The goal of this study was to compare the spatial distribution of craters 8 km diameter on an area of Callisto with that of a lunar highlands area from which craters had been removed to produce the Callisto size/frequency distribution. The region on Callisto was one used earlier by Woronow and Strom (4) for their comparison with the Monte Carlo simulation, and comprises an area of 6.4×10^5 km^2 (Fig 2c). The similar-sized lunar area (6.2×10^5 km^2) is centered at 160°W, 65°N in the farside north polar region (Fig. 2a).

Craters in the lunar area were mapped and classified according to degradational type using the five-fold LPL scheme where Class 1 is the freshest and Class 5 the most degraded. The size/frequency distribution

was then determined and compared with that for the Callisto area (Fig. 1).

Craters were removed from the lunar area so that the size/frequency distribution matched that of the Callisto area. The obliteration sequence was determined by the degradational state of the craters; the older degraded craters were removed first followed by progressively fresher craters. At the larger size even some of the relatively fresh craters had to be removed to reproduce the Callisto curve.

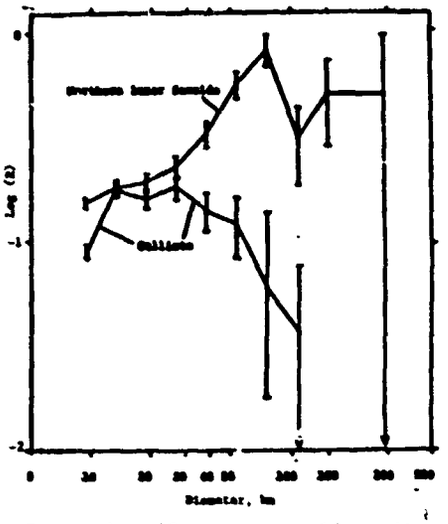

Fig. 1. Size/frequency distributions for the lunar and Callisto areas shown in Fig. 2a and c.

Figure 2a, shows the spatial distribution of craters in the lunar area while Fig. 2b shows the distribution after the appropriate number of craters were removed to produce the observed Callisto size/frequency distribution (Fig. 1). A visual comparison of Figures 2b and 2c shows that the spatial distributions of the two areas are very different despite the similarities in the overall crater density and size/frequency distribution. On the lunar area there are large relatively crater-free regions not observed on Callisto, because of the necessity of removing substantial numbers of large, relatively fresh craters in order to derive the Callisto size distribution. On the other hand, the derived spatial distribution of the lunar area (Fig. 2b) is similar to Figure 2d, which is the spatial distribution derived from the Monte Carlo computer simulation of a lunar-like impact history done by Woronow and Strom (4). This confirms the validity of the earlier Monte Carlo simulations.

The results of this study, together with those of the Monte Carlo computer simulations, strongly suggest that the Callisto (and Ganymede) crater population is basically a production population deficient in large craters relative to that of the terrestrial planets. This indicates that the population of impacting objects responsible for the period of heavy bombardment in the inner Solar System was different from that at Jupiter, and probably had a different origin as well.

References

(1) Parmentier, E.M. and Head, J.W., Internal Processes Affecting Surfaces of Low-density Satellites: Ganymede and Callisto, J. Geophs. Res., 84, 6263-6276, 1979.

(2) Shoemaker, E.M. and Wolfe, R.F., Cratering Time Scales for the Galilean Satellites, The Galilean Satellites, (Morrison, ed.), Chapter 10 Univ. of Ariz. Press, 1982.

(3) Strom, R.G., Woronow, A., and Gurnis, M., Crater Populations on Ganymede and Callisto, Jour. Geophys. Res., 85, 8659-8674, 1981.

(4) Woronow, A. and Strom, R.G., Limits on Large-Crater Production and Obliteration on Callisto, Geophys. Res. Lett., 8, 891-894, 1981.

(5) Gurnis, M., Spatial Distribution of Craters on Callisto and Limits on the Crater Production Population of the Jovian System, Icarus, in Press, 1982.

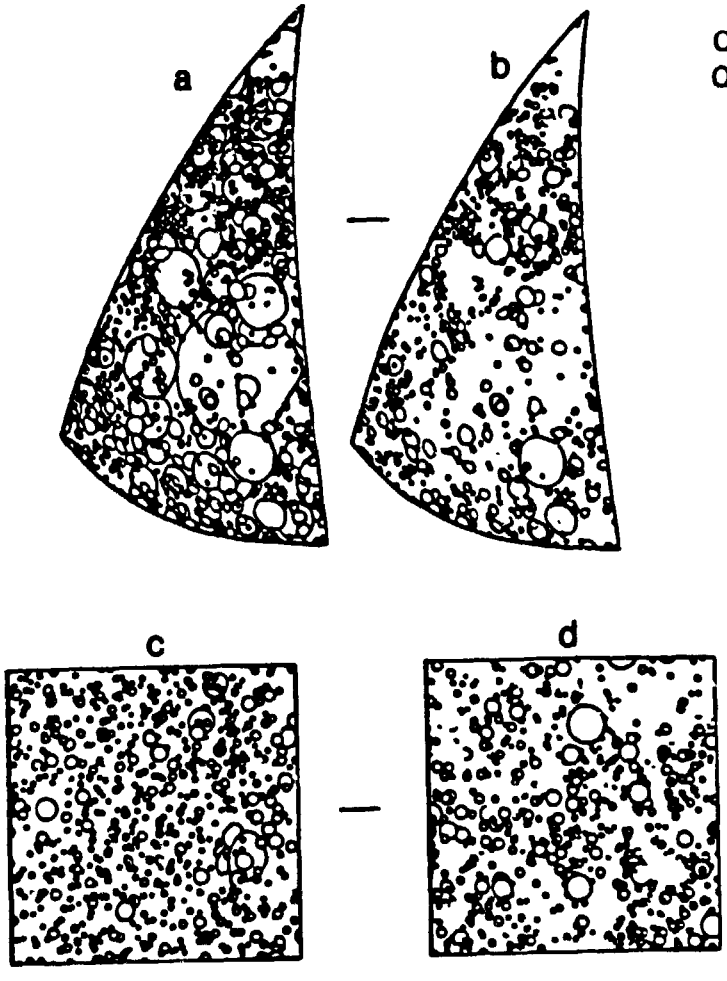

Fig. 2. Spatial distributions of craters observed on the lunar area (a) the Callisto area (c), after crater removal from lunar area to produce Callisto size/frequency distribution (b) and from Monte Carlo computer simulation (d). Scale bars represent 100 km. Fig. 2c and d are from Woronow and Strom (4).

Effects of the Lunar Orientale Impact on the Pre-Existing Crater Population

Robert G. Strom, Alex Woronow and John Spencer
Lunar and Planetary Lab., Univ. of Arizona
Tucson, Aziona 85721

The crater size/frequency distributions were studied in a hemisphere of the Moon centered on the Orientale basin in order to determine the effects of basin ejecta on the pre-existing crater population. The Orientale-centered hemisphere was gridded radially and concentrically into 1440 equal-area segments. Crater diameters down to 8 km have been used over most of this hemisphere, but some regions are measured down to only 20 km. Regions of mare flooding were eliminated from the study.

Basin ejecta has two effects on the pre-existing crater population: (1) a diameter dependent obliteration within the continuous ejecta blanket out to about one basin radius, and (2) the addition of secondary craters beyond this distance. The size/frequency distributions were compared with each other as a function of radial distance and azimuthal direction with respect to the Orientale basin, and these, in turn, where compared with distributions in other highland areas. Finally, all size/frequency distributions were compared to the crater population superposed on the Orientale basin and continuous ejecta deposits (Hevelius fm.). This crater population is a production population uneffected by basin secondary cratering and ejecta blanketing, and represents the pre-mare accumulation of craters near the end of heavy bombardment through the post-mare epoch. The size/frequency distribution of the post-Orientale/pre-mare crater population is different from the post-mare population at the 99% confidence level, and similar to the average highland population at the same confidence level (Fig. 1). The similarity between the post-Orientale/pre-mare crater population and the average lunar highlands implies that in general the highlands crater population is in production and representative of the impacting bodies responsible for the period of heavy bombardment. (1)

Fig. 2 shows the size/frequency distributions of highland craters in the hemisphere surrounding the Orientale basin beyond the continuous ejecta blanket. The dashed line is the distribution on the front side highland portion of the hemisphere while the solid line is the distribution on the farside portion of the hemisphere. The farside hemisphere distribution shows a knee in the curve below a diameter of about 20 km which probably represents a significant contribution of Orientale basin secondaries. However, the knee is not present on the frontside curve. This, together with the asymmetric distribution of the continuous ejecta blanket, suggests that the Orientale basin was formed by an oblique impact coming from the southeast which preferentially distributed secondaries on the farside hemisphere. To test how common this secondary distribution is, the crater size/frequency distribution of two areas of the farside 150° distant from Orientale where studied. These areas were chosen for their lack of plains units and great distance

from Orientale. The size/frequency distribution of one area (Riemam, Fabry, Olcott) shows a knee in the curve below 20 km diameter, while the other (Hertz, Pasteur, King) does not (Fig. 3). This suggests that concentrations of basin secondaries is spotty, but locally can be great enough to significantly alter the shape of the highland crater distribution at diameters less than 20 km, a circumstance first recognized by Wilhelms, et. al. (2). Based on the comparison between the post-Orientale/pre-mare and highland curves, we conclude that locally, in particular the farside region surrounding Orientale, secondaries from Orientale and other basins cause a knee in the size/frequency distribution below 20 km diameter. In other areas the contribution from basin secondaries has not significantly altered the primary crater size/frequency distribution, at least between 8 - 20 km diameter.

The Orientale continuous ejecta blanket out to about a basin radius from the basin rim (Cordillera Mts.) has either obliterated pre-existing craters or degraded them to Classes 4 and 5. Almost all craters superposed on the ejecta blanket are fresh Class 1 craters. Those underlying the blanket are degraded Class 4 and 5. No Class 3 craters are present within the ejecta blanket. This indicates that the ejecta blanket has degraded all pre-existing Class 1 - 3 craters to Class 4 or 5 craters. The obliteration of pre-existing craters within the blanket has been substantial (Fig. 4). The percentage of craters obliterated ranges from about 80% for craters 8 - 12 km diameter to about 40% for craters greater than 50 km diameter. Beyond a basin radius no significant crater obliteration has occurred for diameters greater than 8 km.

In summary, the size/frequency distribution of craters in most areas of the highlands represents the primary production population for diameters greater than 20 km. In the farside region surrounding Orientale out to at least 90° from the basin center, basin secondaries have caused an excess of craters at diameters less than 20 km. This excess of smaller craters is found locally in some other areas of the highlands and also is probably the result of secondaries from other basins. The size/frequency distribution in other areas of the highlands is essentially identical to the post-Orientale/pre-mare population and appears not to be significantly effected by basin secondaries larger than 8 km diameter. Within one basin radius up to 80% of pre-existing craters (8 - 12 km dia.) can be obliterated by the continuous ejecta deposit. Beyond that distance no significant obliteration occurs for diameters greater than about 8 km.

References

1. Strom, R.G. Origin and Relative Age of Lunar and Mercurian Intercrater Plains, Phys. Earth Planet, Interiors, 15, 156, 1977.

2. Wilhelms, D.E., Oberbeck, V.R., and Aggarwal, H.R., Size Frequency Distribution of Primary and Secondary Lunar Impact Craters, Proc. Lunar Planet. Sci. conf. 9th 3735, 1978.

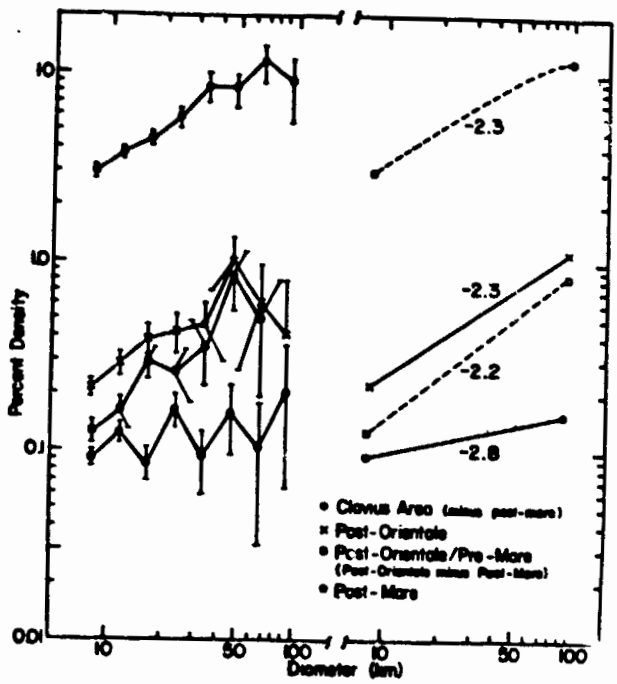

FIGURE 1

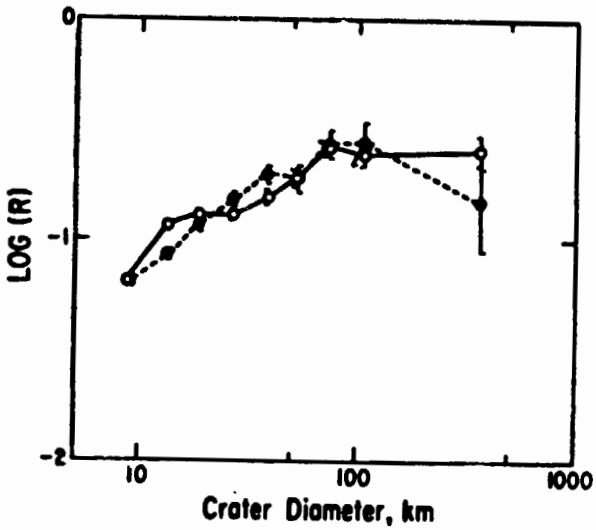

FIGURE 2

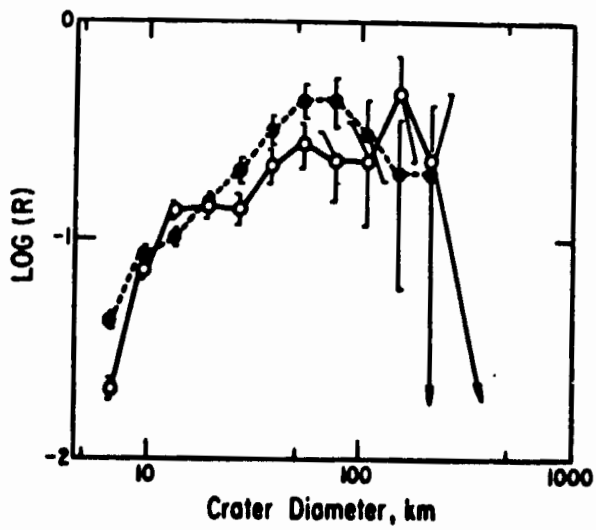

FIGURE 3

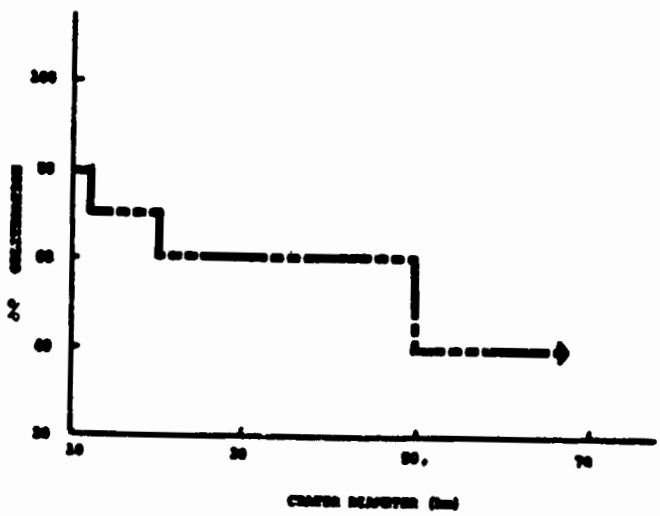

FIGURE 4

PROCELLARUM, A GIANT PLANETARY BASIN

Don E. Wilhelms, U.S. Geological Survey, Menlo Park, CA 94025

Cadogan (1974, 1981) and Whitaker (1981) proposed that a giant impact basin controls the semicircular outline of Oceanus Procellarum and occupies much additional area of the Moon's near side. Cadogan estimated the diameter of the "Gargantuan" basin as 2400 km and its center as 23° N., 29° W. He also suggested that an early volcanic filling by KREEP basalts explains the concentration of KREEP in the Imbrium-Procellarum area, and that ejected "anorthosite" (aluminous terra material) explains the high Al/Mg ratios detected on the limbs and far side by the orbiting X-ray spectrometer. Whitaker showed that many otherwise-unexplained terra and mare features in a large area fit three rings 1700, 2400, and 3200 km in diameter centered at 23° N., 15° W. The basin center lies within the much younger Imbrium basin. Its outer, 3200-km, ring encompases all major near-side maria except Crisium, Fecunditatis, and Nectaris. Orientale and Smythii also lie outside the basin. My studies not only have convinced me that the basin as mapped by Whitaker exists, but have shown that it exerts fundamental control over lunar near-side petrology, structure, geophysics, and stratigraphy.

Most of Procellarum's effects stem from its control of the thickness of the terra crust (Cadogan, 1981; Whitaker, 1981). The lower the surface, the thinner the crust and the higher the underlying mantle. Altimetry data show generally lower terra elevations inside than outside the basin, a fact that is commonly ascribed to a fundamental nearside-farside difference in crustal thickness (Kaula and others, 1974). In detail, the basin undoubtedly has a steplike concentric structure like Orientale and other well-exposed basins, descending in elevation from the exterior terra through two concentric, interring troughs to the central basin. Seismometry suggests a 75-km crustal thickness in the Apollo 16 region (Nakamura, 1981), in the outer trough. This value is close to estimates of the average crustal thickness, which range between 61 and 86 km (Kaula and others, 1974; Bills and Ferrari, 1977; BVSP, 1981, p. 671). The most precise seismic data are from an area of southern Oceanus Procellarum and suggest a 50-60 km thickness for that region (Toksöz and others, 1974; Koyama and Nakamura, 1979), most of which lies within the inner of the two concentric troughs. Hence the 50-60-km figure reflects the crustal thinning under that trough.

The central basin must overlie a still thinner crust. The mantle may have been almost reached by the combined Procellarum and Imbrium impacts, judging from the petrology of one or two small clasts in the Apollo 15 Montes Apeninnus collection (Herzberg and Baker, 1980). Even the Imbrium samples are mostly crustal, however, consisting of KREEP-rich breccias (Apollo 14) and ANT clasts and low-K KREEP matrices (Apollo 15). Therefore Procellarum alone did not pierce the crust, and it was shallower than 61-86 km.

The shallow combined excavation by two of the largest lunar basins supports the hypothesis that basins are much shallower, relative to their diameters, than craters (Baldwin, 1963; Head and others, 1975). If the

outer ring of a basin is also the boundary of excavation (Wilhelms and others, 1977), the depth/diameter ratio of Procellarum was less than 1/37 (86/3200) and probably closer to 1/64 (50/3200). The crust was excavated more by lateral stripping than by the deep, hemispherical scooping observed in simple craters. Because of their shallowness, enormous basins may form without destroying a planet.

The terra surface materials of the three concentric depressions and the exterior terrain differ in composition. The X-ray spectrometers show that the Apollo 16 region and the far side are the most aluminous terra (Adler and others, 1973). The Apollo 15 and 17 tracts, composed mostly of younger basin rims formed closer to the Procellarum center, are more magnesian. The innermost Procellarum basin is KREEP-rich, judging by the Fra Mauro Formation derived therefrom. Composition and crustal thickness are therefore related (Haines and Metzger, 1980). The correlations are consistent with a layered terra crust in which KREEP-rich materials are the deepest, magnesian ANT intermediate, and aluminous ANT highest. The steplike structure of Procellarum has exposed successively deeper layers inward toward its center, and the whole basin has stripped off aluminous material and added it to the surrounding terra (Cadogan, 1974). Thus the differences in crustal thickness and composition that are usually attributed to a nearside-farside dichotomy (Kaula and others, 1974) are partly or entirely effects of the Procellarum impact.

The terra configuration created by Procellarum and superposed basins set the stage for later mare volcanism. The mantle and therefore the source of the basalts was uplifted beneath each basin to compensate for the removed crust. The crustal thinning and the mantle uplifts were additive where the basins were superposed. The most massive maria are Imbrium and Serenitatis, which are superposed on central Procellarum, whereas the least massive maria relative to the size of their containing basins are outside Procellarum. Mare ages and compositions also correlate with Procellarum. For example, the massive, Imbrian-age fillings of Imbrium and Serenitatis are low in Ti. Imbrian high-Ti basalts were extruded in western Tranquillitatis, in the inner Procellarum trough. Eratosthenian and Copernican high-Ti magmas were extruded directly into the western extension of the same trough and from the central basin into the margin of Mare Imbrium. Lunar volcanism endured the longest in this Procellarum-Imbrium region of thin crust. The thin, aluminous basalts of Smythii and Fecunditatis (Hubbard, 1979) were extruded onto the thick crust outside Procellarum. Within an age group, zones of mare composition as indicated by the telescopic and orbital geochemical data are concentric with Procellarum and cut across the younger superposed basins. The basins that are the immediate hosts of the maria only modulate the pattern established by Procellarum.

Lithospheric thicknesses resulting from the steplike Procellarum excavation determined the degree and style of tectonic deformation. The terra crust generally is assumed to deform elastically, and was probably equivalent to the elastic lithosphere during most mare volcanism and tectonism. Subsidence of mare basalts to achieve isostatic compensation

opened arcuate grabens by stretching the lithosphere, and was aided by weak lithospheres and inhibited by strong lithospheres (Solomon and Head, 1980). Therefore most arcuate grabens formed inside Procellarum. The thin lithosphere permitted more complete isostatic compensation than did the thick lithospheres under such maria as Orientale, Nectaris, Smythii, and the far-side maria. Because subsidence of those maria was hindered, they display large mascons despite their relatively small masses of basalt (Solomon and Head, 1980). Most craters with highly uplifted floors are also in or near the basin.

Most mare ridges are concentric with Procellarum (Whitaker, 1981). Even such details as the gravity structure of southwestern Procellarum (Scott, 1974) correlate with its ring structure: positive anomalies with the thickest basalts, parallel negative anomalies with the raised rings underlying thin basalts (compare Scott, 1974, fig. 2).

In summary, so many aspects of lunar geology and geophysics correlate with position relative to a 3200-km, three-ringed Procellarum impact basin that its existence seems firmly established. First-order planetary structures may therefore be of impact origin. One might examine the hemispherical dichotomy of Mars for similar clues to basin origin. A basin three times larger than Procellarum may have stripped several tens of kilometers of crustal material from half of Mars, resulting ultimately in the different geologic styles of the two martian hemispheres.

Adler, I., and 14 others (1973) PLSC 4, p. 2783-2791.
Baldwin, R. B. (1963) The Measure of the Moon: Chicago.
Bills, B. G., and Ferrari, A. J. (1977) JGR, v. 82, p. 1306-1314.
BVSP (Basaltic Volcanism Study Project)(1981) Basaltic Volcanism on the Terrestrial Planets: Lunar and Planetary Institute.
Cadogan, P. H. (1974) Nature, v. 250, p. 315-316.
_____ (1981) The Moon--Our Sister Planet: Cambridge.
Haines, E. L., and Metzger, A. E. (1980) PLPSC 11, p. 289-718.
Head, J. W., Settle, M., and Stein, R. S. (1975) PLSC 6, p. 2805-2829.
Herzberg, C. T., and Baker, M. B. (1980) Proceedings, Conference on Lunar Highlands Crust: Geochim. et Cosmochim. Acta, Suppl. 12, p. 113-132.
Hubbard, N. J. (1979) PLPSC 10, p. 1753-1774.
Kaula, W. M., and four others (1974) PLSC 5, p. 2811-2819.
Koyama, J., and Nakamura, Y. (1979) LPS X, p. 685-687 (abstract).
Nakamura, Y. (1981) Workshop on Apollo 16: Lunar and Planetary Institute Tech. Report 81-01, p. 87-94 (citing earlier unpublished work).
Scott, D. H. (1974) PLSC 5, p. 3025-3036.
Solomon, S. C., and Head, J. W. (1980) Reviews Geophys. Space Phys., v. 18, p. 107-141.
Toksöz, M. N., Dainty, A. M., Solomon, S. C., and Anderson, K. R., (1974) Reviews Geophys. Space Phys., v. 12, p. 539-567.
Whitaker, E. A. (1981) Multi-ring basins: PLPSC 12A, p. 105-111.
Wilhelms, D. E., Pike, R. J., and Hodges, C. A. (1977) Impact and Explosion Cratering, p. 539-562: Pergamon.

THE EXCAVATION OF LUNAR MULTI-RING BASINS

Paul D. Spudis, Dept. of Geology, Ariz. State Univ., Tempe AZ 85287 and U. S. Geological Survey, 2255 N. Gemini Dr., Flagstaff AZ 86001.

Introduction The formation of multi-ring basins is the most important process in the early geologic history of the Moon. Exhaustive study of these enigmatic features has produced no clear consensus on their original size and depth of excavation (e.g., compare 1,2). One problem in the approach of many basin studies is their focus on only one aspect of basin geology (photogeology, sample studies, etc.). This effort utilizes information from photogeologic, lunar sample, geophysical and remote sensing data to address the problem of the original basin cavity diameter and effective depth of excavation. This study extends results for the Orientale basin (3) to the lunar basins Nectaris, Crisium, Serenitatis and Imbrium (4).

Geology and Ejecta of Lunar Basins. This section briefly summarizes the compositions of ejecta from five lunar basins and some constraints on the size of the original basin cavity. Detailed geologic rationale for these constraints may be found in (4).

Orientale. The Orientale basin (930 km diameter) formed in a thick (T=90-100 km; 5) highland crust and contains several pre-basin structures (6,7) that suggest the boundary of the original basin cavity probably occurs within the outer Rook ring of that basin (500-600 km diameter cavity). Mixing models of orbital geochemical data for Orientale ejecta (8) suggest this material is composed of a 2:1 mixture of anorthosite and anorthositic gabbro. These results suggest Orientale effectively excavated to depths no greater than about half the thickness of the crustal target (about 50 km; 3); if the original cavity size was greater than this estimate, a significantly higher mafic content in the basin ejecta would be seen.

Nectaris. The Nectaris basin (860 km diameter) formed within a typical nearside highlands crust (average T=70 km; 5). The northern and western ejecta are covered by Apollo 16 orbital data and the Apollo 16 site lies 200 km NW of the outer Nectaris ring. Nectaris is too degraded to recognize any pre-basin structures within the outer ring but results for Orientale suggest the original cavity was within the outer ring and was about 500-600 km in diameter. Mixing model results for Nectaris ejecta (9,10) indicate a 3:1 mixture of anorthositic gabbro and low-K Fra Mauro basalt. This suggests excavation to middle crustal levels, about 50 km in this region of the Moon.

Crisium. The Crisium basin (635 km diameter) impact occurred into a highlands target (average T=60 km; 5), geochemically similar to the Nectaris basin target. An unusual basin modification style, involving long-term endogenic modification with concurrent mare flooding in ring troughs (4), precludes identification of pre-basin structures. Orbital geochemical coverage of the southern ejecta blanket indicates Crisium ejecta consists of anorthositic gabbro and low-K Fra Mauro basalt (10) in about the same proportions as in Nectaris ejecta (3:1). This suggests Crisium basin excavation to crustal stratigraphic levels comparable to

Nectaris. Due to the thinner crust in this region (5), Crisium probably sampled depths up to 35 to 45 km.

Serenitatis. The Serenitatis basin (880 km diameter) impact occurred within an average thickness crust (60 km; 5) that was geochemically distinct from both Crisium and Nectaris basin targets (4,9). Extensive mare flooding and morphologic degradation by the Imbrium impact prohibit the identification of pre-basin topography. Mixing model studies of the Taurus-Littrow highlands (9) suggest Serenitatis ejecta consists of greater than 90 percent norite with minor amounts of KREEP, mare basalt and anorthosite. This ejecta composition suggests Serenitatis may have excavated nearly the entire crustal column in this region of the Moon, as deep as 50 to 60 km, consistent with the results from other basins in this study (cf. Nectaris, similar in size to Serenitatis).

Imbrium. Imbrium (1200 km diameter) is one of the most complex lunar multi-ring basins. Gravity data (5) suggest a relatively thin crust for the pre-basin target region (average T=50 km) that consisted of complex mare and KREEP volcanic lavas overlying a predominantly noritic highlands crust (4). Numerous pre-Imbrian basins intersect the Imbrium outer ring and in particular, the preservation of an inner basin topographic high near the Apennine Bench (11,12) may have resulted from the Imbrium basin outer ring intersection with the ancient Insularum basin (13). This suggests the original Imbrium cavity may have been about 600-800 km in diameter (4). Mixing model studies of Imbrium ejecta indicate subequal amounts of low-K Fra Mauro basalt, KREEP and mare basalts with minor amounts of anorthositic gabbro (14). A new geochemical map of the Apennine mountains displays a large component of norite within the Imbrium ejecta (15). These results suggest Imbrium excavated at least the entire crustal thickness in this region and possibly some quantity of lunar mantle materials (4).

Discussion. The five basins described here represent a spectrum of basin sizes, ages and morphologies. Where the original cavity diameter can be constrained by preservation of pre-basin topography (Orientale, Imbrium), the original cavity is found to be significantly smaller than the present basin topographic rim. The inferred depths of basin excavation based on ejecta composition and regional crustal thickness are typically less than the local crustal thickness and are on the order of one-tenth the diameter of the inferred basin original cavity. This relationship for lunar basin excavation cavities has been suggested previously from an entirely different line of reasoning (16). An attempt was made to compute the total volume of material excavated by these impacts. This was done by assuming a hemispherical cavity shape with a penetration depth of one-tenth the inferred diameter excavating a spherical Moon (3,4). Results for Orientale range from 4.9 to 9.3 x 10^6 km^3 of ejecta, a result in good agreement with previous estimates from gravity (17) and photogeologic data (18). Analysis of this geometric figure of excavation further indicates that for Orientale, 90 percent of the basin ejecta is derived from depths shallower than about 30 to 40 km (3), in good agreement with the highly anorthositic composition of Orientale ejecta (8). In the case of Imbrium (the largest basin studied), this analysis indicates as much as 16 percent

of the total ejecta volume may be derived from sub-crustal regions. This material may be now largely buried by the mare flows that fill the basin, but detailed study of the orbital geochemical data indicate the presence of minor amounts of ultramafic material within the Apennines (19).

Conclusions. Lunar multi-ring basins form by the topographic modification of initially smaller, shallow transient cavities. The results of this study suggest an initial excavation cavity with a diameter approximately 0.6-0.7 times the present basin topographic rim diameter. The geochemical data suggest a depth about 0.1 times the diameter of this excavation cavity. These results support hypotheses that basin outer rings form by gravity slumping around an initially smaller transient crater (e.g., 20-22). Basin inner rings may result from stratigraphic uplift (23,24) along with minor oscillatory movement (23,25). This excavation model is consistent with a wide variety of studies of Apollo lunar highland samples that indicate a paucity of material derived from the lunar mantle (e.g.,26) within the lunar highlands.

REFERENCES

1) Hodges C.A. and Wilhelms D.E. (1978) Icarus 34, 294.
2) Head J.W. et al. (1975) PLSC 6, 2805.
3) Spudis P.D. (1982) LPS XIII, 760.
4) Spudis P.D. (1982) Ph.D. Dissertation, Ariz. State Univ., 291 pp.
5) Bills B.G. and Ferrari A.J. (1976) PLSC 7, frontispiece.
6) Scott D.H. et al. 1977) USGS Map I-1034.
7) Schultz P.H. and Spudis P.D. (1978) LPS IX, 1033.
8) Hawke B.R. et al. (1982) LPS XIII, 306.
9) Spudis P.D. and Hawke B.R. (1981) PLPSC 12B, 781.
10) Hawke B.R. and Spudis P.D. (1979) Conf. Lunar Highlands Crust, 53.
11) Spudis P.D. and Head J.W. (1977) PLSC 8, 2785.
12) Head J.W. (1977) Imbrium Consort. 2, 120.
13) Wilhelms D.E. (1980) Conf. Multi-ring Basins, 115.
14) Hawke B.R. and Head J.W. (1978) PLPSC 9, 3285.
15) Spudis P.D. and Davis P.A. (1982) Conf. Pristine Rocks, (in press).
16) Croft S.K. (1981) Multi-ring Basins, PLPSC 12A, 207.
17) Scott D.H. (1974) PLSC 5, 3025.
18) Moore H.J. et al. (1974) PLSC 5, 71.
19) Clark P. and Hawke B.R. (1981) PLPSC 12B, 727.
20) Mackin J.H. (1969) GSA Bull. 80, 735.
21) Head J.W. (1974) Moon 11, 27.
22) Schultz P.H. (1976) Moon Morphology, U. Texas Press, 626 pp.
23) Grieve R.A.F. et al. (1981) Multi-ring Basins, PLPSC 12A, 37.
24) Schultz P.H. et al. (1981) Multi-ring Basins, PLPSC 12A, 181.
25) Murray J.B. (1980) Moon and Planets 22, 269.
26) Taylor S.R. (1975) Lunar Science, Pergamon, 372 pp.

CRATER PEAKS TO BASIN RINGS: THE TRANSITION ON MERCURY AND OTHER BODIES

Richard J. Pike, U.S. Geological Survey, Menlo Park, CA 94025

Analysis of the morphologic contrasts between large impact craters and small basins may contribute to a better understanding of both features. Recent efforts have focused on a possible link between central peaks in craters and interior rings in basins [1-8]. In connection with new work on the craters of Mercury, I have reexamined the dimensions of peaks and rings on six planets and satellites. Emphasis was on (1) central-peak basins, small transitional basins that have both a central peak and an inner ("central-peak" or "peak") ring, and (2) the planet Mercury, which has more (12) central-peak basins than the other bodies. The peak ring also is defined as the inner one in two-ring basins; it is designated "ring II" in multiring basins, where the main ring is ranked as IV and the intermediate ring as III [9,10]. All measurements of mercurian basins are new [11,12]; the data for basins elsewhere are either new or were compiled from published sources [e.g., 4]. Basal diameters for central peaks were obtained from work by the Brown University group [e.g., 6]. Analysis of peak-and-ring geometry suggests an interpretation of the crater-to-basin transition, as exemplified here by Mercury (Fig. 1), wherein the morphologic contrasts may not indicate a major discontinuity.

A similar pair of correlations, between central-peak and crater size and between peak-ring and basin size, is observed on the Earth, the Moon, Mercury, Mars, Ganymede, and Callisto. Both resulting linear log-log least-squares fits exclude central-peak basins, which have a different geometry (Fig. 1). Peak rings are fully half the size of their main basin rings, whereas central peaks are barely a quarter the size of their host craters; the respective logarithmic curves do not intersect on the graph [cf. 5-8]. Log_{10} basal diameter of central peaks (D_{cp}) increases monotonically with log_{10} rim diameter of the crater (D_r). Intercepts of least-squares fits at a crater diameter of 50 km range from 10 to 13 km. Log_{10} diameter of the peak ring (D_{pr} or D_{II}) also increases monotonically with log_{10} diameter of the main, or topographic, ring (D_r or D_{IV}). Intercepts of least-squares fits at a basin size of 200 km range from 100 to 110 km. The peak-ring/main-ring curve parallels other log-log monotonic relations between the main and remaining basin rings [9,10]. The 2:1 relation between main- and peak-ring diameter for double-ring basins is identical to that for multiring basins [cf. 2].

Overlap of the D_{cp}/D_r and D_{II}/D_{IV} data marks the transition from craters to basins on each body. The diameter range bracketing the smallest peak ring and the largest central peak generally includes most central-peak basins. The ranges of diameter overlap are approximate; that for the Earth may be about 15 to 25 km, for the Moon 140 to 200 km [cf. 8], for Mercury 75 to 150 km, for Mars 45 to [illegible] km, for Ganymede possibly 70 to 120 km, and for Callisto perhaps 80 to 100 km. Some of these threshold diameters may correlate inversely with surface gravity [13].

The geometry of central-peak basins differs from that of complex craters and other basins in two key respects. First, the relation between

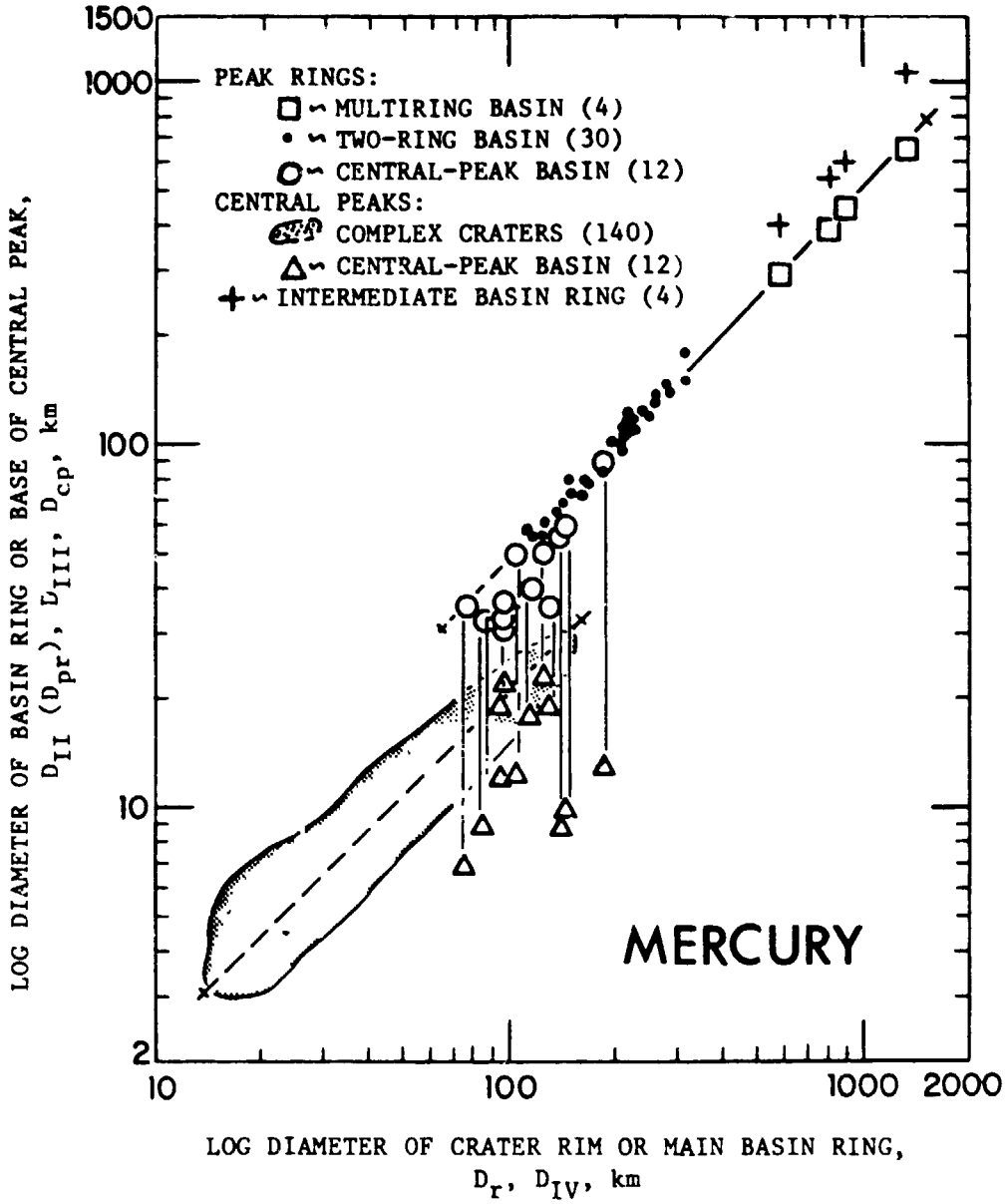

FIGURE 1. A new model for the crater-to-basin transition, exemplified by details for Mercury, showing how peak rings replace central peaks as the size of impact increases. Both peaks and rings follow essentially linear monotonic relations except in central-peak basins, where both (either) peak rings and (or) central peaks systematically diminish in size. Vertical lines connecting the ring and peak of each basin emphasize this complementary relation: either the ring is large and the peak small, or vice versa. The least-squares fit to peak rings (solid line, n=34, central-peak basins excluded) is $D_{II} = 0.460 D_{IV}^{1.015}$; the fit to central-peak data compiled from [6, Fig. 2] (dashed line, n=140) is estimated (only) at $D_{cp} = 0.25 D_r^{0.95}$. The four tentative intermediate rings [4], which are larger than peak rings by a factor of about $\sqrt{2}$ [9, 10], parallel the first two trends.

size of the peak ring and size of the accompanying central peak is complementary. Second, either one or both features are smaller than they would be had they appeared alone in a crater or basin of that diameter. This correlation is especially evident on Mercury (Fig. 1) and Mars (n=11). In at least 7 of the 12 central-peak basins on Mercury, the peaks are substantially smaller in basal diameter than the D_{cp}/D_r data show to be typical of complex craters; similarly, 10 of these basins have smaller peak rings than the D_{II}/D_{IV} data show to be typical of two-ring and multiring basins. In none of the 12 basins do both peak-ring and central-peak diameters attain the larger "normal" values that are found in craters and basins outside the transition zone. Similar, if less clearly defined, complementary relations occur on the Moon (n=2) and the Earth (n=2); Ganymede and Callisto may have no central-peak basins.

Three features of these data suggest that the crater-to-basin transition, wherein rings replace peaks as central features, may be a less drastic physical discontinuity than was previously thought. (1) Central-peak basins are much more common on Mercury and Mars than on the Moon, where breaks in the size-morphology array of impact craters were first defined. This wider occurrence of transitional basins suggests that the crater-to-basin change is less abrupt than once implied by the lunar case. (2) Magnitude of the central disturbance, as reflected by size of peaks or rings, increases monotonically with size of the host crater or basin. The parallel D_{cp}/D_r and D_{II}/D_{IV} plots suggest that "normal" full-sized central peaks and peak rings both form at a level of energy that increases monotonically with the magnitude of impact. (3) The relation between peak and inner-ring size in central-peak basins is complementary. At some physical threshold, rings replace peaks as the more efficient structural expression for this fraction of cratering energy. However, qualitative change in the form of the central uplift does not necessarily indicate a change in the energy fraction itself: where both a peak and a peak ring form in the same small basin, one or both features are smaller than normal. Thus the energy available for the central disturbance probably is shared between the peak and the ring rather than increased to accommodate both features.

References:

[1] Wood, C. A., and Head, J. W. (1976) Proc. Lunar Sci. Conf. 7th, p. 3629-3651.
[2] Head, J. W. (1977) in Impact and Explosion Cratering, N. Y., Pergamon, p. 815-841.
[3] Head, J. W. (1978) Lunar Planet. Sci. IX, Houston, p. 485-487.
[4] Croft, S. K. (1979) Thesis, U.C.L.A., 264 pp.
[5] Hale, W. S., and Head, J. W. (1979) N.A.S.A. Tech. Memo. 80339, p. 160-162.
[6] Hale, W. S., and Head, J. W. (1980a) Proc. Lunar Planet. Sci. Conf. 11th, p. 2191-2205.
[7] Hale, W. S., and Head, J. W. (1980b) Papers presented to Conf. Multi-Ring Basins, Lunar Planet. Inst., Houston, p. 27-29.
[8] Hale, W. S., and Grieve, R. A. F. (1982) Proc. Lunar Planet. Sci. Conf. 13th, in J. Geophys. Res., 87, in press.
[9] Pike, R. J. (1981) N.A.S.A. Tech. Memo. 84211, p. 123-125.
[10] Clow, G. D., and Pike, R. J. (1982) Lunar Planet. Sci. XIII, Houston, p. 123-124.
[11] U. S. Geol. Survey (1976-1979) Atlas o. Mercury, 10 sheets.
[12] Davies, M. E., Dwornik, S. E., Gault, D. E., and Strom, R. G. (1979) Atlas of Mercury, N.A.S.A., 127 p.
[13] Pike, R. J. (1982) Lunar Planet. Sci. XIII, Houston, p. 627-628.

GEOMORPHOLOGY OF CRATERS ON MERCURY: FIRST RESULTS FROM A NEW SAMPLE

Richard J. Pike and Gary D. Clow, U. S. Geological Survey, Menlo Park, CA 94025

Currently we are reexamining in detail the morphology of fresh impact craters on Mercury. One objective is to explain the deviation of mercurian craters from the postulated linear relation between surface gravity, g, and mean diameter, D_t, that marks the transition from a simple to a complex morphology [1]. Another objective is to obtain improved depth/diameter (d/D) values that correlate with the other morphologic features of each crater (Fig. 1). Preliminary results from Mariner 10 images suggest that the simple-to-complex threshold is reached at a smaller crater size than indicated by earlier studies [2-6]. Just how much the revised D_t value for craters on Mercury will differ from the earlier 16-km value [1] must await completion of our d/D work now in progress and, to a lesser extent, expansion of the sample to the planned 200 craters. The data gathered thus far, from 95 craters between 2 km and 150 km across (Fig. 1), indicate that D_t is no greater than 12 km. Our initial attempt at a d/D curve (not shown) from this sample suggests that the intersection of least-squares fits to distributions of simple and complex craters lies below this crater size, between 6-km and 8-km diameter -- a result commensurate with the now-diminished value of D_t.

Figure 1 illustrates the morphologic transition for the 95-crater sample. The largest simple, deep and bowl-shaped, craters on Mercury are no more than 13 km in diameter, whereas the smallest craters in which unambiguous complex-crater characteristics (central peaks, flat and shallow floors, scalloped rims, slump blocks, and wall terraces) can be identified are no less than 11 km across. Craters with a morphology that is transitional between those of simple and complex craters range in diameter from 7 km to 16 km. Three aspects of Figure 1 warrant emphasis. (1) The onset of wall terracing occurs at a much larger crater size (21 km diam.) than does onset of the other five morphologic features (11-12 km diam.). The peaks-before-terraces order on Mercury is consistent with that observed on other planets [1-6] and may figure prominently in a genetic interpretation of the transition [1]. (2) Craters with a transitional morphology, resembling that of such lunar craters as Dawes and Bessel, neatly bracket the simple-to-complex diameter threshold. Our provisional d/D data (not shown) indicate that such craters are systematically shallower than simple craters; this correlation already is evident for craters on the Moon [1; Fig. 9]. (3) Neither central peaks nor wall terraces have been identified in the nine transitional craters studied on Mercury. It may be, however, given evidence from high-resolution lunar pictures, that nascent, low-relief central peaks lie buried beneath the slump deposits.

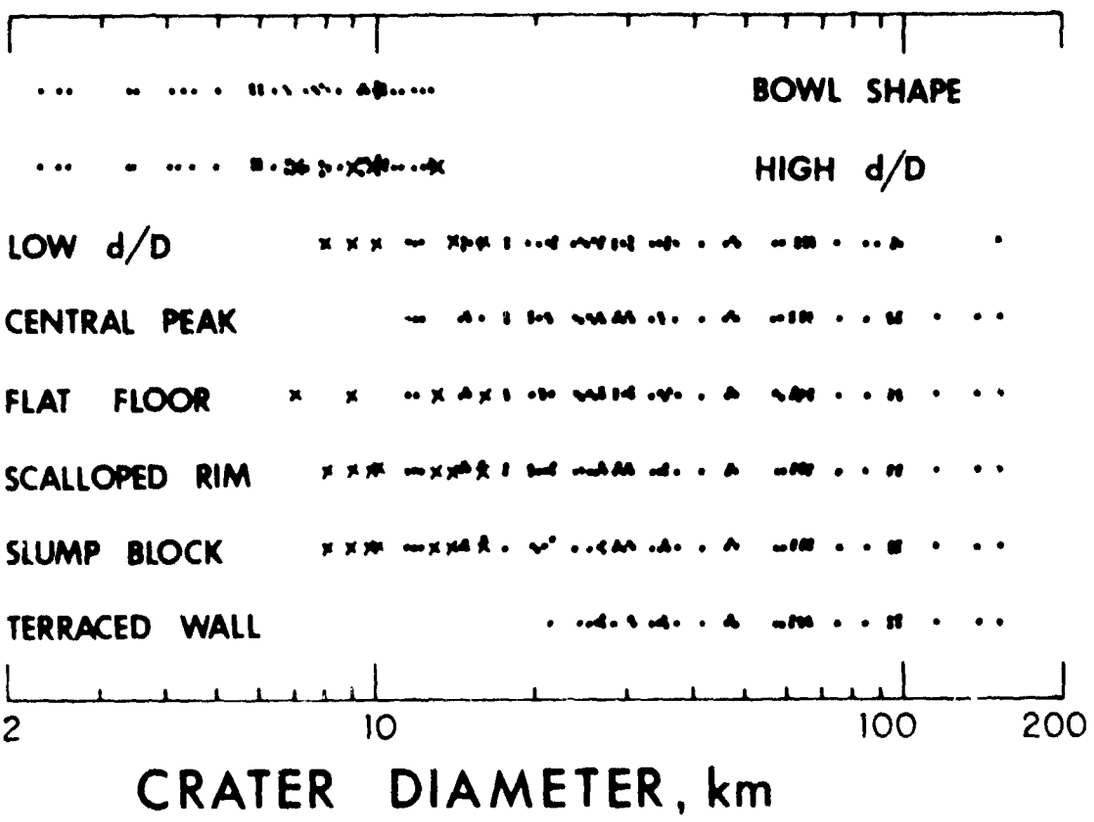

FIGURE 1. Diameter/morphology arrays for eight interior characteristics of mercurian impact craters. Depth/diameter (d/D) results are provisional, but radical changes are not expected. Symbols denote unambiguous identifications of morphologic features on Mariner 10 images for 95 fresh craters: dots, observations on either simple (n=35) or complex (n=51) craters; crosses, observations on craters (n=9) that have a distinctively transitional morphology. Compare with data for Mars [1, Fig. 7].

Our provisional data on crater diameter and especially crater depth, which were obtained from measurements of shadow lengths, are rather crude because the Mariner 10 Supplementary Experimental Data Record (SEDR) [7] contains inaccuracies. Severity of the resulting errors in crater diameter and depth varies considerably, depending mostly on surface latitude and the distance of a given crater from the subspacecraft

point. The 1:15,000,000-scale map of Mercury [8], which used the latest mercurian control net, furnishes the most accurate positions for surface features on the planet. We combine values of latitude and longitude from this map with data on spacecraft altitude and the position of the Sun (from the SEDR but independent of position on the planet and thus not subject to errors in the calculated parameters) and input them to an algorithm that recomputes view angle, sun angle, phase angle, and image scale for each set of points required to generate a crater diameter and a shadow length. This algorithm, which currently is being encoded, enables any crater for which a shadow length can be measured to be used for d/D analysis, no matter how strongly foreshortened its image on Mariner-10 pictures. Besides greatly improving the quality of d/D analysis for Mercury, this added flexibility expands the sample of fresh-looking craters that can be included in morphologic investigations on any planet.

Although the results thus far are preliminary, our data suggest that the transition from simple to complex craters on Mercury occurs at a smaller diameter than indicated by earlier data. However, the 7 km to 12-km-diameter range within which the revised transition probably lies will not necessarily include the 8 km value of D_t that would be consistent with an inverse functional relation with g or silicate bodies (the $g:D_t$ relation for nonsilicate bodies differs [9]). Thus the anomalously high D_t value for Mercury probably is real, if not so large as previously thought. We do not expect the revised D_t value for craters on Mercury to be so low as the 6-km value obtained for craters on Mars [1], a difference almost surely ascribable to the diverse physical properties of the targets. The provisional new value for D_t on Mercury remains consistent with the possible fourth-power scaling recently proposed for the $g:D_t$ relation [10]. Finally, detailed analysis of mercurian craters characterized by a transitional morphology may further elucidate the simple-to-complex problem.

References:

[1] Pike, R. J. (1980) Proc. Lunar Planet. Sci. Conf. 11th., p. 2159-2189.
[2] Malin, M. C., and Dzurisin, D. (1977) J. Geophys. Res., v. 82, p. 376-388.
[3] Malin, M. C., and Dzurisin, D. (1978) J. Geophys. Res., v. 83, p. 233-243.
[4] Cintala, M. J., Wood, C. A., and Head, J. W. (1977) Proc. Lunar Planet. Sci. Conf. 8th, p. 3409-3425.
[5] Wood, C. A., Head, J. W., and Cintala, M. J. (1977) Proc. Lunar Planet. Sci. Conf. 8th, p. 3503-3520.
[6] Smith, E. I., and Hartnell, J. A. (1978) Moon and Planets, v. 19, p. 479-511.
[7] Jet Propulsion Laboratory (1975) Mariner 10 Image Processing Laboratory (IPL) Balloon SEDR.
[8] U. S. Geol. Survey (1979) Misc Inves. Map I-1171, 1:15,000,000.
[9] Basilevsky, A. T. (1981) Dokl. USSR Acad. Sci., v. 258, no. 2, p. 323-325 (in Russian).
[10] Pike, R. J. (1982) Lunar Planet. Sci. XIII, p. 627-628.

A NEW TIME-SAVING CRATER-COUNT TECHNIQUE, WITH APPLICATION TO NARROW FEATURES

Kenneth L. Tanaka, U.S. Geological Survey, Flagstaff, AZ 86001

Standard crater-counting techniques on planetary surfaces (1) have been vital for stratigraphic correlations of geologic and geomorphic units. They have, however, required tedious, time-consuming, and eye-straining effort, and the results have been limited to the average crater density of a given area. A new technique (originally conceptualized by Laurence Soderblom) has been devised that reduces the number of small-diameter craters to be counted. The same method can be employed separately to obtain crater counts for superimposed or protruding geologic features such as faults, scarps, ridges, crater rims, and channels.

The new technique is based on the observation that a linear (or curvilinear) feature(s) of limited or insignificant area has a density of superimposed impact craters that depends on the area defined by the crater diameters. Thus, an areal crater density can be calculated on the basis of the sum of the areas of these linear features, including a surrounding area that depends on the average crater size selected for counting. Because the extent of crater-ejecta blankets may vary considerably for a given crater diameter, only craters whose rims overlap the linear features are counted. For a given linear feature, A_R is defined as the area contained by the envelope circumscribing one crater radius R outward from the outer edge of the feature (see Figure 1). Expressed in equation form,

$$A_R = LW + 2RL + 2RW + \pi R^2 \qquad (1)$$

where L is the length and W the width of the linear feature.

Crater densities may be calculated by summing individually determined counts from largest to smallest crater diameters. Usually, however, crater diameters are binned within size limits. If the individual diameters are measured, their arithmetic mean [the geometric mean, used by (1), is incorrect] can be used as an average diameter. Otherwise, a weighted mean diameter can be calculated on the basis of the observation that most cumulative crater counts are proportional to D^{-3}, where D is the crater diameter; i.e., $N_c \approx (\text{const.})D^{-3}$. The average diameter $\bar{D}$ of D_a and D_b ($D_b > D_a$), weighted by the crater-density function, is

$$\bar{D} = \frac{\int_{D_a}^{D_b} D\,dN_c}{\int_{D_a}^{D_b} dN_c} = \frac{3}{2}\,\frac{(D_b^{-2} - D_a^{-2})}{(D_b^{-3} - D_a^{-3})}. \qquad (2)$$

The cumulative count is the sum of the individual counts, starting with the largest bin size. If the largest bin size, bin 1, contains n_1 craters, the next largest bin size, bin 2, n_2 craters, and so forth,

then

$$N_c = \sum_{j=1}^{k} n_j/A_j, \quad (3)$$

where A_j is the area that corresponds to the average crater diameter of the jth bin. Finally, letting

$$N = \sum_{j=1}^{k} n_j \quad (4)$$

be the number of cumulative craters in the kth and larger diameter bins, the one-σ confidence internal is $\pm N_c/N^{1/2}$.

Crater densities for densely cratered terrain or large areas, or both, can be determined quickly by overlaying the area with a template of line segments and counting the craters that intersect the lines. So as not to count large craters repeatedly, the spacing between line segments should be greater than the largest diameter crater being counted. If these lines are given width, it will cause more smaller craters to be counted. When linear geologic features are being counted, each feature must be measured for length and width. For curvilinear objects, such as crater rims, equation (1) can be modified to more accurately determine the crater-count areas.

The crater line-count method presented above is currently being used in conjunction with 1:15M scale mapping and global stratigraphic studies of Mars, employing the 1:2M photomosaic subquads for the counts. Preliminary results in the Lunae Planum region (MC 18 SW) confirm the usefulness of this technique. Figure 2 compares the crater-density curves of a standard area count, an area line count, and a count of the mare ridges. The area line count used a template of line segments 1 by 90 mm (corresponding to 2 by 180 km) at 10 mm (20 km) intervals. As an expediency, only the central or crestal 0.5 mm (1 km) of the mare ridges were examined to better control the counts of small-diameter craters. Table 1 shows that the compromise of greater error for counting fewer smaller-diameter craters is not overly serious. An unexpected result is the older crater age of the mare ridges. Compatibility of the area line counts with those obtained for Syria Planum lava flows [unit sp_1 (2) of MC 17 SE] indicates that the mare ridges are protruding remnants of an older surface that has been embayed by younger lavas. Locally, this relation is observable (e.g., at lat 20 S., long 80 W.). The older surface is correlative with subdivided ridged plateau materials (3).

References

(1) Crater Analysis Techniques Working Group (1979) Icarus, 37, 467-474.
(2) Scott, D. H., and Tanaka, K. L. (1981) Icarus, 45, 304-319.
(3) Scott, D. H., 1983, this publication.

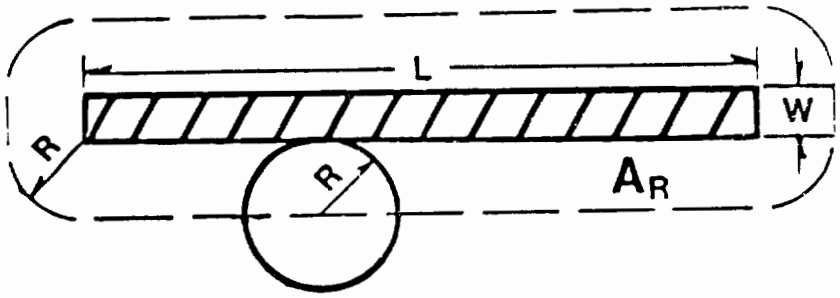

Figure 1. Diagram showing area, A_R, enclosed by dashed line one crater radius, R, away from linear feature of length L and width W.

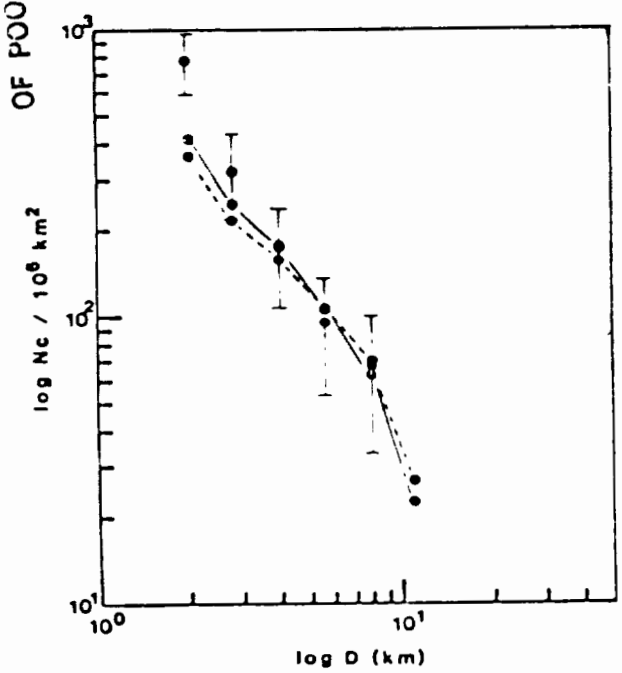

TABLE 1. CRATER COUNT DATA USED IN FIGURE 2

D_a (km)	n	N	A_R (km^2)	N_c (no./10^6 km^2)	σ_{N_c} (no./10^6 km^2)
			Standard area count		
22.4	1	1	344,000	3	3
16.0	1	2	344,000	6	[illegible]
11.2	6	8	344,000	23	8
8.0	13	21	344,000	61	13
5.6	16	37	344,000	108	18
4.0	23	60	344,000	174	23
2.8	25	85	344,000	247	27
2.0	61	146	344,000	424	35
			Area line count		
16.0	2	2	335,555	5	4
11.2	5	7	240,827	26	10
8.0	8	15	177,258	71	18
5.6	5	20	132,730	109	24
4.0	5	25	102,339	158	32
2.8	5	30	80,784	219	40
2.0	10	40	65,937	371	59
			Mare ridge count		
22.4	1	1	147,038	7	7
8.0	3	4	49,808	67	34
5.6	1	5	35,859	95	42
4.0	2	7	26,453	171	64
2.8	3	10	19,841	322	102
2.0	7	17	15,316	779	189

Figure 2. Crater counts on Lunae Planum. Solid curve, standard area count; dashed curve, area line count. Error bars indicate confidence intervals for mare-ridge count.

Chapter 5

VOLCANIC PROCESSES AND LANDFORMS

THICKNESS AND DISTRIBUTION OF VOLCANIC MATERIALS ON MARS: A PROGRESS REPORT

R. A. De Hon, Department of Geosciences, Northeast Louisiana University, Monroe, La. 71209.

Unlike the moon, martian volcanic materials exhibit a wide range of ages, widespread distribution, and multiplicity of surficial characteristics (1, 2). Martian volcanic materials range from positive constructional features to lowlying plains. A minimum volume of material may be derived from the topography of the volcanic constructional features. The thickness of some plains-forming materials may be estimated by the extend these materials bury pre-existing craters. On Mars, with an active erosional regimen, the relationship between crater diameter and rim height is less precise than that of the moon (3, 4), but a general trend is assumed to be preserved if burial is sufficiently rapid.

The current status of martian thickness studies and some generalized trends in distribution of volcanic materials are reporter here (Table 1). Photomosaic base maps of Mars are incomplete ; hence, the thickness studies are incomplete. Isopach maps of volcanic plains materials require more detailed control of unit contacts than are available at this time.

Approximately 600 thickness estimates over 35% of the martian surface are incorporated in the data base. The data distribution is random to clustered depending upon the presence of suitable materials, the age of the subjacent surface, and the thickness of surficial materials. The average thickness of the data is approximately 800 m ± 300 m. Many regions of materials in excess of 2 km thickness are not included in the data; hence, the bulk of the data tends to be weighted in terms of southern highland intercrater materials.

Major volcanic centers dominated by positive constructional forms (such as the Tharsis and Elysium regions) are beyond the capabilities of thickness measurements based on buried craters. The volume of materials within the constructs may be estimated from surface geometry, but thick deposits adjacent and subjacent to these centers have unknown subsurface configurations. Only minimum values may be estimated from surface configurations and from the assumption that thicknesses exceed 1.5-2.0 km. Volcanic materials exceed a thickness of 1.5 km throughout most of the Tharsis Province, Elysium Planum, and Syrtis Major Planum. Measurements less than

TABLE I
CURRENT STATUS AND RESULTS OF THICKNESS STUDIES

PROVINCE SECTION	THICKNESS RANGE	NATURE OF MATERIAL AND OBSERVATION
THARSIS		
Olympus	0.5-0.75 km	Surficial flow materials and aureole of volcanic construct. Total thickness unmeasured.
Alba	0.5-1.0 km	Low patera and flanking materials. Central mass not measured.
Tharsis Montes	0.5-1.0 km	Lobate surficial flows.
Syria-Sinai	0.25-0.75 km	Surficial flows similar to Tharsis.
Lunae	0.0-1.5 km	Ridged plains-forming materials. Measurements are total thickness of exposed materials.
NORTHERN LOWLANDS		
Chryse	0.25-1.0 km	Ridged materials in basin. Deepest portion unmeasured.
Amazonis Arcadia Acidalia Utopia Isidis	Incomplete Data	Scattered measurements with insufficient data distribution to determine trends.
Elysium	>1.5-2.0 km	Volcanic flows associated with Elysium and Hecates Mons.
SOUTHERN HIGHLANDS		
WESTERN SUBPROV.		
Western Highlands	0.0-1.25 km	Discontinuous ridged plains-forming materials in topographic lows. Similar to Lunae Planum materials but more cratered.
CENTRAL SUBPROV.		
Central Highlands	0.0- 1.25 km	Same as Western Highlands.
Argyre	No Data	Basin fill.
Syrtis Major	>1.5-2.0 km	Low patera with in basin. Thin edges and thick center.
Australe	0.5-1.0 km Incomplete Data	Plateau volcanics with patera. Extensive distribution on SW flank of Hellas Basin.
Eastern Highlands	No Data	Same as Western and Central Highlands
Hesperia	No Data	Patera complex with widespread flanking ridged plains material.

1 km are found only along the outer edges of the extensive volcanic piles (3, 4) and on surficial mantling flows (4, 5).

In the highland province, probable volcanic materials exist as low patera, basin fill, and plains-forming materials flooding low lying terrain. Contacts with the more highly cratered materials range from sharp to gradational depending upon the nature of the topographic low into which the meterials are emplaced. Partially buried craters allow reasonable estimates of thickness, but the absence of adequate contact relationships and complete map coverage do not allow volume estimates. Current data suggests that the thickness of volcanic materials averages less than 1 km throughout the cratered highlands with local thicknesses in excess of 1.5-2 km in major basins only (Table I).

References

1. Carr M. H. (1979) Space Sci. Rev. 25, 231-284.
2. Greely, R. and Spudis P. D. (1981) Rev. Geophys. Space Phys., 19, 13-41.
3. Plescia J. B. and Saunders R. S. (1980) Proc. LPSC 11 2423-2436.
4. De Hon R. A. (1982) J.G.R. (in press).
5. Scott D. H. and Tanaka K. L. (1981) Icarus, 45, 304-319.

MAPPING VOLCANIC FEATURES ON MARS

Moore, H. J., U.S. Geological Survey, Menlo Park, CA 94025

Photogeologic analysis and planetwide mapping of martian volcanic features shown in Viking pictures yield the following: (A) identification of volcanic centers with small edifices [1, 2]; (B) identification of lava flows on or near Tyrrhena, Biblis, Ulysses, and Uranius Paterae, the northern plains, and the Mareotis-Tempe uplands; (C) confirmation of the existence of parasitic shields and flank eruptions from Arsia, Pavonis, and Ascraeus Montes [3, 4]; (D) an indication of the distribution of lava flows related to the various montes and other volcanic centers; (E) confirmation of the general concordance between present-day topography and the paleoslopes inferred from some lava flows [5]; (F) identification of locations, including Tharsis, where there are discordances between present-day topography and the paleoslopes inferred from some lava flows; (G) general agreement with other workers on the relative ages of most volcanoes and volcanic centers [6]; (H) concurrence that the elevations and heights attained by the large volcanoes tend to increase over time but that eruptions at low elevations persisted throughout the same interval [7]; and (I) identification of previously unrecognized channel deposits. These results have been compiled on maps at 1:25,000,000 scale.

Detailed mapping of the Elysium Mons region suggests that considerable volumes of water were released during volcanism. Evidence for these large volumes of water includes: channels with streamlined islands that arise from the large "cobrahead" rilles near the outer edges of the Elysium volcanic deposits, a type of chaotic terrain that has formed in the volcanic deposits and subjacent units, and isolated features to the north that resemble möberg hills [8, 9] and hyaloclastite ridges [10]. Intersection of some rilles and chaos with Elysium volcanic deposits, and superposition of Elysium deposits on other rilles prove that volcanism and release of water were contemporaneous. The möberg-like hills suggest that some, if not all, of the water originated from near-surface geologic units, but a primary origin for some of the water cannot be excluded.

References:

[1] Moore, H. J. and Hodges, C. A., 1980, Some martian volcanic centers with small edifices: Repts. Planet. Geol. Prog., 1980, NASA TM 82385, p. 266-268.

[2] Hodges, C. A., 1980, Tempe-Mareotis volcanic province of Mars: Repts. Planet. Geol. Prog., 1979-1980, NASA TM 81776, p. 181-183.

[3] Crumpler, L. S. and Aubele, J. C., 1978, Structural evolution of Arsia Mons, Pavonis Mons, and Ascreus Mons: Tharsis region of Mars: Icarus, v. 34, p. 496-511.

[4] Roth, L. E., Downs, G. S., Saunders, R. S., and Schubert, G., 1980, Radar altimetry of south Tharsis, Mars: Icarus, v. 42, p. 287-316.

[5] Mouginis-Mark, P. J., Zisk, S. H., and Downs, G. S., 1982, Ancient and modern slopes in the Tharsis region of Mars: Nature, v. 297, p. 546-550.

[6] Plescia, J. B. and Saunders, R. S., 1979, The chronology of the martian volcanoes: Proc. Lunar Planet. Sci. Conf. 10th, p. 2841-2859.

[7] Carr, M. H., 1976, Elevation of martian volcanoes as a function of age: Rept. of Accomp. of Planetary Prog., 1975-1976, NASA TM X-3364, p. 152-153.

[8] Hodges, C. A. and Moore, H. J., 1979, The subglacial birth of Olympus Mons and its aureoles: J. Geophys. Res., v. 84, p. 8061-8074.

[9] Allen, C. C., 1979, Volcano-ice interactions on Mars: J. Geophys. Res., v. 84, p. 8048-8059.

[10] Thorarinsson, S., Saemundsson, K., and Williams, R. C., 1973, ERTS-1 Image of Vatnajokull: analysis of glaciological, structural, and volcanic features: Jökull, v. 23, p. 7-17.

GEOLOGIC MAP OF OLYMPUS MONS

E. C. Morris, U.S. Geological Survey, Flagstaff, AZ 86001

Detailed geologic mapping, based on high resolution Viking orbiter photography, has delineated stratigraphic and structural elements of the huge shield volcano, Olympus Mons (Fig. 1). Its flanks are covered by thin, low-viscosity lava flows, and on the northeast and southwest sides of the structure, young flows have partly buried the escarpment that surrounds the volcano and have streamed out onto the basal plains to a distance of almost 200 km (1). Ages of the flows are determined by stratigraphic relations and morphologic characteristics. Flows on the lower and upper flanks differ distinctly in character and in age of emplacement. Flows on the lower flanks are typically long, and narrow and have levees; they are several hundred meters to a kilometer wide and 10-100 km long (1). These flows are the youngest features of the volcano, and they appear fresh and pristine compared to the older flows on the upper flanks and summit. The most recent of the young flows have distinct lobate terminations and sharp boundaries (Fig. 2), and are found mostly on the south and north flanks. Flows on the upper flanks and near the summit have rough, hummocky surfaces and are indistinct; some are stubby and a few others are broad and sheetlike.

Olympus Mons probably grew over a long period of time with many eruptive episodes (2). Lava flows are numerous and extensive; their boundaries are intermeshed and generally indistinguishable. Only the young postscarp flows are mappable as distinct flow units. Consequently only prescarp eruptions and two major postscarp eruptive sequences have been delineated on the flanks of Olympus Mons (Fig. 1).

The basal material upon which Olympus Mons was built is exposed in the north, northwest, west, and southeast segments of the complex scarp that surrounds the volcano. Blocks of this material are found along the rim of the scarp dipping toward the center of the volcano. The surfaces of some of these blocks, where exposed, show channels and grabens similar to those on the fractured plains material east of Olympus Mons. However, a few exposures of scarp material in the west segment have a corrugated or ridged surface suggestive of the surface of some aureole material (Fig. 3).

Landslides and slump blocks are prevalent along the western scarp. Two sections of the scarp, one almost 100 km wide, have collapsed and flowed onto the adjacent plain. The eastern segments of the scarp do not have landslide and slump features which may indicate a difference in the strength of the materials that make up the scarp.

References

(1) Carr, M. H., Greeley, Ronald, Basius, K. R., Guest, J. E., and Murray, J. B. (1977) Some martian volcanic features as viewed from the Viking orbiters, J. Geophys. Res 82, p. 3985-4015.

(2) Carr, M. H. (1981) Yale University Press, 232 p.

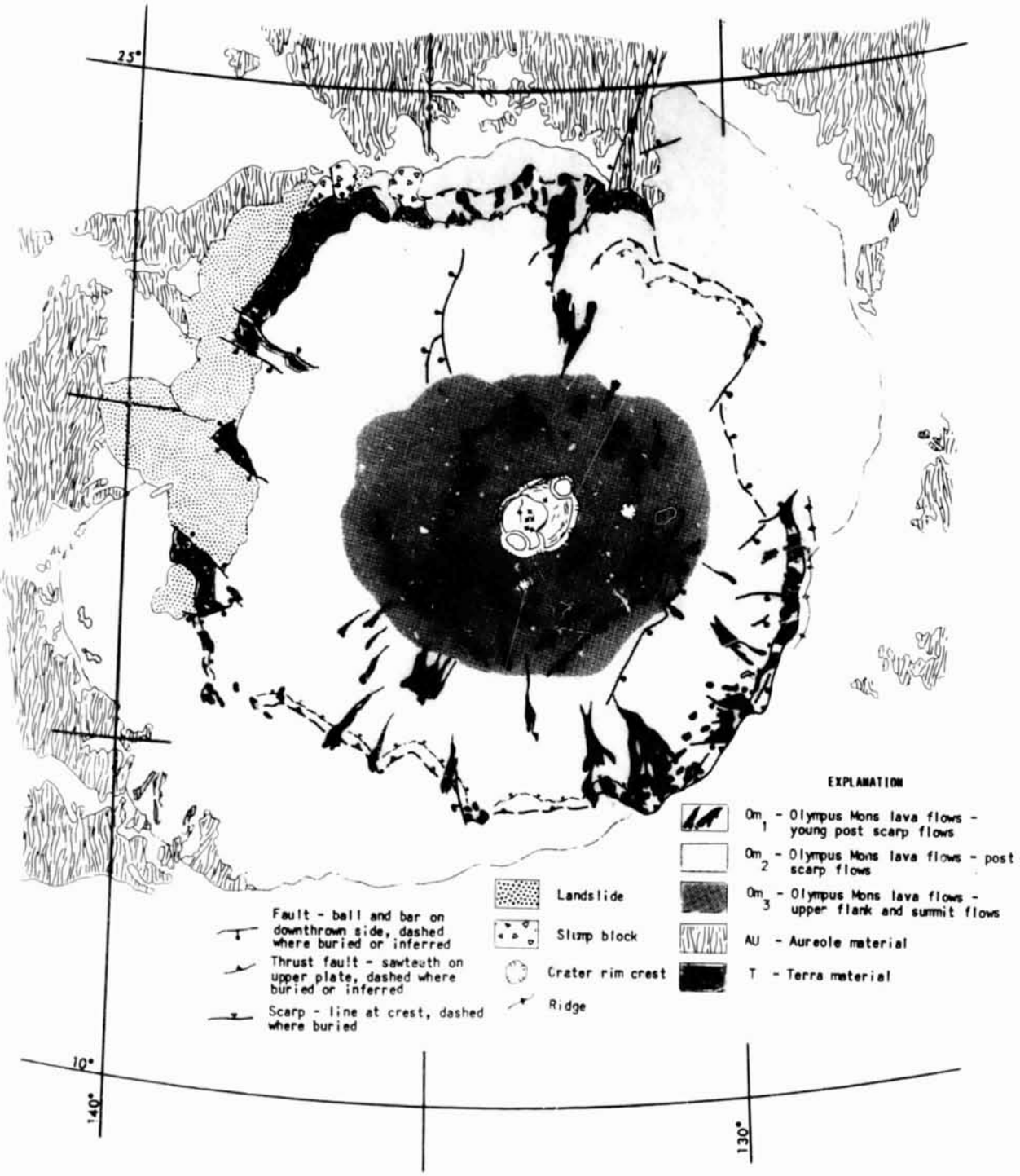

Figure 1. Geologic map of Olympus Mons.

Figure 2. Young post-scarp lava flows on Olympus Mons. Long narrow leeved flows are clearly defined on older indistinct flows. Width of picture 118 km (Viking Orbiter 890A66).

Figure 3. Western segment of the basal scarp of Olympus Mon (138.4° W. long, 19.5° N. lat). Scarp is formed by a block of material dipping inward towards the center of Olympus Mons. The upper exposed surface of the block (a) has a number of subdued anastomosing ridges similar to the surface of the aureole material. Arrows point to dark streaks in talus formed from the weathering of the scarp material. Width of picture 18.5 km (Viking Orbiter 476526).

LAVA FLOW MATERIAL ON THE MOTTLED PLAINS IN MARE ACIDALIUM QUADRANGLE (MC-4), MARS

Witbeck, N.E., and J.R. Underwood Jr., Department of Geology, Kansas State University, Manhattan, Kansas 66506

The mottled plains material has been one of the most difficult of the plains units to define and interpret. There are few clues as to the origin of this extensive unit. In Mare Acidalium quadrangle only a few high-resolution strips of images were taken in the mottled plains region by the Viking Orbiters. One of these high-resolution strips of images suprisingly revealed evidence of relatively recent volcanic activity. This volcanic region is centered at approximately 47°N, 25°W.

Lava-flow lobes are a distinctive characteristic of young volcanic provinces on Earth and Mars (Carr et al., 1977). Several lava flows have been identified on the mottled plains between latitudes 44°-48°N and longitudes 20°-28°W. Figure 1 shows the best example of these lava flows. The source of these flows is uncertain. The flows may have originated from fissures that were subsequently buried, or from central vents (Fig. 1).

This volcanic region was mapped in detail and is included as Figure 2. Dissected and fractured plateau material (pldf) occurs in the northwest corner of the map area. The plateau surface is smooth and is cut by a number of fractures and troughs that commonly trend north-south. Several troughs and a large circular depression on the plateau are embayed by low-albedo plains materials. The knobby terrain (k) is interpreted as erosional remnants of the higher plateau surface. The dissected and fractured plateau material is interpreted to be an isolated remnant of the cratered plateau 800 km to the southeast. The fractures that cut the plateau may be tectonically related to the recent pulse of volcanic activity. Alternatively, they may be the result of more regional stresses.

The subdued patterned mottled plains material (pmps) surrounds the dissected and fractured plateau. Patterned or fractured plains are common in east-central MC-4. In the map area the pattern of troughs is observed to be more discontinuous than that seen in other areas in east-central MC-4. The presence of lava-flow fronts, pressure ridges, and possible volcanic cones on the subdued patterned mottled plains suggests that volcanic flow rock fills or partially fills pre-existing troughs.

Small (<1 km diameter) mound-like domes with or without summit craters are ubiquitous in this region (Figs. 1,2). Several origins have been suggested for these features including: (1) cinder cones (Wood, 1979); (2) pseudocraters formed by lava flowing over water-saturated ground (Frey et al., 1979); (3) pingos produced by the arching of frozen ground forced up by the intrusion of water (Wood, 1979); or (4) small impact craters that were eroded to inverted relief (Masursky and Cradbill, 1976). The association of these domes with volcanic plains tends to support the interpretation of these features as volcanic.

The discovery of recent volcanic features in this region is important because it lends support to the theory that volcanic material has resurfaced parts of the mottled plains.

REFERENCES

Carr, M. H., Greeley, R., Blasius, K. R., Guest, J. B., 1977. Some martian volcanic features as viewed from the Viking orbiters: J. Geophys. Res., v. 82, p. 3985-4015.

Frey, H., Lowry, B. L., and Chase, S. H., 1979. Pseudocraters on Mars: J. Geophys. Res., v. 84, P. 8075-8086.

Masursky, H., and Cradbill, N. L., 1976. Search for the Viking 2 landing site: Science, v. 194, p. 62-68.

Wood, C. A., 1979. Monogenetic volcanoes of the terrestrial planets: Proc. Lunar Planet. Sci. Conf. 10th, p. 2815-2840.

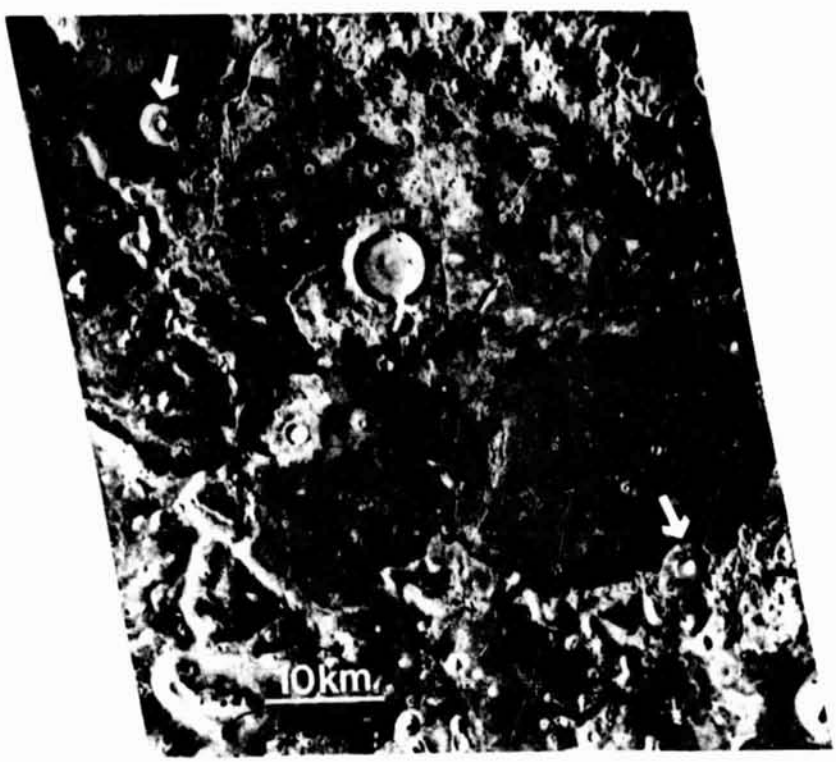

Figure 1. A lava flow on the mottled plains in southern Acidalia Planitia. The flow in the center of the image is approximately 48 x 25 km. The arrows indicate small domal structures that resemble pedestal craters but may in fact be small volcanoes. Small (< 1 km diameter) cratered domes occur at the bottom of the image. Viking frame 35 A 32 (45.4°N, 28.4°W); north is to the top of the image.

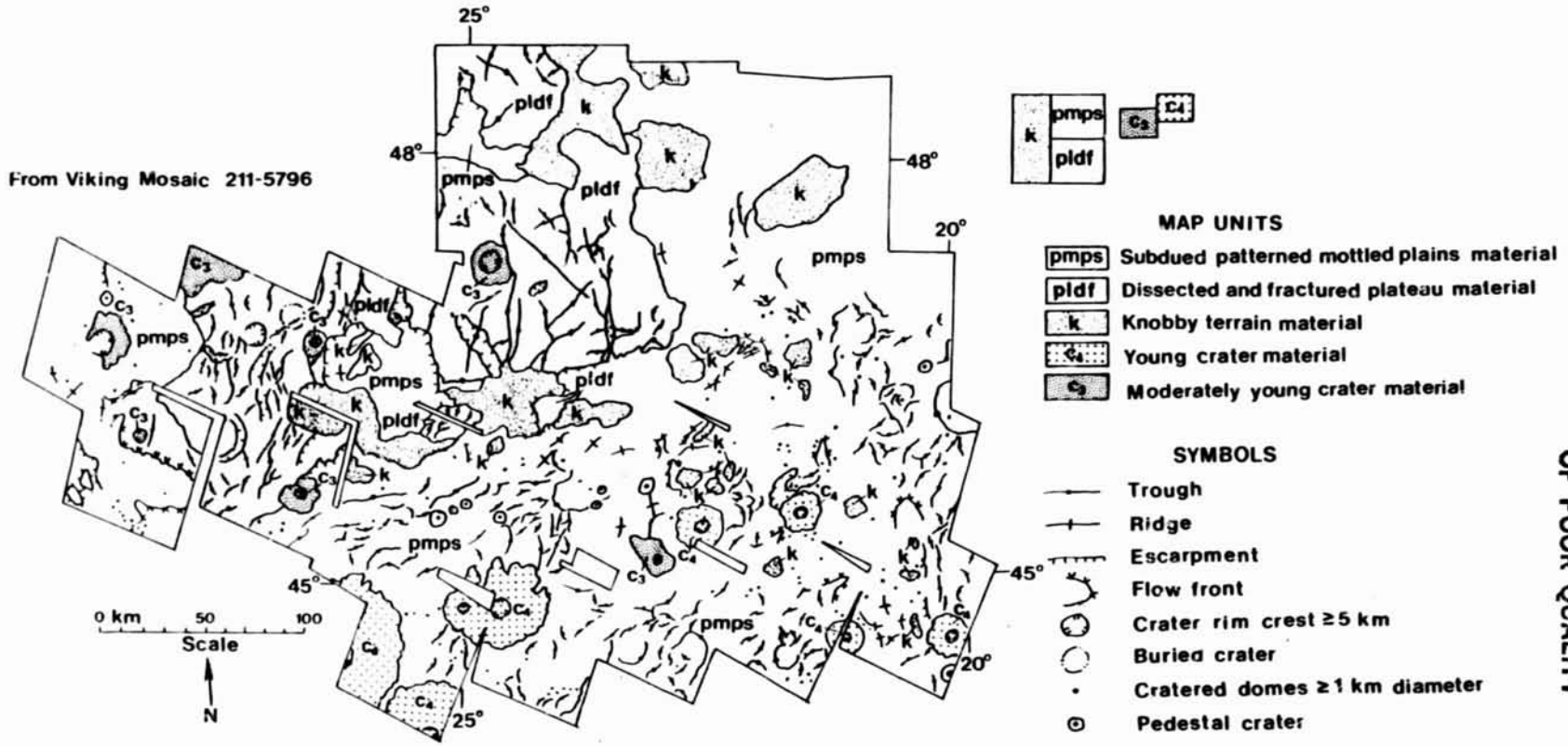

Figure 2. Geology of east-central MC-4

SURFACE TOPOGRAPHY AND EMPLACEMENT MECHANISM OF PYROCLASTIC FLOWS, MT. ST. HELENS: IMPLICATIONS FOR INTERPRETATION OF MARTIAN VOLCANIC TERRAINS

C.A. Neal and S. Self, Department of Geology, Arizona State University, Tempe, Arizona 85287

Six eruptions of Mt. St. Helens during 1980 produced pyroclastic flows. This sequence of deposits, estimated to be equivalent to 0.12 km^3 of dense dacite (1), formed a broad fan extending 8 km N of the mountain. At present, erosion is proceeding very rapidly. As of August 1982, less than 20% of the original pyroclastic flow surfaces remained intact and only small patches of pristine May 18, June 12, and July 22 deposits could be found. Especially erosive were mudflows generated by the explosive eruption of March 19, 1982.

In the extreme western portion of the fan, a local high of primary May 18 material surrounded by deeply incised drainages has escaped modification. Here, good but limited exposures of primary surfaces will probably remain intact for several more seasons. In an effort to document these features and to develop a model for flow emplacement, field work was carried out in October 1980, August 1981, and June-August 1982.

Deposits of the May 18 eruption are characterized by three distinct facies (2) each of which display a different surface morphology. These are: 1) a near-vent veneer deposit on the steep slopes of the volcano with subtle surface dune-like forms ($\lambda < 50$ m); 2) a medial, thick (< 40 m) ponded facies which has a gently undulating surface ($\lambda \cong 1$ km) and subdues topography; and 3) a medial to distal coarse pumice flow facies characterized by channels and levées, breakouts, meter-high flow fronts, ramp structures and distinctive surface pumice concentrations (Figures 1 and 2). These lobate flows were erupted late on May 18 and cover the ponded deposit, extending beyong it in some areas to 10 km from the vent. Facies 3 flows are almost identical in morphology to coarse pumice and ash flows emplaced by the five subsequent eruptions during 1980. However, the May 18 flows are larger in volume and hence possess greater run-out distances than the post-May 18 flows.

Comparative studies of surface morphology and internal structures of each type of Mt. St. Helens pyroclastic flow supports the interpretation that the May 18 flows were more fluidized than those of subsequent eruptions (2,3). Large volume facies 1 deposits contain a higher proportion of fines, were of lower yield strength and were possibly more inflated during run-out. The result was thick, ponded deposits with a generally smooth upper surface. In contrast, surface relief up to 10 m characterizes the late May 18 (facies 3) flows and those from later eruptions. These possess surface features indicative of higher yeild strength (2,3), consistent with a lesser degree of fluidization. Such a trend may be produced by a general decrease in the size of erupted magma batch and a decrease in fragmentation of magma. Both may reflect the tapping of an increasingly volative-poor magma.

Similar observations on coarse, lobate (poorly fluidized), young pumice and ash flows have been made at Fuego, St. Augustine, and Novarupta volcanoes, representing a compositional range from basaltic andesite to rhyolite. Results suggest that such flows are a common, late-stage phenomenon of pyroclastic flow-producing eruptions.

It has been cautiously suggested (4-7) that recognition of extraterrestrial pyroclastic flows on the basis of surface morphology may be possible. So far, no unique identifying morphological feature of appreciable scale has been documented (8-10) for terrestrial pyroclastic flows. Results from our work, unfortunately, imply that this may be the general case. Although the morphology of the small volume pumice and ash flows at Mt. St. Helens is distinctive when viewed at close range, the scale of even the largest features is far too small to be resolved with available Mariner and Viking imagery. No relationship can be demonstrated between the volume of a pyroclastic flow and the scale of surface features. Furthermore, our study suggests that there may be an inverse relationship. We therefore suggest that large and medium volume pyroclastic flow deposits, e.g. Bandelier Tuff, Valley of Ten Thousand Smokes, need not possess large surgace features. Similarly, we suggest that pyroclastic flows on Mars can not be expected to possess resolvable surface features of the type characterized by late-stage, coarse pumice and ash flows.

Inherent in this discussion is the premise that mechanisms of pyroclastic flows on Mars are similar to those operating on Earth. To continue to speculate on this subject, it is necessary to first refine our understanding of terrestrial volcanologic phenomena such as the generation (11), fluidization (12), and deposition (13) of pyroclastic flows. From these efforts, it is conceivable that a list of truly diagnostic criteria - including distribution, style of modification, and surface morphology - will emerge.

REFERENCES

1. Rowley, P.D. et al., 1981, U.S.G.S. Prof. Paper 1250, 489-512.
2. Self, S. and Sykes, M.L., 1982, J.V.G.R., in press.
3. Wilson, L. and Head, J.W., 1981, U.S.G.S. Prof. Paper 1250, 513-524.
4. Malin, M.C., 1979, NASA PUB 2072, 54.
5. Ward, A.W., 1979, Jour. Geophys. Res., 84, 8147-8166.
6. Scott, D.H. and Tanaka, K.L., 1982, Jour. Geophys. Res., 87, 1179-1190.
7. Morris, E.C., 1982, Jour. Geophys. Res., 87, 1164-1178.
8. Greeley, R. and Spudis, P.D., 1981, Rev. Geophys. Space Phys., 19, 13-41.
9. Francis, P.W. and Wood, C.A., 1981, LPI Contrib. 441, 81-83.
10. Criswell, C.W., and Elston, W.E., 1981, NASA Tech. Memo. 84211, 174-176.
11. Wilson, L. and Head, J.W., 1981, LPI Contrib. 441, 281-283.
12. Wilson, C.J.N., 1980, Jour. Volc. Geotherm. Research, 8, 231-249.
13. Wilson, C.J.N., 1982, in press.

Figure 1. Low altitude, oblique aerial photo of western edge of pyroclastic flow fan (7-8 km from vent) showing distal fa ies (facies 3) of May 18 deposits. Note multiple lobate flow fronts, breakouts, and coarse pumice texture. Small pit at lower right is approximately 2.5 m across.

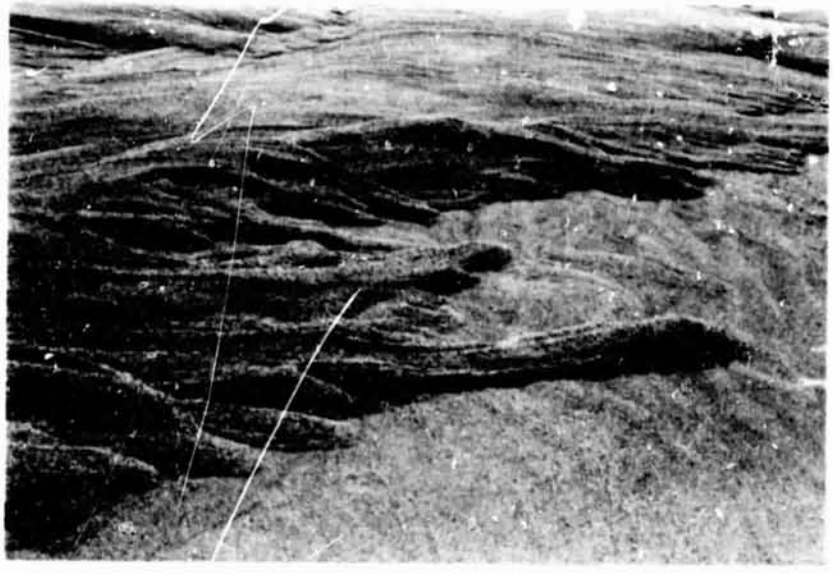

Figure 2. Close-up of boxed area in Figure 1. Prominent leveed flow is approximately 10 m long and averages 50 cm in thickness.

CRITERIA FOR IDENTIFYING PYROCLASTIC FLOWS ON HIGH- AND LOW-RESOLUTION IMAGES: THE MOUNT ST. HELENS PUMICE PLAIN

Charles W. Criswell and Wolfgang E. Elston, Department of Geology, University of New Mexico, Albuquerque, New Mexico 87131

Identification of ignimbrite and related pyroclastic-flow deposits on Mars and Io has been hampered by lack of criteria by which such deposits can be identified on terrestrial air photos or satellite images. An ancient terrestrial ignimbrite tends to be characterized by a flat and relatively featureless surface. This is not a primary surface, but the top of a welded zone from which an upper unwelded zone has been stripped by erosion. The 1980 eruptions of Mount St. Helens gave a rare opportunity to observe primary surface features of unwelded pyroclastic-flow deposits in the continental U.S. This opportunity is passing because of rapid erosion.

Photogeologic and field studies of the Mount St. Helens pumice plain reveal that the sheet-like deposits described by Rowley and others[1] are lobate in outline. Margins along free flow boundaries are serrated due to overbank and breakout flow lobes. Surface features can be grouped into eight categories that may reflect the emplacement processes (numbers also correspond to those used on Figure 1).

1. Ridged channels; characterized by longitudinal channels and one or more sets of longitudinal ridges, 1-3 m high, interpreted as levees. Levees are generally composed of fines-depleted pumice clasts.

2. Ridged plains; characterized by low anastomosing ridges. Topography undulates, with relief of several meters and the surface is marked by low ridges, a few centimeters to decimeters high, with longitudinal, transverse, festoon or eddy patterns. The material comprising the ridged plains is generally finer-grained than in ridged channels and therefore experienced fewer grain-grain interactions during fluidization. This resulted in lower yield strength and lower ridges.

3. Ridged flank deposits; variation of the ridged plains, which occur on the northwest flank of the volcano. Low ($<<$ 1 m) longitudinal braided ridges are interpreted as products of high-energy (high fluidization?) flow. Deposits $<$ 1 to 3 m thick tend to veneer the topography. They are interpreted as having formed from pyroclastic flows that ramped off the steeper slopes of the volcano, expanded, and became diluted with air (P. Rowley, 1982, pers. comm.). Similar features are noted in deposits of June 12, 1980 which are thought to have been more fluidized than other flows of 1980 (R. Hoblitt, 1982, pers. comm.).

4. Corrugated plains, characterized by closely spaced transverse wrinkle ridges and commonly enclosed by a single border levee. The transverse ridges are thought to have formed from low-energy pyroclastic flows with less internal shearing than those producing longitudinal ridges.

5. Smooth cratered plains, characterized by phreatic pits and a nearly flat to gently undulating blanket of ejecta. Phreatic explosions were penecontemporaneous with flow emplacement. Large ($>$ 10 m) phreatic pits are common at Mount St. Helens, but pits below resolution may produce the same effect. Phreatic pits can only form in the presence of surface water, shallow ground water, or ground ice.

6. Low-angle (10-30°) scarps, which truncate primary flow features.

The scarps seem to have resulted from slope failure. Secondary pyroclastic flows, which drained from the failing slopes, are difficult to distinguish morphologically from primary deposits, remnants of scarps may be diagnostic.

7. High-angle (> 30°) scarps, a few meters high, bordering low smooth-surface "mesas". Scarps are best developed on the upstream side. The mesas appear to be isolated remnants of the same flow deposit, probably erupted on June 12, 1980. The landform bears a striking resemblance to certain features on Io. The scarps could have been formed through erosion by subsequent high-energy flows, or by slope failure, or by both. Unfortunately, the June 12, 1980 deposits of Mount St. Helens were nearly totally destroyed by mudflows in the spring of 1982.

8. Scalloped, high-angle scarps that truncate primary flow features, but did not generate secondary pyroclastic flows. The scallops are generally semi-circular. The scarps are believed to have formed by collapse, possibly due to melting ice in the debris-avalanche deposit[2] that underlies the pyroclastic flows. Hummocks at the base of the scarps are evidence for a collapse origin.

Landforms 1, 2, 3, 4 and 8 are not diagnostic of pyroclastic flows; similar features can be seen on lava flows, mud flows, debris flows and glacial deposits. The large pits in the smooth cratered plains, 5, may be diagnostic. Collapse pits on lava flows or glacial moraines have no rims. Rimmed craters without blocks suggest explosion within a low-cohesion material. If other criteria suggest flowage, the material is likely to be pyroclastic. The pits may be difficult to distinguish from small bowl-shaped impact craters and ages based on crater counts would be spurious.

Low- and high-angle scarps, 6 and 7, may be even more significantly diagnostic of pyroclastic flows, because they do not require shallow water or ice, as do phreatic pits. Scarps that fail, releasing secondary flows, should be characteristic of low-cohesion, fluidized material. Isolated mesas bordered by high-angle scarps are probably sculptured by subsequent high-energy flows; the material of the mesas presumably had the low coherence characteristic of pyroclastic deposits.

Would features observed on pyroclastic deposits at Mount St. Helens be of a scale observable at the resolution of spacecraft images? Surface features were mapped on black-and-white air photos, flown in the summer of 1980, with resolution of about 1 meter, far greater than space images. However, several features could also be observed on Landsat III images with 30 m resolution (RBV), within the range of the best space images:

I The pumice plain has a lighter tone than surrounding areas that are mantled by a blast deposit[3] of less vesiculated ash, similar to pumice in composition.

II Tonal variations within the pumice plain suggest that separate flows contributed to the deposit.

III Phreatic pit craters are discernible, associated with the darker and possibly smoother areas. Craters in the more hummocky terrain of debris-avalanche deposits lack ejecta blankets.

IV The light, variably toned pumice plain appears flatter and much less structured than either the surrounding areas of pre-eruption topography mantled by blast deposits or the hummocky debris-avalanche deposits

in valleys below the pumice plain.

Sparks and others[4] noted the same primary stratigraphic features in pyroclastic flows ("standard ignimbrite flow unit") in deposits ranging in volume from <1 to >30 km^3, and ranging in composition from rhyolite to basalt. This suggests that emplacement mechanisms do not vary with volume, but rather, with the nature of fluidization[5]. It is hoped that some features observable under the highest resolution at Mount St. Helens can be extrapolated to larger features on larger volcanos, in the manner that Shoemaker[6,7] extrapolated details of Meteor Crater, Arizona, to Copernicus.

References Cited

1) Rowley et al., 1981, U.S.G.S. PP 1250, p. 489. 2) Voight et al., ibid, p. 347. 3) Hoblitt et al., ibid p. 401. 4) Sparks et al., 1973, Geol., v. 1, p. 115. 5) Wilson, 1980, J. Volcanol. Geotherm. Res., v. 8, p. 231. 6) Shoemaker, 1960a, Proc. 21st Int. Geol. Cong., Sec. 18, p. 418. 7) Shoemaker, 1960b, Lunar Planet. Explor. Colloq., 11, 2, p. 7.

Figure 1. Southwestern portion of Mount St. Helens pumice plain. Numbers correspond to surface features described in text, with not all types shown in photo. Crater to the southeast.

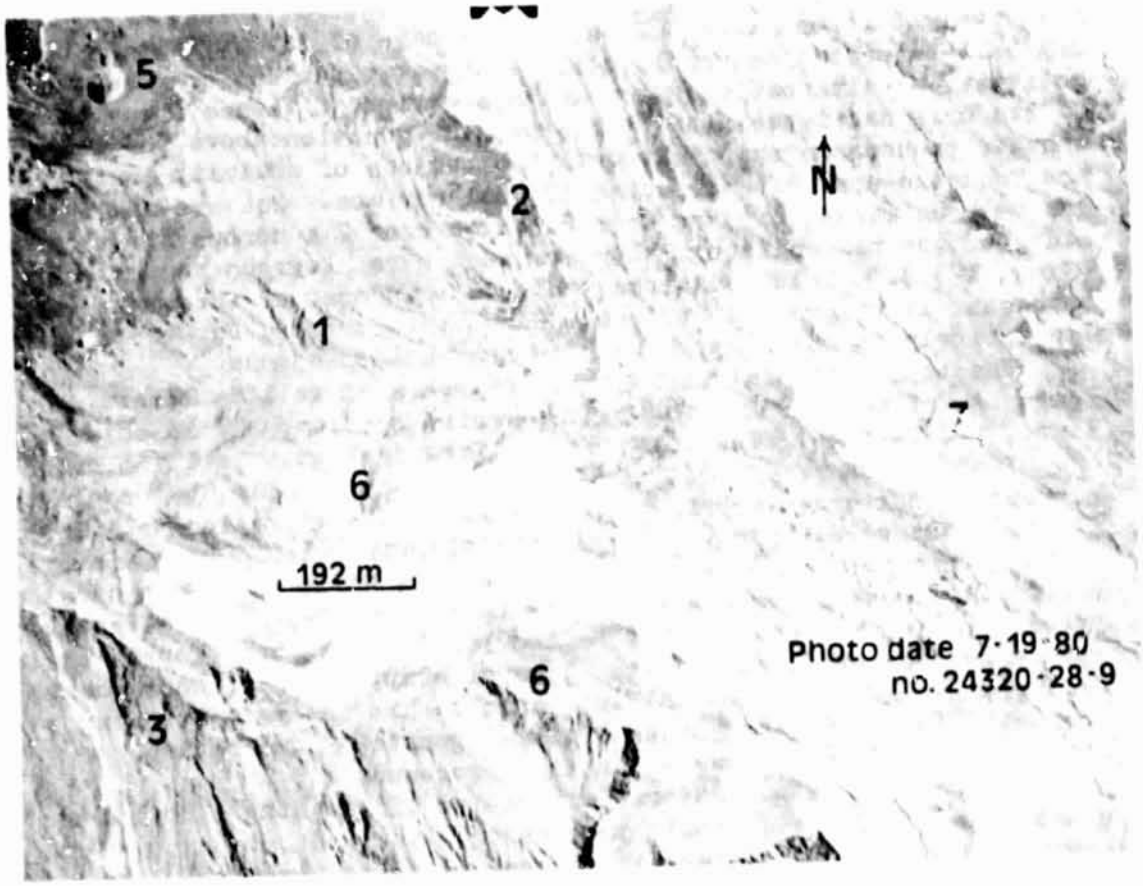

EXAMINATION OF A TEPHRA DEPOSIT ON THE GREAT RIFT OF THE SNAKE RIVER PLAIN IN SOUTHEASTERN IDAHO

Leeda E. Marsh and John S. King, Department of Geological Sciences, State University of New York at Buffalo

King's Bowl is the largest crater located on the King's Bowl rift set, one of the fracture sets of the Great Rift System of Idaho. King's Bowl is located approximately 35 km from American Falls in southeastern Idaho. The King's Bowl lava field represents one of the youngest flows on the Snake River Plain and has been dated at 2130 ± 130 years before present (Prinz, 1970). Field studies indicate that the eruptive sequence at King's Bowl concluded with a period of phreatic activity which covered an area of at least two square kilometers with a blanket of tephra.

The tephra ranges in size from large blocks down to clay size particles. Blocks and larger fragments predominate on the west side of the rift. In contrast, the east side has some blocks but ash predominates due to the prevailing westerly winds at the time of eruption. The surface tephra on the east side of the rift covers a relatively thick layer of loess. A trench was dug revealing the following sequence from surface to depth: tephra, loess, a relatively thin ash layer, loess, and a base of lava. This sequence may be interpreted as representing either two periods of phreatic activity, or alternatively the transportation of tephra from the site of its original deposition to its present position above the loess. Another phenomenon which supports two periods of activity in the area are "squeeze-ups" situated on a loessal surface. Squeeze-ups which are bulbous masses of lava from 0.5 m to over 2 m across exist on both sides of the rift although they are much more numerous on the west (King, 1977). Field relations indicate that most of these masses represent lava squeezed up from beneath the surface, but those which lie entirely on loess may have been semi-molten ejecta.

The tephra consists of vitric fragments as well as lithic fragments of wall rock. The tephra varies considerably in color, shape, and texture. The color ranges from dark gray to a yellowish brown to a brick red. Most particles are very angular, but range to subround. Textures vary from very dense to highly vesicular. The yellowish brown color may represent palagonitization. Preliminary petrographic analysis has revealed a reddish brown isotropic substance surrounding most fragments which may be palagonite. This alteration process (palagonitization) may be the result of interaction of the lava with the water table at the time of eruption or of subsequent weathering. Further chemical and petrographic analysis is being conducted to verify the presence of palagonite and to better characterize the operative alteration processes.

Examination of the interrelationships of the King's Bowl tephra, squeeze-ups, and loess should provide a better understanding of the eruptive sequence and alteration processes active over the last 2,000 years.

King, J.S., 1977, Crystal Ice Cave and King's Bowl Crater, Snake River Plain, Idaho, in Greeley and King, eds, Volcanism of the Eastern Snake River Plain, Idaho: A Comparative Planetary Guidebook, NASA, p.154-163.

Prinz, M., 1970, Idaho rift system, Snake River Plain, Idaho: Geol. Soc. America Bull., vol. 81, p. 941-948.

A typical squeeze-up situated on loess and located on the east side of the rift. Squeeze-up is approximately 1.1 m long, 0.6 m wide, and 0.3 m high.

Tephra blanket on east side of the rift.
Coin (nickel) is used for scale.

LAVA CHANNELS ON THE EASTERN SNAKE RIVER PLAIN, IDAHO AND THEIR RELATION TO SIMILAR LUNAR AND MARTIAN FEATURES

Harris Economou and J.S. King, Department of Geological Sciences, State University of New York at Buffalo

Lava channels are commonly associated with basalt flows of the Eastern Snake River Plain, Idaho. Continuing research has indicated that selected lava channels on the Eastern Snake River Plain resemble some lunar and Martian features. Several channels on the eastern plain were identified and examined in terms of their formation and morphologic evolution. The study also photographically examined numerous channels on the Moon and Mars which are believed to have formed by volcanic processes similar to those responsible for terrestrial lava channels.

One such terrestrial channel located in south-central Idaho is Inferno Chasm (fig. 1). Extensive field research indicates that Inferno Chasm's sinuous 1.5 kilometer-long lava channel formed when the margins of an active lava river which was fed by the vent solidified to form bounding levees. As the eruption proceeded the volume of flow material in the river increased and overflowed the levees bounding the channel. Local blockages in the channel may also have caused the lava river to overflow its banks. Whatever the cause the overflow lava quickly solidified. Repetition of the process heightened and enlarged the levees which now have a maximum height of 30 meters near the vent and progressively decrease down channel.

Figure 1. Vertical aerial photograph of Inferno Chasm. Width of photo equals 2.0 kilometers.

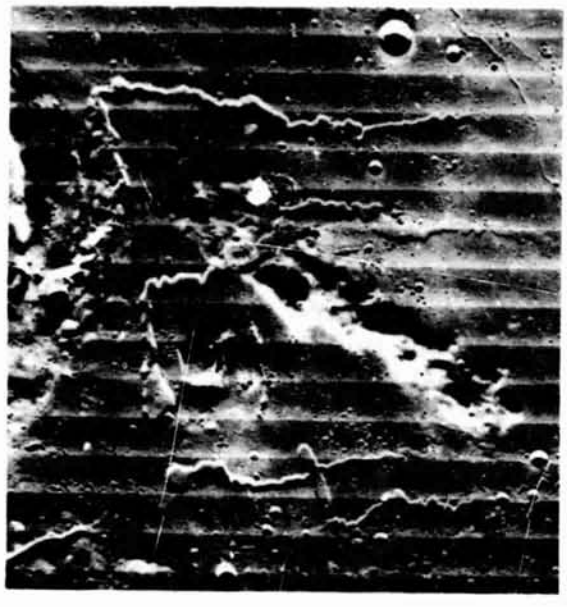

Figure 2. Lunar Orbiter Photograph of sinuous rilles near the crater Prinz. Width of photo equals 60 kilometers.

Figure 3. Lunar Orbiter Photograph of Schroters Valley. Width of photo equals 156 kilometers.

Greeley (1977) first noted the morphologic resemblance of two lunar rilles near the crater Prinz (fig. 2) and hypothesized a similar volcanic origin to Inferno Chasm. Research in this study suggests the rilles formed by a sequence of events much like those responsible for Inferno Chasm. Further research in this study revealed several other sinuous lunar rilles which strongly resemble Inferno Chasm. One of the most striking examples of these is Schroters Valley, a 150 kilometer long rille which flows into Oceanus Procellarum (fig. 3).

Figure 4. Viking Orbiter Image of Elysium Mons summit caldera and associated lava channels. Photo width equals 100 kilometers.

Martian channels such as those located on Elysium Mons (fig. 4) and Hecates Tholus were also examined in this study. Mutch and others (1976) identified the channels as volcanic lava channels. The results of this study agree with Mutch and others and suggest the Martian channels formed by processes similar to those which formed Inferno Chasm and other channels on the Eastern Snake River.

Greeley, R. and P.H. Schultz, 1977, Possible Planetary Analogs to Snake River Plain Basalt Features, In Greeley and King, eds, Volcanism of the Eastern Snake River Plain, Idaho: A Comparative Planetary Guidebook, NASA, p. 233-251.

Mutch et al., 1976, The Geology of Mars: Princeton, N.J., Princeton University Press, 400 pp.

THE ORIGIN OF THE CHENIER CRATER FLOWS

B.R. Hawke, Planetary Geosciences Div., Hawaii Inst. of Geophys., Univ. of Hawaii, Honolulu, HI 96822; J. Whitford-Stark, Dept. of Geology, Univ. of Missouri, Columbia, MO 65211

Introduction: The origin of the flows in Chenier crater on the lunar farside have long been the subject of intense debate. A variety of volcanic (e.g., El-Baz and Worden[1], West[2], Villella[3] and impact (Whitford-Stark and Hawke[4]) origins have been suggested. In particular, Villella[3] argued that the flows originated from the subsurface movement of magma generated as a result of the Tsiolkovsky impact event. As a result of recent studies of lunar impact melt and clastic debris deposits, sufficient evidence now exists to demonstrate an impact melt origin for these enigmatic flows.

Morphology of flow units: The two flows under consideration occur in the floor of Chenier crater which is a 37 km pre-Tsiolkovsky impact structure located 21.5 km northeast of Tsiolkovsky. The longest flow (flow 2) extends for 14.7 km and varies in width from ~3 to ~5 km. The flow thickness is quite variable, being thinnest where the unit crosses a topographic inflection. There is evidence that the flow material originally covered a larger area but moved downslope to merge with the main unit. The surface texture of flow 2 varies from pitted to generally smooth and exhibits neither longitudinal nor transverse ridges. The shorter of the two flows (flow 1) is 8.7 km in length and varies from about 1.5 to 2.3 km in width. Topographic data suggests a maximum thickness of about ~150 m. Lateral ridges exist along portions of the flow and one or more grooves can be seen along much of the length.

Origin and mode of emplacement: Although the flows are concentrated in topographic lows, portions are draped over subjacent terrain from which they failed to completely drain. Such relationships suggest emplacement as fluidized flows and are common in impact melt deposits around other lunar craters (e.g., King crater; Howard and Whilshire[5], Hawke and Head[6]). The lobate form of the deposits also suggests fluid emplacement.

The Chenier flows clearly overlie Tsiolkovsky ejecta deposits and thus were emplaced after the termination of radial flow of crater ejecta. The flows appear to have originated high on that portion of the Chenier crater wall adjacent to Tsiolkovsky. The apparent source can be identified in the vicinity of a major landslide scar visible on Apollo photographs as well as the topograhic map of the area. Abundant lineations clearly demonstrate that the flow material moved down the Chenier wall to the crater floor. The presence of a scar in the source area is a further indication that flow formation was initiated after the deposition of Tsiolkovsky ejecta and hence the fluidization of the flow material cannot be attributed merely to forceful ejection. It is instructive to note that the apparent source area for the flows was adjacent to a hummocky, but generally flat, Tsiolkovsky ejecta unit which is strikingly similar to deposits interpreted to be composed of clast-bearing impact melts by Hawke and Head[6]. Similar material was probably present in the source region of the flows prior to their

development.

An extremely efficient emplacement mechanism is required to account for the transport of flow material far beyond the base of the originating slope. The flow unit traveled a maximum horizontal distance of ~26 km, experienced a maximum vertical drop of ~1.9 km, and has a low effective coefficient of friction (0.073). Flow 2 would have traveled an even greater distance had it not encountered the elevated terrain on the northeast side of the Chenier crater floor. This low coefficient of friction implies an extremely efficient mode of transport. Such mobility would not be expected of a dry flow of clastic debris emplaced after the termination of the cratering event when a radial velocity component due to forceful ejection would no longer be important. Dry lunar avalanches clearly due to local slope failure are not very efficient. Howard[7] noted that only a rare few of the avalanche deposits recognized on crater walls extend beyond the steep crater wall out onto the floor. Typical of these few is the landslide on the wall of Jansen B crater (Diameter = 17 km). The coefficient of friction of this landslide is 0.435, much higher than the 0.073 calculated for the Chenier flows. Additional studies of certain lunar clastic debris deposits that were previously thought to have been very efficient (e.g., the Apollo 17 light mantle) have demonstrated that they were partly propelled by impact processes (Howard[7], Lucchitta[8]). In light of the above considerations, it appears that the Chenier flows are not dry clastic debris deposits but were fluidized by some agent. In view of the absence of a significant lunar atmosphere and the anhydrous nature of the Apollo samples, air and water can be ruled out as fluidizing agents. The one liquid component known to be capable of producing such fluidized deposits is impact melt, which, as discussed above, was probably present in the source region of the Chenier flows.

Morphology and distribution of Tsiolkovsky impact melt deposits: Abundant melt deposits can be recognized in and around Tsiolkovsky and exhibit a number of distinctive morphologies including flow lobes and channels, hard rock veneer, and complexly fractured ponds. Although much of the crater floor is covered by mare basalt, unflooded portions of the floor exhibit both ponded material and hummocky areas which are draped with a thin hard rock veneer. Numerous melt ponds can be seen on the crater walls and are particularly abundant on the eastern walls.

While veneer, flows, and ponds occur on the crater rim, ponds are the dominant morphology and contain the bulk of the recognizable melt volume. Flows of impact melt are not common around Tsiolkovsky but are well-developed on the north wall of Waterman crater[1,4]. Numerous inter-pond areas on the southeastern portion of the crater rim exhibit a subdued appearance associated with melt-draped regions and this veneer material exhibits gradational contacts with pond material. Veneers are particlarly well developed in the region of Waterman crater. Exterior ponds are located around over 180° of the crater perimeter but are most extensive in the southeastern quadrant of the rim. Here, the melt ponds occur at a maximum distance of 30 to 55 km from the rim crest.

Relationship of Chenier flows to other Tsiolkovsky melt deposits: As discussed above, the hummocky, flat unit in the vicinity of the source of the Chenier flows is probably composed of clast-bearing impact melt. This unit is well within the zone of melt deposits seen on other portions of the Tsiolkovsky rim[4,5,6]. In addition, the unit is not in the approach direction for the oblique impact and occurs adjacent to a Tsiolkovsky rim crest low, both factors which have been shown to be important in controlling melt distribution[5,6]. Clearly defined melt ponds have been identified in the vicinity of the hummocky unit and flow source. Impact melt ponds and flow features have been identified between the hummocky region and the Tsiolkovsky rim crest, on that part of the Tsiolkovsky wall adjacent to the hummocky unit, and on the south rim of Chenier crater. Impact melt deposits are quite abundant further to the south.

Conclusions and Implications: An analysis of the Chenier flow units has shown that they are not likely to be clastic debris flows or volcanic deposits. Based on flow unit morphology and morphometry, stratigraphy, and relationship to Tsiolkovsky melt deposits, as well as comparison with other lunar impact melt deposits and landslide deposits, it is concluded that the Chenier flow units are composed of clast-bearing impact melt and were emplaced as melt-fluidized flows after the termination of the Tsiolkovsky impact event.

The criteria developed in this study can be used elsewhere on the Moon to distinguish flows of impact melt from clastic debris deposits. If it can be demonstrated that a given flow was initiated and emplaced after termination of crater ejecta radial flow and if the deposit exhibits a low effective coefficient of friction, an impact melt origin is indicated.

References: 1) El-Baz, F. and Worden, A.M. (1972) Apollo 15 PSR, 25.1-25.27. 2) West, M.N. (1972) Apollo 15 PSR, 25.81-15.83. 3) Villella, C.J. (1977) The Moon, 17, 343. 4) Whitford-Stark, J. and Hawke, B. (1979) NASA TM-80339, 163. 5) Howard, K. and Wilshire, H. (1975) J. Res. US Geol. Survey, 3, 237. 6) Hawke, B. and Head, J. (1977) Impact and Explosion Cratering, 815. 7) Howard, K. (1973) Science, 180, 1052. 8) Lucchitta, B.K. (1977) Icarus, 30, 80.

GEOMORPHIC CLASSIFICATION OF ICELANDIC VOLCANOES

Richard S. Williams, Jr., U.S. Geological Survey, Reston, Virginia 22092; Sigurdur Thorarinsson, University of Iceland, 101 Reykjavík, Iceland; and Elliot C. Morris, U.S. Geological Survey, Flagstaff, Arizona 86001

In 1959 and 1960, Thorarinsson published his first classification of the 13 principal types of Icelandic volcanoes and, in 1968, published a revision of his earlier one. Both landform classifications were based on the relationship of the type of eruptive products (lava, lava and tephra, or tephra), number of eruptions (one or more than one), and the form of the eruptive vent (circular or linear).

In 1980, Thorarinsson, working with Kristján Saemundsson, made a modification to his previous classification schemes. The number of volcanic landforms was reduced to 11 and limited to subaerial basalt volcanoes. The number of eruptions necessary to produce a given landform was eliminated. The stratovolcano (Snaefellsjökull) and the stratified ridge (Hekla) landforms were also eliminated, because they are central (composite) volcanoes.

On the basis of this previous work, many years of direct field observation and study (ground and air), and review of the relevant literature on geomorphology of Icelandic volcanoes, a new geomorphic classification of Icelandic volcanoes has been developed (figures 1-4). The new geomorphic classification, which includes all types of Icelandic volcanoes, distinguishes 29 discrete landforms (Williams and others, 1982). It relates the nature of volcanic activity (effusive, mixed, or explosive); environment during formation (subaerial, subglacial, or submarine); and form of feeder conduit (short fissure/tubular conduit or long fissure) for the three primary compositional classes of Icelandic volcanoes: basalt (figure 1) (effusive: lava ring, lava shield, lava shield row, table mountain, subglacial ridge, seamount, submarine ridge; mixed: spatter cone, spatter cone row, scoria cone, scoria cone row, mixed cone row; explosive: tephra ring, tephra ring row, maar, maar row); rhyolite (figure 2) (effusive: flow dome); and central (figure 3) (mixed composition of basic, intermediate, and acidic lavas and tephra: composite cone, composite ridge, composite volcano massif). A pseudovolcano landform (explosive: pseudocraters, figure 4) is also included in the classification. The new geomorphic classification will form the basis for a National Aeronautics and Space Administration book, "Illustrated Geomorphic Classification of Icelandic Volcanoes" (Williams and others, 1981).

References

Thorarinsson, Sigurdur, 1959, The postglacial volcanism; III. in On the geology and geomorphology of Iceland (Sigurdur Thorarinsson, ed.): Geografiska Annaler, v. 41, no. 2-3, p. 143-150.

Thorarinsson, Sigurdur, 1960, The postglacial volcanism; Chapter 4 in On the geology and geophysics of Iceland: Guide to Excursion No. A2, International Geological Congress, 21st, Norden, 1960, Reykjavík, p. 33-45.

Thorarinsson, Sigurdur, 1968, Iceland; Chapter 10 in A geography of Norden (Axel Sømme, ed.): J.W. Cappelens Forlag, Oslo, p. 204-234.

Thorarinsson, Sigurdur, and Saemundsson, Kristján, 1980, Volcanic activity in historical time; Chapter 3 in Geology of Iceland: Jökull, v. 29 (Special Issue), p. 29-32.

Williams, R.S., Jr., Morris, E.C., and Thorarinsson, Sigurdur, 1981, Illustrated geomorphic classification of Icelandic volcanoes: in Reports of planetary geology program, 1981 (H.E. Holt, compiler): NASA Technical Memorandum No. 84211 (December 1981), p. 183-185.

Williams, R.S., Jr., Thorarinsson, Sigurdur, and Morris, E.C., ____, Geomorphic classification of Icelandic volcanoes: Jökull, v. 32 (in press).

NATURE OF VOLCANIC ACTIVITY	ENVIRONMENT DURING FORMATION	FORM OF FEEDER CONDUIT	
		SHORT FISSURE OR TUBULAR CONDUIT	LONG FISSURE
EFFUSIVE ACTIVITY Landforms resulting from flowing material	Subaerial	LAVA RING Type: Eldborg (Hnappadalssýsla)	--
		LAVA SHIELD Type: Skjaldbreidur	LAVA SHIELD ROW Type: Thjófahraun
	Subglacial/ Subaerial	TABLE MOUNTAIN (STAPI) Type: Herdubreid	SUBGLACIAL RIDGE Type: Kálfstindar
	Submarine/ Subaerial	TABLE MOUNTAIN (STAPI) Type: Surtsey	--
	Submarine	SEAMOUNT Type: Jólnir	SUBMARINE RIDGE Type: Eldeyjarbodi
MIXED ACTIVITY Landforms resulting from flowing and/or airborne material	Subaerial	SPATTER CONE Type: Búrfell (Hafnarfjördur)	SPATTER CONE ROW Type: Threngslaborgir
		SCORIA CONE Type: Búdaklettur	SCORIA CONE ROW Type: Vikraborgir
		--	MIXED CONE ROW Type: Lakagígar
	Subglacial	* Type: Keilir	* Type: Fögrufjöll
EXPLOSIVE (OR PHREATO-MAGMATIC) ACTIVITY Landforms resulting from airborne material	Subaerial	TEPHRA RING Type: Hverfjall	TEPHRA RING ROW Type: Vatnaöldur
		MAAR Type: Graenavatn	MAAR ROW Type: Valagjá
	Subglacial	* Type: Súlufell	* Type: Katlatjarnir

*No landform name available in English.

Figure 1 - Icelandic types of basalt volcanoes (modified from Thorarinsson, 1959, 1960, and 1968; and from Thorarinsson and Saemundsson, 1980).

NATURE OF VOLCANIC ACTIVITY	ENVIRONMENT DURING FORMATION	FORM OF FEEDER CONDUIT	
		SHORT FISSURE OR TUBULAR CONDUIT	LONG FISSURE
EFFUSIVE ACTIVITY	Subaerial	FLOW DOME Type: Laugahraun	FLOW DOME Type: Hrafntinnuhraun
	Subglacial	* Type: Sydri-Háganga	* Type: Hlíðarfjall

*No landform name available in English.

Figure 2 - Icelandic types of rhyolite volcanoes.

NATURE OF VOLCANIC ACTIVITY	ENVIRONMENT DURING FORMATION	MULTIPLE FEEDER CONDUITS AND FISSURES
MIXED ACTIVITY Landforms resulting from flowing and airborne material	Subaerial/ Subglacial	COMPOSITE CONE Stratified cone (stratovolcano) with summit crater Type: Snaefellsjökull
		COMPOSITE RIDGE Elongated stratified cone with crestal fissure and/or crater(s) Type: Hekla
		COMPOSITE VOLCANO MASSIF Contains a single (or multiple) caldera(s) Type: Dyngjufjöll

Figure 3 - Icelandic types of central volcanoes (composition includes basic, intermediate, and acidic rock types).

NATURE OF VOLCANIC ACTIVITY	ENVIRONMENT DURING FORMATION	FORM OF FEEDER CONDUIT
		TUBULAR CONDUIT (Within a Lava Flow)
EXPLOSIVE ACTIVITY	Subaerial*	PSEUDOCRATERS Type: Skútustadagígar

*The prerequisite for the formation of pseudocraters is that the lava flows over terrain rich in ground water, such as marshes (Raudholar near Reykjavík), water-logged Sandur plains (Landbrotsgígar), or over areas where clefts or cavities are more or less filled with water (Skútustadagígar).

Figure 4 - Volcano-like landforms in Iceland.

IMPLICATIONS OF LARGE-SCALE, EXPLOSIVE MELT-WATER INTERACTIONS: PARTICLE CHARACTERISTICS AND DISPERSAL PATTERNS

Michael F. Sheridan[1] and Kenneth H. Wohletz[2]
1) Department of Geology, Arizona State University, Tempe, AZ 85287. 2) Earth and Space Science Division, Los Alamos National Laboratory, Los Alamos, NM 87545.

Fuel-coolant interaction (FCI) results from the mechanical mixing of hot (fuel) and cool (coolant) fluids, the temperature of the fuel being above the vaporizaton temperature of the coolant. Explosive melt-water interaction is a type of fuel-coolant interaction (FCI) that is common in a large fraction of explosive terrestrial volcanic eruptions. Although steam-blast explosions have been recognized for a long time (1), their importance had been underestimated. FCI is the mechanism for surge explosions where magma extrudes beneath a shallow body of water (2,3). However, subsurface water can also promote FCI in chambers as deep as 3 to 5 km (4). A large fraction of terrestrial volcanic events have features that are at least in part controlled by FCI mechanisms.

FCI could occur on the surface of other planets and may be a major process on some. The requirements are that a substance with a low vaporization temperature (coolant) be brought into contact with a high temperature fluid (fuel). Volcanism provides one vehicle for this mechanism, as demonstrated by abundant terrestrial examples. However, other mechanisms, such as those associated with giant impacts, should not be dismissed without a consideration of the processes and time-scales of FCI in relation to current models of cratering events.

What are the sources of information on FCI? Melt-water experiments have been undertaken at Sandia National Laboratories in relation to nuclear plant safety (5,6,7). Larger-scale experiments were done at Los Alamos National Laboratory to model volcanic phenomena (8,9,10). At an even greater scale, a body of data has accumulated in the past 15 years on volcanic base-surge phenomena and deposits. Several new hydromagmatic eruptions occur each year, for example the May 1980 eruption of Mount St. Helens (11), providing abundant new information on this phenomena. Unfortunately, the systematic incorporation of such data into a model of hydrovolcanism is still in its initial stages (12).

What can be said about FCI involving water and a magma-like coolant? Efficiency of conversion of thermal to mechanical energy (9) is dependant on scale, geometry, and composition (melt to water ratio). The maximum experimental efficiency exceeds 30% but natural explosions may approach 50%. Under optimum experimental conditions the melt is fragmented into very small particles (10 to 50 um) that have

a distinctive appearance (7,10). Particles produced by hydrovolcanic explosions have shapes and sizes that are similar to the experimental products (13). If the water content exceeds an optimum value, the exploded system could be "wet" including steam, water, and solid particles (12). The glassy clasts produced would rapidly hydrate and their resulting deposits would lithify due to secondary mineral growth.

Dispersal of FCI products, whether of volcanic or otherorigin, should have a distinctive patterns. Computer-assisted maps of surge deposits can be satisfactorily modeled by an energy-cone algorithm (14,15). Terrestrial volcanic constructs (16) may be sheet-like (tuff rings) to cone-forming (tuff cones). The range of surface textures on FCI products of other planets could be expected to mimic terrestrial pyroclastic flows, pyroclastic surges, and lahars.

REFERENCES

(1) Jagger, T.A. (1949) Hawaii Volcano Obs., 4th Spec. Rept., 137 p.
(2) Colgate, S.A. and Sigurgeirsson (1973) Nature, 244, 552-555.
(3) Peckover, R.S., Buchanan, D.J., and Ashby, D.E. (1973) Nature, 245, 307-308.
(4) Sheridan, M.F., Barberi, F., Rosi, M., and Santacroce, R. (1981) Nature, 289, 282-285.
(5) Buxton, L.D. and Benedict, W.B. (1979) Sandia Laboratories, SAND 79-1399, 62 p.
(6) Nelson, L.S. and Duda, P.M. (1981) Trans. Amer. Nucl. Soc., 38, 453-454.
(7) Corradini, M.L. (1980) Sandia Laboratories, SAND 80-2131, 114 p.
(8) Wohletz, K.H. and Sheridan, M.F. (1982) NASA Tech. Memo. 82325, 134-135.
(9) Wohletz, K.H. and McQueen, R.G. (in prep) Experimental Hydromagmatic Volcanism, submitted to Natl. Res. Council.
(10) Wohletz, K.H. (1983) J. Volcanol. Geotherm. Res., 16, in press.
(11) Lipman, P.W. and Mullineaux, R.R. (1981) U.S. Geol. Survey Prof. Paper 1250, 844 p.
(12) Sheridan, M.F. and Wohletz, K.H. (1981) Science, 212, 1387-1389.
(13) Wohletz, K.H. and Krinsly, D.H. (1982) Scanning Electron Microscopy in Geology, Geoabstrasts, Norwich, England.
(14) Malin, M.C. and Sheridan, M.F. (1982) Science, 217, 637-639.
(15) Sheridan, M.F. and Malin, M.C. (1983) J. Volcanol. Geootherm. Res., 16, in press.
(16) Wohletz, K.H. and Sheridan, M.F. (1982) Am. Jour. Sci. in press.

EXPERIMENTAL MELT-WATER INTERACTIONS

Wohletz, Kenneth H., Earth and space Science Division, Los Alamos National Laboratory, Los Alamos, NM 87545

Experiments in which molten thermite explosively vaporized water have been performed to obtain information on the effects of impact cratering in a wet target. Results of initial experiments (1) in which large masses of melt (100 kg) explosively mixed with water were compared with those of other studies of melt-water interactions (2,3). This analysis showed that the conversion efficiency of thermal to mechanical energy is strongly dependent on the water-to-melt mass ratio for constant confinement pressures and contact geometries. The fine-grained nature (1-100 μm) of ejecta and their ballistic and surge emplacement in vapor-rich flows have been assessed for importance in formation of Martian rampart crater ejecta (4). Present work has been aimed at obtaining more quantitative data relating efficiency to water-to-melt mass ratio. This work also includes shape and size analysis of ejected debris.

1. Series II Experiments

Series II experiments employ a new design (5) in which less than 10 kg loads of melt are used. Explosive energy is scaled by the vertical lift of the confinement vessel produced by a downward directed vent. Records include those of high-speed cinematography and internal-pressure transducers (set 80-81). These records were used to evaluate the trajectory of the vessel and the efficiency of thermal-energy conversion. Set 82 experiments also include oscilloscope records of the vessel's vertical displacement measured by voltage-distance recorders. Figure 1 shows results of the vessel's total lift versus water-to-melt mass ratio. Lift is directly proportional to efficiency and the range of ratios studied complements those reported earlier (1). A marked increase in efficiency is apparent for those experiments using a high initial confinement pressure. The experimental design is currently being modified to use a rigid, large-gauge spring system to measure impulse pressure.

2. Experimental Ejecta Characteristics

Ejected debris recovered from the experiments has been subjected to scanning electron microscopy (SEM) and energy-dispersive spectral analysis (EDS). Size analysis of the debris is only semiquantitative because representative samples of the entire size population have not been successfully recovered.

Smaller-scale experiments conducted at Sandia Laboratories (3) have yielded representative size analyses for less efficient explosions. These data are plotted against calculated efficiencies in Figure 2 and show a range in median diameters from 4000 μm (-2ϕ) to 250 μm (2ϕ). Characteristic sizes observed by SEM in our samples are in the range of 10 to 50 μm for higher efficiency explosive fragmentations.

Representative EDS analyses of ejected debris are shown in Table 1. Quartz sand added to the thermite produces silicate melts and variable chemical compositions that are dependent upon the ejected particle

shape. SEM analysis shows that ejected particles have dominantly moss-like, convoluted shapes and spherical or drop-like shapes (Fig. 3). Subordinant particle shapes are blocky and equant as well as plate-like. These shapes show strong similarities to the shapes of volcanic ash particles produced by explosive magma-water interactions.

The size and shape characteristics of experimental ejecta give additional information that can be used in assessment of the fragmentation mechanism of melt-water interactions. The efficiency of this process is due in part to the fine fragmentation resulting from superheat vaporization, fluid instabilities, and shock-wave propagation (6,7,8,9).

REFERENCES

(1) Wohletz, K. H., and Sheridan, M. F. (1981) NASA Tech. Memo. 82385, 134-135.
(2) Corradini, M. L. (1980) Sandia Laboratories, SAND 80-2131, 114 p.
(3) Buxton, L. D., and Benedict, W. B. (1979) Sandia Laboratories, SAND 79-1399, 62 p.
(4) Wohletz, K. H., and Sheridan, M. F. (in prep.) Martian rampart crater ejecta: experiments and analysis of melt-water interactions, submitted to Icarus.
(5) Wohletz, K. H., and Sheridan, M. F. (1982) NASA Tecn. Memo. 84211, 169-171.
(6) Board, S. J., Hall, R. W., and Hall, R. S. (1975) Nature, 254, 319-321.
(7) Buchanan, D. J. (1974) J. Phys. D: Appl. Phys., 7, 1441-1457.
(8) Drumheller, D. S. (1979) Nucl. Sci. Eng.72, 347-356.
(9) Galloway, W.J. (1954) J. Acoust. Soc. Amer., 26, 849-857.
(10) NASA (1982) EOS 63, 11, p. 193.

TABLE I

Representative chemical analyses* of thermite melt debris

Oxide	1*	2	3	4	5
SiO_2	10.07	10.73	14.34	36.55	18.25
TiO_2	-	-	2.25	1.44	1.90
Al_2O_3	31.24	25.09	11.36	34.41	42.46
FeO	57.94	64.18	57.01	17.32	23.28
MgO	-	-	6.44	3.70	5.84
MnO	-	-	1.58	0.96	1.33
CaO	0.45	-	2.05	1.65	1.90
Na_2O	-	-	3.07	1.98	3.19
K_2O	0.31	-	1.91	1.99	1.85

* Standardless energy dispersive spectral analyses (EDS)

* 1 - Iron-aluminum sphere, large

2 - Iron-aluminum sphere, small

3 - Blocky iron particle

4 - Coating on iron particle

5 - Iron-aluminum spindle

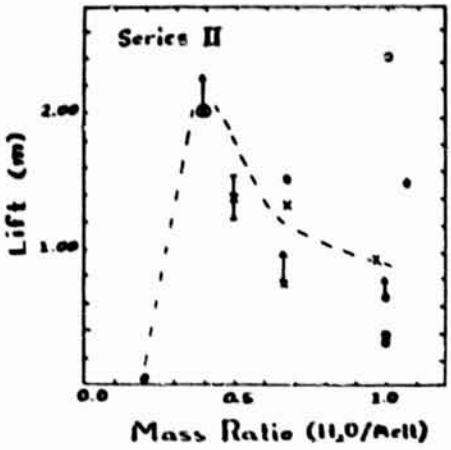

Figure 1. Vertical lift of the experimental device versus water-to-melt ratio. The symbols are:
x - set 80-81 ■ - Hi $P_{conf.}$
o - set 82 ● - Hi $P_{conf.}$

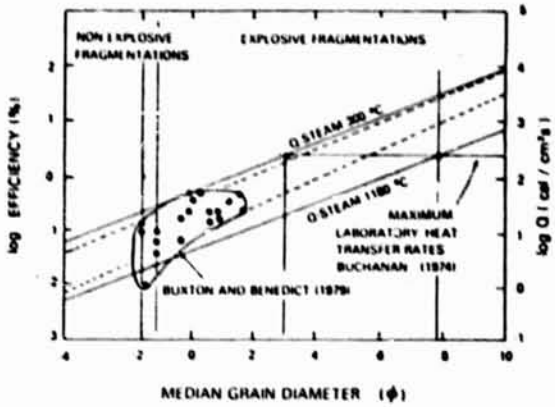

Figure 2. Conversion efficiency of thermal to mechanical energy versus median diameter ($\phi = -\log_2 mm$) of fragments produced (3). Heat transfer rates, Q, are calculated from conductivity equations and compared to maximum measured values (7).

Figure 3. Scanning electron micrograph of a characteristic spherical particle from an experimental melt-water explosion. Note the complex surface texture. Many particles are similar in size and shape to a particle of cosmic dust shown in reference (10).

Chapter 6

AEOLIAN PROCESSES AND LANDFORMS

SIMULATING AEOLIAN PROCESSES ON VENUS WITH A HIGH-PRESSURE N_2 ATMOSPHERE

John Marshall, Rodman Leach, Cheryl Treat, Dept. of Physics, Univ. of Santa Clara, at NASA Ames Research Center, Moffett Field, CA 94035
Ronald Greeley, Department of Geology, Arizona State University, Tempe, AZ 85287

The venusian atmosphere has a surface pressure of ~90 bars and a temperature of 730 K. Although windspeeds near the surface of Venus are probably extremely low -- a few meters per second, aeolian entrainment of particles has been predicted to occur under these conditions. This aeolian action is being investigated with the Venus Wind Tunnel at NASA Ames Research Center, California. Simulation of the Venus atmosphere is done on the basis of comparable densities. Operation of the tunnel with CO_2 at 30 bars and room temperature generates a gas density equivalent to that on Venus.

To date, the tunnel has been operated with CO_2 as the particle-entraining fluid because this is the major constituent of the Venus atmosphere. The CO_2 is stored as a liquid at low temperatures and is released into the tunnel as a gas at room temperature after being heated in an intermediate reservoir stage. This process requires several hours and demands the nearly constant attention of the operator. The concern of this report is the use of nitrogen as a substitute for carbon dioxide. N_2 is supplied as a gas at high pressures, but at room temperature, and simply requires tranfer from a reservoir to the tunnel without an intermediate stage. As a result, operating times are reduced to a few minutes, and is less costly than CO_2. Aside from this practical aspect, it is clearly important to know whether planetary atmospheres, at least in terms of their aeolian action, can be modelled with a gas other than that occurring on the planet in question.

In order for N_2 to act as a substitute for CO_2, it must have the same behavioral characteristics when its density is the same, since fluid density is being used as the comparator for Venus. Its behavior was judged on the basis of two criteria: threshold freestream velocity ($U_{\infty t}$) and threshold friction speed (U_{*t}); N_2 has a lower molecular weight than CO_2 and thus requires considerably higher operating pressures to achieve the same density.

Entrainment thresholds were determined with N_2 for a large range of gas pressures (densities) and a large range of particle sizes and compared to those obtained previously with CO_2. At all densities, both freestream velocities and friction speeds (Fig. 1) were found to be essentially the same for both gases. Although there was some divergence in the viscosities of the two gases at low pressures, this did not appear to have any noticeable effect on threshold. The slightly lower U_{*t} values for CO_2 can be accounted for by the use of a different definition of threshold. Reynolds Numbers for the different pressures (densities) and different particle sizes were also found to be virtually the same for the two gases.

Friction speed is a representation of the velocity profile and as such, can be considered to determine the behavior of the particles once they are airborne. Alone, it is insufficient as a criterion because it can simply define a dimensionless similarity between the velocity profiles of two gases. If absolute velocities for any given height within the profiles were different, this would be reflected in the ballistic behavior of the particles, e.g., saltation heights would differ for the two gases. But, because $U_{\infty t}$ remained constant for both gases, the boundary layer attained the same thickness and the windspeed at any height within the boundary layer was the same. It is concluded, therefore, that nitrogen may be used as a substitute for carbon dioxide to simulate aeolian action on Venus when the density of both gases is the same.

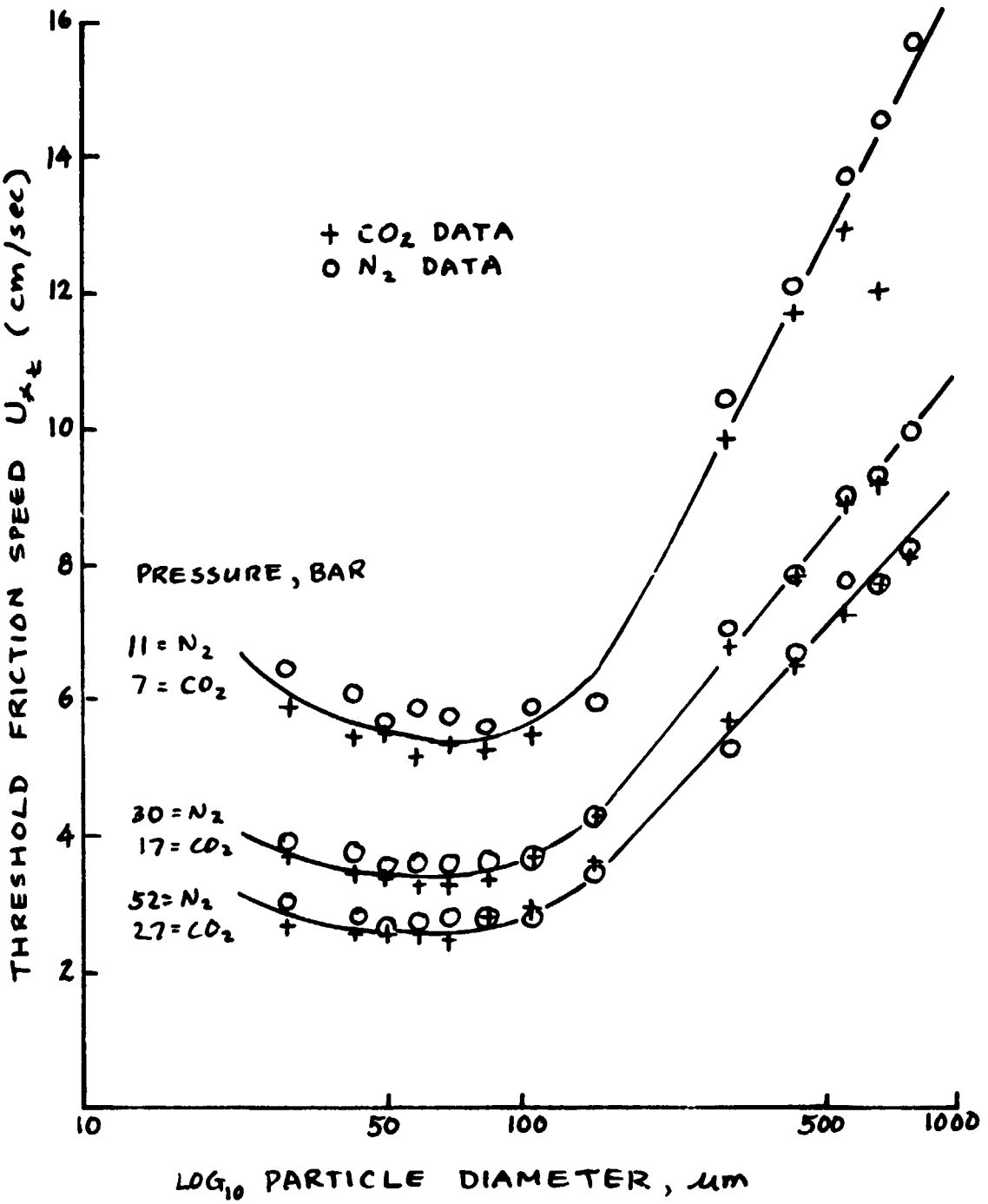

Figure 1. Wind threshold curves for three different atmospheric densities, comparing CO_2 with N_2. The value of u_{*t} for CO_2 being systematically lower than that for N_2 could be due to threshold being determined by different observers.

WINDBLOWN SAND ON VENUS: PRELIMINARY LABORATORY SIMULATIONS

R. Greeley and S. Williams, Department of Geology, Arizona State University, Tempe, Arizona 85287

Aeolian transport of fine-grained material on Venus by the wind is suggested by Venera images of the venusian surface and by Venera and Pioneer Venus measurements of near-surface wind speeds. Aeolian transport of weathering products from the highlands to the lowlands may play an important role in the chemical buffering of the lower part of the venusian atmosphere (Nozette and Lewis, 1982). Theoretically, winds of the strength measured at Venus are well within the range to move particles (Greeley et al., 1976; Iversen et al., 1976; Iversen and White, 1982). In order to investigate the physics of windblown particles on Venus, a wind tunnel capable of operating at venusian atmospheric density was constructed. The tunnel operates with CO_2 at room temperature and 35 bar pressure, which yields the same gas density as the 735 K, 90 bar venusian atmosphere. A series of preliminary tests were conducted to determine the minimum wind friction speed, u_{*t}, required for particle saltation for a range of particle diameters from 23 to 833 μm. The resulting wind threshold curve corresponds fairly well with the theoretical curve (Figure 1). The equation for the theoretical curve is:

$$u_{*t} = A(\rho_p g D_p/\rho_a)^{0.5}$$

$$A = 0.129[[1+0.006/\rho_p g D_p^{2.5}]^{0.5}]/[1.928B^{0.092}-1]^{0.5} \text{ for } D_p<100\mu m$$

$$A = 0.12[[1+0.006/\rho_p g D_p^{2.5}]^{0.5}][1-0.0858e^{[-0.0617(B-10)]}] \text{ for } D_p>100\mu m$$

$$B = u_{*t} \cdot D_p/\nu$$

where ρ_p = particle density
ρ_a = atmospheric density
g = acceleration due to gravity
D_p = particle diameter
ν = kinematic viscosity

Particles with a diameter of ~70 μm are most easily moved by the wind on Venus, with both smaller and larger particles requiring stronger winds for saltation to occur. This is smaller than the ~100 μm particle size most readily moved on the Earth and Mars. The wind friction speed required to move material on Venus is about an order of magnitude less than that required on Earth, and about two orders of magnitude less than that required on Mars. The differences are due to the different densities of gas involved. However, in these preliminary experiments a possible source of error in the determination of threshold friction speeds is as follows: The centerline wind speed, u_∞, is the quantity measured in the wind tunnel tests. This is related to u_* by the coefficient of friction, c_f, that characterizes the surface involved, where: $u_*/u_\infty \equiv [c_f/2]^{0.5}$. The quantity, c_f, is found from basic fluid mechanics. An error in c_f would give an error in u_*, and it is particularly sensitive for small particles. Work is underway to measure the u_*/u_∞ ratio from boundary layer profiles.

The greater density of the venusian atmosphere allows a mode of aeolian particle transport not encountered on Earth or Mars; observations of coarse (~500 μm) particles in the wind tunnel show that they began to roll at wind shear speeds just slightly below those required for saltation. Because the surface winds observed are in the range of threshold wind speed, the rolling mode of transport may move significant quantities of material (see Greeley and Williams, 1982; Williams and Greeley, this volume).

REFERENCES

Greeley, R., B.R. White, J.B. Pollack, J.D. Iversen, and R.N. Leach, 1977, Dust Storms on Mars: Considerations and Simulations, NASA TMX-78423, 30 p.

Greeley, R. and S.H. Williams, 1982, Rolling 'stones' on Venus: A mode of wind transport, submitted to GSA Annual Program with Abstracts.

Iversen, J.D., R. Greeley, and J.B. Pollack, 1976, Windblown dust on Earth, Mars, and Venus, J. Atmos. Sci., v. 33, n. 12, p. 2427-2429.

Iversen, J.D., and B.R. White, 1982, Saltation threshold on Earth, Mars, and Venus, Sedimentology, v. 29, p. 111-119.

Nozette, S. and J.S. Lewis, 1982, Venus: Chemical weathering of igneous rocks and buffering of atmospheric composition, Science, v. 216, p. 181-183.

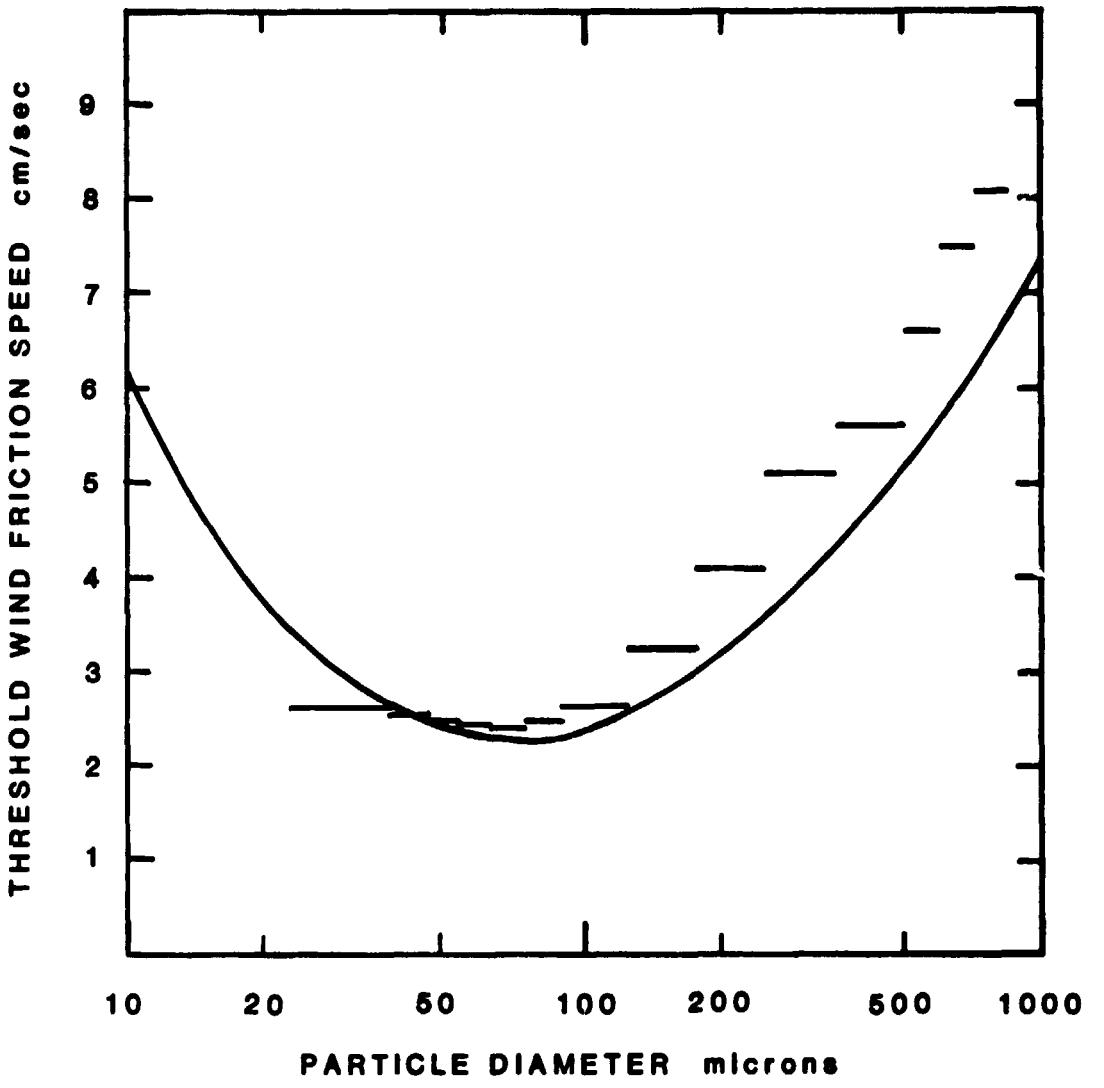

Threshold wind friction speed as a function of particle diameter. The line is the theoretical equations given in text. The horizontal lines are wind tunnel measurements. Quartz sand was used in the tests.

FLUX OF WINDBLOWN PARTICLES ON VENUS: PRELIMINARY LABORATORY RESULTS

Steven H. Williams and Ronald Greeley (Dept. of Geology, Arizona State Univ., Tempe AZ 85287)

Aeolian activity may be important in the distribution of surficial materials on Venus. An aeolian saltation flux equation has been developed from theoretical considerations and wind tunnel tests under terrestrial and martian conditions by White (1979) as follows: $Q = 2.61\ \rho_a/g(u_*-u_{*t})(u_*+u_{*t})^2$; where Q = saltation flux, ρ_a = atmospheric density, g = gravitational acceleration, u_* = wind friction speed and u_{*t} = threshold wind friction speed. In order to test the validity of this flux equation for the environment of Venus, a wind tunnel capable of operating at venusian atmospheric density has been constructed. Very good agreement is found between the wind tunnel data and the flux equation for particle diameters of 75-90 μm, the size most easily moved on Venus (Figure 1). However, flux of particles with diameters in the range of 500-600 μm is not in agreement as closely (Figure 2). The discrepancy may be due to: 1) an inaccurate value of the surface coefficient of friction, c_f, which is used to correlate measured wind tunnel freestream wind speed, u_∞, and the wind friction speed used in the flux equation, with $u_*/u_\infty \equiv (c_f/2)^{1/2}$, 2) improper accounting for the effect of particle diameter in the flux equation, or 3) unknown factors dealing with fluids of densities not previously studied. Current investigations are in progress to derive experimentally determined c_f as a function of particle diameter and to derive a more general flux equation to include particle diameter and particle density.

The theoretical and wind tunnel saltation flux determinations have implications for the geologic evolution of the venusian surface. Even modest winds occurring relatively infrequently can move large quantities of sand-sized particles long distances (Table 1). If winds measured at the surface of Venus by Venera correspond to wind tunnel free-stream wind speeds (a reasonable assumption) then even a conservative estimate of the frequency with which that wind occurs result in large quantities of sand movement. For example, for a wind speed of 1 m/s occurring 5% of the time, 28 kg of sand will pass over a 1 cm width in one terrestrial year. If the average sand speed is 0.5 m/s, a conservative estimate, a typical particle would be capable of moving ~800 km in a terrestrial year. Obviously, such travel over long distances over short times requires unrealistically ideal conditions, such as a smooth surface with no sand traps, however, it is clear that, over geologic time, very large quantities of sand-sized material can be transported great distances. Thus, widespread redistribution of chemically-weathered material could take place, which may explain why only fine and coarse particles are observed at the Venera sites; the intermediate-size (100-500 μm) particles might have been removed by wind deflation. The low, rolling plains units observed by Pioneer Venus may be depositional "sinks" for this aeolian material. The rate of aeolian transport of fines by the venusian wind is apparently sufficient to allow the buffering proposed by Nozette and Lewis (1982) of CO_2, H_2O, SO_2 and HF in the lower atmosphere by reaction with chemically weathered materials from the upland areas.

REFERENCES

Nozette, S. and J.S. Lewis, 1982, Venus: Chemical weathering of igneous rocks and buffering of atmospheric composition, Science, v. 216, p. 181-183.

White, B.R., 1979, Soil transport by winds on Mars, J. Geophys. Res., v. 84, n. B8, p. 4643-4651.

TABLE 1

Saltation Flux, Q, in kg/cm·yr
Smooth surface D_p ~100 μm

Wind Frequency, f, %	Freestream wind speed, u_∞, m/s			
	0.75	1.0	1.25	1.5
5	7.9	28	58	100
10	16	55	120	200
15	24	83	180	300
20	32	110	230	400
25	39	140	290	500
30	47	170	350	610
35	55	190	410	710
40	63	220	470	810
45	71	250	530	910
50	79	280	580	1010

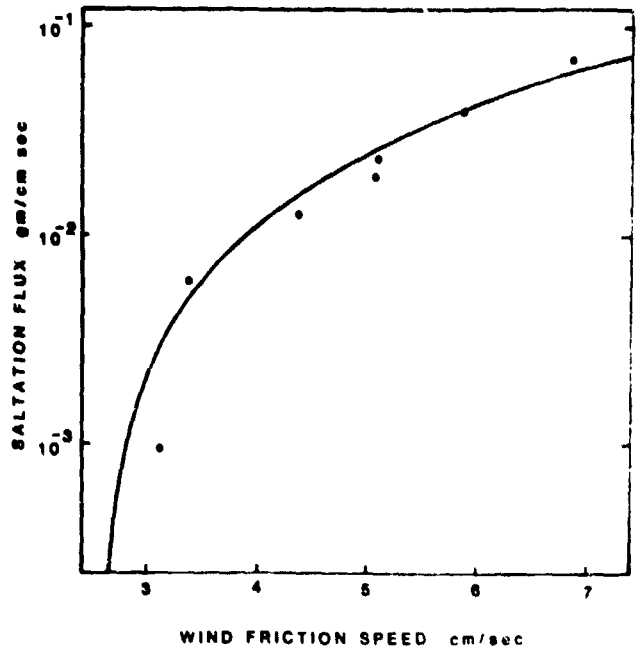

Figure 1. Saltation flux as a function of wind friction speed. The line is from the theoretical equation given in the text. Quartz particles with 75-90 μm diameters were used in the wind tunnel tests.

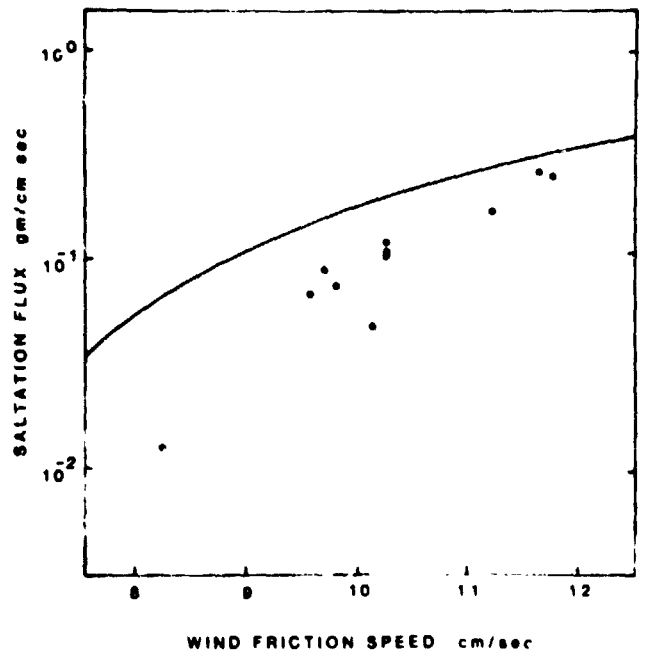

Figure 2. Saltation flux as a function of wind friction speed. The line is from the theoretical equation given in the text. Quartz particles with 500-600 μm diameters were used in the wind tunnel tests.

PARTICLE MOTION OF VENUSIAN SALTATION

B.R. White, Department of Mechanical Engineering, University of California, Davis, California 95616, R. Greeley, Department of Geology, Arizona State University, Tempe, Arizona 85281

Numerical solutions of the equations of motion for particle trajectories on the surface of Venus were calculated. The path lengths and maximum vertical heights that saltating particles achieve were found to be insensitive to variations of the surface pressure within 70 to 100 bars pressure and the surface temperature from 600 to 900°K. Particles in saltation obtained maximum height of only two or less centimeters and path lengths of less than a meter, regardless of particle diameter. These lengths are much shorter than those that occur on either Earth or Mars under similar conditions. Typically, impacting particles collide at the surface with angles varying between 2 and 5° for values of wind speeds at a height of 1 m varying from 1 to 3 m/sec. The ratio of final particle speed to the particle threshold friction speed was found to be many times larger than that of Earth, up to values of 25. For Earth this value is known to be approximately unity.

The spinning of particles in saltation at atmospheric pressure have been shown to have a profound influence on the resulting trajectories (White and Schulz, 1977). The investigation of the present particle motion was accomplished through the study and evaluation of high-speed motion pictures taken in the Venusian wind tunnel. The filmed trajectories were then compared with trajectories obtained by numerical integration of the equations of motion including the spin effect.

The saltating material was 550 micron diameter quartz particles with a density 2.5 g/cm^3. The selection of quartz was made to serve two purposes. First, The shape of quartz was similar to that of natural windblown materials (Greeley et al., 1977). Second, the non-circular geometry of individual particles made measurements of rotation rates possible.

The equations of motion were solved numerically by a computer. The solving scheme was an initial-value ordinary-differential-equation solver using a predictor-corrector computation algorithm. The initial values

(position, velocities, and spin rate) were obtained from experimental measurements taken in the wind tunnel at the beginning of each of the particles' trajectory.

A comparison was made between the filmed path traced out by a particle with two theoretical solutions. The first solution was with no spin, and the second solution used the experimentally measured spin rate. Good agreement was found between the filmed trajectory and the numerical solution with particle spin. The measured and calculated particle speeds along the trajectory were essentially the same for the solution with particle spin. The no spin comparison had poor agreement.

In many other trajectories, the particle spin was not entirely in the vertical longitudinal plane which resulted in a "negative lift" that pushed the particle downward. In some trajectories the spin started out clockwise ("positive lift") and rapidly decelerated, resulting in counterclockwise spin ("negative lift"). The same result was found by Abbott and Francis (1977) for particle motion in water. This phenomenon occurred in approximately 20 percent of all saltating particles observed.

REFERENCES

J.E. Abbott and J.R.D. Francis, 1977. Saltation and suspension trajectories of solid grains in a water stream, Phil. Trans. Roy. Soc. London, 284, 225-254.

R. Greeley, B.R. White, J.B. Pollack, J.D. Iversen, and R.N. Leach, 1981. Dust storms on Mars: Considerations and simulations, from Deser. Dust: Origin, Characteristics, and Effect on Man, ed. Troy L. Pewe, Geological Society of America Special Paper 186, pp. 101-121.

B.R. White and J.C. Schulz, 1977. Magnus effect in saltation, J. Fluid Mech. 81, Part 3, 497-512.

WIND ABRASION OF ROCKS: COMPUTER SIMULATION

Ronald Greeley (Department of Geology and Center for Meteorite Studies, Arizona State University, Tempe AZ 85287)

Three principal factors are involved in calculating rates of wind abrasion of ventifacts (Greeley et al., 1982): 1) wind frequency, 2) various particle characteristics such as speed and flux as functions of wind speed, and 3) the susceptibility to abrasion of various rocks. Data on all three factors have been obtained for terrestrial and martian conditions through experiments. In order to predict the erosion of various rocks a computer program has been written which combines all three factors and calculates the volume eroded as a function of windspeed, particle supply, rock type, etc. The program functions in an interactive mode as part of the Arizona State University Image Processing Facility. "Two-dimensional" rocks of any shape can be entered as a starting condition along with wind speed, and such factors as particle size and rock type. Evolution of the shape of the rock can then be followed as a function of time as it is abraded. Figure 1 shows an example of one run; note that maximum abrasion occurs about 10 cm above the ground, in agreement with results from experiments by Sharp (1964, 1980), and as shown in Figure 2. This height of maximum abrasion results from the optimal combination of particle flux and velocity.

At present, only a limited data base is entered in the program regarding particle velocities, fluxes, and trajectories as functions of freestream windspeed and atmospheric pressure. Work in progress involves expansion of the base for a wide range of conditions appropriate for Earth and Mars; future work will involve incorporation of vales for Venus.

REFERENCES

Greeley, R., R.N. Leach, S.H. Williams, B.R. White, J.B. Pollack, D.H. Krinsley, and J.R. Marshall (1982) Rate of Wind Abrasion on Mars: J. Geophys. Res. (in press).

Sharp, R.P. (1964) Wind-driven sand in Coachella Valley, California: Geol. Soc. Am. Bull. 74, 785-804.

Sharp, R.P. (1981) Wind-driven sand in Coachella Valley, California: further data: Geol. Soc. Am. Bull. Pt. 1, 91, 724-730.

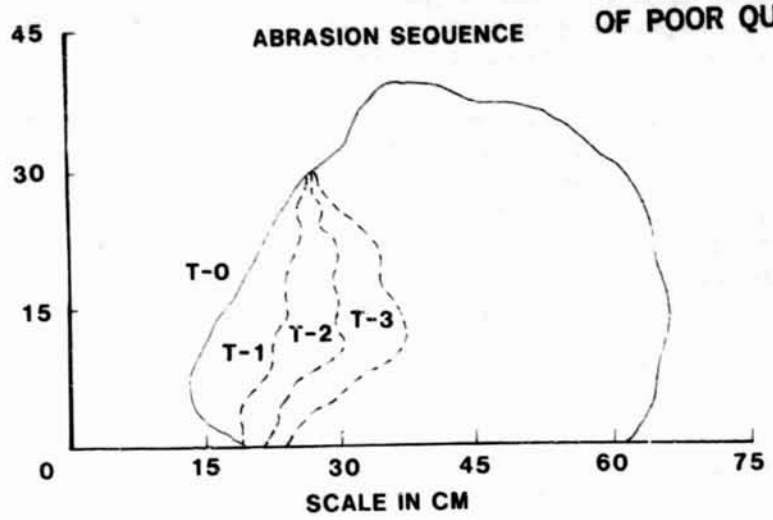

Figure 1. Computer simulation of rock abrasion; T-0 is the rock shape at beginning of run; T-1 through T-3 shows shape through time to the end of run at T-3; wind and particles are from the left to the right. Note that maximum abrasion occurs at about 12 cm above the ground.

Figure 2. Ventifact in Iceland; prevailing wind is from the left; hammer indicates scale. Maximum abrasion occurs about 10 cm above the ground, comparable to the experimental values found in the simulation shown in Figure 1.

DUST STORM ACTIVITY ON MARS DURING THE VIKING MISSION. A. R. Peterfreund, Dept. of Geology, Arizona State Univ., Tempe, AZ 85287. (now at Dept. of Geol. Sci., Brown Univ., Providence, RI 02912).

Contemporary aeolian processes on Mars are best demonstrated by the annual occurrence of local and major dust storms. The characteristics of these storms, their location of origin, and the nature of the surface in the area of origin, are important clues in understanding aeolian processes on Mars. Observations made by the Viking orbiters' instruments, particularly the camera systems (VIS) and the infrared thermal mappers (IRTM), over the four years of mission operation, allow for a detailed documentation of local and global activity.

Thirty-one local dust clouds have been identified from the IRTM daytime data using a search routine that: 1) determined the thermal opacity of the atmosphere at 9μm (1), defined as $\tau 9$, for each IRTM sequence, and 2) using the average $\tau 9$ as a standard, identified anomalies within a given sequence that were indicative of local concentrations of dust (i.e., clouds). The average $\tau 9$, although uncertain in absolute magnitude by a factor of 2 due to uncertainties in the scattering properties of the dust, are used to describe the relative dust abundance of the martian atmosphere over the period of Viking operation (Figure 1).

The two major dust storms of 1977 are apparent in Figure 1 as the large spikes in opacity. The discrepencies between the opacities derived from the two orbiters are the result of the different latitudinal coverage. The earlier increase in opacity observed by VO-2, prior to the first 1977 storm, is attributed to the aeolian activity along the receding south polar cap which increased the dust loading of the atmosphere in the southern hemisphere. VO-1 observations were concentrated in the northern hemisphere at this time and subsequently did not record an increase in the dust loading. Prior to the second storm in 1977, the dust loading was substantially more uniform between the two hemispheres. The IRTM data covering the dust storm season in 1979 were less complete than that of 1977 due to: 1) limited observations by the single operating orbiter (VO-1), and 2) the hiatus in operation (Ls-230°-350°) due to the Voyager Jupiter encounter. However, an increase in opacity can be seen starting at Ls-135°, approximately the same time as the increase was observed in 1977. At Ls-208°, the time of the initiation of the first 1977 major dust storm, the $\tau 9$ values do not exceed 0.2, suggesting that a similar storm did not occur at this earlier time. Whether or not a major storm did occur in the period when IRTM data were not collected is uncertain. Lander data obtained, however, have been interpretted to suggest that a storm did occur at Ls 205° (2).

The catalog of IRTM-observed local dust clouds provides a statistically significant data set of storms for which thermal properties can be described. The nonuniformity of the thermal characteristics of these storms is indicative of the diverse nature of the aerosols that make up the clouds. The observed range in albedo of the local dust clouds, .15 to .40, is interpretted to suggest that the characteristics of local sediments are reflected in the properties of the clouds.

By combining the IRTM record of local dust storm with the VIS data (3) and the wealth of historical Earth-based observations (4), a number of patterns of dust storm activity are evident. Dust storms occur over a broad latitudinal band centered on the sub-solar latitude, and, in time, are concentrated ±90° of perihelion (Ls-250°) (Figure 2). Correlations of dust cloud occurrence with local topography imply that neither elevation nor slope direction is a major

factor in defining where the dust clouds occur. However, slope magnitude is a significant factor. The thermophysical characteristics of the regions where dust storms occur are not unique. However, dust storms rarely originate in regions of high albedo and low thermal inertia (i.e., regions interpretted to be blanketed by substantial dust deposits). Rather, evidence suggests that dust storms generally begin in relatively sandy regions. This hypothesis is based on the observations that: 1) dunes are often present in regions of recurrent dust storm activity, and 2) the majority of dust storms originate in regions where thermophysical properties suggest the presence of sand-size particles. These observations are consistent with experimental studies of threshold velocities (5) which suggest that it is much easier to initiate particle motion in regions where sand is abundant as opposed to regions where it is not.

References: 1) Martin, T. Z. et al. (1979), J. Geophys. Res., 84, 2830-2843. 2) Ryan, J. A. and Sharman, R. D. (1981), J. Geophys. Res., 86, 3247-3254. 3) Briggs, G. A. et al. (1979), J. Geophys. Res., 84, 2795-2820. 4) Wells, R. A. (1980) Geophysics of Mars, Amsterdam, Elsevier, 678 p. 5) Greeley, R. et al. (1980), Geophys. Res. Lett., 7, 121-124.

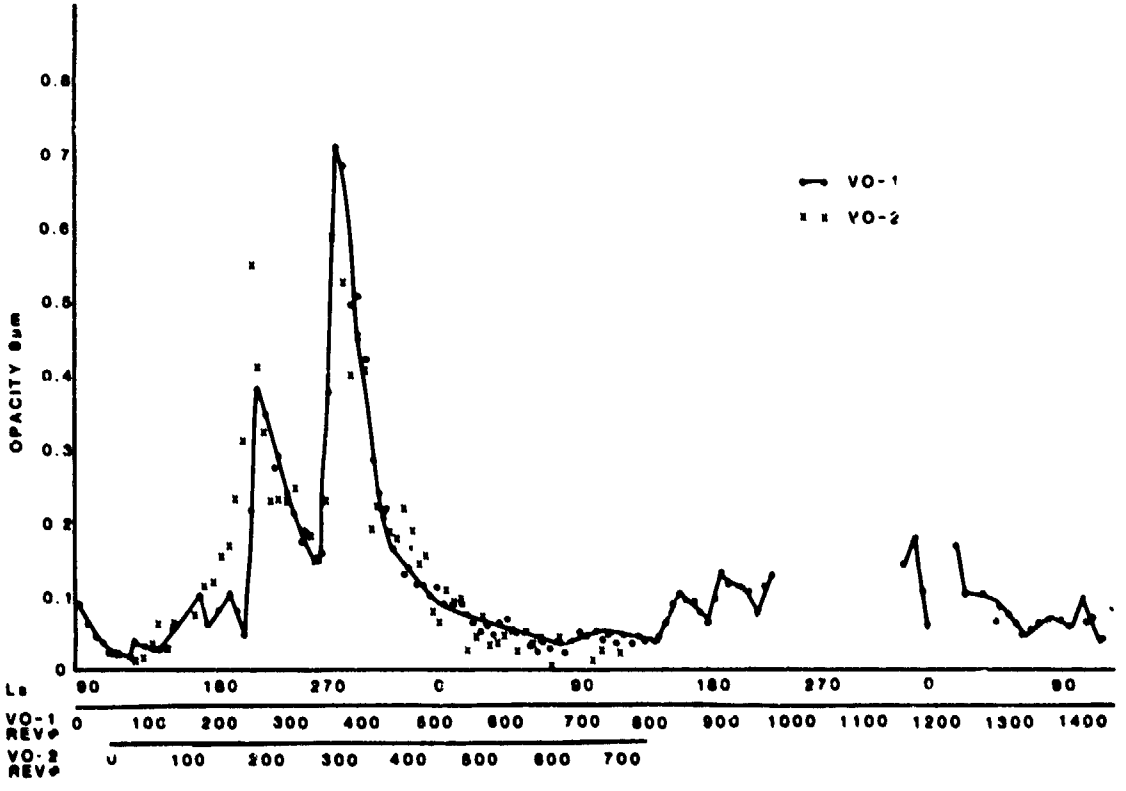

Figure 1. Atmospheric thermal opacity, τ9 derived from the IRTM data for the duration of the Viking orbiters' missions. The opacities are derived from observations obtained within time period of ten revolutions (approximately equal to ten days). Plotted separately are τ9 derived from VO-1 and VO-2 observations. Offsets between the two data sets are due to variations in the coverage by the separate orbiters.

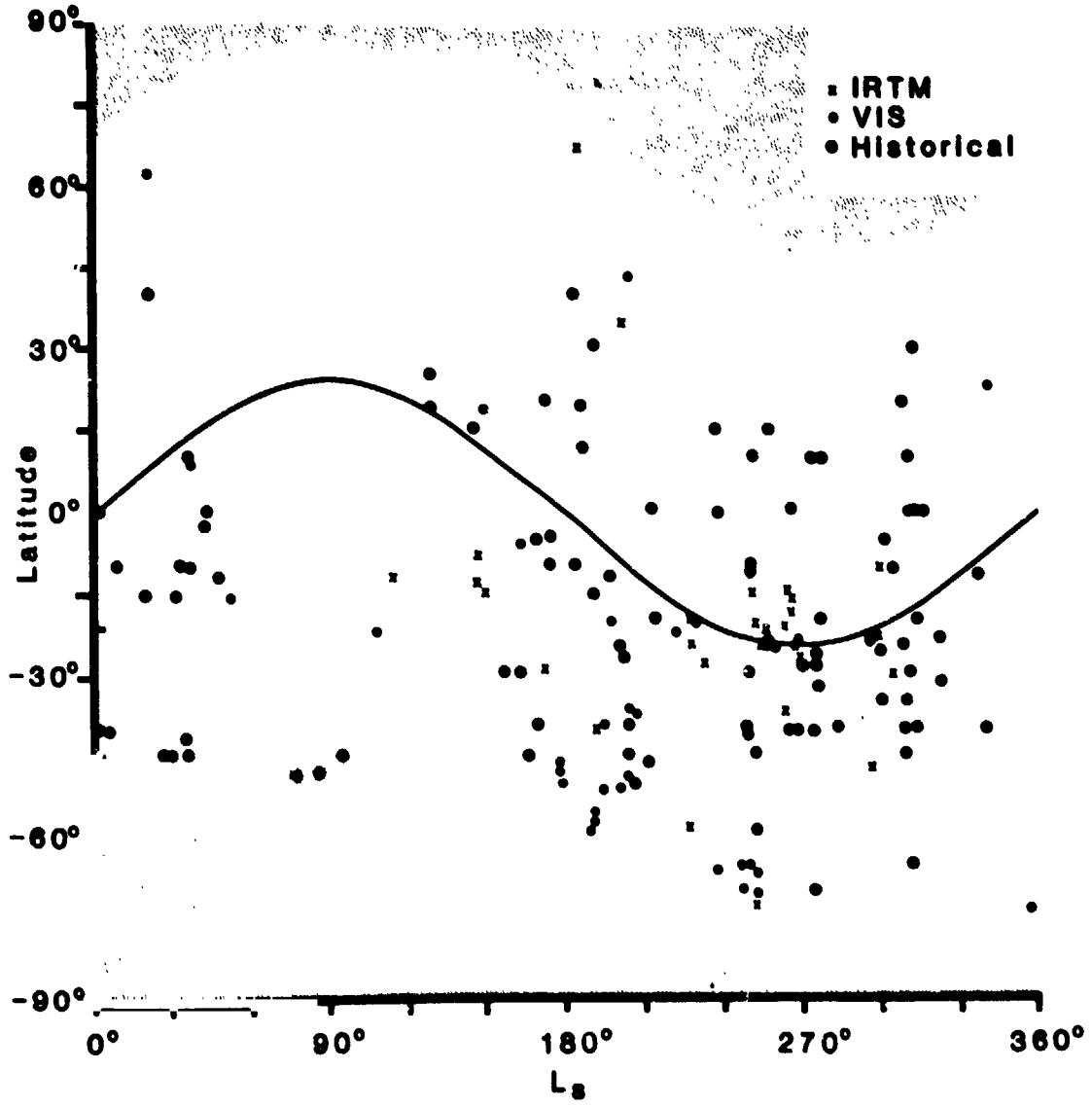

Figure 2. Latitudinal distribution of local dust storms as a function of solar longitude (Ls). The local dust storms plotted are those identified from Viking IRTM and VIS observations, and the historical record of Earth-based observations. The solid line is the sub-solar latitude and the shaded areas represent the maximum extent of the polar caps.

EROSION OF SURFACE MATERIALS AT THE MUTCH MEMORIAL STATION (LANDER 1), MARS

Moore, H. J., U.S. Geological Survey, Menlo Park, CA, 94025

Five conical piles of surface materials were constructed in the sample field of Lander 1 to detect and measure erosion by martian winds and other processes. After about two martian years on the surface, one of these piles finally changed (conical pile 4 of Moore and others, 1979). Conical pile 4 was placed next to a ventifact on Sol 344 (Table 1). During construction, spillage of fines from the surface sampler formed a dark appearing deposit around and downwind of the pile, but the bulk of the material formed a cone about 4-5 cm tall and 9-10 cm wide. By Sol 441, subsequent sedimentation of fines from the atmosphere had almost completely obscured these dark spillage deposits; however, the pile showed little or no evidence of change or reduction in relief up to Sol 921. Pictures taken more than one martian year later on Sol 1765 showed that the relief of conical pile 4 had been substantially reduced and that originally buried edges of the ventifact were exposed.

Although pictures of conical pile 4 were taken 884 sols apart, the changes probably occurred within an interval of 64 sols because the other conical piles appeared to be unchanged on Sol 1601 (Table 1). Conical piles 3 and 5 appeared unscathed on Sol 1543 and conical piles 2 and 5, which were constructed on and near rock 3 (Moore and others, 1979), appeared to have survived intact to Sol 160'. I expect that subsequent pictures, which should be available in October 1982, will show that conical piles 2, 3, and 5 have also changed.

The interval during which the changes are inferred to have occurred was near the winter solstice; it coincides with the stormy season on Mars, when winds are strong in the north (Ryan and Henry, 1979). Conical pile 4 is composed chiefly of very fine grained (0.14-2 μm) cohesive, drift material which would require threshold friction speeds of 10 to 40 m/s for saltation to occur (Iverson and others, 1976, equation 8). Threshold friction speeds must have been smaller than 10 to 40 m/s because objects as large as 1 cm or so should also have moved, but they did not. Minimum threshold friction speeds would be near 2 m/s for cohesionless particles near 150 μm in size (Iverson and others, 1976). Thus, erosion of conical pile 4 could have been caused by impacts of other materials saltated or entrained by the winds or, alternately, there may be small cohesionless "clodlets" in the pile that were entrained by the wind.

References:

Iverson, J. D. and others, 1976, Saltation threshold on Mars: The effect of interparticle force, surface roughness, and low atmospheric density: Icarus, v. 29, p. 381-393.

Moore, H. J. and others, 1979, Sample fields of the Viking Landers, physical properties, and aeolian processes: J. Geophys. Res.. v. 84, p. 8365-8377.

Ryan, J. A. and Henry, R. M., 1979, Mars atmospheric phenomena during major dust storms as measured at surface: J. Geophys. Res., v. 84, p. 2821-2829.

Table 1. Construction Sols, picture frame numbers, and Lander Science coordinates for conical piles at the Mutch Memorial Station (Lander 1), Mars.

Pile No.	Constructed on Sol	Coordinates (m) Z	Y	X	PrePile Frame	Early Frame with Pile	Last Frame Unchanged
1	296	2.24	2.69	0.89	11D034/281	11D092/296	12J008/921
2	324	3.95	-0.63	0.83	12D204/323	11D214/324	12J108/1601
3	324	3.78	-0.20	0.99	11C129/221	11D214/324	11J100/1543
4*	344	2.99	0.74	1.00	11B230/166	11E054/345	11J007/921
5	639	3.77	-0.36	0.99	11D214/324	11I070/690	12J108/1601

* Frame that showed changes of conical pile 4 was 11J130/1765.

NEW METHOD FOR DETECTING CONTRAST CHANGES AT THE MUTCH MEMORIAL STATION (VL1): RESULTS FOR THE FIRST THREE YEARS

E. A. Guinness and R. E. Arvidson, McDonnell Center for the Space Sciences, Washington University, St. Louis, Missouri, 63130

The Viking Lander 1 cameras are based on photodiodes equipped with interferenc filters (Patterson et al., 1977). Because of the rather high optical depths observed on Mars, the diode output voltage, v, produced by the spectral radiance from a given patch of surface, at a given incidence, emission, and phase angle, must be expressed as:

$$V = c \int_0^\infty [S(\lambda)\tau(\lambda) + sky(\lambda)]\, T(\lambda)\, \rho(\lambda)\, d\lambda \qquad (1)$$

where c is a calibration constant, $S(\lambda)$ is the solar spectral irradiance, $\tau(\lambda)$ is the atmospheric transmittance, $SKY(\lambda)$ is the skylight spectral irradiance, $T(\lambda)$ is the camera transfer function, and $\rho(\lambda)$ is the bidirectional spectral reflectance of the surface patch. The relationship between voltage and the 6-bit DN (digital number) returned to Earth can be expressed as:

$$DN = A \times V + B \qquad (2)$$

where A and B are constants. Changes in camera response, which were monitored for the first 1000 sols (Wall, 1981) can be expressed in the following form:

$$DN(T=30,S=0) = M \times DN(T,S) + K \qquad (3)$$

where T is the sensor temperature, S is the sol, and M and K are constants. T=30 is a sensor temperature equivalent to 30 DN and S=0 corresponds to the day of landing. For the red channel (0.60-0.75 micrometers) the values of M and K are such that during the first three years of observations the change in DN due to drift in the camera response is small enough to be well within the quantitization step of the 6-bit encoding from voltage. Thus, drift in the camera response can be ignored. The red channel was chosen because scene contrast is higher than in the blue and green channels.

Given these relations, we derived a new method to measure changes in a given scene imaged at two different times at the same lighting geometry. Consider a scatter diagram of the DN's for a given scene acquired at two different times with a lighting geometry that produces a minimum of shadows (Figure 1A). If there were no surface changes and no change in the characteristics of the illumination, the plot would consist of a straight line with a slope of unity. Changes in the illumination can be shown from equation 1 to only result in a change in slope. However, local changes in scene contrast would tend to increase the spread of points in a direction roughly perpendicular to the main trend (Figure 1B). We utilized principal components analysis to solve for the fractional variance along the direction perpendicular to the main trend. We

also generated images by projecting the data points along the vector direction that is perpendicular to the main trend (Figure 2). This technique eliminates changes due to varying illumination and delineates local surface changes. As a calibration, the fractional variance along the perpendicular vector direction for two scenes acquired one sol apart during the beginning of the mission is 0.05%, while the fractional variance for a scene with and without the surface sampler arm and trenches is 7.73%. Figure 3 is a plot of the fractional variance contained along the perpendicular direction for pairs of images acquired under similar lighting geometries (high sun angle) for the three years of the Lander mission. The fact that the variances are greater than zero and do not form a trend indicates that contrast changes occur on a regular basis, i.e., the scene is dynamic. Since the contrast variations are due to wind erosion and depostion, one can conclude that threshold drag velocities have been reached at the site repeatedly over the three year timescale of the Lander mission.

References

Patterson, W.R., and others, 1977, Calibration and performance of the Viking Lander cameras, J. Geophys. Res., 82, 4391-4400.

Wall, S.D., 1981, Viking Lander camera calibration files, unpublished.

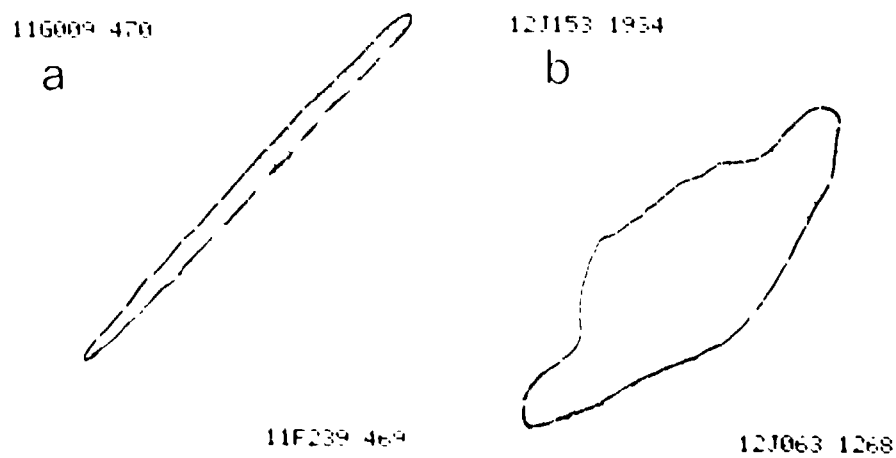

Figure 1 - (a) Scatter diagram for two images acquired on sols 469 and 470; (b) Scatter diagram for two images acquired on sols 1268 and 1934. Diagonal line has a slope of unity. The second scatter diagram shows evidence for local surface changes.

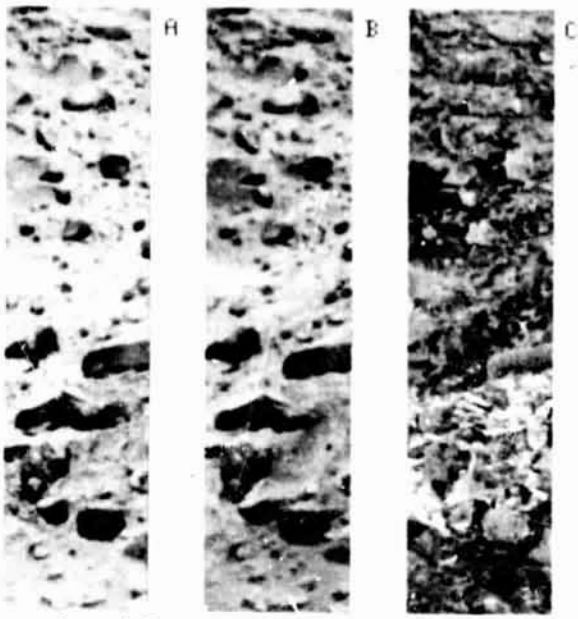

Figure 2 - Images A and B were acquired on sols 1268 and 1934. Image C delineates contrast changes between these two time periods, using the method discussed in the text. Bright areas correspond to regions where the albedo has increased and dark areas to regions where the albedo has decreased.

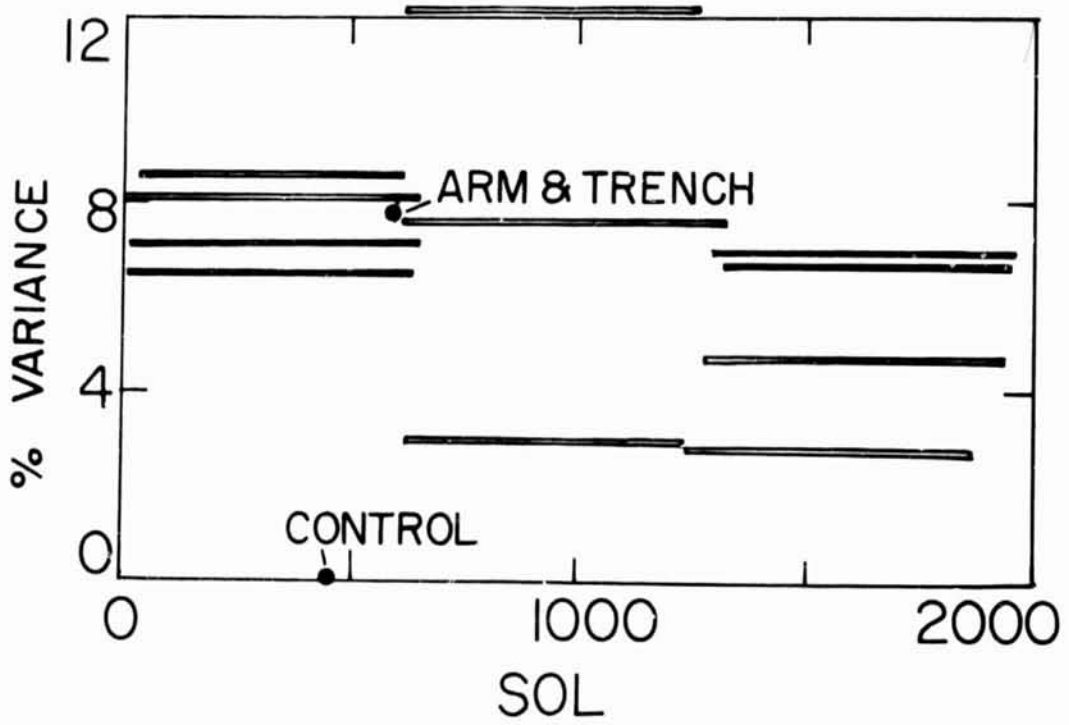

Figure 3 - Plot of variance carried along perpendiculars to main trends of scatter diagrams for image pairs. Ends of bars indicate the time range between each pair. Areas with sampler activity were avoided, except to establish the variance with the arm and trenches in one image and not in the other. The control corresponds to the scatter diagram in Figure 1a.

WIND TUNNEL MODELING OF BRIGHT AND DARK CRATER-ASSOCIATED STREAKS

James D. Iversen, Professor, Iowa State University
Ronald Greeley, Professor, Arizona State University
James B. Pollack, Research Scientist, NASA Ames Research Center

There have been many discussions of the crater-associated wind streaks on Mars, and many conjectural proposals concerning their origin--i.e., are bright streaks depositional, are dark streaks deflational, or is there currently too little information to tell?

We have performed a considerable number of wind tunnel experiments at quite small scale which resulted primarily in deflational streaks. We have also obtained depositional streaks, however, by injecting material through the crater floor or by simply placing erodible material only within the crater rim [Greeley et al. 1974a, 1974b; Iversen et al. 1973, 1975, 1976, 1978; Veverka et al. 1976].

Veverka et al. [1981] propose still a third scenario for the occurrence of depositional (bright) streaks. They have noted that some craters trail both bright streaks and dark streaks in different directions. They conclude that meteorological conditions rather than crater geometry determine whether bright streaks or dark streaks occur. They further contend that bright depositional streaks form during the clearing phases of global dust storms. Because of the dust in the atmosphere, the upper layer of the atmosphere warms, the surface cools, and the atmospheric layer adjacent to the surface becomes very stable. Because of this stability, craters with raised rims block the wind so that it must flow around the lateral sides of the crater rather than over. A quiet zone exists to the lee of the crater (in contrast to the neutral atmospheric layer), and dust falling out of the atmosphere in the clearing stage of the storm deposits preferentially in the lee.

Although simulation of stratified flow in the wind tunnel at small scale is difficult, some recent experiments were performed in the Iowa State University environmental wind tunnel to test the bright-streak stable-layer hypothesis. Figure 1 illustrates the normal neutral layer deflation streak. Figure 2 illustrates an attempt to simulate stable stratification by placing a layer of dry ice at the inlet of the test section. The cold CO_2 gas and cooled air flows along the wind tunnel test section floor, and the much warmer ambient air is drawn into the test section above the colder gas, resulting in stable stratification (the temperature difference in the wind tunnel corresponds to potential temperature difference in the atmosphere). The crater model in Figures 1 and 2 is the same. The particles (glass spheres, diameter <125 μm) are also the same except that in Figure 2 the spheres are damp and more cohesive, with a correspondingly higher threshold speed. The flow pattern in the two tests was obviously quite different. The deflation streak in the crater wake in Figure 1 resulted in the dark streak; the greatest deflation in Figure 2 took place on either side of the wake, leaving a bright streak.

Veverka et al. [1981] present a parameter r (basically a form of the Richardson number) which they indicate must be of the order

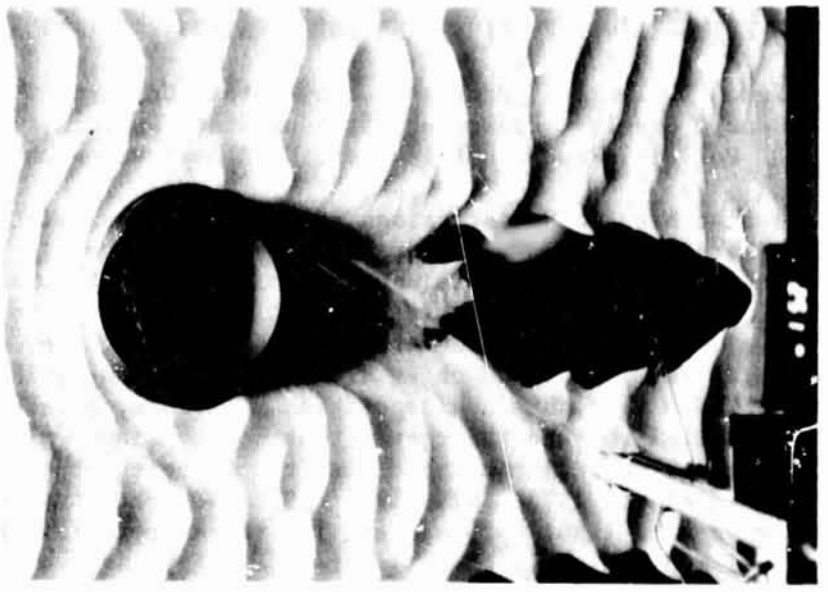

Figure 1. Reference (neutral boundary layer) model test. Model crater rim is 30 cm in diameter and 4 cm above the floor. Particles are glass beads (diameter < 125 μm).

Figure 2. Model test with stably stratified boundary layer. Model and particles are the same as in Figure 1 except for greater particle cohesion because of moisture.

of one for sufficient stability to block the flow. If one assumes that the temperature change from bottom to t p of the crater model is 100° C in the wind tunnel test, then the value of r in the wind tunnel is only 0.02. This seems to be large enough, however, to cause flow blockage to occur. Comparison of parametric values for the wind tunnel model with those for a full-scale crater on Mars with equal and unequal values of Richardson number is shown in Table 1. Although there may be other causes for the difference between bright and dark streaks, such as different ripple wavelengths inside and outside the streaks, the stable-stratification hypothesis seems to be plausible.

Table 1. Comparison of model and full scale parametric values in stably-stratified air.

Model Run	Wind Speed at Crater Rim (m/s)	Richardson Number $\Delta\theta\, gL/\theta_o\, U^2$	Crater Diameter (m)	Crater Rim Height (m)
7-1-2 (Figure 1)	2.4	0	0.3	0.04
7-2-1 (Figure 2)	4.8	0.02	0.3	0.04
Martian Crater	16.0	0.02	1000	130
Martian Crater	2.4	1	1000	130

R. Greeley, J. D. Iversen, J. B. Pollack, N. Udovich, and B. R. White (1974a) Wind Tunnel Simulations of Light and Dark Streaks on Mars. Science, Vol. 183, 847-849.

R. Greeley, J. D. Iversen, J. B. Pollack, Nancy Udovich, and B. R. White (1974b). Wind Tunnel Studies of Martian Aeolian Processes. Proc. R. Soc. London, A, Vol. 341, 331-360.

J. D. Iversen, R. Greeley, J. B. Pollack, B. R. White (1973). Simulation of Martian Eolian Phenomena in the Atmospheric Wind Tunnel. In Space Simulation, NASA SP-36, 191-213.

J. D. Iversen, R. Greeley, B. R. White, and J. B. Pollack (1975). Eolian Erosion of the Martian Surface, Part 1: Erosion Rate Similitude. Icarus, Vol. 26, 321-331.

J. D. Iversen, R. Greeley, B. R. White and J. B Pollack (1976). The Effect of Vertical Distortion in the Modeling of Sedimentation Phenomena: Martian Crater Wake Streaks. Journal of Geophysical Research, Vol. 81, 4846-4856.

J. D. Iversen and R. Greeley (1978). Atmospheric and Wind Tunnel Experiments of the Amboy Crater Sand-covered Lava Flow. Iowa State University Report ERI-78235.

J. Veverka, C. Sagan, and R. Greeley (1976). Variable Features on Mars VI: An Unusual Crater Streak in Mesogaea. Icarus, Vol. 27, 241-253.

J. Veverka, P. Gierasch, and P. Thomas (1981). Wind Streaks on Mars: Meteorological Control of Occurrence and Mode of Formation. Icarus, Vol. 45, 154-166.

MARS: INFLUENCE OF OBSTACLE TYPE AND SIZE ON WIND STREAK PRODUCTION

S. W. Lee, P. Thomas, and J. Veverka, Laboratory for Planetary Studies, Cornell University, Ithaca, New York 14853

We have analyzed the characteristics of wind streaks associated with craters and hills in the size range of ~100 m to 32 km using Viking Orbiter images of Mars. The increased resolution of the Viking coverage allows the results of previous Mariner 9-based studies (Arvidson, 1974; Veverka et al., 1978, to be extended to significantly smaller obstacle sizes.

Our data can be used to test various ideas on how the length of a streak should depend on obstacle height. For example, Veverka et al. (1981) proposed that bright (depositional) streaks result from the blocking of atmospheric flow during times of high static stability and dust loading, and suggested that the maximum streak length should be a constant multiple of obstacle height H.

The major findings and implications of our study are:

1. Both dark and bright Type I streaks (Thomas et al., 1981) form over the entire range of observed obstacle sizes--from ~100 m to ~32 km.
2. Preferred obstacle sizes for producing bright streaks are evident:
   a) 2-8 km craters are most commonly associated with bright streaks; few are found at larger sizes (Fig. 1).
   b) Hills are as effective as comparably-sized craters in producing bright streaks (hill-related dark streaks are rare). This finding supports the earlier conclusion of Chaikin et al. (1981), based on data restricted to the Cerberus region.
   c. Based on the rim height vs. crater diameter data of Pike (1977), and height estimates of hills from shadow measurements, obstacles in the size range of 2-8 km correspond to heights of several tens to a few hundred meters.
3. The situation for Type I dark streaks is much more area-dependent, but if the data for different regions are averaged, a preferred range of crater diameters of 4-16 km is suggested.
4. Streak length to obstacle size ratios (L/D) are similar in mean value and in dependence on obstacle size for both bright and dark streaks. A typical (L/D) vs. D curve for bright streaks is shown in Fig. 2.
5. For bright streaks associated with craters the streak length to rim height ratio (L/H) decreases with increasing H, rather than remaining constant as the simple blocking model of Veverka et al. (1981) suggests. The relationship shown in Fig. 3 is representative of that obtaining for the other regions that we have studied. The implication is that smaller obstacles on Mars are relatively more efficient streak producers than larger ones.

This research was supported by NASA Grant NSG-7546.

References:

Arvidson, R. E., Wind blown streaks, splotches, and associated craters on Mars: Statistical analysis of Mariner 9 photographs. Icarus 21, 12-27, 1974.

Chaikin, A. L., T. A. Maxwell, and F. El-Baz, Temporal changes in the Cerberus region of Mars: Mariner 9 and Viking comparisons. Icarus 45, 167-178 (1981).

Pike, R. J. Size-dependence in the shape of fresh impact craters on the moon. In Impact and Explosion Cratering (D. J. Roddy, R. O. Pepin, and R. B. Merrill, eds.), Pergamon Press (New York), 489-509, 1977.

Thomas, P., J. Veverka, S. Lee, and A. Bloom, Classification of wind streaks on Mars. Icarus 45, 124-153, 1981.

Veverka, J., K. Cook, and J. Goguen, A statistical study of crater-associated wind streaks in the north equatorial zone of Mars. Icarus 33, 466-482, 1978.

Veverka, J., P. Gierasch, and P. Thomas, Wind streaks on Mars: Meteorological control of occurrence and mode of formation. Icarus 45, 154-166, 1981.

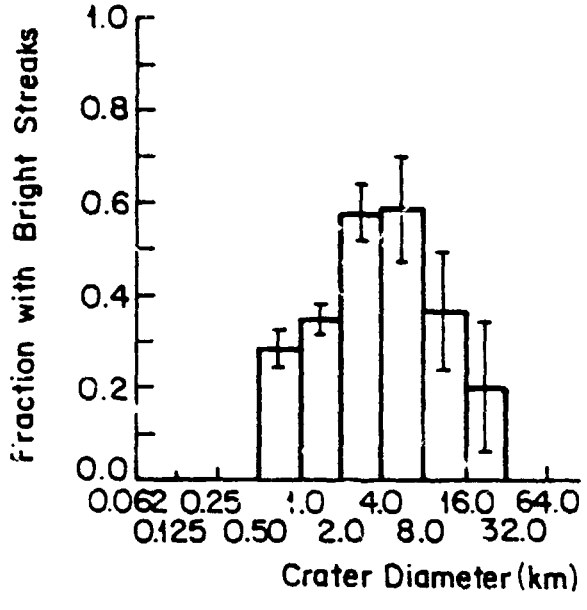

Fig. 1. Occurrence of bright streaks in the vicinity of Kasei Vallis/Lunae Planum. Data are grouped into log (base 2) bins of the crater diameter. Error bars are based on the square root of the number of streaks in each bin.

C-3

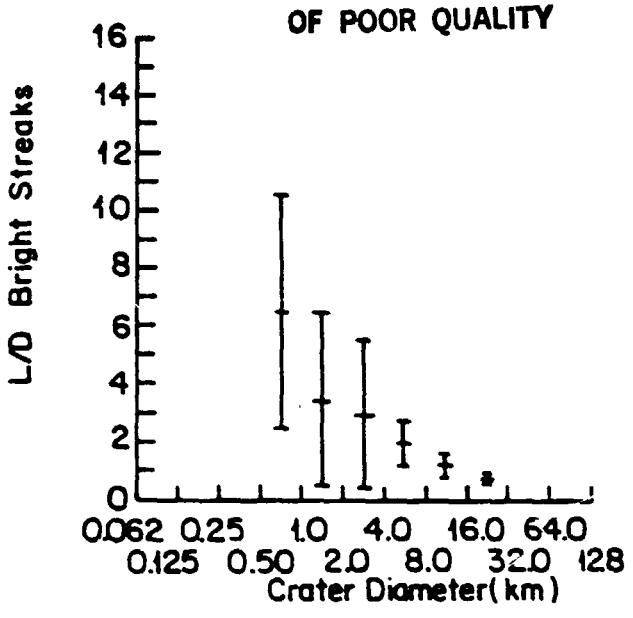

Fig. 2. Mean bright streak length to crater diameter ratio (L/D) as a function of crater diameter. Error bars of one standard deviation are shown. Region: Kasei Vallis/Lunae Planum.

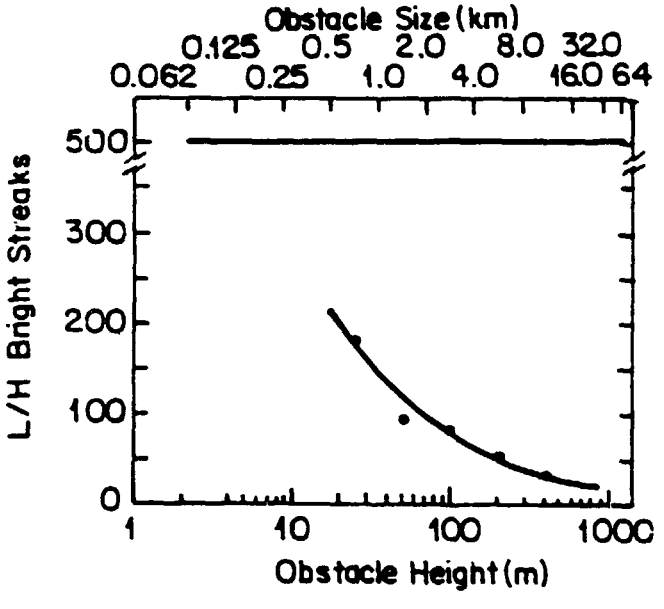

Fig. 3. Mean bright streak length to crater rim-height (L/H). The least-squares fit to the mean values is shown. The line at L/H = 500 is the upper limit predicted by the Veverka et al. (1981) blocking model. The upper scale relates crater diameter to rim height. Region: Kasei Vallis/Lunae Planum.

MARS EOLIAN SEDIMENTATION: HOW MUCH, HOW FAST?

P. Thomas, Laboratory for Planetary Studies, Cornell University

Morphologic, color, and photometric observations of different eolian features on Mars have provided new constraints on the present eolian sediment environments on Mars.

Dust deposition. Color data indicate that simple two-component mixes of bright dust and "background" material describe several dust deposition regions: crater streaks, intra-crater bright deposits, trough and sheet streaks. Crater bright streaks in widely scattered areas of Mars have maximum dust coverage of 10-20% (area), regardless of the type of substrate; intra-crater deposits have 30-50% coverage; and sheet streaks have 20-30% cover of dust. The bright margins of some dark streaks in Oxia Palus appear to be mixes of dust and the exterior material. The amount of dust cover in all these features should be less than 10^{-3} g/cm^2, by comparing the experimental data of Wells (1982). Some dust deposition features end abruptly near their apparent sources. From this relation it is inferred that once entrained this dust was rapidly redeposited and had settling rates of particles greater than 10 μm in diameter.

Dune and crater splotch activity. Color and morphologic data indicate that dark streaks originating at splotches and dunes have complex and variable mixtures of materials (Fig. 1). Although some of these streaks appear to be simple mixtures of dune material and surrounding plains material, most are complex assemblages of at least three materials. Only a small amount of dune material is present in most streaks. The bright margins are time variable and represent dust redistributed by activity within the streak; they are not directly related to the bright deposits in the source craters. The craters in Oxia Palus encompass five separate sedimentary systems: (1) bright intracrater dust deposition, (2) activity of splotches and dunes, (3) erosion of older crater fill, (4) activity in dark streaks, (5) dust deposition and erosion at streak margins. Although the color data show little if any dust can reside on the dunes, activity of these deposits need only be on the order of 0.2 cm^3/cm/y in order to inject a loose surficial layer of dust into suspension. Such low rates would imply rates of motion of dunes of only cm/10^3 yr. The presumed activity within the dark streaks may imply slightly higher minimum rates, but under any circumstance, they do not have to be high by terrestrial standards.

The shapes and sizes of dark "depositional" streaks in several areas of Mars suggest that their forms are controlled by regional meteorology or regional history, rather than strictly by dune size, crater size or the dimensions of the dune field. The dunes, however, occur preferentially in craters that show significant erosion of flat-lying intracrater deposits.

Dark dunes in most areas of Mars appear similar in color; splotches that are well resolved into non-dune flat areas are brighter and redder than those resolved into dunes. Within any one region, however, dunes and splotches make coherent mixes of colors, with dunes being the

dark, bluer end member (Fig. 1). A striking result of the global mapping has been the association of dune fields with areas of both reversing winds and thick, regional dust(?) deposits (Thomas, 1982): The polar dunes are associated with reversing winds and polar layered deposits, Oxia and Hellespontus dunes are associated with both intracrater deposits and nearby regional dust(?) deposits (Arabia; Hellas). The ephemeral nature of most present dust deposition, and the rapid sorting of dust and sand, imply that conditions leading to deposition of the large sediment deposits on Mars are incompletely represented by some of the contemporary, smaller-scale phenomena.

This research is supported by NASA Grant NAGW-111.

References:

Thomas, P. (1982). Present Mars wind activity: relation to large sediment deposits. J. Geophys. Res., in press.

Wells, E. N. (1982). Albedo changes caused by dust deposition; to be submitted to Icarus.

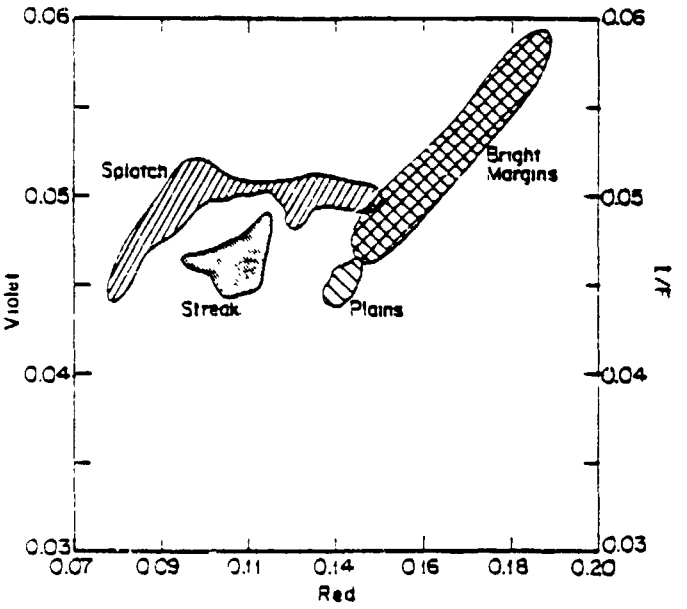

Fig. 1. Example of color groupings of streaks and splotches in Oxia Palus region. Although the streak lies between the dunes and plains, it is not a continuous mixing line. The bright margins, however, do show a continuous mixing with the plains material. Patterns of colors in other Oxia Palus streaks have all or part of this pattern; some show direct mixing of plains and splotches.

Aspects of the aeolian dynamic in the northern circumpolar sand sea of Mars.

M. MAINGUET and C. MOREAU, Laboratoire de Géographie Physique Zonale, Université de Reims, France.

The satellite images of Orbiters 1 and 2 (Viking Mission) revealed the existence of a circumpolar sand sea of 700 000 km^2 (1) (2) (3) around the northern pole of the planet Mars. The sand sheet of this continuous sand sea becomes thinner between 30° and 70° W. A classification of dunes and their dynamical meaning will be exposed.

I- The different types of dunes - More than 90 % of this sand sea is composed of transverse edifices which are isolated or grouped in chains of barchanic edifices. Their form is original on Mars, more ovoid shaped than on the Earth.

MARS: I.S 518827 (77°N. 97°O)

$a = b : 1,5$

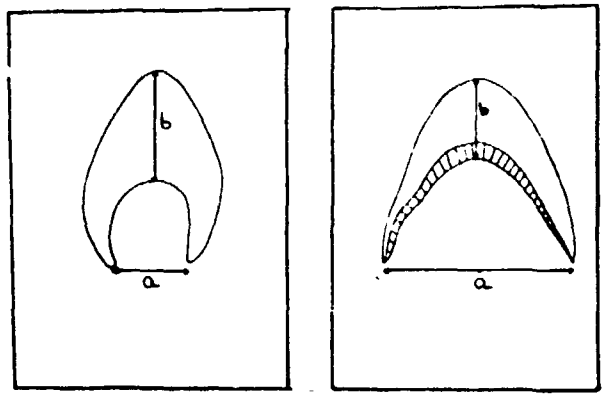

TERRE: AEF 56.57 NE 33. XVI n° 434.435

$a = b \times 2$

$D = \frac{b}{a}$ b = width of the body (up and downwind slopes)
a = distance between the two wings

For the martian barchan : a = b : 1'5
For the terrestrial barchan : a = b x 2

So D Earth < D Mars.

Average width b (Mars) = 250 m, for mega barchan B (Mars) = 4 000 m.
The distance from the polar ice-cap is never less than 100 km.

The isolated barchanic edifices, just like those of the Earth, are on the edge of the sand sea. They are also organized in chain "rempart" or in collective barchanic chains. The last transverse edifices are transverse chains : less frequent and ever located in the Chasma,

The second category is the linear dunes (seif type). Their existence is limited to the regions where the Chasmas arrive in the sand sea, probably where the wind regim is of two main wind directions : one from the Chasma and the general wind direction in the circumpolar sand sea.

Less frequent category of dunes is so called "erosional dunes" of sand-ridge type. These dunes are limited to a very small region (155° W to 210° E) and superimposed on transverse chains. This type of dune exists on Earth when the sand exportation is more important than importation (4).

II- Dynamical interpretation - The majority of transverse edifices is a good indication of the phase of increasing sand deposits. The very few longitudinal dunes are the only indicator of a starting negative sand supply. The heavier form of the barchanic edifices can drive to the hypothesis of less dune movement than on the Earth.

Three main directions of wind were detected : 1- the general circulation in the sand sea in a counter-clockwise direction, 2- from the North to the South as in the Sahara (5) in the Chasma where the wind direction is traced from the direction of the Chasma. Or, better, the carving of the Chasma results dominantly from wind action, 3- a circulation on the southern sand sea border from South to North before joining the general counterclock circulation.

We propose the following hypothesis ; this sand sea is a young one with more sand arriving than exported. The high amount of transverse edifices and their size indicate a long phase of climatic stability with a positive sand supply. But this sand sea is undergoing an evolution as indicated by the appearance of sandridges.

References

(1) TSOAR, H., GREELEY, R., PETERFREUND, R. - 1979 - Mars : the North polar sand sea and related wind patterns.Journal of Geophysical Research, vol.84, n° B14, 12/1979, p. 8167-8180.

(2) BREED, C.S., GROLIER, M.J., MAC CAULEY, J.F. - 1979 - Morphology and distribution of common sand dunes on Mars : Comparison with the Earth. Journal of Geophysical Research, vol. 84, n° B14, 12/1979 , p. 8183-8204.

(3) MAINGUET, M., MOREAU, C. - 1982 - Dunes et transport de particules dans l'erg circumpolaire nord de la planète Mars. Journées de l'A.T.P. Planétologie I.N.A.C., 23, 24 et 25 février, C.N.R.S. Paris

(4) MAINGUET, M., CALLOT, Y. - 1978 - L'erg de Fachi-Bilma (Tchad - Niger). Mémoires et Documents, éditions du C.N.R.S., vol. 18, 184 p.

(5) MAINGUET, M. - 1978 - The influence of trade winds, local air-masses and topographic obstacles on the aeolian movement of sand particles and the origin and distribution of dunes and ergs in the Sahara and Australia. Géoforum, vol. 9, p. 17-28.

0 cm 5
0 km 380
1 cm : 76 km

LEGENDE:

Edifices transverses isolés:

- Mégabarkhanes.
- Boucliers barkhaniques (densité variable)

Barkhanes en organisation collective:

- Chaînes barkhaniques courtes et isolées.
- Chaînes barkhaniques "rempart"
- Chaînes barkhaniques périodiques.
- Chaînes barkhaniques serrées.

Edifices transverses sans organisation:

- Edifices barkhaniques sans organisation.
- Aklés barkhaniques

Autres types de figures éoliennes:

- Chaînes transverses.
- Dunes linéaires de type " sif "
- Cordons longitudinaux ou "Sandridges"
- Dépôts éoliens dans les cratères.

Autres phénomènes éoliens:

- Stries de déflation.
- Effet d'abri.

Autres données:

- Limite méridionale de la calotte polaire Nord.
- Secteurs non couverts.
- Cratères.
- Limites incertaines
- Pôle géographique

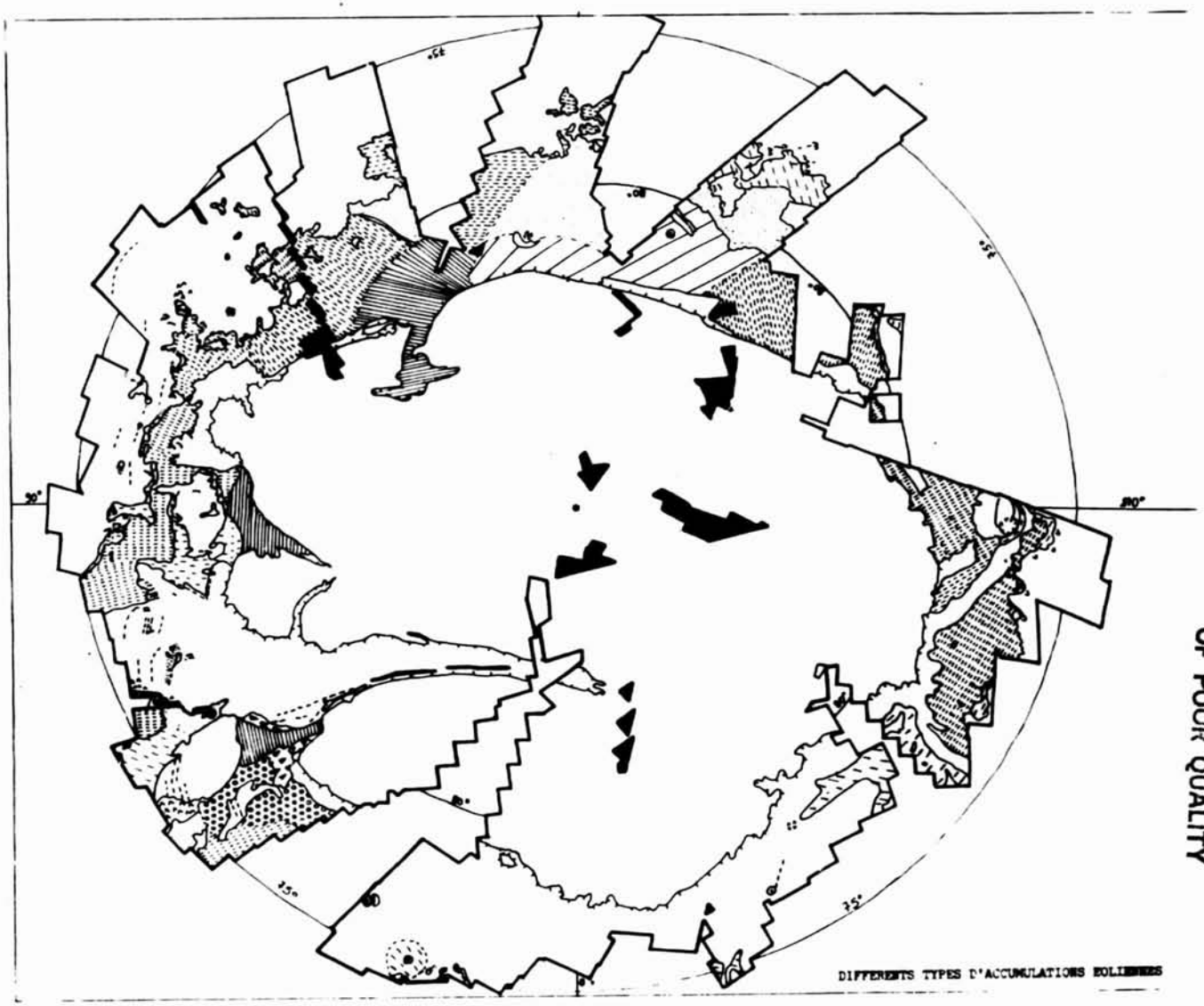

DIFFERENTS TYPES D'ACCUMULATIONS EOLIENNES

LEGENDE:

Sens et directions des vents principaux déduits d'après:

- L'axe des barkhanes. (certitude)
- L'axe des édifices barkhaniques. (moindre certitude)
- Autres critères: chaînes transverses; traînées éoliennes...

AUTRES DONNÉES:

- Limite méridionale de la calotte polaire nord.
- Secteurs non couverts.
- Gros cratère.
- Petits cratères.

Echelle

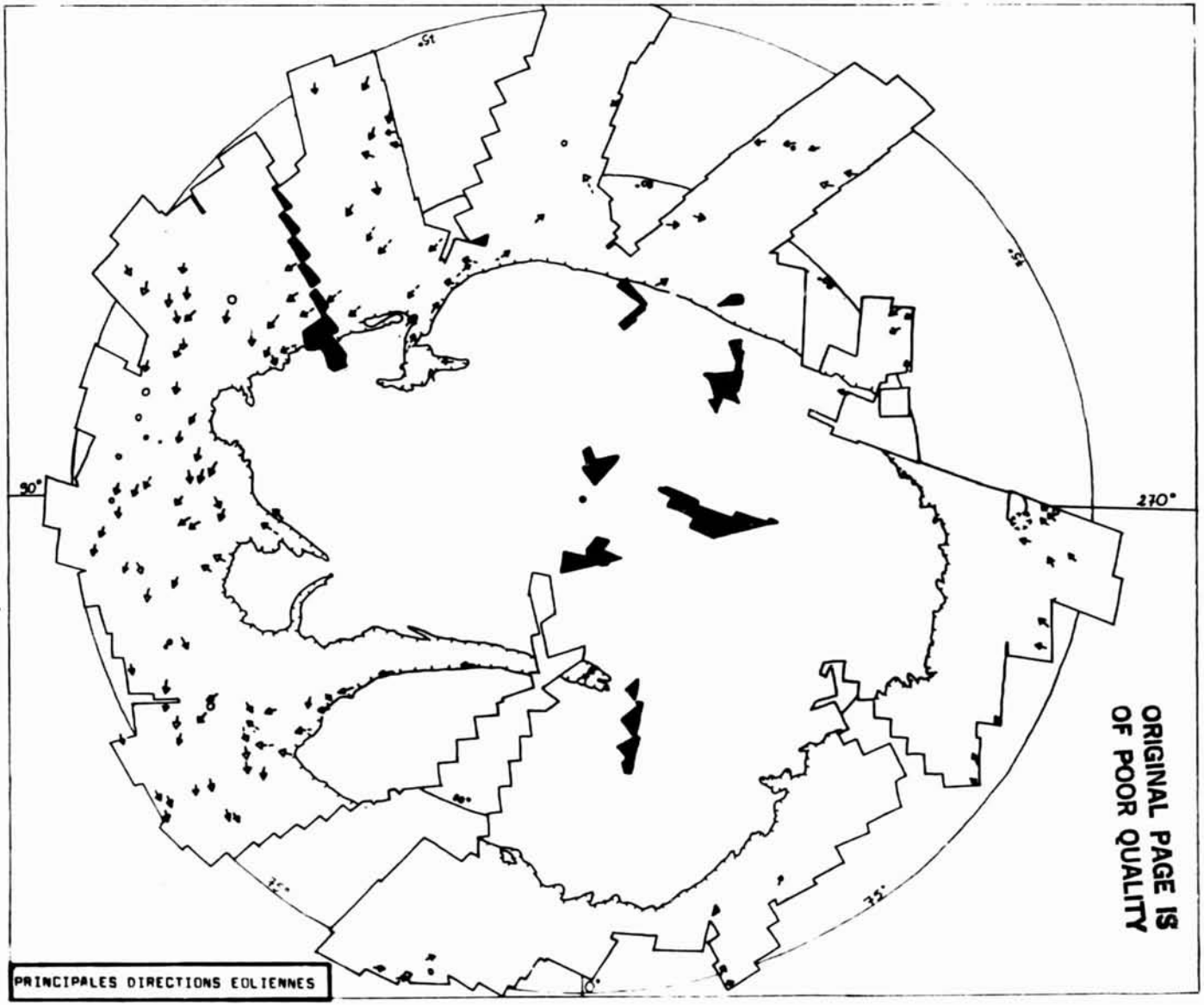

PRINCIPALES DIRECTIONS EOLIENNES

SOIL HUMIDIFICATION AS A TRIGGER OF DUST STORMS ON MARS

R.L. Huguenin and S.M. Clifford, Dept. Physics/Astronomy,
Hasbrouck Lab, UMassachusetts, Amherst, MA 01003

One of the most striking dynamical phenomena on Mars is the equatorial dust storm. They have occurred nearly every Martian year since observational records have been kept. The major storms have developed preferentially near perihelion. They have also appeared at certain specific locales on the planet. Initial plumes appeared suddenly, often by dawn, extending several hundred kilometers across in regions that were clear the previous days. Frequently the major storms initiated with brilliant white plumes that later turned yellow.

What triggers these equatorial storms? A prevailing idea is that dust might be raised by saltation impact of sand grains ($\sim$160μm). Threshold saltation velocities were estimated to be 50 $\pm$ 25ms^{-1} (1), which are somewhat higher than observed wind velocities. Hourly averaged wind speeds at the Viking lander sites around the onsets of the 1977 storms, for example, were 17.7 ms^{-1} (VL1) and 13.6 ms^{-1} (VL2), with gusts to 26 ms^{-1} (2). Similar wind velocities were deduced from Viking IRTM observations of apparent plume velocities at the storm sites (3). It has been proposed that combinations of regional topography and insolation-induced modifications of thermal gradient may produce high enough local turbulance to raise the dust (e.g. 3,4). That high enough wind speeds could be generated has been questioned, however (5). In addition, the saltation models do not adequately explain the appearance of plumes by dawn on Day 1 of the storms. They predict instead that the onset of activity should occur closer to midday during peak insolation and maximum prevailing winds. Furthermore, there is inadequate agreement between the regions of predicted highest surface velocities and the observed sites of dust plume generation (6). Finally, the color change from an initial white plume to yellow is not explained by the saltation models.

An alternative dust injection hypothesis was proposed by Johnson et al (7). It was argued from laboratory data that solar heating rates of $\sim$50^{o} hr^{-1} could produce a rapid desorption of gas within the upper few cm. Subsurface pressures could build to the point that the surface could explosively rupture, injecting dust into the atmosphere. Gas jets could also develop along microfissures in the dust layer, according to the model, that could raise additional dust into the atmosphere. A modification of the Johnson et al model has been proposed by Huguenin et al (8,9), and Greeley and Leach (5). It was argued by Huguenin et al that if the soils contained adsorbed H_2O as well as CO_2, $\sim$ 4 times as much gas (12 mg cm^{-2} CO_2 + 36mg cm^{-2} H_2O) might be desorbed during the diurnal heating cycle. As a result the heating rate could be $\sim$ 4 times lower ($\sim$ 13^{o} hr^{-1}) and release the same amount of gas as in the Johnson et al experiments. The heating rates are close to the observed average heating rates near perihelion at the Southern hemisphere dust storm sites ($\sim$ 15^{o} hr^{-1}); consequently it was proposed that dust storms may initiate at those sites due to enhanced levels of adsorbed H_2O in the soils there. Greeley and Leach presented bell jar and wind tunnel experiments that supported this model, and they showed that the presence of adsorbed H_2O could act to reduce the threshold velocity for

saltation.

The role that H_2O plays in triggering the equatorial storms may be even more direct. A phenomenon was observed during the Viking Gas Exchange experiments on Mars that suggests that H_2O may produce a catastrophic desorption of gas from the soil under appropriate conditions. Such conditions could develop around perihelion on Mars, and it is possible that this phenomenon may trigger some of the storms. In particular, when samples of Martian soil were humidified in the GEx test cells, there were sudden and spontaneous releases of gas from the samples. Over 9600 nmol of gas was released per gram of sample, and most was generated within the first few hours (10). All gases, with the exception of some of the O_2, were derived from adsorbed atmospheric constituents (10). While most attention has focused on the unusual production of O_2 during the GEx experiments, the explosive release of adsorbed gases by simple humidification was spectacular.

It has been proposed that the mechanism for driving off the adsorbed gas was base hydrolysis (11), whereby adsorbed gases were replaced by the H_2O. This is a common reaction, but not with the intensity that occurred during the GEx experiment. The difference in intensity can be attributed to the apparently highly dessicated state of the Martian soils, revealed in part by near-IR telescope stectra (12). At the low Martian surface temperatures, H_2O is more stable as ice than as adsorbed H_2O and minimal H_2O (less than 1 monolayer equivalent) would exist in the adsorbed state (13). The ice is unstable in the regions where the equatorial storms occur (14), and hence the soils are highly desiccated. When these soils were exposed to H_2O vapor at $\sim 5^oC$ during the GEx experiment, the H_2O would be expected to spontaneously replace the adsorbed gases. With such a small fraction of the adsorbed species being H_2O, the intensity of the GEx desorption reaction can be explained. If the soils on Mars were similarly humidified by some means, a similar desorption reaction could conceivably occur.

We have recently reported evidence for H_2O vapor source regions on Mars (15), and it was noted that the outgassing activity peaked during the perihelic dust storm periods. It was argued that seasonal melting of ground ice within the upper meter of soil possibly occurs during this period (15). If true, the melted ice would tend to migrate upward into the dry overburden and dampen the soil. This would provide a similar condition to that which drove off adsorbed gases during the GEx experiment.

If it is assumed that: 1) humidification during the melting event can drive off adsorbed gases to the same extent ($\sim$ 9600nmol g^{-1}) as in the GEx experiment; 2) soil porosities in the surface layer are $\sim$ 0.5; 3) soil temperatures are $\sim$ 0 -5°C; and 4) that the escape of gas is diffusion-inhibited, as discussed by Farmer (14), Bernoulli's equation indicates that pore-space pressures of up to 0.4 atmosphere could develop. Escape velocities of up to 450m/s could develop along microfissures in the soil. These pressures and jetting velocities would be more than adequate to inject dust into the atmosphere. Indeed a mini dust storm event inside the GEx chamber may have produced the clogging of the drain line, as discussed by Huguenin (16).

In addition to providing a mechanism for raising dust on Mars, the

soil humidification/desorption model could explain some other dust storm characteristics. Firstly, the high initial moisture contents of the escaping vapor could explain the white coloration of the initial plumes. Secondly, the onsets by dawn could be accounted for. In particular, the events would be triggered by seasonal warming of the soil to the melting point of ice. During the cold nighttime and early morning hours escaping H_2O vapor would be expected to freeze out near the surface. This could form barriers along the microfissures and pores that would inhibit the rate of outgassing, and it could conceivably permit pressures to build and result in explosive outgassing/dust injection events. Thirdly, the model could account for the repeated occurrences of the storm events at certain specific locales. Indeed, the primary storm sites coincide with the three sites where H_2O outgassing repeatedly occurs (15).

Acknowledgement. This research was supported by grants NSG 7397, NSG 7405, and NAGW 40.

References. 1) R. Greeley et al, Geophys. Res. Lett. 3, 417, 1976; 2) J.A. Ryan and R.M. Henry, J. Geophys. Res., 84, 2821, 1979; 3) A.R. Peterfreund and H.H. Kieffer, J. Geophys. Res. 84, 2853, 1979; 4) S.L. Hess, Planet Space Sci., 21, 1549, 1973; 5) R. Greeley and R. Leach, NASA TM 80339, 304, 1979; 6) G. Briggs, W. Baum, and J. Barnes, J. Geophys. Res., 84, 2795, 1979; 7) D. Johnson, P. Harteck, and R. Reeves, Icarus 26, 441, 1975; 8) R.L. Huguenin et al, NASA TM 80339, 208, 1979; 9) R.L. Huguenin, S.M. Clifford, and R. Greeley, NASA TM 81776, 215, 1980; 10) V.I. Oyama and B.J. Berdahl, J. Mol Evol 14, 199, 1979; 11) R.L. Huguenin, K.J. Miller, and W.S. Harwood, J. Mol Evol 14, 103, 1979; 12) R.L. Huguenin, K.G. Clark, and T.B. McCord, Proc Sec. Coll. Planetary Water Polar Processes, 100, 1978; 13) D.M. Anderson and A. R. Tice, J. Mol Evol 14, 33, 1979; 14) C.B. Farmer, Icarus, 28, 279, 1976; 15) R.L. Huguenin and S.M. Clifford, J. Geophys. Res., Mars Special Issue, in press, 1982; 16) R.L. Huguenin, J. Geophys. Res., Mars Special Issue, in press, 1982.

Chapter 7

FLUVIAL PROCESSES AND LANDFORM DEVELOPMENT

MARS VALLEY NETWORKS AS INDICATORS OF FORMER CLIMATIC CONDITIONS.

Michael H. Carr, U.S. Geological Survey, Menlo Park, CA

The presence of fluvial features on the martian surface is commonly cited as evidence for different climatic conditions in Mars' past. This paper is a progress report on work to assess more precisely what the presence of channels implies about past martian climates.

Mars has two main types of channels, outflow channels and runoff channels (valley networks). The outflow channels are commonly believed to have formed by floods with high discharge rates and short durations (e.g. Milton, 1973, Baker and Milton, 1974). Large floods would undergo insignificant losses by freezing, evaporation, and sublimation, even on the Moon (Lingenfelter et al., 1968), and thus could probably carve the large martian outflow channels under present climatic conditions. The conditions under which the branching valleys could form are, however, more problematic. The valleys appear to result from slow, sustained erosion by streams of modest discharge, much like terrestrial valleys (Pieri, 1976). Such streams would freeze faster than the large floods, and the question arises whether they could accomplish a significant amount of erosion before freezing. The object of the work reported here is to determine the conditions under which small streams could form and survive on the martian surface to cut the observed channels. The problem falls naturally into two parts. The first is to determine how long a stream of a given discharge will flow before it freezes. The second part of the problem is to determine how such a stream could originate. Significant progress has been made only on the first part of the problem.

Freezing rates of martian streams were calculated for various surface temperatures and pressures. The calculations are similar to those of Wallace and Sagan (1979) but differ in several important respects as elaborated on below. A range of atmospheric pressures was considered, and the surface temperatures appropriate to each pressure were derived from the atmospheric models of Pollack (1979), Toon et al. (1980) and Hoffert et al., (1981). Following Wallace and Sagan (1979) and Colbert (1980), it was assumed that on any body of water a thin ice cover will form. Under given conditions of atmospheric temperature, pressure, and wind velocity, the energy budget at the ice-atmosphere interfaces can be calculated. The upper surface of the ice recieves direct solar radiation in the visible, infrared radiation mostly from the atmosphere, and heat conducted upward through the ice. The incoming energy is balanced by heat reradiated at the surface temperature of the

ice and heat lost through sublimation. Heat may be also lost or gained by conduction to the atmosphere and convection depending on the relative temperatures of the ice and air at the surface.

The first step in the calculation is to determine the temperature of the ice surface at which the energy inflow and outflow are equal. Once this surface temperature is known, then heat lost by conduction from the ice-water interface can be calculated, and because this heat loss is balanced by radiation penetrating the ice and by the latent heat of fusion released by freezing, the rate of freezing can be calculated. The ice is appropriately thickened for the time interval under consideration and the calculations repeated. In this way the growth of ice on a stream can be tracked over a wide range of climatic conditions.

The most complex part of the problem is calculation of the surface temperature of the ice. The calculations here differ from those of Wallace and Sagan (1979) as follows: (1) Radiation in the visible and infrared are treated separately; (2) empirical extinction coefficients are used to calculate absorption of the visible radiation by the ice (Wallace and Sagan assumed that a fixed fraction was absorbed); and (3) a conduction term is introduced to account for the heat lost or gained by the ice through conduction to or from the atmosphere. The method used here to calculate conduction is similar to that used by Gierasch and Toon (1973). In the initial calculations, the infrared flux was derived from the differences between the surface temperatures predicted from the various atmospheric models and those that would prevail with no atmosphere. A more refined method of estimating the infrared flux is reported on elsewhere in this volume (Clow, 1982). Sublimation rates were calculated by a method identical to that used by Wallace and Sagan. The estimates of the freezing rate were tested against known freezing rates at two localities in Alaska and predictions were within 30 percent of the observed rates.

The results indicate that freezing rates are relatively insensitive to climatic conditions. For example, for the model atmosphere of Hoffert et al. (1981), and a frictional wind velocity of 100 cm/s, and an ice albedo in the visible of 0.8, a standing body of water 1 meter deep will take 18 days to freeze on Mars at an atmospheric pressure of 10 mb. Under a pressure of 300 mb it will take 42 days to freeze. Freezing of a stream would be slower because of frictional heating. The freezing rates are slow compared with flow velocities of streamds. During 18 days a stream initially 1 meter deep could travel 500-2,000 km for a plausible range of slopes (Komar, 1979). Thus it appears that if flow can be initialized then even the valley networks could form under climatic conditions similar to those

that currently prevail.

The main difficulty is initiating the flow. If the channels are cut entirely by sapping (Pieri, 1980) then surface flow is initiated simply by leakage from the groundwater system and climatic constraints on formation of the valleys are loose. On the other hand, if the streams form by surface runoff, such as by melting of surface ice, then the climatic constraints on their formation are likely to be severe. The specific conditions under which streams could be initiated by runoff are currently being investigated.

REFERENCES

Baker, V.R., and Milton, D.J., 1974, Erosion by catastrophic floods on Mars and Earth. Icarus, v. 23, p. 27-41

Clow, G.D., 1982, Downward travelling infrared flux at the martian surface for past CO_2/H_2O atmospheres. (this volume)

Gierasch, P.J., and Toon, O.B., 1973, Atmospheric pressure varation and the climate of Mars. J. Atmos. Sci., v. 30, p. 1502-1508

Hoffert, M.I., Callegari, A.J., Hsieh, C.T., and Ziegler, W., 1981, Liquid water on Mars: An energy balance climate model for CO_2/H_2O atmospheres. Icarus, v. 47, p. 112-129.

Komar, P.D., 1979, Comparisons of the hydraulics of water flows in martian outflow channels with flows of similar scale on Earth: Icarus, v. 37, p. 156-181.

Lingenfelter, R.E., Peale, S.J., and Schubert, G., 1968, Lunar rivers. Science, v. 161, p. 266-269.

Milton, D.J., 1973, Water and processes of degradation in the martian landscape. J. Geophys. Res., v. 78, p. 4037-4047.

Pieri, D.C., 1976, Martian channels: Distribution of small channels on the martian surface. Icarus, v. 27, p. 25-50.

Pieri, D.C., 1980, Martian valleys: Morphology, distribution, age and origin. Science, v. 210, p. 895-897.

Pollack, J.B., 1979, Climate change on the terrestrial planets. Icarus, v. 37, 479-553.

Toon, O.B., Pollack, J.B., Ward, W., Burns, J.A., and Bilski, K., 1980, The astronomical theory of climate change on Mars. Icarus, v. 44, p. 552-607.

Wallace, D. and Sagan, C., 1979, Evaporation of ice in planetary atmospheres: Ice covered rivers on Mars. Icarus, v. 39, p. 385-400.

VALLEY NETWORKS ON MARS: MAPPING AND MORPHOGENESIS

Victor B. Baker, Department of Geosciences, University of Arizona, Tucson, Arizona 85721; G. Robert Brakenridge, Department of Earth Sciences, Dartmouth College, Hanover, New Hampshire 03755; R. Craig Kochel, Department of Environmental Sciences, Clark Hall, University of Virginia, Charlottesville, Virginia 22903

Geomorphic mapping of valley networks in the heavily cratered terrains of Mars (Figures 1 and 2) has revealed a complex history of valley morphogenesis. The valleys show prominent local structural control by lineaments, anastomosing reaches, local zones of relatively high drainage density, unusual widening and narrowing, and very indistinct sink relationships.

Many areas show a very complex history that involved valley development over a long time span marked by continued impact cratering. Depositional phases followed by exhumation phases may be required to explain inverted topography in network systems such as Auqakuh Vallis (Figure 2). The valleys also appear to have been extensively modified by mass movement, thermokarstic, and eolian processes.

Valleys of the Aeolis region (Figure 1) are developed in the Cratered Plateau Material mapped by Scott and others (1978). Flow is directed down the regional topographic gradient, here estimated at 0.5 to 1 m/km (U.S. Geological Survey, 1976).

Auqakuh Vallis (Figure 2) is developed in a layered plateau material that thickly mantles an older densely cratered surface. Large craters have been extensively reduced to subcircular depressions by burial. High-resolution Viking pictures reveal an intricate landscape of mesas, scalloped valley sides, pitting, and "inverted" topography.

Past statements concerning the paleoenvironmental significance of valley networks on Mars have heretofore been generalized and or restricted to a few special cases (e.g. Baker, 1972; Mars Channel Working Group, in press). However, the developing body of detailed morphogenetic mapping studies of individual network systems is now providing new data with which to assess this important, but difficult problem. Future work needs to concentrate on a synthesis of descriptions, genetic models, and large-scale implications similar to that achieved for studies of the outflow channels.

References

Baker, V.R., 1982, The channels of Mars: The University of Texas Press, Austin, 198 p.

Mars Channel Working Group, in press, Channels and valleys on Mars: Geological Society of America Bulletin.

Scott, D.H., Morris, E.C., and West, M.N., 1978, Geologic map of the Aeolis Quadrangle of Mars: U.S. Geol. Survey Misc. Inv. Map I-1111.

U.S. Geological Survey, 1976, Topographic map of the Aeolis Quadrangle of Mars: U.S. Geol. Survey Misc. Inv. Map I-1001.

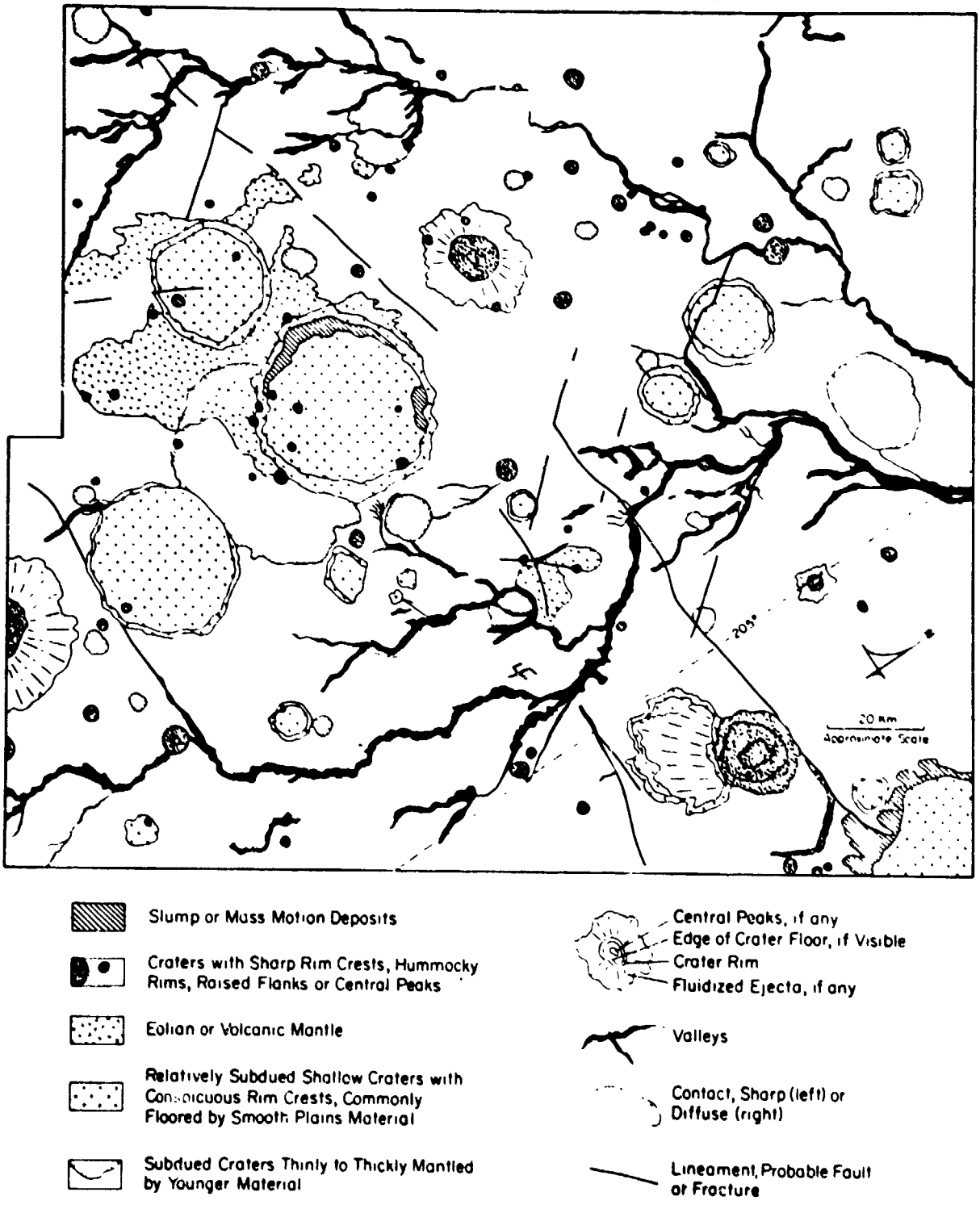

Figure 1. Large-scale geomorphic map of a valley network on the Aeolis Quadrangle at 14° S, 206° W. Valleys trend to the NE from the heavily cratered uplands toward Elysium Planitia.

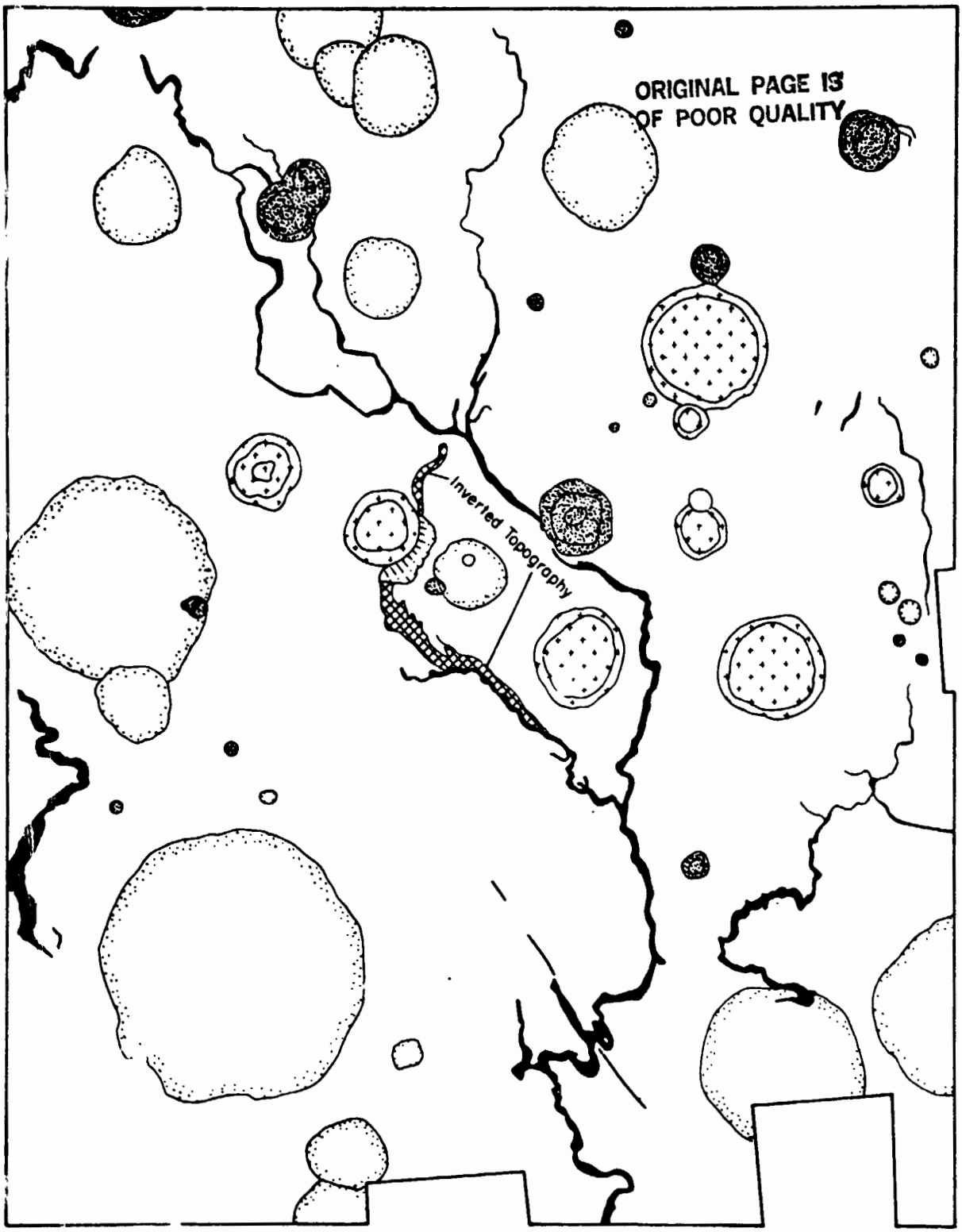

Figure 2. Geomorphic map of Auqakuh Vallis in the Syrtis Major region of Mars, 30° N, 300°W. The system represents northward flow (to the bottom of the map).

ANCIENT FLUVIAL DRAINAGE SYSTEMS: MARGARITIFER SINUS AREA, MARS

BOOTHROYD, Jon C., Dept. of Geology, Univ. of Rhode Island, Kingston, RI 02881

Stereo pairs of Viking Orbiter images have been used to map fluvial drainage systems in the west central area of the Margaritifer Sinus Quadrangle (MC-19) (Fig. 1) and in the northernmost part of the Argyre Quadrangle (MC-26). It is possible, with this technique, to determine drainage basin boundaries, to delineate source areas for small outflow channels, and to identify depositional basins. Preliminary studies indicate that some valley networks were tributary to old outflow channel system, or flowed into depositional basins formed in regional lows. Other networks show reactivation after mantling by crater ejecta or presumed eolian material; still others have been beheaded by later development of chaotic terrain. These observations suggest that while some of the valley networks are very old, others were active during the time of formation of the large outflow channels and chaotic terrain.

The Ladon Valles drainage system occupies the largest segment of the area mapped to date, with a source area to the northeast of the crater Holden, an array of outflow channels (Ladon Valles proper), and a probable depositional basin northwest of Ladon Valles. The Ladon system may be part of an older Uzboi-Holden-Ladon system as reported by Pieri (1980). The Ladon drainage continues northward to the presumed depositional plain inside an older, highly degraded, multi-ringed basin, the boundaries of which were mapped by Saunders (1979) and discussed by Schultz and Glicken (1979). Figure 2 illustrates the structural control imparted to the Ladon Valles drainage course by another old-basin margin (Pieri and Parker, 1981), as well as a valley network draining toward the depositional basin.

Many workers, including Pieri (1980) and Carr (1980), consider the valley networks to be very old, whereas outflow channels may have spanned a considerable period of martian history (Masursky et al., 1977). However, the period of valley network formation is quite complex and is interwoven, in part, with the development of chaotic terrain and outflow channels. Figure 3 shows several old stem valleys adjacent to fresher appearing valleys and a small, unnamed outflow channel. Stereo mapping together with earth-based radar profiles (Downs et al., 1978; Roth et al., 1980), indicate that the paleoslope was away from Eos chasma to a depositional area now exhibiting chaotic collapse. The drainage is, in effect beheaded. In addition, the Osuga Valley outflow channel (Fig. 3) cuts through a substantial ridge which may have been actively growing during formation of the channel system.

REFERENCES

Carr, M.H., 1980, The morphology of the martian surface: Space Sci. Rev., v. 25, p. 231-284.

Downs, G.S., Green, R.R., and Reichly, P.E., 1978, Radar studies of the martian surface at centimeter wavelengths: the 1975 opposition: Icarus, v. 33, p. 441-453.

Figure 1. Topographic map of part of the Margaritifer Sinus quadrangle (USGS, 1976) with superimposed drainage basins determined by mapping using Viking Orbiter stereo pairs of images. Arrows indicate presumed direction of fluvial transport.

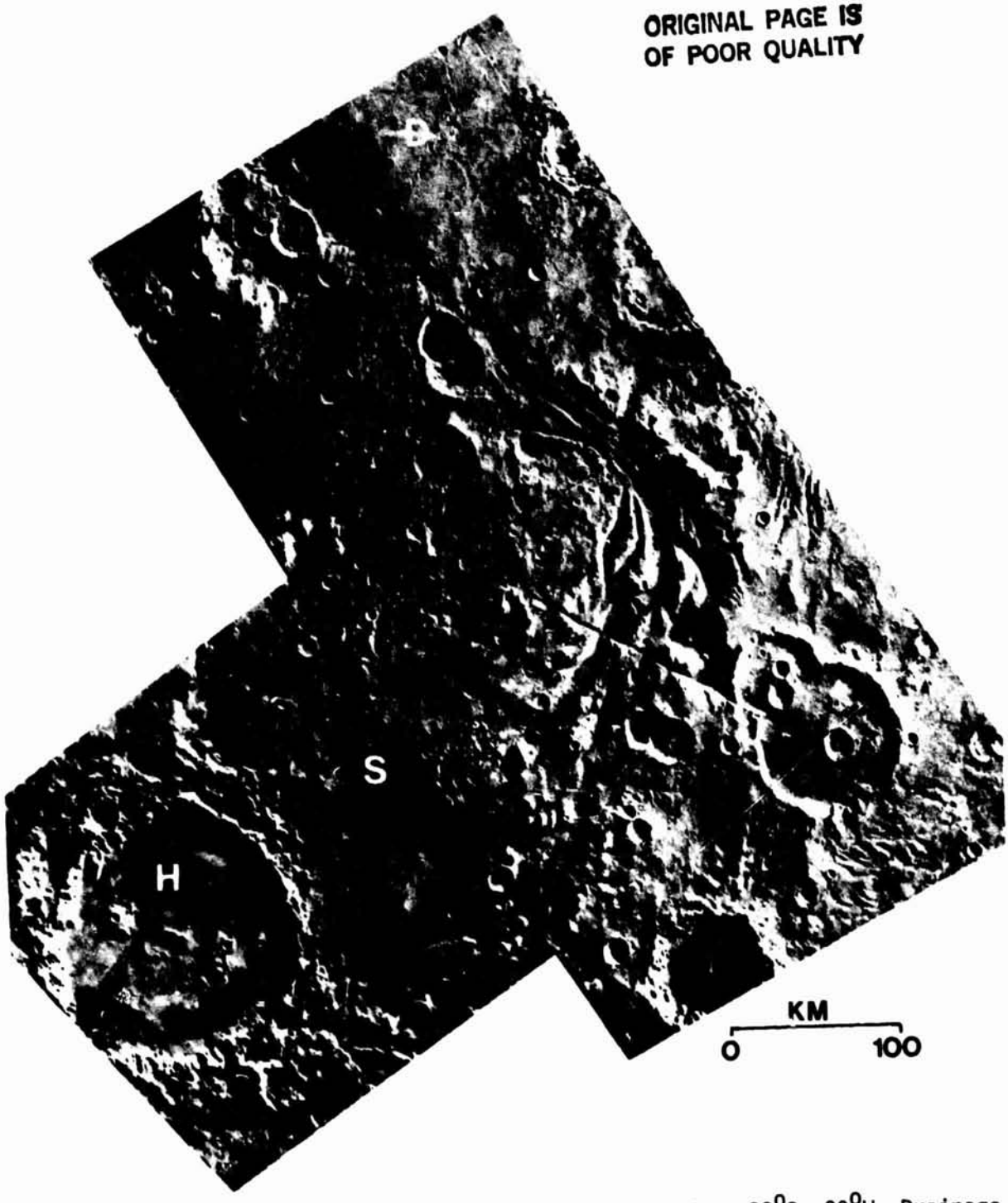

Figure 2. Ladon Valles and adjacent area centered on 22°S, 29°W. Drainage flowed from a late source area (S) to a depositional area in an ancient multi-ringed basin (D). The crater Holden (H) may have disrupted an older through-going drainage from the south (611A30, 650A18,19).

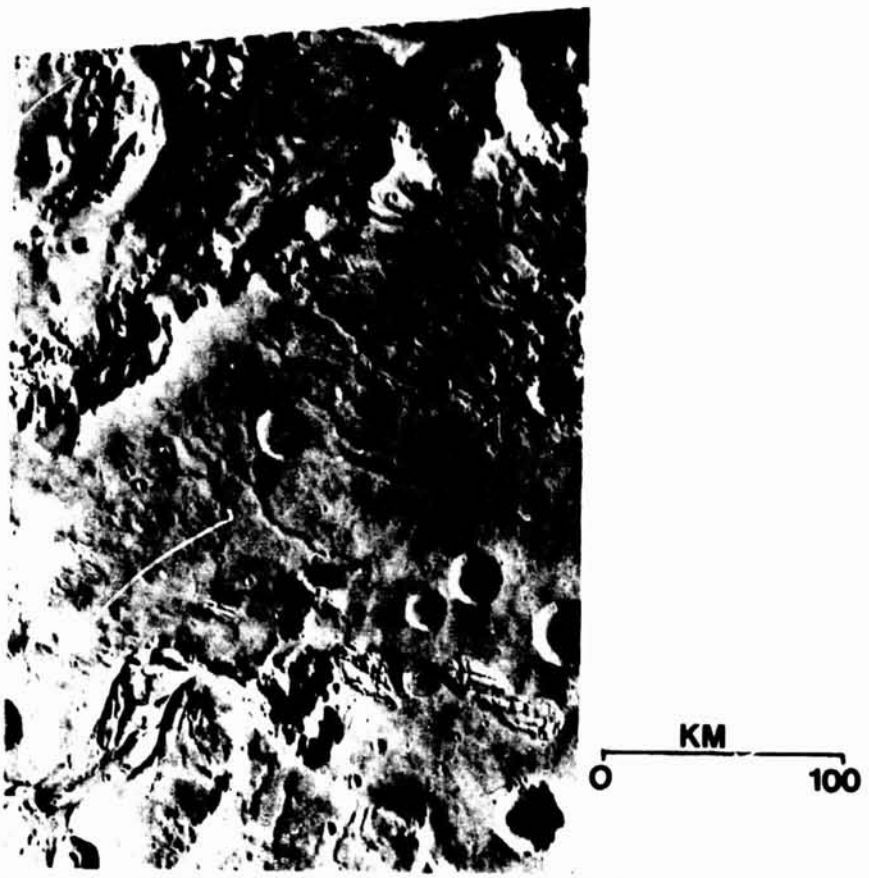

Figure 3. Area southeast of Eos Chasma centered on 13S, 38W. Degraded stem valleys are adjacent to fresher valleys and an unnamed outflow channel (top right). Paleoslope is from left to right. Osuga Valles (lower left) flowed north east through a ridged area into the depositional basin (365S84).

REFERENCES (Cont.)

Masursky, H., Boyce, J.M., Dial, A.L., Schaber, G.G. and Strobell, M.E., 1977, Classification and time of formation of Martian channels based on Viking data: Jour. Geophys. Res., v.82, No. 28, p. 4016-4038.

Pieri, D.C., 1980, Geomorphology of martian valleys: p. 1-160, in Advances in Planetary Geology, NASA Tech. Memo. TM-81979, 325 p.

Pieri, D.C., and Parker, T., 1981, Geologic mapping of martian valley systems I: Nirgal Vallis and vicinity: Reports of the Planetary Geology Program, 1981, NASA Tech. Memo 84211, p. 503.

Roth, L.E., DOwns, G.S., and Saunders, R.S., 1980, Radar Altimetry of south Tharsis, Mars: Icarus, v. 42, p. 287-316.

Saunders, R.S., 1979, Geologic map of the Margaritifer Sinus quadrangle of Mars: USGS Map I-1144 (MC-19).

Schultz, P.H., and Glicken, H., 1979, Impact crater and basin control of igneous processes on Mars: Jour. Geophys. Res., v. 84, No. B14, p.8033-8047.

CHANNEL DEPOSITS ON MARS

Moore, H. J., U.S. Geological Survey, Menlo Park, CA 94025

A search of Viking Orbiter photographs has revealed that some martian channels have associated deposits. The purpose of this abstract is to make the existence and locations of these channel deposits known to other workers (Table 1) and to briefly describe them.

The Amazonis channel deposits apparently have not been recognized previously. Fluids that carved the channels originated somewhere near the Equator from a vast expanse northwest of Apollinares and then flowed northeastward, where well-defined broad channels occur (fig. 1). These well-defined broad channels with streamlined islands can be traced northeastward from 180°W., 10°N., to 175°W., 12°-19°N., where they become partly filled. The channels disappear and the deposits become progressively thicker and more extensive to the northeast, where they terminate against mountains and as thick lobes and fronts. According to crater counts, these deposits may be younger than Olympus Mons.

Table 1. Locations of channels and channel deposits, crater ages of channels, and selected Viking Orbiter picture frames.

Channel Name	Location of Channel(s)	Location of Deposits	Crater Age N/km^2 ($D \geq 1$ km)	Selected Orbiter Picture Frames
Amazonis	10°N, 180°W	20°N, 175°W	$8(\pm5)\times10^{-5}$	583A77-80,96
	20°N, 175°W	29°N, 179°W		545A41-46,22
Elysium	28°N, 230°W	33°N, 237°W	$7(\pm3)\times10^{-4}$	612A44-56,21-24
	32°N, 236°W	37°N, 246°W		538A11,13; 239S09
Hrad	34°N, 218°W	41°N, 230°W	--	009B1-60
	41°N, 230°W	44°N, 240°W	--	
Kasei	29°N, 71°W	29.5°N, 71°W	--	555A10,12
Mangala	to south of deposits	6°S, 145°W	$<7\times10^{-4}$	460S19-22
				458S10-14
		4°S, 151°W	$>5\times10^{-4}$	459S15-18
				454S12-16
Harmakhis	39°S, 265°W	39.5°S, 267°W	--	408S74,76
	43°S, 273°W	41.0°S, 268°W	--	329S,330S,363S
				406S,407S

Elysium channel deposits could be extensive. Fluids that carved the channels probably issued from huge, elongate chasms radial to Elysium Mons such as the one near 223°W., 26°N. Nearby narrow deep channels coalesce to form a wide channel that distributes near 232°W., 31°N. The southern branch of these distributary channels becomes progressively filled by deposits that appear to overflow the channel locally, but evidence for the channel persists to 242°W., 37°N. The deposits terminate near 246°W., 37°N., as abutments against higher terrane and as lobes and fronts. The crater-retention age of these deposits is compatible with the age of the channels, according to my interpretation of the counts of Carr and Clow (1981), i.e. $1\pm0.8\times10^{-3}$ craters/km^2.

Dark deposits occur in and adjacent to Hrad Vallis south of the Viking Lander 2 site. In some places, the Hrad channels are filled with dark-appearing material in varying amounts up to the point of overflowing; in other places, overflow is indicated by dark levees, dark lobes that extend away from Hrad, and dark marginal plains. Dark deposits that abut against and are superposed as a lobe on the ejecta of crater Chincoteague appear to be related to the Hrad channel. In still other places, the Hrad channel appears to be free of deposits.

Demonstrable deposits created by overflows of Kasei Vallis are scarce, if they exist at all. One possible example is shown in picture frame 555A10, where thin lobes and sheets can be traced away from an arcuate "bayou" of the northern edge of Kasei. These sheets and lobes may represent an overflow of sediment laden-fluids. Farther upstream there are additional lobes that may be lavas from the general direction of Ascraeus Mons. Similar flow deposits may be present near the mouth of Joventa Chasma, near 58°, 63°, and 64°W., 5°N.

Channel deposits occur at the mouths of the Mangala Valles along with convincing examples of superposed lava flows. On the plains below the Mangala scarp, these smooth-appearing deposits have irregular shallow rimless depressions and steep, in some places leveed, margins where they border the scarp and valley walls. Near 150°W., 5°S., the smooth deposits can be traced upstream about 60 km; a second segment of the channel floor appears smooth as far as 8°S. In some places, wide leveed channels can be traced to the scarp, where they narrow, and onto a fanlike structure at the base of the scarp, where they widen again.

Deposits occur near the edge of the head of Harmakhis Vallis, where a partly leveed sheet, as much as 20 km wide, extends 50 km southward and narrows to 10 km. Other flowlike deposits, with flow units 10 km wide, converge from the east.

The origins of the deposits are puzzling. The intimate and gradational relation between the Amazonis channel and deposits, in combination with an absence of evidence for a volcanic source, suggest that the

deposits may be sedimentary--possibly mudflows or alluvial deposits peculiar to Mars. The same possibilities should be considered for the Elysium and Hrad channels, even though the source of the fluids and deposits appears to be the Elysium volcanic center. The deposits on the Mangala plains do not resemble the nearby lava flows from the Arsia region; perhaps the rimless depressions may be kettles and represent the sites of ice that has vaporized. The deposits of Harmakhis could be mud-flow deposits (Nummedal and Prior, 1981) or even glaciers (Lucchitta and others, 1981).

Whatever their possible origins, these deposits deserve further careful study.

References:

Carr, M. H., and Clow, G. D., 1981, Martian channels and valleys: their characteristics, distribution, and age: Icarus, v. 48, p. 91-117.

Lucchitta, B. K., Anderson, D. M., and Shoji, H., 1981, Did ice streams carve martian outflow channels?: Nature, v. 290, p. 759-763.

Nummedal, Dag, and Prior, D. B., 1981, Generation of martian chaos and channels by debris flows: Icarus, v. 45, p. 77-86.

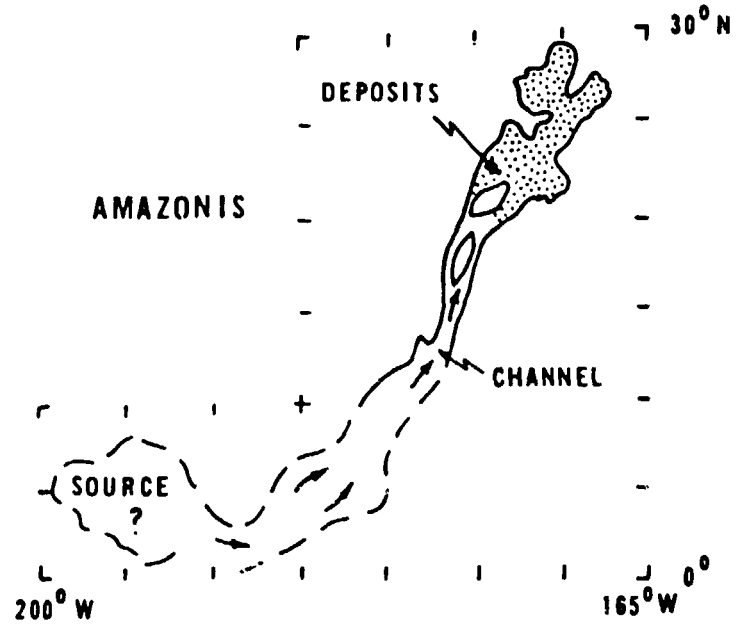

Figure 1. Map of Amazonis channel and deposits

MEANDER RELICS: EVIDENCE OF EXTENSIVE FLOODING ON MARS

David H. Scott - U.S. Geological Survey, Flagstaff, AZ 86001

Many morphologic features whose formation is commonly associated with running water also can be duplicated by other processes. On Mars this ambiguity has caused some controversy over the formation of channels (1). Although most planetary investigators now agree on the fluvial origin of the larger channels, there is less evidence and agreement on the extent of floodwaters into the plains beyond the immediate vicinity of channel mouths. Previous studies (2) indicated that alluvial channels within the Chryse basin extended farther into the northern plains than had been mapped. This work was based primarily on the recognition of scour and depositional features associated with the rapid and turbulent flow of water; their identification did not extend much beyond lat 30° N.

One characteristic that is probably unique to formation by running water is the meander pattern developed along the courses of mature streams and rivers. As rivers swing from side to side in flowing across their flood plains, meanders gradually migrate downstream as bends in their channels are eroded. Cutoffs are formed where erosion creates shorter courses, and eventually a pattern of abandoned meanders is marked by scars, scrolls, and oxbows on the flood plain.

Relict crescentic depressions that are nearly identical both in shape and size to meander patterns of terrestrial streams occur in Chryse Planitia (Fig. 1). These postulated meander scars are especially well developed along the lower course of Ares Vallis, where they are confined within the sculptured banks of the main channel. However, the increasingly subdued shape downstream of the walls of the channel as the meander remnants become more conspicuous suggests that slope gradients had decreased sufficiently to allow a less turbulent type of discharge as floodwaters spread out over the plains. In places, these presumed meander loops appear to terminate near the valley walls, where they may have been covered by slump material or debris flows. Elsewhere within the Chryse-Acidalia Planitia region, meander remnants have been buried more completely and do not show such well-developed forms. They generally can be recognized, however, by a narrow near-central ridge within the channel troughs, although such ridges do not occur in similar appearing crescentic troughs in the Cebrenia quadrangle (lat 45° N, long 185°). The origin of these medial ridges is uncertain; they may represent coalesced point bars along the inside bends of meander channels or elongate sandbanks down the middle of the channels, where there is less bottom turbulence. On terrestrial flood plains, scroll-like patterns of ridges form where shifting of meander flow channels has occurred.

It may also be that the channel ridges formed in a periglacial environment. Subsurface pore water migrates and accumulates mostly toward the lower-central part of an abandoned river channel. With decreasing temperatures after a warm period that induced flooding, encroaching permafrost would further concentrate the remaining pore water toward the channel center (Fig. 2). Eventual freezing and expansion of the water would

a b c

Fig.1 a - Ares Vallis (Viking frame 364A02). Meander scars (1), channels banks (2), streamlined erosional forms (3). Diagrams b and c show configurations of meanders in Ares Vallis and Missisippi river at same scale; arrows show direction of flow.

create an ice-cored ridge along the valley floor beneath a cover of alluvium. Highly elongate pingos occur in valley-floor sediment on Prince Patrick Island, Northwest Territories, Canada, where they may be related to freeze-thaw processes associated with invasion and retreat of the sea along low-lying areas (3).

Whatever the origin of the martian ridges, they appear to be diagnostic of meander channels in this region and thus afford a means of identifying fluvial channels from troughs created by tectonic and other processes. Their recognition as far as lat 45° N. in Acidalia Planitia suggests that water flooding was pervasive in the northern plains.

References:

(1) Carr, M. H. and Clow, G. D. (1981) Icarus 48, 91-117.
(2) Tanaka, K. L. and Scott, D. H. (1980) Proc. Third Colloquium on Planetary Water, 76-79.
(3) Embleton, C. and King, C. H. M. (1975) Periglacial Geomorphology, Halsted Press, 1-203.

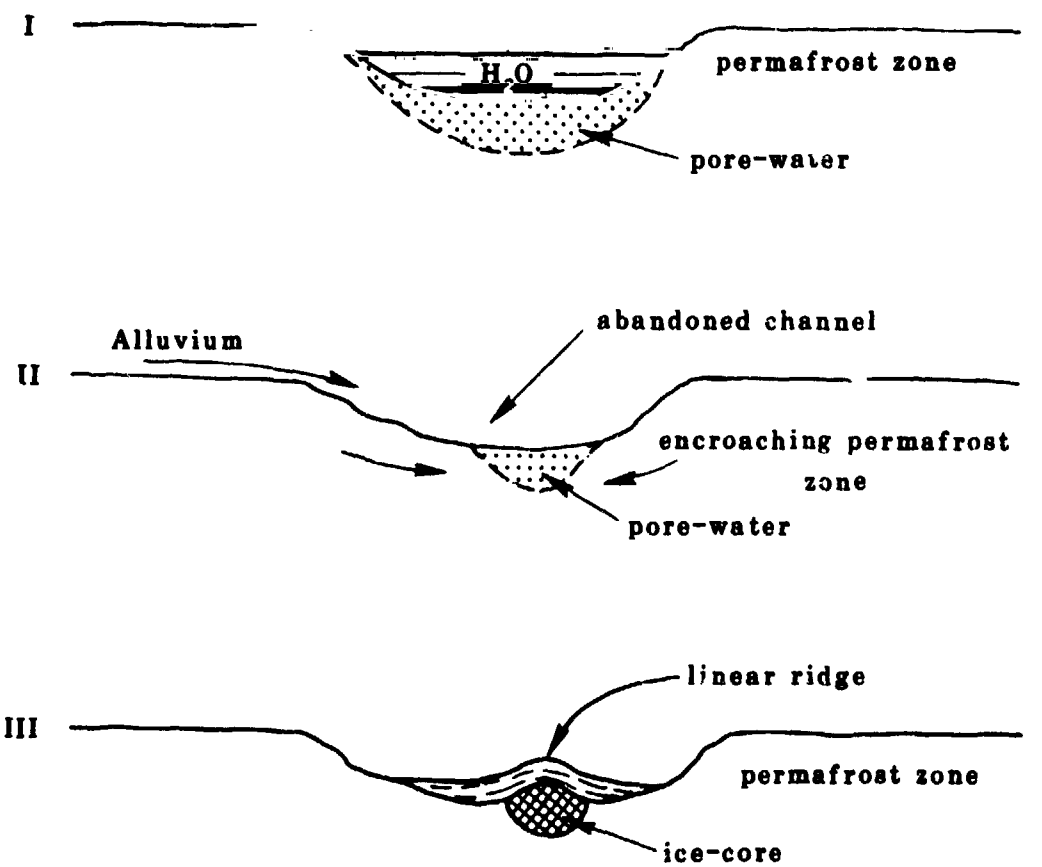

Figure 2 Stages in development of linear pingo ridges along channel floors

SPECTRAL ANALYSES OF MEANDERING CHANNELS ON EARTH AND MARS

Komar, Paul D., School of Oceanography, Oregon State University,
Corvallis, Oregon 97331

It is well established that the meandering characteristics of a river depend mainly on the discharge, several investigators having arrived at empirical relationships for the meander "wavelength" as a function of the discharge (Inglis, 1949; Leopold and Wolman, 1957; 1960; Dury, 1965; Carlston, 1965). The data upon which these relationships are based are highly scattered. Part of the reason for this may be the subjectivity of the measurement methods of the "wavelength" for a stretch of irregular river. According to Speight (1965; 1967), the traditional methods of measuring meander wavelengths are probably the most serious obstacle to progress in quantifying the meander relationships. This was a major factor in Speight's first turning to the spectral analysis approach in an attempt to obtain more reliable and repeatable evaluations of meander wavelengths.

Speight (1965) focused on the Angabunga River in New Guinea, a river which originates in a mountainous region where it is confined between rock walls but then passes through an alluvial plain where it has well developed meanders. Analyses were carried out for both courses. Speight (1967) continued the analysis of the Angabunga River, but also included a number of rivers in the Melbourne area of southern Australia in order to obtain data at different discharges.

In these studies a stretch of river is first digitized at equal increments of channel distance, the increment being on the order of twice the channel width. Rather than performing the spectral analyses directly on these measurements, due to the river doubling back it was instead necessary to analyze the angles made between successive segments of the river length. In spite of this the spectral analyses do yield evaluations in terms of wavelengths that dominate the "energy" or "intensity" of the meandering.

All of the spectra obtained by Speight are complex with many peaks, the dominant peaks representing wavelengths considerably longer than those

selected visually according to traditional approaches. The peaks in the spectra were found to be stable along the channel length, even up into the mountainous reaches where the channel would not normally be characterized as "meandering" although there was some tendency for organized irregularities. Speight was able to relate the wavelengths of the various peaks to the flow discharge, much as in the traditional analyses, but of course obtaining different relationships for the several peaks. His C peak, that with the third highest wavelength, corresponded most closely to the former empirical relationships such as that of Leopold and Wolman (1960). But in many cases this C peak appeared rather insignificant in the spectra in comparison with other peaks with greater energy.

Subsequent investigations that have employed spectral analysis techniques to study channel meandering are those of Toebes and Chang (1967), Chang and Toebes (1970) and Ferguson (1975). The spectra obtained by Chang and Toebes are similar to those of Speight (1965), but they were able to discern an influence from the local geology and soils as well as from the flow discharge and channel slope. Ferguson (1975) analyzed nineteen rivers in Britain. First performing spectral analyses on the angle changes as did Speight (1965), Ferguson did not obtain significant polymodal spectra as did Speight, attributing this to the complete dominance by high or infinite wavelengths caused by valley bends (which he did not filter out). Ferguson obtained improved spectra and better wavelength estimates by analyzing directional changes of the meandering channels, the differences between successive angles of channel directions rather than the angles themselves. This improvement results mainly from the new analysis approach eliminating the effects of large valley bends. However, the wavelengths obtained are still substantially larger than those determined by the traditional methods. Ferguson did find that the wavelength estimates correlated well with channel widths and river discharges, but were apparently unaffected by other variables.

These few studies using spectral analysis techniques to investigate channel meandering have left many issues unresolved. In some cases they even conflict in their final conclusions. Yet clearly the approach has promise, not only for the more rational selection of meander wavelengths

but also as a tool for more fully investigating meander properties. It was for this reason that the present investigation was begun. At present I am still in the initial stages of the study, examining the usefulness of filtering to remove the longer wavelengths and testing whether maximum entropy power spectrum methods will provide better results than Fourier analysis. My analyses to date have focused on the terrestrial rivers utilized by Leopold and Wolman (1957, 1960) in their classic examination of channel meandering. Their data form the basis of most of the standard empirical relationships for channel meandering, yet it is somewhat inconsistent with other data sets, so that it will be worthwhile to reexamine those rivers utilizing refined techniques. Once this has been accomplished and I feel more confident about our analysis procedures, and hopefully have learned more about the spectral characteristics of terrestrial rivers, I then plan to turn to the martian channels in an attempt to obtain quantitative comparisons with the terrestrial systems.

References

Carlston, C.W. (1965) The relation of free meander geometry to stream discharge and its geomorphic implications: Amer. Jour. Sci., v. 263, p. 864-885.

Chang, T.P., and G.H. Toebes (1970) A statistical comparison of meander planforms in the Wabash basin: Water Resources Res., v. 6, p. 557-578.

Dury, G.H. (1964) Principles of underfit streams: U.S. Geol. Survey, Prof. Paper 452-A.

Inglis, C.C. (1949) The behaviour and control of rivers and canals: Central Power Irrigation and Navigational Res. Station, Poona, India.

Leopold, L.B., and M.G. Wolman (1957) River channel patterns: braided, meandering and straight: U.S. Geol. Survey, Prof. Paper 282-B, p.37-86.

Leopold, L.B., and M.G. Wolman (1960) River meanders: Geol. Soc. Amer. Bulletin, v. 71, p. 769-794.

Speight, J.G. (1965) Meander spectra of the Angabunga River: Jour. Hydrol., v. 3, p. 1-15.

Speight, J.G. (1967) Spectral analysis of meanders of some Australasian rivers: in Landform Studies from Australia and New Guinea, eds. Jennings and Mabbutt, Canberra, Austrl. Nat. Univ. Press, p.48-63.

Toebes, G.H., and T.P. Chang (1967) Planform analysis of meandering rivers: Proc. 12th Congr. Int. Assoc. Hydraul. Res., v. 1, p. 362-369.

FLUME EXPERIMENTS ON THE FORMATION OF STREAMLINED ISLANDS

Komar, Paul D., School of Oceanography, Oregon State University,
Corvallis, Oregon 97331

Streamlined islands in rivers and comparable landforms in the Channeled Scabland of Washington and in the outflow channels on Mars have shapes that are closely similar to symmetrical airfoils with length to width (L/W) ratios of 3 to 4 on average (Baker, 1979; Baker and Kochel, 1979; Komar, 1981). Direct comparisons with drag measurements on airfoils have shown that these average L/W values correspond closely to the shape having the minimum total drag or resistance to the flowing fluid eroding the landforms (Komar, 1981; in review).

A series of flume experiments have been completed with model islands to examine how the prototypes achieved their streamlined shapes. The models were composed of mixtures of medium-grained sand with just enough clay to provide cohesive strength. In most of the experiments the islands initially were given a circular shape of about 15 cm diameter. A few experiments involved highly elongated islands with large initial length to width ratios. The experiments were conducted in the 7.6 meter long, 50 cm wide flume at Oregon State University.

One main variation between different experimental runs involved the flow depth in comparison with the island height. Evidence from the Channeled Scabland islands and those in the Martian outflow channels indicates that some islands were fully submerged during formation while others extended above the water surface. For this reason, the present experiments included runs for both conditions. Otherwise the main variable between runs was the flow discharge.

The figure illustrates the results obtained when the water depth was the same or slightly less than the initial island height. The discharge increases from left to right in the diagram, the vertical giving a time sequence of changes for each experiment. The discharge increase also represents a progressive increase in the island Reynolds number Re and the flow Froude number Fr, values being given in the figure. In this series of experiments the development of the streamlined form is due more

STREAMLINED ISLAND MODELS

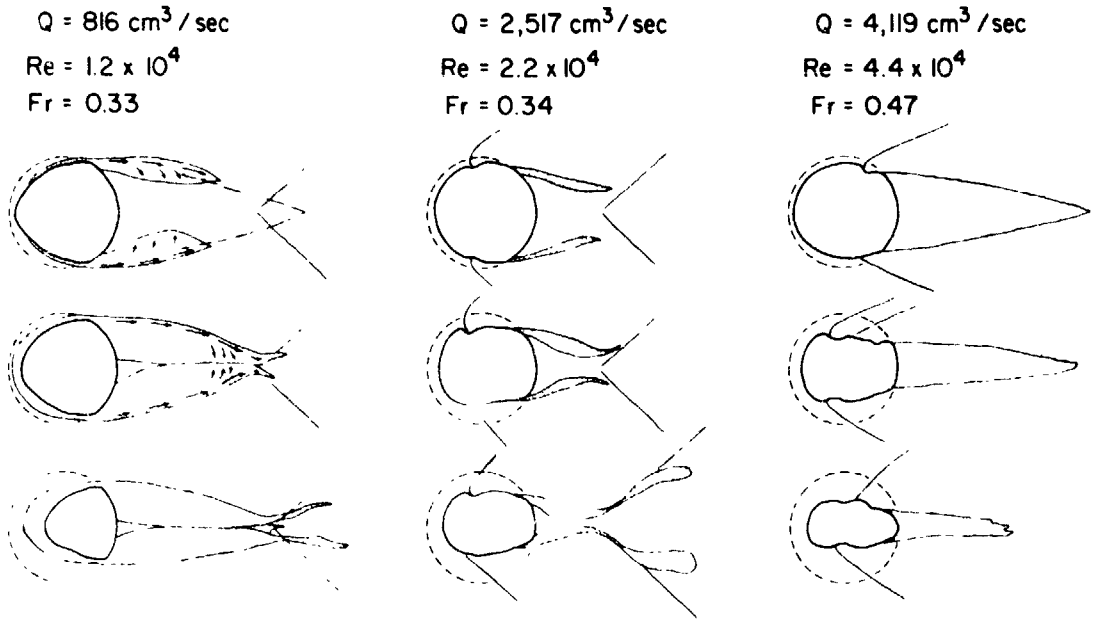

to deposition in the island's wake than to island erosion. This is especially the case at the lower discharges where the deposited sand completely filled in the wake region. At the intermediate discharge a strong V-wave in the island's lee diverted the sand movement, producing a rather unusual depositional pattern (see figure). At the same time, more intense oblique waves formed on the island's flanks and these became significant in eroding the island, the positions where these waves "attach" to the island being the focal points of maximum erosion. At the highest discharge these oblique waves were able to erode the island down to a streamlined shape, whereas the lee waves became less effective in diverting the sand movement. In these experiments notches tended to form at the "attachment" points of the oblique waves. I have been unable to conclusively identify such notches on the streamlined islands in the Channeled Scabland and in the Martian outflow channels.

The processes of streamlining are more effective and rapid if the island is slightly submerged, the water depth being just sufficient to "top" the island. Under such a circumstance the flow becomes

supercritical over the island due to the low flow depths and high velocities, producing a hydraulic jump along the island's lee. The hydraulic jump combines with the still-present oblique waves on the island's flanks to quickly erode away the sides and shape the lee into a point. The modification of the island form is at first very rapid, but as it approaches a streamlined shape the erosion rate declines so that the streamlined island can persist for a considerable time. At this stage the model island looks much like a miniature island from the Channeled Scabland, having length to width ratios in the range 2.4 to 3.0. In some of the experiments the oblique waves tended to focus the flow coming over the top of the island, producing a cross-over channel comparable to those described by Baker (1978) on the streamlined islands in the Channeled Scabland and also observed on islands in active rivers. Therefore, with the model islands only slightly submerged, in addition to developing good streamlining, they also duplicate other features seen on prototype streamlined islands.

References

Baker, V.R. (1978) Large-scale erosional and depositional features of the Channeled Scabland: in The Channeled Scabland, edited by Baker and Nummedal, NASA Planetary Geology Program, Washington, D.C. p. 81-115.

Baker, V.R. (1979) Erosional processes in channelized water flows on Mars: Jour. Geophys. Res., v. 84, n. B14, p. 7985-93.

Baker, V.R., and R.C. Kochel (1979) Martian channel morphology: Maja and Kasei Valles: Jour. Geophys. Res., v. 84, n. B14, p. 7961-83.

Komar, P.D. (1981) Streamlined islands: An analysis of their minimum-drag shape: Repts. of Planetary Geology Program – 1981, NASA Tech. Memo. 84211, p. 266-268.

Komar, P.D. (in review) The lemniscate loop – Comparisons with the shapes of streamlined landforms: submitted to Geol. Soc. Amer. Bulletin.

Komar, P.D. (in review) The shapes of streamlined islands on Earth and Mars: Experiments and analyses of the minimum-drag form: submitted to Geol. Soc. Amer. Bulletin.

GROUNDWATER SAPPING STUDIES

Alan D. Howard and Charles McLane, Department of Environmental Sciences, University of Virginia, Charlottesville, VA 22903

The role of groundwater sapping in the development of valley networks on Earth and Mars is being studied by a combination of experimental, theoretical, and simulation approaches:

Flow tank experiments: Extensive experiments have been conducted in a narrow groundwater flow tank of sapping processes in fine-grained sediments. A theoretical model of conditions for initiation of sapping erosion has been developed (Howard and McLane, 1981). Three zones occur in the flow tank experiments: 1) an interior zone with groundwater flow through the sediment with negligible erosion; 2) the sapping face, where a combination of gravitational forces and flow forces due to emergent groundwater control the rate of sapping; and 3) a zone of fluvial transport of sediment derived from the sapping face and channel bed erosion (Figure 1). The last two zones intergrade. Experiments to date indicate the following relationships among flow, geometric, and sapping-rate parameters:

q_s = sediment outflow (g/s)

q = discharge (g/s)

v = water viscosity (g/(s cm))

S = channel gradient (Fig. 1)

i = groundwater gradient (Fig. 1)

f = form ratio (Fig. 1)

R^2 = proportion of variance explained

$$q \propto i^{.32} f^{.56} v^{-.25} \qquad R^2=0.5$$

$$q_s \propto (i - i_c)^{1.09} S^{2.19}, \text{ where } i_c = 0.08 \qquad R^2=.70$$

$$S \propto q^{-.79} q_s^{.29} \qquad R^2=.70$$

These experiments confirm the linear relationship between sapping rate and the excess hydraulic gradient ($i-i_c$) reported previously (Howard and McLane, 1981). Additional experiments now underway are investigating the effects of particle grain size and sorting upon these relationships.

Numerical modelling of flow conditions: Two characteristics of our experiments make numerical simulation of the flow conditions near the sapping face essential. Firstly, the sapping rates are determined by flow conditions at the sapping face, which can be considerably different than the overall flow gradients. Secondly, because of the interaction between channel and sapping processes, the experiments are inherently transient. Finite-element groundwater flow models are being used to calculate the detailed flow net and are being compared with extensive piezometric measurements made

during the experiments.

Analogue experiments: A series of experiments on valley development will be conducted in a small chamber (about 1' x 4' x4') under a wide-range of boundary conditions, with a wide range of materials, and with additional processes considered, such as freeze-thaw. These experiments will be a continuation of those already conducted by Craig Kochel (this volume) and will be made in collaboration with Mr. Kochel. These experiments will investigate the effects of such factors as wide variations in flow gradients, substrate inhomogeneities (such as layering and simulated craters), and freeze-thaw effects upon valley network geometry developed by sapping.

Simulation modelling: Sapping processes are presumed to lead to development of dendritic valley networks by a process of "groundwater capture" in which an extending network gains a competitive advantage by virtue of the high-gradient flow path to the head of the eroding stream. The flow-tank experiments reported above demonstrate the competitive advantage of sapping faces with short flow paths (high hydraulic gradients). This process should be amenable to simulation modelling, and such a model is presently being developed. The experiments in non-cohesive sediments will serve as a test of the model, which can then be extended to arbitrary flow geometries and for different assumed processes of groundwater sapping to investigate their effects upon valley development.

References:

Howard, A.D. and McLane (1981), Groundwater sapping in sediments: Theory and experiments: NASA Tech. Mem. 84211, p. 283-285.

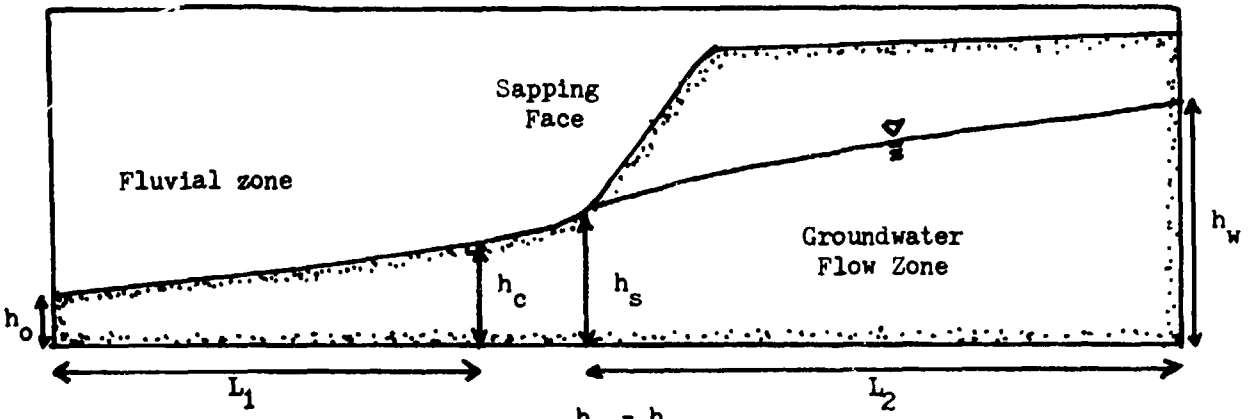

$$i = \text{hydraulic gradient} = \frac{h_w - h_s}{L_2}$$

$$f = \text{form ratio} = \frac{h_s}{L_2}$$

$$S = \text{channel gradient} = \frac{h_c - h_o}{L_1}$$

Figure 1. Geometrical definitions for flow tank experiments.

SURFACE CHANNEL NETWORKS DEVELOPED BY GROUNDWATER SAPPING IN A LABORATORY MODEL: ANALOGY TO SAPPING CHANNELS ON MARS

R. Craig Kochel, Department of Environmental Sciences, University of Virginia, Charlottesville, VA 22903, Victor R. Baker, Department of Geosciences, University of Arizona, Tucson, AZ 85721, David W. Simmons and Carl J. Lis, Department of Geology, State University College, Fredonia, NY 14063

Crudely dendritic channel networks in many areas of Mars have been interpreted as having been produced by groundwater sapping processes. Investigations of the morphology of terrestrial channel networks created by groundwater sapping processes is limited because of modification of these systems by overland flow. Howard and McLane (1981) discussed groundwater flow theory applied to a two-dimensional model. Our experiments with a three-dimensional sapping chamber were designed to empirically investigate valley morphometry in channel systems formed by groundwater sapping and compare these to presumed sapping networks developed on Mars.

A mixture of 90% 2.25Ø fine sand and coal fly ash was used as a sedimentary medium in a sapping box constructed from marine plywood and sealed with roofing tar (Fig. 1). A constant head was maintained throughout the experimental runs by using a reservoir in the rear of the tank (Fig. 1). Before each of 23 runs the box was drained, regraded, and a new slope recorded. Time zero was taken as the time when sapping was first observed at the surface somewhere along the slope. Once channels were initiated headward and lateral extension occurred by sapping at the base of channel walls and subsequent collapse. The average duration of sapping runs was about 100 minutes.

In most cases an initial escarpment of 2 to 5 cm was cut near the slope base prior to the run. Once sapping was initiated a period of rapid ascarpment retreat and channel extension occurred for 15 to 60 minutes (Fig. 2). After the adjustment period, sapping processes caused escarpment retreat by slumping but at a much reduced rate (Fig. 2). Major sapping channels formed with regular inter-channel spacing. Channels enlarged most rapidly in the reentrant areas of major escarpment slumps where subsurface flows bacame concentrated. Channel bifurcation occurred and tributaries appeared to extend headwardly at similar rates (Fig. 2). Subsurface piracy was common (Fig 2, Run 16) during later stages of network development. The channels formed were steep-sided, flat-floored, and terminated in blunt, amphitheater heads similar to presumed sapping channels on Mars. Temporal and spatial development of sapping channel networks was recorded by tracing channel patterns at selected time intervals on a transparent frame mounted above the sand surface (Fig. 2).

Morphometric parameters were calculated for 69 channel networks formed in the sapping box and compared to 70 sapping

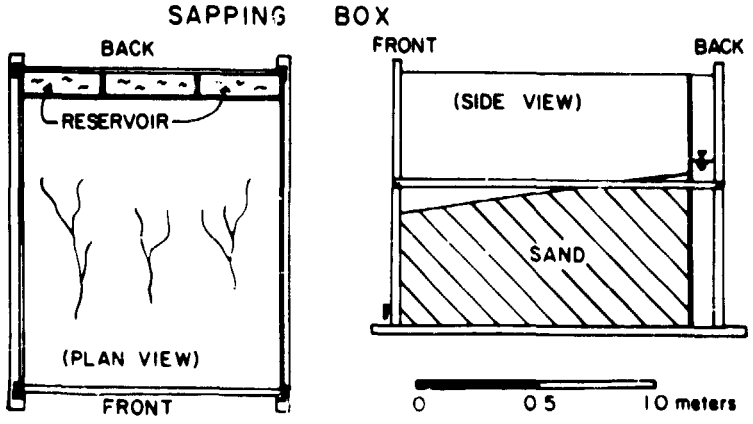

Figure 1. Schematic of the experimental sapping box.

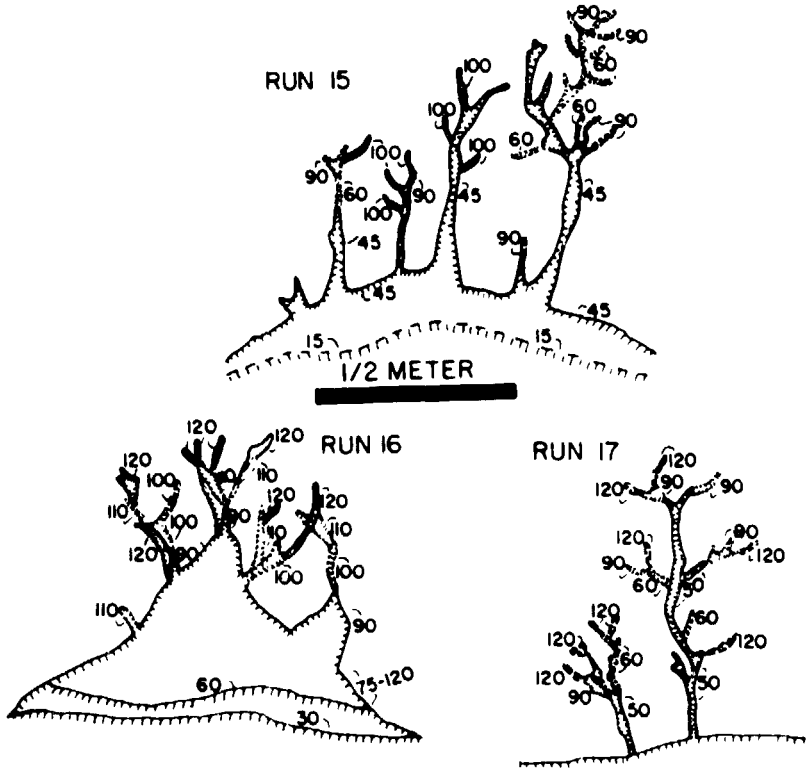

Figure 2. Examples of surface channel patterns developed by groundwater sapping in the sapping box. Numbers indicate time in minutes from the onset of sapping at the surface.

channel networks observed in Viking imagery of the Valles Marineris and western Kasei Vallis regions of Mars (Table 1).

TABLE 1 MORPHOMETRIC PARAMETERS OF SAPPING VALLEYS

MEANS OF LINEAR MORPHOMETRIC PARAMETERS

	n samples	Channel Length 1:2	1:3	2:3	Shreve Magn.	Bifurcation Ratio.	Interchannel Ratio
SAPPING BOX	69	1.13	1.36	1.20	4.45	2.28	60
MARS	70	1.35	1.69	1.18	4.89	3.32	64

MEANS OF AREAL MORPHOMETRIC PARAMETERS

	n samples	First Order Frequency	Shape k	Drainage Density	Junction Angles
SAPPING BOX	69	$0.05/cm^2$	2.18	$0.27cm/cm^2$	42.3^c
MARS	70	$0.01/km^2$	2.12	$0.15km/km^2$	51.3^c

Space limitations preclude a detailed discussion of the comparative morphometries of Martian sapping channels and those developed in the sapping box experiments. However, several similarities are readily apparent. Sapping channel systems on Mars and in the sapping box exhibit some degree of organization to their spatial occurrence manifest by the regular interchannel distance along the basal escarpments. This spacing is about 20 km on Mars and about 9 cm in the sapping box (Fig. 2). This organization is also apparent in the dimensionless interchannel spacing ratio (lateral escarpment distance divided by the average interchannel spacing). Channel networks on Mars and in the box have similar channel length values. Junction angles developed by sapping processes averaged 40 to 50 degrees. Lubowe (1964) showed that junction angles in 1st, 2nd, and 3rd order dendritic terrestrial stream networks averaged 60 to 85 degrees.

Our next series of experiments will attempt to integrate a quantitative monitoring of flow conditions and look at surficial morphologies developed in varied sedimentary media and environmental conditions.

References:

Lubowe, J.K., 1964, Stream junction angles in the dendritic pattern: Amer. J. Sci., v. 262, p. 325-339; Howard, A.D., and McLane, C., 1981, Groundwater sapping in sediments: Theory and experiments: N.A.S.A. Tech. Mem.84211, p. 283-285.

GEOMORPHIC MAPPING OF MANGALA VALLIS, MARS

R. Craig Kochel, Dept. of Environmental Sciences, University of Virginia. Charlottesville, VA 22903, Cassandra J. Runyon, Dept. of Geology, Southern Illinois University, Carbondale, IL 62901, and Victor R. Baker, Dept. of Geosciences, University of Arizona, Tucson, AZ 85721

Mangala Vallis is one of the large outflow channels on Mars carved by enormous volumes of northerly-flowing fluids. Mangala Vallis occurs at longitude 153° and extends from -10 to -4° south latitude. The channel bifurcates into two distributaries before terminating in the Amazonis Planitia basin (Figure 1).

Geomorphic mapping of Mangala Vallis followed the format of Baker and Kochel (1979) and is shown in Figure 2. It is apparent that the hilly and cratered host terrain has been extensively modified by catastrophic fluvial flow(s) and was later subjected to post-diluvial modification processes. Table 1 summarizes the comparative geomorphology of Mangala, Maja, and Kasei Vallis. Mangala Vallis most closely resembles Maja Vallis. Their geomorphic similarities may be largely due to similarities of host terrain materials in which these channels were eroded, i.e. hilly and cratered terrain. Unlike the Kasei Vallis channel developed in lunae planum material, Maja and Mangala show minor post-diluvial modification of channel walls. These differences are probably due to contrasting behavior of different ground-ice and regolith character between the two host terrain types. The absence of extensive fracture systems in the region of Maja and Mangala Vallis relative to Kasei Vallis also indicates contrasting regoliths and/or structural histories. Channel floor bedforms developed in Mangala are similar to those described in Kasei and Maja Vallis (Baker and Kochel, 1979) with the exception of a sinuous flat-topped mesa in the eastern part of the study area (Fig. 1, site 5; Fig. 2, site IR). This feature may represent the former floor of a valley filled with some resistant material such as lava. The lava may have acted like a caprock causing relief inversion. Eolian deposits and landforms are more significant in Mangala Vallis than in Kasei or Maja Vallis. Crater streaks are abundant as are large areas of low-relief eolian mantles in some breached craters and protected channel floors. Large dune fields also occur at the mouths of the two Mangala distributaries and may represent reworked fluvio-deltaic sediments.

References:

Baker, V. R., and Kochel, R. C., 1979, Martian channel morphology: Maja and Kasei Vallis: J. Geophys. Res., v. 84, p. 7961-7983.

TABLE 1 -- GEOMORPHIC COMPARISON OF OUTFLOW CHANNELS

GEOMORPHIC FEATURES	KASEI VALLIS	MAJA VALLIS	MANGALA VALLIS	FIG 1	FIG 2
Host Terrain	lunae planum	hilly and cratered terrain		1	HC
Channel Pattern	alternating zones of divergence/convergence				
Channel Floor					
Long. grooves	abundant	common	abundant	2	
Streamlined hills	abundant	abundant	abundant	3	SH
Obstacle scour	abundant	common	abundant		
Crater breaches	rare	abundant	abundant	4	
Cataracts	common	rare	rare		
Inverted relief			common	5	IR
Terraces	common	common-rare	common	6	T
Eolian Deposits	crater streaks common	crater streaks minor	crater streaks dune fields	7	D
Post-diluvial	extensive	minor	minor		
Wall Modifications	debris fans, aprons, flows talus	talus slumps debris	talus slumps sapping	8	S
Chaotic Terrain	rare		common-rare	9	CdT
Fracture Systems	abundant	rare	rare		

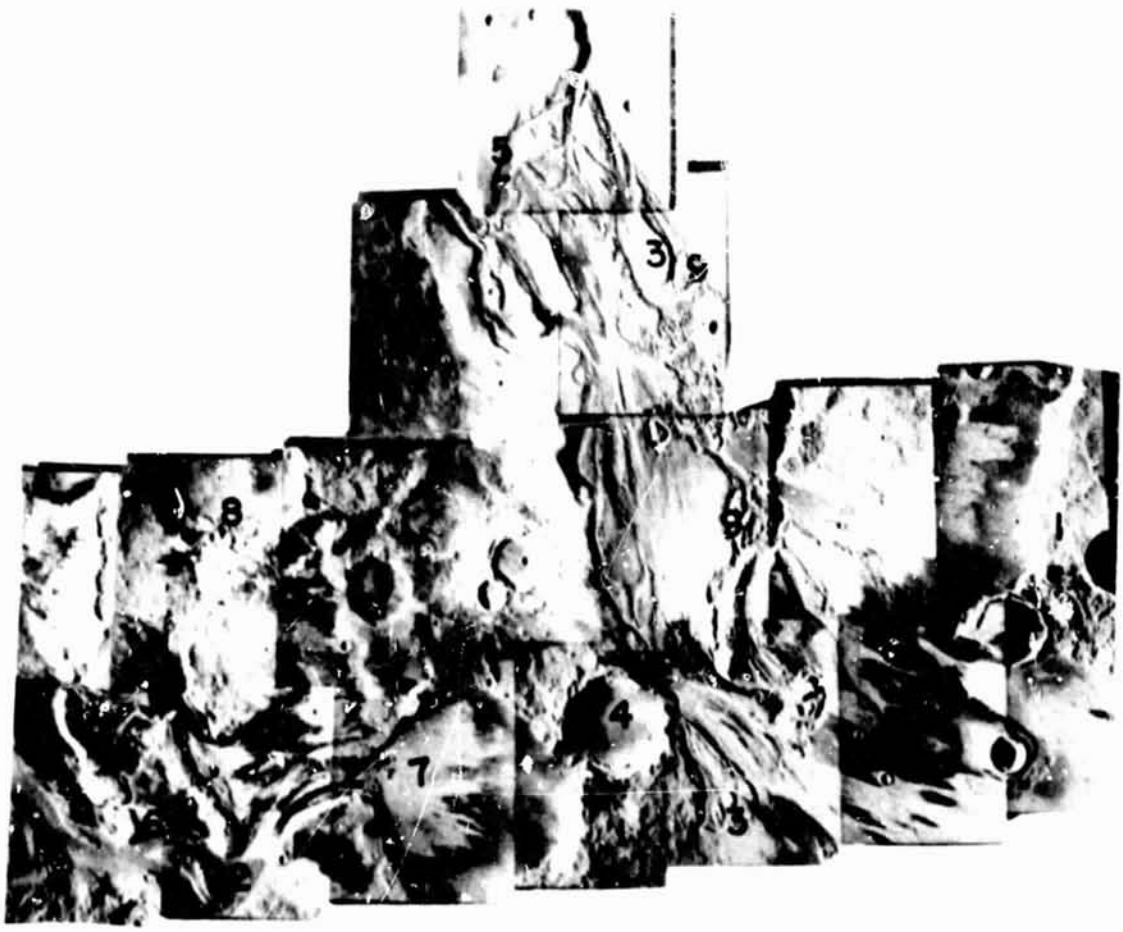

Figure 1. Viking orbiter photomosaic of part of Mangala Vallis (frames 451S17-35). Sites are referred to in Table 1.

Figure 2. Geomorphic map of Mangala Vallis. HC=hilly and cratered terrain, SH=streamlined hills, CHg=channel floor, T=terraces, D=dunes and eolian mantle, P=plains in hilly and cratered terrain, PC=craters with rims breached by floods, C1=fresh, young crater, C2=older crater, indistinct rim, C3=crater modified but not breached by floods; SW=possible slackwater deposit.

LAKES OR PLAYAS IN VALLES MARINERIS

B. K. Lucchitta, U.S. Geological Survey, Flagstaff, AZ 86001

Layered materials in Valles Marineris, which were first recognized on Mariner 9 pictures, were attributed to deposition in lakes (1). Moderate- and high-resolution Viking images, some with stereoscopic coverage, now permit a critical evaluation of this hypothesis. These new images clearly show that the layered materials are interior deposits and not erosional remnants of formerly more extensive plateaus. The interior materials are finely and evenly layered, whereas the walls of the plateaus are not. Overlap of the highly eroded interior remnants of the plateau by the layered materials indicates that these layered materials postdate the plateau rock and extensive erosional activity. Both deposits differ in erosional aspects: the slopes of the layered materials are dissected into numerous parallel gullies and show few landslides, whereas the wallrock is characterized by anastomosing spurs and gullies with many landslides. Also, unlike the wallrocks, the interior deposits are highly susceptible to wind erosion; thus they are probably less well indurated and differ in composition.

Evidence from Viking images also supports a sedimentary depositional origin associated with water. The fine and even bedding in the layered materials is consistent with emplacement in playas or lakes; turbulent winds associated with the rugged relief of Valles Marineris are unlikely to have created such even bedding. Also, similarly layered wind deposits would then occur on the surrounding plateau, but they do not. If the interior deposits were former polar deposits, as suggested for layered deposits elsewhere in the equatorial area (2), they should, again, not be restricted to the troughs. However, the volume of the interior deposits appears to be larger than that of materials eroded from the trough walls, many of which are fault scarps; the additional materials are probably from volcanism inside the troughs (3).

Involvement of water in the deposition of the interior beds is also suggested by relative-elevation data (4). The position of the highest points of the interior deposits about 2,000 m below the plateau rims indicates that slopes existed toward the interior. Even though the floor elevations of Ophir and Candor Chasmata differ by as much as 4,000 m, the fact that the contained beds reached similar elevations strongly suggests fluvial deposition at a common base level. The physical resemblance of the interior beds to basin beds in fault troughs of the Basin and Range province of the American West also supports deposition of these martian beds in lakes or playas.

Runoff from the surrounding plateaus, in addition to sapping, may have contributed water and sediment to former lakes in Valles Marineris. Generally, tributary canyons to the troughs lack visible drainages above the canyon heads, and they presumably eroded headward by sapping (5). However, debouchment of integrated valley networks from the Sinai Planum plateau into tributary canyons south of Ius Chasma suggests that runoff from the plateaus played a significant role in some places. Other such valley networks may have existed elsewhere but now are not recognized because they were poorly developed in the resistant lavas that cap the plateaus, and were later buried by wind deposits.

A difference in wall morphology between old and young wall segments of Valles Marineris suggests that a climatic change took place during development of the walls and that old wall segments developed during a fluvial epoch. Old wall segments, characterized by spur-and-gully morphologies, occur on the upper part of the fault scarps that form the walls, whereas young wall segments, characterized by smooth talus slopes, occur on the lower part of the same fault scarps; the transition between these two wall types is abrupt. Also, all young landslide scars are smooth walled and do not show transitional forms to spur-and-gully morphologies. The old spur-and-gully type of wall dates back to the time of valley-network formation on Mars and thus is linked to an epoch of fluvial activity. Because interior deposits are associated with the spur-and-gully morphology, they also belong to the older fluvial epoch. This association supports the hypothesis that the interior deposits were emplaced by water.

Spur-and-gully morphology may be an erosional style that develops preferentially in a subaqueous environment. Radio-echo sounding on the Earth reveals remarkably similar erosional forms on the walls of submarine canyons. This similarity suggests that the spur-and-gully morphology on Mars developed in deep bodies of water that filled Valles Marineris, although the resemblance of many subaerial erosional forms on Mars to subaqueous forms on Earth weakens the argument.

Circumstantial evidence also supports the idea that Valles Marineris may have contained lakes or were filled to high levels by deposits from ephemeral lakes and playas. The headwaters of Simud Vallis once extended into Valles Marineris. The present floor gradient on Simud Vallis between Valles Marineris and the Chryse Basin is virtually flat, and movement of water through the valley would have been difficult. Flow would have been greatly facilitated if Valles Marineris were once enclosed and formed lakes that eventually overflowed at high spillway levels, and thus provided the necessary gradient for Simud Vallis. Breaching of the containing dam by headward erosion along the ancestral Simud Vallis could have caused a gigantic flood that created the necessary gradient and gave Simud Vallis its present configuration.

None of the above observations alone conclusively demonstrates that lakes or playas ever existed in Valles Marineris, but altogether the evidence is highly suggestive. Therefore, the early hypothesis (1) is supported by more detailed observations. Valles Marineris once, during a more fluvial epoch on Mars, probably contained water in permanent or ephemeral lakes, and received sediment that was deposited in the interior.

References

(1) McCauley, J. F. (1978) U.S. Geol. Survey Misc. Inv. Map I-897, scale 1:5,000,000.
(2) Schultz, P. H. and Lutz-Garihan, A. B. (1981) Lunar and Planet. Sci. XIII, 946-948.
(3) Lucchitta, B. K. (1981) NASA Tech. Memo 84211, 419-421.
(4) Wu, S. S. C., Schafer, F. J., and Jordan, R. (1980) NASA Tech. Memo 82385, 453-461.
5) Sharp, R. P. (1973) J. Geophys. Res. 78, 4063-4072.

PREFERENTIAL DEVELOPMENT OF CHAOTIC TERRAINS ON SEDIMENTARY DEPOSITS, MARS

B. K. Lucchitta, U.S. Geological Survey, Flagstaff, AZ 86001

Chaotic terrains on Mars are characterized by polygonal fracture systems, angular mesas, and rounded hummocks arranged disorderly in irregular hollows, circular depressions, or at the base of scarps. Sharp (1) ascribed the origin of chaotic terrains to possible collapse through the degradation of ground ice. Here, I examine the proposition that some chaotic terrains are associated with fluvial depositional centers and suggest that chaotic terrains may have developed preferentially on sedimentary deposits.

Polygonally fractured ground occurs in several low areas (2) in Valles Marineris. One such area is in the center of Candor Chasma, where outwash from landslides apparently converged and pooled (3). The deposit from this former pool has a level surface, embays the surrounding terrain, and has a surface texture of irregular plaques and hummocks traversed by numerous cracks. Two other, smaller low spots in East Candor Chasma show a similar surface texture. These observations suggest that sediment deposited in ponded water on Mars may yield surfaces that are traversed by cracks and broken into plaques and hummocks similar to chaotic terrains.

Chaotic terrains are also associated with fluvial activity elsewhere on Mars. In Margaritifer Terra (MC-19 SE), several valley networks, including Paraná Vallis, drain toward a regional low; this depression is occupied by deposits with chaotic arrangements. Chaotic terrain occurs where Nirgal Vallis debouches into Holden Vallis (4), where Mawrth Vallis empties into the Chryse Basin, and where Ma'adim Vallis enters a crater. These observations suggest that deltaic or fan deposits formed locally along the course of martian valleys and that such deposits favored the development of chaotic textures.

Other depressions on Mars contain chaotic terrains. Three large circular lows in Sirenum (MC-24 NW) contain materials that have chaotic arrangements. These depressions are probably ancient crater scars that were filled with sediment from local runoff. Volcanic activity in this region (5) may have contributed to the release of water from the ground or from emanated volatile materials. Here, as in Valles Marineris, there appears to be an association between depositional centers and the eventual development of chaotic terrains.

The main area of chaotic terrains on Mars lies in Margaritifer Sinus, where it occupies the regional low between the Tharsis uplift to the west and the martian cratered highlands to the east. Carr (6) suggested that subterranean aquifers emerged and formed springs in this low area, and Boothroyd (7) discovered that ancient valley networks converged on this low, where they may have coalesced to form trunk streams ancestral to the present outflow channels. These observations support the view that the present chaotic terrain may lie on a former flood plain and its water-saturated sediment. Chaotic terrains also occur in many places along the north highland boundary; there, also, they may have formed on the deltas or flood plains of some of the ancient valleys that flowed toward the low area of the northern plains.

In summary, the association of chaotic terrains with apparent former fluvial activity and ponding suggests that sedimentary deposits may have been favored materials for the eventual development of chaotic terrains. The reason for this may be threefold. [1] Cracking upon freezing or drying of water-saturated materials may have led to the typical polygonal structures; [2] segregated ice masses may have formed in the fluvial sediment, which has grain sizes that favor the development of segregated ice (sand and gravel furnish the needed aquifers, and silt is most susceptible to the massive growth of ice); and [3] degradation of the segregated ice masses led to eventual collapse of the ground.

References

1) Sharp, R. P. (1973) J. Geophys. Res. 78, 4073-4083.
2) Wu, S. S. C., Schafer, F. J., and Jordan, R. (1980) NASA Tech. Memo 82385, 458-461.
3) Lucchitta, B. K. and Ferguson, H. M., Proc. Lunar Planet. Sci. Conf. XIII, in press.
4) Pieri, D. C. (1981) NASA Tech. Memo 84211, 503.
5) Scott, D. H. and Tanaka, K. L. (1981) Proc. Lunar Planet. Sci. Conf. 12B, 1449-1458.
6) Carr, M. H. (1979) J. Geophys. Res., 84, 2995-3007.
7) Boothroyd, J. C. (1982) NASA Tech. Memo, in press.

Modification of Martian Fretted Terrain

Dean B. Eppler and Michael C. Malin, Department of Geology, Arizona State University, Tempe AZ 85287

Fretted terrain is one of several lowland landscapes found on Mars that suggest intense geomorphic activity. First described by Sharp (1), subsequent studies have concentrated on description and classification (2), age relationship (3,4), and mechanisms and vigor of modification processes (3, 5,6,7). This study is concerned principally with the temporal, material, and environmental constraints that can be placed on the modification of fretted terrain by, in particular, the formation and maintenance of reasonably smooth surfaced, convex, lobate aprons that surround high standing mesas and occur at the base of many scarps.

Measurements of apron width perpendicular to the superjacent scarp, scarp height above the apron, and scarp azimuthal orientation, as well as crater counts, were performed in Deuteronilus Mensae on 52 aprons and associated plains and highland units. Flow width shows no particular relationship to scarp height, nor do high scarps have preferred orientations. The clustering of scarp heights does imply, however, detectable layering in the materials underlying the upland surface. There is a strong suggestion of a correlation of average apron width with orientation: those between N75°E and N165°E are wider than those at other azimuths. We will return to this observation shortly. Aprons have few, if any, superimposed impact craters (5). Surrounding terrains have a more normal compliment of such craters. From this it may be inferred that: 1) the aprons are young with unmodified surfaces, 2) the aprons are young with surfaces modified by young or on-going processes, or 3) the aprons are old but with surfaces modified by young or on-going processes. In each case, however, we appear to be dealing with relatively recent (perhaps contemporary) process(es).

Material factors must also be considered when evaluating potential candidates for mechanisms of degradation. The distinct change in landform character from scarp to apron implies a variation in material. Possible explanations for the observed relationships include, alternatively, aprons made of coherent bedrock, coherent fragmental debris, or unconsolidated fragmental debris. The fragments could be coarse, fine, or mixed. Each of these alternatives implies certain properties and emplacement histories, yet to choose one is not possible at present. Examination of IRTM high resolution observations may permit this problem to be resolved.

Environmental factors, including temperature, atmospheric pressure, and the abundance of H_2O in solid or liquid form, are, intuitively, extremely important to the evolution of fretted terrain, though this is by no means proved. The current conditions do not permit liquid water in the near surface materials (8,9), although climatic changes induced on 10^5 yr timescales by astronomical perturbations may produce conditions allowing but not necessarily ensuring the presence of liquid water (10). The presumed importance of liquid water to apron formation rests principally on the ability of many processes, relying on water-related erosion and transport, to create landforms similar to those seen in fretted terrain. The relationship between scarp azimuthal orientation and apron width suggests a possible link between rapid morning temperature changes and apron forming processes. Processes of planation operating on bedrock, or mass movement

phenomema, particularly debris avalanches, flows, or creep, seem most likely responsible for the aprons in the fretted terrain. It is most probable that these processes are active during periods of high obliquity, and may now be less active or inoperative.

References:

1. Sharp, R. P. (1973) J. Geophys. Res. 78, 4073-4083.
2. Eppler, D. B. and Malin, M. C. (1981) Lunar Science XII (Abstr.) 260-261.
3. Malin, M. C. (1976) Ph.D. Dissertation, Calif. Inst. Technology, Pasadena, CA 91125, 176 p.
4. Arvidson R. and Coradini, M. (1975) Trans. Am. Geophys. UN (EOS) (Abstı), 56, 1014.
5. Carr, M. H. and Schaber, G. G. (1977) J. Geophys. Res., 82, 4039-4054.
6. Squyres, S. W. (1978), Icarus, 34, 600-613.
7. Squyres, S. W. (1979), J. Geophys. Res., 84, 8077-8076.
8. Kieffer, H. H., Martin, T. Z., Peterfreund, A. R., Jakosky, B., Miner, E. D. and Palluconi, F. D., (1977) J. Geophys. Res., 82, 4249-4292.
9. Palluconi, F. D. and Kieffer, H. H., (1981), Icarus, 45, 415-426.
10. Toon, D. B., Pollack, J. B., Ward, W. Burns, J. and Bilski, K. (1980) Acarus, 44, 552-607.

POSSIBLE EVIDENCE OF HYDROCOMPACTION WITHIN THE FRETTED TERRAINS OF MARS

D. Weiss, and J. J. Fagan, Department of Earth and Planetary Sciences, City College of CUNY, New York, N. Y. 10031

Many researchers have been concerned about the erosional history and maintenance of the Martian Highlands-Lowlands boundary in the vicinity of the fretted terrain of the Deuteronilus Mensae. The geomorphic development of this north-facing front and its associated valleys, channels, and outliers was originally described by Sharp (1) as being the result of undermining caused by the evaporation of ground ice exposed at the escarpment face or by groundwater emerging at the foot of the escarprment. Squyres (2) proposed that the removal of debris produced by the receding escarpment could be accomplished by aeolian deflation after weathering or by fluvial transport under different climatic conditions than those presently active on Mars.

The presence of debris aprons at the base of many valley and outlier escarpments were described by Squyres (2) as being lobate with a distinct convex profile. Carr (3) indicates that erosion by mass wasting along the boundary around the mesas and outliers is persuasive. The debris aprons can extend as far as 20 Km from escarpment surfaces and do not appear to be cratered.

An examination of "Survey" series high resolution Viking imagery taken along the northern highlands boundary area indicates the presence of a "moat-like" depression or swale on the debris apron at its contact with various excarpment surfaces. These features appear to be about 3 Km wide and, at the most, a few tens of meters deep. When found on the debris aprons surrounding the outliers the "moats" do not have a preferred orientation or side on which they develop. Figure 1 illustrates a typical "moat" surrounding an outlier. A few moats were observed to encircle the outlier, but most did not go around completely. When observed on the debris aprons along the valley escarpments (Fig. 2), the "moats" follow the trend of the valley walls. Thusly many of the debris aprons initially described by Squyres (2) as having continuous convex surfaces are, as shown in Figures 1 and 2, topped by a "moat-like" depression.

The origin of the "moats" has led us to examine four possibilities: aeolian erosion, sapping, basal slip or slumping, hydrocompaction. When first observed it was assumed that the "moats" were aeolian in origin. They generally appeared to have a preferred orientation. Further examination of the area indicated a non-randomness to their distribution and the lack of other wind-derived features such as dunes. A wind induced streamlining affect was also set aside. Sapping also presented itself as a possible mechanism especially when the "moats" were observed in several of the valleys south of the outliers. Laity and Saunders (4) have invoked sapping as a process responsible for the continued development of the valleys along the highlands northern

escarpment. The removal of debris apron material would be initiated by the sapping process to be then entrained in the down valley movement of sediment. Unfortunately down elevation outflows were not observed for the "moats" surrounding the outliers. The depressions could also be the result of basal slip/slumping activity within the debris aprons. Slope instability leading to the development of slip surfaces could produce en masse downslope movement of the debris apron. The depressions could thusly be analogous to the grabens developed at the head of slump blocks and other similar mass wasting features.

The fourth possibility is that of hydrocompaction. On earth, the introduction of water into under-saturated or moisture deficient low density sediments can cause the reorientation of the sedimentary particles and the collapse of the internal sedimentary structure occurs. Thusly the weight of the overburden compacts the material as former pore space is reduced. Where observed on Earth, most hydrocompacted materials include alluvial fan, alluvial, and wind-blown silts such as loess and related sediments. The phenomena is generally restricted to material with bulk densities of less than 1.3 g/cm^3 which has a high void ratio. Where observed on earth, the water needed to bring about hydrocompaction is introduced into the sediment as a result of irrigation, leakage from canals and wells, and storm runoff. Subsidence of up to 6 m has been reported for alluvial sediments of the San Joaquin Valley of California.

On Mars one can speculate about the possible discharge sources for water that can bring about hydrocompaction. Sharp (1), Squyres (2), Sharp and Malin (5), and Carr (3) indicate that the release of ground-ice and/or groundwater have brought about the erosion of the fretted terrain and valleys of the highlands northern front. Laity and Saunders (4) and Howard and McLane (6) also invoke the release of water in order to develop sapping features on Mars. Carr (7) proposed a mechanism for the rapid release of water from subsurface aquifers. It is quite possible that a similar mechanism, acting much slower, would bring about the release of water needed to produce the observed "moat-like" features. Thusly, along the escarpment faces of outliers and valleys, the release of water in suitable quantities to bring about hydrocompaction is possible.

REFERENCES: 1) Sharp, R. P., 1973, JGR, 78, p. 4073-4083. 2) Squyres, S.W., 1978, Icarus, 34, p. 600-613. 3) Carr, M. H., 1980, Space Sci. Rev., 25, p. 231-284. 4) Laity, J. E., and Saunders, R.S., 1981, NASA-TM 84211, p. 280-282. 5) Sharp, R. P. and Malin, M. C., 1975, G.S.A. BULL. 86, p. 593-609. 6) Howard, A. D., and McLane, C., 1981, NASA-TM 84211, p.283-285. 8) Carr, M. H., 1979, JGR, 84, p. 2995-3007.

1A. 0 10 km

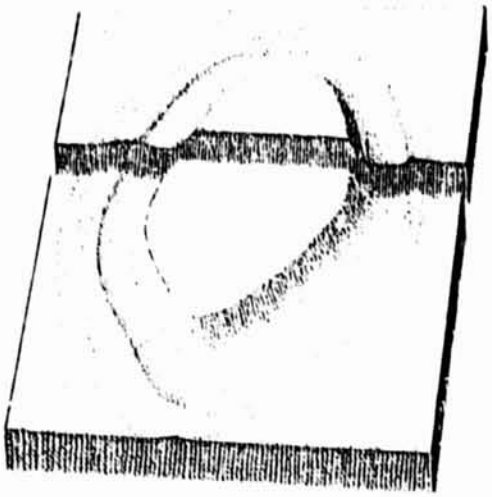

1B. Not to scale.

Figure I. "Moat-like" depression around outliers of fretted terrain. A. Viking image 267S41. B. Idealized block diagram.

2A. 0 20 km

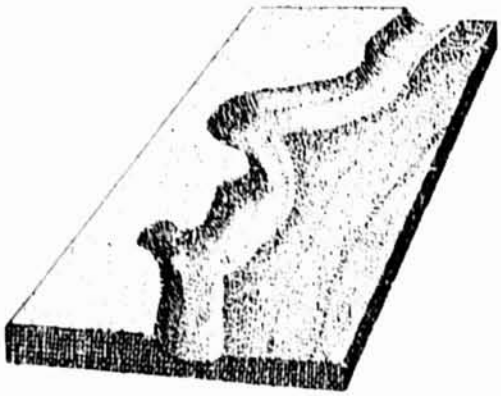

2B. Not to scale.

Figure 2. "Moat-like" depression along escarpment near fretted terrain. A. Viking image 302S04. B. Idealized block diagram.

QUANTITATIVE MORPHOLOGY OF THE VALLES MARINERIS SCARPS

P. C. Patton, Department of Earth and Environmental Sciences, Wesleyan University, Middletown, CT 06457

Analysis of the network characteristics of the Valles Marineris spur and gully topography can be used to infer a sequential development to the chasma scarps. Observations of the regional distribution of wall scarp morphology in the Valles Marineris and comparitive studies of large scarps on Earth can be used to place limits on the processes that are important in the formation of the martian scarps.

Measurements were made of the quantitative morphology of nearly 600 spur networks throughout the Valles Marineris. An individual spur network is defined by the master spur that connects the hillslope system to the crest of the scarp (1). Scarp networks have the inverse pattern of the intervening gully networks. Network samples included both spur networks that are truncated by apparent fault scarps as well as scarp networks whose slope bases are more sinuous and lacking in structural control. Spur networks were also sampled along the length of the Valles Marineris in order to ascertain any regional variations in scarp morphology. The additional quantitative data on spur network topology confirms many of the initial results of this study (1). Networks that have fault scarps at their base have a greater density of bedrock spurs and are apparently weathering limited slopes where transport processes are dominant. Scarp crests are also more linear suggesting a more uniform rate of headward erosion. In contrast slopes which lack basal scarps have lower bedrock spur densities and are apparently transport limited hillslopes where debris is stored on the slope masking the spur topography. Slope crests are more sinuous implying uneven rates of headward erosion as a few master gullies become dominant. This is reflected in the increased width of the hillslope networks which coalesce concommittantly with the capture of adjacent gully networks. The correlation of fine-textured spur topography with basal fault scarps implies that regolith removal by dry mass-movement processes is the most important process on these slopes. Where the slope base is not rejuvenated by faulting more debris is produced on the slope than can be transported and a more subdued topography results.

Observations on the regional distribution of spur and gully topography provide addition evidence for this process. The northern walls have a fine-textured spur and gully topography which terminates against an apparent basal fault scarp. In contrast the southern wall lacks a basal scarp, has a lower spur density and has a more sinuous crest and base. It is logical to assume that both scarps were created at the same time. If both scarps are the same age, then a radically different scarp evolution has occurred on either side of the chasma. A regional comparison of north and south scarps throughout the Valles Marineris does not reveal any preferential development of either scarp form. Therefore, the difference is scarp morphology does

not appear to be related to regional geology or other spatial variables such as slope aspect. Instead these observations further argue that the spur and gully topography is related to the tectonic control of the scarp base and that other processes are less efficient in transporting regolith off the slopes.

Comparitive studies of the chasma scarps with fault scarps in the Basin and Range Province of the western U.S. provide important contrasts. Mountain fronts in the Basin and Range of various tectonic activity (2,3) were studied. The density of spur and gully topography is largely independent of the morphology of the mountain front scarp. This is because the fluvial processes which dominate these scarps are efficient removers of slope regolith. This negative evidence further supports the suggestion that the Martian spur and gully topography evolves by mass wasting processes that require a continually lowered base level.

References Cites

1) Patton, P.C., 1981, Evolution of the spur and gully topography on the Valles Marineris wall scarps: Reports of the Planetary Geology Program, NASA T.M. 84211, p. 324-325.

2) Bull, W.B. and McFadden, L.D., 1977, Tectonic geomorphology north and south of the Garlock Fault, California: in Doehring, D.O., ed , Geomorphology in arid regions, Publications in Geomorphology, Binghamton, N.Y. p. 115-136.

3) Wallace, R.E., 1978, Geometry and rates of change in fault generated range fronts, north-central Nevada: U.S. Geol. Survey Jour. of Research, v. 6, n. 5, p. 637-650.

COLLAPSE: A MECHANISM FOR MARTIAN SCARP RETREAT

BASKERVILLE, Charles A., U.S. Geological Survey, 952 National Center, Reston, VA 22092

Collapsed channel walls and collapsed depressions have been interpreted from images taken on the Viking mission around Mars. The question that arises is, where did the missing material go? All of the collapse based on degradation of contained ground ice does not seem to account for all the material formerly occupying the depressions. Some suggestions are made toward explaining this loss.

On scenes 206S21 (Fig. 1) and 231S35 (Fig. 2), slumps or collapse structures can be seen along valley walls which are many times larger than similar Earth features (Mutch and others, 1976). It is suggested that the lowermost materials along the valleys were removed by fluid flowing down the channel, undermining the outside channel walls along meander bends. The broadly arcuate fissures along the plateau edge (arrows on photos) above the channel are surface expressions of slumps in the early stages of development.

A possible explanation for slumping along these valley walls is that the lowermost material may be an engineering-like soil, which is defined as all loose weathered material including decomposed bedrock with no cemented strength of its own, which contained interstitial ice - permafrost or ground ice (Mutch and others, 1976); the ice may have been warmed by fluids moving in the channel reducing strength. The overburden weight of the channel walls could then squeeze out the weakened soil and cause collapse of the overburden mass along the arcuate stress relief fractures. Martian channel, valley, and chasma walls can range from many tens of meters to kilometer dimensions in height. If this lower unit is silt- or clay-rich (Mutch and others, 1976), it may have had large amounts of ice in the pore spaces. When heated by the aforementioned fluids, formerly ice-laden riged silt or clay could have flowed plastically and caused subsidence by loss of supporting power. A similar reaction is reported in periglacial environments on Earth by French (1976).

An illustrative phenomenon, though non-static, can take place on earth-bound engineering projects where the weight of a surcharge, which may be 3 or 4 meters thick, is used in an attempt to consolidate and strengthen silts and clays with little or no shear strength. When the placing of the surcharge is not properly controlled, a "mud wave" may result, which is the engineer's terminology for a failed mass flowing from beneath the over-burden surcharge.

On Viking images 232S13 (Fig. 3), 212S21 (Fig. 4) and

212S28 (Fig. 5), there are large (± 5 Km) flat-floored craters which appear to be craters formed by collapse into an underlying large void; these craters lack ejecta blankets and raised rims as seen associated with impact craters. Similar features called alases are found on Earth (Washburn, 1973). In 212S28 the inner material of the crater has broken into blocks. Scene 212S21 indicates slumping and centripetal drainage, shown by drainage lines leading into the crater, around the scarp of the crater. Similar features are present around the scarp of the large crater in the northeast corner of 232S13. 232S13 additionally has a window-like closed lower surface exposed beneath the main crater floor.

Fagan and others (1961) have studied collapse craters and shown hypothetical sequences for their formation along the highlands - lowlands boundary. They indicate that these forms may be fracture controlled, as evidenced, in some instances, by subcircular outlines of the crater rims and linear edges--a hypothesis this author supports based on examination of a number of these features on Mars photography. Viking image 216S26 (Fig. 6) depicts an elongated non-circular collapse structure, many kilometers in length, that appears to be aligned with a fracture striking east-northeast (see arrow on 216S26). Rossbacher and Judson (1980) discuss similar depressions which they attribute to wastage or degradation of large volumes of ground ice in segregated masses and in pore spaces, giving rise to thermokarst topography.

It is indicated that the breakup of the material in subcircular depressions, as in scene 212S28, could have been initiated by tectonism locally affecting fracture sets related to a large regional fracture system (Mutch and others, 1976). This type of mechanism is probably the control for the elongate closed depression in scene 216S26. The erosion by fluids and gravitational wasting of the material in the subcircular depressions could have been started by the aforementioned tectonic deformations which opened these fractures, allowing more rapid erosion of their walls. The apparent internal drainage systems have been instrumental as channelways in carrying away the material eroded in these depressions. Sediment transport was probably initiated by volcanic heat which could degrade pore ice such as postulated by Rossbacher and Judson (1980). This heat was transferred through some of the fractures. The resulting melt water transported sediment by traction and suspension into the open fractures within the depressions, and thence into subterranean channelways and caverns. These subterranean caverns and channelways may be in soluble strata, analogous to caverns in karst regions on Earth such as the recent Florida sinkholes, or in buried lava tunnels, as found in volcanic regions on Earth; both instances on Mars being of much larger scale.

Acknowledgments

This work is supported by NASA Contract W-14, 730. Mars imagery was obtained from the NASA National Space Science Data Center, Greenbelt, MD.

References

Fagan, J.J., Weiss, D., Steiner, J., Franke, O.L., 1981, Subsidence depressions on Martian plateau terrains: NASA Tech. Mem. 84211, p. 308-311.

French, H.M., 1976, The Periglacial Environment: Longman Inc., New York, 309 p.

Mutch, T.A., Arvidson, R.E., Head, J.W. III, Jones, K.L., and Saunders, R.S., 976, The geology of Mars: Princeton, N.J., Princeton Univ. Press. 400 p.

Rossbacher, Lisa and Judson, Sheldon, 1980, Thermokarst on Mars: NASA Tech. Mem. 81776, p. 283-285.

Washburn, A.L., 1973, Periglacial processes and environments: St. Martins, New York, 320 p.

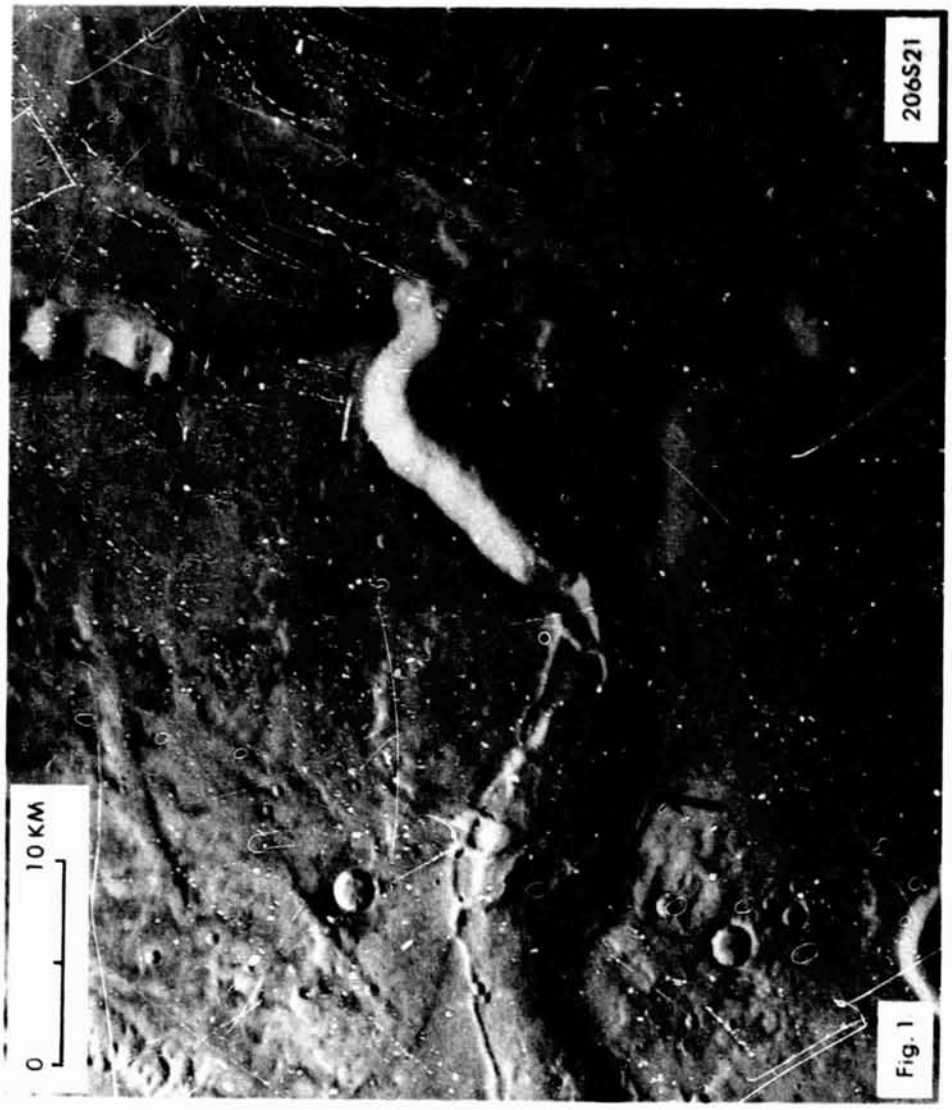

Fig. 2.

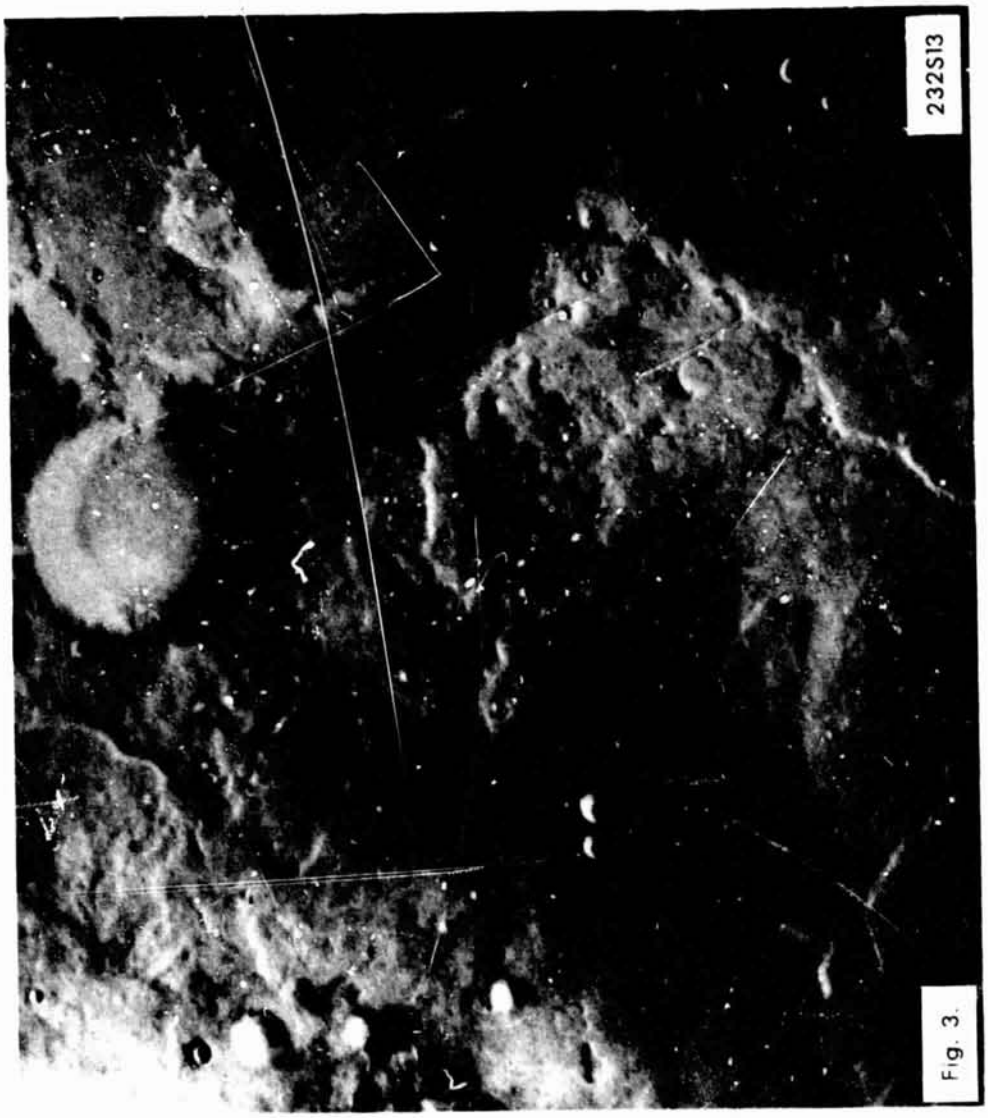

Fig. 3.

Fig. 4.

Fig. 5.

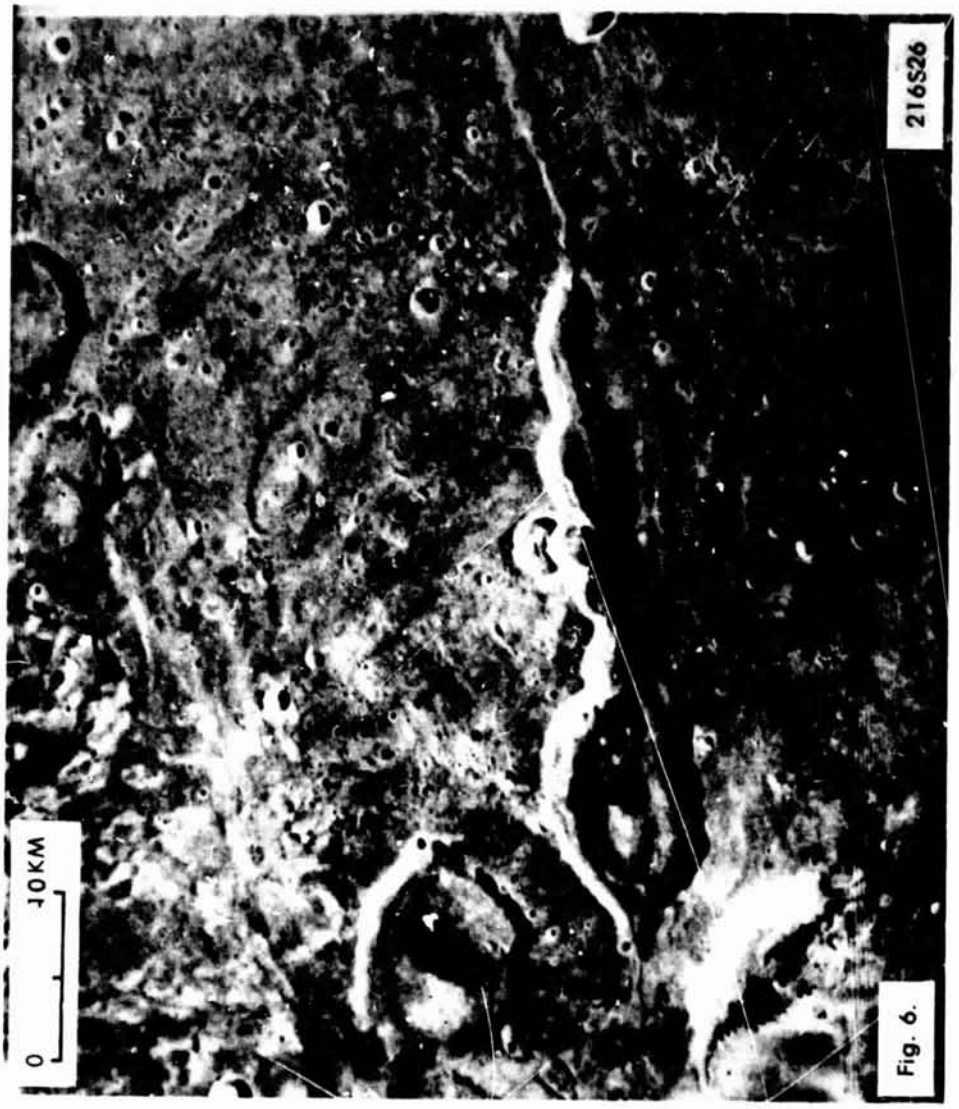

Fig. 6.

LANDSLIDES OF VERMILLION CLIFFS, ARIZONA: APPLICATION TO MARS

Kenneth L. Tanaka, U.S. Geological Survey, Flagstaff, AZ 86001

Rotational blockslides and plastic-flow landslides appear to be end members of landslide styles found along the base of 50 km of the Vermillion Cliffs in northern Arizona, as well as along a few kilometers of the neighboring Echo Cliffs. These cliffs are composed of the following continental, Mesozoic formations (from oldest to youngest): Moenkopi Formation ($\overline{R}$m), Chinle Formation ($\overline{R}$c), Moenave Formation ($\overline{R}$mo), Kayenta Formation ($\overline{R}$k), and Navajo Sandstone ($\overline{R}$Jn). Reconnaissance mapping has partly shown the extent, geologic relations, and morphometry of the landslides (1,2,3,4). Further field investigation of some of the largest landslides has revealed their structural details and mechanisms of emplacement.

The rotational blockslides in the vicinity of long. 112°00' W. and lat. 36°45' N. involve 400-500 m of sandstone and siltstone from the lower part of the Moenave Formation to the present surface of the Navajo Sandstone (Fig. 1.), which overrode and, in some cases, carried along parts of the underlying bentonitic shale beds of the Chinle Formation. The slide deposits have a total length of up to 2000 m and a width of over 8000 m at this locality. The initial slides next to the cliffs underwent later collapse of their distal portions, as a result three successive stages of rotational blockslides extend outward from the cliff. These slides produce the characteristic stair-step appearance of the cliffs. Thicknesses are generally less than 150 m for the first stage slides and 100 m for succeeding stage slides. Individual slides are as much as 2000 m in width and 700 m in length. Vestiges of an older, more eroded sequence form a belt less than 1000 m long and 6000 m wide at a distance of 2500 m from the cliff face (I in Fig. 1).

Slides of the first two stages emplaced adjacent to the cliffs are well preserved (IIa and IIb in Fig. 1), whereas only local remnants of blockslides of the third stage are present. Beds within the slides have been rotated backward 15-50° from an initial dip of 4° N. The landslides have steep head faults which flatten out into sole faults on the overridden erosion surface or within the Chinle Formation. Because they are generally linear in strike the head faults are probably controlled by joints. Obvious shearing and local faulting and tight folding has taken place in the underlying Chinle Formation. Sandstone beds immediately above the sole fault have been broken up into meter-scale blocks which are brecciated or fractured into centimeter- to decimeter-size fragments. Small thrust faults occur locally in siltstone beds of the Moenave and Kayenta Formations incorporated in the blockslides. Another area of blocksliding, similar in size and style of movement to the one just described, is found at lat. 111°51' W. and long. 36°45' N.

Farther east a plastic-flow type of landslide dominates. Here a lower set of cliffs, as much as 100 m high, was formed because of the erosional resistance of the Shinarump Member at the base of the Chinle Formation which overlies the Moenkopi Formation. The bentonitic shale beds of the Chinle Formation, carrying chaotic mixtures of the overlying

formations, have been pushed over these cliffs. This kind of landslide generally occurs when the lower cliffs are within 2000 m of the upper cliffs.

One of the larger slides at long. 111°47' W. and lat. 36°43' N. was inspected first hand. This lobate slide flowed about 600 m past the lower cliff face, splaying out from 300 m in width at the cliff to a maximum of 750 m. At the toe, the slide is about 25 m thick, 5-10 m of the Chinle Formation at the base is overlain by 5-20 m of chaotically mixed red sandstone and siltstone, and a few boulders of the Navajo Sandstone and lenses of shale and limestone from the Chinle Formation are mixed in. The slide surface is characterized by roughly transversely oriented swales 20-30 m in wavelength and 5-8 m in amplitude. The surface gradient dips in the direction of transport at 6-10°. Other plastic-flow slides exposed along the lower cliffs appear to have the same morphology and stratigraphy.

Rotational blockslides are typical of areas in which the slide mass overrode flat terrain; plastic-flow landslides occur where the slide material has been transported over a cliff or a steep slope. It is supposed that the landslides in this area are Pleistocene in age because the wet climate of that period would have facilitated their movement and because of the limited amount of erosion since landslide emplacement. Other rotational blockslides similar in nature to the first type described have been documented elsewhere in the western U.S. (5,6,7). They all have the same stratigraphy - a mechanically strong material such as sandstone, lava, or welded ash overlying shale or loosely consolidated volcaniclastic material in which failure occurs.

Application to Mars: Many landslides and suspected landslides have been documented along martian scarps. The slides within Valles Marineris appear to have been rapidly emplaced, perhaps aided by volatiles in the slide material (8). Landslides along the northwest and northeast flank of the Olympus Mons escarpment are of at least three different types; one style has a stair-step morphology similar to the rotational blockslides described above, however, the martian examples are larger in size, in accordance with the large escarpment. One martian example, at long. 135°20' W. and lat. 23°30' N., fell from a 9000 m cliff (Fig. 2). The slide is 40 km long and as much as 30 km wide; it has four major slide segments that probably were formed in the same successive slide stages as those inferred for the Vermillion Cliff blockslides. Each slide block is capped by cliff-forming, resistant material whose surface dips backward, implying backwards rotation. The slide has a 45 km northwest-trending linear scar; the scar indicates fault control. Other slide sequences along the Olympus Mons escarpment have one to four segments. No landslides of the plastic-flow type have been found; however, these may be less plentiful because of the lack of a bench or steep terrain over which low strength material can flow and because of the difficulty of distinguishing plastic-flow types from other types of landslide found along the escarpment owing to limitations in image resolution. Another possible major locality of rotational landslides occurs along the southeastern, stair-step appearing

escarpment of Olympus Mons. Partial burial by lavas, however, make interpretations tentative.

The occurrence of rotational blockslides and other slides along the Olympus Mons escarpment suggest the presence of low-strength material below the lavas. This material could be the previously proposed ash flows or landslide materials within the escarpment (9,10). The blockslides probably occurred soon after escarpment formation because they are embayed by post escarpment lavas; other exposed landslide types mostly post date the lavas.

References

(1) Petersen, R.G. (1959) U.S.G.S. Map MF-215.
(2) Wells, J.D. (1959) U.S.G.S. Map MF-189.
(3) Petersen, R.G. (1961) U.S.G.S. Map MF-196.
(4) Petersen, R.G. and Wells, J.D. (1961) U.S.G.S. Map MF-197.
(5) Reiche, P. (1937) Jour. Geol., 45, 538-548.
(6) Howe, E. (1909) U.S.G.S. Prof. Paper 67, 19-20.
(7) Russell, I.C. (1898-99) U.S.G.S. 20th Ann. Rept., II, 193-200.
(8) Lucchitta, B.K. (1979) JGR, 84, B14, 8097-8113.
(9) Morris, E.C. (1982) JGR, 87, B2, 1164-1178.
(10) Tanaka, K.L. (1981) Third Intl. Coll. on Mars (abs.), 261-263.

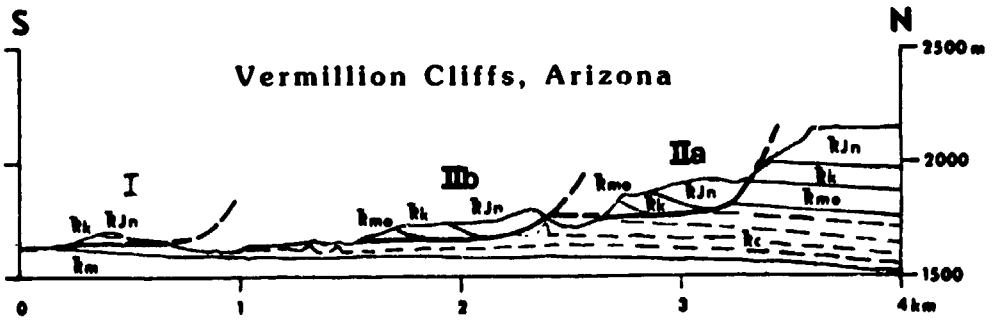

Figure 1. Rotational blockslides mapped along the Vermillion Cliffs, Arizona; I is an older sequence, II is youngest sequence; a,b refer to slide stages of II.

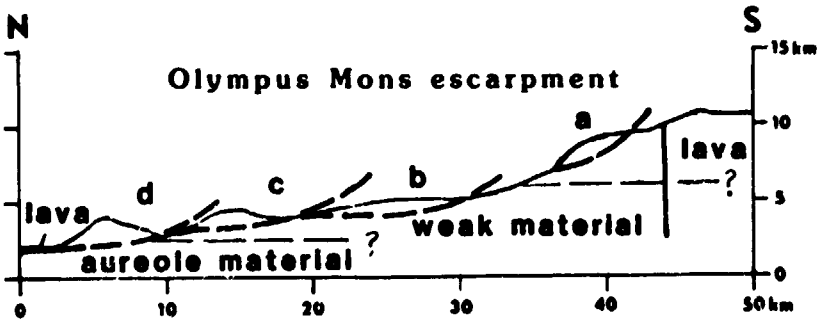

Figure 2. Inferred rotational blockslides, basal faults (heavy dashed lines) and weak material along the northwestern escarpment of Olympus Mons, Mars; a,b,c,d are proposed slide stages.

CONTINENTAL MARGIN SEDIMENTATION: ITS RELEVANCE TO THE MORPHOLOGY ON MARS.

Dag Nummedal, Department of Geology, Louisiana State University, Baton Rouge, LA 70803.

The continental margin (slope and rise) constitutes one of the most extensive geologic provinces on earth, accounting for as much as 9 per cent of the surface. Sediment movement on the continental margin is dominated by mass movement, including sliding, slumping, debris flowage and turbidity current transport (Saxon and Nieuwenhuis, 1982). In contrast, sediment transport elsewhere on earth is heavily dominated by fluid bottom traction and suspension transport (rivers, longshore currents, shelf tides and storm waves, winds). As a consequence, on all scales the earth's slope and rise morphologically are distinct from other, and traditionally better known, geologic provinces.

Mass movement appears to be the dominant mode of sediment transport also on Mars, probably because there are no effective competing processes. Wind is the only exogenic sediment transport agent on Mars today, and aeolian erosion appears not to be very effective (Arvidson et al., 1979, Nummedal et al., 1982). The frustration expressed by many authors in attempting morphological comparisons between the earth's continental surface and Mars is easily understandable. Comparisons were made between surfaces subject to fundamentally different mechanisms of erosion and sediment transport. In those cases where subaerial terrestrial analogs to specific "fluvial" features on Mars have been proposed, the analogies appear rather strained.

Recent continental slope mapping with side scan sonar of long range (e.g. "Gloria", slant range: 70 km), medium range (e.g. "Sea MARC", slant range 6 km) and short range (e.g. E.G. & G, slant range 0.5 km) permit the following generalized characterization of continental margin morphology. The examples which have been summarized in this description all come from tectonically passive continental margins.

The continental slope is incised by numerous canyons (Emery and Uchupi, 1972). On the U.S. Mid-Atlantic slope canyons occur every few kilometers along slope (Farre, 1982). Some of the larger canyons connect with fluvial paleo-channels on the shelf (Hudson, Baltimore canyons) others appear totally unrelated to paleo-drainage systems. The upper reaches of the canyons display trellis-like drainage patterns formed by second and third-order tributaries with a spacing of about 300 m and 100 m respectively. Tributaries of adjacent canyons generally meet, and have completely dissected the intervening spurs. The major canyons display a highly meandering thalweg. The channel walls are scalloped; debris on the channel floor in some places suggests that these scallops are crescent-shaped slump scars. The smaller canyons (which do no indent the shelf edge) are straighter and display longitudinal channel-floor ridges. Large lenticular avalanche scars sculpt the regional slope between the major canyons (Ryan, 1982; Farre, 1982; Malahoff et al., 1980).

Submarine slides and slumps have now been identified on nearly all continental margins. These range in size from a slide covering more than 45,000 km^2 on the continental rise off Northwest Africa (Embley and Jacobi, 1977) to individual slides measuring less than 1 km^2 on the Mississippi delta front (Nummedal and Prior, 1981). Mass-movement appears to be the dominant mechanism for transport of sediment from shallow to deep water on all continental margins. Marine geologic evidence indicates that many submarine slides are transformed downslope into debris flows and turbidity currents (Hampton, 1972; Embley, 1982, Heezen and Ewing, 1952). The morphologic expression of the debris flow deposits and turbidities is inadequately known largely due to the scarcity of deep-water side scan sonar surveys. It is known, however, that long, continuous gently

sinuous channels traverse the continental rise and abyssal plains away from major canyon systems (Curray and Moore, 1974). Some of these channels are more than 1000 km long, a few km wide and up to 100 m deep. Dee-sea fans appear to include both bifurcating and meandering channel segments.

The assemblage of features due to mass-movement on the earth's continental margins is identical in scale, topographic setting and morphologic detail to the complex erosional features on Mars.

REFERENCES

Arvidson, R. E., E. Guiness and S. Lee, Differential aeolian redistribution rates on Mars, Nature, 278, 533-535, 1979

Curray, J. R., and D. G. Moore, Sedimentary and tectonic processes in the Bengal deep sea fan and geosyncline, in, The Geology of Continental Margins; C. A. Burk and C. L. Drake (eds.), Springer-Verlag, N.Y., 617-627, 1974.

Embley, R. W., Anatomy of some Atlantic margin sediment slides and some comments on ages and mechanisms, in, Marine Slides and Other Mass Movements, S. Saxon and J. K. Nieuwenhuis (eds.), Plenum Press, N.Y., 189-213, 1982.

Embley, R. W., and R. Jacobi, Distribution and morphology of large submarine sediment slides and slumps on Atlantic continental margins, Marine Geotechnology, 2, 205-228, 1977.

Emery, K. O., and Uchupi, E., Western North Atlantic Ocean: Topography, Rocks, Structure, Water, Life and Sediments, Am. Assoc. Petroleum Geologists Memoir, 17, 1982.

Farre, J., Ideas on submarine canyon development and evolution, Abstracts, 11th International Congress on Sedimentology, 97, 1982.

Hampton, M., The role of subaqueous debris flows in generating turbidity currents, J. Sed. Petrol., 42, 775-793, 1972.

Heezen, B. C., and M. Ewing, Turbidity currents, submarine slumps and the 1929 Grand Banks turbidity current, Am. Jour. Science, 250, 849-873, 1952.

Malahoff, A., R. W. Embley, R. Perry, and C. Fefe, Submarine mass-wasting of sediments on the continental slope and upper rise south of Baltimore Canyon, Earth and Planet. Sci. Letters, 49, 1-7, 1980.

Nummedal, D. H. Masursky and M. Mainguet, Discussion of "Origin of Martian Outflow channels: the aeolian hypothesis" by J. A. Cutts and K. R. Blasius, J. Geophy. Res. (in press), 1982.

Nummedal, D. and D. B. Prior, Generation of Martian chaos and channels by debris flows, Icarus, 45, 77-86, 1981.

Saxon, S. and J. K. Nieuwenhuis, Marine Slides and Other Mass Movements, Plenum Press, N.Y., 353, 1982.

Chapter 8

PERIGLACIAL AND PERMAFROST PROCESSES

POLAR BASAL MELTING ON MARS.

Stephen M. Clifford, Department of Physics and Astronomy, University of Massachusetts, Amherst, MA 01003.

The possibility of polar basal melting on Mars has been discussed as a potentially important process in understanding the climatic history of H_2O on Mars and the evolution of the martian polar terrains (Clifford, 1980a,b,c; Howard, 1981). In this abstract several key points of this subject will be reviewed.

On Earth, the term "basal melting" is usually applied only when melting occurs at the interface between an ice sheet and the bed on which it rests. That is, if an ice sheet is thick enough for the combination of the Earth's geothermal heat flux and any frictional heat produced by glacial sliding to raise the temperature at its base to the melting point - then basal melting is said to occur. However, consider the case where the thickness of the ice sheet falls short of that required for melting to occur at the ice sheet's base. In this instance the melting isotherm will lie at some depth below the base of the ice sheet but within the bed on which the ice sheet rests. It is important to note that, if the bed is porous, pore ice is likely to exist in the region between the melting isotherm and the base of the ice sheet. If additional snow or ice accumulates on the surface of the ice sheet, then the melting isotherm will rise higher in the frozen bed in response to the added insulation. As the isotherm rises it will release, as a liquid, any ice which may have previously existed within the pores of the frozen bed. While melting will not technically occur at the actual base of the ice sheet, an increase in the ice sheet's thickness will nevertheless result in the melting of pore ice beneath the ice sheet. In the discussion which follows, the use of the term "basal melting" will be broadened to include any situation where pore, or glacial, ice is melted as the result of a change in the position of the melting isotherm.

Basic assumptions. The extent of the martian cryosphere is determined by both the latitudinal variation of mean annual surface temperatures and by the value of the martian geothermal gradient. Present thermal models suggest that the depth to the 273 K isotherm varies from approximately 1 km at the equator to perhaps as much as 3 km at the martian poles (Fanale, 1976; Rossbacher and Judson, 1980). Recent estimates of the total inventory of H_2O on Mars (Pollack and Black, 1979; Lewis, personal communication, 1980) are sufficiently large that the ground ice capacity of the martian cryosphere, at least near the poles, is likely to be saturated. Therefore, as in the example discussed in the previous paragraph, the deposition of any additional material in the martian polar regions will result in a situation where the equilibrium depth to the melting isotherm has been exceeded - thus, basal melting will begin, and continue, until the equilibrium depth to the melting isotherm is once again established. Any meltwater produced as the result of this readjustment will fill the available pore space that exists beneath the martian cryosphere. Calculations, based on a lunar analog indicate that the martian crust may remain porous to a depth of almost 10 km (Clifford, 1981a). Indeed, the availabe pore volume beneath the martian cryosphere appears sufficient to store a sizable reservoir of H_2O as groundwater. This storage potential may have important consequences for the climatic behavior of water on Mars - a subject which will be discussed in greater detail later in this abstract.

Thermal calculations. The thickness of the martian polar deposits required for basal melting can be calculated from:

$$H = k_{eff} \frac{(T_{mp} - T_s)}{Q_g + Q_f} \qquad (1)$$

where k_{eff} is the effective thermal conductivity of the polar deposits, T_{mp} is the melting point temperature of the ice (which may be depressed below 273 K due to pressure and solute effects), T_s is the mean annual surface temperature, Q_g is the geothermal heat flux, and Q_f is the frictional heat due to glacial sliding (Clifford, 1980a).

The effective thermal conductivity of the polar deposits is dependent on the quantity of dust entrained in the ice. After de Vries (1963, 1975) the effective conductivity, k_{eff}, of this two component mixture can be calculated from the relation:

$$k_{eff} = \frac{f_i k_i + F f_d k_d}{f_i + F f_d} \qquad (2)$$

where k_i and k_d are the thermal conductivities of the ice and dust, f_i and f_d are their respective volume fractions ($f_i + f_d = 1$), and where F is a weighting factor that represents the ratio of the average temperature gradient through the dust grains versus the average

TABLE 1. THICKNESS OF POLAR DEPOSITS REQUIRED FOR GEOTHERMAL MELTING (T_s = 165 K).

Dust Content of Polar Ice	Required Thickness (km) T_{mp} = 220 K	T_{mp} = 250 K	T_{mp} = 273 K
80%	.81	1.2	1.6
60%	1.7	2.7	3.4
40%	2.9	4.5	5.7
20%	4.5	7.0	8.8

Adopted values: $k_i = 2.7 \times 10^5$ cal/(cm yr K), $k_d = 3.1 \times 10^3$ cal/(cm yr K), Q_g=22 cal/(cm^2 yr), Q_r= 0, F=2.05.

temperature gradient through the ice. The actual value of F is also dependent on the size distribution, shape, and orientation of the dust grains (the derivation of Equation 2 and the appropriate formula for calculating the weighting factor F can be found in de Vries (1963, 1975)).

Calculated values of H for various dust contents and melting temperatures are presented in Table 1; assumed values for the various constants in Equations 1 and 2 are also listed in the table. The listed value of F was calculated for ellipsoidal particles with a major axis six times the length of each minor axis; the particle orientation is assumed to be random (McGaw, 1969). The melting point temperatures of 220 K and 250 K were included to allow for the possibility that salts contained in the dust (specifically: $CaCl_2$ and $NaCl_2$) might significantly lower the temperature required for basal melting. The presence of even a small quantity of salt may be important - for it opens the possibility that melting may occur, not at a discrete depth defined by a particular isotherm, but over a broad range of temperatures representing an equally broad range of depths within the polar deposits.

Storage of a primitive ice sheet. Based on the possible identification of table mountains and related morphologies on Mars, it has been proposed that an extensive ice sheet may have once covered sizable areas of both the northern and southern hemispheres (Allen, 1979a; Hodges and Moore, 1979). Arvidson et al. (1980) have argued against such a proposal on the basis that the difficulties involved in the removal and storage of such a large volume of ice appear insurmountable. However, the process of basal melting may resolve both of these major objections (Clifford, 1980c).

Ice will remain stable on the martian surface only at latitudes where the daily temperature remains continuously below the frost point. If Mars once possessed extensive polar ice sheets, then this fact may help to account for their subsequent disappearance. Consider for example that, after the ice sheets had reached their maximum areal extent, the martian climate warmed. As mean annual temperatures increased in the equatorial and temperate zones, the position of the frost point latitude migrated towards the poles. When this latitude passed the outer perimeter of the ice sheet, the ice began to ablate and redistribute itself poleward via cold-trapping. As a consequence, what the ice sheet lost in areal extent it gained in thickness at the poles. With this added thickness, the melting isotherm readjusted to maintain its equilibrium depth from the surface - resulting in the initiation of basal melting. If the area involved in basal melting was equal to the present extent of the north and south polar deposits, and if the geothermal heat flux had a value of approximately 22 cal cm^{-2} yr^{-1} (Fanale, 1976), then a 500 m thick ice sheet that once covered 40% of the planet's surface could be introduced into the martian crust as groundwater in just a few million years.

The origin of Chasma Boreale It has been suggested (Clifford, 1980a,b) that Chasma Boreale (85°N, 0°W), and similar features in both the north and south polar terrains, may have been formed by the catastrophic release of a large subsurface reservoir of glacial meltwater. This hypothesis is consistent with the depths for basal melting presented in Table 1 and with certain morphologic similarities between Chasma Boreale and features, found elsewhere on the planet, whose origin is popularly attributed to a catastrophic release of groundwater. Of particular interest are the similarities between Chasma Boreale and Riva Vallis (2°S, 43°W). The differences that

exist between these two features can reasonably be attributed to their differing geologic environments. For example, the large blocks of disrupted crustal material which are visible on the floor of Riva Vallis would not be expected in Chasma Boreale. The reason for this is that the polar deposits apparently consist of fine dust particles entrained in a matrix of water ice. The disruption of these deposits, by the catastrophic release of a subglacial lake, would alter the sensitive insolation balance that had previously preserved this polar material. The change in sun angles and the exposure of low albedo dust would likely result in the evaporation of interstitial ice from the disrupted blocks of polar deposits. The removal of this binding agent would allow strong polar winds, confined by the channel, to erode and transport the resulting sediment along the channel floor (Cutts, 1973). While a fluvial origin for Chasma Boreale is not the only explanation for this feature, it is consistent with what one might expect if polar basal melting were widespread on Mars. It should be noted that a similar idea for the origin of Chasma Boreale was proposed in a slightly different context by Wallace and Sagan (1979).

The climatic behavior of H_2O. Recent calculations on the stability of ground ice in the equatorial region of Mars suggest that any ground ice, emplaced earlier than 3.5 billion years ago, may have long since been lost by sublimation to the atmosphere (Clifford and Hillel, 1982). Yet various lines of morphologic evidence suggest that substantial quantities of ground ice have existed in the equatorial region of Mars throughout its geologic history (Johansen, 1978; Allen, 1979; Rossbacher and Judson, 1981). In an attempt to address this apparent conflict, a model for the climatic behavior of H_2O on Mars has been proposed (Clifford and Huguenin, 1980; Clifford, 1981b). This model suggests that as equatorial ground ice is depleted, it may be replenished by the thermal migration of H_2O from an extensive subpermafrost groundwater system. The groundwater system is in turn replenished when H_2O, resulting from the sublimation of equatorial ground ice, is cold-trapped into the polar regions - where, as before, the added layer of insulation results in basal melting. The prinicipal asset of this model is that it represents an essentially steady-state hydrologic cycle which does not require any significant periods of climatic change to account for the global redistribution of H_2O. A major uncertainty and potential shortcoming of this model is whether the H_2O inventory on Mars is large enough to support the required planet-wide groundwater system.

The potential importance of polar basal melting on Mars is not limited to the examples discussed above. For instance, Howard (1981) has recently suggested that polar basal melting may be responsible for the origin of the etched plains and braided ridges of the south polar region. To address these and other questions, a more detailed treatment of polar basal melting on Mars is in preparation. This research was supported under NASA Grant NSG 7405.

References: Allen, C.C. (1979a) JGR 84, 8048; Allen, C.C. (1979b) Icarus 39, 111; Arvidson et al. (1980) Rev. Geophys. Space Phys. 18, 565; Clifford, S.M. (1980a) Lunar Plan. Sci. Conf. XI, 165; Clifford, S.M. (1980b) BAAS 12, 678; Clifford, S.M. (1980c) NASA TM 82385, 405; Clifford, S.M. (1981a) Proc. 3rd Int. Colloq. Mars, 46; Clifford, S.M. (1981b) Proc. 3rd Int. Colloq. Mars, 44; Clifford, S.M. and R.L. Huguenin (1980) NASA TM 81776, 144; Clifford, S.M. and D. Hillel (1982) JGR, in press; Cutts, J. (1973) JGR 78, 4211; de Vries, D.A. (1963) in: Physics of Plant Environment, (Van Wijk, W.R., ed.), Chpt. 7, North-Holland Publ. Co., Amsterdam; de Vries, D.A. (1975) in: Heat and Mass Transfer in the Biosphere, (de Vries, D.A. and N.H. Afgan, eds.) Chpt. 1, Scripta Book Co., Washington, D.C.; Fanale, F.P. (1976) Icarus 28, 179; Hodges, C.A. and H.J. Moore (1979) JGR 84, 8061; Howard, A.D. (1981) NASA TM 84211, 286; McGaw, R. (1969) Highway Res. Brd. - Special Rept. 103, 114; Pollack, J.B. and D.C. Black (1979) Science 205, 56; Rossbacher, L.A. and S. Judson (1981) Icarus 45, 39; Wallace, D. and C. Sagan (1979) Icarus 39, 385.

PHYSICAL AND MECHANICAL PROPERTIES OF PERMAFROST ON MARS

Duwayne M. Anderson
State University of New York at Buffalo

Terrestrial permafrost varies widely in its physical and mechanical properties and behavior. Ice content, for example, may range from 0 to 100%. Moreover, the ice content of permafrost is only a fraction, albeit the predominant one, of the total water content. A significant fraction of the total water present exists in an unfrozen state and is distributed throughout the pore space and interfacial volumes. The proportion of ice to unfrozen water varies in a characteristic manner with temperature and solute concentration. These basic facts determine, for example, the strength and deformation properties of permafrost and also its hydrological and electrical properties. Reliable relationships among these properties are derivable from basic thermodynamic theory and from empirical relationships recently established by laboratory and field data.

Permafrost exists at all latitudes on Mars. The temperatures and pressures characteristic of the various locations and regions determine, to a large extent, the depth and distribution of permafrost and together with ground water salinity, control its ice content, strength and deformation characteristics, hydrological and electrical properties, etc. Calculations based on the Viking Mission Data results indicate that permafrost thicknesses range from about 3.5 kilometers at the equator to approximately 8 kilometers in the polar regions. The depth to the bottom of Martian permafrost are more than three times the depths characteristic of permafrost in terrestrial polar locations. Martian permafrost is much colder than terrestrial permafrost. Consequently, the proportion of unfrozen water to ice is, in general, much lower. This, however, may be somewhat offset by the higher salinity of Martian permafrost. The combination of low temperatures and great thicknesses of Martian permafrost, coupled with the low atmospheric pressure and very small snowfall, enhance the stability of the Martian surface. The "active layer" on Mars is extremely thin compared to that of terrestrial permafrost, making Martian permafrost much more resistant to erosional processes than is the case on Earth.

ICE-WEDGE POLYGONS, BAYDJARAKHS, AND ALASES IN LUNAE PLANUM AND CHRYSE PLANITIA, MARS. George A. Brook, Department of Geography, University of Georgia, Athens, Georgia 30602

Based upon the estimated temperature regime permafrost must exist everywhere at shallow depth below the Martian surface. Furthermore, the morphological evidence, including patterned ground, possible thermokarst depressions, massive slumps (chaotic terrain), and rampart craters (1, 2) strongly suggests the present or former existence of considerable volumes of ground ice. At the present time water in the form of ice could exist in equilibrium with the atmosphere in the polar latitudes to approximately ± 40° (3) and meandering stream channels are persuasive evidence that water was much more common at or near the Martian surface in the past.

Two landforms common in terrestrial permafrost areas, namely ice-wedge polygons and thermokarst alases, have attracted a great deal of attention because morphologically similar forms have been identified on Mars. Polygonal patterns on the Martian surface are abundant throughout the northern latitudes. Individual polygons, however, range from 2-20 km in diameter and most are therefore much larger than terrestrial examples which rarely exceed 100 m across (4). Black (5) points out that on Mars the reduction of gravity to a tenth of that on Earth would permit some enlargement of polygons but not to ten times the size. Although it is likely that Martian ice-wedge polygons could exceed 100 m in diameter, the larger features identified are more likely to be developed in rock rather than in ice-rich sediments, and may have formed in response to tectonic tensional stresses (6).

Depressions that resemble terrestrial thermokarst alases in morphology and size have been identified in Chryse Planitia in a tableland comprised of layered deposits (1) and in suspected aeolian deposits in Lunae Planum (7). In both areas depressions have flat floors, steep sides, and circular to irregular planimetric outlines. Coalesced forms are common. In addition, Theilig and Greeley report that in the Lunae Planum examples, a knobby texture tends to occur along the sides which may indicate areas where the process of alas formation did not go to completion. If these Martian depressions are indeed alases, the various stages of development from ice-wedge polygon to alas topography should be evident. Neither Carr and Schaber nor Theilig and Greeley report having seen the full range of forms typical of alas topography on Earth.

As described by Soloviev (8) development of terrestrial alas topography begins with the formation of high centered polygons and intersecting networks of trough-like depressions as the polygonal system of ice-wedges begins to thaw. Further melting deepens the troughs causing the sides of the polygons to slump and to form conical mounds called baydjarakhs. As degradation continues the baydjarakhs collapse and decay with the formation of uneven-floored depressions (dujodas) within the baydjarakh field. Continued collapse ultimately produces circular to oval depressions with steep sides and flat floors (alases).

Detailed examination of Viking orbiter images of the areas of Lunae Planum and Chryse Planitia previously examined by Theilig and Greeley (7) and Carr and Schaber (1) has revealed landforms typical of the various stages of alas development on Earth. The sequence of forms is best seen on Viking image 8A74, which covers a small part of Chryse Planitia (Fig. 1). In this area light-toned polygonal patterns 0.1-1.0 km in diameter are visible adjacent to several flat-

floored, steep-walled depressions which resemble alases. The polygons appear to be of the low-centered variety and intersect the walls of some depressions (e.g., at A and B in Fig. 1). Their scale is only slightly larger than ice-wedge polygons on Earth suggesting that they may have been produced by thermal contraction of ice-rich sediments. Small-scale polygonal patterns are also visible on Viking images 8A72 and 34A83 of Chryse Planitia.

Polygons 250 m across at location C in Figure 1 are high-centered and form a knobby terrain where they merge with a flat-floored depression to the west. The topography at C is similar to knobby terrain around the margins of flat-floored depressions in Lunae Planum (7) and closely resembles terrestrial baydjarakh topography produced by degradation of ice-wedge polygons. Individual knobs in Lunae Planum (Viking images 74 A09 and 74A10) are 0.4-1.0 km across and are therefore of comparable size to knobs and polygons in Chryse Planitia, and to small-scale, low-centered polygons 0.4-1.0 km across at 17.6°N, 57.0°W in Lunae Planum (9).

The sequence of landform development in Lunae Planum and Chryse Planitia from small-scale, high- and low-centered polygons, through knobby terrain resembling baydjarakh topography, to flat-floored, steep-walled, rimless depressions similar to alases and alas valleys, exactly parallels landform evolution in terrestrial ice-wedge thermokarst regions. Moreover, morphologically similar landforms on Earth and Mars have comparable dimensions. This similarity, and the presence of well-developed rampart craters near possible thermokarst topography in Chryse Planitia, suggests that the sedimentary blankets in Lunae Planum and Chryse Planitia presently contain (or once contained) large volumes of ground ice, and that ground ice degradation has produced thermokarst features.

References

(1) Carr, M. H. and Schaber, G. G. (1977) J. Geophys. Res., 82: 4039-4054.
(2) Lucchitta, B. K. (1981) Icarus, 45: 264-303.
(3) Fanale, F. R. (1976) Icarus, 28: 179-202.
(4) Washburn, A. L. (1973) Periglacial Processes and Environments. St. Martin's Press, New York.
(5) Black, R. F. (1978) p. 127-129 in Proc. of the Second Colloquium on Planetary Water and Polar Processes, U.S. Army Cold Regions Research and Engineering Laboratory, Hanover, NH.
(6) Pechmann, J. C. (1980) Icarus, 42: 185-210.
(7) Theilig, E. and Greeley, R. (1979) J. Geophys. Res., 84: 7994-8010.
(8) Soloviev, P. A. (1973) Biuletyn Peryglacjalny, 23: 135-155.
(9) Evans, N. and Rossbacher, L. A. (1980) NASA Tech. Mem., 82385: 376-378.

(a)

(b)

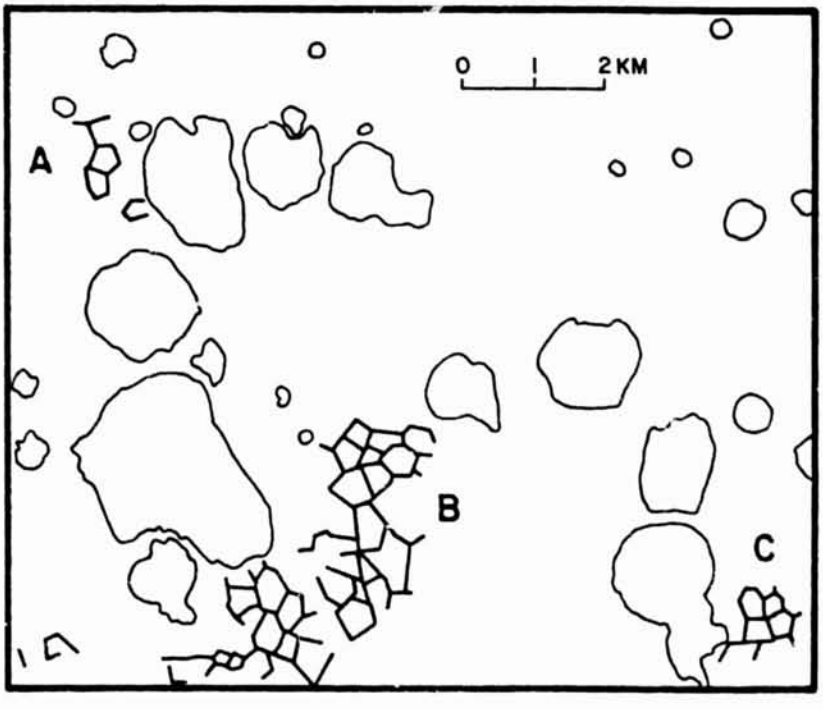

Fig. 1 Ice-wedge thermokarst in Chryse Planitia, Mars. (a) is part of Viking orbiter image 8A74, (b) is a morphologic map of the region. Low-centered polygons at A and B intersect the walls of alas-like depressions. High-centered polygons at C resemble terrestrial baydjarakh topography.

GROUND ICE AND DEBRIS FLOWS IN THE FRETTED TERRAIN, MARS

Baerbel K. Lucchitta, U.S. Geological Survey, Flagstaff, AZ 86001 and
J. H. Persky, Dept. of Geology, Boston University, Boston, MA 02215

The highland boundary in Protonilus and Deuteronilus Mensae is dissected into flat-floored valleys and angular mesas, the so-called fretted terrain. Sharp (1) attributed its origin to the sublimation of ice on scarps, mass wasting, and possibly removal of the material by wind. Viking pictures show debris with apparent linear flow markings in valleys and below scarps. The inferred mass movement was attributed by Carr and Schaber (2) to gelifluction and by Squyres (3) to rock-glacial flow. The present study, based on an examination of Viking images, offers a new interpretation for the origin of fretted terrain.

Our study confirms previous observations which noted that debris blankets extend, on average, no more than 20 km from the scarps (3,4). Because the debris blankets are young and too small to account for scarp retreat of more than about 5 km, Squyres (3) proposed that the major dissection of the fretted terrain belonged to a former epoch and was done by a different mechanism, and that the presently observed mass movement is only a minor reactivation of erosion on the scarps. He believed that the origin of the debris blankets is the result of incorporation of seasonal frost into talus that then flowed from the scarps like rock glaciers. We disagree with the view that a different mechanism was responsible for the formation of fretted terrain in the past and that seasonally added ice is the mechanism responsible for the flow of debris. Even though trunk valleys such as Mamers Vallis may have formed when water erosion played a significant role in the past, the major dissection of the highland scarp into fretted terrain has probably been due to the same debris-flow process that we observe today. Moreover, seasonal frost appears to be insufficient to act as a lubricant. Reasons for these assertions are given below.

1) The seasonal water frost observed at the Lander 2 site is very thin and sublimated after some months (5). Percolation of this water into a talus pile is unlikely under present martian conditions. Squyres (3) visualized burial of such frost layers, but burial would imply rapid talus accumulation; such rock piles, however, would dilute the ice to an extent that would prohibit effective lubrication and flow of rock glaciers.

2) Most tributary canyons to fretted channels are filled with young lineated debris whose surfaces are graded toward the main channels. The debris comes from round, cirquelike valley heads that apparently extended headward by sapping. This sapping process and the accompanying debris flows created the fretted channels that we see today; there is no need to call on a former different process for the formation of older fretted channels. Also, the typical angular shape of outlying mesas appears to be a direct result of the rapid removal of material from cliffs by debris flows; again, the shape of the scarps and the flow of debris appear to be intimately related, and a different mechanism for the original formation of the angular mesas seems unlikely.

3) Bent and tilted surface layers at the edge of scarps, and layers collapsed over linear troughs indicate that subsurface material was removed. Such removal could have been by flow or by loss of substance to the ground or the atmosphere. In either case, the presence of ice would facilitate the removal of material; ice would lubricate rocks and promote flow or ice would sublimate or melt. Thus, it is likely that the ground in the vicinity of the fretted terrain contains ice. Such ice, freshly exposed in steep scarps, could have mobilized the material in the scarps, and served as lubricant for the rock-glacial flow.

4) The volume of material removed from tributary canyons is larger than that deposited in debris aprons in the main channels. Similarly, as pointed out by Squyres (3), the volume of material removed from isolated mesas is not matched by the volume in debris blankets surrounding the mesas. Additionally, elongate and enclosed troughs contain debris blankets, but, because of the enclosure, the loss of material cannot be due to flow. In all the above cases there is a problem with the mass balance; because the deposits are too small, one infers that material disappeared. Erosion by wind has been cited previously (1) to account for the loss. However, even though fine-scale wind features can be detected on very high-resolution pictures, the overall landscape does not suggest intensive erosion by wind; for instance, parallel ridges and gullies typical of wind erosion in Memnonia and the Valles Marineris are absent, instead, the landscape is dominated by smoothly curved debris aprons with flow-lineated surfaces and broadly scalloped scarps indicative of mass wasting processes. Wind erosion appears to have been restricted to the lifting of fine materials already chemically disintegrated or mechanically dispersed. Our preferred explanation for the loss of large amounts of material from the debris blankets is that the blankets contained more ice than previously thought (30 percent estimated by Squyres (3)) and that, perhaps, they are more like glaciers than rock glaciers. The ice could disappear eventually by sublimation into the atmosphere or by percolation into the ground at the base of the aprons. Because we believe, as pointed out above, that the ice in the aprons is derived from ground ice, it follows that the ground underlying the fretted terrain is also highly charged with ice.

Squyres (3) noted that debris aprons on Mars are concentrated in two latitudinal belts; the belts, about 25° wide, are centered on latitude 40° N and 45° S. He attributed this zoning to climatic control and the acquisition of seasonal frost. We agree with the climatic control but disagree with the frost hypothesis, and we offer an alternative explanation. According to Farmer and Doms (6), ice at a depth of about 1 m is in equilibrium with the atmosphere north and southward of 40° lat. This latitude coincides roughly with the belt occupied by the debris blankets, and in this region, near-surface ice could remain in the ground for an extended period of time. Farther south, in the equatorial area, ice exposed in scarps would sublimate from the ground and the scarps would stabilize through the shedding of talus; farther north, the temperature would probably be too cold to

permit glacial or rock glacial flow. In the latitudes of the fretted terrain, where the debris blankets occur, conditions would permit both retention of near-surface ice in the ground and movement of ice-rich material.

Thus, the following setting can be envisioned for the formation of the fretted terrain: ice-rich ground underlying scarps of tectonic or, perhaps, ancient fluvial origin became mobilized and the ice-rich debris flowed away under its own weight, resulting in collapse of the scarps or undermining and sapping at valley heads. The collapsed material also became mobilized giving rise to continued fresh exposures on scarp surfaces and continued retreat of the scarps. Many years of exposure of the flowing material to the atmosphere eventually caused sublimation of the ice; the small amounts of rock contained in the debris blankets may have disintegrated and been dispersed by the wind. The young age of the debris blankets suggests that the process that formed the fretted terrain is currently active (3). If this process were rapid, then the fretted terrain would be young; if this process were slow, which is more probable under present martian environmental conditions, then the inception of the formation of fretted terrain could be old. The process could also have been intermittent and related to astronomical climatic cycles. Further study may shed light on these alternatives.

References

(1) Sharp, R. P., (1973) J. Geophys. Res. 78, 4073-4083.
(2) Carr, M. H. and Schaber, G. G., (1977) J. Geophys. Res. 28, 4039-4054.
(3) Squyres, S. W., (1978) Icarus 34, 600-613.
(4) Carr, M. H. and Clow, G. D., (1981) Icarus 48, 91-117.
(5) Jones, K. L., Bragg, S. L., Wall, S. D., Carlston, C. E., and Pidek, D. G., (1979) Science 204, 799-806.
(6) Farmer, C. B. and Doms, P. E., (1979) J. Geophys. Res. 84, 2881-2888.

DOWNWARD-TRAVELLING INFRARED FLUX AT THE MARTIAN SURFACE FOR PAST CO_2/H_2O ATMOSPHERES

Gary D. Clow, U.S. Geological Survey, Menlo Park, CA 94025

The martian polar laminae and quasi-dendritic valley networks indicate that the climate of Mars has changed with time. The morphology of the valley networks is most consistent with formation by running water [1]. Although periodic orbital variations may cause the surface pressure to oscillate between <1 mb and 20 mb as CO_2 is exchanged between the regolith, atmosphere, and polar caps [2,3], such variations cannot induce climate change of the magnitude necessary for the formation of valley networks. Despite occasional midday equatorial temperatures above 273°K [4], the present climate is simply too cold to supply enough liquid water to support valley network formation. Wallace and Sagan [5] found that the evaporation rate of ice is sufficiently slow even with the present martian climate that liquid water could flow beneath a 10 to 30 m thick ice layer for hundreds of kilometers with discharges on the order of 10^{-1} $m^3 s^{-1}$. However, the source of the running water remains a problem. Although the melting of subsurface ice or permafrost by geothermal activity may have supplied water for some valley networks [5], nearly all the valley networks are restricted to the old cratered terrain and they themselves probably ceased to form shortly after the decline in the intense bombardment 3.9 billion years ago [6]. As discussed by many authors, a greenhouse effect may have enhanced surface temperatures during a period of high surface pressure, to the point that liquid water could exist on or in the ground that might subsequently run off or seep into the valley networks. A comparison of the volatile inventories of the terrestrial planets by Pollack and Black [7] showed that the equivalent of from 1 to 3 bars of CO_2 may have been outgassed from Mars. Pressures of at least 500 mb are required for the mean global surface temperature to reach 273°K with a CO_2/H_2O greenhouse effect [3,8,9].

The thermal structure of the lower atmosphere, the disposition of volatiles in the soil, and the evaporation rates of surface water ice and CO_2 frost, all partially depend on the exchange of energy at the ground-surface interface. The downward-travelling infrared flux emitted by the atmosphere is likely to have been a significant component of the surface energy balance for past martian climates. To aid in the study of near surface processes, the downcoming IR flux from the atmosphere reaching the ground ($I_\downarrow$) was calculated for various surface pressures and temperatures for atmospheres composed primarily of CO_2 with traces of water vapor. Carr [10] is currently incorporating the effect of $I_\downarrow$, a term that was ignored in the study by Wallace and Sagan [5], into his investigation of the stability of ice overlying running water. In the calculation of $I_\downarrow$, each atmospheric level was assumed to emit black-body radiation at the local temperature. Absorption of the propagating radiation by CO_2 and H_2O molecules was approximated through the use of absorption bands that were modified from those used by Hoffert et al.[9] to yield the band absorptances for downward-travelling radiation and to guarantee that the

absorption of upward- and downward-travelling IR radiation would be the same when traversing the same atmospheric path. The bands include the effects of the 15 μm fundamental transition of CO_2, the hot bands of CO_2 at 10 and 15 μm, the rotation bands of H_2O from 18 to 100 μm, and the e-type continuum of H_2O from 8 to 12 μm. Atmospheric pressure was assumed to decrease exponentially with altitude using a scale height appropriate for CO_2 while the H_2O vapor pressure was scaled with the fourth power of atmospheric pressure. The relative humidity was assumed to be 100% at the surface for this set of caluclations. In an attempt to duplicate the approximate radiative equilibrium conditions for the present martian atmosphere, temperatures were assumed to drop exponentially with altitude to a limiting value of 160°K (75% of the effective planetary temperature, 212°K) with a thermal scale height of 40 km.

The calculated downcoming infrared fluxes ($I_{\downarrow}$) are shown in figure 1 along with the envelope of values for mean global surface temperature as a function of surface pressure as determined by Cess et al.[8], Hoffert et al.[9], and Pollack [11]. As expected, $I_{\downarrow}$ is a rapidly increasing function of surface temperature which is in turn an increasing function of surface pressure. The downcoming IR flux approaches the values for the upward-travelling infrared flux emitted by the ground as surface pressure increases, when the ground temperature and the surface air temperature are equal. For situations where the ground temperature is significantly below the mean surface air temperature, such as for soils at night or small bodies of surface ice, the difference between the upward-travelling IR flux from the ground and the downcoming IR flux from the atmosphere can become quite small. The value of $I_{\downarrow}$ associated with the mean global surface temperature exceeds the current mean absorbed solar flux (113 W/m^2) for surface pressures greater than 100 mb. However, much of the solar flux is absorbed by the atmosphere. Assuming an atmospheric optical depth of 0.3, the mean global solar flux absorbed by a soil with an albedo of 0.2 is about 90 W/m^2 while that for thick ice with an albedo of 0.5 is about 55 W/m^2. Although the downcoming infrared flux is small in comparison with the absorbed solar flux for the present climate, it was an important component of the surface energy balance if the surface pressure ever exceeded 30 mb on Mars.

References:

[1] Pieri, D. (1980) Science, v.210, p.895-897.
[2] Fanale, F.P., and Cannon, W.A. (1979) J. Geophys. Res., v.84, p.8404-8414.
[3] Toon, O.B. et al. (1980) Icarus, v.44, p.552-607.
[4] Kieffer, H.H. et al. (1977) J. Geophys. Res., v.82, p.4249-4291.
[5] Wallace, D., and Sagan, C. (1979) Icarus, v.39, p.385-400.
[6] Carr, M.H., and Clow, G.D. (1981) Icarus, v.48, p.91-117.
[7] Pollack, J.B., and Black, D.C. (1979) Science, v.205, p.56-59.
[8] Cess, R.D. et al. (1980) Icarus, v.41, p.159-165.
[9] Hoffert, M.I. et al. (1981) Icarus, v.47, p.112-129.
[10] Carr, M.H. (1982) Reports of Planetary Geology Program-1982, in press.
[11] Pollack, J.B. (1979) Icarus, v.37, p.479-553.

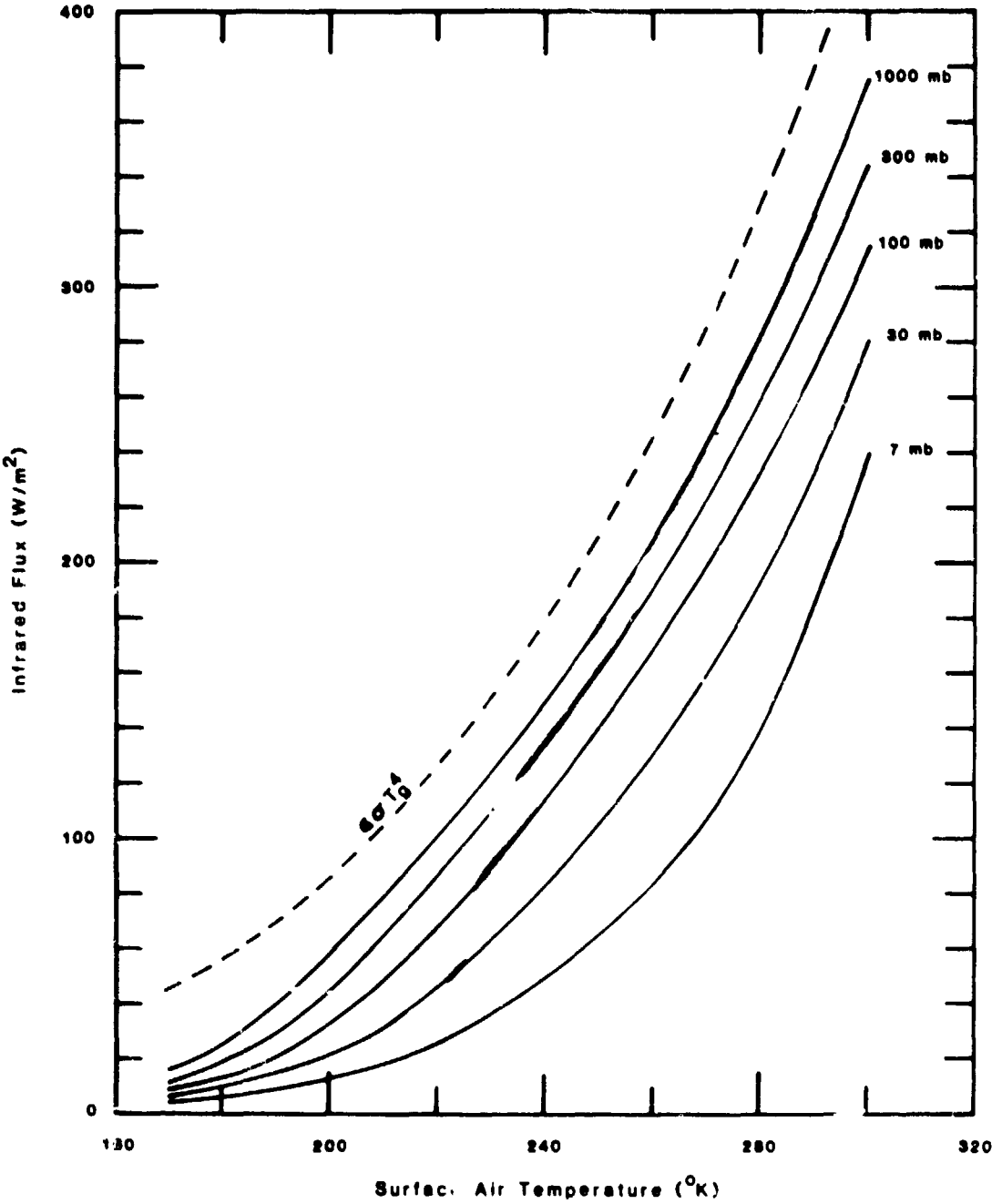

Figure 1. Downcoming infrared flux evaluated at ground level as a function of surface pressure and air temperature. Dashed line is the upcoming infrared flux from the ground at temperature T_g (emissivity=0.95). The stippled area shows the range of values for mean global surface temperature as a function of surface pressure as determined by several workers [8,9,11].

Chapter 9

STRUCTURE, TECTONICS AND STRATIGRAPHY

PLAINS RIDGES: INDICATORS OF COMPRESSIONAL STRESS ON THE MOON, MARS AND MERCURY

Ted A. Maxwell, National Air and Space Museum, Smithsonian Institution, Washington, D.C. 20560

The morphology and orientation of planetary ridge systems have been studied locally in detail but also provide evidence of compressional stress on a global scale. These ridges, similar to lunar mare ridges or wrinkle ridges, are here called "plains ridges" for applicability to the Moon, as well as Mars and Mercury. Plains ridges can be used for both qualitative and quantitative estimates of the extent and magnitude of compression occurring after periods of plains volcanism. On the Moon, ridges formed primarily in late Imbrian through Eratosthenian time (3.8 to 2.0 b.y.), as judged from crater counts, correlation with Apollo ages, and superposition of mare basalt units in which they form. On Mars, ridges surrounding the Tharsis volcanic province occur on plains of the Hesperian system, roughly the equivalent of the Eratosthenian system on the Moon (1). Mercurian ridges in intercrater plains are often gradational with the more well-known scarps, and formed after the period of high impact bombardment, but before the Caloris basin (2). Independent of age, the orientations of plains ridges are useful for determining the geographic extent of local, regional and possibly global compressive stress.

Local Effects. The rims of partially and completely buried craters provide one example of the influence of subsurface structure and topography on the formation of plains ridges. Such ridge rings may be used to estimate the minimum thickness of superposed plains, since the unit must be greater than the rim height of the underlying crater. Ridge rings on the Moon and Mars are morphologically identical (3), and generally occur in regions of thin volcanic fill (although a notable exception is the Lamont structure on the Moon). Mapping of plains ridges surrounding the Tharsis region of Mars indicates that ridge rings occur predominantly on the eastern edge of the Lunae Palus and Coprates ridged plains, and suggest a minimum thickness of about 1 km for volcanic plains in this region. The geologic setting and radar topography for north-south oriented ridges in eastern Coprates provides further evidence for local effects. Although the main ridge systems south of Valles Marineris are developed on plains that slope gently to the west, those in eastern Coprates (50° to 57°W longitude) occur in a topographic trough aligned north-south with an axis at 55°W (see Figure 16 in reference 4). It is likely that ridge formation here was aided by subsidence of plains material, similar to methods proposed for lunar basins, but resulting in linear north-south trends rather than the concentric and radial arrangements of ridges in lunar basins (5).

Regional Stress Indicators. Ridge systems within multi-ring basins indicate the importance of both radial and concentric compression that accompanied the downdropping of the central basin fill (6, 7). Several geometric models for crustal shortening due to basin subsidence and global compression have been proposed, including collapse of the fill from a

spherical to planar surface (8), reduction of circumference due to inward-dipping bounding faults (6), and combinations of local and global-scale compression on a bending plate (7, 9). In contrast to the dominantly circumferential pattern of ridge systems of multi-ring basins on the Moon and the Caloris basin on Mercury, ridges within martian basins are controlled primarily by regional and possibly global tectonic forces. Circumferential or arcuate orientations of ridges are present surrounding the basin edges of seven martian basins, although those closest to the Tharsis region are strongly influenced by regional compression generated by the Tharsis load.

The degree of correspondence between the modeled stress field and actual ridge orientations has been quantitatively compared east of the Tharsis province (5). Comparison of ridge orientations in Lunae Palus and Coprates to a Tharsis center at 1°N, 122°W (10) indicates that more than 60% of the total length of ridges is orthogonal to a normal from this center. Non-orthogonal ridges are seen to have general northerly orientations after removal of the Tharsis orthogonal population. Comparison of the frequency of orthogonal and non-orthogonal ridges further suggests that loading due to the Tharsis plateau was effective in producing compressional features as far as 4000 km from the center of the load; additional sources for compressional stress are necessary to account for ridge systems at greater distances from the Tharsis plateau. Further studies are in progress to determine whether there is any systematic trends of those ridge systems that do not conform to modeled stress orientations on both the Moon and Mars.

Global Compression. In order to account for the excess of northerly-trending ridges in lunar basins (11), and the pronounced northerly trend of ridges on Mars after removal of those orthogonal to Tharsis (5), global scale E-W compression has been suggested as a probable source mechanism. Preliminary estimates of linear shortening in martian ridged plains and lunar basins indicate values of 0.5 to 1.5% strain based on simple fold models, although greater values are possible if significant thrust faulting has occurred. If the strain represented by lunar basin ridge systems were averaged over the entire Moon, these values would suggest a decrease of radius on the order of 15 km, an order of magnitude greater than that estimated for Mercury (2). Consequently, the delineation of local and regional sources for compressive stress is an important prerequisite to estimating the amount of strain represented by ridge systems.

References

(1) Scott, D.H. and M.H. Carr, USGS Map I-1083, 1978. (2) Strom, et al., JGR, 80, 2478-2507, 1975. (3) Gifford, A.W., NASA TM-82385, 90-92, 1980. (4) Roth, L.E. et al., Icarus, 42, 287-316, 1980. (5) Maxwell, T.A., Proc. LPSC 13th, JGR supplement, in press, 1982. (6) Maxwell, T.A., Proc. LPSC 9th, 3541-3559, 1978. (7) Solomon, S.C. and J.W. Head, RGSP, 18, 107-141, 1980. (8) Bryan, W.B., Proc. LSC 4th, 93-106, 1973. (9) Muehlberger, W.R., Proc. LSC 5th, 101-110, 1974. (10) Wise, D.U. et al., Icarus, 38, 456-472, 1979. (11) Maxwell, T.A. and A.W. Gifford, Proc. LPSC 11th, 2447-2462, 1980.

STRAIN ESTIMATES FOR THE RIDGED PLAINS OF MARS: EVIDENCE OF COMPRESSION IN THE COPRATES QUADRANGLE

Thomas R. Watters and Ted A. Maxwell, National Air and Space Museum, Smithsonian Institution, Washington, D.C. 20560

The compressional ridge systems surrounding the Tharsis province of Mars comprise some of the most interesting structural features on the planet. The intensity and complexity of the systems are best represented in the Coprates and Lunae Palus quadrangles. Saunders and Gregory (1980) measured the spacing of ridges in various localities in these regions. They suggested that a Biot (1961) type dominant wavelength of folding (Figure 1) could account for the observed mean ridge spacing. Biot's theory involves the folding of a viscoelastic media in response to compressive stress. The dominant wavelength (Ld) of a single folded unit of thickness (h) is related to the ratio of the viscosity of the folded unit (n) to that of the underlying unit (n_1) by the following equation:

$$Ld = 2\pi h \sqrt[3]{n/3n_1}$$

Using thicknesses for the plains unit obtained from methods of DeHon (1979), Saunders and others (1981) used this relationship to show that the ratio of ridge spacing to plains thickness is approximately 30, corresponding to a viscosity ratio (plains to substrate) of 500.

With appropriate assumptions, Biot's theory of folding may be more extensively applied to the ridged plains to provide estimates of 1) the strain represented by the ridges, 2) the viscosity ratio between plains and substrate, and 3) the thickness of the plains unit. If any two of the three variables are known, and ridges in the region represent a single folded unit, then the third factor can be calculated on the basis of this model. In order to estimate the degree of strain in the ridged plains, both the height and width of the ridges must be determined. The ridge height can be calculated from Viking orbiter images using a sine function involving the width of the shadow and the solar incident angle. Measurements of two parallel ridges, 63.2 km apart in SW Coprates (measurements were made from a 4X enlargement of Viking frame # 608A45) indicate heights of 410 and 440 meters. Comparison measurements made using pixel listings support the measurements from the prints. Assuming the ridges are simple symmetric folds (Fig. 1), the cross-sectional area of the fold was estimated by multipying ½ the width of the ridge by height. The volumetric strain ($\Delta V/V$) was calculated for a range of plains thickness (0.5-2.5 km) for one wavelength. A range of approximately 0.5 to 2.5% strain was obtained. This strain estimate is independent of viscosity contrast, but as shown, is dependent on thickness of the folded layer and dominant wavelength of folding.

Using Biot's theory it is possible to calculate the viscosity ratio (n/n_1) for a given thickness holding Ld constant. Viscosity ratios for thicknesses with an Ld of 40, 63.2, 80 km were calculated (Fig. 3). The most realistic range of viscosity ratios (500-3000) suggests a thickness of 1.0 to 2.0 km for the plains unit in Coprates. The selected range of

viscosity ratios seems reasonable since as Saunders and Gregory (1980) pointed out, the ridged plains (most likely volcanic in origin) are probably underlain by an extensive regolith with a low effective viscosity relative to the plains unit. The resulting thickness value, however, is greater than the 0.5 km estimated by DeHon (1981), but agrees with a 1.5 km estimate by Saunders and Gregory (1980) for W. Solis Planum. A thickness of between 1.0 and 2.0 km suggest a strain of between 0.6 and 1.1% (Fig. 2).

These strain estimates may be further tested using the Biot theory. Once a dominant wavelength of folding is established, the degree of development is dependent on the extent of amplification (Ad) of the wavelength. The amount of amplification represents the factor by which a fold of a given wavelength is multiplied after a period of time. The amplification intensity at any one time (t_0) during the fold history is calculated with respect to a time (t_1) when the layer has been shortened 25% and is related by the following equation:

$$\log_e Ad = t_0/t_1(n/3n_1)^{2/3} = x/25(n/3n_1)^{2/3} \qquad (2)$$

where x is the % strain at time t_0. An upper limit of 25% strain is chosen since strains exceeding this amount would erase all effects of folding (Biot, 1961). Using this equation, strain for a range of viscosity ratios and amplification factors were calculated (Fig. 4). Based on strain of 0.6 to 1.1% calculated above, a viscosity contrast of approximately 3000 satisfies the largest range of amplification factors (Fig. 4).

In conclusion, preliminary studies of the ridged plains in SW Coprates indicate: 1) ridge heights of approximately 400 m; 2) the plains unit is between 1.0 and 2.0 km thick; 3) the viscosity ratio between the plains unit and the substrate is approximately 3000; and 4) the strain recorded in the ridges is between 0.6 and 1.1%. Other methods to estimate strain are under investigation to provide checks on the internal self-consistency of this model.

Supported by NASA Grant NAGW-129.

REFERENCES:

Biot, M. A., Theory of folding of stratified viscoelastic media and its implications in tectonics and orogenesis. Bull. G.S.A., 72, 1595-1620, 1961.

DeHon, R. A., Thickness of the western mare basalts. Proc. Lunar Planet. Sci. Conf. 10th, 2935-2955, 1979.

DeHon, R. A., Thickness distribution of Tharsis volcanic materials (abstract). Reports in Planetary Geology Program, 1981, NASA Tech. Mem. 84211, 144-146, 1981.

Saunders, R. S. and T. E. Gregory, Tectonic implications of Martian ridged plains (abstract). Reports in Planetary Geology Program, 1980, NASA Tech. Mem. 82385, 93-94, 1980.

Saunders, R. S., F. G. Bills and L. Johansen, The ridged plains of Mars (abstract). Lunar and Planetary Science XII, LPI, Houston, 924-925, 1981.

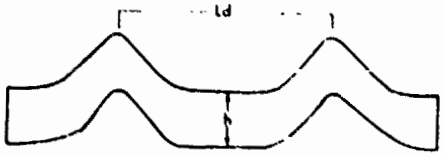

Figure 1.

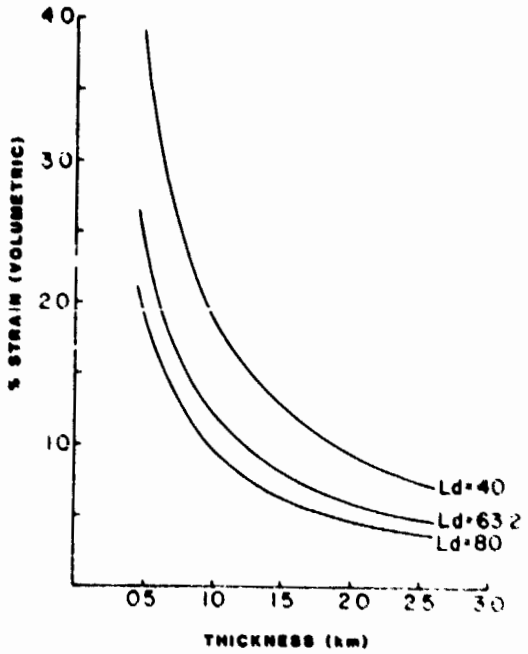

Figure 2.

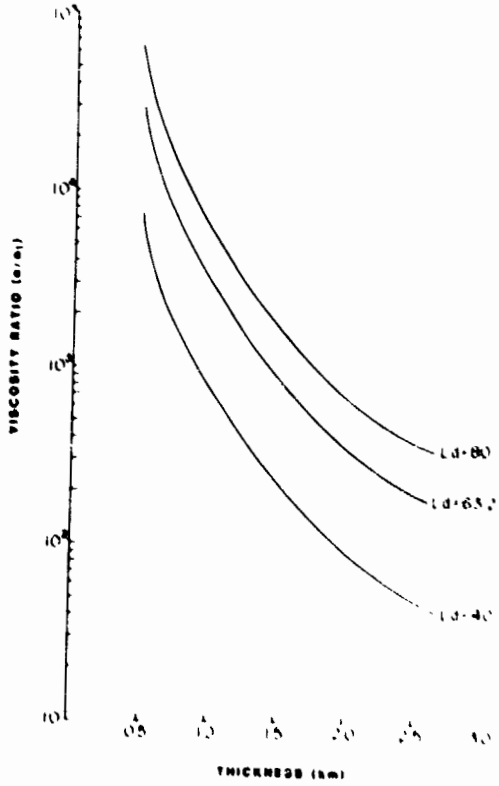

Figure 3.

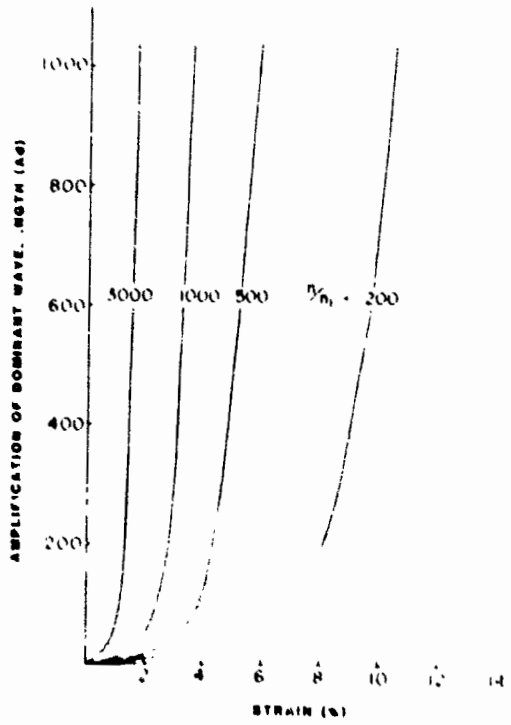

Figure 4.

(see text for explanation)

RIDGES RELATED TO IMPACT CRATERS AND BASINS ON MARS

Chicarro A. F. and Masson Ph., Laboratoire de Géologie Dynamique Interne, (ERA 804/02), Université Paris-Sud, 91405 Orsay, France.

Most large (over 100 km) impact craters and basins on Mars exhibit numerous positive structures in their floor material (1). In contrast to the relative concentricity to the basin rim of most mare wrinkle-ridges on the Moon, impact structures ridge patterns on Mars show a greater variety of structural directions (2, 3).

In Schiaparelli basin for instance (4), almost all ridges are randomly oriented (few showing a NW trend), and there is also a non-oriented pattern in the ridged plains north of the basin (fig. 1). In other cases, a clearly concentric pattern can be seen, such as in Huygens and Herschel basins. Then, other ridge systems transect basins without altering their directions like in Copernicus, thus showing a structural pattern which probably respond to regional compressive stresses.
Small craters (50-100 km), also exhibit some ridge patterns in their interior (fig. 2), and in some cases, ridge formation has been altered by the existence of a crater, as some ridges tend to follow the rim crest.

Therefore, ridge formation seem to be a common phenomenon in crater floor material, as all basins and many impact craters are ridge bearers. Even Argyre, a supposed ridge-free basin, shows a couple of ridges in the northern and eastern parts of the basin, which do not seem to have been covered by recent floor deposits (fig. 3). Naturally, those are not to be interpreted as the sinuous "polar-like" structures one can see in the southern part of the basin.

So, why crater floor material tend to show a ridge morphology when deformed ? Concentric ridge patterns may suggest (as on the Moon), that this material is relatively thick (several hundred meters), and then may be deformed by subsidence due to the crater filling material load. And in the much more frequent crossing or randomly oriented patterns, subsidence may play a role but cannot account for the whole deformation.
Then, we may suggest that the smooth, relatively young, and probably fine grained crater floor material (which may be interpreted as aeolian and/or volatile rich deposits (5, 6)) is more likely to show a ridge morphology in response to local or regional compressive stresses, than the crater surroundings material. However, flow deposits in bounded chasma, which may be comparable to crater filling materials for their physical properties, are rarely ridged.

Therefore, ridges are probably not the only morphological feature responding to compressive stresses. But it seems that certain materials (e.g. crater floor filling material), tend to be deformed as ridges, rather than other more resistant units, which may not respond the same way to compressive stresses.

References :

(1) Wood C.A. & Head J.W. (1976): Comparison of impact basins on Mercury, Mars and the Moon. Proc. L.S.C. 7th p. 3629-3651.
(2) Chicarro A.F. & Masson Ph. (1981): Different kinds of ridges on Mars. 1st meeting of E.U.G., April 13-16, Strasbourg, France.
(3) Gifford A.W. (1981): Ridge systems on Mars. 3rd Int. Coll. on Mars, Aug. 31-Sept. 2, Pasadena, California, p. 93-94.
(4) Mouginis-Mark P.J. & Sharpton V.L. (1980): Schiaparelli Basin, Mars. Conf. on Multi-ring basins, Nov. 10-12, Houston, Texas, p. 65-67.
(5) Hawke B.R. & Mouginis-Mark P.J. (1981): Studies of martian crater and basin deposits. NASA PGPI meet., Baton Rouge, Louisiana, p. 152.
(6) Wood C.A., Head J.W. & Cintala M.J. (1978): Interior morphology of fresh martian craters. Proc. L.P.S.C. 9th, p. 3691-3709.

Figure captions :

fig. 1: Schiaparelli basin, 500 km across, showing an almost randomly oriented ridge pattern (locally NW trends are visible).
fig. 2: Ridges located in the old terrains of Aeolis quadrangle (207°, -12°), transecting young crater floor material without altering significantly their original direction.
fig. 3: Oblique view of the northern part of Argyre Basin, showing an important ridge which probably has not been covered by younger floor deposits, or has been made visible by erosion. (Viking Orbiter picture n° 079 A 21).

fig. 1

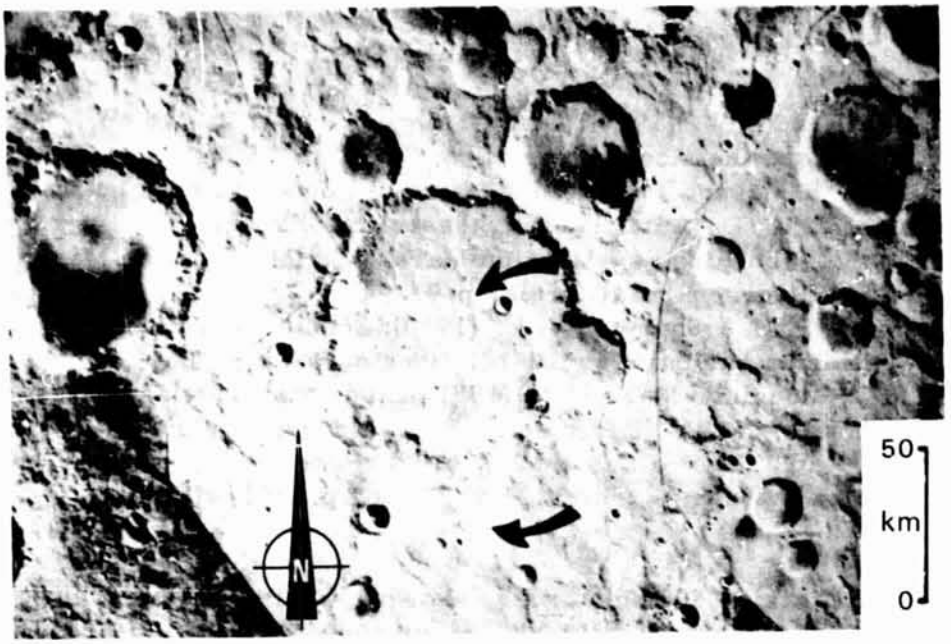

fig. 2

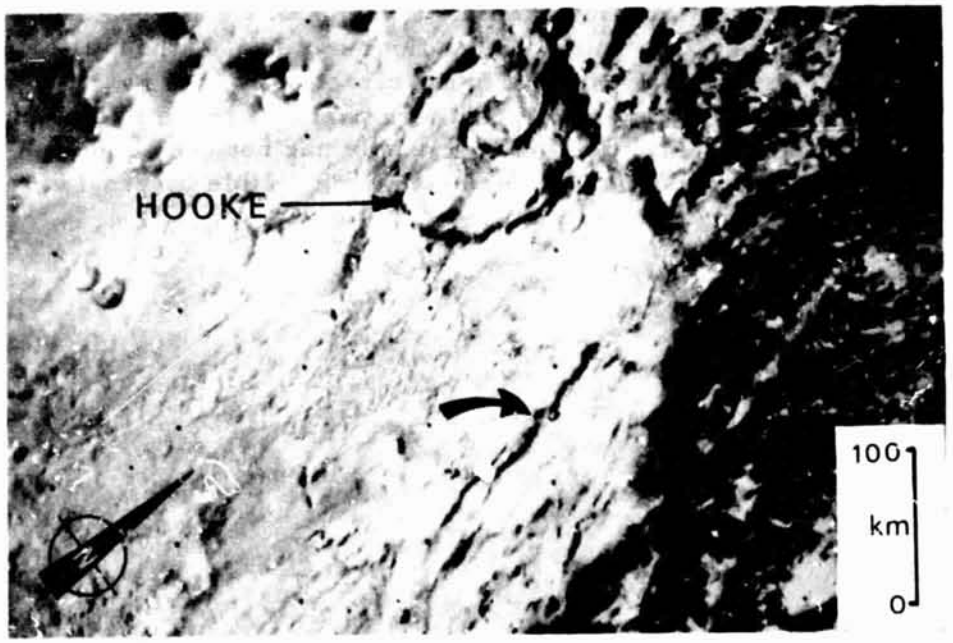

fig. 3

Acknowledgments :

This study was supported by INAG in the framework of ATP "Planétologie 1982" (contract n° 47.25), and compiled at the Lunar and Planetary Institute, Houston, Texas, during a Visiting Graduate Fellow appointment of A. F. Chicarro.
The Lunar and Planetary Institute is operated by the Universities Space Research Association under contract n° 09-051-001 with the National Aeronautics and Space Administration.

COMPARATIVE GEOLOGY OF ORIENTALE, CALORIS, AND ARGYRE BASINS

THOMAS, P. G., MASSON, Ph., Laboratoire de Géologie Dynamique Interne (ERA 804/02), Université Paris-Sud, 91 405 ORSAY Cedex, France.

The geologic and tectonic mapping of three large impact basins -Orientale on the Moon, Caloris on Mercury, and Argyre on Mars- is undertaken at the Laboratoire de Géologie Dynamique Interne (Université Paris-Sud, Orsay, France) in cooperation with the U. S. Geological Survey, Branch of Astrogeologic Studies (Flagstaff, Az.). The shaded relief maps (1:5,000,000 scale, Comparative Planetology Series) of these three basins are used as base maps (1), (2), (3).

The Orientale and Caloris stratigraphy is now well known (4), (5). The outer limit of the transient cavity is characterized by "massif and blocky" mountains up to 1 or 2 km above the surrounding terrains : the Montes Rook formation (Orientale), and the Caloris Montes formation (Caloris). The transient cavity is surrounded by ejecta blankets which show hummocky or radial facies. The Argyre stratigraphy established from Viking images is apparently different of the stratigraphy Based on Mariner 9 images (6), and does not look like its lunar and mercurian counterparts. There is no radial facies, and only few patches of hummocky facies are observed around Argyre. But, the "massif and blocky" facies appears to be more important than on Mercury and on the Moon. This facies is 300 km wide (equivalent to 1 transient cavity radius), and apparently shows blocks and ridges separated by rectilinear troughs (fig. 1). The directions of the ridges and of the troughs seem to indicate that they are not resulting of ejecta deposition, as the Hevelius formation's on the Moon, but that they are controlled by faults. This indicates that the Argyre blocky facies is not the result of an overturned flap, as proposed for the Orientale Montes Rook formation (5), but that it corresponds essentially to the preimpact faulted basement.

The three basins are surrounded by concentric scarps, usually interpreted as gravity slumping downward an inward the transient cavity. Importance and distribution of the scarps differ in the three basins : Orientale shows one continuous scarp, a weak and discontinuous scarp is seen around Caloris, and numerous and discontinuous scarps surround Argyre (fig. 1).

The outer scarp surrounding areas of Orientale and Caloris do not show basin related tectonic features. But, the Caloris ejecta exhibit uplifted and downwarped blocks (7), indicating important tectonic movements directly or indirectly related to impact mecanism (8).

Argyre interior is completely embayed by recent plains material and does not show any tectonic features related to impact mecanism. The Orientale non more flooded interior shows elongated and complexly fractured domes produced by compressional stress during the final stages of the cratering sequence. The Caloris floor is intensively ridged and fractured by tectonic movements. It has been proposed (8) that these tectonic features could be the consequence of Caloris radius shortning under global compression of the mercurian lithosphere.

Despite of their morphologic similarities, the detailed comparative geologic and tectonic studies of Orientale, Caloris, and Argyre basins show important differences due to external factors (martian erosion) and to internal evolution (crustal and lithospheric properties).

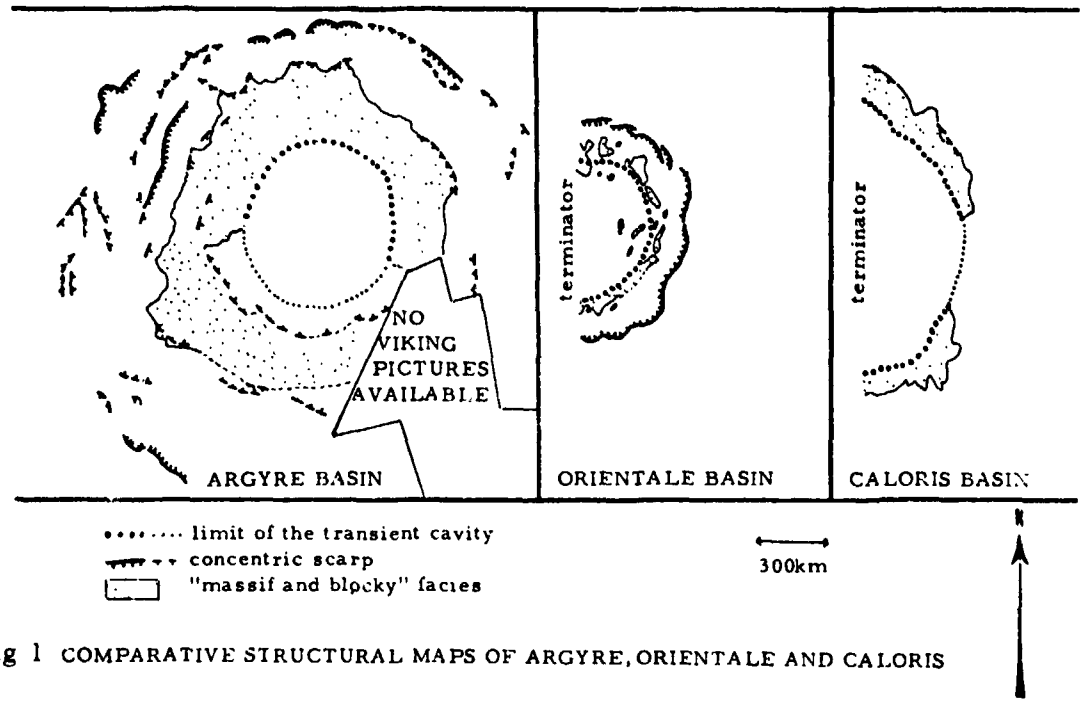

fig 1 COMPARATIVE STRUCTURAL MAPS OF ARGYRE, ORIENTALE AND CALORIS

References

(1) Marc Orientale Area, Atlas of the Moon - Comparative Planetology Series, U. S. Geological Survey, Misc. Inv. Series, I. 1089, 1978.

(2) Caloris Planitia Area, Atlas of Mercury - Comparative Planetology Series, U. S. Geological Survey, Misc. Inv. Series, I. 1089, 1979

(3) Argyre Planitia, Atlas of Mars - Comparative Planetology Series, U. S. Geological Survey, Misc. Inv. Series, I.1264, 1980.

(4) Mc Cauley, J. F. (1977), Orientale and Caloris - Phys. Earth Plan. Int. 15, 220-250.

(5) Mc Cauley, J. F. et al. (1981), Stratigraphy of the Caloris basin - Icarus 47, 184-202.

(6) Hodges, C. A. (1980), Geologic Map of the Argyre Quadrangle of Mars - U. S. Geological Survey, Misc. Inv. Series, I-1181.

(7) Thomas, P. G. (1978), Structural lineament pattern analysis of Caloris surroundings : a pre-Caloris pattern on Mercury - In : Report of Planetary Geology Program, 1977-1978, NASA Technical Memorandum 79729, 78-82.

(8) Fleitout, L. and Thomas, P. G. (1982), Far Field tectonics associated with a large impact basin : application to Caloris on Mercury and Imbrium on the Moon. E. P. S. L. 58, 104-115.

Aknowledgment. This study was supported by INAG in the framework of ATP "Planétologie - 1982" (Contract n° 47-24).

STRUCTURAL CONTROL OF GEOMORPHIC FEATURES IN THE KASEI VALLIS REGION OF MARS

R. Craig Kochel and Cynthia M. Burgess, Department of Environmental Sciences, University of Virginia, Charlottesville, VA 22903

Schumm (1974) suggested that large Martian outflow channels such as Kasei Vallis may have a structural origin related to regional tectonic processes. Baker and Kochel (1979) suggested that outflow channels may have initially inherited their geometry from structural features and were extensively modified by later catastrophic flooding.

Major geomorphic features of this region include: outflow channels with grooved floors, streamlined hills in outflow channels, lunae planum plateau material which served as host terrain, and craters. Major structural elements visible in the region include: NE-SW trending grabens, N-S trending wrinkle ridges, sapping channels extending away from channel escarpments and on channel floors, and major fracture systems of undetermined origin (probably joints). Figure 1 is a simplified geomorphic map of the study area showing these structural and geomorphic features. Details of these features is found in Baker and Kochel (1978,1979).

Orientations of these features were measured from Viking images and are summarized in Figure 2. Comparison of Figures 1 and 2 indicate that only a fair correlation exists between orientations of major straight outflow channel segments and major fracture and graben systems. The poor correspondence may result from the local variation in fracture orientations over the region (Fig. 2). Large-scale outflow channel orientations appear most closely alligned with graben trends (Fig. 1), which may suggest that originally found more accessable outlets through grabens but were inhibited by the normally trending wrinkle ridges. Baker and Kochel (1979) have shown that although some wrinkle ridges appear to post-date channeling, most were formed prior to the channeling episode and served as flow obstacles. As expected, tensional fractures (grabens) and compressional features (wrinkle ridges) exhibit an orthogonal relationship and both have very well-defined trends. Features interpreted as sapping channels show some correlation to graben orientation and regional fracture patterns. This may be indicative of structurally-controlled groundwater flow patterns through zones of enhanced secondary permeability.

References:

Schumm, S.A., 1974, Structural origin of large Martian channels: Icarus, v. 22, p. 371-384. Baker, V.R., and Kochel, R.C., 1978, Morphological mapping of Martian outflow channels: Lunar Planet. Sci. Conf., 9th, p. 3181-3192. Baker, V.R. and Kochel, R.C., 1979, Martian channel morphology: Maja and Kasei Vallis: J. Geophys. Res., v. 84, p. 7961-7983.

ORIGINAL PAGE IS OF POOR QUALITY

Figure 1. Simplified geomorphic map of western Kasei Vallis.

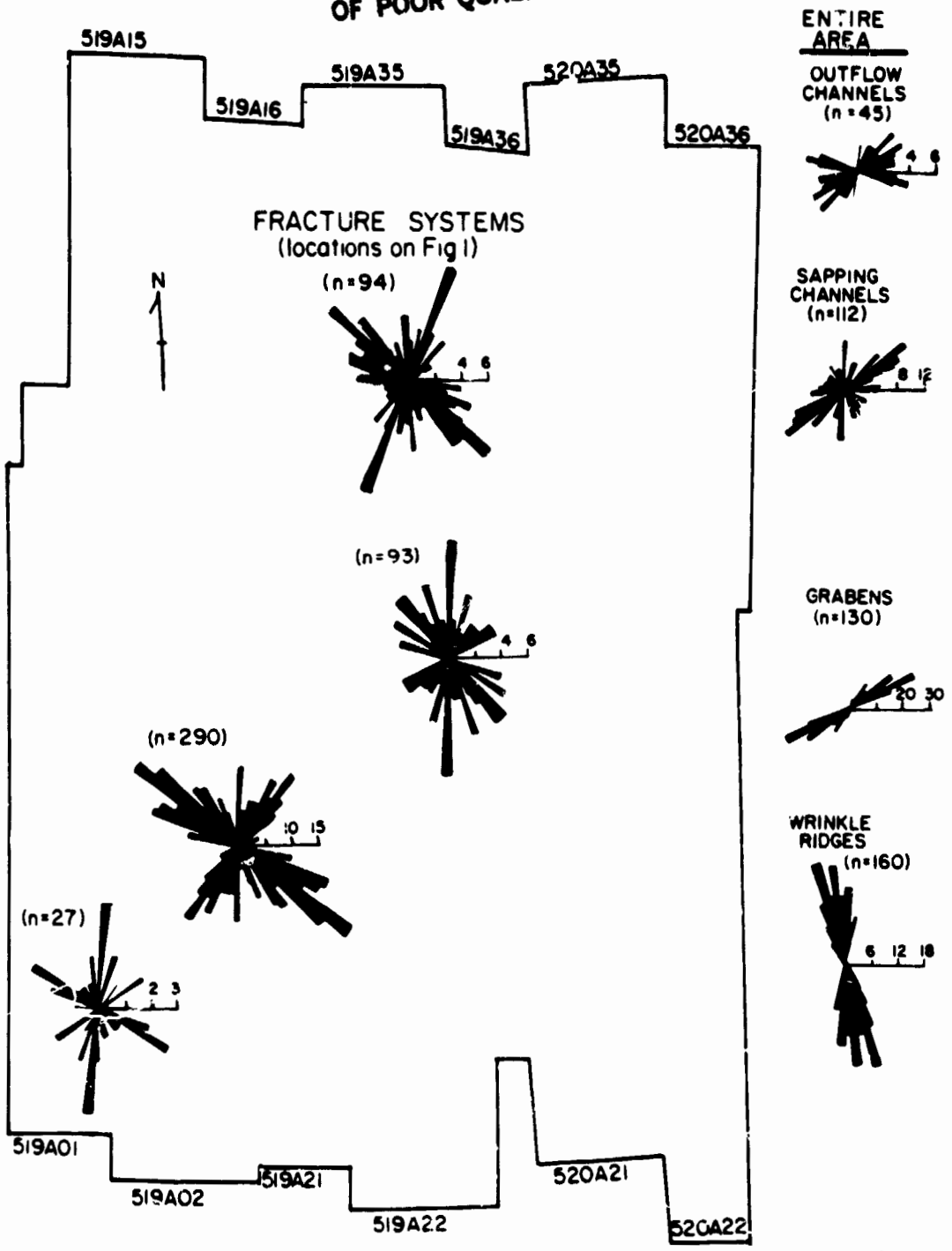

Figure 2. Rose diagrams of azimuthal orientations of geomorphic and structural elements in western Kasei Vallis. Data is grouped in 5 degree intervals. Plots in the outlines area are local fracture patterns. Plots oiut:ide the area are data from the entire study area.

Martian Global Tectonics

Richard A. Schultz and Michael C. Malin, Department of Geology, Arizona State University, Tempe, AZ 85287

Scarps, ridges, and graben within the heavily cratered terrain of Mars define distinct groups of structural trends on a regional scale, and a pattern of crustal deformation on a global scale. These trends are the result of regional deformation of the crust, rather than the imposition of a single planetwide stress system. Centers of deformation are spatially related by a systematic global pattern. As the relative ages of measured structures seem to generally predate both the emplacement of Lunae Planum-aged volcanic units and the structural and volcanic activity near Tharsis, this structural pattern is thought to reflect a fundamental global organization of volcanic and tectonic activity. This pattern was established early in martian history, and served to localize subsequent crustal modification. The earliest manifestation of this pattern was in primarily mechanical deformation of the crust. This was globally asymmetric and most intense in the northern third of the planet; it guided the formation of the planetary dichotomy boundary, much of the original structure of the associated fretted terrain and, in addition to local volcanism, may have contributed to the NE-SW asymmetry of the later Tharsis-related graben sets. The other major phase of activity was primarily thermal: this produced the extensive volcanic plains of Lunae Planum-age near Tharsis and, to a lesser extent, in Syrtis Major and Hesperia Planitiae. Subsequent, more local activity along this global pattern seems to have contributed to plains volcanism southwest of Hellas, constructional volcanism in the Tharsis region, and modification of surface landforms in areas of fretted terrain.

FRACTURE ORIENTATIONS IN THE THARSIS PROVINCE OF MARS

R.Bianchi, M.Fulchignoni and R.Salvatori, Istituto di Astrofisica Spaziale del C.N.R., viale dell'Universita' 11 00185 Roma - Italy

The martian region Tharsis-Valles Marineris, because of its peculiar volcanic structures, has been carefully investigated by many authors. Several tectonic structures near Tharsis Plateau, as graben, suggest an evident relation between volcanism and tectonism. Morphologic studies have been carried out on the region Tharsis-Valles Marineris (1,2), and the obtained results made it necessary to further investigate the tectonism of this region, in order to clarify the geologic evolution of the whole planet. The study of the lineaments of Mars (3,4), allowed scientists to put forward the hypoteses that a certain mechanism of plate tectonic took place on Mars. On the other hand the study of fractures and ridges orientation in this region (5,6,7) made it possible to guess that geologic evolution occurred under different circumstances. The solution of the problems concerning the correlation between surface stress directions and the orientation of tectonic features would enable the scientific community to reconstruct the geologic evolution of the whole planet. Different types of stresses have disturbed the surface producing extensive and compressive tectonic features. The fracturing modalities in the region

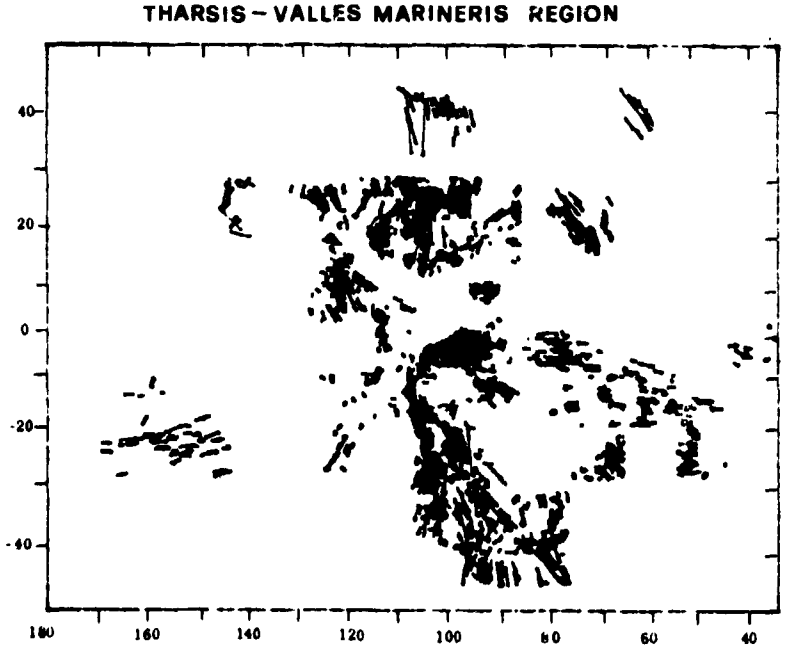

Fig. 1 - Geographical distribution of all the fractures.

Tharsis-Valles Marineris can be related both to the possible stresses caused by the ancient mantle movements and to the load of the volcanic material on the surface. The area surrounding the volcanic region of Tharsis probably presents all the features produced by the tectonic events that determined the current aspect of the region. The distinction between different types of fracture systems would be very important to gain further information on the orientation and nature of the stresses that characterized the region during its history. In order to attempt a preliminar distinction among fracture systems in more significant directions we have statistically examined 6723 fractures in the region limited between 170° and 40° long. and ±50° lat. (fig. 1). In a previous work (7,8), using azimuth frequency and cumulative lenghts diagrams, we found a main azimuthal trend in a N-S direction and a secondary one along an E-W axis. In fig. 2 is reported the frequency distri-

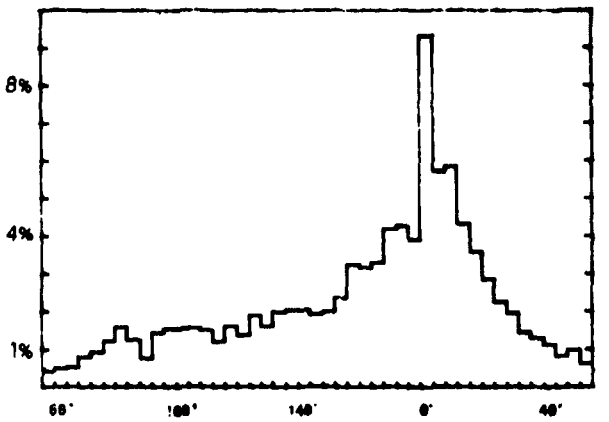

Fig. 2 - Fracture azimuths frequency distribution.

THARSIS – VALLES MARINERIS REGION

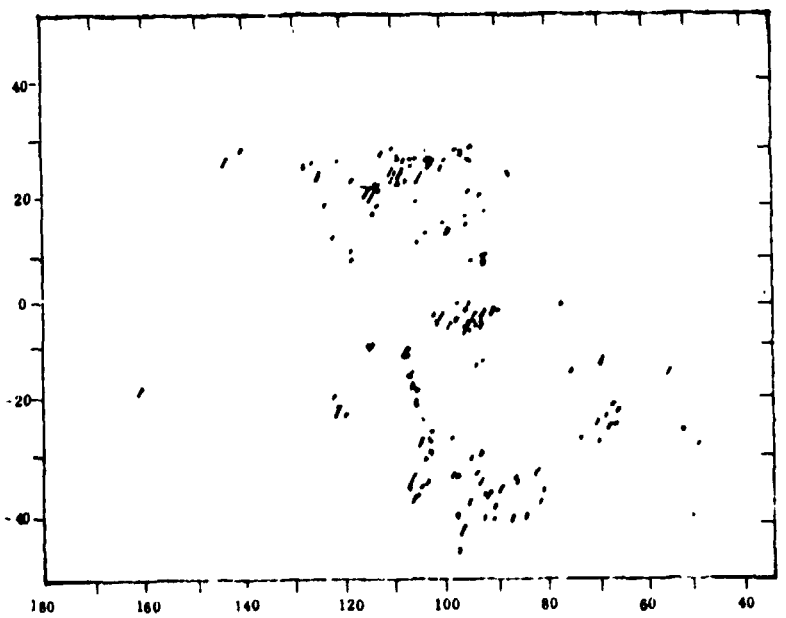

Fig. 3 - Fracture orientated along the direction 28°±3° from North.

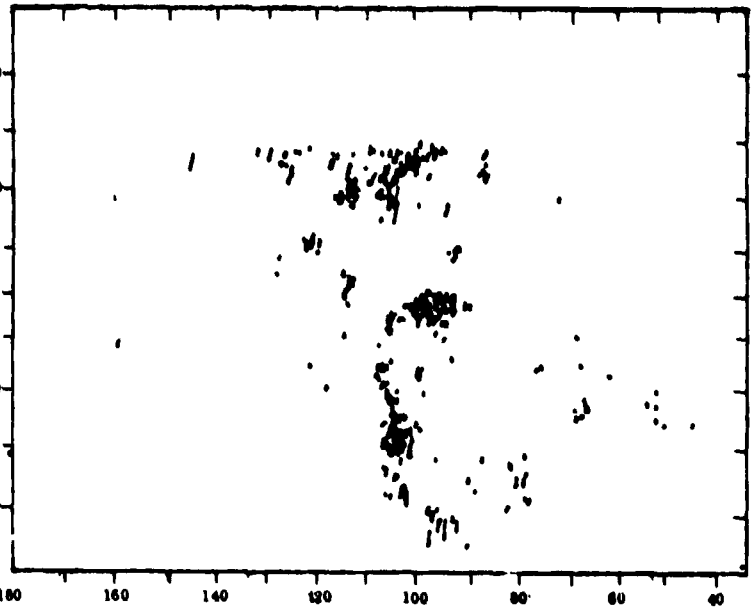

Fig. 4 - Fracture oriented along the direction 13°±3° from North.

bution of all the fractures azimuths grouped in 45 classes of 4° each. In order to group the azimuthal values in very narrow angular trends the angular interval was chosen to be just larger than the instrumental error due to the digitizing operation, i.e. ±3°. Gaussian distributions were fitted to the peaks in the fracture azimuths histogram obtaining several directional families. Assuming the mean value (± the instrumental error) of each gaussian curve as the statistically significant orientation we extracted the fractures belonging to each family. For example, in fig. 3 and 4 are shown two groups, respectively along the directions 28°±3° and 13°±3° from N. Examining the geographical distribution of the fractures in each direction and considering the mutual distances among fractures in the areas where they are more frequent it is possible to attempt some speculation on the fracturing modalities in Tharsis region.

References: 1) Blasius K.R. et al.(1977) J.Geophys.Res. 82, 4067. 2) Lucchitta B.K. (1979) J.Geophys.Res. 84, 8097. 3) Masson P. (1977) Icarus 30, 49. 4) Masson P. (1979) The Moon and the Planets 22, 212. 5) Wise D.U. et al. (1979) Icarus 38, 456. 6) Maxwell T.A. (1982) Proc. 13th Lunar and Plan. Sci. Conf. in press. 7)Salvatori R. et al.(1981) NASA TM 84211, 386. 8) Salvatori R. et al. (1982) submitted to Icarus.

STRUCTURAL CONTROL OF SAPPING VALLEY NETWORKS ALONG VALLES MARINERIS, MARS

R. Craig Kochel and Allan P. Capar, Department of Environmental Sciences, University of Virginia, Charlottesville, VA 22903

Valles Marineris is widely accepted to be of structural origin. Support for this interpretation is provided by the parallelism of extensive graben systems along the southern rim of the canyon. Considerable geomorphic modification has occurred along the canyon escarpments since their formation. This modification is apparent as extensive landslides, slumps. flows, and talus accumulation (Lucchitta, 1979). A simplified geomorphic map of the study area including the western chasms is shown in Figure 1. Crudely dendritic networks of deep blunt-end valleys have developed along the canyon rims (Figure 1) and have been interpreted as having formed by groundwater sapping processes. These sapping networks are particularly well-developed along the northern rim of Valles Marineris. If these channels were formed by groundwater sapping it is likely that they would show a strong structural control because of structural effects such as increased secondary permeability along fracture/fault zones. To determine if the proposed sapping channels are structurally controlled the orientations of 257 channels and 147 grabens were measured and compared (Fig. 2). From Figure 2 it can be seen that when all sapping channels are included in the data there aren't any clear trends or correlations with structure. However, if the smaller sapping channels less than 15 kilometers long are filtered out of the analysis a clear orthogonal set of orientations is visible (Fig. 2). Although the channel trends do not correspond precisely with the graben orientation trends, there is a strong suggestion of structural control in the orthogonal pattern. This pattern is similar to patterns developed in joint-controlled drainage networks on earth.

A fair correspondence exists between the overall graben trends of WNW-ESE and NE-SW and sapping channel orientations of NE-SW and NW-SE. Some of the deviations from perfect correspondence could be explained by modification of sapping valleys by mass wastage processes and the effects of secondary fracture systems unrelated to the grabens. Viking frames used to prepare Figure 1 show clear evidence at several locations of sapping channels that have extended headwardly along the axis of grabens along the southern rim of Valles Marineris.

References:

Lucchitta, B.K., 1979, Landslides in Valles Marineris, Mars: J. Geophys. Res., v. 84, p. 8097-8113.

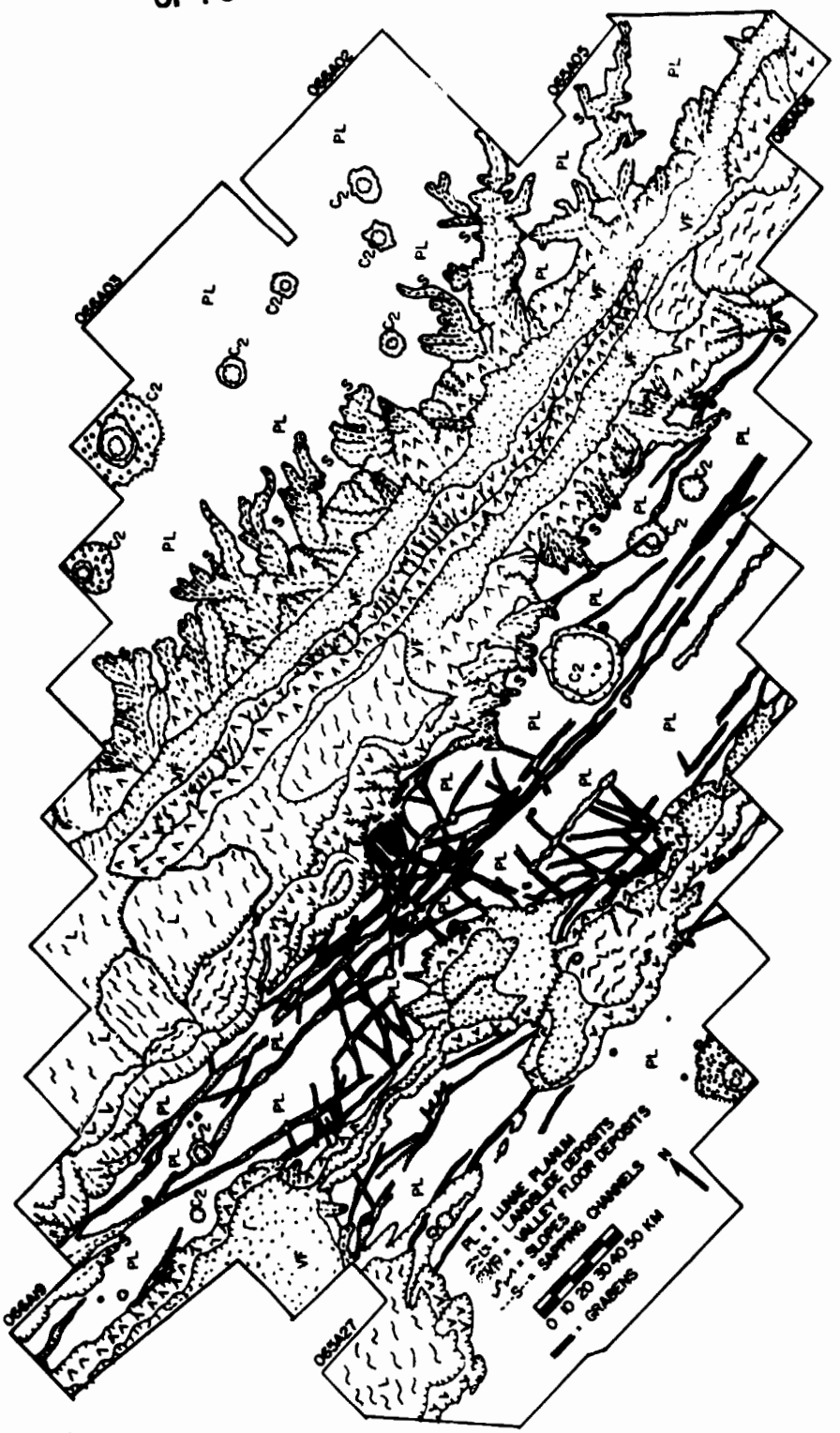

Figure 1. Simplified geomorphic map of western Valles Marineris. C2 craters are young craters with raised rims.

Figure 2. Rose diagrams of azimuthal orientations of sapping channels and grabens in western Valles Marineris. Data was organized in 5 degree groupings.

ALIGNED SUBSIDENCE DEPRESSIONS IN THE VICINITY OF CERTAIN MARTIAN VALLEYS

J. Steiner, C. Sodden and D. Weiss, Department of Earth and Planetary Sciences, City College of CUNY, New York, N. Y. 10031

Large valley forms, commonly with amphitheater terminations, dissect the steep walled escarpment of the northern plateau terrain. Elongate graben-like and monocline-like forms which contribute to the formation of patterned ground on highlands (figure 1), comprise a subset of structures which logically relate to the development of valleys. To these elongate features may be added the tendency for depressional basins, impact craters, and subsidence depressions to be elongate in a systematic manner in relation to major lineations.

Of particular importance in this regard are subsidence basins, characterized by steep-walled boundaries, flat floors, and the absence of ejecta blankets, which occasionally offset ejecta of adjoining impact craters (1). These basins can be separated into two major groups: relatively small diameter basins which punctuate the floor of upland terrains, and distinctly larger basins which can be included in the beds of sinuous valley channels. These latter features, together with channels, define much of the discernable accordant lowland surface which abuts highland rocks. About 3500 of these and related basins have been digitized according to various parameters of morphology in an attempt to arrive at meaningful discriminations between basin forms.

The degree of elongation of basins can be expressed as the eccentricity of the basins in relation to an ellipse (2), and plotted as a vector whose direction is that of the major axis, and whose length is defined as the eccentricity ($e = c/a$) of the ellipse. Figure 1 shows a vector field made up of all vectors related to the more obvious subsidence basins, as presently recognized. It is readily apparent that the basins on highlands in the vicinity of the valley walls comprise a set conformable to that of basins on the lowlands (e.g. within sinuous channels, or, in other locations, at levels close to valley floors). This set of vectors is also subparallel to the east-west direction of the valley floor (mosaic unresolved to true north). Thusly, there appears to be an evolutionary relationship between subsidence depressions and large valleys.

Valley formation and headward erosion have been related to sapping at the headwalls (3,4). It has also been speculated to occur along valley walls and portions of the major escarpment (5). Present observations suggest that depletion of the Plateau terrain may occur internally as well as marginally,

and that basin form growth may involve the production of the large subcircular forms visible in sinuous channels. In this context, graben-like features may reflect subsidence structures which in general have a transverse orientation in respect to vectors.

REFERENCES

1. Fagan, J.J., Weiss, D., Steiner, J., and Franke, O.L. (1981) Subsidence Depressions on Martian Plateau Terrains, NASA Tech Mem 84211, 308-309.

2. Steiner, J., Sodden, C., Weiss, D., Fagan, J.J. (1981) A Morphological Comparison of Depressional Features in Plateau Materials of the Deuteron Mensae Region Based on Ellipsoidal Characteristics, NASA Tech Mem 84211, 312-315.

3. Laity, J.E., and Saunders, R.S. (1981) Sapping Processes and the Development of Theater-Headed Valleys, NASA Tech Mem 84211, 280-282.

4. Howard, A.D., and McLane, C. (1981) Groundwater Sapping in Sediments: Theory and Experiments, NASA Tech Mem 84211, 283-285.

5. Weiss, D., and Fagan, J.J. (1982) Possible Evidence of Hydrocompaction Within the Fretted Terrains of Mars (this report).

Figure 1. Map of eccentricity vectors connected to subsidence basins in fretted terrain at 38N 345W. Alignment of vectors subparallel to the traced east-west valley relates subsidence to valley forms.

Figure 1

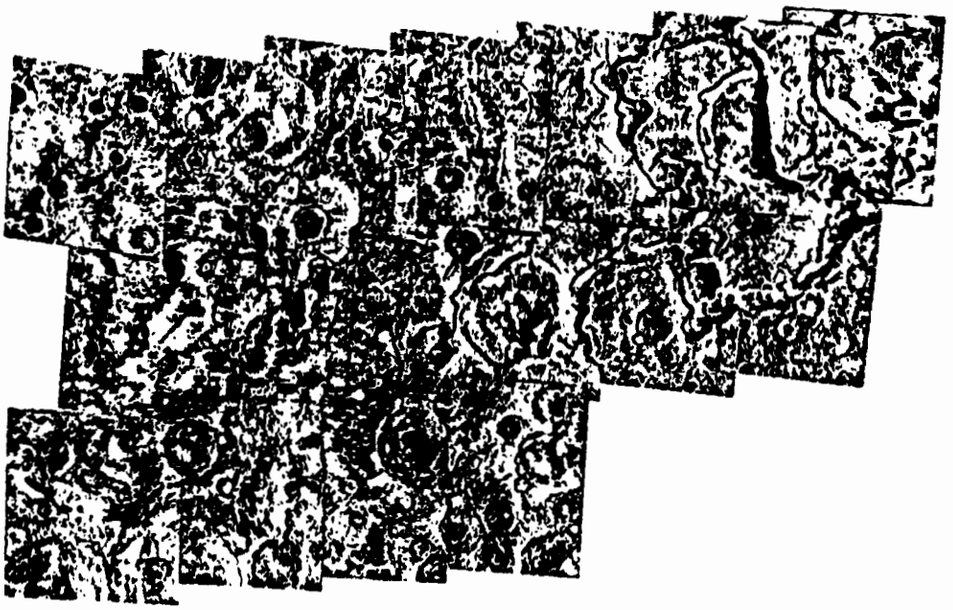

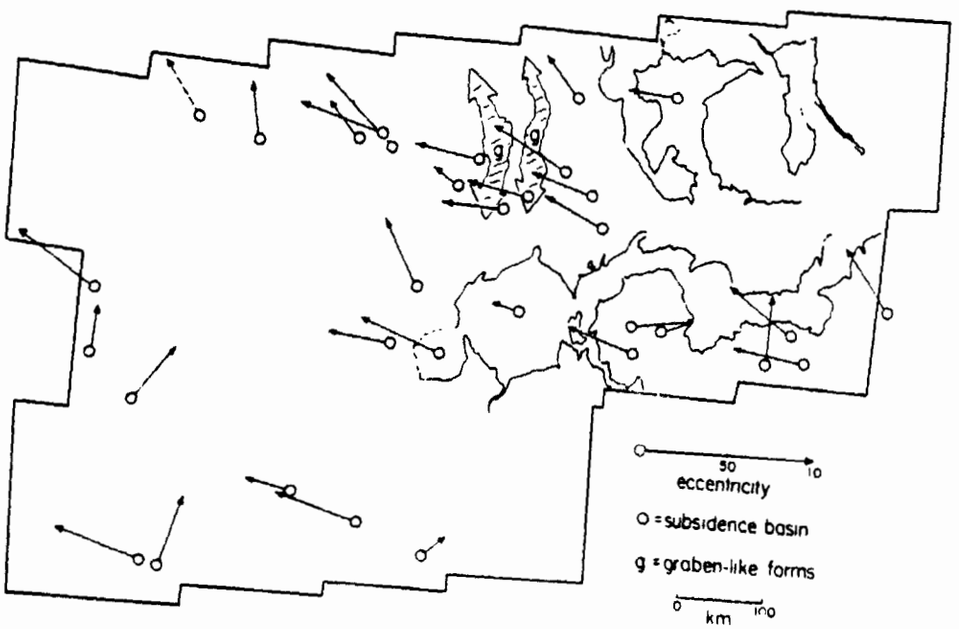

PRELIMINARY SURVEY OF KNOBS ON THE SURFACE OF MARS.

L. S. Manent, National Air and Space Museum, Smithsonian Institution, Washington, D. C. 20560, and Farouk El-Baz, Itek Optical Systems, Lexington, MA. 02173

Positive isolated features or knobs have been observed on Mars since Mariner 9 first photographed the planet in 1972. More recently, the Viking Orbitors photographed the surface at increased resolution. With the use of Viking photomosaics, a systematic search for these features was completed. Data collected on the knobs are from U.S. Geological Survey photomosaics at 1:2,000,000 scale (Figure 1). Of the 68 mosaics, 19 contained isolated positive features. These mosaics cover the Diacria (MC-2), Arcadia (MC-3), Mare Acidalium (MC-4), Cebrenia (MC-7), Amazonis (MC-8), Syrtis Major (MC-13), Elysium (MC-15), Aeolis (MC-23), and Noachis (MC-27) regions.

The knobs were characterized by length (long axis), width (perpendicular to the length at widest point), geographic location, proximity to streaks and geologic surroundings. These knobs occur in three surface units: a) the lowlands, consisting of plains material, b) a rugged upland terrain, and c) the plains/highlands border areas.

The Diacria Quadrangle (MC-2) contains knobs in the smooth and mottled plains unit, which dominates the area (Morris and Howard, 1981). The knobs are disseminated throughout the northern part of the quad between 140°W and 160°W, and are relatively small. Their average length and width is 4.8km and 3.6km respectively, with a length to width ratio of 1.34. The knobs are more rounded but elongate ones are oriented south to southwest. Wind streaks are not prominent but Thomas and Veverka (1979) indicate a southerly wind regime, based on global wind streak directions (Figure 2). There is an area of knobby terrain in the southwest section of the quad that extends to the Elysium volcanic province. These knobs are surrounded by plains material, but form a rugged upland terrain. They are associated with old crater rims and walls. They are slightly larger with an average length and width of 6.2km and 4.8km and the same proportion of rounded to elongate forms. Morris and Howard (1981) interpret these as remnants of ancient crater terrain that was dissected by faults and fractures and embayed by plains units.

Eastward in the Arcadia Quadrangle (MC-3) in the northern section, small knobs are also disseminated throughout. Along 50°N in the northeast section of Arcadia, large isolated knobs are present at the northwest edge of Tempe Plateau in the etched-upland material. Knobs in this region have an average length and width of 13km and 8.8km respectively, and a length to width ratio of 1.56. They are more elongate than those in the plains material and are oriented in a southwesterly direction. Global distribution of wind streaks indicate a south to southwest wind direction (Figure 2). Structural trends in the area are also to the southwest. The knobs are probably fracture-controlled erosional remnants, with wind as a modifier of their forms.

In the northeast section of Mare Acidalium (MC-4), knobs are present in the mottled plains material with average length and width of

5.4km and 3.6km. The length to width ratio is 1.5. Streaks are absent but knobs are oriented in a southerly direction. In the plains material in the southeast section, knobs are scattered throughout, and their average length and width is 4.1km and 3.3km. Similarily in the south-central section, the knobs are scattered and small in size, with an average length and width of 4.8km and 3.4km. However, in the southeast section, there are also some knobs forming a rugged upland terrain that are closely spaced and slightly larger. Their average length and width is 5.8km and 4.2km.

In the Cebrenia Quadrangle (MC-7), knobs occur along the eastern side in the Phelegra Montes and surrounding hilly terrain. They are grouped together in an uplifted area of an intensely cratered ancient surface that has been degraded. Their average length and width in the northeast is 8.72km and 6.48km, and in the southeast 6.92km and 4.9km. In the south-central part, scattered smaller knobs without streaks occur with an average length and width of 5.19km and 3.52km.

Knobs occur in the western half of the Amazonis Quadrangle (MC-8) in a rugged upland terrain forming parts of old crater rims and walls. Their average length and width is 6.9km and 4.8km in the northwest and 5.3km and 3.6km in the southwest. Streaks are abundant in the area and show a southwest wind direction. Similarly, the knobs have a southerly and southwesterly orientation.

In the Elysium Quadrangle (MC-15) knobby landforms occur in highly cratered and rugged terrain that extends in an arc from the south-central part to the northeast part of the quadrangle. Northeast-trending streaks are present throughout and are concentrated in the Cerberus region. The average length and width of the knobs in the northeast is 7.0km and 4.8km, in the southeast 5.7km and 3.9km, and in the southwest 6.3km and 4.6km. Length to width ratios are 1.58, 1.52, and 1.58 respectively.

Knobs are present along the plains/highland border of the Aeolis Quadrangle (MC-23). These are significantly larger and appear to have been produced by erosional retreat of the boundary scarp (Scott, Morris and West 1978). Their average length and width is 11km and 9.1km and their length to width ratio is 1.58. These knobs are oriented in a northwest-southeast direction.

In the Noachis Quadrangle (MC-27), knobs are located in the transitional zone between Hellespontus and Hellas, in the ancient cratered highlands of Mars. These knobs are the largest, with average length and width being 12.5km and 8.5km. Length to width ratio is 1.55. These knobs are generally oriented in a northwest-southeast direction.

These observations suggest that in the plains region, northern hemisphere of Mars, knobs are disseminated throughout and are significantly smaller than anywhere else on Mars. They are commonly less than 5km in diameter and tend to be oriented along the global wind regime. Streaks are not dominant in the region. North of the plains/highland boundry in a rugged upland terrain region, knobs are slightly larger and associated with streaks. They are commonly between 5km and 10km in diameter. Faulting, fracturing, slumping, and wind erosion appear to be the knob-forming processes. Knobs along the plain/highland border and highland terrain region are larger and more structurally controlled, with

the wind being a secondary eroding process. They are generally concentrated in groups and larger than 10km in diameter. Splotches are present but no streaks are associated with the knobs.

References:
Thomas, P. and Veverka, J., 1979, JGR, vol. 84, no. B14.
Morris, E. C. and Howard, K. A., 1981, U.S.G.S. map I-1286 (MC-2)
Scott, D. H., Morris, E. C. and West, M. N., 1978 U.S.G.S. map I-III (MC-23).

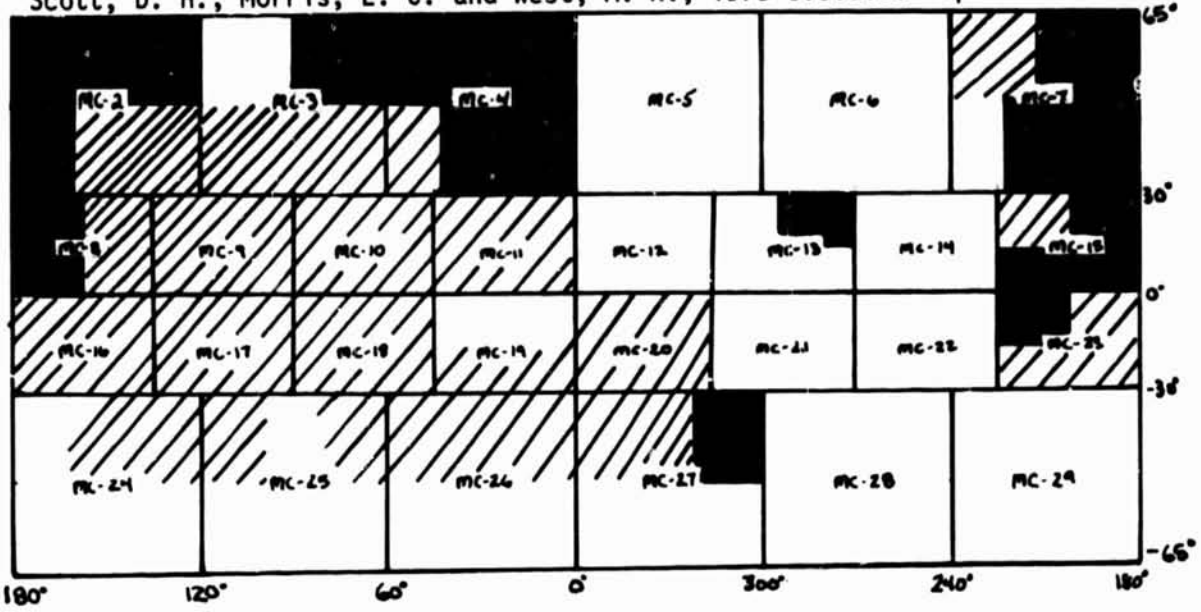

Figure 1. Location of positive isolated features
■ Knobs present /// No knobs present

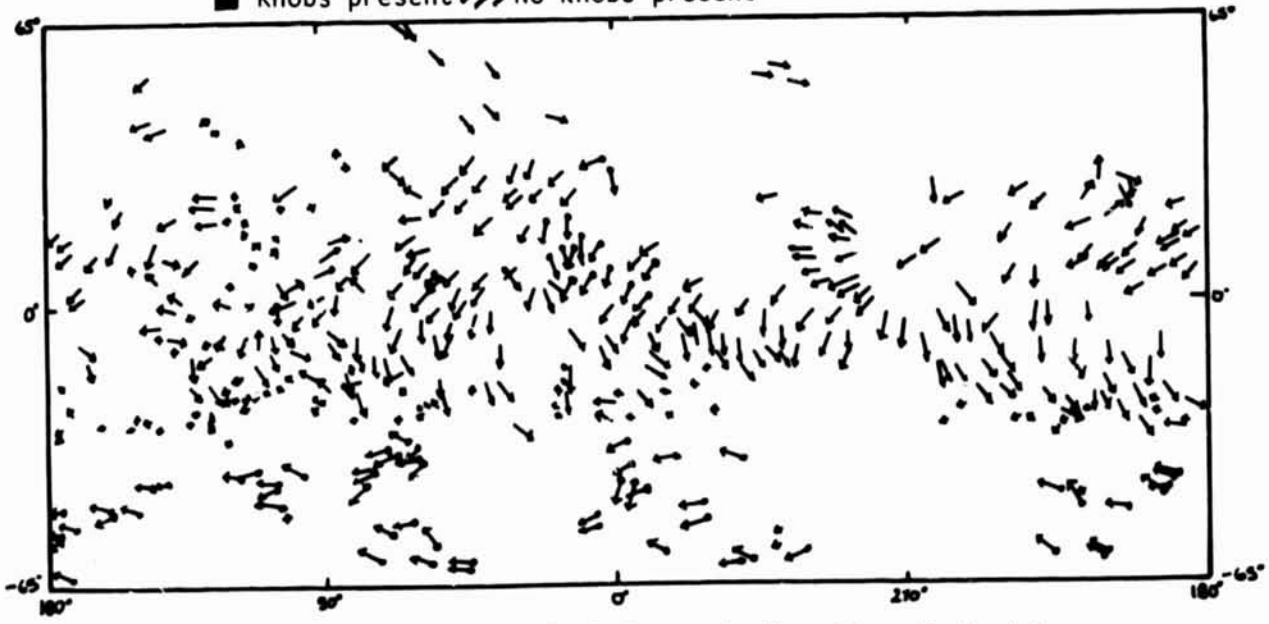

Figure 2. Global distribution of wind streak direction plotted from Viking data. ← Bright streaks; • dark, erosional streaks; ↔ dark, splotch-associated streaks.

MARS: SUBDIVISIONS OF HIGHLAND ROCKS

David H. Scott - U.S. Geological Survey, Flagstaff, AZ 86001

The highland terrains of Mars were only coarsely subdivided into four basic rock units during the Mariner geologic-mapping program. Other geologic units were recognized in the highlands from the Mariner images but were more or less ubiquitous to the planet as a whole. Geologic mapping and paleostratigraphic studies currently in progress have revealed many new highland rock units and have allowed the further subdivision of others. Figure 1 illustrates the general relations between the Viking map units and those previously established from Mariner pictures; these units are presently assigned only provisionally to the martian time-stratigraphic systems. As on other planetary maps, the names of the various rock units reflect their most outstanding observable physical features but not necessarily their primary surface forms or constructional morphologic characteristics.

In many places, boundaries between units are not sharp contacts but represent gradational zones whose surfaces show varying degrees of modification by resurfacing and fracturing. The plateau units (fig. 1) generally exhibit a regular transition between the hilly (plh), cratered (plc), and smooth (pls) materials that suggests increasing amounts of volcanic or eolian deposits. The ridged plateau (plr) and ridged plains (pr) units, on the other hand, may have different origins. Ridges within the plateau material typically are more prominent, broader, and more nearly resemble elongate mountain chains than their plains counterparts. The plains-type ridges, also, are more likely to occur in topographically low areas, where they appear to be associated with infilling materials, such as lava flows. Although the end members of these two ridge-forming units are readily distinguishable, gradations between them are common, and in such areas their assignment to one or the other particular type is less reliable.

Another, possibly unique, problem of ridge identification has arisen in the Lunae Planum region. Here, the ridge systems resemble typical plains-type wrinkle ridges; the ages of the ridges, however, as determined by crater counts (1), are consistently older than those of the smooth plains that encompass them. These ridges may belong to the older ridged plateau unit, whose surface has been mostly buried by later lava flows; the exposed narrow crestal parts of the plateau ridges resemble those more typical of the plains.

Several new plains units (Atp_{1-3}) have been mapped in the Tempe Terra (lat 40° N., long 75° W.) part of the highlands. These units appear to be embayed in places by early lava flows from Tharsis Montes and thus may be slightly older than the Amazonian system to which they have been assigned; possibly, the age of these units should be designated Amazonian-Hesperian (AH).

The oldest appearing martian rocks (unit Nbc) are exposed along the southern part of Claritas Fossae (lat 30° S., long 100° W.). In this general region, they also occur as islands of rugged mountains surrounded by lava flows of Tharsis Montes. In places, this basement complex is also gradational with other units, particulary the hilly plateau (Nplh) and fractured plains (Npf_1) materials.

References:

(1) Tanaka, K. L., 1982, A new time-saving crater count technique, with applications to narrow features (this issue).
(2) Scott, D. H., and Carr, M. H., Geologic Map of Mars; U.S. Geol. Survey, Misc. Geol. Inv. Map I-1083.

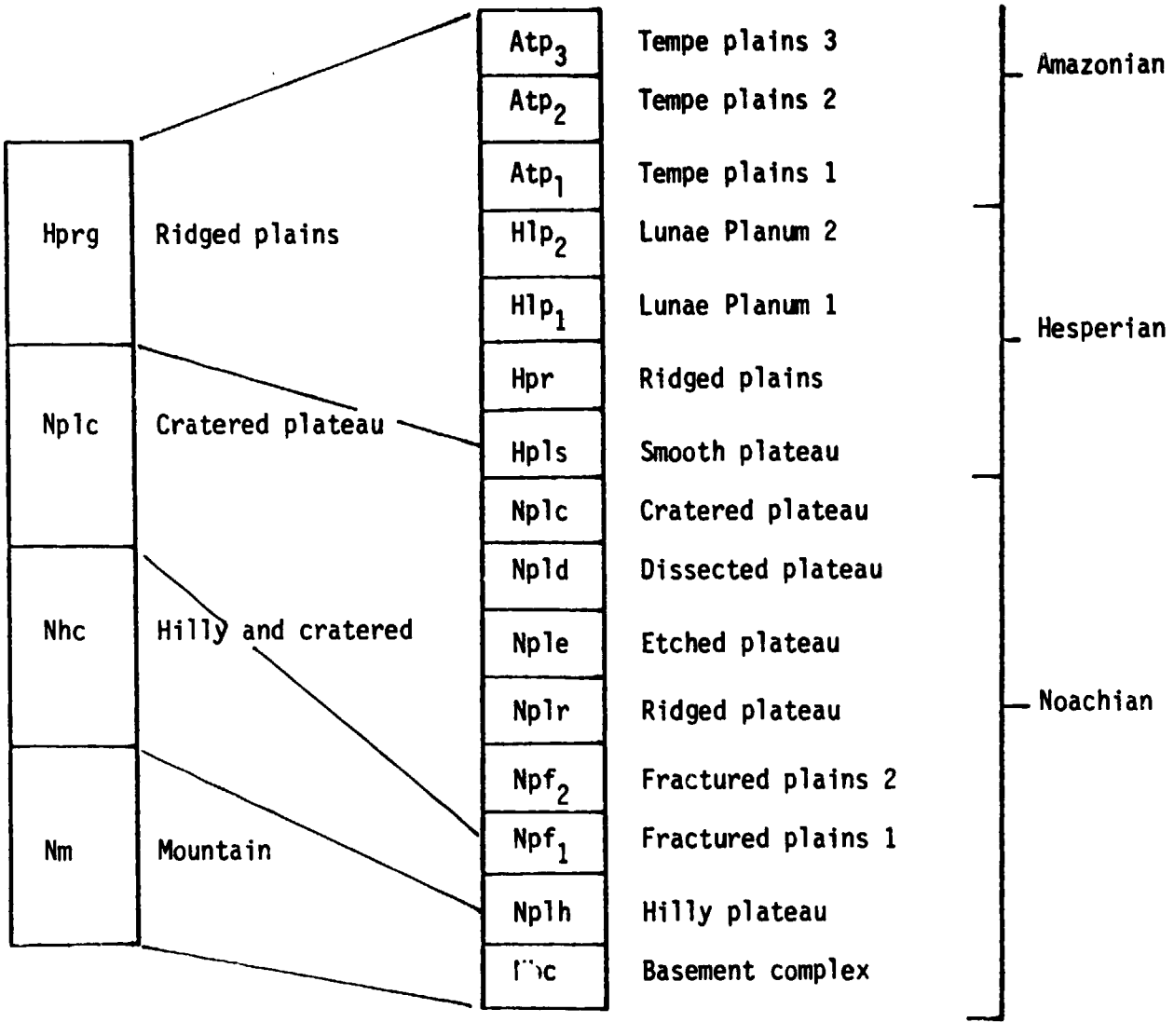

Figure 1. Subdivisions of major highland geologic units from Mariner and Viking mapping. Correlations shown are only approximate; some of the new (Viking) map units occur within more than one of the original Mariner units shown on the 1:25 million-scale geologic map of Mars (2).

COMPUTER ENHANCEMENT AS AN AID TO THE INTERPRETATION OF GEOLOGIC FEATURES ON VIKING IMAGERY: A PRELIMINARY PROGRESS REPORT

Baskerville, Charles A., U.S. Geological Survey, 952 National Center, Reston, VA 22092

Initial analysis of Viking Orbiter scenes suggested the presence of subtle tonal differences that might be expressions of geologic features. Digital-image processing was used to adjust the scene contrast as an aid to the interpretation of a subset of frame no. 534A04. The computer programs used are part of the Office of Remote Sensing of Earth Resources (ORSER) package developed at The Pennsylvania State University for enhancement of multispectral images recorded from aircraft and the Landsat and Skylab satellites (Turner and others, 1978; Sabins, 1978).

In the standard, unenhanced scene, which was recorded in the 555 - 650 nanometers (K. Klaasen, personal commun., 1982) wavelength region, a bright linear zone was noted along the middle of a valley wall. This feature was interpreted tentatively as a lithologic unit. However, in the contrast-enhanced image (Lillesand and Kiefer, 1979) this feature was determined to be a topographic bench. Apparently, the strata above the bench have eroded more rapidly than the lower strata, possibly suggesting a lithologic difference.

Other tonal features of possible geologic importance (Verstappen, 1977) will be analyzed using the ORSER program.

ACKNOWLEDGMENTS

This work is supported by NASA Contract W-14,730. Mars imagery was obtained from the NASA National Space Science Data Center, Greenbelt, Md. Computer tapes were procured from the NASA-Jet Propulsion Labs, Pasadena, Calif.

REFERENCES

Lillesand, T.M. and Kiefer, R.W., 1979, Remote sensing and image interpretation: John Wiley & Sons, p. 442-487, 528-559.

Sabins, Jr., F.E., 1978, Remote sensing principles and interpretation: W.H. Freeman, p. 233-275.

Turner, B.J., Applegate, D.N. and Merembeck, B.F., 1978, Satellite and aircraft multispectral scanner digital data user manual, ORSER Technical Report 9-78, The Pennsylvania State University, 378 p.

Verstappen, H.T., 1977, Remote sensing in geomorphlogy: Elsevier Scientific Publishing Co., 214 p.

ILLUSTRATION

Figure 1.-534A04 Apparent bright stratigraphic unit on valley wall indicated by arrow in lower center of scene.

Chapter 10

REMOTE SENSING AND REGOLITH STUDIES

SIR-A IMAGES REVEAL MAJOR SUBSURFACE DRAINAGES IN THE EASTERN SAHARA: APPLICATIONS TO MARS

J. F. McCauley, G. G. Schaber, C. S. Breed, and M. J. Grolier, U.S. Geological Survey, Flagstaff, AZ 86001

The Shuttle Imaging Radar (SIR-A), carried on Columbia in November 1981, penetrated the extremely dry Selima Sand Sheet and associated dunes and drift sand of the Eastern Sahara to reveal previously unknown buried valleys, geologic structures, and possible stone-age occupation sites. Radar responses from bedrock and gravel surfaces beneath several centimeters to possibly meters of windblown sand delineate sand- and alluvium-filled relict stream valleys, some nearly as wide as the Nile Valley and perhaps as old as middle Tertiary (fig. 1). Underfit and incised wadis, many superimposed on the large valleys, represent the effects of intermittent running water, probably during Quaternary pluvial episodes.

The presence of these otherwise invisible drainage networks beneath the eolian veneer (fig. 2) was suspected on the basis of earlier field and Landsat studies of the Gilf Kebir region. There numerous steep-walled incised dry wadis debouch from a dissected plateau onto the surrounding desert plains, from which nearly all traces of former fluvial activity have been eroded or buried by wind (Breed and others, 1982; McCauley and others, 1982a, b). In the Eastern Sahara, the size and regional extent of old buried fluvial networks has now been confirmed by radar images. Radar-brightness units were mapped, using techniques first applied to lunar mapping (McCauley, 1967), these maps show a terrain formed under earlier, less arid climatic conditions (McCauley and others, 1982a, b). The now-vanished major river systems revealed by SIR-A probably accomplished most of the erosional stripping of this now extraordinarily flat hyperarid region.

The presently hyperarid Eastern Sahara provides numerous analogs for surface geologic processes and landforms on Mars, including relict fluvial channels, yardangs, dunes, conical hills, and pitted rocks (McCauley and others, 1979, 1980, 1982a; Grolier and others, 1980; Breed and others, 1980, 1982; Grolier and Schultejann, 1982). Most of these features are of hybrid origin and reflect an interplay of wind with episodic running water and with mass wasting. The Eastern Sahara, though on a much shorter time scale, clearly shows the effects of eolian takeover of a previous fluvial terrain, as described for Mars.

The theoretical penetration of sand (or ice) by radar depends on the wavelength and incidence angle of the radar beam (in the case of SIR-A, 24 cm and 47° at the surface) and on the electrical properties of the material, which are largely determined by soil moisture (Chilar and Ulaby, 1974; Elachi and others, 1982). The calculated depth of radar penetration of dry sand and granules, based on laboratory measurements of the electrical properties of samples from the Selima Sand Sheet, is at least 5 m. Penetration of dry sand by imaging radar thus provides a new tool for geologic investigations of hyperarid regions whose palimpsest fluvial features are obscured by a veneer of dry (or frozen) sediment. A similar imaging-radar experiment for Mars should result in

hitherto unknown views of the martian terrain beneath the polar icecaps and the eolian dust blankets and dune fields that presently obscure much of its surface.

References:

Breed, C. S., McCauley, J. F., and Grolier, M. J., 1980, Evolution of inselbergs in the hyperarid Western Desert of Egypt--comparisons with martian fretted terrain: National Aeronautics and Space Administration Technical Memorandum 82385, p. 307-311.

Breed, C. S., McCauley, J. F., and Grolier, M. J., 1982, Relict drainages, conical hills, and the eolian veneer in Southwest Egypt--applications to Mars: Journal of Geophysical Research, Third International Mars Colloquium Issue (in press).

Chilar, J. and Ulaby, F. T., 1974, Dielectric properties of soils as a function of moisture content: CRES Technical Report 177-47, University of Kansas Center for Research Inc., Lawrence, Kansas.

Elachi, C., Roth, L., and Schaber, G. G., 1982, Radar subsurface imaging in hyperarid regions: IEEE Transactions (in press).

Grolier, M. J., McCauley, J. F., Breed, C. S., and Embabi, N. S., 1980, Yardangs of the Western Desert: Geographical Journal, v. 146, pt. 1, p. 86-87.

Grolier, M. J. and Schultejann, P., 1982, Geology of the Gilf Kebir Plateau, Western Desert, Egypt, in El-Baz, F. and Maxwell, T. (eds.), Desert Landforms of Western Egypt: A basis for comparison with Mars: National Aeronautics and Space Administration Contractor's Report (in press).

McCauley, J. F., 1967, The nature of the lunar surface as determined by systematic geologic mapping, in Runcorn, S. K., ed., Mantles of the Earth and Terrestrial Planets: New York, Interscience, p. 431-460.

McCauley, J. F., Breed, C. S., El-Baz, Farouk, Whitney, M. I., Grolier, M. J., and Ward, A. W., 1979, Pitted and fluted rocks in the Western Desert of Egypt: Viking comparisons: Journal of Geophysical Research, v. 84, no. 14, p. 8222-8232.

McCauley, J. F., Breed, C. S., and Grolier, M. J., 1980, The Gilf Kebir and the Western Desert of Egypt--insights into the origin of the North Polar Erg on Mars: National Aeronautics and Space Administration Technical Memorandum 82385, p. 312-313.

McCauley, J. F. Breed, C. S., and Grolier, M. J., 1982a, The interplay of fluvial, mass-wasting, and eolian processes in the eastern Gilf Kebir region, in El-Baz, F., and Maxwell, T. eds., Desert Landforms of Southwest Egypt: A basis for comparison with Mars: National Aeronautics and Space Administration Contractor's Report (in press).

McCauley, J. F., Schaber, G. G., Breed, C. S., Haynes, C. V., Grolier, M. J., Issawi, B., Elachi, C., and Blom, R., 1982b, Subsurface valleys and geoarchaeology of the Eastern Sahara revealed by Shuttle Radar: Science (in press).

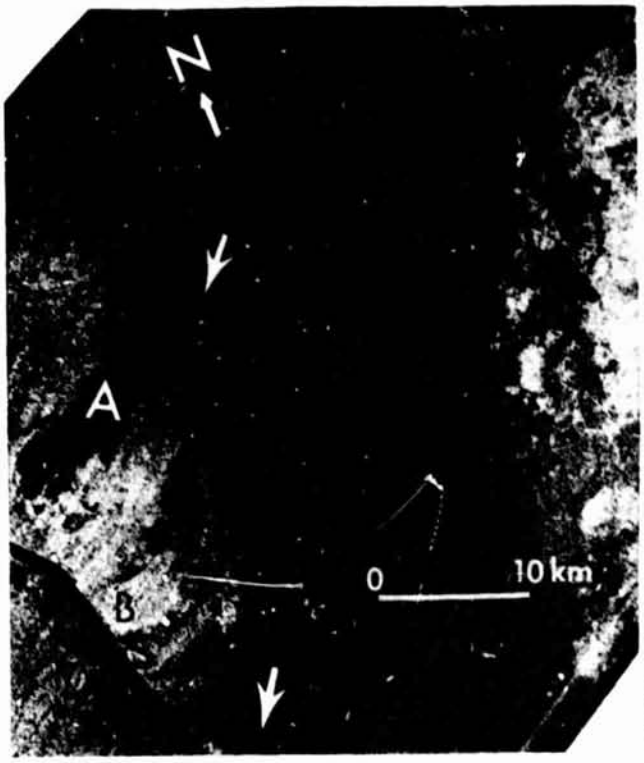

Figure 1. SIR-A image showing 20-km-wide valley with a stubby beveled tributary (at A) and much smaller superimposed channels at B and C. Note fans (arrows). All these fluvial features are buried beneath a veneer of windblown sand (see fig. 2).

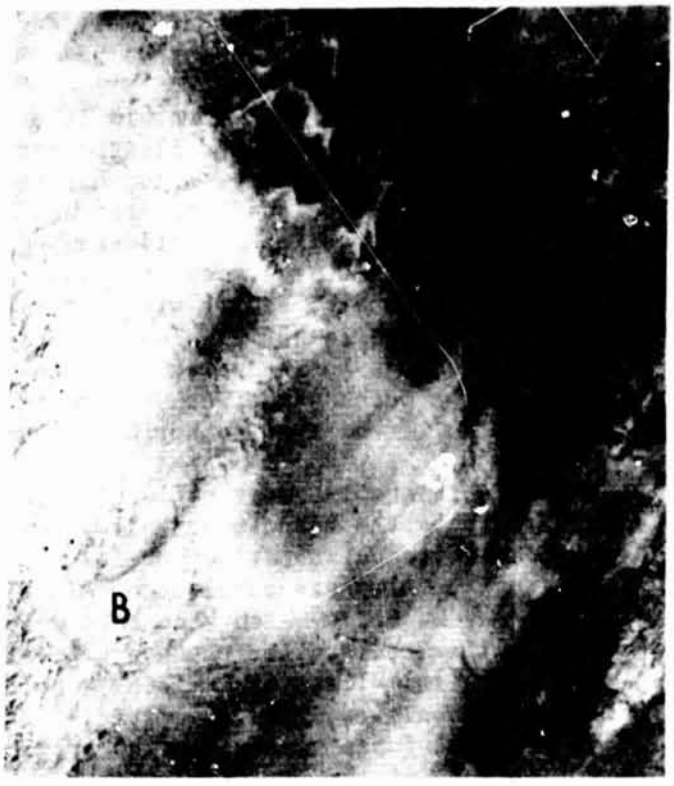

Figure 2. Landsat image of area of figure 1 at same scale shown on radar image. Large valley is obscured by sand sheet and dunes. Faint trace of sand-filled incised channel is visible at B.

SIR-A RESULTS FROM COASTAL NORTHERN CALIFORNIA

J.B. Plescia and R.S. Saunders, Jet Propulsion Laboratory, California Institute of Technology, Pasadena, CA 91109

Two SIR-A images of the coastal northern California area were acquired during the STS 2 flight in November 1981, during orbits 20 and 21 and are referred to as takes 24A and 24B respectively.

The northern coast of California is a heavily forested area composed predominantely of Mesozoic clastic marine units. Most notable of these units is the Franciscan complex which has been interpreted as a subduction complex. The Franciscan lies between Tertiary-Cretaceous clastics to the west and Paleozoic clastics and alluvium of the Sacramento Valley to the northeast and east. Contacts between each major units are generally tectonic rather than depositional. Faults within the region are generally northwest striking (N20-30^{o}W) paralleling the coast. The most important structural feature is the Coast Range Thrust which forms the eastern margin of the Franciscan units. The Coast Range Thrust, and other associated thrusts in the Paleozoics, trend east to northwest and dip north to northeast.

Major contrasts in radar reflectivity are largely confined to the area underlain by the Franciscan units. Within that region elongate zones and smaller rectangular patches of low reflectivity occur. Many, but by no means all, of the elongate zones occur along ridge crests. These low reflectivity zones may be areas which have been deforested exposing the ground surface. The smaller rectangular patches generally have their long axes oriented north to northwest. These may reflect outcrops of ultramafic serpentine-rich rocks which commonly occur in the Franciscan. The ultramafics do not support substantial forest growth. Other reflectivity contrasts are associated with the courses of the larger rivers which cross the region. All are marked by low return. This is most likely due to flat valley bottoms filled with fine grained material of much smaller size than the radar wavelength.

We have examined the azimuthal distribution of lineaments observed between the coast and the western margin of the Sacramento Valley from both strips. This was done in order to compare the lineament observed on the radar with the known structure of the region.

Few mapped faults were directly observable on the radar image. Only the Coast Range Thrust is readily identifiable apparently because of its correlation with the south fork of the Trinity River. The absence of identifiable faults on the radar image may result from several interrelated causes. First the region is heavily forested and therefore the ground is not exposed, thus any reflectivity contrast between rock types across a fault which might produce a lineament are hidden from view. Secondly, all the rock types in the region are fairly similar marine clastics and probably would have low reflectivity contrasts. Finally the stuctures do not seem to have produced pronounced topographic expressions which would result in observable lineaments.

There are some examples of correlations between lineaments and features observable on the ground. Along the coast, within the Tertiary-Cretaceous clastics, a series of short lineaments broken by numerous canyons which cut the coastal region parallel the coast. These lineaments can be correlated

with bedding within the clastic section. Distinct bedding apparently occurs only within the Tertiary-Cretaceous section and not within the Franciscan to the east. A second series of lineaments which occur along the western margin of the Sacramento Valley can also be correlated with sedimentary bedding. Here the Cretaceous clastic section has been uplifted exposing bedding in a curvilinear pattern along the margin of the valley. The lineaments observed closely parllel the outcrop pattern of the unit.

Three types of angular frequency histograms were prepared from the data. These include a) the number of lineaments independent of their length as a function of azimuth, b) the same data weighted for length of the lineaments and c) only those lineaments greater than 5 km length. Figure 1 illustrates the histograms of lineaments greater than 5 km length for takes 24A and 24B. The average directions for each of these analysis is listed in Table I in terms of direction relative to the flight line and to geographic north. The majority of lineaments are oriented at an angle of approximately 50° to a direction parallel to the flight track (40° from a normal to the flight track). As the two orbit flight tracks differ by approximately 20° in orientation (N78°E vs. N100°E), hence the lineaments seen on them are not oriented in the same direction. The observed difference is well outside any probable error in such an analysis. Additionally none of these directions are similar to the generally N20-25°W orientation of the structural features observed in the region. Such a distribution of lineaments suggests that they are not a direct result of structure but rather are an artifact in the data.

The results observed here indicate that extreme caution must be exercised when attempting to map structural features in such regions from radar images. Similar results to those resented here, that all lineaments do not represent real structure, has also been reported by Elder et al., 1974 and Johnston et al., 1975.

REFERENCES:

Elder, C.H., Jeran, P.W., and Keck, D.A., 1974, Geologic structure using radar imagery of the coal mining area of Buchanan County, VA., U.S. Bur. Mines Rept. Inv. 7869.

Johnston, J.E., Miller, R.L. and Englund, K.J., 1975, Applications of remote sensing to structural interpretations in the southern Appalachians: U.S. Geological Survey Jour. Research, v. 3, 285-293.

TABLE I

	Number		Length weighted		Length	5km	
Take	relative	absolute	relative	absolute	relative	absolute	orbit
24A	55° - 58°	N47°W - 20°E	54° - 55°	N48°W - 22°E	53° - 61°	N49°W - N17°E	N78°E
24B	49° - 50°	N31°W - 50°E	49° - 50°	N31°W - 50°E	50° - 45°	N30°W - 55°E	N100°E

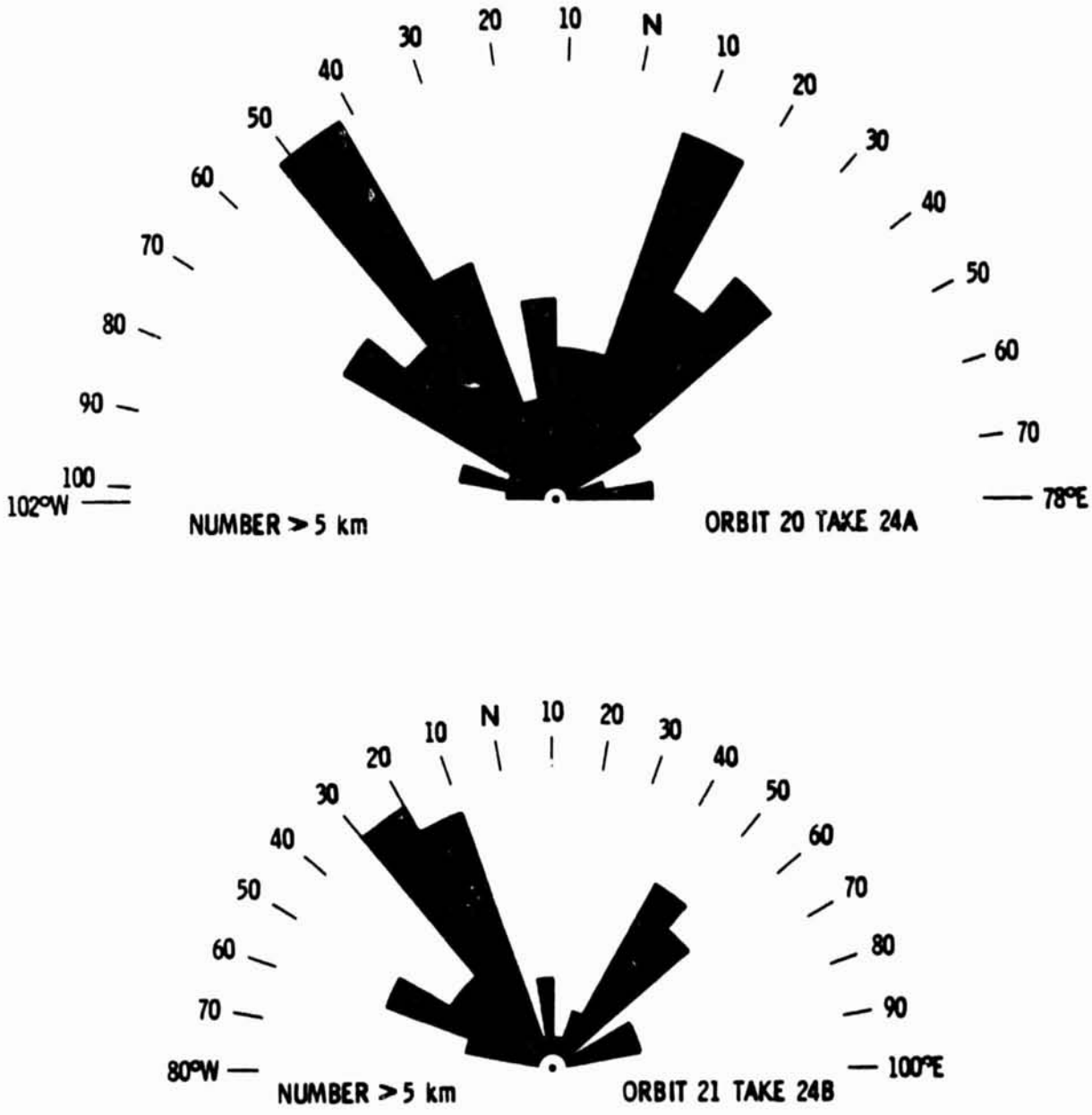

Figure 1. Angular frequency histograms for all lineaments greater than 5 km length for coastal northern California from takes 24A (top) and 24B (bottom).

MARS SURFACE PROPERTIES FROM VIKING BISTATIC RADAR

Richard A. Simpson, G. Leonard Tyler, and H. Taylor Howard
Center for Radar Astronomy, Stanford University, Stanford, CA 94305

Data from Viking bistatic radar observations at λ = 13 cm wavelength have been fitted to power spectrum templates calculated using the Hagfors (J. Geophys. Res., 69, 1964) scattering function

$$\sigma_H(C,\theta) \propto (\cos^4\theta + C \sin^2\theta)^{-3/2}$$

Surface roughness estimates from this analysis (Table I) agree closely with values obtained from earth-based observations (Downs et al., Icarus, 26, 1975; Simpson et al., Icarus, 36, 1978) where ground tracks intersect -- in cratered terrain as well as in plains. There are no striking correlations between the radar results and photogeology. This reaffirms our earlier conclusion (Simpson et al., Icarus, 32, 1977; Icarus, 49, 1982) that processes which dominate Mars surface texture at scales important to radio wave scattering (<100 m) cannot be easily inferred from orbital images.

Values of surface roughness determined using the Hagfors function are 30-40% lower than those derived previously with gaussian templates (Simpson and Tyler, Icarus, 46, 1981). Previously published estimates from the permanent north polar cap should be reduced, therefore, to about 2°. Inversions of power spectra (Fig. 1) suggest that $\sigma_H(C,\theta)$ only adequately describes surface tilt on Mars. There is usually a higher proportion of surface elements with near-zero tilts than the Hagfors function would predict. On the moon $\sigma_H(C,\theta)$ was judged the best of three functions (gaussian, Hagfors, and exponential) in comparisons with radar data (Simpson and Tyler, IEEE Trans., AP-30, 1982). The difference on Mars may be the way in which aeolian and other processes modify the small-scale surface structure.

Comparison of roughness estimates from data in which two approximately equal orthogonally polarized echoes were received shows no significant differences in the spectra of the two components. Separation of the echo into deterministic (polarized) and random (unpolarized) components showed occasional presence of the latter. In particular, near (72°W, 17°S) where Downs et al. (Icarus, 26, 1975) reported detection of a depolarized echo, we found unpolarized echo power. Though existing models are inadequate for quantitative interpretation of polarization data there is general agreement that unpolarized and depolarized power indicates the presence of blocks or other irregular structure on the surface.

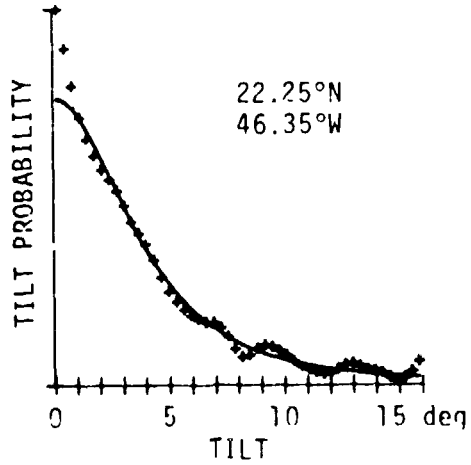

Fig. 1 - Tilt probability density function for Chryse Planitia Viking Lander 1 site.

TABLE I

Surface Roughness from Viking Bistatic Radar
Template Fits Using Hagfors' Scattering Law

(arranged approximately in order of decreasing latitude)

Area	DOY*	Ground Track Start °W	Start °N	Stop °W	Stop °N	RMS Roughness** (deg)
North Polar Cap	020	129.60	85.38	175.59	88.70	1.79±0.11
South of VL-2	016	239.64	34.33	230.39	37.41	4.98±0.95
Olympus Mons	066	142.23	25.75	132.10	34.04	7.67±3.46
VL-1	038	45.55	21.33	46.95	23.55	4.42±0.18
Tritonis Lacus	343	247.52 250.26	18.28 21.85	249.43 250.11	20.03 23.90	4.15±0.18 1.78±0.08
Syrtis Major	042	291.11	8.98	298.98	9.57	1.18 to 0.46
Lunae Planum	029	51.53	8.42	69.62	9.80	4.99 to 2.29
Arsia Mons	001	125.46	-13.85	131.18	-9.32	8.00±1.32
Apollinaris	324 359	166.33 193.29	-19.86 -21.86	167.88 190.57	-13.13 -16.26	3.16±0.44 2.33±0.24
Sinai/Solis Plana	045 006	80.46 83.16	-25.07 -24.27	73.92 78.12	-13.34 -17.20	1.01 to 2.04 0.99 to 1.84
Soviet Site	339	26.65	-24.56	22.72	-21.73	4.82±0.09
Hellas	002 042	295.96 295.14	-46.25 -49.90	300.50 294.54	-37.24 -45.46	3.97-7.95 3.34±0.53 3.40±0.64

* Day of year. Day numbers larger than 300 were from 1977; the remainder were 1978.

** Generally given as a mean value and standard deviation -- e.g., "5.68±0.54." High and low values along the ground track are indicated by "3.97-7.95;" assume considerable variation. An approximately monotonic trend from ground track start to stop is indicated by "3.40 to 4.27." Dual entry for Hellas 042 gives results derived independently from two polarizations.

ANALYSIS OF THE APOLLO LUNAR SOUNDER EXPERIMENT DATA - A PROGRESS REPORT. V. L. Sharpton, J. W. Head, Depart. of Geological Sciences, Brown University, Providence, RI 02912, and R. W. Shorthill, Univ. of Utah Research Institute, Research Park, Salt Lake City, UT 84108.

Background: ALSE was a three channel, synthetic-aperture radar experiment in operation during orbits 16, 17 and 18 of the Apollo 17 mission [1,2]. The primary objective was to detect variations in the lunar subsurface electrical properties and thereby determine subsurface layering and structure. The HF-1 channel (λ = 5m) provided the deepest subsurface sounding.

Processing: All HF-1 raw data signal film was transformed to holographic format using coherent optical-processing techniques [3]. Unlike photographs, holograms preserve the full dynamic range and phase information of the processed data. A specially designed hologram viewer [2] allows the observer to adjust the Doppler bandwidth and magnify the reconstructed radar image on a viewing screen. These Doppler-filtered images can then be photographed and mosaicked.

Interpretation: Early digital and holographic analysis illustrated that radar data collected during a single lunar orbit was not sufficient to determine subsurface reflections from off-track surface clutter. In order to reduce this ambiguity, a multiple orbit data correlation technique was devised which involved comparing the holographically processed radar data from two adjacent E-W orbits and filtering out those reflections which did not occur in both orbits at the same time delay (depth) and azimuth (longitude) [5]. This technique was tested for traverses across Maria Serenitatis and Crisium. Spatially coherent radar returns were detected across both maria: two horizons in Serenitatis and one in Crisium [4]. Calculations of power reflection coefficients indicate that these radar horizons are most likely regolith layers interbedded with more massive lithologies [4]. The subsurface horizons in Mare Serenitatis have recently been assigned to major stratigraphic boundaries on the basis of detailed surface analysis, thus permitting the structural and stratigraphic evolution of the basin to be better ascertained [5].

Present Investigation: The ALSE coverage included a number of mare regions in addition to Serenitatis and Crisium: the north flank of Mare Vaporum, the southern shelf of Mare Imbrium and an extensive traverse across Oceanus Procellarum. We have recently undertaken an effort to analyze these remaining ALSE data in holographic format and correlate the data between adjacent orbits. The hologram viewer at the University of Utah has been reassembled and fine tuned. Second and third generation signal and hologram film for all lunar regions covered by ALSE has been examined and catalogued. We have conducted test runs for the traverse (orbit 17) across Oceanus Procellarum in the vicinity of 5°N, 50°W and are currently analyzing these images.

References: [1] R. J. Phillips, et al. (1973) Apollo Lunar Sounder Experiment in Apollo 17 Preliminary Science Report, NASA SP-330, 22-1--22-26. [2] L. J. Procello et al. (1974) The Apollo Lunar Sounder Radar System, Proc. IEEE, 62, 769-783. [3] L. J. Cutrona et al. (1966), On the application of coherent optical processing techniques to synthetic-aperture radar, Proc. IEEE, 54, 1026-1032. [4] W. J. Peeples et al. (1978) Orbital radar evidence for lunar subsurface layering in Maria Serenitatis and Crisium, Journ. Geophy. Res., 83, 3459-3468. [5] V. L. Sharpton and J. W. Head (1982) Stratigraphy and structural evolution Mare Serenitatis: A reinterpretation based on Apollo Lunar Sounder (ALSE) data, Journ. Geophys. Res., in press.

CLASSIFICATION OF SURFACE UNITS IN THE EQUATORIAL REGION OF MARS BASED ON VIKING ORBITER COLOR, ALBEDO, AND THERMAL DATA

R.E. Arvidson and E.A. Guinness, McDonnell Center for the Space Sciences, Washington University, St. Louis, Missouri 63130

A considerable amount of Viking Orbiter data now exists that is pertinent to understanding the distribution of surficial and perhaps bedrock units on Mars. The most applicable data sets consist of three color (0.45 to 0.59 micrometers) image data (Soderblom et al., 1978), together with thermal inertia estimates and broadband (0.3 to 2.5 micrometers) albedo data derived from the Infrared Thermal Mapper (Kieffer et al., 1977). We have quantitatively searched for clusters within the 3 dimensional data set consisting of Red/Violet ratios from the approach mosaic (northern late spring), together with albedo and thermal inertia estimates for the first 300 days of the Viking Orbiter mission. These Mars Consortium data were first placed in registered image format and then a principal components rotation was performed to obtain three new axes that better explain the variance patterns inherent in the data (Arvidson et al., 1982). We find that about 50% of the variance (information content) for the region spanning 15 degrees on either side of the equator is carried along the first principal component vector direction. In essence, this means that the data form an elongate swarm in R/V, albedo, thermal inertia space. The swarm was "stretched" into a spherical shape, to remove the dominate trend and to emphasize the distribution of clusters, by increasing the dynamic range along the principal component directions. An inverse coordinate rotation was then performed to obtain the decorrelated values of R/V, albedo, and themal inertia. The new values were then plotted in a triangular diagram and clusters were visually defined and tested for statistical validity (Arvidson et al., 1982). Unit maps for the region bounded by 0 to 50° and 280 to 360° W. longitude were generated based on the clusters. Five main clusters were identified that are part of a trend with two end members: A bright, red region with low thermal inertia (Arabia), and a dark, gray region with high thermal inertia. The fact that three discrete units can be discerned between these end members may be related to discrete mixing of "bright" and "dark" components by aeolian processes. Mantling by sediments is prevalent in Arabia, while the darker, grayer units, with higher thermal inertia, exhibit mare-like plains. The mantling is apparent in Viking Orbiter images with resolutions from 8 to 30 meters per pixel. These results imply a correlation in the study area between color, albedo, and thermal inertia, which are probes of near surface materials, and debris mantles, which extend to depths of meters. However, caution must be exercised in interpreting the units maps for at least two reasons. First, results of Jacobberger et al. (1982), who used the same techniques to map rocks and soils in eastern Egypt using Landsat MSS data, demonstrate that mineralogically distinctive rocks can be grouped within a single cluster because of limited spectral coverage (i.e. broad bands, only 4 bands, limited part of spectrum). Second,

Strickland (1982) examined the Martian study area with orbital color data and has been able to delineate color clusters that correspond to units not resolved at the relatively coarse spatial resolution of the approach mosaic. We are presently including the orbital color data in our cluster analyses.

References

Arvidson, R.E., E.A. Guinness, A.P. Zent, 1982, Classification of surface units in the equatorial region of Mars based on Viking Orbiter color, albedo, and thermal data, J. Geophys. Res., in press.

Jacobberger, P.A., R.E. Arvidson, D. Rashka, 1982, Application of Landsat MSS data and sediment spectral reflectance measurements to mapping of the Meatiq dome, Egypt, Geology, submitted.

Kieffer, H.H., T.Z. Martin, A.R. Peterfreund, B.M. Jakosky, E.D. Miller, and F.D. Palluconi, 1977, Thermal and albedo mapping of Mars during the Viking primary mission, J. Geophys. Res., 82, 4249-4291.

Soderblom, L.A., K. Edwards, E.M. Eliason, E.M. Sanchez, and M.P. Charette, 1978, Global color variations on the Martian surface, Icarus, 34, 446-464.

Strickland, E.L., 1982, Eolian Stratigraphy of the west central equatorial region of Mars, Abstracts, Lunar and Planetary Sci. 13, 780-781.

CORRECTIONS FOR ELEVATION OF VIKING ORBITER MEASUREMENTS OF MARTIAN THERMAL INERTIAS

James R. Zimbelman, Department of Geology, Arizona State University, Tempe, Arizona 85287

Thermal inertias determined from Viking Infrared Thermal Mapper data display a general trend of decreasing value with increasing elevation (1,2). Three atmospheric effects contribute to this trend: decreasing thermal conductivity of particulate materials with decreasing atmospheric pressure (3), decreasing atmospheric thermal radiation to the surface with increasing elevation, and decreasing dust optical depth with increasing elevation (2). These effects are particularly pronounced for topographically high areas such as the volcanic constructs (4,5). New radar-derived topography indicate that the 1976 Mariner 9 topography (6) is 2 to 5 km too high in parts of the northern hemisphere (7); earlier studies using the 1976 elevations may require some reevaluation. We are working on removing the elevation-dependent effects from the observed thermal inertias so that the resulting spatial variations of surface properties are enhanced.

Laboratory experiments with a variety of particulate materials have established the pressure-dependent variations in thermal conductivity (8,9). The thermal conductivity varies as the square root of the pressure for martian conditions so that the thermal inertia varies as the fourth root of the pressure (3). Pressure can be associated with elevation through the atmospheric scale height and an appropriate correction made to the thermal inertias at that elevation.

Jakosky (1) showed that the removal of the atmospheric thermal radiation term from the standard models resulted in a significant increase in the derived thermal inertia for the Arsia Mons caldera. We have run thermal models with varying atmospheric radiation contributions and the resulting thermal inertia changes can again be related to the elevation through the atmospheric pressure.

The contribution of atmospheric dust to the thermal radiation incident on the surface is considerably more difficult to model. Several approaches have been taken to this problem (1,10,11). Visual (12) and infrared (13) measurements provide dust optical depths for the Viking operations period which should allow the dust contribution to thermal inertia values to be evaluated.

1. Jakosky, B.M., 1979, J. Geophys. Res., 84, 8252-8262.
2. Palluconi, F.D. and H.H. Kieffer, 1981, Icarus, 45, 415-426.
3. Kieffer et al., 1973, J. Geophys. Res., 78, 4291-4312.
4. Kieffer et al., 1977, J. Geophys. Res., 82, 4249-4291.
5. Zimbelman, J.R. and R. Greeley, 1981, Pap. Third Mars Coll., LPI Cont. 441, 291-293.
6. U.S. Geological Survey, 1976, Map I-961.
7. Downs et al., 1982, Science, (in press).
8. Wechsler, A.E. and P.E. Glaser, 1965, Icarus, 4, 335-352.
9. Wechsler et al., 1972, Thermal Characteristics of the Moon, J. Lucas, ed., MIT Press.
10. Gierasch, P. and R. Goody, 1972, J. Atmos. Sci., 29, 400-402.
11. Zurek, R.W., 1978, Icarus, 35,196-208.
12. Pollack et al., 1979, J. Geophys. Res., 84, 2929-2945.
13. Martin et al., 1979, J. Geophys. Res., 84, 2830-2842.

EFFECTS OF LAYERING ON REFLECTANCE AND ABSORPTION BAND CONTRAST

Bruce Hapke, Dept. of Geology and Planetary Science, University of Pittsburgh, Pittsburgh, PA 15260

Approximate solutions to the equation of radiative transfer have been obtained which give the reflectance of a horizontally-stratified, two-layered medium. It is found that the dependence of the reflectance on the optical thickness τ of the upper layer depends strongly on the albedos of the upper and lower layers. Here, $\tau = N\sigma Q_E t$, where N is the number of particles per unit volume, σ is the particle cross-sectional area, Q_E is the extinction efficiency (for soils $Q_E \simeq 1$), and t is the thickness of the upper layer. When a dark material overlies a bright surface, a covering of $\tau = 1$ (corresponding to about a monolayer) is sufficient to reduce the reflectance to nearly that of the dark substance. However, when a light material overlies a dark surface, a covering of $\tau > 10$ is required to make the reflectance approach that of the bright substance. This theoretical prediction is consistent with experimental results of Wells and Veverka.

If one of the layers has an absorption band, the relative contrast between the center and wings of the band is strongly affected by layering. If the band is in the bottom layer, a covering of $\tau = 1.5$ is sufficient to reduce the contrast by more than 90%, independent of whether the darker or lighter material is on the top. If the band is in the top layer, the contrast reaches nearly its full value when $\tau = 1$ if the dark material is on top; however, if the light material is on top, a covering of $\tau > 10$ is required.

This theory should be useful in interpretations of many topics in planetary geology, including effects of dust deposits on the Martian surface, effects of the Martian atmosphere on surface photometry, and effects of frost deposits on outer planet satellites. For instance, in the latter application, the results of this study imply that frost layers only a few mg/cm^2 thick on a silicate soil would be sufficient to completely hide characteristic silicate absorption bands.

SPECTRAL EVIDENCE FOR ALUMINOUS IRON OXIDES ON MARS

Richard V. Morris (NASA Johnson Space Center, Houston, TX 77058) and Howard V. Lauer, Jr. (LEMSCO, Houston, TX 77058).

INTRODUCTION

One prominent feature in the reflectance spectra of both the bright and dark regions of Mars is an absorption edge that extends from about 0.75 to 0.40 μm (e.g., Singer et al., 1979). This edge is generally attributed to some combination of interelectronic and charge-transfer transitions involving ferric iron (e.g., Huguenin et al., 1977; Singer et al., 1979; Sherman et al., 1982). Because the spectral data do not give tight mineralogical constraints, there is not general agreement on the nature of specific ferric oxide phases inferred from the spectral data. Some workers suggest a Fe_2O_3/FeOOH assemblage (e g., Singer et al., 1979) which may be amorphous (Singer, 1982). Other suggestions include maghemite γ-Fe_2O_3, (e g., Hargraves et al., 1979) and the magnetic FeOOH polymorph δ-FeOOH (Burns, 1980). While some aspects of the spectral properties of the above phases satisfy the constraints of the observational data, there are other aspects which agree poorly or not at all. For example, the absorption edge for hematite (α-Fe_2O_3) is not at a short enough wavelength.

It is possible and even likely under natural conditions on Mars that impurity ion substitution occurs at least to some degree for ferric iron. On the earth, aluminum commonly substitutes for ferric iron in natural situations, and consequently we anticipate a similar situation may occur on Mars. The work reported by Sommer and Buckingham (1981) suggests that aluminum substitution in ferric oxides is important optically. Although they did not report on the spectral behavior of the absorption edge, they did report that the band minimum near 0.86 μm in hematite shifts to longer wavelengths with increasing aluminum content. We report here preliminary results of our studies of the optical properties of the solid-solution series between α-Al_2O_3 and α-Fe_2O_3 in synthetic systems and discuss the implications of the results for the reflectance spectra of Mars.

EXPERIMENTAL PROCEDURES

The starting point for the synthetic procedure was solutions of appropriate amounts of iron and aluminum sulfate salts. Addition of excess base resulted in precipitates which were subsequently washed repeatedly with neutral water. The precipitates were then hydrolyzed in either neutral water or a PARR pressure vessel at ~100°C, washed in neutral water, dried in air, and finally heated in air at temperatures above ~600°C. Formation of solid solutions was verified by shifts in the positions of peaks in the x-ray diffraction patterns.

The diffuse reflectance spectra were recorded at room temperature over the spectral range ~0.30-2.2 μm on a Cary-14 spectrophotometer configured with a 9-inch diameter integrating sphere. The spectra were recorded relative to HALON and subsequently converted to absolute reflectance using the data of Weidner and Hsia (1981).

RESULTS AND DISCUSSION

In Figure 1 we plot the position of the band minimum for the band near 0.86 μm in pure hematite and the short-wavelength position of the absorption edge as a function of the aluminum content as the Al/Fe atomic ratio. There are additional bands between the above band and the absorption edge in the spectra, but we will not consider them here. All of the samples used in the plot gave definable x-ray diffraction lines and so are not amorophous.

In agreement with Sommer and Buckingham (1981) we find that the band minimum shifts to longer wavelengths with increasing aluminum content. The 1.05 μm band minimum for the most aluminum-rich compositions is essentially the same as the value reported by Lehmann and Harder (1970) for natural corundum samples containing ferric iron impurities. In contrast to the band minimum, the absorption edge shifts to shorter wavelengths with increasing aluminum content. The position of the edge for the most aluminum-rich compositions, which is below the 0.30 μm limit of our data, also appears to be consistent with the data of Lehmann and Harder (1970), but a direct comparison is difficult since they report transmission spectra.

The above results suggest that the shortward shift relative to hematite of the absorption edge in the martian spectra is spectral evidence for aluminous iron oxide phases on Mars. We have not yet attempted to estimate a value of Al/Fe for the martian case because we have not yet determined the positions of the spectral features at temperatures appropriate for Mars and because we have found that the positions of the features also seems to depend on the degree of crystallinity. Additionally, data in region Al/Fe = 0.1 to 0.4 are required. We anticipate that, since the positions of the band minimum and the absorption edge vary in opposite directions, an estimate of an Al/Fe ratio from the martian spectral data will be reasonably well constrained.

REFERENCES

Burns (1980) Nature 285, 647.
Hargraves et al. (1979) J. Geophys. Res. 84, 8379-8384.
Huguenin et al. (1977) LS VIII, Lunar and Planetary Institute, 478-480.
Lehmann and Harder (1970) Amer. Min. 55, 98-105.
Sherman et al. (1982) J. Geophys. Res., in press.
Singer (1982) J. Geophys. Res., in press.
Singer et al. (1979) J. Geophys. Res. 84, 8415-8426.
Sommer and Buckingham (1981) IEEE IGARSS, June 8-10, 603-607.
Weidner and Hsia (1981) J. Opt. Soc. Am. 71, 856-861.

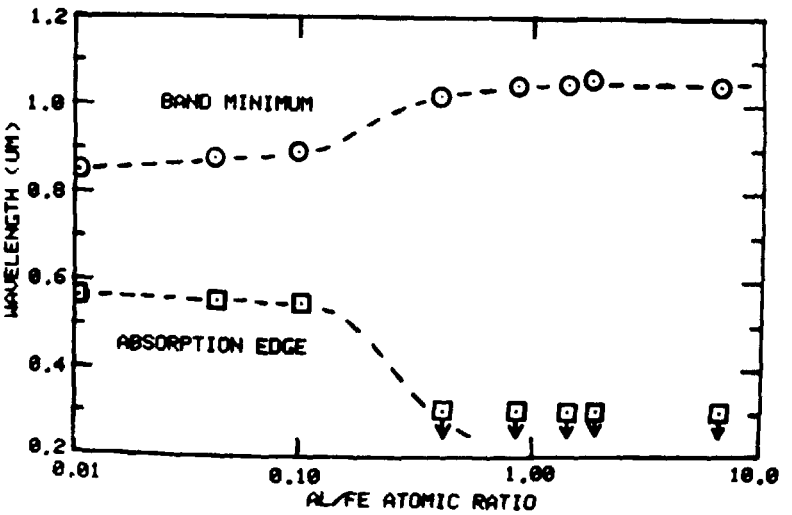

Figure 1. Plot of the positions of the band minimum and absorption edge as a function of the atomic ratio Al/Fe for members of the solid solution series of α-Al_2O_3 and α-Fe_2O_3. Arrows indicate upper limits due to instrumental limitations.

ALTERATION OF ROCKS IN HOT CO_2 ATMOSPHERES: FURTHER EXPERIMENTAL RESULTS AND APPLICATION TO MARS

J. L. Gooding, SN2/Planetary Materials Branch, NASA Johnson Space Center, Houston, TX 77058.

INTRODUCTION. Reaction of rock materials with hot, high-pressure atmospheres rich in CO_2 may have been a significant process during the respective geologic histories of Mars and Venus. On Venus, such reactions should have been a natural consequence of the hot, dense CO_2 atmosphere which envelops the planet. On Mars, similar reactions might have occurred in response to transient high-pressure atmospheres generated by impact cratering or volcanic events which thermally disturbed regolith rich in adsorbed or condensed CO_2. Previous experimental work (1) explored possible effects of hot, dry CO_2 on rocks as a simulation of the Venusian weathering environment. This report summarizes additional observations on some of those products but also describes results of a simulated Martian "hydrothermal" event.

BASALT IN HOT, DRY CO_2. As described previously (1), the principal change observed in powdered samples of U.S. Geological Survey standard basalt BHVO-1 exposed to hot CO_2 was progressive decrease in spectral reflectivity. However, the x-ray diffraction (XRD) pattern of a CO_2-treated sample included a peak at 3.97±0.02Å which was negligible to absent in patterns of both unheated and N_2-treated samples (Fig. 1). The 3.97Å peak is not attributable to any common oxide or carbonate mineral but can be provisionally explained as the (004) peak of pachnolite, $NaCaAlF_6 \cdot H_2O$, or as the $(11\bar{1})$ peak of ludlamite, $Fe_3(PO_4)_2 \cdot 4H_2O$. It is at least conceivable that such phases could have formed by alteration of primary fluorapatite although the required reactions remain unidentified. The spectral darkening effect was probably unrelated to the 3.97-Å phase(s) but could have arisen by oxidation of Fe-rich silicates according to reactions of the type

$$3\ FeO + CO_2 \rightarrow Fe_3O_4 + CO.$$

Unfortunately, complicated overlap of silicate and oxide mineral XRD peaks prevented positive identification of possible Fe^{3+}-oxide reaction products. However, the XRD peak-height ratio I(2.52Å)/I(2.58Å) increased by ~10% during heat treatment of the sample with CO_2. The 2.52Å peak should have included contributions from the strong (311) peaks of any existing magnetite or maghemite whereas the 2.58Å peak should have been defined principally by pigeonite or Fe-rich diopside $(13\bar{1})$. Thus, spectral darkening of the samples by oxidation remains unconfirmed but at least consistent with the observations.

BASALT IN HOT CO_2/H_2O. A 0.59-g aliquot of powdered BHVO-1 (held in an Al_2O_3 crucible) and 18g of distilled H_2O were placed in the pressure bomb used previously (1). After evacuation of air, the bomb was sealed and heated to 200°C at which point it was back-filled to a measured pressure with CO_2 gas (> 99.5% pure). The mixture was then heated to 350°C and 100 atm and held under those conditions for 48 hrs. The relative proportions of H_2O and CO_2 used gave a final molar ratio $H_2O/CO_2 \simeq 9$. The run product was "quenched" as before (1).

The final BHVO-1 product was dry but sufficiently indurated that it broke into clods upon removal from the crucible. After gentle re-pulverization of

the friable clods, the sample gave a reflectance spectrum which showed considerable darkening (Fig. 2). Its XRD pattern included a weak 3.97Å peak and an apparent increase in the I(2.52Å)/I(2.58Å) ratio discussed above. However, both XRD and spectrophotometric evidence for hydrous minerals was negative.

IMPLICATIONS FOR MARS. Previous workers (2) suggested that impact cratering in volatile-rich regolith might lead to hydrothermal rock alteration on Mars. Vaporization of adsorbed H_2O and CO_2 from a powdered basalt model regolith (3) should produce a molar ratio $H_2O/CO_2 \approx 6$ in the hydrothermal fluids. However, exposure of a crystalline basalt to $H_2O/CO_2 \approx 9$ (equivalent to model regolith with adsorbed gases plus water ice) at a reasonable hydrothermal temperature and pressure produced only minor alteration after 48 hrs. Thus, it seems that longer-lived hydrothermal systems, abundant liquid water (as opposed to water vapor), or more susceptible rock materials would be required for significant amounts of hydrous minerals to form in impact craters on Mars. Hydrothermal longevity would be favored by hot initial temperature and deep burial whereas alteration susceptibility would increase with glass content of the rock. Hydrous mineral formation should probably be limited to areas of glassy melt-rock, liquid water circulation, and slow cooling. Hydrothermal alteration at small, shallow craters and at craters in H_2O-poor regolith may be limited to oxidation effects.

Acknowledgment. This work was performed at the Jet Propulsion Laboratory, California Institute of Technology, when the author was a senior scientist in the Earth and Space Sciences Division.

References: (1) Gooding, J.L. (1981) Reports Planet. Geol. Program-1981, NASA Tech. Memo. 84211, p. 460-462. (2) Kieffer, S.W. and Simonds, C.H. (1980) Rev. Geophys. Space Phys., 18, p. 143-181. (3) Fanale, F.P. and Cannon, W.A. (1974) J. Geophys. Res., 79, p. 3397-3402.

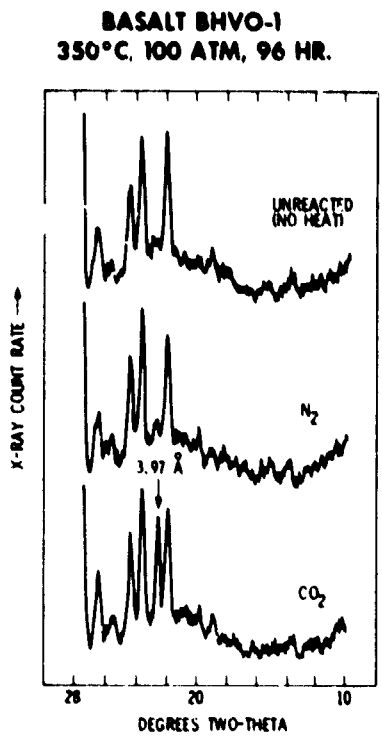

Figure 1. X-ray diffraction patterns of experimentally treated basalt samples. The 3.97Å phase formed in the CO_2 experiment may be pachnolite or ludlamite.

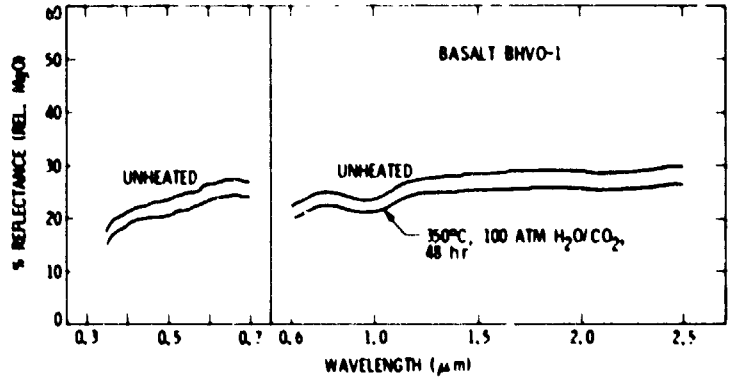

Figure 2. Visible (0.35-0.70μm) and near-infrared (0.6-2.5μm) reflectance spectra of experimentally treated basalt. The sample reacted in H_2O/CO_2 (molar ratio≈9) darkened, possibly by oxidation of mafic minerals.

MARS SOIL/WATER/ATMOSPHERE DYNAMICS INTERACTIONS INVESTIGATIONS, R. Stephen Saunders, James B. Stephens, Bruce Banerdt[1], and Fraser P. Fanale[2], [1]Jet Propulsion Laboratory, California Institute of Technology, Pasadena, CA 91109, [2]University of Hawaii at Manoa, Honolulu, HI 96822.

The current set of experiments in our investigations of soil, water, and atmosphere dynamic interactions addresses the question of thermal interactions on a diurnal and seasonal basis. The earlier experiments reported in Fanale et al. (1 and 2) provided basic parameters for atmospheric and soil interactions for the isothermal case. The present experiments will determine the thermal properties of dry martian soil in a CO_2 atmosphere under martian pressure and temperature conditions.

In order to perform the thermal wave experiment, we designed, fabricated, installed and tested a martian solar simulator (a heated aluminum grid buried under the surface of the soil) for the Mars Soil Thermodynamic and Fluid Dynamic Properties Chamber. The chamber was pumped down, the soil was vacuum dried, leaks were fixed and the first cold run was attempted. After some catastrophic backfills (a hose fell off a manometer and the electric power was shut off) and more leaks were fixed, the chamber and all its associated systems were ready for the cold thermal wave experiment.

The cold (-50°C soil temperature) thermal wave experiment was started with the chamber at Mars atmospheric pressure (5 to 7 mmHg). The solar simulator was turned on (42 watts into a 2 foot diameter aluminum grid) and the progress of the thermal wave down through the soil was monitored by the soil pressure and temperature probes. The thermal wave was shown to have moved only a few inches in a week's time. We suspect that the thermal conductivity of the soil is strongly dependent upon the CO_2 pressure over a range of 5 to 10 mmHg at temperatures typical of Mars. We accidently allowed the pressure to briefly rise to 10 mmHg and noticed a marked increase in the thermal conductivity.

The chamber was warmed up and various repairs were made. The soil in the chamber was dried out again and a room temperature (+ 20°C) thermal wave experiment was performed at martian CO_2 pressure (6 mmHg) with the martian solar simulator plate held at + 54°C. After 4 weeks the thermal wave traveled to the bottom of the soil container (1 meter depth). A room temperature pressure wave experiment will follow.

References:

(1) Fanale, F. P. et al. (1982) Mars: The Regolith-Atmosphere-Cap System and Climate Change, Icarus, 50, 381-407.

(2) Fanale, F. P. et al. (1982) Seasonal and Long Term Exchange of CO_2 Between the Regolith and Atmosphere of Mars: Experimental and Theoretical Studies, J. Geophys. Res., Third International Colloquium on Mars Special Issue, in press.

RAPID ESTIMATION OF MARTIAN TOPOGRAPHY FROM VIKING ORBITER IMAGE PHOTOMETRY

Philip A. Davis, Laurence A. Soderblom, and Eric M. Eliason, U.S. Geological Survey, Flagstaff, AZ 86001

We have developed a rapid method of estimating martian topography with a computer-based interactive system that uses calibrated accurate Viking Orbiter image data in iterative photometric and tensor calculations. First, an estimate of the brightness of light scattered by the atmosphere is made and subtracted from the image. This step is extremely important because the scattered component can be a large fraction of the total image brightness. Two models are currently operable in the interactive program. The first model is designed specifically for features with cylindrical symmetry in topography and albedo, for example, craters; this model assumes that the crater has radial symmetry in its albedo and topography, and compares two traverses extending from the center of the crater to beyond the rim. In simplified concept, ratioing the two brightness traverses cancels out the brightness changes due to symmetrical albedo patterns, and remaining variations in the ratio are due only to changes in slope. The second model is designed for asymmetric topography (e.g. dunes, ridges, and valleys) but can also be used on craters; this model requires identification of a flat surface along the profile and cannot compensate for changes in albedo.

Both models involve the same iterative loop of photometric and tensor analysis. The relative-height profile along the designated traverse paths is first determined by using a user-supplied photometric function to solve for the slope in each pixel; tensor analysis is then used to map the original traverse across the undulating topography. For example, a traverse across a crater floor, on an oblique image, will appear as an arc that bows toward the spacecraft and will be longer than the original straight line designated by the user. The traverse must then be expanded to accommodate the additional pixels; the brightness values along the corrected traverses are used to recalculate the slopes. These photometric and tensor calculations are repeated iteratively until the total height along the profile does not change.

To test the derived profile, a synthetic image of the crater (or other landform) is calculated from the derived albedo and topography profiles, the model photometric function, and the viewing, illumination, and range of the original image. The observed brightness values of the crater in original image are then divided by those of the synthetic image of the crater; the result is examined visually. If the match is poor, the user refines the photometric function or chooses different profile directions so as to continue. In most cases, crater interiors do not have completely symmetrical albedos. Thus, if the derived albedo and topography profiles are accurate, the ratio image will show irregular scattered patches or crescentic concentrations of low- or high-albedo areas in the craters. If the user happened to choose the original profile direction to pass over one of these irregular patches of albedo or topography in the crater, the ratio image will show

concentric rings. In this case, the user should repeat the profiling routine and choose a profile direction that does not include areas of topography or of a symmetric albedo; if this repetition is not possible, the crater cannot be profiled.

The accuracy of the methods described above was tested by profiling craters whose topography had been derived by stereo photogrammetry and by shadow measurements. Table 1 compares the results; the accuracy of the computer methods is 1 to 5% for diameters, 5 to 8% for rim heights, and 2 to 5% for slopes.

Table 1. Comparison of results from computer profiling methods with those from shadow measurements and stereo photogrammetry*.

Viking Frame	Crater Type	Measured Diameter (km)	Computer Diameter (km)	Measured Depth (m)	Computer Depth (m)	Measured Slope	Computer Slope
Computer model versus Shadow Measurement							
693A03	Bowl-shaped	3.3	3.1	520	507	---	---
467A10	Flat-floored	9.4	9.4	850	770	---	---
Computer model versus Stereo Photogrammetry							
64A18	Bowl-shaped	2.7	2.6	600	570	35.9°	33.9°
64A18	Flat-floored	5.4	5.1	808	830	25.4°	26.1°

* Shadow measurements by method of D. W. G. Arthur; stereophotogrammetry results from S. S. C. Wu and colleagues.

BEHAVIOR OF WATER-SOLUBLE CATIONS AND ANIONS IN COLD DESERT ENVIRONMENTS

Everett K. Gibson, SN7, NASA Johnson Space Center, Houston, TX 77058
Sarah A. Hokanson, Dept. of Geology, Wellesley College, Wellesley, MA
(formerly Lunar and Planetary Institute Summer Intern)
Susan J. Wentworth, LEMSCO, 1830 NASA Rd. 1, Houston, TX
Roberta Bustin, Dept. of Chemistry, Arkansas College, Batesville, AR

Weathering, diagenesis, and chemical alteration of various soil profiles from the Dry Valleys of Antarctica have been studied as an analog of soil development within the Martian regolith. Horowitz et al. (1) had earlier suggested that the Dry Valleys should be the best terrestrial analog of the Martian surface. Our previous studies have shown that the Dry Valleys have weathering processes operating which may be similar to those observed on Mars (2-5). Surface processes operating in the Dry Valleys are similar to Martian surface processes in the following respects: low temperatures (mean temperature of -17°C in Wright Valley), low absolute humidities, diurnal freeze-thaw cycles, low annual precipitation, desiccating winds, salt-rich regolith, and oxidizing environment. Previous studies have suggested that physical or mechanical weathering (6) predominates over chemical weathering processes. Even though chemical alteration is a secondary weathering process in the Dry Valleys, it plays an important role in regolith development (5).

During the 1979-80 austral summer a suite of core and surface samples near evaporite and brine ponds were collected from Wright and Taylor Dry Valleys. Previously, we reported results from the study of water-soluble cations and anions from four cores (4) and now the results from seven additional cores have been examined. A detailed description of the chemical weathering and diagenesis of a one-meter deep soil pit has recently been reported (5). We wish to discuss the analysis and our interpretations of the results from the eleven core samples (ranging from 13 to 32 cm in length and analyzed in 1 cm segments) for their water-soluble ions which represent ionic transport processes above the permanently frozen zone. Abundances of these soluble ions reflect the nature of the secondary minerals which have been produced by evaporation and weathering processes.

The sample suite includes core samples from: (1)regions of permanent mature brine ponds (DJ-2074, DJ-33, DJ-39) associated with Don Juan Pond, (2) brine ponds which are intermediate in maturity associated with Don Quixote Pond (DQ-35, DQ-20), (3) temporal brine ponds from the VXE-6 site (WV-42), (4) seasonal evaporite ponds which contain standing water for only short periods of time in the South Fork, Wright Valley (DJ-21, WV-38, WV-52), (5) regions near Lake Hoare, a fresh-water lake (TV-50), and (6) Prospect Mesa which has the oldest soils within the Antarctic Dry Valleys (WV-11). Petrographic studies of the Dry Valley soils indicated that most silicate minerals and lithic fragments exhibit some degree of alteration (5). Chemical alterations occur in samples from both above and from within the permanently frozen zone. Concentrations of water-soluble cations (Na^+, K^+, Ca^{2+}) and anions (Cl^-, SO_4^{2-}, NO_3^-) decrease significantly from the surface to the permanently frozen zone, suggesting major movement of water-soluble species. Enrichments in secondary mineral abundances correlate with water-soluble ion concentrations. Authigenic secondary minerals in the Dry Valley soils include: halite, gypsum, thenardite, soda niter, bloedite, calcite, limonite, chabazite, aragonite, trona, mirabilite, epsomite, drapskite, sylvite, antarcticite, tachydrite, bischofite, and "clay" minerals(5).

Chloride and calcium abundances within the cores generally reflect the nature of the secondary mineralogy. Chloride ions are associated with salt (NaCl) and antarcticite ($CaCl_2 \cdot 6H_2O$), whereas the calcium ion abundances reflect phases such as gypsum, calcite and antarcticite. Chloride abundances ranged from as low as 10 μmoles for samples collected in Taylor Valley near Lake Hoare to values as great as 3600 and 3800 μmoles in salt-rich evaporite layers in soils from the edge of Don Juan Pond and on Prospect Mesa (Table 1). Soils from near permanent brine ponds (i.e.,Don Juan Pond and VXE-6) typically contain approximately 400 μmoles Cl throughout the soil column with the exception of salt-rich layers (usually within 4 to 10 cm of the surface) which contain as much as 3800 μmoles Cl. Soils from the seasonal ponds generally contain between 40 and 100 μmoles Cl throughout the soil column with the exception of salt-rich layers, where Cl concentrations increase to 400 μmoles.

In common with soils from other arid parts of the world, soluble salt concentrations are characteristic of Dry Valley soils and cores. The origin of the water-soluble ions forming the Dry Valley salts is controversial: proposed origins include chemical weathering of rocks, hydrothermal fluids, marine aerosols, and the evaporation of water from marine incursions. Ratios of Na^+/Cl^-, Mg^{2+}/SO_4^{2-}, Na^+/SO_4^{2-}, and Cl^-/SO_4^{2-}, which are uniform regardless of surface soil location and similar to those of sea water (7), suggest that Na^+, SO_4^{2-}, and Cl^- are of marine origin. Pastor and Bockheim (7) concluded, however, that the less abundant ions Ca^{2+}, Mg^{2+} and K^+ were derived mainly from rock weathering because the ratios of Mg^{2+}/Ca^{2+}, Mg^{2+}/K^+, and Ca^{2+}/K^+ resemble those for the lithosphere.

Isotope measurements verify that most sulfate is probably of marine origin, although some may be of hydrothermal origin; $\delta^{34}S$ of gypsum in Wright Valley ranges from +14.1 to 20.3 $^0/_{00}$ (8). Nakai et al. (8) also concluded that carbonate is mainly of marine origin; for calcite, $\delta^{13}C$ = -14.4 to +17.6 $^0/_{00}$ and $\delta^{18}O$ = -0.4 to +22.3 $^0/_{00}$. Calcite encrustations, however, are found only in areas containing carbonate country rocks, indicating that leaching and redeposition take place. Strontium isotope measurements suggest that the salt content of Lake Vanda (Wright Valley) and nearby soils originated by rock weathering (9).

From the above data, it seems probable that a large portion of the water-soluble ions in Dry Valley soils and cores is of marine origin (especially Na^+, Cl^-, and SO_4^{2-}), but some of the ions were derived by rock weathering. According to (10), most Ca^{2+} and Mg^{2+} come from pyroxenes and amphiboles in diabasic rocks and from biotite in granitic rocks. Muscovite and potash feldspar contributed most of the K^+.

Keys and Williams (11) studied the distributions of salt minerals in the McMurdo region. They discovered that surface soils containing Na^+ and Cl^- decrease in abundance with increasing distance from the coast, which is consistent with a marine aerosol origin for these ions. Sulfates are evenly distributed, but SO_4^{2-} still appears to be of marine origin because of the isotope data discussed above. Salts containing Mg^{2+} are found mainly in areas containing basic igneous country rocks. (11) concluded that for surface soils, salts of marine origin are the most important with respect to volume but that chemical weathering of rocks and soils is also significant. Chemical weathering would contribute to the localized enrichments of salts observed in cores.

It is known that the Martian surface conditions may be favorable for chemical weathering (12,13). Primary silicates would be expected to be reactive minerals such as pyroxene, olivine, and feldspars. Because of the possible

existence of an extensive subsurface system of water-ice and maybe even liquid water just beneath the Martian surface (14), it seems likely that water is available to assist in the weathering of the reactive minerals. Such weathering could result in the formation of clays, sulfates, carbonates, hydrates, and zeolites. Formation of pedogenic zeolites (14, 15) under cold, arid Antarctic conditions opens the possibility that zeolites may also form in the Martian regolith. Terrestrial zeolites are especially common soils derived from volcanic ejecta (16), and such soils may be common on Mars. Zeolites are well-known for their volatile exchange and storage properties. Consequently, the possible presence of a significant abundance of zeolites in the Martian regolith might have a profound effect on the volatile inventory and budget of Mars. Specifically, zeolites could be a repository of atmospheric gas including CO_2, O_2 and H_2O. Changes in pressure and temperature might induce Martian zeolites to take up or release large quantities of volatiles. Movement of water within the regolith would assist in the chemical weathering, leaching and salt-forming processes operating in the near surface region of Mars.

References.

1. Horowitz N.H. et al. (1972) Science 176, 242-245.
2. Gibson E.K. and B. Ransom (1981) Lunar and Planet. Sci. XII, 342-344.
3. Gibson E.K. (1981) Third International Mars Colloquium, pp. 90-92.
4. Gibson E.K. et al. (1982) Repts. Planet Geol., NASA Tech. Memo 84211, 463-465.
5. Gibson E.K. et al. (1983) Proc. 13th Lunar Planet Sci. Conf., JGR (in press).
6. Kelly W.C. and J.H. Zumberge (1961) J. Geol. 69, 433-446.
7. Pastor J. and J.G. Bockheim (1980) preprint.
8. Yokai N. et al. (1975) Geochem. J. 9, 7-24.
9. Jones L.M. and G. Faure (1967) EPSL 3, 101-106.
10. Claridge G.G.C. and I.B. Campbell (1977) Soil Sci. 123, 377-384.
11. Ness J.R. and K. Williams (1981) Geochim. Cosmochim. Acta 45, 2299-2309.
12. Gooding J.L. (1978) Icarus 33, 483-513.
13. Smith M.B. and H.H. Kieffer (1978) J. Geophys. Res. 83, 1809-1815.
14. Clifford S.M. (1981) Third International Mars Colloquium, pp. 44-45.
15. Mora, C.S. et al. (1982) Repts. Planet Geol., NASA Tech. Memo 84211, 466-468.
16. Hay, R.L. (1977) M.S.A. Short Course Notes on Natural Zeolites pp. 53-64.

TABLE 1

WATER-SOLUBLE CHLORIDE AND CALCIUM ABUNDANCES IN CORE SAMPLES

Core Location	Core Number	Length	Chloride Concentrations, μmoles		Calcium Concentrations, μmoles	
			Typical	Highest Value	Typical	Highest Value
Don Juan Pond Center	DJ-2074	14 cm	450	1500	200	480
Don Juan Pond Edge	DJ-11	4 cm	250	400	90	350
Don Juan Pond Basin	DJ-19	24 cm	100	1500	70	185
Don Quixote Pond Center	DQ-15	16 cm	50	450	10	70
Don Quixote Pond Edge	DQ-20	11 cm	100	450	8	27
VEE-6 Pond, South Fork	WV-42	15 cm	400	750	200	288
Pond 3, South Fork	DJ-21	17 cm	50	150	10	118
Pond 1, South Fork	WV-38	24 cm	40	40	15	152
Pond 1, South Fork	WV-52	22 cm	45	150	25	340 (gypsum)
Prospect Mesa	WV 11	16 cm	800	1000	60	127
Taylor Valley, Lake Hoare	TV-50	25 cm	10	45	3	8

INCIPIENT WEATHERING OF LOW TEMPERATURE SOLAR SYSTEM OBJECTS

R.L. Huguenin, Dept. Physics/Astronomy - Hasbrouck Laboratory,
University of Massachusetts, Amherst 01003

There is significant evidence that low-temperature objects in the Solar System have undergone incipient weathering. Evidence for contemporary weathering on Mars, for example, has been recently discussed (1,2). Analysis of carbonaceous chondrites have indicated that low-temperature *in situ* weathering apparently occurred in those objects (3). There is also spectroscopic evidence for alteration products on the surfaces of low-albedo asteroids (4).

The apparent occurrence of incipient weathering on such low-temperature objects has been a subject of considerable interest. Firstly, the occurence of weathering implies that precursor phases were subsequently exposed to disequilibrium environments. Secondly, it has been broadly assumed that liquid H_2O was the medium of alteration for at least the meteorites and asteroids. The latter assumption in particular has raised numerous unanswered questions about the histories of these objects and the Solar System. A major question is whether liquid H_2O was really required to produce the weathering phases on these objects.

We have argued that on Mars the exposure of primary silicates to H_2O vapor at low temperatures can produce a chemical alteration of the minerals (2,5). Could such processes have occurred in meteorites, asteroids, and other low-temperature objects in the Solar System? The required conditions would be consistent with current models of ice/mineral assemblages for meteorites, asteroids, and outer Solar System satellites.

The exposure of mafic silicates to H_2O at ice temperatures would be predicted to result in reaction, whereby H^+ from dissociated H_2O at the mineral/ice interface would be drawn into the mineral to negative defects (2). The excess OH^- at the mineral surface and H^+ in the mineral, according to the model, creates a charge imbalance that is relieved by: 1) removal of electrons from surface OH^- and incorporation into the crystal at positive defects; and 2) migration of metal ions (during prolonged exposure to ice) toward grain surface and into the ice layer (2,5). The mineral becomes hydrated ($2H^+$ + lattice $O^{2-} \rightarrow$ lattice H^+ + lattice OH^-) and it loses metal ions in the process. There is also a chemical reduction of the mineral and an oxidation of the ice ($OH^-_{ice} \rightarrow OH_{ice} + e^-_{mineral}$). Laboratory studies indicated that the oxidation product is apparently chemisorbed hydrogen peroxide and its decay product, chemisorbed O (2). The lifetime of the H_2O_2 was estimated to be 10^4 - 10^6yr at -50°C (2).

The chemically reduced and hydrated mineral was proposed to break down into poorly characterized phases (2,5). Redistribution of ions toward the surface and into the ice was predicted to result in the breakdown of the precursor mineral to clay, metal oxices, carbonates, and salts (5). The weathering products would be predicted to be colloidal or possibly amorphous, since the liquid H_2O medium in which more well-developed minerals polymerize would not be present. It was suggested that prolonged exposure to the frozen H_2O may possibly drive the polymerization of some gels into clay, oxide, carbonate, and salt crystallites; however, well-developed crystals should probably not be expected (5). The redox gradient between the mineral

and ice could produce further complexities in the phases that are ultimately produced.

Evidence from meteorites. Are the weathered phases in meteorites consistent with the predicted frost-weathering assemblages? For the carbonaceous chondrites, at least, they do in fact appear to share some of the principal characteristics.

Firstly, the weathering products are extremely fine grained and poorly developed. The weathered matrix material consists of intimate mixtures of extremely fine grained or metacolloidal clay, oxides, carbonate, salts (primarily sulfate) and sulfides. A significant fraction of the mixture is PCP (poorly characterized phases), which is largely formless or amorphous silicate, oxide, carbonate, and sulfate material enriched in metal ions (3).

Secondly, the petrographic data are consistent with the proposed redistribution of metal ions toward and beyond the grain surface. In Murray, for example, relatively iron-depleted ($FeO + Fe_2O_3 = 20.9$; $SiO_2 = 37.2$) phyllosilicate was situated adjacent to olivine, and spreading outward from this was a sequential development of more Fe rich phyllosilicate and finally iron-enriched PCP ($FeO + Fe_2O_3 = 54.4$; $SiO_2 = 11.5$) over distances ranging from a few microns to a few tens of microns (3). In Nogoya, similar sequences could be seen within altered clasts. There precursor clasts were nearly completely pseudomorphed during *in situ* alteration with the original shape outlines sharply preserved. Layers of phyllosilicates extend from poorly crystallized or amorphous Mg-Si-rich interior portions to more Fe-rich layers toward fracture boundaries. The fractures, where the ice would have been situated, were filled with magnetite in Nogoya. In other meteorites, where weathering was less advanced, fractures are filled with metal ion-rich PCP. In numerous cases the phyllosilicates that contain the redistributed metal ions developed into a layered colloform texture. Such a texture would be consistent with the predicted long-term ordering of the disordered phases (perhaps under the influence of ice), analogous to long-term devitrification of glasses. Colloform textures are also seen in hydrothermally altered rocks, however.

Thirdly, phase relationships and isotopic data point to low temperatures of alteration (3). Alteration phases were apparently formed with upper limit temperatures of 400°K. Thermally labile carbonaceous compounds, some of which appear to have formed before or during alteration, argue for prolonged upper limit temperatures of 300°K or lower. Isotopic data, particularly $\delta^{34}S$, point to 273°K or lower temperature for the sulfur-bearing phases (J.S. Lewis, private communication).

A fourth property of weathered phases that is consistent with a possible frost-weathering origin is the relatively broad range of redox potentials represented within the assemblages, ranging from hydrated iron oxides , through magnetite, to reduced carbonaceous material. While such distributions would not be unique to a frost-weathering origin, they are at least consistent. Of particular interest in this context are observations of ubiquitous coatings of amorphous carbonaceous coatings on phyllosilicates from CM matrices (6,7). An intimate association of extractable organics with phyllosilicates in PCP was also noted (3). The phyllosilicates would be predicted by the frost-weathering model to be strongly chemically reduced, with up to $\sim 10^{22} H^+$ and e^- incorporated per gram (2). Such highly

reduced minerals should tend to return to a redox state that is in equilibrium with their surroundings, i.e., they would be predicted to transfer electrons and chemically reduce their surroundings until the redox potentials reach equilibrium. This may account for the association of the highly reduced phases with the phyllosilicate. Production of highly oxidized phases in the ice during weathering might explain the occurence of hydrated ferric oxides and sulfates in nearby areas of the matrix.

It can be concluded that the meteorite data is consistent with possible alteration by frost-weathering. It has been argued that weathering may have been by liquid H_2O, and as discussed by Bunch and Chang (3), the observed phases could be explained by that model as well. The principal advantage of the frost-weathering model, however, is that complex scenarios for stabilizing liquid H_2O ($T > 273^oK$, $pH_2O > 5mb$) are not needed. Simple H_2O ice/mineral assemblages in relatively small asteroid or comet-sized parent bodies would be predicted to lead to phases similar to those that are observed.

Evidence from asteroids. Unlike the meteorites, compositional information about asteroids and outer Solar System objects is derived from remote sensing observations. A synthesis of high resolution IR spectra (0.9 - 2.5μm) and narrow band photometric data (3.0 - 3.5μm) for asteroids 1 Ceres, 2 Pallas, and 324 Bamberga led to the proposal that clays and salts with interlayer water may be present on the surfaces of these objects (4). The spectrum of 324 Bamberga shows additional evidence below 2.5μm for abundant magnetite. It was argued that alteration by aqueous or analogous processes processes is implied (4).

Implications for other outer Solar System objects. Models of nebular condensation and accretion argue that H_2O ice may have been an abundant phase in the outer Solar System. Remote spectral observations of Galilean, Saturnian, and Uranian satellites and Saturn's Rings indeed point to the presence of abundant H_2O ice. If the H_2O condensed on mafic silicate grains, frost-weathering type reactions could have conceivably occurred. Conditions on these objects would in theory support such reactions, and it is possible that significant alteration might have occurred. The near-IR spectra of these objects contain significant structure, and their interpretations have been subjects of considerable controversy.

Acknowledgements. This research was supported by NSG-7397, NSG-7405, and NAGW-40. Conversations with S. Chang and J.S. Lewis are gratefully acknowledged.

References. 1) E.L. Strickland III, Contrib. Lunar and Planetary Institute, 441, 253, 1981; 2) R.L. Huguenin, J. Geophys. Res., Mars Colloq. issue, in press, 1982; 3) T.E. Bunch and S. Chang, Geochem. Cosmochem. Acta, 44, 1543, 1980; 4) M.A. Feierberg, L.A. Lebofsky, and H.P. Larson, Geochem. Cosmochem. Acta, 45, 971, 1981; 5) R.L. Huguenin, J. Geophys. Res., 79, 3895, 1974; 6) T.R. McKee and C.B. Moore, Proc. 10th Lunar Plan. Sci. Conf., 1, 921, 1979; 7) D.R. Mackinnon and P.R. Buseck, Nature, 280, 219, 1979.

GEOLOGIC AND REMOTE SENSING STUDIES OF THE SCHICKARD-SCHILLER REGION

B.R. Hawke and J.F. Bell, Planetary Geosciences Div., Hawaii Institute of Geophysics, Univ. of Hawaii, Honolulu, HI 96822

Introduction: The Schickard-Schiller region (40°-60° S; 35°-68° W) is a major expanse of largely highland terrain located southwest of Mare Humorum. The region contains Schickard, Schiller, Wargentin, Phocylides, and Mee craters as well as the Schiller-Zucchius basin[1-3]. Numerous Imbrian-aged light plains deposits occur in region[4-5]. Schultz and Spudis[6] noted the presence of abundant dark-haloed impact craters on non-mare units in the Schickard-Schiller region and proposed that the region had been the site extensive volcanic flooding early in lunar history and the resulting basalt deposits were subsequently covered with varying thicknesses of highlands ejecta. More recently, Hawke and Bell[7,8] presented the preliminary results of spectral studies of three dark-haloed craters (Schickard R, Noggerath F, and Inghirami W) in this region. While analyses of these spectra suggested that these craters had excavated basaltic material, it was clear additional spectra with higher spatial and spectral resolution were needed. These were recently (August and September, 1981) obtained using the Mauna Kea 2.2m telescope. The purposes of this study include the following: 1) to confirm the existence and determine the composition of the postulated basaltic component in the ejecta deposits of dark-haloed impact craters in the Schickard-Schiller region, 2) to reassess the geolcgic history of the region, and 3) to investigate the processes responsible for light plains formation.

Dark-Haloed Impact Craters: Figure 1 shows the three spectra which are critical to understanding the origin of dark-haloed impact craters in the Schickard-Schiller region. Noggerath F is a relatively young dark-haloed impact crater. The spectrum of its bowl is very similar to that of the fresh crater in the mare deposit located on the northern portion of the Schickard crater floor. The Noggerath F bowl spectrum is very distinct from that of Schickard X, a fresh highlands crater in the wall of the Schickard. The Schickard X spectrum is similar to those obtained for other fresh highlands craters on the western limb. These spectra were treated to continuum removal and Gaussian function band fitting procedure[9]. Both the Noggerath F and the Schickard mare crater exposed high-Ca pyroxenes, indicative of mare basalts[10]. Schickard X crater exposed material with low-Ca orthopyroxene, typical of highland rocks. The spectrum obtained for the Inghirami W bowl is almost identical to that of the Noggerath F bowl. Fresh mare basalts are exposed on the interiors of both of these dark-haloed impact craters.

Spectra obtained for the dark-halo of Noggerath F exhibit characteristics which are intermediate between those of fresh mare basalts and the mature mare surfaces of the ponds in the NW and SE portions of the floor of Schickard. This dark material is mare basalt which is considerably more mature than that on the crater interior. Fresher material would be expected to be exposed on the interior because of mass wasting on steep inner slopes.

Inghirami W crater excavates material from beneath the inner faces of the Havelius Formation as mapped by Scott et al.[11]. Both Schickard R and Noggerath F are located in Imbrian-aged light plains deposits[5-7] which are

interpreted to have been emplaced as a consequence of the Orientale impact event[11]. Noggerath F, Inghirami W, and Schickard R excavate mare basalts from beneath light plains and other Orientale-related deposits. Dark-haloed impact craters are both abundant (N=15) and widely distributed in the Schickard-Schiller region and are concentrated on Orientale-related deposits. Hence, it seems likely that pre-Orientale mare volcanic activity not only occurred but was extensive in the region. Perhaps the deposition of highland ejecta on pre-existing mare surfaces has been an important process in light plains formation elsewhere on the Moon.

Some newly acquired spectral data exists for other lunar regions. A preliminary analysis of the spectrum of the dark-halo impact crater NE of Petavius strongly suggests that basaltic material was excavated from beneath Petavius crater ejecta. Similar results were obtained from analyses of the spectra of dark-haloed craters SE of Poseidonus and south of Hercules.

Geologic Studies of the Schickard-Schiller Region: Additional geologic studies were conducted in the Schickard-Schiller region in order to better understand its volcanic history. A variety of additional factors would favor the existence of an ancient pre-Orientale phase of volcanism in the region[7]: 1) The Schiller-Zucchius basin is situated within the region[1,2]. Impact basin formation produces topographic lows and extensive crustal facture systems, both of which are conducive to the extrusion and accumulation of volcanic material[12]. 2) The unusual interior morphology of Wargentin crater is most easily explained by early flooding of the structure by basalts which were subsequently covered by a thin layer of light plains material emplaced as a result of the Orientale event. 3) The proximity of the Schickard-Schiller region to Orientale suggests that any pre-existing mare deposits could have been buried by Orientale-related deposits.

Post-Orientale volcanic activity may have been more prevalent in the region than has been commonly recognized. In particular, there is strong evidence that the Schiller plains, which occupy a portion of the Schiller-Zucchius basin (southwest of Schiller crater), are of volcanic origin. These plains exhibit both a lower albedo and a lower crater density than nearby highlands plains[4] and are distinct on Whitaker's color difference photography as well as on the multispectral image mosaic of Soderblom[13]. These plains embay adjacent highlands terrain and Orientale secondary craters and display mare-type ridges which are generally radial to Orientale. These ridges are probably the result of the shallow burial of ridges associated with Orientale secondary chains by post-Orientale volcanics.

References: 1) W. Hartmann and G. Kuiper (1962) Commun. Lunar and Planetary Lab., Univ. of Arizona 1, 51. 2) W. Hartmann and C. Wood (1971) The Moon 3, 3. 3) D. Wilhelms (1981) NASA-TM 84211, 405. 4) T. Offield (1971) USGS Map I-546. 5) D. Wilhelms and J. McCauley (1971) USGS Map I-703. 6) P. Schultz and P. Spudis (1979) PLPSC 10, 2899. 7) B. Hawke and J. Bell (1981a) PLPSC 12, 665. 8) B. Hawke and J. Bell (1981b) NASA-TM 84211, 135. 9) T. McCord et al. (1981) JGR 86, 10883. 10) J. Adams (1974) JGR 79, 4829. 11) D. Scott et al. (1977) USGS Map I-1034. 12) S. Solomon (1975) PLSC 6, 1021. 13) La Jolla Consortium (1977) PLSC 8, frontispiece.

Figure 1. Spectra of craters in the Schickard-Schiller region. All have been divided by Apollo 16.

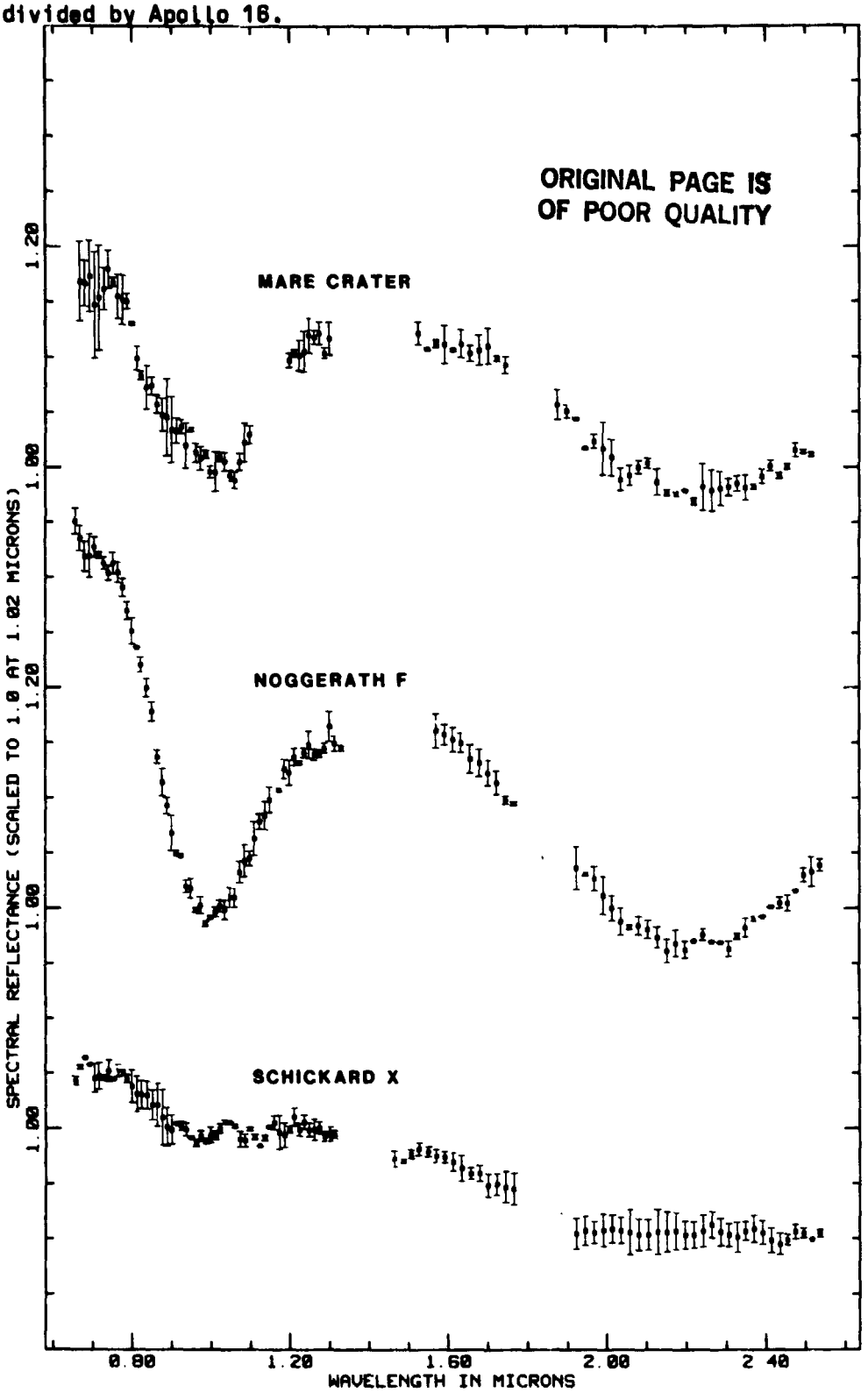

MAGNETIC EFFECTS ASSOCIATED WITH HYPERVELOCITY IMPACTS

Coradini M., Capaccioni F., Flamini E., Martelli G.
Istituto di Astrofisica Spaziale, Reparto di Planetologia
Roma, Italy
Cerroni P., Hurren P., Smith P.N.
University of Sussex
Brighton, U.K.

The problem of the origin of lunar magnetism has been a controversial topic since the magnetic mapping of the Moon carried out by the Apollo 14 and 15 sub-satellites and the discovery of the surprisingly high remanent magnetism of lunar samples. Whether lunar magnetism is due to a primordial ambient field or to the effect of cratering is still debated. Both effects are probably contributory. In our experiments of macroscopic hypervelocity studies we have shown that magnetic effects do accompany hypervelocity cratering (1, 2, 3). However, a better understanding of this phenomenon can be achieved by further measurements with diagnostic instrumentation improved in the light of past experience. In particular our experiments are devoted to the comprehension of the following problems: a) the exact three-dimensional morphology of the remanent magnetic field in the neighberhood of the impacted area; b) target typical time for viscous relaxation; c) the effects of the transient magnetic fields produced in the impact region on the magnetism of the target material both in the crater region and in the ejecta blanket; d) the effects of the enhancement of the pre-existing magnetic field just before impact.

The impacting projectile is obtained from a shaped charge by using only the foremost part of the jet which is composed of the fragment with the highest speed, the remainder of the jet being removed by a deflecting charge (4). Estimates of the projectile mass during flight are obtained from optical and soft X-ray photographs. A time of flight technique provides the projectile velocity, which results to be of the order of 10 km/s or so. These projectiles impact onto atificial ferromagnetic concrete targets which provide both mechanical and magnetic isotropic response.

Preliminary measurements of the surface magnetic field of the impacted targets have been carried out and the results have been numerically elaborated in order to produce magnetic isomaps. A first analysis of these isomaps yielded fairly homogeneous results for all the examined targets and evidenced a common trend both for the vertical and for the

horizontal components of the magnetic field. A striking feature present in all the isomaps of the vertical component is a concentrical trend of the magnetic lines of force around the physical crater (see figure below). This could imply the existence of some magnetising mechanism connected to the formation of the crater. A number of effects could be invoked to explain this behaviour, such as for example those proposed in refs. 5 to 7.

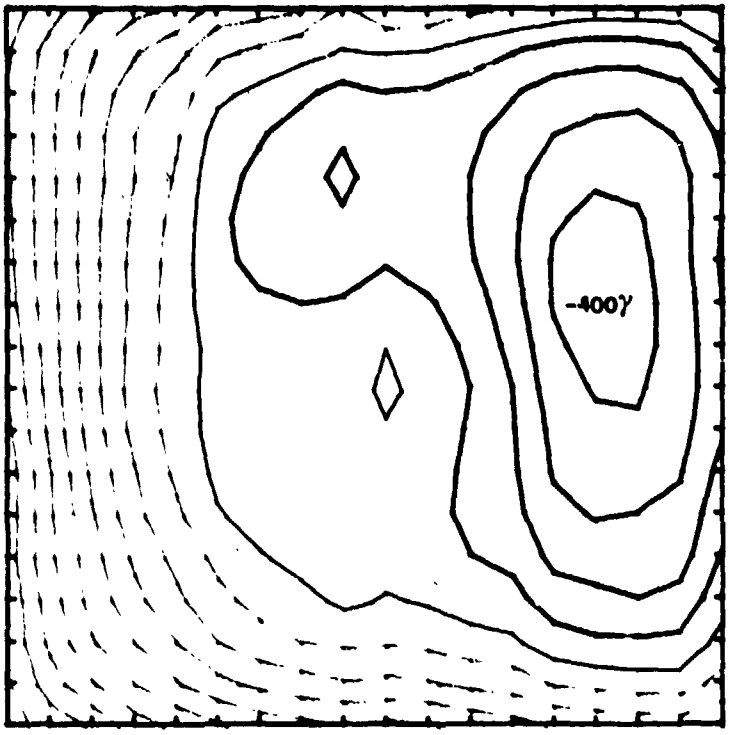

Fig.1: Isomap of the vertical component of the superficial magnetic field of the impacted target.
The intensity difference between two adjacent isolines is 100 gammas.
Minimum value of the magnetic field is shown.

REFERENCES

1. Martelli G. and Newton G.: 1977. Nature 269,478-480
2. Srnka et al., 1979. Earth and Planet Sci. Lett.,42, 127-130
3. Martelli G. et al., 1982. " The Comparative Study of the Planets", ed. Reidel Pub. Company, pp.333-357
4. Bond J.W., Keyse R.J. and Newton G., 1980. Planet. Space Sci. 28, 599-608
5. Cerroni P. and Martelli G.,1982. Planet. Space Sci., , -
6. Dachille A., 1978. Meteoritics, 13, 135
7. Ivanov B.A. et al.,1977. "Impact and explosion cratering",eds. Roddy Pepin and Merrill, pp.861-865

Chapter 11

GEOLOGICAL MAPPING, TOPOGRAPHY AND GEODESY

PRELIMINARY GEOLOGICAL MAP OF RA PATERA QUADRANGLE (J12a), IO

R. Greeley (Dept. of Geology, Arizona State Univ., Tempe AZ 85287), P. D. Spudis (U. S. Geological Survey, Flagstaff AZ 86001 and Arizona State Univ.) and J. E. Guest (Univ. of London Observatory)

The Ra Patera quadrangle is one of three areas on Io covered by highest resolution Voyager images selected for detailed geological mapping at a scale of 1:2M to provide insight into volcanic processes and material units. Covering an area of nearly 1.3×10^6 km^2, preliminary photogeological mapping (Fig. 1) shows that the quadrangle area can be subdivided into five principal types of geological units:

1) Shield volcanoes: consist of radial or subradial flows emanating from relatively small central vents; includes Ra Patera, a broad shield 760 x 270 km across composed of at least 7 principal flow units including channel- and tube-fed flows and broad sheet flows, all originating from a vent 25 x 40 km. The wide range of color and albedo of the Ra flows may indicate various allotropes of sulfur and may include active sulfur flows. Hephaestus Patera and an asymmetric shield (Vent E) are included in this category. Vent E, located on the northeast flank of Ra Patera, consists of 4 flow units and may be an incipient shield volcano in the early stages of development.

2) "Pit" craters and associated flows: consist of vent complexes as large as 100 km across and associated flows; includes Mazda Catena (4 or possibly 5 seperate vents, including a cone), Mihr Patera (circular caldera 60 km across with near-vent flows and a plateau-forming flow unit), Gibil Patera, Horus Patera, and Vent D.

3) "Break-out" shield (Mihr A): a complex vent/flow system displaying numerous "tongue"-like flows that appear to have broken out from a single massive cooling unit; may represent a style of volcanism unique to the rheological properties of sulfur (1,2).

4) Miscellaneous vents: occur at random in the map area, ranging in size up to 80 km; some occur within pit crater flows and may be rootless vents.

5) Intervent flows and plains: flows and plains not having identifiable source vents, named intervent plains in preliminary geological mapping (3,4); may be older central vent flows blanketed by plume deposits or may represent fissure-style eruptions.

These five types of volcanic units combine to form a surface on Io which may be analogous to "plains" volcanism on Earth, i.e. a series of coalescing low-profile shield volcanoes and intervening sheet flows (5).

Preliminary mapping suggests the following stratigraphic sequence (oldest- to- youngest): 1) eruption of plains units and flows associated with oldest central vents; some plains units may represent "flood"-type volcanism, probably active throughout the geological history of the mapped area; 2) eruption of older pit crater flows and associated caldera formation (Mihr, Horus and Gibil Paterae) and old shield materials (Hephaestus Patera); 3) eruption of young pit crater flows (Mazda Catena) and "breakout" shield flows (Mihr A); 4) formation of Ra Patera shield volcano (possibly active).

References

1) Greeley R. et al. (1981) EOS 62, 1080.
2) Fink J. et al. (1981) NASA TM 84211, 36-37.
3) Masursky H. et al. (1979) Nature 280, 725-729.
4) Schaber G. (1980) Icarus 43, 302-333.
5) Greeley R. (1982) JGR 87, 2705-2712.

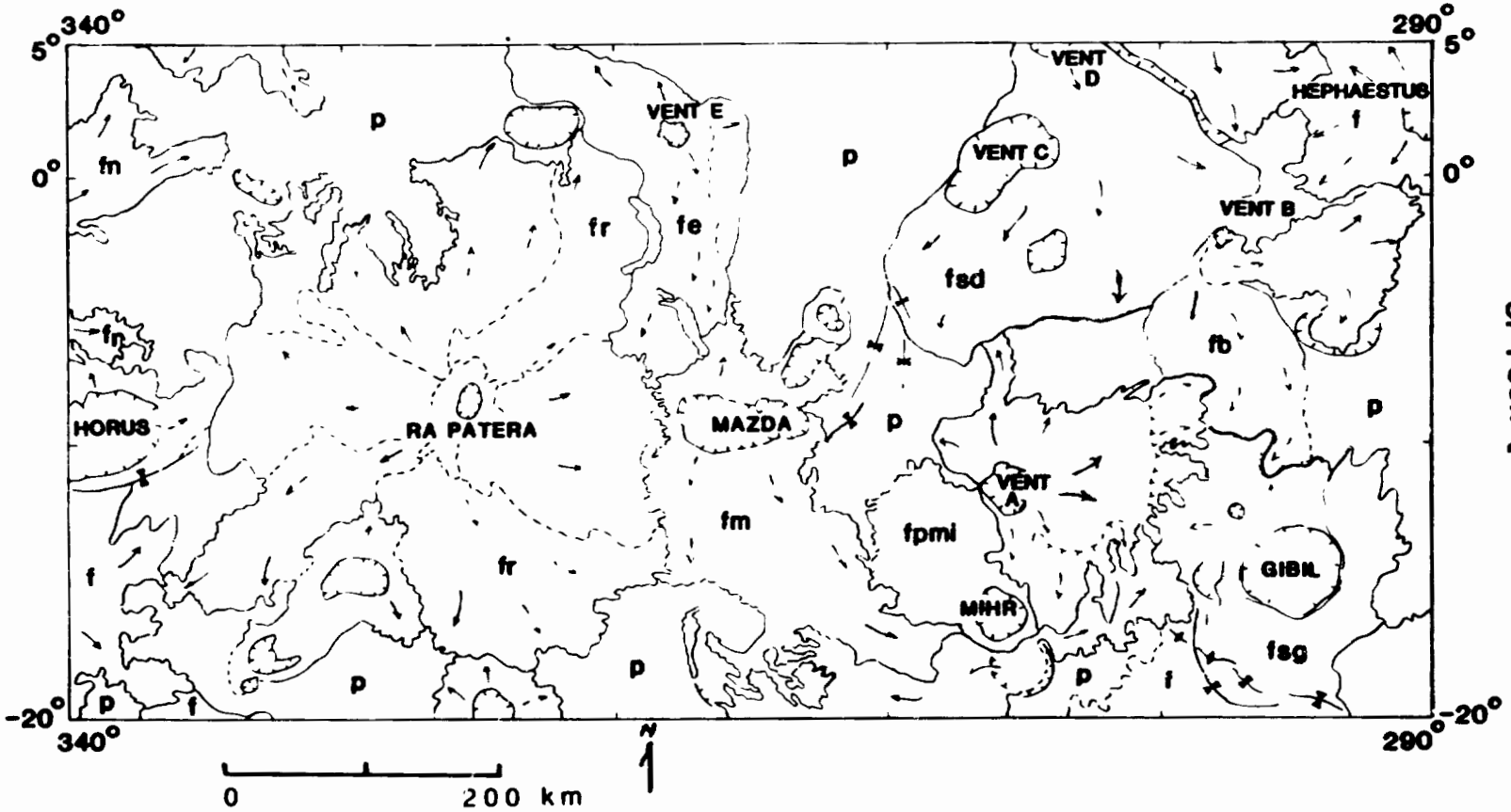

Figure 1. Photogeological sketch map of the Ra Patera Quadrangle, Io; fr = flows from Ra Patera; fn = flows from Nyambe Patera; fe = flows from vent E; fm = flows from Mazda Cataena; fpmi = flows from Mihr Patera; fsd = flows from vent D; fb = flows from vent B; fsg = flows from Gibil Patera; p = undifferentiated plains units; f = undifferentiated flows.

PRELIMINARY GEOLOGIC MAP OF THE SOUTH POLAR REGION OF GANYMEDE

R. A. De Hon, Department of Geosciences, Northeast Louisiana University, Monroe, La. 71209.

Preliminary photogeologic mapping of the south polar region of Ganymede is based on 35 unrectified Voyager images. Resolution of the imagery varies greatly depending upon the distance of the spacecraft from the surface and a wide range of viewing and illumination angles. Approximately one-half of the quadrangle is beyond the terminator, and about 10% of the illuminated portion is at such an extreme viewing angle is to be unusable. Rectified frames and photomosaics are not presently available; hence, preliminary mapping includes a wide range of scales, and positional accuracy varies.

The major physiographic/geologic units in the region consist of various types of grooved or furrowed terrain, hummocky materials, crater and basin deposits (Fig. 1). The oldest materials are rugged cratered terrain materials (unit tc) and dark, cratered plains materials (unit pc). The cratered plains unit is modified by the later formation of bright, grooved terrain material (unit tg) which consists of multiple sets of grooves (graben) Together, the dark plains and bright grooved terrain form a mosaic of dark polygonal patches bounded by linear swaths of bright terrains. In contrast, polar furrowed terrain material (unit tf) constitutes a large continuous region of subparallel ridge and trough development with persistent directional trends. Younger, dark plains-forming material (unit p) occurs in small patches filling some craters and in topographic lows overlying most other materials.

The largest basin in the polar region is Gilgamesh which consists of a 150-175 km diameter central depression surrounded by hummocky and radial basin ejecta (unit b). Several arcuate scarps in the rugged materials define basin concentric rings, but none are continuous. Hummocky and lineate materials extend roughly two basin diameters from the central depression. A well-defined secondary crater field extends beyond the rugged basin deposits and is clearly superposed on both dark cratered plains material and bright grooved terrain materials.

Crater materials may be dated by superposition on terrain units and by degradation morphology. The oldest craters within crater plains and cratered plain materials are incomplete and highly degraded. Some craters superposed

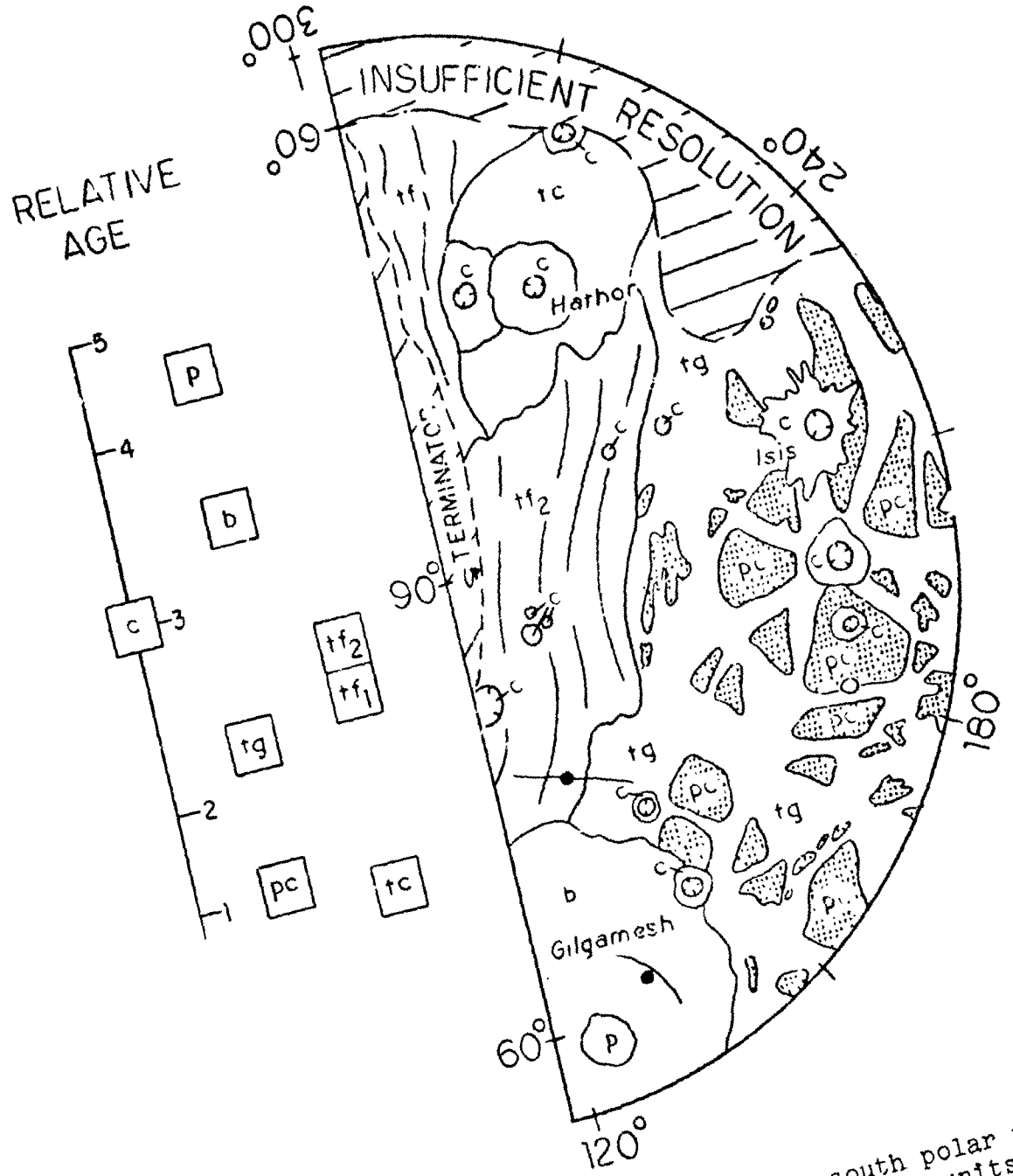

FIGURE 1. Geologic sketch map of the south polar region of Ganymede. See text for description of units.

on grooved terrain material are overlapped by secondaries from Gilgamesh. Younger craters are superposed on Gilgamesh ejecta. The youngest craters are well-developed, bright rayed features that are superposed on all other materials. Many bright patches near 190°-210° longitude are part of the extensive ray pattern associated with the crater Osiris outside the region.

The earliest period of high impact rates is poorly preserved on Ganymede. Most of the early cratered terrain was obliterated by crater relaxation and subsequent overprinting by the formation of grooved and furrowed terrains (1). The grooved terrain has formed over a long time span (2) in response to planet-wide tectonism related to the planetary thermal state and the changing thickness of the lithosphere (4, 5, 6). Retention of basin and crater forms after the formation of furrowed terrains indicates that the crust has been fairly stable since the period of grooved terrain formation and that meteor impact has been a major though declining process for most of geologic time.

Acknowledgements. This study represents one phase of research conducted under NASA Planetology Programs Grant NSG 7628, Northeast Louisiana University. Geologic mapping of the South Polar Region of Ganymede (Jg-15, 1:5M) by Hal Massursky, U.S.G.S., Ray Arvidson, Washington University, and Rene De Hon, Northeast Louisiana University is part of the Jovian Satellite Mapping Program.

References

1. Smith B.A., et al. (1979) Sci. 206, 927-950.
2. Golombek M. P. and Allison M. L. (1981) NASA Tech. Mem. 84211, 54-56.
3. Squyres S. W. (1980) Geophys.Res.Lett.7, 593-596.
4. Fink J. H. and Fletcher R. C. (1981) LPSCX11, 277-279.
5. Lucchitta B. K. (1980) Icarus 44, 481-501.
6. McKinnon W. B. (1981) Proc. LPSC X11, 1585-1597.

GEOLOGIC MAPPING OF EUROPA: PROGRESS REPORT

Konrad Hiller, Ludwig-Maximillians Universitat and DFVLR, Munich, FRG
David Pieri, Jet Propulsion Laboratory, Pasadena, California, USA

Work is continuing on the geological mapping of the Je-3 quadrangle of Europa as part of the Galilean Satellite Mapping Program. We have tried to differentiate terrain units by morphology, texture, and color as well as by lineament character of the predominate lineament type within the terrain units. In addition we are trying to formulate a lineament generation sequence and to couple such a sequence to the larger questions of the interior evolution of Europa.

The suggestions of Luccitta and Soderblom (1981) as to differentiation by spectral type are under study as well as detailed confirmation of earlier global studies (e.g. Pieri, 1981). Broad diffuse patterns of albedo and spectral differentiation are also under study in the context of implantation of exotics (e.g. SO_2) from circum-Jovian space (Johnson, 1982-personal communication).

REFERENCES

Luccitta, B.K. and L.A. Soderblom, 1981, A Geologic Map of Europa, p.508 in Reports of the Planetary Geology Program 1981, NASA TM 84211, H.E. Holt, ed., 582pgs.

Pieri, D.C., 1981, Lineament and Polygon Patterns on Europa, Nature, 289, p.17-21.

GEOLOGICAL MAP OF MARS, 1:15M SCALE, NORTHEAST QUADRANT

R. Greeley, Department of Geology and Center for Meteorite Studies, Arizona State University, Tempe, AZ 85287

As part of the U.S. Geological Survey program, geological maps of Mars are currently being prepared at a scale of 1:15M by D. Scott (Principal Investigator), M.H. Carr, J.S. King, R. Greeley, and J.E. Guest, with each investigator being responsible for major regions; this global mapping is based on Viking images. This report concerns the northeast quadrant of Mars (0^{o} to 65^{o} North; 180^{o} to 360^{o} West); individual 1:2M photomosaics (total of 30) were mapped geologically and then compiled on the new U.S.G.S. 1:15M airbrush map base. Preliminary compilation shows that the approximately 36 mapped units can be classified into the following major groups: 1) plains units, 2) plateau units, 3) volcanic units, 4) various crater units, and 5) surficial units.

Plains units (excluding obvious volcanic units) occur primarily in the northern lowlands and are interpreted to be the result of various periglacial and aeolian processes. Plateau units are found principally in the cratered uplands in the southwestern part of the map; they appear to be mantling materials of possible volcanic and/or aeolian origin; some of the plateau units have been incised by valley networks and "etched" by wind, water, and/or sapping processes. Volcanic units occur principally in association with the Elysium region and in Syrtis Major. They include shield-building lava flows, flood-and plains-type lava flows, and possible lahars; small conical hills (many with summit craters) found in some of the northern latitude plains may be cinder cones and/or "psuedocraters" of the Icelandic type. Crater units include materials associated with craters of all sizes, including basins; however, crater materials (rim and/or ejecta deposits) smaller than about 100 km across were not mapped. Surficial units include albedo, various mass-movement materials, channel deposits, and patterns presumed to be aeolian in origin.

The mapping is now in review. When completed, the 1:15M series will serve as the primary data base for the Mars Consortium Project.

GEOLOGIC MAPPING OF MARTIAN VALLEY SYSTEMS II: AEOLIS REGION

D.C. Pieri[1] and T. Parker[2]

[1]Jet Propulsion Laboratory, Pasadena, California 91109
[2]Department of Geology, California State University at Los Angeles

As part of a continuing effort to produce a series of maps of selected small valley systems across Mars, we are mapping an area of the heavily cratered terrain near Al Qahira Vallis in the Aeolis region. This is one of the oldest areas of Mars and shows extensive valley network development in various stages of obliteration. Our data base is almost exclusively the new high-resolution Survey Mission data obtained during the last operational period of Orbiter 1.

Our mapping area consists of a region of heavily cratered terrain which has been heavily eroded and faulted. Impact craters are ubiquitous, superimposing and being superimposed by valley networks. In this area valley networks appear to occur preferentially in lower smoother intercrater plains units, although they exist in all of our preliminary units. Impact crater morphologies range from highly degraded to fresh, with large (25 km) craters showing well-developed and extensive rampart ejecta blankets. Units downcut by the flows forming Al Qahira Vallis have intricate digitate valley networks superimposed on them which were truncated by the Al Qahira flows.

Preliminary crater counts show the valley networks to be quite old, with faint integrated networks appearing to be the oldest. Steep-walled stem systems, rare in this area, appear younger, and are confined to the intercrater plains. This area appears to be quite complex with regard to valley formation, and it appears that a variety of network morphologies span much of the period of regional development and are present in older substrate as well as the newer intercrater plains. In any case, however, the systems are probably older than 2by BP.

VOYAGER CARTOGRAPHY

R. M. Batson, U. S. Geological Survey, Flagstaff, AZ 86001

The Jovian and Saturnian satellites are being mapped at several scales from Voyager 1 and 2 data. Details of the Galilean satellite mapping program are given by Batson and others (1980). The Saturnian satellite mapping plan and other details of methods used in Voyager cartography are summarized by Batson and others (1981).

Compilation of airbrush maps of the Galilean satellites at a scale of 1:5,000,000 are progessing well. Two maps of Europa, two of Io, and three of Ganymede are in press. One map of Io and three of Ganymede are in compilation. Six preliminary pictorial maps of the Saturnian satellites, compiled with Voyager 1 and 2 data, have been published.

An atlas containing the preliminary maps of the Saturnian satellites is in press. The atlas contains both conformal and equal-area projections of each map, Voyager 1 and 2 images that were specially processed and perspective grids for each of the images.

References

Batson, R. M., Bridges, P. M., Inge, J. L., Isbell, C. E., Masursky, Harold, Strobell, M. E., and Tyner, R. L., 1980, Mapping the Galilean Satellites of Jupiter with Voyager data: Photogrammetric Engineering and Remote Sensing, v. 46, no. 10, p. 1303-1312.

Batson, R. M., Bridges, P. M., and Mullins, K. F., 1981, Voyager cartography: in Reports of the Planetary Geology Program, NASA TM 84211, p. 484-485.

1:2,000,000 SCALE CONTROLLED PHOTOMOSAICS OF MARS

R. M. Batson and R. L. Tyner, U. S. Geological Survey, Flagstaff, AZ 86001

Compilation of a series of 140 controlled photomosaics of Mars at a scale of 1:2,000,000 is in progress. Details of the series are discussed by Batson and Tyner (1981). To date, 94 mosaics have been published, 12 are in press, and 34 are in preparation. The latter include mosaics of the polar regions, where illumination angles, surface frost conditions, and cloud cover vary widely. Consequently these mosaics have a patchy appearance, and, in many cases, a dynamic range not well accommodated by the printing process. Some of the mosiacs published earlier did not have complete coverage or contained areas of coverage by pictures of questionable quality because all the Viking pictures had not been cataloged at the time of compilation. Current plans call for upgrading these maps with newly located photographic coverage.

References

Batson, R. M., and Tyner, R. L. 1981, 1:2,000,000 scale controlled photomosaics of Mars: in Reports of the Planetary Geology Program, 1981, NASA TM 84211, p. 487-488.

REVISIONS OF 1:5,000,000 SCALE MARS MAPS

R. M. Batson and P. M. Bridges, U. S. Geological Survey, Flagstaff, AZ 86001

Several of the 1:5,000,000 shaded relief maps of Mars originally compliled from Mariner 9 pictures are being upgraded by adding details from the Viking Orbiter pictures to the original airbrush drawings. No attempt is being made to reposition features according to new control data; the maps remain tied to the Mariner 9 datum (Davies, 1973). The maps in the northern hemisphere of Mars are particularly improved by these revisions because the resolution of Mariner 9 pictures was very poor in that region. Also, Mariner 9 pictures taken near periapsis in the martian equatorial region are often degraded by cloud or haze cover. The maps are therefore improved considerably by the addition of information from the Viking Orbiter pictures. The status of the revisions is as follows:

Quadrangles published or in press:	9
Quadrangles in revision process:	5
Quadrangles yet to be done	16

Reference

Davies, M. E., 1973, Mariner 9: primary control net: Photogrammetric Engineering, v. 39, no. 12, p. 1297-1302.

SPECIAL PURPOSE MARS MAPPING

R. M. Batson, U. S. Geological Survey, Flagstaff, AZ 86001

Two special maps of Mars are in press. These are the Chryse Planitia map and the topographic map of the Phoenicis Lacus NW quadrangle of Mars; the shaded relief was done by Patricia Hagerty and the contour overprint was described by Wu and others (1980).

A special series of controlled photomosaics has been designed for compilation at the scale of 1:500,000. These maps will contain the highest resolution pictures taken by Viking, many of which have resolutions of 10-30 m per pixel. Some spacecraft telemetry required for computation of image rectification parameters is not available for a very large number of these pictures, so W. T. Borgeson and Kathleen Edwards have developed special software for synthetic rectification by digital-image processing methods. Compilation of the first quadrangles in the series has begun.

Reference

Wu, S. S. C., Schafer, F. J., and Jordan, Raymond, 1980, Topographic mapping of Mars: the 1:2,000,000 contour map series, in Reports of the Planetary Geology Program, 1980, NASA TM 82385, p. 458-459.

ALBEDO MAP OF MARS

R. M. Batson and Susan L. Davis, U. S. Geological Survey, Flagstaff, AZ 86001

A large number of pictures were taken by the Viking 1 spacecraft from near apoapsis under near zenith illumination. One large set was taken during revolutions 614 through 699, and a second set during revolutions 1323 through 1347. The martian season, or L_s during which the pictures were taken, ranges from 52° through 87°. These seasons cover approximately 85 percent of the area shown on the two equatorial sheets of the newly published 1:15,000,000 map of Mars. The pictures constitute the largest available image data set taken over a narrow time-frame, under clear atmospheric conditions, from which a synoptic albedo map of Mars can be made.

The map is being compiled in two phases. The first phase, now complete, consists of an airbrush drawing superposed on the two 1:15,000,000 equatorial map sheets. Pictures taken through the red filter on the Viking 1 camera were used for this drawing. The pictures taken during revolutions 614 through 699 were radiometrically processed to produce color images and were digitally transformed to Mercator projections (Batson and others, 1979). The second set has not undergone such processing, and the albedo patterns were interpreted visually from standard images available from the Planetary Data Facility. Absolute albedo levels on a planetwide basis were controlled by the Viking Infrared Thermal Mapper (IRTM) Solar albedo image available from the Mars Consortium data set (Pleskot and Miner, 1981). Digital processing and mosaicking of all the images, which constitutes the second phase of the effort, is now underway.

References

Batson, R. M., Hall, D. G., and Jordan, JoAnne, 1979, Color pictures of Mars: in Reports of the Planetary Geology Program, 1978-1979, NASA TM 80339, p. 439.

Pleskot, L. and Miner, E. D., 1981, A preliminary reference map of martian bolometric albedos: Icarus (in press).

THE CONTROL NETWORKS OF THE SATELLITES OF JUPITER AND SATURN

Davies, Merton E., The Rand Corporation, Santa Monica, California 90406

Geodetic control networks are being computed photogrammetrically for the large satellites of Jupiter and many of the satellites of Saturn using pictures from the Voyager 1 and 2 encounters. Control points have been identified on the satellites and their coordinates computed by single-block analytical triangulations. The status of the control nets is summarized in the following table:

Satellites	Points	Pictures	Measurements	Normal Equations	Overdeterminations	σ(μm)
Jupiter						
Io	598	240	9812	1916	5.12	12.36
Europa	174	120	3664	708	5.18	11.88
Ganymede	1669	295	17212	4223	4.08	21.37
Callisto	575	207	8736	1771	4.93	17.95
Saturn						
Mimas	110	32	1356	316	4.29	13.43
Enceladus	71	22	1052	208	5.06	19.19
Tethys	110	27	924	301	3.07	13.32
Dione	126	28	1322	336	3.93	16.63
Rhea	336	84	3554	924	3.85	20.93
Iapetus						
(Vgr 1)	15	14	218	72	3.03	22.62
(Vgr 2)	44	66	1632	286	5.71	11.84

Coordinates for the control points on the Galilean satellites have been reported in Davies and Katayama, 1981. The mean radii as measured by the triangulations are Io, 1815 km, Europa, 1569 km, Ganymede, 2631 km, and Callisto, 2400 km. The longitude systems of Europa, Ganymede, and Callisto are defined by craters on their surfaces; because of the extensive volcanism on Io, no feature has been chosen for this purpose on Io.

The surfaces of the Saturnian satellites Mimas and Enceladus are ellipsoidal. For Mimas the best fit axes are a = 200 km, b = 196 km, and c = 194 km; for Enceladus the axes are a = 256 km, b = 250 km, and c = 248 km (see Davies and Katayama, 1982). The mean radii of the other Saturnian satellites are Tethys, 525 km, Dione, 560 km, Rhea, 765 km, and Iapetus, 725 km. In the computation of the control nets it is important that the pictures and points completely encircle the body; with flyby missions this is sometimes difficult to achieve because of the great difference in resolution between pictures taken early and late in the flyby. Sometimes pictures from a second flyby help fill gaps; thus the control nets of Tethys, Dione, and Rhea contain pictures from both Voyager 1 and 2 encounters and do encircle the satellites. The control net of Mimas contains pictures taken by Voyager 1 and does encircle the satellite, whereas the control of Enceladus contains pictures taken by Voyager 2 and does not encircle the satellite. The control net of Iapetus contains two regions, one from pictures taken by Voyager 1 and another from pictures taken by Voyager 2. The regions do not overlap and it has not been possible to tie them photogrammetrically.

References

Davies, M. E., and F. Y. Katayama, "Coordinates of Feature on the Galilean Satellites," J. Geophys. Res., Vol. 86, No. A10, Sept. 30, 1981, pp. 8635-8657.

Davies, M. E., and F. Y. Katayama, "The Control Networks of Mimas and Enceladus," accepted by Icarus, 1982.

THE CONTROL NETWORK OF MARS: September 1982

Davies, Merton E., The Rand Corporation, Santa Monica, California 90406

Strips of Viking mapping pictures are being added to the planetwide control networks of Mars. These high resolution strips run from the Viking 1 lander site east to Airy-0, north along the 0° meridian to 60° latitude, southwest through the Viking 1 lander site to the equator, and west along the equator to 180° longitude. Everywhere along these strips, old points are incorporated in the measurements thus assuring that the strips and planetwide net make up a single large data set. The control points are much denser in the areas covered by the strips than in those regions not covered by strips and as they are usually associated with smaller craters their coordinates will be more accurate. Within the strips the standard error of the coordinates of the control points is estimated to be less than 3 km and the error in longitude of a few points near Airy-0 is less than 40 m.

The horizontal coordinates of the control points on Mars have been updated with a single-block planetwide analytical triangulation computed in September 1982. Coordinates of the points will be published later this year. The computation containd 47524 measurements of 6853 points on 1811 pictures. These comprised 1054 Mariner 9 and 757 Viking frames. The overdetermination factor was 2.48 and 19139 normal equations were solved. The standard error of measurement was 18.06 μm. The longitude of the Viking 1 lander site was 47°.962 and the latitude of Airy-0 was -5°.152. The last published control net (Davies et al., 1978) contained coordinat of 4138 control points and gave the longitude of the Viking 1 lander site as 47°.968 and the latitude of Airy-0 as 5°.142 thus the location of the Viking 1 lander site was moved 360 m and Airy-0 was moved about 600 m.

References

Davies, M. E., F. Y. Katayama, and J. A. Roth, Control Net of Mars: February 1978, The Rand Corporation, R-2309-NASA, February 1978.

MAPPING PRECISION OF THE VIKING LANDER IMAGES

Sherman S.C. Wu, Loretta Barcus, and Francis J. Schafer, U. S. Geological Survey, Flagstaff, AZ 86001

The solution to the problem of photogrammetric mapping of the Viking Lander images includes two approaches: Off-line and on-line (Wu, 1979; Wu et al., 1982). The off-line digital image processing introduces errors in linear interpolation from the GEOM stretch method. Therefore the most accurate method is the on-line approach, where all conversions and corrections are made in real time on an analytical plotter. However, map precision is limited by the performance of the facsimile cameras and the image resolution. Images from the Viking Lander cameras include two different resolutions with pixel sizes of 0.04° and 0.12°, i.e. high and low resolutions respectively. Because each image element is obtained by scanning in both the azimuth and elevation directions (Wu, et al., 1982), the photogrammetric accuracy is indirectly determined by the performance of the servo mechanisms. Analyses by Huck et al. (1975) give maximum angular errors of ±0.15° and ±0.30° for azimuth and elevation, respectively, in the low-resolution images; and ±0.1° and ±0.2° for azimuth and elevation respectively, in the high-resolution images. These figures include all errors of the servo mechanisms, position of the photosensor array and the camera mounting deviations. Therefore these figures will determine the absolute precision, where as the image resolution, the smallest resolvable image element can be used to determine the relative precision, in the analysis of the mapping precision of the Viking Lander images.

If X_c, Y_c, and Z_c, in the Viking Lander camera coordinate system are coordinates of a ground object (Wu, et al., 1982), of which ΔA_{z1} and ΔA_{z2}, and E_1 and E_2, are azimuth and elevation elements on photographs from cameras 1 and 2 respectively, and the base between the two cameras is designed by b which has a calibrated distance of 0.821 m, then

$$Z_c = \frac{b}{\tan \Delta A_{z1} - \tan \Delta A_{z2}} \tag{1}$$

$$Y_c = -\tfrac{1}{2} Z_c \, (\tan \Delta A_{z1} \bullet \tan \Delta A_{z2}) \tag{2}$$

$$X_c = -\tfrac{1}{2} Z_c \left(\frac{\tan E_1}{\cos \Delta A_{z1}} + \frac{\tan E_2}{\cos \Delta A_{z2}}\right) \tag{3}$$

The standard errors of these three coordinates can be determined based on the theory of error propagation by partially differentiating these three coordinates with respect to their variable components. They can be expressed as:

$$\sigma_Z = \frac{Z^2}{b} \left(\sec^4 \Delta A_{z1} + \sec^4 \Delta A_{z2}\right) \sigma_{A_z} \tag{4}$$

$$\sigma_Y = \frac{1}{Z}\left[Y^2 + \left(\frac{b}{2}\right)^2\right]^{1/2}\sigma_Z \qquad (5)$$

$$\sigma_X = X\left[\frac{Y^2}{Z^2}\sigma_{A_z}^2 + \frac{1}{Z^2}\sigma_Z^2 + (\sin 2E_1 + \sin 2E_2)\cdot\sigma_E^2\right]^{1/2} \qquad (6)$$

Using equations 4, 5, and 6, relative and absolute mapping precision from Viking Lander images are calculated respectively with the image resolution and the uncertainties due to the performance of the cameras.

Relative Precision - With a 0.04° and a 0.12° smallest resolvable image element (pixel) for both azimuth and elevation, respectively for the high- and low-resolution images, the relative mapping precisions are calculated separately for each resolution as listed in Table 1. Z-coordinates, the ranges of objects, are calculated every 2 m from 1 m to 9 m; Y-coordinates, which are 90° to Z, and are at left and right of the range, are calculated from +5 m to -5 m; and X-coordinates, which are elevations of object points with positive toward the ground, are calculated from 1.0 m to 2.0 m with an increment of one-half meter. These figures cover the mappable areas of the two Viking Landers. For example in Table 1, the standard errors of Z, Y, and X from high resolution images are 3 mm, 3 mm, and 5 mm respectively for a point at the location of Z = 1 m, Y = 1 m, and X = 1.5 m.

Absolute Precision - With angular errors 0.1° and 0.2° respectively for azimuth and elevation of high-resolution images, and 0.15° and 0.30° respectively for azimuth and elevation of low-resolution images, limited by the performance of the camera, the absolute mapping precision are calculated separately for each resolution as listed in Table 2. The actual mapping precision is considered better than the precision as listed in Table 2 due to the fact that the camera bolt down errors had been carefully calibrated and had been corrected in the mapping process (Wolf, 1976, Wu, et al., 1982).

References

Huck, F. O., H. F. McCall, W. R. Patterson and G. R. Taylor, 1975. The Viking Mars Lander camera, Space Science Instrumentation I, pp 189-241.

Wolf, M. R., 1976. Jet Propulsion Laboratory memorandum to S. S. C. Wu. Reference 824-IPL/SIPG/76-192.

Wu, Sherman S.C., 1979. Topographic Mapping of Viking Lander Area, NASA Tech. Memorandum 80339: Report of Planetary Geology Program, 1978-1979, pp.425.

Wu, Sherman S.C. and F. J. Schafer, 1982. Photogrammetry of the Viking Lander Imagery, Photogrammetric Engr. and Remote Sensing, vol. 48, no. 5, May 1982, pp. 803-816.

TABLE 1 - RELATIVE MAPPING PRECISION OF BOTH HIGH- AND LOW-RESOLUTION IMAGES FROM FACSIMILE CAMERAS OF THE TWO VIKING LANDERS

Z(m)	Resolution		High Resolution						Low Resolution					
	Y(m)		0	±1	±2	±3	±4	±5	0	±1	±2	±3	±4	1±5
1		σ_z(mm)	1	3	7	13	21	32	4	8	20	38	63	96
		σ_y(mm)	1	3	13	38	85	160	2	9	40	114	254	479
	x(m)													
	1.0	σ_x(mm)	2	3	7	13	21	32	5	9	20	38	64	96
	1.5		3	5	10	19	32	48	9	14	30	57	95	144
	2.0		4	6	14	26	42	64	12	19	41	77	127	192
3		σ_z(mm)	11	12	16	22	31	41	33	37	48	66	92	124
		σ_y(mm)	2	4	11	22	41	69	5	13	33	67	123	208
	x(m)													
	1.0	σ_x(mm)	4	4	5	7	10	14	12	13	16	22	31	42
	1.5		6	6	8	11	15	21	18	19	25	34	46	62
	2.0		8	9	11	15	21	28	24	26	33	45	62	83
5		σ_z(mm)	30	31	35	41	50	61	91	94	105	124	149	182
		σ_y(mm)	2	7	14	25	40	61	7	20	43	75	120	182
	x(m)													
	1.0	σ_x(mm)	6	6	7	8	10	12	18	19	21	25	30	36
	1.5		9	10	11	13	15	18	28	29	32	38	45	55
	2.0		12	13	14	17	20	24	37	39	43	50	60	73
7		σ_z(mm)	59	60	64	70	78	89	177	181	192	210	235	268
		σ_y(mm)	3	9	19	30	45	64	10	28	56	91	135	192
	x(m)													
	1.0	σ_x(mm)	9	9	9	10	11	13	26	26	28	30	34	38
	1.5		13	13	14	15	17	19	38	39	42	45	51	58
	2.0		17	17	18	20	23	26	51	52	55	61	68	77
9		σ_z(mm)	98	99	102	108	117	128	293	296	307	325	351	383
		σ_y(mm)	4	12	23	36	52	71	13	36	70	109	157	214
	x(m)													
	1.0	σ_x(mm)	11	11	11	12	13	14	33	33	34	36	39	43
	1.5		16	17	17	18	20	21	49	50	52	55	59	64
	2.0		22	22	23	24	26	29	66	66	69	73	78	86

TABLE 2 - ABSOLUTE MAPPING PRECISION OF BOTH HIGH- AND LOW-RESOLUTION IMAGES FROM FACSIMILE CAMERAS OF THE TWO VIKING LANDERS

Z(m)	Resolution	High Resolution						Low Resolution					
	Y(m)	0	±1	±2	±3	±4	±5	0	±1	±2	±3	±4	1±5
1	σ_z(mm)	4	7	16	31	53	80	5	10	24	47	79	119
	σ_y(mm)	1	8	33	95	211	400	2	11	50	143	317	599
	x(m)												
	1.0	6	8	17	32	53	80	10	13	25	48	80	120
	1.5 σ_x(mm)	11	14	26	48	80	120	17	21	39	72	119	180
	2.0	16	19	35	64	106	160	23	29	52	96	159	240
3	σ_z(mm)	28	31	40	55	76	103	41	46	60	83	114	155
	σ_y(mm)	4	11	27	56	102	173	6	17	41	83	153	260
	x(m)												
	1.0	11	12	14	19	26	35	16	17	21	28	39	52
	1.5 σ_x(mm)	17	18	22	29	39	52	26	27	33	44	59	79
	2.0	23	25	30	39	53	70	35	37	45	59	79	105
5	σ_z(mm)	76	79	88	103	124	151	114	118	132	154	186	227
	σ_y(mm)	6	17	36	62	100	152	9	26	54	94	150	228
	x(m)												
	1.0	16	17	18	21	25	31	24	25	28	32	38	46
	1.5 σ_x(mm)	25	26	28	32	38	46	37	38	42	49	58	69
	2.0	33	34	38	43	52	62	50	52	57	65	77	93
7	σ_z(mm)	148	151	160	175	196	223	222	226	240	263	294	335
	σ_y(mm)	9	23	47	76	113	160	13	35	70	114	169	240
	x(m)												
	1.0	22	22	23	26	29	32	33	33	35	38	43	48
	1.5 σ_x(mm)	33	34	36	39	43	49	50	51	54	58	65	73
	2.0	44	45	48	52	58	65	67	68	72	78	87	98
9	σ_z(mm)	244	247	256	271	292	319	366	371	384	407	438	479
	σ_y(mm)	11	30	58	91	131	178	17	45	87	137	196	267
	x(m)												
	1.0	28	28	29	31	33	36	42	42	43	46	49	54
	1.5 σ_x(mm)	42	42	44	46	50	54	63	64	66	69	75	81
	2.0	56	57	59	62	66	72	84	85	88	93	100	109

PLANETWIDE CONTROL NETWORK OF MARS

Sherman S. C. Wu and Francis J. Schafer, U. S. Geological Survey, Flagstaff, Arizona 86001

Pictures taken by Viking Orbiters 1 and 2 are being used to make planetwide contour maps of Mars (Wu, et al., 1982). Publication at 1:2,000,000 and 1:15,000,000 is planned. The photographs are used in a block adjustment to produce a planetwide control network in an equatorial band and a polar band. The equatorial band covers approximately 60° of latitude. The two polar regions beyond the latitude of 65° are almost entirely covered by the polar band.

A total of 800 photographs are used with 500 for the equatorial coverage and 300 for the coverage of the polar band outside of the equatorial region (Table 1). Footprints of photo coverage are shown in

TABLE 1 - CATGORIES OF VIKING ORBITAL PHOTOGRAPHS USED FOR THE PLANETARY CONTROL NETWORK OF MARS

BAND	EQUATORIAL		POLAR		
MISSION	VO-1	VO-2	VO-1	VO-2	TOTAL
RMAG (KM)					
<24,000	40		43	10	93
24,000 TO 37,000	400	21	117	127	705
	480	20	160	137	
TOTAL	501		297		798

Figures 1 and 2 respectively for the equatorial and the polar bands. Geodetic coordinates of ground points are calculated by analytical aerotriangulation through a block adjustment using the U. S. Geological Survey's GIANT program. Control data for the adjustment include the spacecraft positions determined by Earth-based tracking, occultation points from both Mariner 9 and Viking missions (Kliore et al., 1970, Lindal, 1978), Earth-based radar observations (Downs et al,1982) and the planimetric control net derived by Davies (Davies et al, 1982). Spacecraft positions are given very high weighting in the computations, because they cannot be determined accurately any other way. Similarly, the horizontal components of the Davies planimetric net and the vertical components of the radar and occultation net are given high weight. New vertical values are computed for the points in the planimetric net, and new horizontal values for the radar and occultation measurements. Camera positions and orientations are also adjusted for their internal consistency. The final net includes not only the above points, but the horizontal and vertical locations of a third set of image points required to control photogrammetric mapping.

The planetwide control network of Mars is expected to be completed in the first half of fiscal year 83.

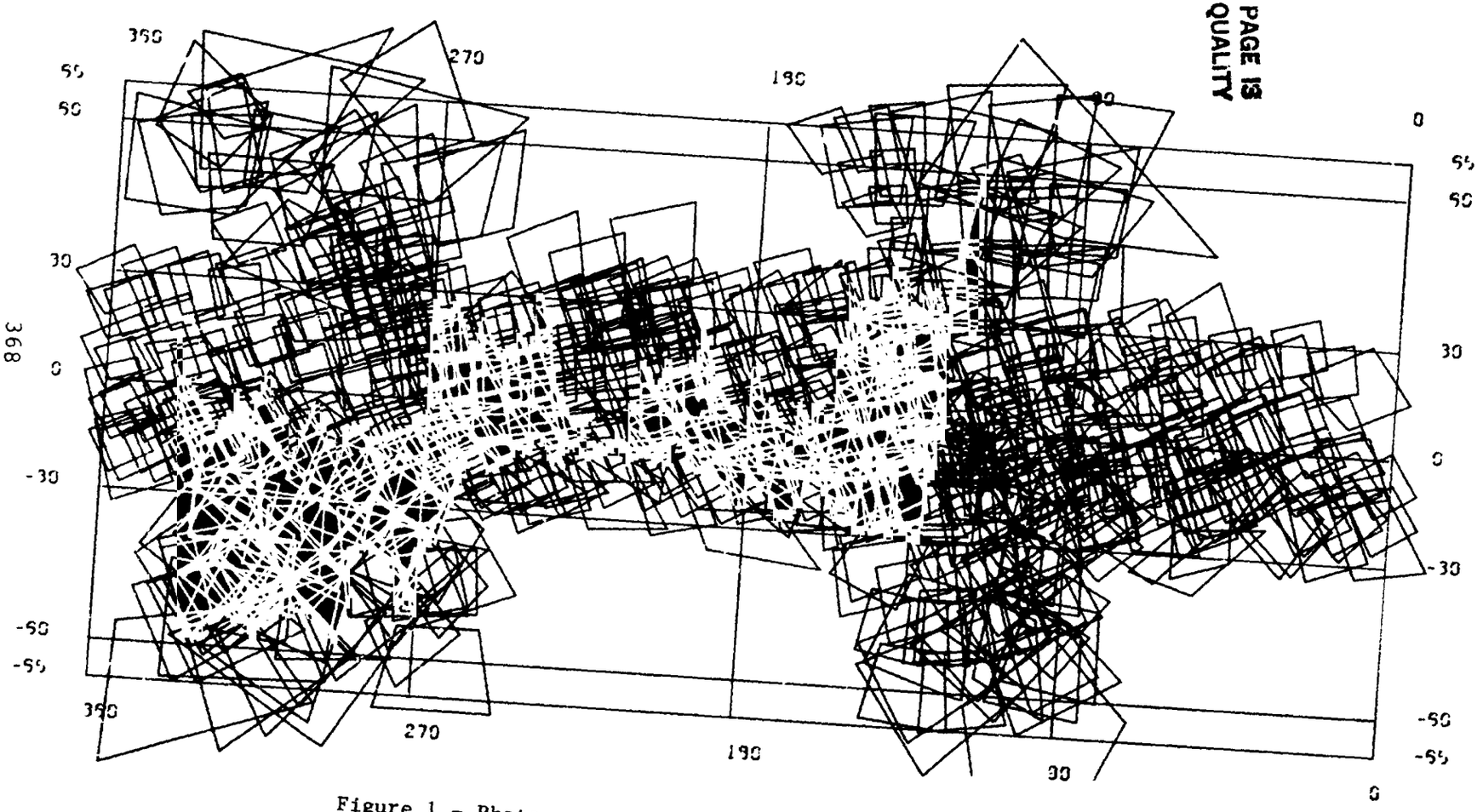

Figure 1 - Photo coverage of Mars control net (equatorial band)

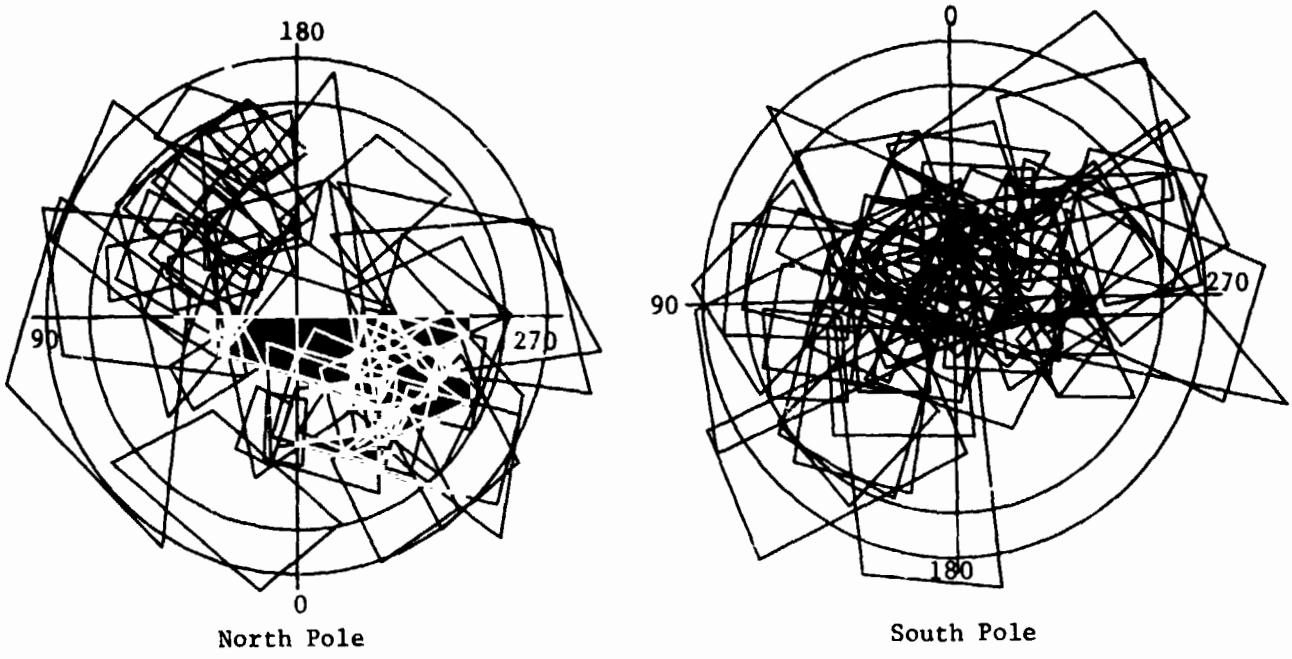

Figure 2 - Photo coverage of Mars control net (polar band)

References

Davies, M. E., Katayama, F. Y., and Roth, J. A., 1979, Control net of Mars: The Rand Corporation, R-2039-NASA, Feb., 1978, 91 p.

Downs, G. S., Mouginis-Mark, P. J., Zisk, S. H., and Thompson, T. W., 1982, New radar-derived topography for the northern hemisphere of Mars (in press).

Kliore, A., Cain, D. L., Seidel, B. L., and Fjeldbo, G., 1970, S-band occultation experiment for Mariner Mars 1971, Icarus, vol. 12, no. 1, pp. 82-90.

Lindal, G. F., 1978, Occultation data update, Viking Mars Physical Properties Working Group Report, NASA Langley/JPL/MMC, Viking Project, p. 106-116.

Wu, Sherman S. C., Elassal, A. A., Jordan, Raymond, and Schafer, F. J., 1982, Photogrammetric application of Viking orbital photographs, Planetary and Space Science, vol. 30, no. 1, pp. 45-55.

THE SOLUTION OF THE LAYOVER PROBLEM OF SIDE-LOOKING RADAR IMAGES

Sherman S.C. Wu, U. S. Geological Survey, Flagstaff, Arizona 86001

Because of its method of illumination and image formation, the direct use of radar images for map compilation is precluded on conventional photogrammetric equipment. Both radar shadow, which occurs at low depression angles, and radar layover (non-unique return at high depression angles) make stereo mapping difficult and complicated. However, radar shadow can be eliminated from the stereo coverage area with images taken from the same side, where as the layover problem is mathematically solvable.

Layover is caused by the fact that the radar measures range from the radar antenna to an object regardless of the terrain relief. For airborne systems, higher elevation terrain features appear closer to the antenna and may overlap lower elevation terrain features; radar energy scattered off the tops of mountains returns to the antenna before that scattered off the mountains' toes. This phenomina is just the opposite from conventional aerial photography, therefore the radar image displacements due to elevated terrain are toward to the nadir point of the camera (radar station) where as displacements of conventional aerial photography are away from the nadir point of the camera station. This is perhaps one of the most severe obstacles in stereo radar mapping.

The mathematical solution to the radar layover problem involves two equations, each of which represents a circle or a sphere, and relates the radar station and radar range to a ground point in each of a pair of overlapped radar images. As shown in figure 1, P_1 and P_2 are two flight paths, from which stereo radar images are taken; S_1 and S_2 are two radar stations from which radar images of ground point G are taken; and R_1 and R_2 are ranges of G measured respectively from S_1 and S_2. By assuming that the coordinates of the beginning and the ending points of each path, B and E are known, or any other control points along the radar paths are known, then the coordinates X_1, Y_1, H_1, and X_2,Y_2, H_2 of S_1 and S_2 can be interpolated. P_1 and P_2 can be straight lines, or can be curves if additional intermediate control points, I's, are known along the paths. The two equations, C_1 and C_2, respectively for the two circles are:

$$C_1 = f_1 (S_1, R_1, G)$$

$$C_2 = f_2 (S_2, R_2, G)$$

and the unknown coordinates, X_G,Y_G, and H_G are the ground coordinates of G, which is then one of the two intersections of the two circles. The two equations are:

$$(X_G - X_1)^2 + (Y_G - Y_1)^2 + (H_G - H_1)^2 = R_1^2$$

$$(X_G - X_2)^2 + (Y_G - Y_2)^2 + (H_G - H_2)^2 = R_2^2$$

Where $H_G = \frac{1}{2}[(H_1 + H_2) - (R_1 \sin \Theta_1 + R_2 \sin \Theta_2)]$
and, Θ_1 and Θ_2 are depression angles of G respectively at radar stations S_1 and S_2. If Θ_1, and Θ_2 are in the same vertical plane, they can be determined by the following equations:

$$\Theta_1 = \text{arc cos } [\frac{R_1^2 + B^2 - R_2^2}{2 R_1 B}]$$

$$\Theta_2 = 180^0 - \text{arc cos } [\frac{R_2^2 + B^2 - R_1^2}{2 R_2 B}]$$

B is the air base between the two radar stations.

This will leave only two unknowns, X_G and Y_G, to be solved in two equations. Of course two solutions will be obtained for each of X_G, Y_G. Only one of those two answers is correct and is determined by the depression angles.

On the analytical stereo plotter, once X_G, Y_G and H_G are determined, the computer will cause the radar images to be displaced as in conventional aerial photography, so that the stereo model can be retained.

Combined with techniques of image correlation, this concept of the solution of the radar layover problem is a new approach which can be used in the future design of a radar stereoplotter, and which will also certainly include general cases such as where the ground points and the two radar stations are not in a vertical plane

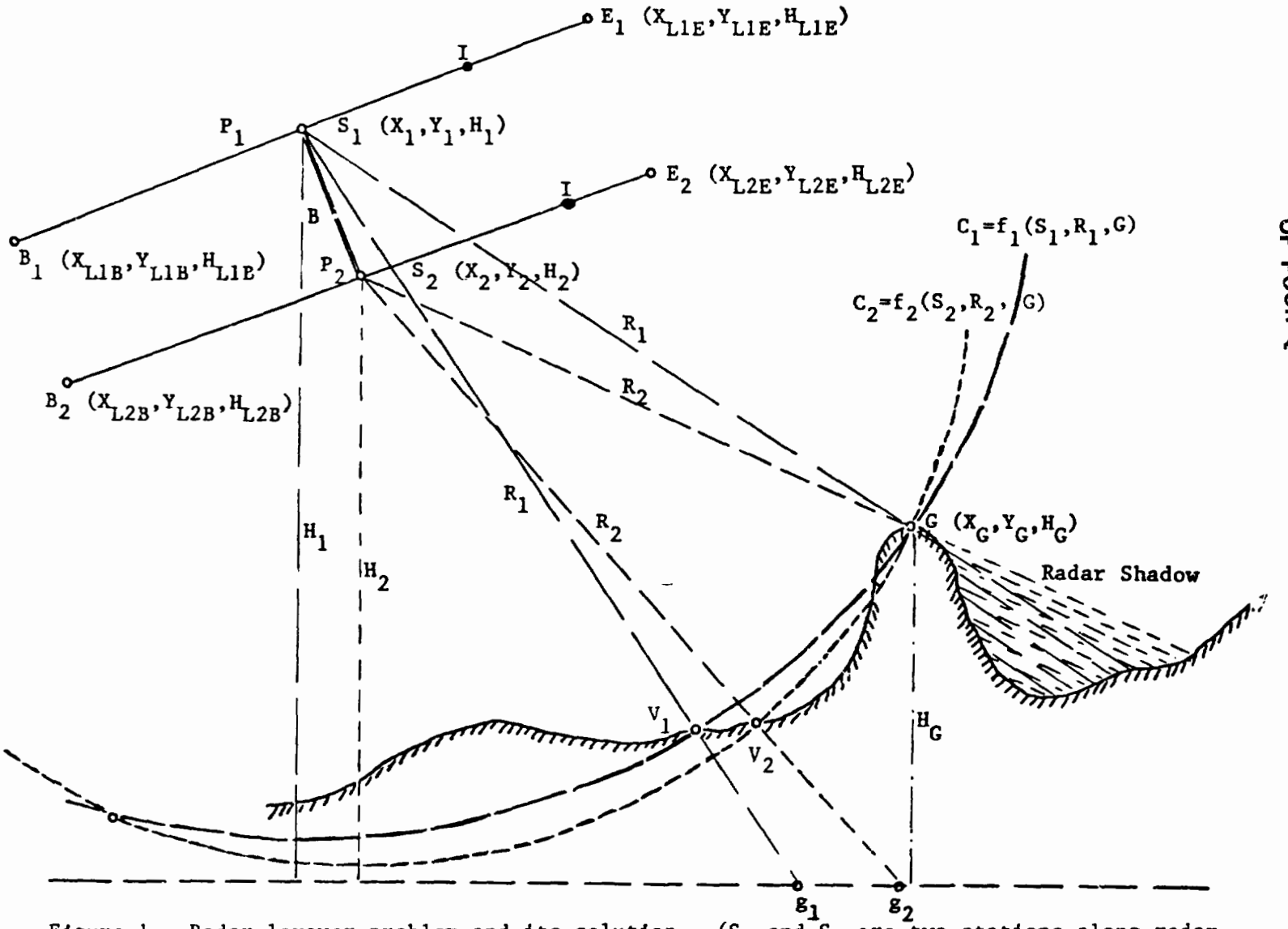

Figure 1 - Radar layover problem and its solution. (S_1 and S_2 are two stations along radar paths P_1 and P_2, from which ground point G is measured and recorded. The layover problem, G to V_1 and V_2, is resolved by solving simultaneous equations of two circles, C_1 and C_2, which are formed by two radar stations and their ranges.

THE COMPLETION OF PHOTOGRAMMETRIC COMPILATION OF THE GLOBAL TOPOGRAPHIC MAP OF THE MOON

Sherman S. C. Wu, U. S. Geological Survey, Flagstaff, Arizona 86001

A new global topographic map of the Moon, based on a new topographic datum (Wu, 1981a), is under compilation at a scale of 1:5,000,000 with a contour interval of 500 meters. The coordinate system used is the same as that of the control nets derived by the Defense Mapping Agency (Doyle et al, 1977).

Contour maps compiled by photogrammetric methods using all available stereo pairs of metric photographs from the Apollo 15, 16, and 17 missions (Wu, 1981b) were compiled as an intermediate step, and will be published as special maps in the DMA LOC format, at a scale of 1:2,750,000. Preliminary copies of the LOC-3 map (Wu, 1981b) have been distributed to principal investigators in the Planetary Geology Program.

Figure 1 is an example of the map formats of LOC-1, -2, and -4. Figure 2 shows the stereo coverage of the models used to compile LOC-4. Publication of all four sheets in fiscal year 83 is planned. Completion and publication of the global map is also planned for fiscal year 83.

This compilation was done on analytical stereoplotters from 566 stereo models (see table) with the collaboration of Raymond Jordan, Francis Schafer, Michelle Kerrick, Annie-Elpis Howington, Patricia Garcia, Colleen Maurer, Carol Hildeman, Sherri Bergstrom, Susan Roeming, and Loretta Barcus.

LOC No.	LOC-1	LOC-2	LOC-3	LOC-4	TOTAL
Apollo Mission					
15	6	43	218	17	334
16		35	62	8	105
17		11	60	56	127
TOTAL	6	139	340	81	566

References

Doyle, F. J. Elassal, A. A. and Lucas, J. R., 1977, Selenocentric geodetic reference system, NOAA Tech. report NOS 70-NG55, 53 p.

Wu, Sherman S. C., 1981a, A method of defining topographic datums of planetary bodies, Ann. Geophys. t, 37, fasc, 1, 1981, pp. 147-160.

Wu, Sherman S. C., 1981b, Photogrammetric compilation of the global map of the Moon, in Report of Planetary Geology Program-1981, NASA Tech. Memo. 84211, pp. 497-499.

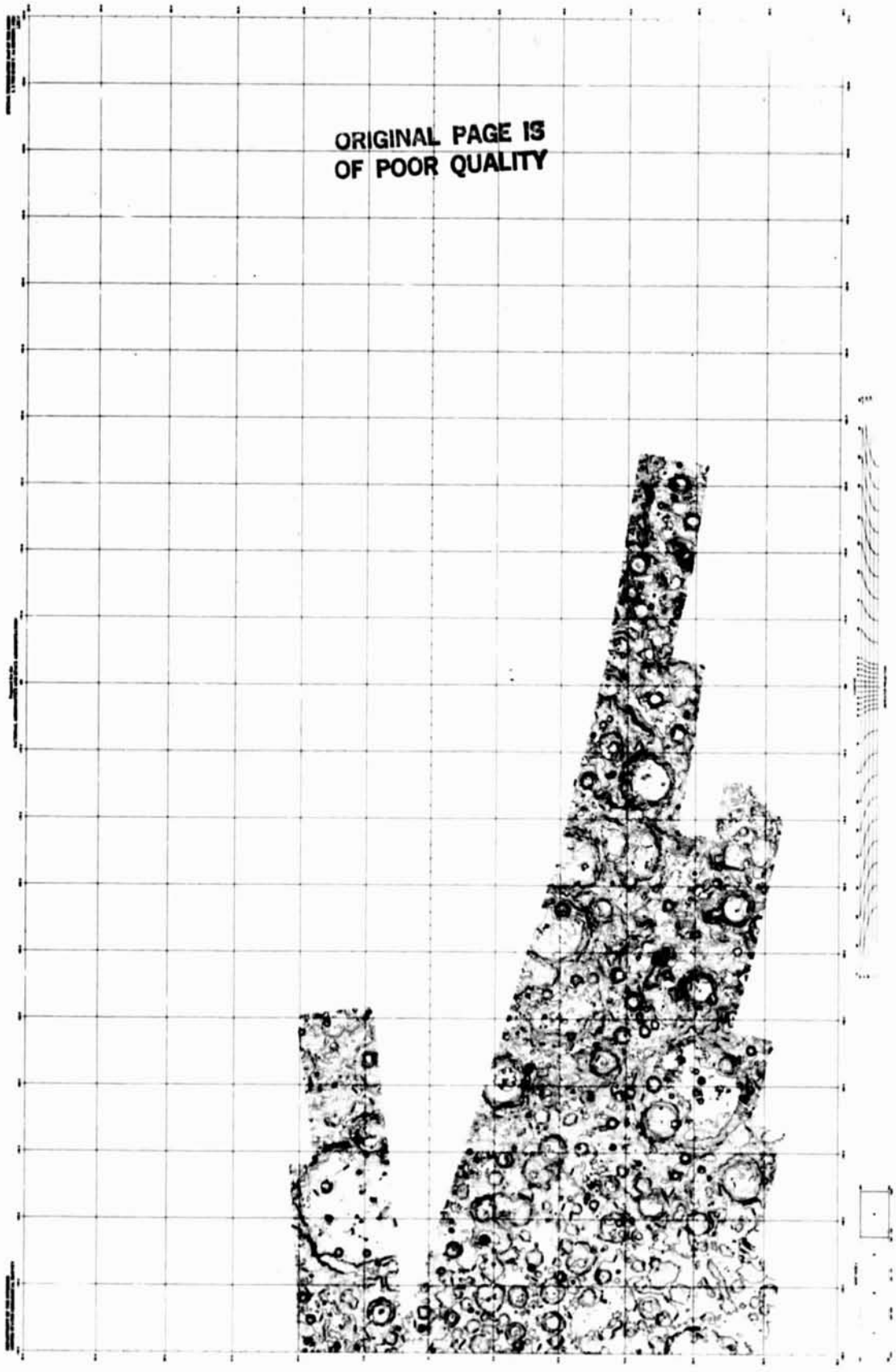

Figure 1 - Topographic map of the Moon, LOC-4. The map is compiled by Photogrammetric methods using Apollo metric photographs. Contour interval is 500 meters.

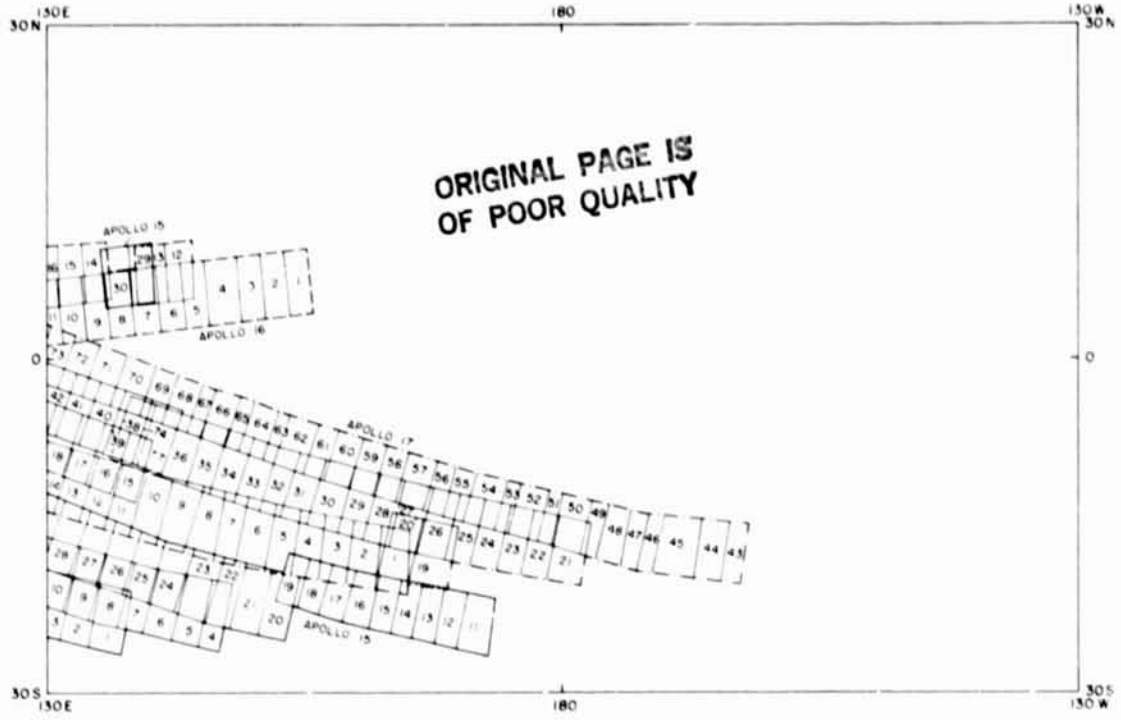

LUNAR PLANNING CHART (LOC-4) STEREOMODEL COVERAGE

APOLLO 15

Index No.	Picture No.	Index No.	Picture No.
1	1568-1566	16	88-86
2	1570-1568	17	90-88
3	1572-1570	18	92-90
4	877-875	19	94-92
5	878-876	20	292-290
6	880-878	21	294-292
7	882-880	22	296-294
8	884-882	23	298-296
9	886-884	24	300-298
10	888-886	25	302-300
11	78-76	26	304-302
12	80-78	27	306-304
13	82-80	28	308-306
14	84-82	29	1857-1855
15	86-84	30	1859-1857

APOLLO 16

Index No.	Picture No.
1	51-49
2	53-51
3	55-53
4	57-55
5	59-57
6	61-59
7	63-61
8	65-63
9	67-65
10	69-67
11	71-69
12	1854-1852
13	1856-1854
14	2083-2081
15	2085-2083
16	2087-2085

APOLLO 17

Index No.	Picture No.	Index No.	Picture No.	Index No.	Picture No.
1	1696-1694	26	486-484	51	191-190
2	1698-1696	27	488-486	52	192-191
3	1700-1698	28	490-488	53	194-193
4	1702-1700	29	492-490	54	195-194
5	1704-1702	30	494-492	55	197-196
6	1706-1704	31	476-494	56	198-197
7	1708-1706	32	498-49[illegible]	57	200-199
8	1710-1708	33	500-49[illegible]	58	202-201
9	1712-1710	34	502-500	59	203-202
10	1714-1712	35	504-502	60	206-205
11	1716-1714	36	506-504	61	207-106
12	1718-1716	37	508-506	62	209-208
13	1720-1718	38	510-508	63	210-209
14	1722-1720	39	368-366	64	212-211
15	707-705	40	370-368	65	214-212
16	709-707	41	372-370	66	215-214
17	711-709	42	374-372	67	217-215
18	713-711	43	178-177	68	218-217
19	1390-1388	44	179-17[illegible]	69	220-218
20	1392-1390	45	1[illegible]-180	70	222-220
21	476-474	46	184-183	71	224-222
22	478-476	47	185-184	72	226-224
23	480-478	48	186-185	73	228-226
24	482-480	49	188-187	74	366-364
25	484-482	50	189-188		

Figure 2 - Apollo photo coverage and list of stereo models used for the photogrammetric compilation of the contour map of the Moon (LOC-4)

Chapter 12

SPECIAL PROGRAMS

VIKING LANDER MONITOR MISSION IMAGING INVESTIGATION

STATUS REPORT

Stephen D. Wall, Jet Propulsion Laboratory

The Viking Lander Monitor Mission operatis the Mutch Memorial Station, formerly the Viking I lander, which continues to provide imagery, meteorology and ranging data on a weekly basis from Mars. The lander is programmed to continue operations through 1994, and current indications are that the lander may survive until then if the storage capacity of the four onboard batteries can be maintained. Considerable engineering effort is being devoted to prolonging battery life through conditioning (charge-discharge) cycles. Flight software changes have been made this year which have performed conditioning excercises. As a result three of the four batteries have been restored to about 80% of their original capacity. All other critical systems on the lander are operating nominally.

Imaging data is processed routinely by JPL's Image Processing Lab and released periodically to the NASA Regional Planetary Libraries. The imaging strategy is to monitor a few areas approximately monthly, and otherwise to repeat previous images with the same lighting geometry to identify changes. Such images ("repros") have shown that the scene is dynamic, though not strikingly so. Fine material is periodically redistributed, both eroded and deposited, and there is no clear sign that either dominates. Figure 1 is a repro pair comparing sol 1402 with sol 2068 showing typical redistribution of a thin layer above the cemented surface near the lander. More evidence of redistribution can be seen near the horizon. Figure 2 is not a repro pair, but despite differences is lighting it is clear that a centimeter or two has been removed from a pile made by the surface sampler. These images were taken on sols 441 and 1765. Although it is not possible to determine the times of these events, repro and other pairs can bracket them, and the times are consistent with a third year dust storm in the same season or perhaps somewhat later than the first two years' storms (Ryan and Sharman, J. Geophys. Res. 86, C4). We hope that meteorology data can further localize these occurences in time.

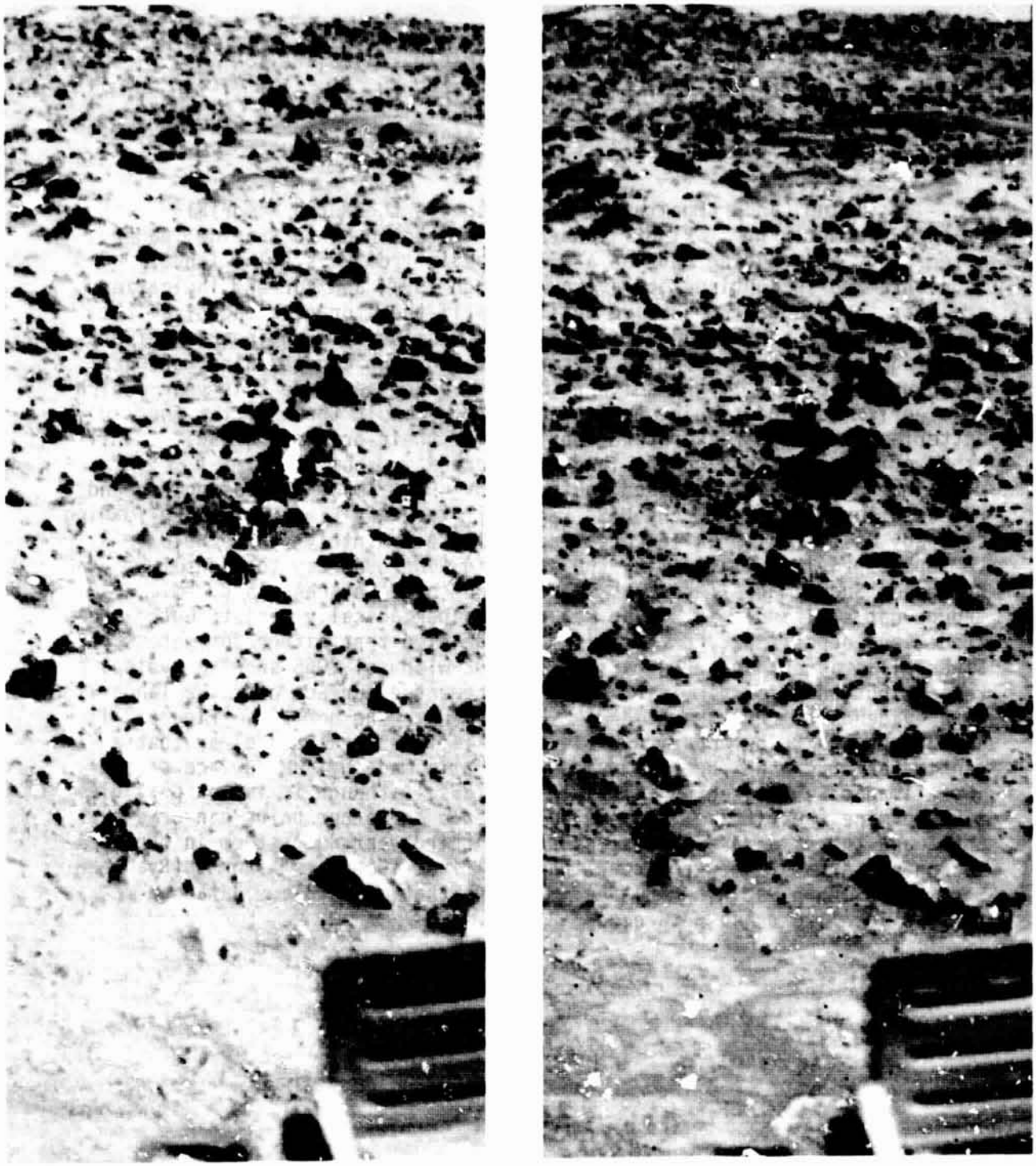

Figure 1.- Lander images 11J081/1402 and 11J171/2068

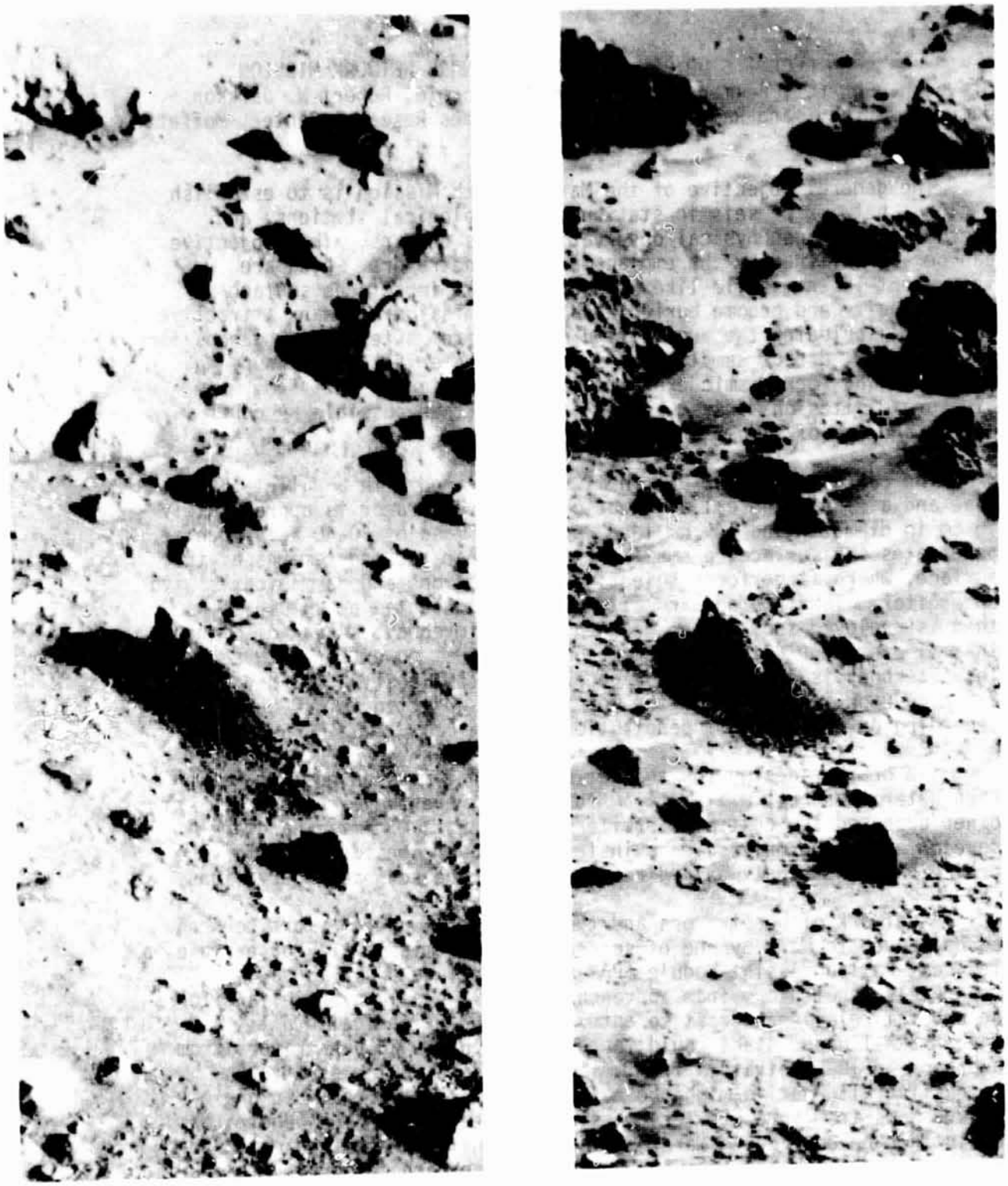

Figure 2.- Lander images 11F205/441 and 11J130/1765

RECENT STUDY IN SUPPORT OF A MARS NETWORK MISSION

Steven W. Squyres, Palmer Dyal, Robert M. Haberle, Robert W. Jackson, James P. Murphy, and Ray T. Reynolds, NASA-Ames Research Center, Moffett Field, CA 94035.

The general objective of the Mars Network Mission is to establish a global network of seismic stations, meteorological stations, and geochemical and geophysical observation sites on Mars. This objective can be accomplished by the emplacement of penetrators, which are instrument-laden missile-like projectiles that impact the surface at high velocity and become buried. A network mission has many attractive features, including the acquisition of data from sites too dangerous for soft landers, direct sampling of subsurface material, solid coupling to the ground for seismic experiments, acquisition of data from many widespread sites on Mars at a cost far lower than possible by other means, and use of simple and tested technology.

The basic penetrator design is rocket-shaped with a bullet-like nose and a flared conical aft section. The penetrator is approximately 10 cm in diameter and 140 cm long, and has a mass of 30-40 kg. When it penetrates the surface, a small afterbody separates and remains at the surface, where it performs scientific observations and communicates with an orbiter. The forebody and afterbody are connected by an umbilicus that is deployed from a storage area in the forebody. A radioisotope thermal generator (RTG) in the forebody provides power for both sections. The afterbody is subjected to a deceleration of about 20,000 g for 2-3 msec upon impact, while the forebody is subjected to 2,000-20,000 g depending on the depth of penetration.

The orbiter design for the network science mission has not yet been determined, but will closely follow that eventually chosen for other proposed low cost Mars orbiters in order to minimize hardware development. The only science instruments under consideration for the orbiter are ones that would directly support the surface observations.

A network of penetrators and the communications relay orbiter can be delivered to Mars by one of several types of missions. For example, a low-cost Payload Assist Module (PAM-A) upper stage could target and separate 4 penetrators from approach and provide enough propellant for an orbital relay spacecraft to enter a 24-hour elliptical orbit. A larger SRM-1 upper stage could target and separate 20 penetrators from approach or 10 penetrators from a low altitude circular orbit. An attractive alternative might be to use a spacecraft already in orbit around Mars from some previous mission for the relay. The penetrators could then be carried to Mars on a simple penetrator bus and would be targeted and separated from the bus during approach to Mars. A separate launch penetrator mission using a PAM-A could easily carry 6 penetrators and possibly as many as 8 if a lightweight bus could be designed.

Two major considerations govern the selection of penetration sites: establishment of effective local and global seismic and magnetic networks, and acquisition of data from areas of widely varying meteorologic and geologic characteristics. At least three closely-spaced penetrators should be placed in an area of suspected high seismicity. A good candidate would be the Tharsis region. The penetrator spacing should be close enough to make detection of weak or infrequent seismic events likely (on the order of 500 km). As many additional penetrators as possible should be widely distributed to give good global seismic, magnetic, geochemical, and meteorological coverage at sites of high geologic interest. At least 4 penetrators separated by distances of roughly 5000 km would be required for an effective global seismic network. One of these could of course be part of the local network. Prime target candidates would include the polar layered deposits, major outflow channel floors, areas of suspected ice-rich permafrost, and ancient cratered highlands. A major volcano could presumably be included in a seismic array in the Tharsis area.

A wide variety of scientific experiments could be conducted by a network mission. These include:

Seismometry - One attractive design for a penetrator seismometer would be a combined bubble tiltmeter and force balance accelerometer that has been investigated at Caltech. A bandwidth of 0.01-5 Hz and a resolution of 10^{-8} g would be desirable and should be achievable. The principle areas where work is required for a penetrator seismometer are event detection, data compression, and impact survival. A data compression algorithm for the tiltmeter/accelerometer instrument has been devised that would produce 1.5×10^5 bits per day. Some successful high g-load testing has been performed on seismometer components.

Magnetometry - The best magnetometry instrument for a penetrator would probably be three orthogonal fluxgate magnetometers. Determination of the bulk electrical conductivity properties of Mars would also require simultaneous monitoring of changes in the forcing magnetic field by a magnetometer on the orbiter.

Heat Flow - Heat flow measurements could be conducted with temperature sensors in the penetrator forebody, in the afterbody, and spaced at regular intervals along the umbilicus. The sensors could be platinum resistance thermometers, solid-state temperature sensors, thermistors, or low temperature thermocouples.

Gamma Ray Spectrometry - An active gamma ray experiment for a penetrator would consist of a pulsed neutron source and a NaI or CsI gamma ray detector. Pulsed neutron sources are currently available that would be well suited to a penetrator mission. Such sources emit 10 μs pulses of 14 MeV neutrons at an intensity of 10^6 n^0 μs^{-1} produced by a deuterium-tritium reaction. Typical sources have diameters of 5 cm and lengths of 15 cm. These neutron sources have been thoroughly tested in penetrators on Earth. A NaI or CsI detector would be capable of

giving relative abundances of all the major rock-forming elements. Typical detectors are 20-25 cm long. NaI detectors have better resolution than CsI by a factor of 2, but single crystal NaI detectors are considerably more fragile than single crystal CsI detectors. A recently developed NaI polycrystal detector, however, has NaI's resolution with substantially improved strength.

Material Properties (Stratigraphy) - The instrument required for determination of subsurface material properties and stratigraphy is an accelerometer. This instrument would sense the deceleration experienced by the penetrator forebody as it slowed and came to rest beneath the surface. Variations in material properties would appear as irregularities in the deceleration record. An instrument of this type is also required to determine the depth of penetration. Such accelerometers exist and have been extensively tested on penetrators.

Imaging - One attractive type of imaging system for a penetrator would be a small charge-coupled device (CCD). The camera would of course be mounted on the highest part of the penetrator afterbody. A typical design would have about 8 bits per picture element, and no filters for mechanical simplicity. CCD arrays have been successfully tested to very high g-loads.

Meteorology - Several instruments would be required to make up a meteorology package in the penetrator afterbody. These include pressure, temperature, humidity, opacity, wind direction, and wind velocity sensors. As yet, no instrument prototypes have been developed for use in penetrators. Much additional information could be gained from an infrared radiometer onboard the orbiter that gives atmospheric thermal profiles. These profiles, when combined with simultaneous meteorological observations from a network of surface sites, would substantially improve our understanding of the martian atmospheric circulation.

Costs for Mars network missions have been estimated by Science Applications Incorporated (SAI). The costs for these missions are comparable to those for Mars orbiters, and very much less than those for soft landers or rovers.

SPATIAL RESOLUTION AND AREAL COVERAGE OF MARS BY THE VIKING ORBITER CAMERAS

M.H. Edwards and R.E. Arvidson, McDonnell Center for the Space Sciences, Washington University, St. Louis, Missouri 63130

As noted by Davies and Murray (1971), the areal coverage at some stated spatial resolution (or better) is a useful way to visualize how well a given planetary object has been covered by imaging data. The Viking Orbiter VIS system has provided the best coverage to date for Mars (Snyder, 1979). However, because of competing imaging needs during the beginning of the mission and because of orbital changes, the image coverage is not uniform. Thus, we have investigated both how much of the surface area of Mars is covered by a given resolution (or better) and the distribution in map form of the coverage.

If we assume that the VIS vidicon sample array of 1056 lines and 1182 samples properly samples the system limiting spatial frequency (e.g., the resolving power in cycles/mm) then no more than about 373 x 418 cycles could be properly sampled on the vidicon face plate, since $2\sqrt{2}$ TV lines are needed to assure proper sampling of a given spatial frequency. These values correspond to a resolving power of about 30 cycles/mm when the dimensions of the image on the vidicon are considered. According to Benesh and Thorpe (1975), at ~30 cycles/mm, the cameras have a contrast attenuation of ~0.5, or ~50% of the scene contrast is attenuated. This contrast attenuation value is typically used to define the limiting spatial frequency or the resolving power of a system. We can thus consider the ground resolution of the VIS images to be $\sim 2\sqrt{2}$ times the width covered by a picture element on the ground.

To determine the areal coverage at some stated ground resolution or better we utilized data from frames 003A01 to 973A10, 004B01 to 705B52, and 122S01 to 485S24. The planet was treated as an array of elements with 1° x 1° spacing and a computer search was conducted to find frames that cover a given grid intersection. If the ground resolution for a given frame was better than the value already assigned to the intersection, the new resolution value replaced the old value. The result is a map of the coverage with a stated ground resolution, which can be displayed as an image (Figure 1). The image was generated both as a simple cylindrical projection and as a Lambert equal area projection. The brightness histogram from the latter image was used to generate the plot of ground resolution vs. areal coverage shown in Figure 2. These two data presentations are valuable adjuncts to understanding how well Mars has been covered by imaging data. For instance, according to Figure 2, somewhat less than 10% of the surface has been covered with image data that have a ground resolution of better than ~100 meters. Less than 1% is covered with a resolution of better than ~30 meters and most of that coverage is in the northern midlatitudes.

References

Benesh, M. and T. Thorpe, 1976, Viking Orbiter 1975 visual imaging subsystem calibration report, JPL Pub. 611-125.

Davies, M.E. and B.C. Murray, 1971, The view from space, Columbia Univ. Press, 163 p.

Snyder, C.W., 1979, The extended mission of Viking, J. Geophys. Res., 84, 7917-7933.

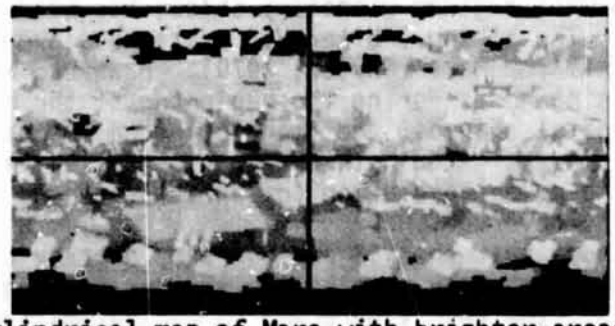

Figure 1-Cylindrical map of Mars with brighter areas covered with higher resolution images than darker areas.

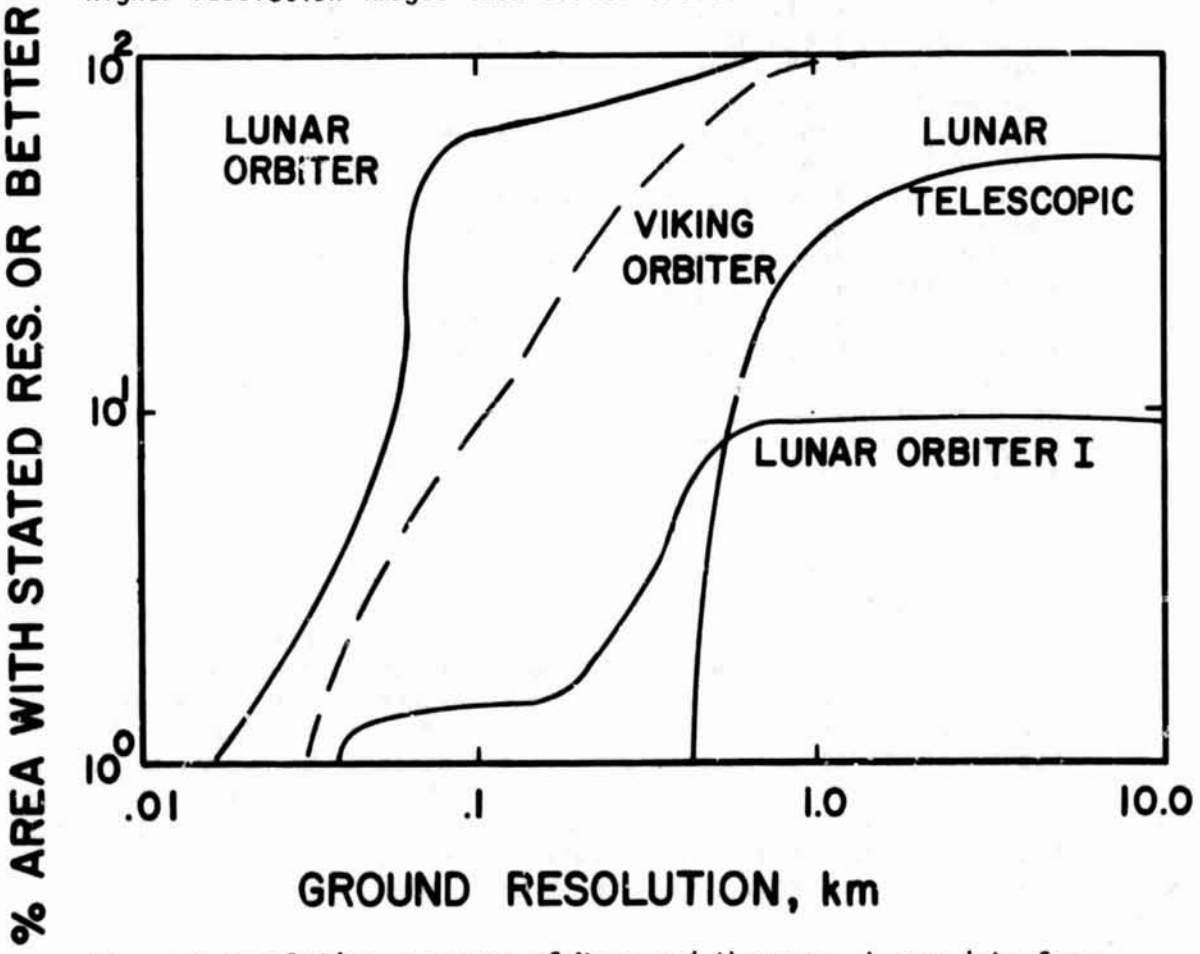

Figure 2-Resolution coverage of Mars and the moon. Lunar data from Davies and Murray (1971).

VIKING ORBITER IMAGING STATUS REPORT

S. Winterhalter, Jet Propulsion Laboratory, California Institute of Technology, Pasadena, California 91109

During Fiscal Year 1982 201,586 Viking Orbiter products were processed. These products were broken down into the following groups and distributed: original negatives- 5,929; duplicate positives- 17,787; duplicate negatives- 71,148; strip contact prints- 83,006; enlargements- 23,716.

Systematic processing produced shading corrected and high pass filtered orthographic projection versions of these images in the form of negative rolls, strip contact prints and 8x10 inch enlargement prints. Systematic processing, lagging the receipt of data by years, finished the negative products in April 1982. As the photoproducts become available, they are distributed to Viking investigators, Regional Planetary Image Facilities, NASA and NSSDC.

The strip contact prints are mosaicked to produce the most useful presentation of the Viking Orbiter images. Approximately 700 mosaics have been generated from the first 1,000 orbits of Viking Orbiters 1 and 2 about Mars. Thirty of these cover areas mapped during the Survey and Extended Missions. Nearly 400 more mosaics need to be produced. They will be comprised of 20 to 100 individual picture frames. Each mosaic will be annotated with Mars regional identification, ground scale bars, surface coverage and orientation indication as well as picture identification.

The mosaics are then photographed for distribution. 8x10 inch negatives and prints, 4x5 inch negatives and 20x24 inch enlargements were distributed to the Regional Planetary Image Facilities, NASA and NSSDC. In order to cut down on costs, only 8x10 inch prints and 4x5 inch negatives will be distributed from October 1, 1982 on.

The most recent Survey Mission mosaics produced are:

211-5913	Global Monitoring: Syrtis Major and Hellas	0 Lat/320 Lon
5914	Global Monitoring: Elysium and Amazonis	-18 Lat/148 Lon
5915	Global Monitoring: Tharis and Valles Marineras	-6 Lat/ 43 Lon
5930	Olympus Mons	17 Lat/133 Lon
5931	Arsia-Pavonis Bore Wave Study Board 1	.5 Lat/125 Lon & 20/107
5932	Arsia-Pavonis Bore Wave Study Board 2	-12 Lat/119 Lon &-1.6/98
5934	Mangala, Survey II	-6 Lat/159 Lon
5936	Survey 1 Mosaic 1979	32 Lat/312 Lon
5937	Survey 1 Mosaic 1979	31 Lat/312 Lon
5938	Survey 1 Mosaic 1979	30 Lat/294 Lon
5939	Survey 1 Mosaic 1979	29 Lat/291 Lon
5944	South of Olympus, IMC Mapping	7 Lat/140 Lon
5945	Al Qahira Mapping	-19 Lat/190 Lon
5946	Al Qahira Mapping	-14 Lat/198 Lon
5947	Al Qahira Mapping	-22 Lat/181 Lon
5948	Mangala Mapping	-7 Lat/152 Lon
5949	Mangala Mapping	-2 Lat/145 Lon
5950	Memnonia Block Mapping	-11 Lat/163 Lon
5951	Memnonia Block Mapping	-15 Lat/154 Lon
5952	Memnonia Block Mapping	-10 Lat/163 Lon
5953	Memnonia Mapping	-12 Lat/178 Lon
5954	Memnonia Mapping	-20 Lat/166 Lon

211-5955	Chryse Planitia	35 Lat/13 Lon
5956	Chryse Planitia	35 Lat/20 Lon
5957	Mangala and Memnonia	-.01 Lat/145 Lon
5958	Mangala and Memnonia	5 Lat/140 Lon
5959	Survey 1 Mosaic	340 Lat/32 Lon
5960	Survey 1 Mosaic	350 Lat/33 Lon
5961	Survey 1 Mosaic	353 Lat/33 Lon
5962	Survey 1 Mosaic	335 Lat/32 Lon
5963	Mareotis Fossae	70 Lat/51 Lon & 87 Lat/43 Lon
5964	Tempe Fossae	63 Lat/47 Lon & 52 Lat/43 Lon
5965	North Polar Monitor	

An atlas containing the location of all the Viking Orbiter mosaics is being compiled at this time. The mosaics are being located and outlined on 1:5,000,000 maps.

This present research conducted at the Jet Propulsion Laboratory, California Institute of Technology under contract NAS 7-100 sponsored by the Planetary Geology Program, Office of Space Science and Applications, National Aeronautics and Space Administration.

Data from Planetary Science Missions Available to Researchers

Robert W. Vostreys, National Space Science Data Center,
Goddard Space Flight Center, Code 601, Greenbelt, MD 20771

With the advent of a new era of decreased planetary exploration, data from past missions become of increasing importance to researchers. The repository for most of the planetary data (as well as data from other space science missions) is the National Space Science Data Center (NSSDC).

NSSDC was established by the National Aeronautics and Space Administration (NASA) to provide data and information from space science experiments in support of additional studies beyond those performed by principal investigators. In addition to its main function of providing selected data and supporting information for further analysis of space science flight experiments, NSSDC produces relevant publications. Among these are a report on active and planned spacecraft and experiments, a data listing, and various users guides.

The Planetary and Heliocentric Spacecraft and Investigations volume of the Data Catalog Series of Space Science and Applications Flight Missions was recently published. It contains information, by planet, on the investigations conducted for which NSSDC has data. The Data Set description volume will be published later this year. For lunar missions, the *Catalog of Lunar Mission Data* is available. Virtually all the data available at or through NSSDC result from individual experiments carried on board individual spacecraft. The Data Center has developed an information system utilizing a spacecraft/investigation/data identification hierarchy. Table 1 summarizes the lunar and planetary investigations by planet. Table 2 summarizes them by discipline area.

Table 1

Spacecraft and Investigations by Planet
for which NSSDC has Data

	Spacecraft	Investigations
Mercury	3	14
Venus	13	54
Moon	29	93
Mars	8	54
Jupiter	4	46
Saturn	3	13
Interplanetary	7	56
	67	330

Table 2

Investigations by Discipline Area
for which NSSDC has Data

	Lunar	Planetary	Interplanetary
Imaging	29	22	6
Particles and Fields	24	49	32
Ultraviolet	1	8	-
Infrared	-	20	-
Radio Science and Celestial Mechanics	12	33	6
Atmospheres	1	40	-
Physical/Chemical Properties	21	9	-
Interplanetary Particles	5	-	12
	93	181	56

NSSDC provides facilities for reproduction of data and for onsite data use. Resident and visiting researchers are invited to study the data while at the Data Center. The Data Center staff will assist users with additional data searches and with the use of equipment. In addition to satellite data, the Data Center maintains some supporting information and other supporting data that may be related to the needs of researchers.

The services provided by NSSDC are available to any individual or organization resident in the United States and to researchers outside the United States through the World Data Center A for Rockets and Satellites (WDC-A-R&S). Normally a charge is made for request data to cover the cost of reproduction and the processing of the request. The researcher will be notified of the charge, and payment must be received prior to processing the request. However, as resources permit, the Director of NSSDC/WDC-A-R&S may waive the charge for modest amounts of data when they are to be used for scientific studies or for special educational purposes and when they are requested by an individual affiliated with: (1) NASA installations, NASA contractors, or NASA grantees; (2) other U.S. Government agencies, their contractors, or their grantees; (3) universities or colleges; (4) state or local governments; or (5) nonprofit organizations. A researcher may obtain data by a letter or telephone request, or an onsite visit.

Data can be provided in a format or medium other than that originally supplied by the principal investigators. For example, magnetic tapes can be reformatted, computer printout or microfilmed listings can be reproduced from magnetic tape, enlarged paper prints are available from data on photographic film and microfilm, etc. The Data Center will provide the requester with an estimate of the response time, and when appropriate, the charge for such requests. When requesting data on

magnetic tape, the user should specify whether he will supply new tapes after the data have been copied, or pay for new tapes.

The Data Center's address for requests is as follows:

National Space Science Data Center
Code 601.4
Goddard Space Flight Center
Greenbelt, Maryland 20771
Phone: (301) 344-6695

Researchers who reside outside the U.S. should direct requests for data to the following address:

World Data Center A for Rockets and Satellites
Code 601
Goddard Space Flight Center
Greenbelt, Maryland 20771 U.S.A.
Phone (301) 344-6695

IMAGE STORAGE AND DISPLAY USING CONSUMER VIDEO TECHNOLOGY

L.K. Bolef, McDonnell Center for the Space Sciences, Washington University, St. Louis, Missouri, 63130

Lunar and planetary image data can be examined in pictoral form, the data can be digitally processed to extract information, and in some cases data acquired for the same region over some time span can be viewed in movie form. We have examined ways of utilizing videotapes and videodisks as relatively inexpensive (i.e. consumer technology) but information dense media. We have interfaced our BIRP search and retrieval software to a SONY LDP-1000 industrial videodisk player to examine in analog, pictoral form those frames that meet BIRP search constraints. This "electronic browsing" system provides a user with a capability to search through image engineering data and to then interactively examine the frames. We have also used a SONY PCM-1600 (used in recording studio audio) to encode a digital Viking Lander image and to store the data on 3/4" videotape in NTSC compatible format. The inverse operation was then performed to decode the data and to generate a digital image. The two images and the picture difference are shown in Figure 1. With the error corrections intrinsic to the PCM-1600, there was no degradation in image quality. A one hour videotape would hold 5x10**9 bits of data at the recording density used to store the Viking Lander frame. We have also used the videotape recorder in animation studies where color-coded values of the topography of Earth and Venus were projected onto globes seen from an orbiting spacecraft. Several thousand frames were generated that show an approach and orbit sequence for each planet. The frames were then written onto videotape in sequential form in order to generate the appropriate animation sequence. In order to properly sequence the placement of frames on the videotape, an encoder was built that places time code markers in the audio track. The frame locations were then keyed to the code markers through the use of appropriate software. The overall intent of these activties is to utilize existing, consumer-driven technologies to help reduce the costs of electronic handling and analysis of data.

PCM ENCODING OF DIGITAL DATA
VIKING LANDER FRAME 11J130

WASHINGTON UNIVERSITY 5/28/82

DIFFERENCE OF TWO IMAGES

PCM ENCODED IMAGE

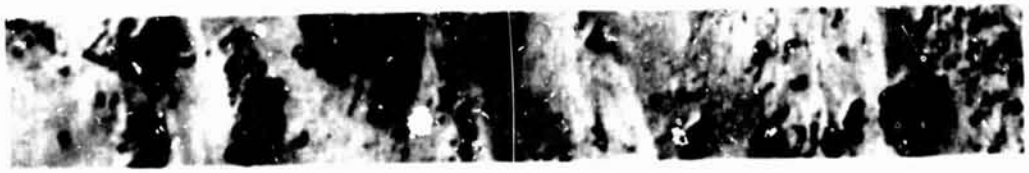

ORIGINAL IMAGE

Figure 1 - Results of encoding digital image, storing the data on videotape, decoding the data and comparing the data to the original.

THE MARS CHANNEL WORKSHOP: A REPORT

Komar, Paul D., School of Oceanography, Oregon State University,
Corvallis, Oregon 97331

The Third Mars Channel Workshop was held at Timberline Lodge, east of Portland, Oregon, on 27-28 April 1982. This was followed by a two-day field trip to the Mount St. Helens region. Thirteen NASA investigators interested in martian channels participated in the workshop and field trip.

In total, sixteen presentations were made at the workshop, summarizing our newly completed or on-going research. On average each talk lasted about an hour, although two individuals persisted for an hour and a half. There were also shorter "show-and-tell" sessions where we could inspect the products of mapping efforts related to the martian channels.

Several of the presentations dealt with the small valley systems, the origin and significance of which are still under debate. J. Laity presented the results of her investigation of sapping processes on the Colorado Plateau and comparisons with martian valleys. A. Howard and C. Kochel are involved in laboratory experiments and numerical models of sapping processes. V. Baker focused on the dissection of volcanoes by small channels where sapping has been important, comparing the dissection of Hawaiian volcanoes with those on Mars, suggesting that it may have been a significant process on the martian volcanoes. D. Pieri presented his results on the mapping of Margarifer Sinus. J. Boothroyd is in the midst of the first detailed analysis of "drainage basins" in the Ladon Vallis region, determining the areas of contribution to the small valleys. M. Carr is concerned with the stability of water and ice on Mars under various atmospheric conditions, especially focusing on the smaller-scale flows one presumably had in the valley networks.

Other studies related more to the large outflow channels, investigations of their processes of formation, secondary alterations and mapping. C. Kochel and V. Baker have prepared a morphological map of Mangala Vallis. B. Lucchitta has used the Earth based radar transits of Mars to determine elevations and then gradients of four of the outflow channels, concluding

C-5

that Tiu and Simud are essentially level or even slightly reversed. She presented a model of origin for these channels which involved ponding of water into lakes which then overflowed catastrophically, carving the channels. M. Malin described his field studies in north-central Iceland of the catastrophic floods produced by volcanic eruptions suddenly melting glaciers, relating the channels and deposits of these floods to their flow conditions. D. Nummedal described channels in the oceans formed by collapse and gravity flows, the observations being relevant to channel formation and slope processes on Mars. P. Komar has completed an analysis of streamlined islands on Earth and Mars, concluding that those on Mars did approach a least-drag configuration and must have formed in fluid flows at high Reynolds numbers, most likely catastrophic water flows.

It is of significance that all of the presentations acknowledged that water flows played the primary role in formation of both the small valleys and the large outflow channels. Although problems of interpretation remain, the flow of water is identified as a necessary ingredient. There also appears to be a growing impression that there might have been a significant recycling of the water, especially in connection with the sapping processes. This and other evidence suggests that Mars has undergone climatic changes in the past with periods of more clement conditions. The small channel networks also appear to be more systematic than previously thought. They are not just random small channels, distributed over the martian surface without much order, but instead appear to belong to well-developed drainage systems. Locally they flow toward ancient trunk streams that may be precursors of the outflow channels. Some small valley networks and outflow channels may have belonged to the same integrated systems.

The field trip to Mount St. Helens following the workshop was organized by Mike Malin and Dan Dzurisin. We first took a two-hour charter flight around the volcano in order to obtain an overview of the blast area, the large mudflows and the effects of the flows that travelled down the river valleys. Two full days were then spent on the ground, mainly

focusing on the mudflow deposits and the changes produced within the north and south branches of the Toutle River. The field trip was both scientifically worthwhile and exciting, the excitement including playing "chicken" with logging trucks and the discovery of a new sub-human species, *Homo logmanicus*, characterized by having one continuous eyebrow and a sadistic grin.

THE GALILEAN SATELLITE GEOLOGICAL MAPPING PROGRAM, CONTINUED.

B. K. Lucchitta, U.S. Geological Survey, Flagstaff, AZ 86001

The Galilean Satellite Geological Mapping Program was established to illuminate detailed geologic relations on the four large satellites of Jupiter. The program involves about 40 investigators from various universities, research institutes, and government offices in the United States, England, Germany, and Italy. A total of twenty-four researchers have been assigned to map 10 quadrangles on Ganymede, 15 to map 6 quadrangles on Io, and 4 to map 2 quadrangles on Europa. All maps are at a scale of 1:5,000,000 except for three of the Io maps, where high-resolution pictures permitted compilation of selected areas at large scales.

During 1982, the production of base materials has proceded as planned. Preliminary airbrush maps of central and southern Europa were completed and sent to the mappers to initiate geologic mapping and for review. Collections of photographs prepared in Flagstaff were also supplied to the mappers; these photographs consisted of unfiltered (shading corrected) and high-pass-filtered versions of level 1 (cosmetic and radiometric corrections) and level 2 (map projection) images. For Io, the final photomosaics and brownline Cronaflexes of the three special (largescale) maps (Ra Patera, Kane Patera, and Maasaw Patera) were transmitted to the mappers. Also completed and mailed was the airbrush version of the Io 1:5,000,000 map, Ji2. Image packages containing level 1 and level 2 pictures and available color composites of their respective quadrangles were forwarded to all Io mappers, including those whose base maps are not yet prepared. Preliminary airbrush versions of the 1:5,000,000-scale Jg7 and Jg8 quadrangles of Ganymede, as well as newly processed images, were distributed to the respective mappers. The remaining Ganymede quadrangles exist as controlled photomosaics, and airbrushing is in progress.

A meeting of all mappers was convened in Pasadena, Calif., in January 1982. The participants were informed about the status of the program, updated production schedules for the delivery of base materials, and a change in the coordinates of the special map for Io's Ra Patera. Furthermore, preliminary small-scale geologic maps of Io, Europa, and Ganymede, published in the book "Satellites of Jupiter" (1), were discussed at the meeting. It was concluded that more detailed mapping than that on the preliminary maps is essential to thoroughly understand the geologic history of the satellites and that the Galilean Satellite Geologic Mapping Program is necessary to accomplish this task.

References

(1) Morrison, David, Satellites of Jupiter, University of Arizona Press, in press.

PLANETARY GEOLOGY SPEAKERS BUREAU: THE SECOND YEAR

R. Greeley, Department of Geology and Center for Meteorite Studies, Arizona State University, Tempe, AZ 85287.

The Planetary Geology Speakers Bureau was established in the Spring of 1981 and is now in its second year of operation. Fifteen Planetary Geology Principal Investigators comprise the Bureau and are available to universities and research institutes to speak on a variety of topics (Table 1). Twice a year announcement for the program and a list of speakers and topics are sent to geoscience departments as listed in the American Geological Institute directory. Arizona State University serves as coordinator for the program by securing the initial point of contact for the host institution and scheduling potential speakers. The host institution is expected to pay reasonable and customary expenses associated with the speaker's travel.

Experience has shown thus far that most speakers present a general lecture open to the public plus a more specialized seminar at the host institution.

For additional information contact R. Greeley, Department of Geology, Arizona State University, (602) 965-7045.

Table 1

R.E. Arvidson	McDonnel Center for the Space Sciences Washington University St. Louis, MO 63130	Geologic Evolution of Mars and Venus Remote Sensing of the Earth
J.M. Boyce	Mail Code EL-4 NASA Washington, D.C. 20546	Impact Cratering Studies Strategy of Solar System Exploration Science Planning & Admin.
F. El-Baz	National Air & Space Museum Smithsonian Institution Washington, D.C. 20560	The Deserts of Earth and Mars Studying the Earth from Space
R. Greeley	Dept. of Geology Arizona State University Tempe, AZ 85287	Geologic Exploration of the Solar System Planetary Volcanism Aeolian (Wind) Processes
J.W. Head, III	Dept. of Geological Sciences Brown University Providence, RI 01912	Tectonic, Geologic Evolution of the Terrestrial Planets Lunar and Planetary Impact Basins
E.A. King	Dept. of Geology University of Houston Houston, TX 77004	Origin of Tektites, Chondrites, Chondrules Apollo Explorations of the Moon The Lunar Samples The Origin of Asteroids

H. Masursky	U.S. Geological Survey 2255 N. Gemini Drive Flagstaff, AZ 86001	Satellites of the Outer Planets Geology of Venus Martian Polar & Channel Deposits
G.E. McGill	Dept. of Geology & Geography University of Massachusetts Amherst, MA 01003	Kinematics of Utah Graben Tectonics of Venus
D. Nummedal	Dept. of Geology Louisiana State University Baton Rouge, LA 70803	The Channels on Mars General Geology of Mars
R.S. Saunders	Jet Propulsion Laboratory 4800 Oak Grove Blvd., 183-501 Pasadena, CA 91103	Extraterrestrial Geology The Geology of Venus Exploring the Solar System
P.H. Schultz	Lunar & Planetary Institute 3303 NASA Road 1 Houston, TX 77058	Target Earth Planetary Catastrophes Polar Wandering on Mars View from the Moon Martian Impacts: Clues for Geologic History
D.H. Scott	U.S. Geological Survey 2255 N. Gemini Drive Flagstaff, AZ 86001	Regional Geology of Mars Volcanic Provinces on Mars Terrestrial and Planetary Geology
E.M. Shoemaker	U.S. Geological Survey 2255 N. Gemini Drive Flagstaff, AZ 86001	Earth-crossing Asteroids The Galilean Satellites
J. Veverka	Center for Radiophysics & Research Cornell University Ithaca, NY 14853	Phobos & Deimos, Companions of Mars The Exploration of Comets Martian Weather: Dry, Cold & Windy Io: The Solar System's Strangest Moon A Voyager View of Saturn & its Satellites

DEVELOPMENTS OF PLANETARY GEOLOGY PROGRAMS IN FRANCE

MASSON Ph., MERCIER, J. L., Laboratoire de Géologie Dynamique Interne (ERA C /02), Université Paris-Sud, 91 405 Orsay Cedex, France.

Since the previous report on Planetary Geology Activities and Developments in France has been published in 1980 (1), the Planetary Image Facility located in the Laboratoire de Géologie Dynamique Interne (LGDI) of the Université Paris-Sud (UPS) at Orsay (France) developed and served as a Regional Facility for french users.

The facility contains most of the Mariner, Viking and Voyager images provided by the World Data Center A for Rockets and Satellites (NASA Goddard Space Flight Center, Greenbelt, Md.) and by the NASA-Caltech Jet Propulsion Laboratory (Pasadena, Ca.). These data are available for consultation under different formats (paperprints, negative and positive films, and photomosaics). The retrieval system based on microfiche library is in the process of beeing replaced by the Planetary Image Videodisc produced by JPL. Computerized data files for use by BIRP (2) in preparation at JPL will be available with the laboratory computers. In addition to planetary images, the facility contains complete sets of currently published maps (shaded relief, topographic, geologic) of the Moon, Mars, Mercury, Venus and the satellites of Jupiter and Saturn. These maps are provided by the U. S. Geological Survey, Branch of Astrogeologic Studies (Flagstaff, Az.). The facility located on the Campus of UPS at Orsay, is supported by the Institut National d'Astronomie et de Géophysique (INAG) du CNRS, and by the Centre National d'Etudes Spatiales (CNES).

In addition to the optical equipments, such as microfiche reader, light table, image analyzer, zoomtransferscope and stereoscope, available for in situ image retrieval and analysis, a videodisc player and two computers with digital plotter and printer are now available for quick image retrieval and consultation. An image processing facility (Centre de Dépouillement et de Synthèse des Images, CDSI) operated by the Institut d'Optique (UPS, Orsay) and supported by CNRS, is available for image computerized processes and colorvideo enhancements. A new facility involving a digitizing table interfaced with the CNRS regional computer center (CIRCE, Orsay) is under completion, and will allow production of thematic digitized maps.

The Planetary Geology Programs under development or under completion in France with the planetary data available at Orsay, are mainly conducted in the framework of the NASA Planetary Geology Program, the Mars Data Analysis Program (MDAP), and the Jupiter Data Analysis Program (JDAP), by five groups : LGDI (UPS, Orsay), Laboratoire de Géographie Physique Zonale (Université de Reims), Institut de Géographie (Université de Nantes), Département de Géographie (Université d'Orléans) and Institut de Physique du Globe (Universités de ParisVI-VII). These groups are supported by INAG in the framework of ATP "Planétologie". They conduct four main types of studies :

- structural analysis of Mars,
- Comparative study of large basins in the Solar System,
- Studies of erosional landforms and processes on Mars,
- Theoritical studies and laboratory simulations of ice deformation on the icy satellites of the giant planets.

The structural analysis of Mars is conducted at Orsay (LGDI, UPS). It aims to relate the tectonic structures (faults, grabens, scarps, ridges) observed on the martian surface, to the internal structure of the planet and to its structural evolution. A general inventory of compressive-type structures (scarps, ridges) is under completion (1 Ph D in preparation) in cooperation with the Lunar and Planetary Institute (Houston, Tx), (3). A geomorphic study of scarps and ridges is initiated at the Departement de Géographie (Université d'Orléans).

Comparative study of large basins in the Solar System are conducted at Orsay (4) in cooperation with the U. S. Geological Survey, Branch of Astrogeologic Studies (Flagstaff, Az.). This study aims to compare Mare Orientale on the Moon with Caloris Basin on Mercury and Argyre on Mars. Three geologic maps, at the same scale (1:5,000,000) and in stereographic projections centered on the basin centers, will be published jointly. Two preliminary maps (Orientale and Caloris) are completed. The third map (Argyre) is under completion.

Comparative studies of eolian processes around the north polar cap of Mars with terrestrial analogs (especially North African deserts) are under completion at the Laboratoire de Géographie Physique Zonale (Université de Reims). These studies were conducted in cooperation with the U. S. Geological Survey, Branch of Astrogeologic Studies (Flagstaff, Az.), the University of Arizona (Tucson, Az.), and the Smithsonian Institute (Washington, D. C.). Detailed geomorphic studies of channels, fluvial-like features, erosional processes, and slope evolution of the Valles Marineris and the Maja Vallis regions of Mars, are conducted at the Institut de Géographie (Université de Nantes). A preliminary geomorphic map of Valles Marineris is completed (5).

Theoritical studies and laboratory simulations of ice deformation are conducted at the Institut de Physique du Globe (Université Paris VI-VII) in order to contribute to the interpretation of the grooved terrains observed on Ganymede (6). These studies are conducted in cooperation with the Groupe de Recherches en Géodésie Spatiale (CRGS/CNES, Toulouse).

Most of the results related to the research programs described above, were presented during the Planetology Workshop organized in Paris (February 1982) by INAG (7).

References

(1) MASSON, Ph., MERCIER, J. L. (1980). Planetary Geology Activities and Developments in France, in : Reports of Planetary Geology Program-1980, NASA Technical Memorandum 82385, p. 488-490.

(2) ARVIDSON, R. E., BOLEF, L. K., GUINNESS, E. A., NORBERG, P. (1980). BIRP : Software for Interactive Search and Retrieval of Image Engineering data - NASA Contractor Report 3299.

(3) FERNANDEZ-CHICARRO, A., MASSON, Ph. (1983) - Ridges related to impact craters and basins on Mars, (this issue).

(4) THOMAS, P. G., MASSON, Ph. (1983) - Comparative Geology of Orientale, Caloris, and Argyre basins, (this issue).

(5) BOUSQUET, B., BODART-JOURDAIN, J. (1982) - Valles Marineris, cartographie et analyse morphologique des pentes, in : Nouveaux développements dans la connaissance du système solaire, Journées d'Etudes de l'ATP de Planétologie de l'INAG, Paris (23, 24, 25 février 1982), p. 179-181.

(6) POIRIER, J. P., MASSON, Ph., SOTIN, C. (1982) - A possible mode of formation of grooves in Uruk Sulcus, Ganymède. Icarus (submitted for publication).

(7) Nouveaux Développements dans la Connaissance du Système Solaire, Journées d'études organisées par le Comité de l'ATP de Planétologie de l'Institut National d'Astronomie et de Géophysique (CNRS), Paris (23, 24, 25 février 1982), 208 p.

Chapter 13

LATE ABSTRACTS

BACKSCATTER TECHNIQUES AS APPLIED TO FINE GRAINED ROCKS WITH POSSIBLE APPLICATION TO MARTIAN AND LUNAR ROCKS. D.H. Krinsley and K. Pye.
Dept. of Geology, Arizona State University, Tempe, AZ 85287
Dept. of Earth Sciences, University of Cambridge, CB2 3EQ, U.K.

In the course of scanning electron microscopic observation of rock thin sections for use in martial eolian studies, we utilized a technique which has great potential in the study of fine grained materials of all kinds. It is use of the backscatter electron (BS) mode for the examination of rock thin sections: the technique produces, under the proper operating conditions, Z (atomic number) contrast and simulated 3-dimensional topography (Robinson, 1975; Robinson and Nickel, 1979; Hall and Lloyd, 1981). We concentrate here on the description of mudrock thin sections.

Sedimentary petrologists have not studied mudrocks in thin section frequently because they are extremely fine grained, and using light microscopy, many of the rock constituents cannot be resolved. Difficulties also arise due to the intermixing of various clay minerals and the common occurrence of opaque hematite stain or organic material. Additionally, it is almost impossible to distinguish between quartz and feldspar in mudstones except in the few circumstances when feldspar is twinned. Since mudrocks comprise more than 50 percent of the stratigraphic column, the lack of data in this area comprises one of the most important unknowns in sedimentary geology. The technique is also applicable to other fine grained igneous and metamorphic rocks (Blatt, 1982).

Standard thin sections of mudrocks were prepared in the normal manner, polished as finely as possible, and left uncovered. The specimens were then coated with approximately 100Å of carbon to eliminate charging (Goldstein, et al., 1981), mounted on SEM stubs, and examined with the SEM in the backscatter mode at kVs ranging from 20 to 30. Useful photographs can be made up to about 10,000X; a non-dispersive X-ray unit should be available to determine elemental composition.

Two samples were studied, a Devonian gray shale from Pennsylvania and an Upper Ordovician black mudstone from Wales, U.K. Three different types of backscatter detectors and microscopes, in both the U.K. and the U.S.A., were used. Figure 1 is a normal secondary electron micrograph (SEM) of the Devonian shale; the magnification (0.55kX, 550X) should be doubled to give the actual magnification (1100X). The last line under the X is a 10 micron marker. Figure 2 is a backscatter electron micrograph of the same area, at magnification of double 740X, or 1480X. The 10 micron bar below the X is correct. Figure 3 is a backscatter electron micrograph of the Wales mudstone; figure 4 was taken at another point in the same mudrock section. All of the bars at the bottom of these photographs represent 10 microns.

Figure 1, an uncovered thin section tilted at about 45°, demonstrates the type of detail and information that normally can be obtained from thin sections. Mineral alignment from southeast to northwest is very noticeable, but as always, it is next to impossible to locate individual minerals, or to study their textural relationships, orientation, etc. Figure 2, however, displays a great deal of additional information when examined in conjunction with a non-dispersive X-ray unit — both atomic number contrast and topographic

relief. At least four mineral phases (quartz, dspar, pyrite, illite) can be identified on the basis of their contrast, supported by X-ray microanalysis. Each mineral has its own topographic relief. The two large minerals in the approximate center of the photograph "lap" against each other and display a wealth of detail. The white mineral to the right (pyrite) has thin, dark planes running trough it, representing a different chemical composition or mineral, and is shattered. The composition, orientation, area, surface expression, and fracture/cleavage patterns could be studied in detail. Closeups of the same area have been taken at 7,000X, and the contacts between the mineral phases can be seen in great detail.

Figure 3, the Wales mudstone, contains an egg-shaped group of pyrite framboids in the center of the micrograph, surrounded by a large number of phases, including illite, quartz, feldspar, and chlorite-mica stacks. In particular, the large chlorice-mica stack on the lower left of the framboid group consists of a series of light, brick-like fragments of chlorite, while the mica portion of the stack is composed of twisted fibers. Figure 4 is a detailed micrograph of one of these stacks, the lower portion being the fibers of mica and the upper, the "bricks" of illite. It looks as if the mica fibers were the last to grow, and disrupted the illite. If this is true, it points the way toward an interesting solution of a complex diagenetic growth problem.

It is obvious, we believe, that the technique can be used to initiate a new or revitalized shale petrology, in which it will be possible to study in great detail grain orientation, contacts between grains, relative hardness, composition, pore space, surface area, etc., and finally, presumed paragenesis. The technique can also be used to examine the details of fine grained cements in sandstones and limestones, and the fine grained components of metamorphic and igneous rocks. It should be of great value in planetary geology, not only in the study of rock thin sections, but also with respect to the fabric of presumed analogs to martian rocks.

REFERENCES

Blatt, H. (1982). "Sedimentary Petrology," W. H. Freeman & Co.
Hall & Lloyd (1981). Am Min. 66, 362-368.
Robinson, V.N.E. (1975). In "Scanning Electron Microscopy", IIT Res.Inst., Chicago, 41-44.
Robinson & Nickel (1979). Am.Min. 64, 1322-1328.

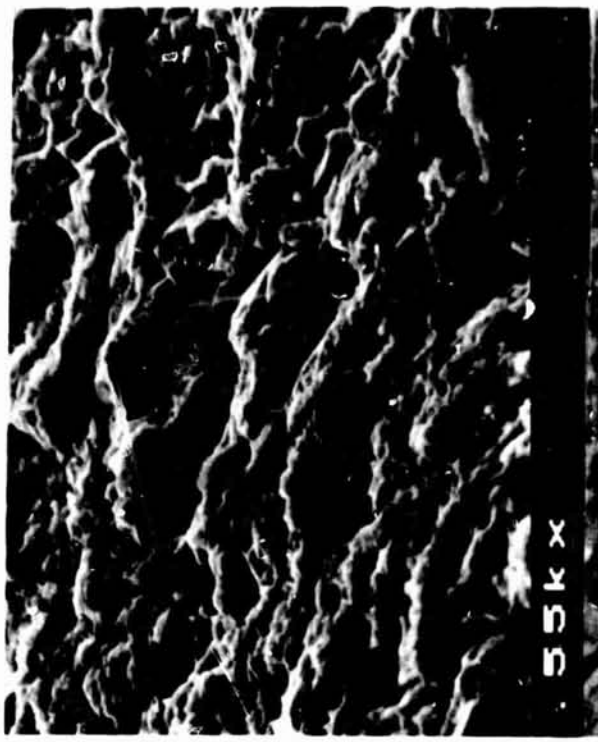

Figure 1

Figure 2

Figure 3

Figure 4

PARTICLE ATTRITION DEVICE FOR EARTH AND MARS. D.H. Krinsley and J.R. Marshall.
Dept. of Geology, Arizona State University, Tempe, AZ 85287
Mail Stop 242-6, NASA-Ames Research Center, Moffett Field, CA 94035

This investigation is concerned with the extent to which various basic mineral grains derived from basalt and associated rocks, which are presumed to exist on Mars, can withstand extensive abrasion. Hardly any information is available on the degree to which sand-size mineral grains will withstand extensive eolian transport, particularly under conditions characteristic of the martian surface. Glassy basalt, olivine, basic feldspar, pyroxene, augite, and quartz (for comparison, as a great deal is known about the eolian abrasion characteristics of this mineral) are prepared for abrasion in an eolian device specifically designed for this purpose, and described below. It is then hoped to plot the transport distance survival rate of the various basic minerals. Additionally, information may be produced on the composition of eolian sands and dune fields on Mars.

The particle attrition device (which has been constructed and is ready for use) consists of six particle-circulation chambers in which mobilization is achieved by air jets from a compressed air/regulator filtration system. It will eventually be equipped with electrostatic precipitators so that fines which have been generated by the attrition process can be collected. The apparatus permits long-term testing of as much as several years, if necessary, and can handle particles between 100 and 5000um in diameter at any required velocity.

Although the device does not appear to function like a natural, open system, the surface textures produced on quartz particles bombarded in it are absolutely similar to natural surfaces, unlike the textures produced in a number of other experimental devices (Marshall, Whalley, and Krinsley, manuscript). Thus we feel confident that it will permit analog situations to be studied with a fair degree of accuracy.

The tests will include studies of the longevity strength of particles under Earth and Mars conditions, textural evolution with time, abrasion mechanism changes with time, and rates of rounding. Later, when electrostatic precipitators are attached to the columns, rates of fines production and the types and amounts of fines produced will be examined. Particle velocity will be measured by high speed photography.

Active Volcanism on Io: A Unified Model and Mechanism

L.S.Crumpler and Robert G. Strom
Dept. of Planetary Sciences, Univ. of Arizona
Tucson, Arizona 85721

Numerical models indicate that the observed lifetimes, the structure and the low-latitude concentration of active calderas and volcanic plumes on Io can result from the injection of silicate sills at the interface between a solid sulfur crust a few kilometers thick and a silicate lithosphere from 100 to 200 km thick [1].

The silicate magma trigger model of Io volcanism has been evaluated by considering the one-dimensional heat transfer between hot silicate magma and initially cold sulfur. For a proable range of initial magma temperatures and initial sulfur crust temperatures, the contact between silicate magma and sulfur will be on the order of 700 K, or approximately the vapor point of elemental sulfur (Figure 1). Taking the thickness of the silicate sill into account, this contact temperature will be maintained for periods of several months to several years for intrusive sills of the order of 10m and 100 m respectively. This is in agreement with inferred lifetimes for volcanic plumes on Io.

Similar methods have been used to demonstrate that the lifetime of sulfur lava lakes or dark-floored calderas, and the time scale for surface freeze-over is consistent with initially molten sulfur ponding to depths of between 10 to 100 m. Many of the structural features and albedo markings on the floors of dark-floored calderas may be the result of vertical movements (i.e., sinking) of solidified sulfur crusts on molten lava lakes in which subsequent extrusion of molten sulfur has occurred. Concentric fractures resulting from such movements may provide the channels for additional plume-like activity resulting in the dark diffuse deposits also associated with many calderas.

Detailed area measurements of the various albedo types in dark-floored calderas have been fitted with model temperatures assuming correlation with various sulfur allotropes. The total radiant heat flow from all dark-floored calderas estimated by this means is 10^{21} to 10^{22} ergs s^{-1}, or about the same as that derived from recent terrestrial observations of Io at infrared wavelengths [2].

A unified model of Io volcanism has been developed which favors the following: Most of the heat flow from Io is dissipated by advection, not conduction, and the heat flow is modulated by the efficient transfer of heat from silicate melts generated at 100 to 200 km depth, injected at the sulfur-silicate crustal interfaces and interacting with a sulfur crust about 2 km thick.

For uniform global conductive heat flow, the prevailing temperature at the base of the sulfur crust will be lower at polar latitudes. Model results indicate that there is no sulfur vapor generated at the sulfur crust-silicate crust interface when the initial planetary surface temperature is about 80 to 90 K. Therefore, the lack of observable plumes at the poles of Io may be a consequence of the colder surface temperatures at high latitudes.

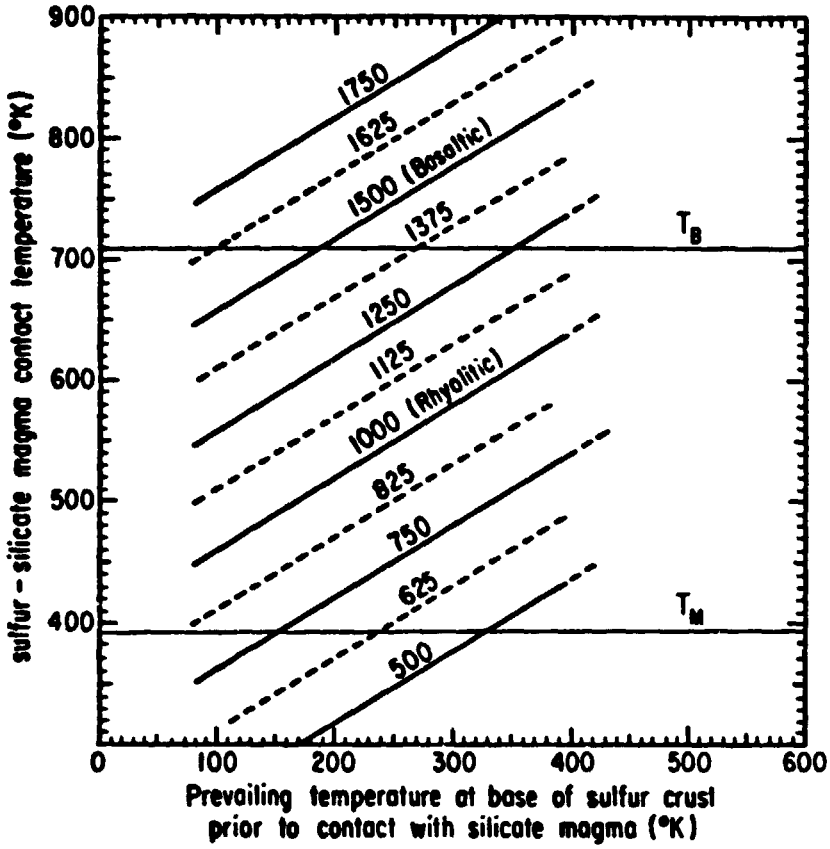

Figure 1. Temperatures of the contact between molten silicate and solid sulfur for various initial sulfur and silicate melt temperatures.

References

1. Crumpler, L.S., Thermal models of sulfur and silicate magma interaction, Io, Lunar and Planetary Science XIII, part 1, 137, 1982.

2. Matson, D.L., and others, Jour. Geophy. Res., 86, 1664, 1981.

INTERFACING VIDEODISC PLAYERS AND MICROCOMPUTERS

Michael D. Martin and R. Stephen Saunders, Jet Propulsion Laboratory, Californnia Institute of Technology, Pasadena, CA 91109

This abstract describes activities within JPL's Planetary Image Facility utilizing an Apple II microcomputer to control the display of planetary image data stored on optical videodiscs. These activities resulted in the development of two software/hardware systems which demonstrated the potential for providing a user-friendly access capability to stored information.

The first demonstration system consists of an Apple II computer with 48K of memory, an MCA/Discovision PR7820-2 Videodisc player and a Coloney Productions VAI-2 Videodisc Interface Card for the Apple II. Software for the system was written in The Applesoft BASIC language. The interface card and accompanying software allow the user to control the videodisc player from the BASIC program by PRINT'ing control commands with a special prefix character which are then captured by an object code routine stored in the Apple's memory and converted into the appropriate one byte codes for transmission to the Videodisc player. Some of the commands are listed below:

INIT	-	Initialize videodisc player.
PLAY (adr)	-	Initiate play mode at specified track address.
SLOWFWD (adr)	-	Initiate slow forward mode at address.
SLOWREV (adr)	-	Initiate slow reverse mode at address.
STEPFWD	-	Step videodisc one frame forward.
STEPREV	-	Step videodisc one frame backward.
FIND (adr)	-	Search for frame.
FDSPON	-	Turn frame display on.
FDSPOFF	-	Turn frame display off.
APPLE	-	Display Apple video on the monitor.
VIDEO	-	Display videodisc image on the monitor.
ABORT	-	Abort current command.
REJECT	-	Reject videodisc player.

The play and slow commands also allow specification of an ending address (adr1, adr2) which will terminate that mode when that address is reached. Other commands turn the audio channels on and off, check the status of the player and return the frame number currently being displayed by the player. An attractive feature of the Coloney interface is the internal switching of the video display so that two separate monitors are not required.

The demonstration developed using this interface consists of a program which explains the capabilities of the videodisc player for storing single frame imagery then cycles through a sample of each of the various commands utilizing material from the planetary image test disc produced by Discovision Asso. At the end of the automatic demonstration the user is prompted to take control of the playback by pressing any key on the Apple keyboard. If no response is made in 30 seconds the automatic demonstration continues. If a key is typed a menu display appears which allows the user

to type one letter commands to activate the various features of the videodisc player, including the play, slow and step modes, frame display on/off and frame search capabilities. The user may also list a set of frequently accessed segments on the disc and select a sequence for playback. This menu list is stored in a text file and can be modified for any given application.

The second system utilized the Apple II with a SONY Videodisc player Model LDP-1000 and an interface card supplied by SONY (not a commercially available product). This system was also developed using Applesoft BASIC. The interface to the player was implemented in a more rudimentary fashion than with the Coloney system and required command values (represented by 1-byte integers) to be put in certain memory locations then transferred to the player by an object code routine stored on the interface card. This system required the use of two monitors (one for Apple display and one for videodisc images) and presented a graphic control screen featuring the various playback modes and capabilities of the SONY player. User input was via a joystick equipped with pushbuttons. By manipulating the joystick a flashing cursor could be placed over the desired option. In the play mode simply moving the joystick from left to right cycled the player through 22 different playback speeds (11 forward and 11 reverse).

Both demonstration systems were developed for specific events (the Coloney system for Planetfest '81 and the SONY system for the San Francisco Video exposition) and were designed more to demonstrate potential rather than to serve as working tools within the Image Facility.

We are currently developing software to allow the production and playback of geology tutorials, using the Apple II to store and display text files which describe the images contained on the Planetary Image Videodisc.

THE ROLE OF PERMAFROST IN LARGE SCALE FAILURE ON MARS.

Dag Nummedal, Department of Geology, Louisiana State University, Baton Rouge, LA 70803.

Over most of Martian history it appears as if mass movement, including sliding, slumping and gravity flowage, has been the dominant mode of sediment transport. This may be due to lack of effective competing processes. Wind is the only exogenic sediment transport agent on Mars today, and aeolian erosion appears not to be very effective (Nummedal et al., 1982). As a consequence, the morphology of the Martian surface assumes an overall appearance very different from most of the subaerial surface of the Earth.

In terms of scale, topographic setting and morphologic detail, the assemblage of erosional features found on Mars is most closely related to the mass-movement morphology found on the earth's submarine continental margins (Nummedal, 1982; Nummedal and Prior, 1981). There is no indication, however, that a submarine environment was ever present on Mars. Rather, this paper presents the argument that the processes responsible for this remarkable morphologic suite were those presently active in terrestrial permafrost terrains.

Mapping on Mars has identified features morphologically similar to those commonly found in terrestrial permafrost regions. These include clast polygons and stripes (Carr and Schaber, 1977), a range of thermokarst features (Sharp, 1973; Gatto and Anderson, 1975; Carr and Schaber, 1977), mass-movement deposits (Squyres, 1979; Lucchitta, 1978, 1981) and hillslope features commonly found in permafrost terrains (Squyres, 1979; Lucchitta, 1981). It is demonstrated in this paper that small, poorly integrated drainage systems on Mars (valleys) also have their close analogs in arctic Alaska.

This paper argues that also the larger-scale erosional features on Mars, channels, valleys and chaos, are permafrost-related. The process scenario is envisioned to be as follows: (1) Initial deposition of sediment in hydrologic basins permitting growth of ice-bonded permafrost. Mapping on Mars has indicated many areas of large-scale sediment "ponding" (Lucchitta and Boothroyd, pers. comm.). (2) Long-term decay of the ice matrix, probably by sublimation. This process is most effective in equatorial latitudes where the adsorbed ice is most readily exchanged with the atmosphere (Fanale and Cannon, 1974). (3) The reduction in sediment strength through ice matrix decay would ultimately lead to failure due to gravity-induced stress even on very gentle slopes. Gravity flowage occurs on slopes as gentle as 0.2° on the Mississippi delta (Nummedal and Prior, 1981). (4) Retrograde failure of oversteepened headscarps formed in step (3) could expand the failure scar upslope. Loading of debris on unstable downslope sediments could cause renewed failure and consequent expansion of the failure scar downslope. If meltwater was part of the process, these failures would be similar to arctic "thaw slumps" (Washburn, 1980). Similar features, however, could probably also occur in Martian "freeze dried" sediments. Morphologically, they would be expected to resemble submarine failure scars (Nummedal, 1982).

On Earth such permafrost featuers are of limited size because of modification by vegetation and rainfall. On Mars, however, where processes of mass movement would lack effective competition, the failures would grow to reach immense size. Consequently, the morphology would assume scales and characteristics similar to those of the submarine continental slope, the only morphogenetic province on Earth where mass-movement controls sediment transport.

REFERENCES

Carr, M. H., and Schaber, G. G., 1977, Martian permafrost features: Jour. Geophysical Research, v. 82, p. 4039-4054.

Fanale, F. P., and Cannon, W. A., 1974, Exchange of adsorbed H_2O and CO_2 between the atmosphere and the regolith of Mars caused by changes in surface insolation: Jour. Geophysical Research, v. 79, p. 3397-3402.

Gatto, L. W., and Anderson, D. M., 1975, Alaskan thermokarst terrain and possible Martian analog: Science, v. 188, p. 255-257.

Lucchitta, B. K., 1978, Survey of cold-climate features on Mars, in Proc. Second Colloquium on Planetary Water and Polar Processes. NASA Washington, D.C. Planetary Geology Program, p. 131-134.

Lucchitta, B. K., 1981, Mars and Earth: comparison of cold-climate features: Icarus, v. 45, p. 264-303.

Nummedal, D., 1982, Continental margin sedimentation: its relevance to the morphology on Mars: in Reports of the Planetary Geology Program 1982 (in press).

Nummedal, D., Masursky, H., and Mainguet, M., 1982, Discussion of "Origin of Martian Outflow Channels: the Aeolian Hypothesis", by J. A. Cutts and K. R., Blasius, Jour. Geophysical Research (in press).

Nummedal, D., and Prior, D. B., Generation of Martian chaos and channels by debris flows, Icarus, v. 45, p. 77-86.

Sharp, R. P., 1973, Mars: fretted and chaotic terrains: Jour. Geophysical Research, v. 78, p. 4073-4083.

Squyres, S. W., 1979, The distribution of lobate debris aprons and similar flows on Mars: Jour. Geophysical Research, v. 84, p. 8087-8096.

Washburn, A. L., 1980, Geocryology, John Wiley & Sons, New York, 406 p.

Volcanism in Ice on Europa

A.F.Cook, Herzberg Institute of Astrophysics, National Research Council, Ottawa (on leave from Smithsonian Astrophysical Observatory, Cambridge, Massachusetts), E.M. Shoemaker, L.A. Soderblom, K.F. Mullins, U.S. Geological Survey, Flagstaff and R. Fiedler, Dibias, Oberpfaffenhofen.

The final frame of a crescent Europa taken during the third day after Voyager 2's encounter with Jupiter exhibits a bright spot on the southern part. This spot appears at a contrast far greater than seen for any other albedo feature on Europa. Image processing has shown that this bright feature extends beyond the bright limb at low light level. It cannot be seen to extend beyond the terminator. Its projected centre lies at longitude 27° E, latitude -31°. This is an area viewed in several other frames from both Voyager 1 and Voyager 2. No special feature is seen on these down to approximately 2% contrast. Also, all observed dark albedo features on the crescent match those on the USGS map of Europa.

All low and high resolution images of Europa have been searched and yield no other variable feature. The observed active region did not show a deposit pattern, perhaps because it was either a new eruption or one which reappeared in a long dormant area. On the other hand there are a few unusually bright regions which exhibit a reduced contrast compared to most of Europa, but these showed no evidence of current activity aloft.

Johnson et. al. (1982) have constructed multispectral mosaics of Europa. They suggest that sulfur ion implantation may explain a rather obvious difference between the trailing and leading faces of Europa. The former is exposed to an overtaking magnetosphere loaded with ions injected from Io. It must also be subject to sputtering by magnetospheric ions. Europa is also undergoing continuous erosion by meteoroids. The ionized atoms and smallest charged solid particles ejected by this bombardment will be swept away by the overtaking magnetosphere of Jupiter. The remaining spall will either escape or be redeposited over a rather large area. This spall does not completely obscure the structure of the ice field which must be active rather than a relic of the distant past. Evidently, multispectral composite images at the highest resolutions are required for further progress in estimating the relative importance of these processes.

It is entirely possible that the scattered light beyond the bright limb from this eruption is caused by a plume of very small ice crystals carrying electrical charges and being transported by Lorentz forces. Accordingly we abstain from calculations based on a ballistic model.

We wish to call attention to the fact that a liquid ocean under Europa's ice field is subject to a resonant effect from Jupiter's tidal action at latitudes ± 30°. This is a resonance of the forcing frequency with the Coriolis frequency at these latitudes These may be enhanced by non-uniform bottom topography below possibly combined with non-

uniform thickness of ice above.

This represents one phase of research carried out at JPL, Cal. Tech., under Contract NAS 700, sponsored by NASA and supported by JPL at SAO and USGS and supported by the NASA Planetary Geology Program at SAO under Grant 953617.

Reference

Johnson, T.V., Soderblom, L.A., Mosher, J.A., Danielson, G.E., Cook, A.F., and Kupferman, P., 1982. Global multispectral mosaics of the icy Galilean satellites, submitted to J. Geophys. Res.

AUTHOR INDEX